



Theses and Dissertations

2011-12-13

A Performance-Based Model for the Computation of Kinematic Pile Response Due to Lateral Spreading and Its Application on Select Bridges Damaged During the M7.6 Earthquake in the Limon Province, Costa Rica

Kevin W. Franke
Brigham Young University - Provo

Follow this and additional works at: <https://scholarsarchive.byu.edu/etd>



Part of the [Civil and Environmental Engineering Commons](#)

BYU ScholarsArchive Citation

Franke, Kevin W., "A Performance-Based Model for the Computation of Kinematic Pile Response Due to Lateral Spreading and Its Application on Select Bridges Damaged During the M7.6 Earthquake in the Limon Province, Costa Rica" (2011). *Theses and Dissertations*. 2748.
<https://scholarsarchive.byu.edu/etd/2748>

This Dissertation is brought to you for free and open access by BYU ScholarsArchive. It has been accepted for inclusion in Theses and Dissertations by an authorized administrator of BYU ScholarsArchive. For more information, please contact scholarsarchive@byu.edu, ellen_amatangelo@byu.edu.

A Performance-Based Model for the Computation of Kinematic Pile Response Due to Lateral
Spread and its Application on Select Bridges Damaged During the M7.6

Earthquake in the Limon Province, Costa Rica

Kevin W. Franke

A dissertation submitted to the faculty of
Brigham Young University
in partial fulfillment of the requirements for the degree of

Doctor of Philosophy

Kyle M. Rollins, Chair
T. Leslie Youd
Norman L. Jones
Paul W. Richards
Fernando S. Fonseca

Department of Civil and Environmental Engineering

Brigham Young University

December 2011

Copyright © 2011 Kevin W. Franke

All Rights Reserved

ABSTRACT

A Performance-Based Model for the Computation of Kinematic Pile Response Due to Lateral Spread and its Application on Select Bridges Damaged During the M7.6 Earthquake in the Limon Province, Costa Rica

Kevin W. Franke

Department of Civil and Environmental Engineering, BYU
Doctor of Philosophy

Lateral spread is a seismic hazard associated with soil liquefaction in which permanent deformations are developed within the soil profile due to cyclic mobility. Lateral spread has historically been one of the largest causes of earthquake-related damage to infrastructure. One of the infrastructure components most at risk from lateral spread is that of deep foundations. Because performance-based engineering is increasingly becoming adopted in earthquake engineering practice, it would be beneficial for engineers and researchers to have a performance-based methodology for computing pile performance during a lateral spread event. This study utilizes the probabilistic performance-based framework developed by the Pacific Earthquake Engineering Research Center to develop a methodology for computing probabilistic estimates of kinematic pile response. The methodology combines procedures familiar to most practicing engineers such as probabilistic seismic hazard analysis, empirical computation of lateral spread displacement, and kinematic pile response using p-y soil spring models (i.e. LPILE).

The performance-based kinematic pile response model is applied to a series of lateral spread case histories from the earthquake that struck the Limon province of Costa Rica on April 22, 1991. The M7.6 earthquake killed 53 people, injured another 193 people, and disrupted an estimated 30-percent of the highway pavement and railways in the region due to fissures, scarps, and soil settlements resulting from liquefaction. Significant lateral spread was observed at bridge sites throughout the eastern part of Costa Rica near Limon, and the observed structural damage ranged from moderate to severe. This study identified five such bridges where damage due to lateral spread was observed following the earthquake. A geotechnical investigation is performed at each of these five bridges in an attempt to back-analyze the soil conditions leading to the liquefaction and lateral spread observed during the 1991 earthquake, and each of the five resulting case histories is developed and summarized.

The results of this study should make a valuable contribution to the field of earthquake hazard reduction because they will introduce a procedure which will allow engineers and owners to objectively evaluate the performance of their deep foundation systems exposed to kinematic lateral spread loads corresponding to a given level of risk.

Keywords: Kevin W. Franke, liquefaction, lateral spread, performance-based engineering, kinematic pile response, Costa Rica, Limon earthquake

ACKNOWLEDGMENTS

I would like to extend thanks to my Ph.D. advisory committee for the many hours spent in my behalf. In particular, I would like to thank my advisor, Dr. Kyle M. Rollins. His counsel, guidance, and friendship have been invaluable to me throughout this entire experience.

I have benefitted much from the advice and guidance from several trusted colleagues and friends. In particular, I thank Dr. Travis M. Gerber, Dr. Norman L. Jones, Dr. T. Leslie Youd, Dr. Steven L. Kramer, Dr. Zia Zafir, Jim Gingery, Dr. Jorge Meneses, Scott Anderson, Dr. Bret Lingwall, Corbett Hansen, Scott Davis, and Mathew Francis. I would also like to thank Dave Anderson, Kevin Hicks, and Insuma S.A. Geotechnical Consultants for their help during the Costa Rica field investigations. I thank Joshua Prettyman for his assistance in drafting many of the figures in Chapters 10 through 12.

I would like to express thanks to Kleinfelder, Inc. and to URS Corporation, my employers during my Ph.D. studies. The flexibility and computer/software resources they provided were an invaluable component to the completion of my Ph.D.

Funding for this study was provided by a grant from the US Geological Survey External Research Program (Award No. G10AP00047). This support is gratefully acknowledged. However, the conclusions and opinions do not necessarily reflect those of the US Geological Survey. I also thank Maria Ramirez of the Costa Rican Ministry of Transportation for providing data and access to sites along with Daniel Avila of the Utah Dept. of Transportation for their invaluable assistance with drilling and SPT energy measurements.

I extend deep gratitude to the many individuals and organizations that provided financial support for my Ph.D. studies. These individuals and organizations include the Earthquake

Engineering Research Institute (EERI); Ralph and Betty Rollins and family; T. Leslie Youd and family; Geo-Engineers; Elder H. Burke Peterson and family; the International Association of Foundation Drillers (ADSC); and BYU Graduate Studies.

Finally, I express special thanks to my family. Thank you to my parents, who taught me to never give up. And to my dear wife Ruby and my five children (Shari, Chad, Abby, Julie, and Russell) - thank you for your endless patience, love, and encouragement. We did it!

TABLE OF CONTENTS

LIST OF TABLES	xv
LIST OF FIGURES	xvii
1 Introduction.....	1
2 Review of Liquefaction	3
2.1 Introduction.....	3
2.2 Liquefaction	3
2.3 Liquefaction Susceptibility	4
2.3.1 Critical Void Ratio	6
2.3.2 Steady State of Deformation	8
2.4 Liquefaction Initiation	10
2.4.1 Flow Liquefaction Surface.....	11
2.4.2 Phase Transformation and Limiting Shear Strain	13
2.4.3 Flow Liquefaction and Estimating Steady State Strength	14
2.4.4 Cyclic Mobility	20
2.4.5 Evaluation of Initiation of Liquefaction.....	22
2.5 Liquefaction Effects.....	31
2.5.1 Alteration of Ground Motion	31
2.5.2 Ground Settlement	31
2.5.3 Loss of Bearing Capacity	32
2.5.4 Increased Lateral Pressure on Walls	33
2.5.5 Flow Failures	34
2.5.6 Ground Oscillation	36

2.5.7	Lateral Spread	36
2.6	Chapter Summary	36
3	Review of Lateral Spread	41
3.1	Introduction.....	41
3.2	Understanding Lateral Spread	41
3.2.1	Experimental Studies of Lateral Spread	42
3.2.2	Summary Lateral Spread Theory	47
3.3	Analytical and Empirical Methods for Predicting Lateral Displacements	48
3.3.1	Analytical Methods.....	48
3.3.2	Empirical Methods.....	50
3.3.3	Comparison of Analytical and Empirical Methods	52
3.4	Deterministic Procedures for Estimation of Displacements Using Empirical Models	55
3.4.1	Early Empirical MLR Procedures.....	55
3.4.2	Modern Empirical MLR Procedures.....	58
3.4.3	Youd et al. (2002) Procedure	60
3.4.4	Bardet et al. (2002) Procedure	63
3.4.5	Baska (2002) Procedure	65
3.5	Incorporation of Uncertainty in the Estimation of Lateral Spread Displacements.....	68
3.5.1	Special Considerations of Baska (2002) Statistical Procedure	72
3.6	Estimating Lateral Spread Displacement Versus Depth.....	72
3.7	Depth Limitations When Developing Lateral Spread Displacement Profiles	77
3.8	Chapter Summary	79
4	Review of Kinematic Pile Response Analysis	83
4.1	Introduction.....	83

4.2	Kinematic Versus Inertial Loading of Piles.....	84
4.3	Estimation of Lateral Spread Soil Deformations	87
4.4	Computing Kinematic Pile Response	89
4.4.1	p-y Analysis Methodology.....	91
4.4.2	p-y Development for Soil Layering	94
4.4.3	Equivalent Single Pile for Kinematic Group Response	101
4.4.4	Additional Discussion Regarding Kinematic Loading and the Pile Cap	115
4.5	Chapter Summary	118
5	Performance-Based Earthquake Engineering Design.....	121
5.1	Introduction.....	121
5.2	Basic Philosophy of PBEE	122
5.3	Seismic Hazard Analysis	124
5.3.1	Estimating Earthquake Ground Motions Using Attenuation Relationships	125
5.3.2	Review of DSHA	127
5.3.3	Review of PSHA.....	132
5.4	Introduction to PEER PBEE Framework.....	152
5.4.1	PEER PBEE Framework Variable Definitions.....	153
5.4.2	PEER PBEE Framework Equation	154
5.5	Chapter Summary	157
6	Performance-Based Kinematic Pile Response.....	159
6.1	Introduction.....	159
6.2	Assumptions of the Procedure	159
6.3	Steps in the Performance-Based Kinematic Pile Response Procedure.....	161
6.4	Soil Site Characterization	162

6.5	Characterization of Site Geometry/Topography.....	166
6.6	Characterization of Site Seismicity.....	167
6.6.1	Site-Specific PSHA.....	167
6.6.2	USGS National Seismic Hazard Mapping Project.....	170
6.6.3	Liquefaction Triggering Analysis.....	172
6.7	Evaluation of Flow Liquefaction.....	175
6.8	Development of the Intensity Measure.....	177
6.9	Development of Fragility Functions for Lateral Spread Displacement.....	180
6.10	Development of Probabilistic Lateral Spread Displacements.....	184
6.11	Development of Fragility Functions for the Kinematic Pile Response.....	189
6.12	Development of Probabilistic Kinematic Pile Response.....	194
6.13	Performance-Based Software Development.....	198
6.13.1	LPILE MC Simulator.....	198
6.13.2	Performance-Based Pile Response Software (PPRS).....	199
7	Introduction to the Costa Rica Case Histories.....	201
7.1	Introduction.....	201
7.2	1991 Limon Earthquake.....	201
7.3	Site Investigation.....	204
8	Rio Cuba Bridge.....	209
8.1	Introduction.....	209
8.2	Observed Damage Following the 1991 Earthquake.....	210
8.3	Soil Site Characterization at the Rio Cuba Bridge.....	213
8.4	Characterization of Site Geometry/Topography at the Rio Cuba Bridge.....	215
8.5	Deterministic Pile Response Analysis at the Rio Cuba Bridge.....	217

8.5.1	Deterministic Ground Motion Evaluation From the 1991 Earthquake.....	217
8.5.2	Deterministic Liquefaction Evaluation From the 1991 Earthquake	218
8.5.3	Post Earthquake Slope Stability	218
8.5.4	Deterministic Evaluation of Lateral Spread.....	222
8.5.5	Pile Response Analysis	222
8.5.6	Summary of Deterministic Results	227
8.6	Performance-Based Pile Response Analysis at the Rio Cuba Bridge	228
8.6.1	Probabilistic Ground Motions	228
8.6.2	Probabilistic Liquefaction Triggering	230
8.6.3	Development of the Loading Parameter, \mathcal{L}	234
8.6.4	Development of the Fragility Functions for Lateral Spread Displacement	235
8.6.5	Development of Probabilistic Lateral Spread Displacements.....	237
8.6.6	Development of Fragility Functions for the Kinematic Pile Response	239
8.6.7	Development of Probabilistic Kinematic Pile Response	242
8.6.8	Discussion of Results	245
9	Rio Blanco Bridge	247
9.1	Introduction.....	247
9.2	Observed Damage Following the 1991 Earthquake	248
9.3	Soil Site Characterization at the Rio Blanco Bridge.....	250
9.4	Characterization of Site Geometry/Topography at the Rio Blanco Bridge	251
9.5	Deterministic Pile Response Analysis at the Rio Blanco Bridge	253
9.5.1	Deterministic Ground Motion Evaluation From the 1991 Earthquake.....	253
9.5.2	Deterministic Liquefaction Evaluation From the 1991 Earthquake	253
9.5.3	Post Earthquake Slope Stability	255

9.5.4	Deterministic Evaluation of Lateral Spread.....	256
9.5.5	Pile Response Analysis	258
9.5.6	Summary of Deterministic Results	262
9.6	Performance-Based Pile Response Analysis at the Rio Blanco Bridge.....	263
9.6.1	Probabilistic Ground Motions.....	263
9.6.2	Probabilistic Liquefaction Triggering.....	265
9.6.3	Development of the Loading Parameter, \mathcal{L}	269
9.6.4	Development of the Fragility Functions for Lateral Spread Displacement	270
9.6.5	Development of Probabilistic Lateral Spread Displacements.....	272
9.6.6	Development of Fragility Functions for the Kinematic Pile Response	272
9.6.7	Development of Probabilistic Kinematic Pile Response	275
9.6.8	Discussion of Results	275
10	Rio Bananito Highway Bridge	279
10.1	Introduction.....	279
10.2	Observed Damage Following the 1991 Earthquake	281
10.3	Soil Site Characterization at the Rio Bananito Highway Bridge.....	286
10.4	Characterization of Site Geometry/Topography at the Rio Bananito Highway Bridge.....	292
10.5	Deterministic Pile Response Analysis at the Rio Bananito Highway Bridge.....	292
10.5.1	Deterministic Ground Motion Evaluation From the 1991 Earthquake.....	292
10.5.2	Deterministic Liquefaction Evaluation From the 1991 Earthquake	295
10.5.3	Post Earthquake Slope Stability	296
10.5.4	Deterministic Evaluation of Lateral Spread Displacement.....	301
10.5.5	Pile Response Analysis	307
10.5.6	Summary of Deterministic Results	310

10.6	Probabilistic Analysis at the Rio Bananito Highway Bridge.....	310
10.6.1	Probabilistic Ground Motions.....	313
10.6.2	Probabilistic Liquefaction Triggering.....	315
11	Rio Bananito Railway Bridge	319
11.1	Introduction.....	319
11.2	Observed Damage Following the 1991 Earthquake	320
11.3	Soil Site Characterization at the Rio Bananito Railway Bridge	325
11.4	Characterization of Site Geometry/Topography at the Rio Bananito Railway Bridge.....	332
11.5	Deterministic Pile Response Analysis at the Rio Bananito Railway Bridge	335
11.5.1	Deterministic Ground Motion Evaluation From the 1991 Earthquake.....	335
11.5.2	Deterministic Liquefaction Evaluation From the 1991 Earthquake	336
11.5.3	Post Earthquake Slope Stability	336
11.5.4	Deterministic Evaluation of Lateral Spread.....	339
11.5.5	Pile Response Analysis	341
11.5.6	Summary of Deterministic Results	343
11.6	Performance-Based Pile Response Analysis at the Rio Bananito Railway Bridge	345
11.6.1	Probabilistic Ground Motions.....	345
11.6.2	Probabilistic Liquefaction Triggering.....	348
11.6.3	Development of the Loading Parameter, \mathcal{L}	350
11.6.4	Development of the Fragility Functions for Lateral Spread Displacement	350
11.6.5	Development of Probabilistic Lateral Spread Displacements.....	353
11.6.6	Development of Fragility Functions for the Kinematic Pile Response	355
11.6.7	Development of Probabilistic Kinematic Pile Response	356
11.6.8	Discussion of Results	357

12 Rio Estrella Highway Bridge	361
12.1 Introduction.....	361
12.2 Observed Damage Following the 1991 Earthquake	363
12.3 Soil Site Characterization at the Rio Bananito Railway Bridge	365
12.4 Characterization of Site Geometry/Topography at the Rio Estrella Bridge	366
12.5 Deterministic Pile Response Analysis at the Rio Estrella Bridge	369
12.5.1 Deterministic Ground Motion Evaluation From the 1991 Earthquake.....	369
12.5.2 Deterministic Liquefaction Evaluation From the 1991 Earthquake	372
12.5.3 Post Earthquake Slope Stability	378
12.5.4 Deterministic Evaluation of Lateral Spread.....	378
12.5.5 Pile Response Analysis	379
12.5.6 Summary of Deterministic Results	387
12.6 Performance-Based Pile Response Analysis at the Rio Estrella Bridge.....	392
12.6.1 Probabilistic Ground Motions.....	392
12.6.2 Probabilistic Liquefaction Triggering.....	395
12.6.3 Development of the Loading Parameter, \mathcal{L}	397
12.6.4 Development of the Fragility Functions for Lateral Spread Displacement	397
12.6.5 Development of Probabilistic Lateral Spread Displacements.....	400
12.6.6 Development of Fragility Functions for the Kinematic Pile Response	402
12.6.7 Development of Probabilistic Kinematic Pile Response	404
12.6.8 Discussion of Results	405
13 Summary and Conclusions.....	407
REFERENCES.....	413
Appendix A. Geotechnical Study Reports	A-1

Appendix B. PSHA Seismic Source Model Documentation	B-1
Appendix C. LPILE MC Simulator	C-1
Appendix D. Performance-Based Pile Response Software	D-1

LIST OF TABLES

Table 2-1: Correction Factors for Computing Clean Sand Corrected SPT Blowcount for Estimation of Residual Shear Strength of Liquefied Soil (After Seed and Harder, 1990).....	17
Table 2-2: Correction Factors for Computing Clean-Sand Equivalent SPT Blowcounts (After Youd et al., 2001)	19
Table 3-1: Regression Coefficients for the Youd et al. (2002) MLR Model.....	62
Table 3-2: Recommended Range of Parameters for the Youd et al. (2002) Procedure.....	62
Table 3-3: Regression Coefficients for the Bardet et al. (2002) FFGS4 Model	64
Table 3-4: Recommended Range of Parameters for the Bardet et al. (2002) FFGS4 Model.....	65
Table 3-5: Regression Coefficients for Baska (2002) Model	67
Table 3-6: Recommended Range of Parameters for Baska (2002) Model	68
Table 4-1: Coefficients to Account for Inertial Loading With Kinematic Loading in Liquefied Soil (After Boulanger et al., 2007)	86
Table 4-2: Recommended Lateral Earth Pressure Coefficients for Use in the β Method (After Kulhawy et al., 1983; Kulhawy, 1991).....	109
Table 4-3: Recommended Ranges of δ for Various Soil-Pile Interfaces.....	110
Table 6-1: Probability of Liquefaction Model Coefficients for Cetin et al. (2004).....	174
Table 6-2: Coefficients of Variation for Commonly-Used Soil Input Parameters for Many p-y Soil Spring Models (After Duncan, 2000).....	193
Table 8-1: Generalized Soil Profile for the East Abutment at the Rio Cuba Bridge.....	215
Table 8-2: EZ-FRISK Faults Within About 100 km of the Rio Cuba Bridge	230
Table 8-3: Site Parameter \mathcal{S} for the Rio Cuba Bridge	236
Table 9-1: Generalized Soil Profile for the East Abutment at the Rio Blanco Bridge	253
Table 9-2: EZ-FRISK Faults Within About 100 km of the Rio Blanco Bridge	265
Table 9-3: Site Parameter \mathcal{S} for the Rio Blanco Bridge.....	271

Table 10-1: Lateral Deformations at the South Abutment of the Rio Bananito Highway Bridge as Measured by Youd et al. (1992) (After McGuire, 1994)	286
Table 10-2: Tabular Summary of Boring T-2 at the South Abutment of the Rio Bananito Highway Bridge	289
Table 10-3: Generalized Soil Profile for the South Abutment at the Rio Bananito Highway Bridge	291
Table 10-4: EZ-FRISK Faults Within About 100 km of the Rio Bananito Highway Bridge	313
Table 11-1: Measured Displacements From Method #1 (After Youd et al., 1992; McGuire, 1994)	325
Table 11-2: Generalized Soil Profile for the North Abutment at the Rio Bananito Railway Bridge.....	332
Table 11-3: EZ-FRISK Faults Within About 100 km of the Rio Bananito Railway Bridge.....	346
Table 11-4: Site Parameter \mathcal{S} for the Rio Bananito Railway Bridge	352
Table 12-1: Measured Distances at the Rio Estrella Bridge Following the 1991 Limon Earthquake (After Youd et al., 1992; McGuire, 1994)	364
Table 12-2: Generalized Soil Profile for the South Abutment at the Rio Estrella Bridge.....	368
Table 12-3: Summary of Boring T-2 at the North Abutment of the Rio Estrella Bridge	377
Table 12-4: EZ-FRISK Faults Within About 100 km of the Rio Estrella Bridge	393
Table 12-5: Site Parameter \mathcal{S} for the Rio Estrella Bridge.....	399

LIST OF FIGURES

Figure 2-1: CVR Line (After Kramer, 1996).....	7
Figure 2-2: Observances of Castro, 1969 (After Kramer, 1996)	9
Figure 2-3: The Steady State Line (After Kramer, 1996).....	10
Figure 2-4: Use of SSL in Flow Liquefaction Determinability (After Kramer, 1996).....	10
Figure 2-5: Flow Liquefaction Surface (After Kramer, 1996)	12
Figure 2-6: Stress Path and Stress-Strain Plots for a Medium-Dense Sand (After Wu, 2002).....	14
Figure 2-7: Zone Susceptible to Flow Liquefaction Shown in p' - q Space (Shown as Shaded; After Kramer, 1996).....	15
Figure 2-8: Relationship Between Residual Shear Strength and Clean-Sand SPT Resistance (After Seed and Harder, 1990).....	19
Figure 2-9: Zone Susceptible to Cyclic Mobility as Shown in p' - q Space (Shown as Shaded; After Kramer, 1996).....	20
Figure 2-10: Three General Cases of Cyclic Mobility (After Kramer, 1996)	21
Figure 2-11: (a) Probabilistic SPT-Based CRR Correlation for $M_w = 7.5$ and $\sigma'_v = 1$ atm, and (b) Deterministic SPT-Based CRR Correlation for $M_w = 7.5$ and $\sigma'_v = 1$ atm (After Cetin et al., 2004)	28
Figure 2-12: Example of Plotting CSR Versus CRR With Depth (After Kramer, 1996).....	30
Figure 2-13: Settlement Around a Structure in Kobe, Japan Following 1995 Hyogoken- Nanbu Earthquake (Courtesy of EERC, Univ. of Calif.)	32
Figure 2-14: Bearing Capacity Failures Following 1964 Niigata, Japan Earthquake (Courtesy of EERC, Univ. of Calif.)	33
Figure 2-15: Graben Formed Behind a Displaced Quay Wall in Kobe, Japan Following 1995 Hyogoken-Nanbu Earthquake (Courtesy of NISEE, Univ. of Calif.)	34
Figure 2-16: Portion of Lower San Fernando Dam That Experienced Flow Liquefaction Following 1971 San Fernando Earthquake (Courtesy of EERC, Univ. of Calif.).....	35
Figure 2-17: Lateral Spread at the Port in Port-au-Prince, Haiti Following the 2010 Earthquake (Courtesy of EERI)	37

Figure 3-1: Schematic Depiction of Lateral Spread Resulting From Soil Liquefaction (After Varnes, 1978)	43
Figure 3-2: Determination of Site Geometry for Empirical MLR Equation	61
Figure 3-3: Compiled Grain-Size Data With Ranges of F_{15} and $D50_{15}$ for Use With the Youd et al. (2002) Procedure (After Youd et al., 2002)	63
Figure 3-4: Mixed Discrete-Continuous Probability and Cumulative Density Functions.....	73
Figure 3-5: Types of Soil Profiles Evaluated Numerically by Valsamis et al. (After Valsamis et al., 2007).....	75
Figure 3-6: Deflection and Strain Profiles at the Wildlife Array (After Holzer and Youd, 2007)	75
Figure 3-7: Select Deflection Profile From Moss Landing Lateral Spread (After Boulanger et al., 1997).....	76
Figure 4-1: Inertial and Kinematic Loading of a Foundation System (After Boulanger et al., 2007)	85
Figure 4-2: Example of a Post-Liquefaction Limit Equilibrium Analysis Evaluating the Potential for Liquefaction Flow Failure.....	90
Figure 4-3: Depiction of Procedure for Using p-y Curves to Account for the Kinematic Loading of Piles (After Juirnarongrit and Ashford, 2006; Modified From Reese et al., 2000).....	92
Figure 4-4: p-y Analysis Model for Kinematic Loading (After Juirnarongrit and Ashford, 2006)	93
Figure 4-5: Process for Computing Site-Specific p-y Curves From the Measurement of Pile Strain (After Hales, 2003).....	95
Figure 4-6: Recommended p-Multipliers to Compute p-y Behavior of Liquefied Sand (After Brandenburg et al., 2007).....	100
Figure 4-7: Equivalent "Single" Pile for a Simplified Four-Pile Group (After Juirnarongrit and Ashford, 2006)	104
Figure 4-8: Creation of the Equivalent Single Pile $M-\phi$ Curve for Nonlinear Analysis (After CalTrans, 2011).....	105
Figure 4-9: Linear Relationship Assumption Between M and θ for the Rotational Stiffness (After Juirnarongrit and Ashford, 2006).....	106

Figure 4-10: Various Published Estimates for α as a Function of Undrained Shear Strength (After Vesic, 1977)	108
Figure 4-11: Group Efficiency Factor for Use in Computing Skin Resistance of Piles in Sand (After Kishida and Meyerhof, 1965)	111
Figure 4-12: Range of Recommended Values for N_q Published in Literature (Adapted From Coyle and Costello, 1981)	111
Figure 4-13: Summing the Moments About Downward-Moving Piles (Adapted From Juirnarongrit and Ashford, 2006)	113
Figure 4-14: Ultimate Angular Rotation of the Pile Cap for Both the Frictional Pile Group and the End-Bearing Pile Group (After Juirnarongrit and Ashford, 2006; Originally Adapted From Mokwa and Duncan, 2003).....	114
Figure 4-15: Normalized Load-Displacement Curves for Non-Liquefied Crust Over Liquefied Soil From Centrifuge Study (After Brandenberg et al., 2005)	117
Figure 5-1: Schematic Diagram of DSHA Steps for a Given Site (After Kramer 1996)	130
Figure 5-2: Example Probability Density Functions for Source-to-Site Distance for a (a) Point Source, (b) Fault Source, and (c) Area Source (After Kramer, 1996).....	133
Figure 5-3: (a) Graphical Representation of the Parameters a and b Used in the Gutenberg-Richter Recurrence Law; (b) Gutenberg-Richter Recurrence Law Applied to Two Tectonic Belts (After Kramer, 1996).....	137
Figure 5-4: Bounded Gutenberg-Richter Recurrence Relationships, Given $m_0 = 4.0$ for (a) Constant Rate of Seismicity, and (b) Constant Rate of Seismic Moment (Based on Youngs and Coppersmith, 1985; After Kramer, 1996)	138
Figure 5-5: Inconsistency of Mean Annual Rate of Exceedance as Determined From Seismicity Data and Geologic Data (After Youngs and Coppersmith, 1985)	140
Figure 5-6: Schematic Illustration of Conditional Probability of Exceeding a Particular Value of Ground Motion Parameter for a Given Magnitude and Distance (After Kramer, 1996)	141
Figure 5-7: Schematic Diagram of the Steps Involved in Completing a PSHA for a Given Site (After Kramer, 1996)	147
Figure 5-8: Example of Seismic Hazard Curves for the Peak Horizontal Acceleration (PHA) Computed for a Given Site With Three Separate Seismic Sources (After Kramer, 1996)	150

Figure 5-9: Seismic Hazard Deaggregation Plot of the PHA for a Site in Downtown Seattle, WA (Courtesy of Wessel and Smith, USGS, 2002).....	152
Figure 5-10: Example for Fragility Curves for Some <i>EDP</i> Given Some <i>IM</i>	155
Figure 5-11: Visual Representation of Equation (5-24) (Courtesy of Steven Kramer, From a NEES Presentation in 2005)	156
Figure 6-1: MASW Technique and Typical Output for Obtaining an Average Measurement of Shear Wave Velocity at a Given Site (Courtesy of Kansas Geological Survey; After Park Seismic, 2010).....	164
Figure 6-2: Example of a Logic Tree for Seismic Hazard Analysis of Gridded Seismic Sources in the Western United States (After Petersen et al., 2008).....	169
Figure 6-3: Seismic Hazard Curves at a 6-m Depth of a Fictional Soil Profile for the Factor of Safety Against Liquefaction Initiation (Modified From Kramer and Mayfield, 2007).....	174
Figure 6-4: \mathcal{L} Parameter for the Youd et al. (2002) Model.....	178
Figure 6-5: Deaggregation Plots for (a) PGA and for (b) \mathcal{L}_{Youd} Parameter for a Site in Costa Rica. Return Period is 475 Years.....	180
Figure 6-6: Computing the Fragility Curve for $EDP_i = \log(d)$ for the Youd et al. (2002) Empirical Model	184
Figure 6-7: Schematic Illustration of the (a) "Stripes" Approach and the (b) "Cloud" Approach to <i>EDP/IM</i> Characterization (After Kramer, 2008)	188
Figure 6-8: Example of Mean Pile Response with +/- 1 Standard Deviation Computed From a Monte Carlo Simulation in LPILE	195
Figure 6-9: Example of Seismic Hazard Curve for Pile Displacement at the Pile Head.....	197
Figure 6-10: Screenshot of LPILE MC Simulator Spreadsheet.....	199
Figure 6-11: Screenshot of PPRS	200
Figure 7-1: Shakemap for April 22, 1991 Costa Rica Earthquake (After USGS, 2008).....	203
Figure 7-2: Bridge Location Map (Image Courtesy of Google Earth TM 2011)	204
Figure 7-3: Sketch of the Standard Penetration Method (ASTM D-1586) (After Insuma S.A. Geotechnics, 2010 [Appendix A]).....	206

Figure 7-4: Details for the 64 kg (140 lb) Hammer and Split-Spoon Sampler Used in the Field Investigation (After Insuma S.A. Geotechnics, 2010 [Appendix A])	207
Figure 8-1: The East Abutment of the Rio Cuba Bridge	209
Figure 8-2: Rotation of the East Abutment at the Rio Cuba Bridge	211
Figure 8-3: Transverse Displacements at the Bridge Deck at the Rio Cuba Bridge.....	212
Figure 8-4: Displacement at the Base of the Bridge Girders	212
Figure 8-5: Pile Cracking Observed at the East Abutment of the Rio Cuba Bridge	213
Figure 8-6: Boring P-1 Performed at the Rio Cuba Bridge	216
Figure 8-7: Simplified Sketch of the Plan and Profile Views of the Rio Cuba Bridge as Shown on the Bridge Plans Provided by the Costa Rican Ministry of Transportation	219
Figure 8-8: Computed Deterministic Response Spectra for the Rio Cuba Bridge From the 1991 Earthquake. $N = 1$	220
Figure 8-9: Deterministic Liquefaction Triggering Results for the M7.6 1991 Limon Earthquake at the Rio Cuba Bridge	221
Figure 8-10: Post Earthquake Slope Stability Analysis at the Rio Cuba.....	223
Figure 8-11: Deterministic Median and 95-Percentile Evaluations of Lateral Spread Displacement Using Select Empirical Models for the Rio Cuba Bridge	224
Figure 8-12: Computed Lateral Spread Displacement Profile at the Rio Cuba Bridge for the M7.6 1991 Limon Earthquake.....	224
Figure 8-13: Moment-Curvature and Moment-Stiffness Curves for the Rio Cuba Bridge	227
Figure 8-14: Deterministic Computed Pile Response for the Rio Cuba Bridge East Abutment From the 1991 Limon Earthquake.....	229
Figure 8-15: Seismic Hazard Curve for the PGA at the Rio Cuba Bridge	231
Figure 8-16: Source Contributions to Probabilistic Seismic Hazard for the Rio Cuba Bridge	232
Figure 8-17: Probabilistic Response Spectra (5-Percent Damping) for the Rio Cuba Bridge	232
Figure 8-18: Deaggregation Plots for the PGA at the Rio Cuba Bridge.....	233

Figure 8-19: Performance-Based Liquefaction Triggering Results for the Rio Cuba Bridge	234
Figure 8-20: Hazard Curves for the Loading Parameter \mathcal{L} for the Rio Cuba Bridge	235
Figure 8-21: Lateral Spread Fragility Curves for $DISP^* = 0.1$ Meter and $DISP^* = 1$ Meter at the Rio Cuba Bridge	236
Figure 8-22: Lateral Spread Hazard Curves for the Rio Cuba Bridge.....	237
Figure 8-23: Probabilistic Lateral Spread Displacement Profiles for the Rio Cuba Bridge	238
Figure 8-24: Probabilistic Pile Response Curves (Absolute Values) Assuming No Bridge Deck for the Rio Cuba Bridge	243
Figure 8-25: Probabilistic Pile Response Curves (Absolute Values) Assuming a Bridge Deck at the Rio Cuba Bridge.....	244
Figure 9-1: The Rio Blanco Bridge	248
Figure 9-2: Rotation of the Pile Cap at the East Abutment of the Rio Blanco Bridge	249
Figure 9-3: Boring P-1 Performed at the Rio Blanco Bridge	252
Figure 9-4: Simplified Sketch of the Plan and Profile Views of the Rio Blanco Bridge as Shown on the Bridge Plans	254
Figure 9-5: Computed Deterministic Response Spectra for the Rio Blanco Bridge From the 1991 Earthquake. $N = 1$	255
Figure 9-6: Deterministic Liquefaction Triggering Results for the M7.6 1991 Limon Earthquake at the Rio Blanco Bridge.....	257
Figure 9-7: Post Earthquake Slope Stability Analysis at the Rio Blanco	259
Figure 9-8: Deterministic Median and 95-Percentile Evaluations of Lateral Spread Displacement Using Select Empirical Models for the Rio Blanco Bridge	260
Figure 9-9: Computed Lateral Spread Displacement Profile at the Rio Blanco Bridge for the M7.6 1991 Limon Earthquake	260
Figure 9-10: Moment-Curvature and Moment-Stiffness Curves for the Rio Blanco Bridge	262
Figure 9-11: Deterministic Computed Pile Response for the Rio Blanco Bridge East Abutment From the 1991 Limon Earthquake.....	264
Figure 9-12: Seismic Hazard Curve for the PGA at the Rio Blanco Bridge	266

Figure 9-13: Source Contributions to Probabilistic Seismic Hazard at the Rio Blanco Bridge	267
Figure 9-14: Probabilistic Response Spectra (5-Percent Damping) for the Rio Blanco Bridge	267
Figure 9-15: Deaggregation Plots for the PGA at the Rio Blanco Bridge.....	268
Figure 9-16: Performance-Based Liquefaction Triggering Results for the Rio Blanco Bridge	269
Figure 9-17: Hazard Curves for the Loading Parameter \mathcal{L} for the Rio Blanco Bridge.....	270
Figure 9-18: Lateral Spread Fragility Curves for $DISP^* = 0.1$ Meter and $DISP^* = 1$ Meter at the Rio Blanco Bridge	271
Figure 9-19: Lateral Spread Hazard Curves for the Rio Blanco Bridge.....	273
Figure 9-20: Probabilistic Lateral Spread Displacement Profiles for the Rio Blanco Bridge	274
Figure 9-21: Probabilistic Pile Response Curves (Absolute Values) Assuming No Bridge Deck for the Rio Blanco Bridge	277
Figure 9-22: Probabilistic Pile Response Curves (Absolute Values) Assuming a Bridge Deck at the Rio Blanco Bridge.....	278
Figure 10-1: The Current Rio Bananito Highway Bridge	280
Figure 10-2: Rotated Pile Cap at the South Abutment of the Rio Bananito Highway Bridge	282
Figure 10-3: Liquefaction Deformations at the South Approach Embankment for the Rio Bananito Highway Bridge	283
Figure 10-4: Ground Deformations at the South Abutment of the Rio Bananito Highway Bridge as Measured by Youd et al. (1992) (After McGuire, 1994)	284
Figure 10-5: Pre- and Post-Earthquake Profile Geometries of the Southern Approach Embankment at the Rio Bananito Highway Bridge	285
Figure 10-6: (a) Boring P-1 and (b) Boring P-2 Performed at the Rio Bananito Highway Bridge	288
Figure 10-7: Averaged SPT Blowcounts for the Southern Abutment at the Rio Bananito Highway Bridge	290

Figure 10-8: Simplified Sketch of the Plan and Profile Views of the Rio Bananito Highway Bridge (After Priestley et al, 1991; McGuire, 1994)	293
Figure 10-9: Contour Sketch of the Rio Bananito Highway Bridge.....	294
Figure 10-10: Computed Deterministic Response Spectra for the Rio Bananito Highway Bridge From the 1991 Earthquake. $N = 1$	295
Figure 10-11: Deterministic Liquefaction Triggering Results From Boring P-1 for the M7.6 1991 Limon Earthquake at the Rio Bananito Highway Bridge	297
Figure 10-12: Deterministic Liquefaction Triggering Results From Boring P-2 for the M7.6 1991 Limon Earthquake at the Rio Bananito Highway Bridge	298
Figure 10-13: Post Earthquake Slope Stability Analysis at the Rio Bananito Highway Computed Using Residual Strength Ratios	302
Figure 10-14: Post Earthquake Slope Stability Analysis at the Rio Bananito Highway Computed Using Uniform Residual Strength	303
Figure 10-15: Back-Analysis of the Residual Strength Ratio at the Rio Bananito Highway Bridge	304
Figure 10-16: Back-Analysis of the Uniform Residual Strength at the Rio Bananito Highway Bridge	305
Figure 10-17: Residual Strength Comparisons for (a) Uniform Residual Strength (After Seed and Harder, 1990), and (b) Residual Strength Ratio (After Ledezma and Bray, 2010)	306
Figure 10-18: Empirically Computed Lateral Spread Displacements at the Southern Abutment of the Rio Bananito Highway Bridge	307
Figure 10-19: Moment-Curvature and Moment-Stiffness Curves for the Rio Bananito Highway Bridge	309
Figure 10-20: Deterministic Computed Pile Response for the Rio Bananito Highway Bridge South Abutment Before Bridge Deck Fell From Its Supports	311
Figure 10-21: Deterministic Computed Pile Response for the Rio Bananito Highway Bridge South Abutment After the Bridge Deck Fell From Its Supports	312
Figure 10-22: Seismic Hazard Curve for the PGA at the Rio Bananito Highway Bridge.....	314
Figure 10-23: Source Contributions to Probabilistic Seismic Hazard for the Rio Bananito Highway Bridge	315

Figure 10-24: Probabilistic Response Spectra (5-Percent Damping) for the Rio Bananito Highway Bridge	316
Figure 10-25: Deaggregation Plots for the PGA at the Rio Bananito Highway Bridge	317
Figure 10-26: Performance-Based Liquefaction Triggering Results for the Rio Bananito Highway Bridge	318
Figure 11-1: The Rio Bananito Railway Bridge	320
Figure 11-2: Caisson and Support System for the Rio Bananito Railway Bridge (After McGuire, 1994)	321
Figure 11-3: Dynamic Wave Equation Analysis Performed at the Rio Bananito Railway Bridge	322
Figure 11-4: Rotated Caissons at the North Abutment of the Rio Bananito Railway Bridge Following the 1991 Limon Earthquake (After Youd, 1993).....	322
Figure 11-5: Damaged Rio Bananito Railway Bridge Following the 1991 Limon Earthquake (After Youd, 1993).....	323
Figure 11-6: Schematic Plan View of the Rio Bananito Railway Bridge and Surrounding Structures at the Time of the 1991 Earthquake (After McGuire, 1994).....	324
Figure 11-7: Pre- and Post-Earthquake Positions of the Soccer Field Boundaries as Measured in Method #2 (After McGuire, 1994)	326
Figure 11-8: (a) Boring P-1 and (b) Boring P-2 Performed at the Rio Bananito Railway Bridge	328
Figure 11-9: Averaged SPT Blowcounts for the North Abutment at the Rio Bananito Railway Bridge.....	329
Figure 11-10: Torvane Testing at the Rio Bananito Railway Bridge	331
Figure 11-11: Shear Strength Data From the North Abutment at the Rio Bananito Railway Bridge	331
Figure 11-12: Contour Sketch of the Rio Bananito Railway Bridge	333
Figure 11-13: Simplified Sketch of the Plan and Profile Views of the Rio Bananito Railway Bridge.....	334
Figure 11-14: Computed Deterministic Response Spectra for the Rio Bananito Railway Bridge From the 1991 Earthquake. $N = 1$	335

Figure 11-15: Deterministic Liquefaction Triggering Results From Boring P-1 for the M7.6 1991 Limon Earthquake at the Rio Bananito Railway Bridge	337
Figure 11-16: Deterministic Liquefaction Triggering Results From Boring P-2 for the M7.6 1991 Limon Earthquake at the Rio Bananito Railway Bridge	338
Figure 11-17: Post Earthquake Slope Stability Analysis at the Rio Bananito Railway Bridge	340
Figure 11-18: Deterministic Median and 95-Percentile Evaluations of Lateral Spread Displacement Using Select Empirical Models for the Rio Bananito Railway Bridge.....	342
Figure 11-19: Computed Lateral Spread Displacement Profile at the Rio Bananito Railway Bridge for the M7.6 1991 Limon Earthquake.....	343
Figure 11-20: Deterministic Computed Pile Response for the Rio Bananito Railway Bridge North Abutment From the 1991 Limon Earthquake	344
Figure 11-21: Seismic Hazard Curve for the PGA at the Rio Bananito Railway Bridge.....	347
Figure 11-22: Source Contributions to Probabilistic Seismic Hazard for the Rio Bananito Railway Bridge.....	347
Figure 11-23: Probabilistic Response Spectra (5-Percent Damping) for the Rio Bananito Railway Bridge.....	348
Figure 11-24: Deaggregation Plots for the PGA at the Rio Bananito Railway Bridge	349
Figure 11-25: Performance-Based Liquefaction Triggering Results for the Rio Bananito Railway Bridge.....	351
Figure 11-26: Hazard Curves for the Loading Parameter \mathcal{L} for the Rio Bananito Railway Bridge	352
Figure 11-27: Lateral Spread Fragility Curves for $DISP^* = 0.1$ Meter and $DISP^* = 1$ Meter at the Rio Bananito Railway Bridge.....	353
Figure 11-28: Lateral Spread Hazard Curves for the Rio Bananito Railway Bridge	354
Figure 11-29: Probabilistic Lateral Spread Displacement Profiles for the Rio Bananito Railway Bridge.....	355
Figure 11-30: Mean Displacements and ± 1 Standard Deviations for a Single Caisson at the Rio Bananito Railway Bridge Computed From a Series of Monte Carlo Simulations.....	357

Figure 11-31: Probabilistic Caisson Response Curves (Absolute Values) for the Rio Bananito Railway Bridge	358
Figure 12-1: Southern Abutment of the Rio Estrella Bridge	362
Figure 12-2: (a) Boring P-1, (b) Boring P-2, and (c) Boring P-3 Performed at the Rio Estrella Bridge	367
Figure 12-3: Averaged SPT Blowcounts for the South Abutment at the Rio Estrella Bridge	368
Figure 12-4: Simplified Sketch of the Profile View of the Rio Estrella Bridge	370
Figure 12-5: Sketch of the Current Elevation Contours and the Insuma Boring Locations at the Rio Estrella Bridge	371
Figure 12-6: Computed Deterministic Response Spectra for the Rio Estrella Bridge From the 1991 Earthquake. $N = 1$	372
Figure 12-7: Deterministic Liquefaction Triggering Results From Boring P-1 for the M7.6 1991 Limon Earthquake at the Rio Estrella Bridge	374
Figure 12-8: Deterministic Liquefaction Triggering Results From Boring P-2 for the M7.6 1991 Limon Earthquake at the Rio Estrella Bridge	375
Figure 12-9: Deterministic Liquefaction Triggering Results From Boring P-3 for the M7.6 1991 Limon Earthquake at the Rio Estrella Bridge	376
Figure 12-10: Deterministic Liquefaction Triggering Results From Boring T-2 at the North Abutment of the Rio Estrella Bridge.....	380
Figure 12-11: Deterministic Median and 95-Percentile Evaluations of Lateral Spread Displacement Using Select Empirical Models for the Rio Estrella Bridge	381
Figure 12-12: Computed Lateral Spread Displacement Profile at the Rio Estrella Bridge for the M7.6 1991 Limon Earthquake	381
Figure 12-13: Simplified Sketch of the Soil Profile Relative to the Foundation Elements at the Southern Abutment of the Rio Estrella Bridge.....	382
Figure 12-14: Deterministic Computed Pile Response for the Rio Estrella Bridge South Abutment From the 1991 Limon Earthquake.....	388
Figure 12-15: Lateral Spread Distribution Versus Normalized Depth in the Liquefiable Layer (After Boulanger et al., 2003)	389

Figure 12-16: Deterministic Lateral Spread Displacement Profile With the Void Redistribution/Water Film Assumption for the Rio Estrella Bridge	389
Figure 12-17: Deterministic Pile Response Results With the Void Redistribution/Water Assumption for the Rio Estrella Bridge	390
Figure 12-18: Seismic Hazard Curve for the PGA at the Rio Estrella Bridge	394
Figure 12-19: Source Contributions to Probabilistic Seismic Hazard for the Rio Estrella Bridge	394
Figure 12-20: Probabilistic Response Spectra (5-Percent Damping) for the Rio Estrella Bridge	395
Figure 12-21: Deaggregation Plots for the PGA at the Rio Estrella Bridge	396
Figure 12-22: Performance-Based Liquefaction Triggering Results for the Rio Estrella Bridge	398
Figure 12-23: Hazard Curves for the Loading Parameter \mathcal{L} for the Rio Estrella Bridge	399
Figure 12-24: Lateral Spread Fragility Curves for $DISP^*=0.1$ Meter and $DISP^*=1$ Meter at the Rio Estrella Bridge	400
Figure 12-25: Lateral Spread Hazard Curves for the Rio Estrella Bridge	401
Figure 12-26: Probabilistic Lateral Spread Displacement Profiles for the Rio Estrella Bridge	403
Figure 12-27: Mean Displacements and ± 1 Standard Deviations for the Equivalent Single Pile at the Rio Estrella Bridge Computed From a Series of Monte Carlo Simulations	404
Figure 12-28: Probabilistic Pile Response Curves (Absolute Values) for the Rio Estrella Bridge	406

1 INTRODUCTION

Lateral spread is a seismic hazard associated with soil liquefaction in which permanent deformations are developed within a soil profile. Lateral spread has historically been one of the largest causes of earthquake-related damage to infrastructure. One of the infrastructure components most at risk from lateral spread is that of deep foundations. Although deterministic methods have been developed for evaluating pile displacements within lateral spreads, performance-based engineering is increasingly becoming adopted in earthquake engineering practice. Therefore, engineers and researchers would benefit from having a performance-based methodology for predicting pile performance during a lateral spread event.

This dissertation presents a new performance-based methodology for computing kinematic pile response due to lateral spread soil displacements and validates it against a number of actual lateral spread case histories. The study utilizes the probabilistic performance-based framework developed by the Pacific Earthquake Engineering Research (PEER) Center to develop a robust and flexible procedure to compute probabilistic estimates of kinematic pile response for a given single pile or pile group. The procedure incorporates performance-based empirical lateral spread and liquefaction triggering procedures with Beam-on-Winkler Foundation methods to develop the probabilistic pile response estimates.

In order to demonstrate the new performance-based kinematic pile response procedure, five new lateral spread case histories are developed from select bridge sites damaged following the M7.6 earthquake that occurred in the Limon Province of Costa Rica on April 22, 1991. While

a generic lateral spread scenario would adequately demonstrate the new performance-based procedure, greater value is placed on the development and analysis of actual lateral spread case histories that subsequently could be of use to future engineering researchers. Both deterministic and probabilistic pile response analyses are performed where appropriate for each case history, and the computed results are compared against the observed performance of the bridges and their foundations.

The ultimate goal of this study is to develop and demonstrate a procedure that will allow engineers and owners to make probabilistic estimates of the kinematic response of deep foundation systems exposed to lateral spread displacements. In addition, the study seeks to introduce new lateral spread case histories which may shed further light on the phenomenon and provide researchers with an additional tool for the validation and calibration of their models/procedures associated with kinematic pile response due to lateral spread.

2 REVIEW OF LIQUEFACTION

2.1 Introduction

Lateral spread is a term commonly used to describe the permanent deformation of the ground resulting from soil liquefaction due to earthquake shaking. Its effects on infrastructure and critical lifelines can be devastating. Soil deformations can range from millimeters to several meters, with the greatest displacements usually occurring near free-faces at the margins of rivers and oceans. Bridges spanning bodies of water with underlying soils prone to liquefaction, as well as pile foundations placed through liquefiable layers are especially at risk sustaining damage due to lateral spread.

Because the occurrence of lateral spread is conditional on liquefaction, this chapter will review the basic mechanics behind liquefaction. Kramer (1996) provides an excellent summary of the mechanics behind the phenomenon of liquefaction, and is referenced heavily in this chapter. Lateral spread will be discussed in greater detail in Chapter 3.

2.2 Liquefaction

Liquefaction involves the reduction of stiffness and strength of saturated, cohesionless soils caused by monotonic, transient, or repeated disturbance of saturated cohesionless soils under undrained conditions (Kramer, 1996). Liquefaction occurs in two general forms: *flow liquefaction* and *cyclic mobility*. Flow liquefaction generally occurs more rarely and can

potentially be very dangerous. Much more common is cyclic mobility, which tends to produce far less dramatic displacements, but can be extremely damaging to infrastructure just the same. Both flow liquefaction and cyclic mobility will be discussed later in this chapter.

The phenomena of liquefaction became the topic of focused research following the occurrence of two significant earthquakes in 1964. The first occurred on Good Friday near the Prince William Sound in Alaska ($M_w = 9.2$). Liquefaction caused by that earthquake damaged roads, lifelines, and the foundations of several structures located in Anchorage (approximately 120 km northwest of the epicenter). The second occurred three months later in Niigata, Japan ($M_S = 7.5$), where soil liquefaction caused similar lifeline damage, as well as the destruction of several structures which failed in bearing capacity and experienced large post-liquefaction settlements. Since that time, geotechnical engineers have learned much about the phenomenon of liquefaction and how to approach it. Kramer (1996) provides some systematic and logical steps that should be considered in the evaluation of liquefaction hazard – *liquefaction susceptibility*, *liquefaction initiation*, and *liquefaction effects*.

2.3 Liquefaction Susceptibility

Not all soils are susceptible to liquefaction. When evaluating liquefaction hazard, it is important to know which criteria are required for the occurrence of liquefaction to even be possible. Kramer (1996) divides susceptibility criteria into four general categories: *historical*, *geologic*, *compositional*, and *state*.

Historical criteria recognize that if a soil has liquefied before, there is a strong probability that it will liquefy again as long as the soil and groundwater conditions remain relatively unchanged (Youd, 1984). By noting similarities in soil and groundwater characteristics at such

sites, researchers can then take that knowledge and look for other sites possibly prone to liquefaction. Sites that contain prehistoric evidence of the occurrence of liquefaction (termed *Paleoliquefaction*) have been used in such studies in recent decades (Obermeier and Pond, 1999).

Geologic criteria are based on the fact that the nature of soil's environment may determine whether or not it is susceptible to liquefaction. The environment in which a soil was deposited, hydrological conditions in that environment, and the age of the soil deposit all help contribute to liquefaction susceptibility (Youd and Hoose, 1977). Alluvial, fluvial, and aeolian deposits have a high potential for liquefaction when saturated due to the loose configuration in which they were deposited. Saturated man-made soil deposits are also prone to liquefaction unless properly compacted. Finally, liquefaction probability tends to increase as groundwater levels are near the ground surface. Most liquefaction seems to occur within 15 meters of the ground surface (Kramer, 1996).

Compositional criteria state that the soil itself may determine whether or not it is susceptible to liquefaction. In general, most engineers recognize that soils need to be cohesionless and saturated in order to liquefy. Also, liquefaction susceptibility increases with increasing soil-grain uniformity, and decreases with increasing fines content and soil-grain angularity. Initially, it was believed that only sands were prone to liquefaction. However, liquefaction in gravels and even coarse silts has been witnessed in the field and replicated in the laboratory (Chen et al., 2009; Ishihara, 1984, 1985; Coulter and Migliaccio, 1966; Wong et al., 1975). Additionally, much debate has occurred recently regarding the liquefaction susceptibility of fine-grained silts and clays. To evaluate liquefaction susceptibility of fine-grained soils, Youd et al. (2001) recommended adherence to the 'Chinese criteria,' which is a simple set of criteria

based on Atterberg limits, water content, and clay content. However, Bray and Sancio (2006) published observed case histories from recent earthquakes in Turkey that seemed to suggest that low-plasticity clays could potentially liquefy. As a result, Bray and Sancio presented a set of susceptibility criteria that was significantly more conservative than the Chinese criteria. Idriss and Boulanger (2008) later acknowledged that some low-plasticity clays could experience behavior similar to liquefaction, calling it “cyclic softening.” However, they were much more adamant in defining the difference between “sand-like behavior” and “clay-like behavior.” As a result of these recent publications, most engineering professionals currently disregard the Chinese criteria for evaluating the liquefaction susceptibility of fine-grained soils, choosing instead to apply the susceptibility criteria recommended by Bray and Sancio (2006) or Idriss and Boulanger (2008). However, Youd et al. (2009) point out that liquefaction in clay-like materials often does not result in the same secondary hazards associated with liquefaction in sand-like materials, using lateral spread as a particular example.

State criteria infer that the actual “state” (i.e. density and initial stress conditions) of the soil may determine whether or not it is susceptible to liquefaction, and if so, which type of liquefaction.

2.3.1 Critical Void Ratio

To understand how state criteria can influence liquefaction susceptibility and type, it is first necessary to review the idea of a critical void ratio and the critical void ratio (CVR) line as presented by Casagrande (1936) with his experiments in drained, strain-controlled triaxial tests of sands. From his tests, Casagrande observed that for the same type of sand confined at the same constant pressure, loose and dense specimens respectively contracted and dilated to achieve the same terminal or critical void ratio at large strains. If one were to plot the critical void ratio

for all confining stresses, then one would have the CVR line for that particular soil. Figure 2-1 shows a CVR line plotted in $e-\sigma'$ space with two initial points plotted: one above the CVR line and one below. Points plotted below the CVR line represent “dense” soils, or those prone to dilation, while points plotted above the CVR line represent “loose” soils, or those prone to contraction.

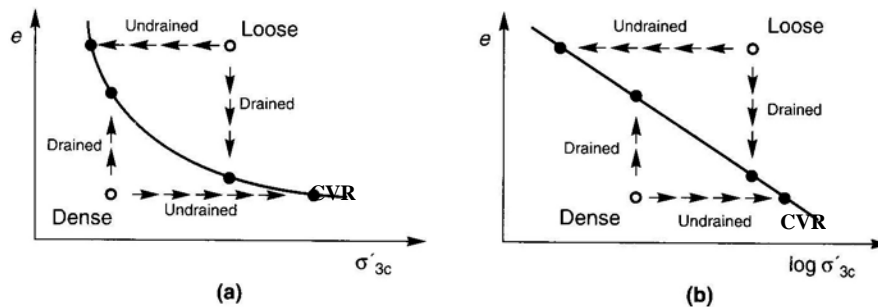


Figure 2-1: CVR Line (After Kramer, 1996)

Casagrande further hypothesized that if the soil were to be sheared in undrained conditions, thus allowing no changes in volume or void ratio, that the loose specimens would be forced to follow a horizontal (i.e. constant void ratio) path to the left on the plot (i.e. lose effective stress and, hence, strength) and the dense specimens would be forced to follow a horizontal path to the right (i.e. gain strength) until the CVR line was reached. Therefore, Casagrande postulated that loose specimens, or those plotting *above* the CVR line, were prone to liquefaction, while dense specimens, or those plotting *below* the CVR line, were not. This theory, however, appeared flawed when back-calculations of the Fort Peck Dam failure of 1938 showed that the failed soil plotted slightly below the CVR line.

2.3.2 Steady State of Deformation

As the technology to measure pore water pressure later became available, further advances were made in understanding the differences between drained and undrained shear failures in liquefaction-prone soil. Castro (1969) performed static and cyclic undrained triaxial tests on isotropically and anisotropically consolidated sand specimens. Three general types of stress-strain behavior were observed, as shown in Figure 2-2. Very loose specimens (shown as Specimen A in Figure 2-2) showed the tendency to contract and then suddenly collapse, showing only a fraction of the initial strength. Castro called this behavior “liquefaction.” Dense specimens (shown as Specimen B in Figure 2-2) showed a tendency to contract slightly and then dilate, showing an increase in strength due to negative pore pressure. Castro called this behavior “dilation.” Medium-dense specimens (shown as Specimen C in Figure 2-2) showed the tendency to contract and collapse, like a loose specimen, but when strained further would reach a point where it would begin to dilate and regain strength, like a dense specimen. Castro called this behavior “limited liquefaction.”

When the void ratio at large strains was plotted against the corresponding confining stress, a line below and roughly parallel to the CVR line was formed. This line was later termed the steady state line (SSL). The difference between the two lines was hypothesized to be due to the development of a “flow structure” which forms under stress-controlled conditions (Casagrande, 1976). Later research confirmed that the difference between the CVR and SSL lines can vary considerably for any given soil and seems to be a function of the soil’s potential for collapse (Alarcon-Guzman et al., 1988; Poulos et al., 1988). The SSL is reached only when soil specimens are sheared to large enough strains so as to achieve a state in which the soil flows continuously under constant shear stress and constant effective confining pressure at constant

volume and constant velocity. This state was termed the *steady state of deformation* (Castro and Poulos, 1977). The strength that the soil exhibits while in this state is called the steady state strength, S_{su} .

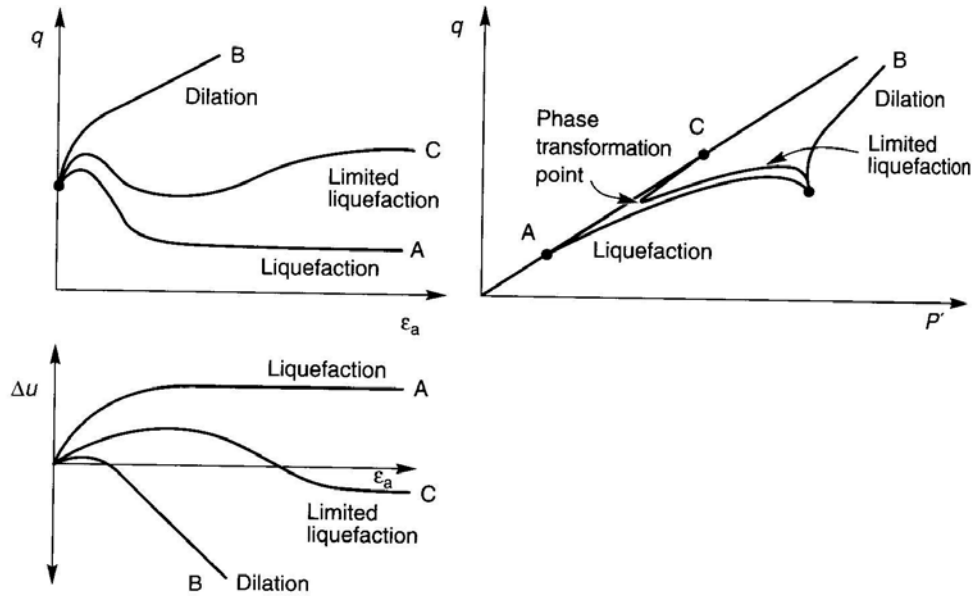


Figure 2-2: Observances of Castro, 1969 (After Kramer, 1996)

The SSL is really a three-dimensional line that can be viewed in $e-\tau-\sigma'$ space and is shown in Figure 2-3. The SSL has real convenience because it has the potential of showing if a particular soil is susceptible to flow liquefaction. A soil is considered susceptible to flow liquefaction if it plots above the SSL ($e-\sigma'$ space) and its steady state strength is less than the initial static stress acting upon it, as shown in Figure 2-4.

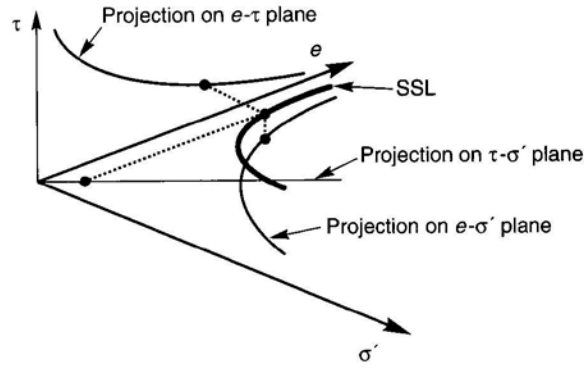


Figure 2-3: The Steady State Line (After Kramer, 1996)

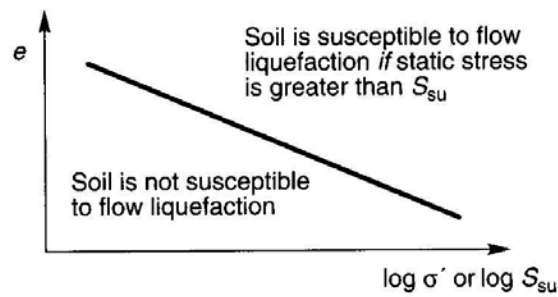


Figure 2-4: Use of SSL in Flow Liquefaction Determinability (After Kramer, 1996)

2.4 Liquefaction Initiation

Because a certain soil meets the criteria for liquefaction susceptibility does not necessarily mean that liquefaction is certain to occur. A chain of events must take place in order to initiate liquefaction, and even the occurrence of those events does not necessarily mean that catastrophic soil failure will happen. Prediction of the types of deformations that would occur

upon the initiation of liquefaction greatly depends on understanding the state of the soil when liquefaction is triggered (Kramer 1996).

2.4.1 Flow Liquefaction Surface

Hanzawa et al. (1979) were the first to demonstrate the use of stress paths, or p' - q space in determining whether or not strain-softening behavior (i.e. flow liquefaction) would occur for a specimen of soil at a given initial state of stress. Figure 2-5 shows the stress path of five separate soil specimens initially consolidated to the same void ratio, but confined under different effective pressures.

The stress paths in Figure 2-5 indicate that the specimens were loaded monotonically. All of the stress paths converge to a point on the failure envelope which represents the steady state strength of the soil, which is determined from plotting the SSL of the soil shown in the lower plot. Following the stress path for Specimen E, it can be seen that a gradual, but accelerating loss of strength takes place, which is characterized by its movement in the direction of the origin. The stress path then reaches an apex where the path then travels rapidly back to the steady state point. This type of stress path indicates flow liquefaction. The stress paths for Specimens A and B do not behave in a similar manner, but instead show an increase in strength, which is characterized by their movement away from the origin. This type of stress path indicates dilation. The stress paths for Specimens C and D initially exhibit a form of behavior similar to Specimen E, but their stress paths show a period of dilation before reaching the steady state strength. These specimens are experiencing limited liquefaction, in their behavior will be discussed in more detail in the next section.

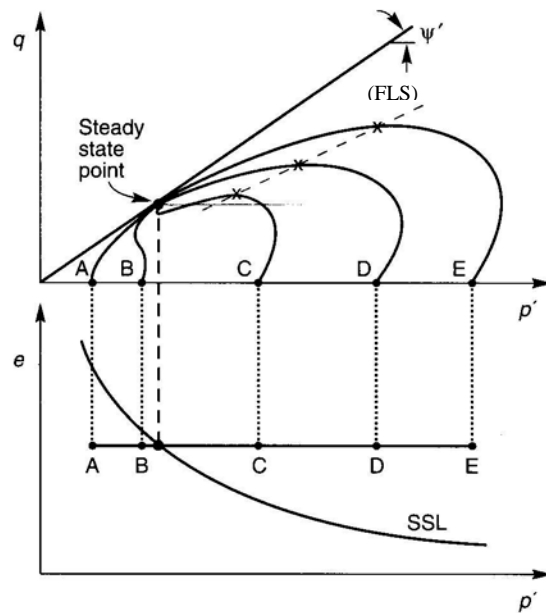


Figure 2-5: Flow Liquefaction Surface (After Kramer, 1996)

If one were to pass a line through the apexes of the stress paths of Specimens C, D, and E of Figure 2-5, it would be seen that the line would approximately extend through the origin. This line is called the *Flow Liquefaction Surface (FLS)* and represents the location in p - q space at which flow liquefaction is initiated for a given soil at a given effective confining pressure (Sladen et al., 1985). The actual FLS is truncated at the q value of the steady state strength due to the fact that flow liquefaction cannot occur if the stress path is below the steady state point. The FLS can vary for any given soil and depends on the density of the soil and the effective confining stress. If a soil that is loaded either monotonically or cyclically under undrained conditions such that excess pore pressures cause the stress path of the soil to reach the FLS, then flow liquefaction will be initiated.

2.4.2 Phase Transformation and Limiting Shear Strain

It was previously mentioned that Specimens C and D from Figure 2-5 experienced what is termed limited liquefaction, characterized by the signature dilation of the soil specimens following a temporary loss of strength, but prior to achieving a steady state of deformation. The point at which contraction ceases and dilation begins was termed the *phase transformation point*, and the line connecting the locus of such points for various confining pressures in p' - q space is called the *phase transformation line*, or PTL (Ishihara, et al., 1975; Ishihara, 1985). Because the soil exhibited stress-strain behavior at the phase transformation point that was similar to the behavior expected at the steady state of deformation, Alarcon-Guzman, et al. (1988) called this state the *quasi-steady state*, or QSS. Figure 2-6 shows the stress path and stress-strain curve for a specimen of Monterey 0/30 sand tested cyclically by Wu (2002).

Notice in Figure 2-6 that as the specimen continues to be loaded cyclically after the stress path first reaches the failure envelope, the stress path begins looping back on forth between the two failure envelopes, essentially passing through the origin twice during every cycle. During the instant that the stress path is at the origin, the pore pressure ratio r_u , which is defined as the excess pore water pressure divided by the effective confining pressure, is equal to unity and the soil technically has no effective strength. Seed and Lee (1966) defined this state as *initial liquefaction*. This definition can be misleading, however, and has led many to believe that a liquefied soil has no strength at all. If a liquefied soil in this state continues to be strained, either due to continued loading or to achieve static equilibrium, it will eventually begin to dilate and regain some strength due to phase transformation. Observance of this behavior and the fact that a permanent state of zero effective stress could not be maintained led early researchers to theorize the existence of an absolute *limiting shear strain* for any given liquefiable soil (De Alba et al.,

1975; Tokimatsu and Seed, 1984; Seed et al., 1984). Wu (2002) points out that more modern research in post-liquefaction stress-strain behavior has proven this idea erroneous in that there is no “absolute” limiting shear strain, but instead, the apparent limiting shear strain serves as an index of soil damage inflicted on the specimen (i.e. the number of loading cycles the soil was exposed to), and it increases monotonically with additional stress cycles. Therefore, the limiting shear strain for a soil should be considered in addition to the number of cycles the soil element was exposed to.

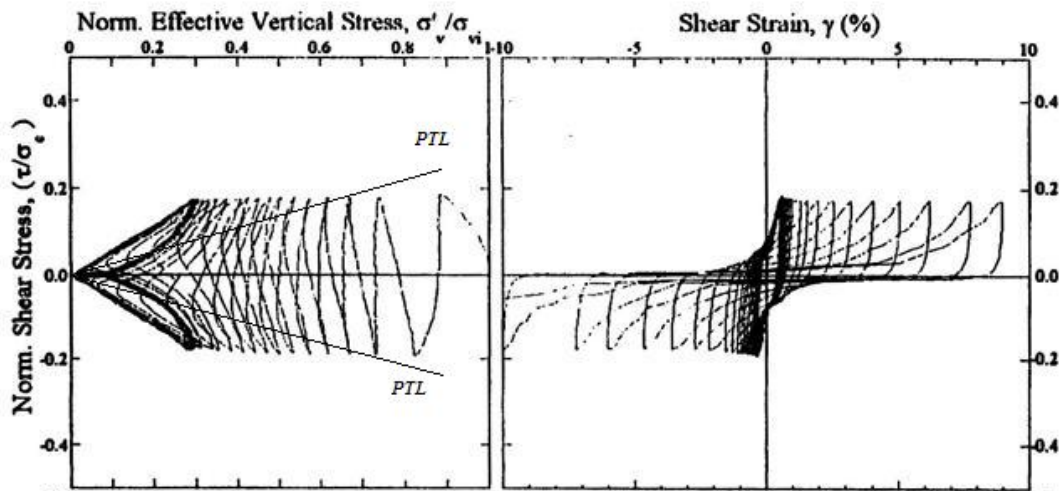


Figure 2-6: Stress Path and Stress-Strain Plots for a Medium-Dense Sand (After Wu, 2002)

2.4.3 Flow Liquefaction and Estimating Steady State Strength

As mentioned earlier, once the effective stress path of the soil specimen that is being monotonically or cyclically disturbed reaches the FLS, flow liquefaction is initiated. Kramer

(1996) points out that initiating flow liquefaction is only the first of two requirements needed for the occurrence of a flow slide, often recognized as the most devastating and dangerous hazard of liquefaction. The other requirement involves the presence of driving stresses which continue to push the soil to its steady state strength. Driving stresses are static shear stresses that already exist in the soil prior to liquefaction and are caused by gravity.

Figure 2-7 shows the FLS and the initial states in p' - q space where a liquefiable soil has the potential of initiating flow liquefaction if loading is sufficient to move the effective stress path to the FLS.

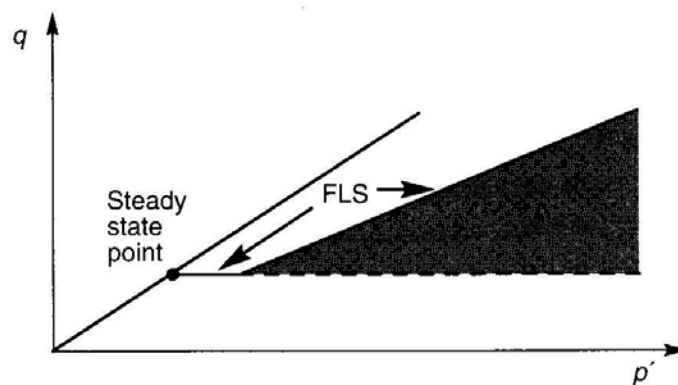


Figure 2-7: Zone Susceptible to Flow Liquefaction Shown in p' - q Space (Shown as Shaded; After Kramer, 1996)

Flow liquefaction can trigger when an undrained soil disturbance pushes the effective stress path of the soil to the FLS. Kramer and Seed (1988) note that if large static stresses already exist in a particular element of soil under drained conditions, very little excess pore pressure may be needed to initiate flow liquefaction.

The critical key when considering flow liquefaction hazard is to obtain an accurate estimate of the liquefiable soil's steady state strength. Unfortunately, for being such a critical aspect to evaluating flow liquefaction potential, obtaining an accurate estimate of the steady state strength of a soil is extremely difficult to do in practice. With that said, there are three general types of techniques that are used today to estimate the shear strength of liquefied soils: *laboratory techniques* (Poulos et al., 1985), *in situ techniques*, and *normalized strength techniques*. Only in situ techniques and normalized strength techniques will be discussed at any further length in this thesis; the reader may refer to the listed references for further information on laboratory techniques.

In situ strength measurement was first proposed by Seed (1986), and was later updated by Seed and Harder (1990). The idea of the approach is to correlate SPT or CPT resistance with the apparent shear strength back-calculated from observed flow slides. This back-calculated strength is termed the *residual strength*. The Seed and Harder (1990) approach remains a very popular approach among geotechnical engineers today, and it still constitutes the “state of practice” in many seismic-prone regions. The method requires that the soil either have 10% or less fines content, or that the measured standard penetration test (SPT) resistance be corrected for fines. The clean sand corrected SPT blowcount, $N_{1,60-CS}$ as recommended by Seed and Harder (1990) can be computed using Equation (2-1) in conjunction with Table 2-1 below.

$$N_{1,60-CS} = \alpha + (N_{1,60}) \quad (2-1)$$

Once the value of $N_{1,60-CS}$ is obtained, the residual shear strength can be estimated from Figure 2-8 for clean-sand blowcounts less than 16 blows/foot.

Table 2-1: Correction Factors for Computing Clean Sand Corrected SPT Blowcount for Estimation of Residual Shear Strength of Liquefied Soil (After Seed and Harder, 1990)

Fines content, FC	α
$FC \geq 75\%$	5
$75\% > FC \geq 50\%$	4
$50\% > FC \geq 35\%$	3
$35\% > FC \geq 25\%$	2
$25\% > FC \geq 10\%$	1
$FC < 10\%$	0

Normalized strength techniques are based on the idea that if the consolidation curve and the steady state line for a given liquefiable soil are parallel, then the steady state strength should be proportional to the consolidation stress (Kramer, 1996). The application of this technique, however, is complicated by the fact that liquefiable soils do not portray unique consolidation characteristics, which are largely a function of the state of the soil and can vary significantly even within the same soil deposit. In addition, the residual strength back-calculated from field case histories may be strongly influenced by the presence of water interlayers which are not replicated from standard laboratory tests.

However, if a specimen of soil can be prepared to resemble the in-situ conditions (i.e. void ratio, density, effective confining pressures) and tested in undrained shear, then the resulting *residual strength ratio*, or S_r / σ_{vo}' , is theorized to closely represent field conditions (Vasquez-Herrera et al., 1990; Baziar et al., 1992; Ishihara, 1993). Several researchers (e.g., Olson and Stark, 2002; Idriss and Boulanger, 2007) have performed such tests and utilized field data to back-calculate residual strength ratios from multiple case histories where flow liquefaction has

occurred in the past. Ledezma and Bray (2010) used many of these models to develop a mean estimate of the residual shear strength ratio, (μ_{s_u}/σ'_v) which is given as:

$$\mu_{s_u}/\sigma'_v \approx \exp\left(\frac{\mu_{N_{1,60,CS}}}{8} - 3.5\right) \times \left[1 + \frac{(0.3\mu_{N_{1,60,CS}})^2}{158}\right] \quad (2-2)$$

$$\sigma_{s_u}/\sigma'_{vc} = 0.4 \left(\mu_{s_u}/\sigma'_{vc} \right) \quad (2-3)$$

where $\mu_{N_{1,60,CS}}$ is the mean estimate of clean-sand equivalent SPT blowcount and σ_{s_u}/σ'_v is the standard deviation. Youd et al. (2001) recommends that the clean-sand equivalent SPT blowcount, $N_{1,60,CS}$ be computed as:

$$N_{1,60,CS} = \alpha + \beta(N_{1,60}) \quad (2-4)$$

where α and β are correction factors and are provided in Table 2-2.

It is important to apply good engineering judgment when using methods involving residual strength ratios, bearing in mind that they provide only an approximation of the true steady state strength of liquefied soil. In addition, many engineers call into question the validity of residual strength ratios at shallow depths, claiming that the computed residual strengths often seem extraordinarily low and unrealistic. No published references and or research supporting this

claim could be identified; however, such a concern is valid and should warrant further research and investigation.

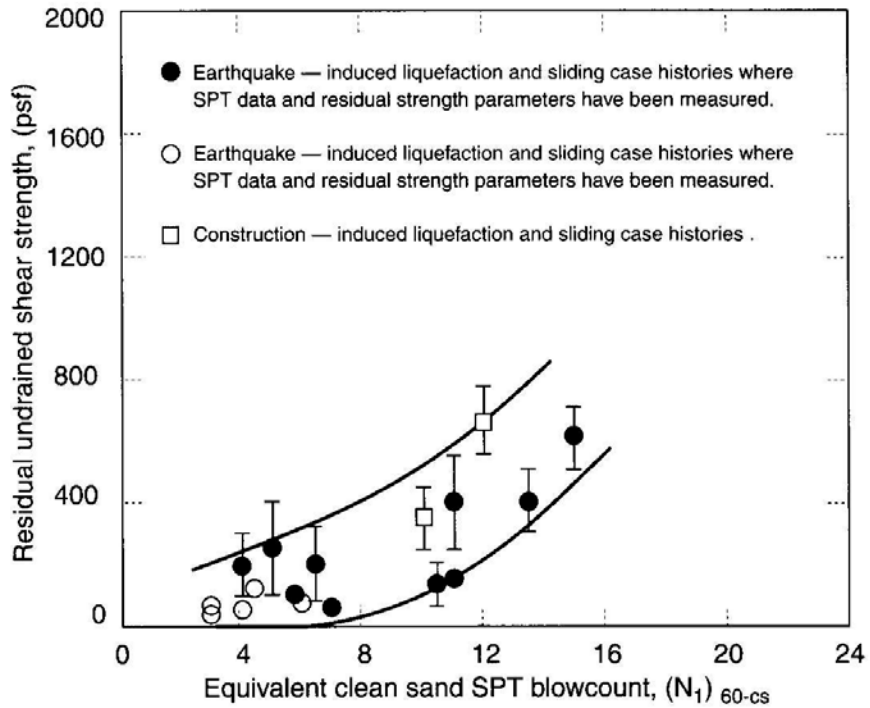


Figure 2-8: Relationship Between Residual Shear Strength and Clean-Sand SPT Resistance (After Seed and Harder, 1990)

Table 2-2: Correction Factors for Computing Clean-Sand Equivalent SPT Blowcounts (After Youd et al., 2001)

Fines content, FC	α	β
$FC \leq 5\%$	0	1.0
$5\% < FC < 35\%$	$\exp[1.76 - 190/FC^2]$	$0.99 + FC^{1.5}/1000$
$FC \geq 35\%$	5.0	1.2

2.4.4 Cyclic Mobility

When initial stress conditions exist such that static shear stresses in a liquefiable soil element are less than the steady state strength, S_{su} of the soil, as shown in Figure 2-9, then the soil is generally considered safe from flow failure. However the soil is still susceptible to cyclic mobility. *Cyclic mobility* is the gradual strain and loss of strength that occurs in a soil due to incremental buildup of pore water pressures induced by cyclic loading under undrained conditions.

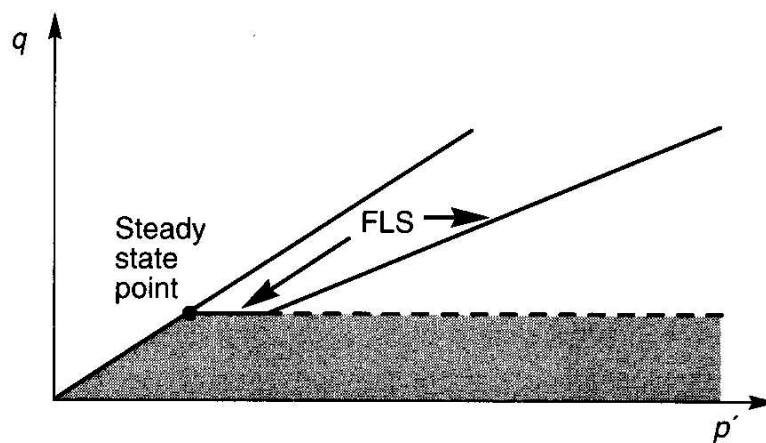


Figure 2-9: Zone Susceptible to Cyclic Mobility as Shown in p'-q Space (Shown as Shaded; After Kramer, 1996)

There are three general ways in which the initial stress conditions and cyclic loading conditions can produce cyclic mobility in a given soil (Kramer, 1996). The first, as shown in Figure 2-10(a) occurs when the sum of the initial static shear stress, or τ_{static} , and the shear stress induced by cyclic loading, or τ_{cyc} , is less than S_{su} .

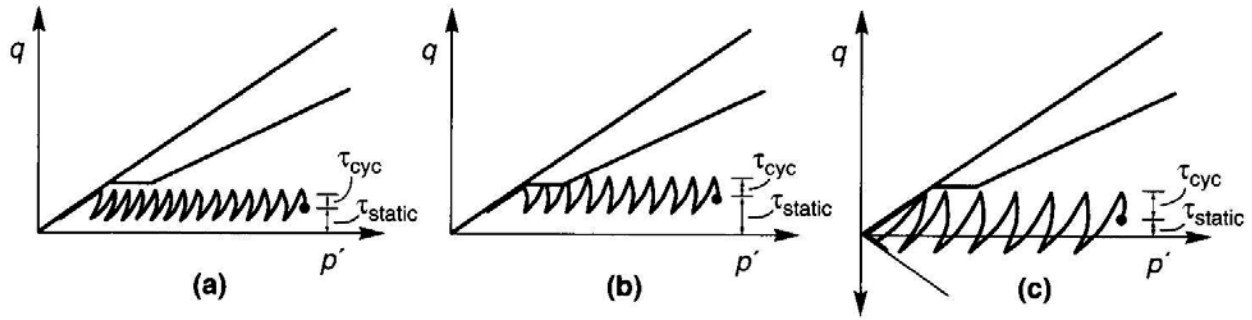


Figure 2-10: Three General Cases of Cyclic Mobility (After Kramer, 1996)

Case (a) generally produces a very gradual loss of stiffness and strength and can result in shear failure of the soil if enough cycles of loading take place to move the effective stress path to the failure envelope. However, “failure” does not mean that the soil would flow continuously if a steady load were to then be applied because the soil would dilate due to phase transformation and cause the soil’s effective strength to increase until reaching the steady state strength, at which point further dilation would cease.

The second way in which cyclic mobility is generally produced, as shown in Figure 2-10(b), occurs when $\tau_{static} + \tau_{cyc} > 0$ and $\tau_{static} + \tau_{cyc} > S_{su}$. This case resembles the first case; however, due to the fact that the initial shear stress and cyclic shear stress collectively are greater than the steady state strength, momentary instances of flow liquefaction are triggered every time the loading causes the effective stress path to cross the FLS. During these brief instances, large strains can occur, which can lead to very significant cumulative strains by the end of loading.

The third way in which cyclic mobility is generally produced, as shown in Figure 2-10(c), occurs when $\tau_{static} - \tau_{cyc} < 0$ and $\tau_{static} + \tau_{cyc} < S_{su}$. This case includes both compressional and extensional loading, and experimental evidence suggests that pore pressures within a soil

specimen increase relatively rapidly when exposed to such loading conditions (Dobry et al., 1982). Figure 2-6 shows the stress path of a soil specimen that experienced cyclic mobility in this manner.

2.4.5 Evaluation of Initiation of Liquefaction

Now that much of the basic mechanics behind the occurrence of liquefaction has been discussed, actual methods used in engineering practice today to estimate a particular site's vulnerability to liquefaction will be considered. Most of these methods can be divided into two general categories: *cyclic strain approach* and *cyclic stress approach*.

Few practicing engineers and researchers today utilize the cyclic strain approach, but it is appealing because excess pore pressures have been shown to be very closely correlated to strain amplitude. The principle reason that few practicing professionals prefer this approach, however, stems from the difficulty of accurately predicting soil strains in a given soil profile when subjected to earthquake loading (Seed, 1980). For this reason, the cyclic strain approach will not be discussed further in this dissertation, but the inquiring reader may refer to the following references for more information on the approach: Dobry and Ladd (1980); Dobry, et al. (1982); Dobry, et al. (1984); and Vasquez-Herrera and Dobry (1988).

The cyclic stress approach is currently employed by most practicing professionals to predict whether or not liquefaction will initiate at a given site assuming some level of earthquake loading. The final product of this approach is typically a factor of safety which is calculated by dividing the soil's resistance to liquefaction initiation by the demand (loading) induced in the soil. A factor of safety equal to or less than unity would imply that liquefaction was likely to initiate if the soil was loaded to the level of ground shaking considered in the analysis. The resistance to liquefaction for a given soil is often quantified by using the cyclic shear stress

required to initiate liquefaction at a given level of loading, $\tau_{cyc,L}$, or by normalizing that parameter with the effective overburden pressure, σ_{vo}' , to obtain the *cyclic resistance ratio*, *CRR* (sometimes denoted as *CSR_L*). The demand for liquefaction placed on the soil is often quantified by using the equivalent cyclic shear stress induced by an earthquake, τ_{cyc} , or by normalizing that parameter with σ_{vo}' to obtain the *cyclic stress ratio*, *CSR*. Therefore, the equation for the factor of safety against liquefaction can be expressed as:

$$FS_L = \frac{\tau_{cyc,L}}{\tau_{cyc}} = \frac{CRR}{CSR} = \frac{CSR_L}{CSR} \quad (2-5)$$

The shear stress required to trigger liquefaction used to be estimated from cyclic uniform harmonic tests performed in the laboratory. Researchers originally hypothesized that the controlling factors in liquefaction initiation had to do with only the initial density and stress conditions (Kramer, 1996). However, it was soon observed that such factors as specimen preparation technique, strain history, overconsolidation, and length of time under confining pressure affected the liquefaction potential of a soil specimen (Pyke et al., 1975; Ladd, 1974; Finn et al., 1970; Seed and Peacock, 1971; Ohsaki, 1969), and as a result of these findings, determination of liquefaction resistance by means of laboratory testing is rarely performed today. Because researchers observed that there are several parameters which contribute to the liquefaction resistance of a given soil, many of which are quite sensitive and very difficult to replicate in a laboratory, in-situ methodologies for estimating liquefaction resistance began to be developed. First suggested by Whitman (1971), various in-situ tests could be performed at sites where liquefaction was known to have occurred in order to characterize the liquefaction resistance in terms of various in-situ field investigation parameters. Such procedures were

developed for *cone penetration tests* – or CPT (Douglas et al., 1981; Robertson and Campanella, 1985; Seed and De Alba, 1986; Mitchell and Tseng, 1990; Kayen et al., 1992; Martin, 1992; Suzuki et al., 2004; Carraro et al., 2003; Baziar et al., 2004; Ku et al., 2004; Andrus et al., 2004; Moss et al., 2006), *shear wave velocity* (Stokoe, et al., 1988; Finn, 1991; Tokimatsu, et al., 1991; Kayen et al., 1992; Suzuki et al., 2004; Andrus, et al., 2004), *dilatometer index* (Marchetti, 1982; Robertson and Camponella, 1986; Reyna and Chameau, 1991), and *standard penetration tests* – or SPT. Only the SPT-based procedure will be discussed at length in this dissertation because it is the most commonly used procedure for evaluating liquefaction triggering potential in engineering practice today, though CPT-based methods appear to be quickly gaining ground.

The SPT resistance correlates fairly well with liquefaction resistance because the same factors which cause the liquefaction resistance to increase (i.e. density, overconsolidation, non-uniformity, angularity, fines content) also cause the SPT resistance to increase. Beginning with the charts created by Seed and Idriss (1971) which plotted the *CSR* versus SPT resistance for several sites known to have liquefied and several sites known not to have liquefied during earthquakes with magnitudes of approximately $M_w = 7.5$, many researchers have since been creating similar approaches for both deterministic and probabilistic scenarios. Of these many approaches, three appear to have become widely accepted among the engineering community today, though they tend to differ significantly from one another in various aspects: Youd et al. (2001), Cetin et al. (2004), and Idriss & Boulanger (2008). Since about 2006, there has been a significant amount of disagreement and confusion regarding which of these methods should be applied in engineering practice. In particular, recent arguments between Idriss & Boulanger and Cetin et al. regarding the validity of various aspects of their respective procedures have become quite heated. The basis of these arguments transcends the scope of this research, however, and

defense of a particular approach will not be attempted in this dissertation. However, a performance-based procedure for liquefaction triggering has already been developed and published by Kramer and Mayfield (2007) which incorporates the Cetin et al. (2004) probabilistic model for liquefaction triggering. Because the performance-based pile response analyses performed as part of this study incorporate the Kramer and Mayfield (2007) performance-based liquefaction procedure, only the Cetin et al. (2004) procedure will be summarized at length in this dissertation. However, until greater consensus is reached by the professional community on this issue, one should evaluate all three simplified methods for deterministic evaluation of liquefaction triggering. In addition, sound engineering judgment should be applied in interpreting the results. Such an approach was applied to the deterministic case histories in this study and will be explained later in this dissertation.

The cyclic resistance ratio for a given soil layer must be computed to evaluate the factor of safety against liquefaction triggering for that layer. Traditionally, the *CRR* was obtained from charts prepared from hundreds of case histories where liquefaction was either known to have occurred or to have not occurred. Cetin et al. (2004) utilized Bayesian statistical analysis with these case histories and developed an equation for computing *CRR*, which is given as:

$$CRR = \exp \left[\frac{\left(N_{1,60} \cdot (1 + 0.004 \cdot FC) - 29.53 \cdot \ln(M_w) - 3.70 \cdot \ln \left(\frac{\sigma'_v}{P_a} \right) + 0.05 \cdot FC + 16.85 + 2.70 \cdot \Phi^{-1}(P_L) \right)}{13.32} \right] \quad (2-6)$$

where $N_{1,60}$ is the SPT blowcount corrected for hammer energy and overburden, FC is the fines content in percent ($5 \leq FC \leq 35$), M_w is the moment magnitude of the design earthquake, σ'_v is the effective vertical stress at the depth of interest, P_a is atmospheric pressure (= 1 atm = 100 kPa

= 1 tsf) and has units consistent with the effective vertical stress, P_L is the probability of liquefaction in decimals (common to use 15% or 0.15), and $\Phi^{-1}(P_L)$ is the inverse of the standard cumulative normal distribution (i.e. mean = 0, standard deviation = 1). Figure 2-11 shows a plot of these CRR curves for both (a) probabilistic liquefaction evaluation, and (b) deterministic liquefaction evaluation (i.e. P_L is assumed to be 15%).

The most commonly used method for calculating the *CSR* in current practice is the simplified procedure for estimating τ_{cyc} (Seed and Idriss, 1971). This procedure was developed for correlating cyclic shear stresses observed during harmonic uniform cyclic loading in the laboratory with cyclic shear stresses anticipated in the field. By comparing several lab test results and earthquake ground-motion recordings, Seed and Idriss hypothesized that the cyclic equivalent shear stress in the field is approximately equal to 2/3 of the peak cyclic shear stress from the laboratory.

Seed and Idriss therefore approximated the uniform cyclic shear stress amplitude for level or gently sloping sites as:

$$\tau_{cyc} = 0.65 \frac{a_{max}}{g} \sigma_v r_d \quad (2-7)$$

where a_{max} is the peak ground surface acceleration (typically estimated from a separate seismic hazard analysis, which will be explained in Chapter 5), g is the acceleration of gravity, σ_v is the total vertical stress at the depth of interest, and r_d is a depth stress reduction factor. Several researchers have developed predictive relationships for the term r_d over the years (e.g.

Golesorkhi, 1989; Idriss, 1999; Youd et al., 2001; Idriss and Boulanger, 2008). In the Cetin et al. (2004) procedure, a relationship for r_d was developed using Bayesian statistical updating. Applying this approach, r_d can be computed as:

$$r_d = \left[\frac{1 + \frac{-23.013 - 2.949 \cdot a_{\max} + 0.999 \cdot M_w + 0.0525 \cdot V_{s,12}^*}{16.258 + 0.201 \cdot e^{0.341(-d + 0.0785 \cdot V_{s,12}^* + 7.586)}}}{1 + \frac{-23.013 - 2.949 \cdot a_{\max} + 0.999 \cdot M_w + 0.0525 \cdot V_{s,12}^*}{16.258 + 0.201 \cdot e^{0.341(0.0785 \cdot V_{s,12}^* + 7.586)}}} \right] \pm \sigma_{\varepsilon_{rd}} \quad (d < 20m) \quad (2-8)$$

$$r_d = \left[\frac{1 + \frac{-23.013 - 2.949 \cdot a_{\max} + 0.999 \cdot M_w + 0.0525 \cdot V_{s,12}^*}{16.258 + 0.201 \cdot e^{0.341(-20 + 0.0785 \cdot V_{s,12}^* + 7.586)}}}{1 + \frac{-23.013 - 2.949 \cdot a_{\max} + 0.999 \cdot M_w + 0.0525 \cdot V_{s,12}^*}{16.258 + 0.201 \cdot e^{0.341(0.0785 \cdot V_{s,12}^* + 7.586)}}} \right] - 0.0046(d - 20) \pm \sigma_{\varepsilon_{rd}} \quad (d \geq 20m) \quad (2-9)$$

where d is the depth in meters, M_w is the moment magnitude of the design earthquake, a_{\max} is the horizontal peak ground acceleration in units of gravity, and $V_{s,12}^*$ is the average shear wave velocity in the upper 12 meters (~40 feet) of soil in meters/second. The parameter $\sigma_{\varepsilon_{rd}}$ is the standard deviation of the stress reduction factor and is given as:

$$\sigma_{\varepsilon_{rd}} = d^{0.85} \cdot (0.0198) \quad (d < 12m) \quad (2-10)$$

$$\sigma_{\varepsilon_{rd}} = 12^{0.85} \cdot (0.0198) \quad (d \geq 12m) \quad (2-11)$$

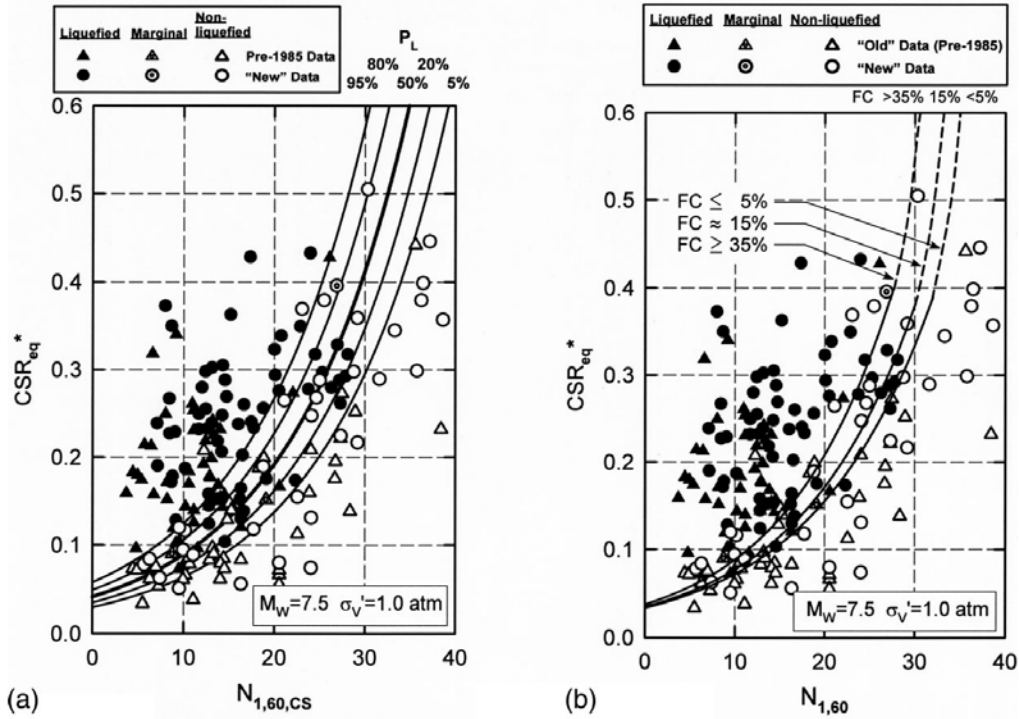


Figure 2-11: (a) Probabilistic SPT-Based CRR Correlation for $M_w = 7.5$ and $\sigma'_v = 1$ atm, and (b) Deterministic SPT-Based CRR Correlation for $M_w = 7.5$ and $\sigma'_v = 1$ atm (After Cetin et al., 2004)

Two factors known to affect the CSR must be accounted for in order to use the simplified procedure to estimate FS_L . First, because the Seed and Idriss (1971) procedure was based on earthquakes with a known magnitude of $M_w = 7.5$, a Duration Weighting Factor (DWF), also known as the Magnitude Weighting Factor (MWF), must be applied for earthquakes of different magnitudes in order to obtain a CSR value valid to use with $CRR_{M_w=7.5}$ obtained from plots like that in Figure 2-11. The DWF as recommended by Cetin et al. (2004) can be approximated as:

$$DWF \approx e^{(-0.3353 \cdot M_w + 2.5281)} \quad (5.5 \leq M_w \leq 8.5) \quad (2-12)$$

The second factor that should be accounted for when computing the CSR in accordance with the Cetin et al. (2004) procedure is the effective overburden stress. Cyclically loaded laboratory test data indicate that liquefaction resistance increases with increasing confining stress. The rate of increase, however, is nonlinear (Youd et al., 2001). Therefore, an overburden correction factor, K_σ is used to account for this phenomenon. Both Cetin et al. (2004) and Youd et al. (2001) recommend that K_σ be computed as:

$$K_\sigma = \left(\frac{\sigma'_v}{p_a} \right)^{f-1} \quad (2-13)$$

where p_a is in the same units as the effective overburden pressure, σ'_v ; and f is a function of relative density and is equal to 0.8 for loose soils, 0.7 for medium-dense soils, and 0.6 for dense soils. Cetin et al. (2004) state that this relationship is valid for effective overburden pressures greater than about 0.3 atmospheres.

Thus correcting the CSR for both magnitude (i.e. duration) and overburden stress, the corrected cyclic stress ratio can now be computed as:

$$CSR_{eq} = \frac{\tau_{cyc}}{\sigma'_{v0}} = 0.65 \left(\frac{a_{max}}{g} \right) \cdot \left(\frac{\sigma'_{v0}}{\sigma'_{v0}} \right) r_d \quad (2-14)$$

$$CSR_{eq, M_w=7.5, 1 \text{ atm}} = CSR_{eq}^* = \frac{CSR_{eq}}{DWF \cdot K_\sigma} = 0.65 \left(\frac{\sigma'_{v0}}{\sigma'_{v0}} \right) \cdot \left(\frac{a_{max}}{g} \right) \cdot \frac{r_d}{(DWF \cdot K_\sigma)} \quad (2-15)$$

Combining Equations (2-6) and (2-15), the factor of safety against liquefaction can be computed as:

$$FS_L = \frac{CRR}{CSR_{eq}^*} \quad (2-16)$$

By plotting the variation of CRR and CSR_{eq}^* with depth as shown in Figure 2-12, the factor of safety against liquefaction triggering can conveniently be visualized over a cross section of the soil profile of interest.

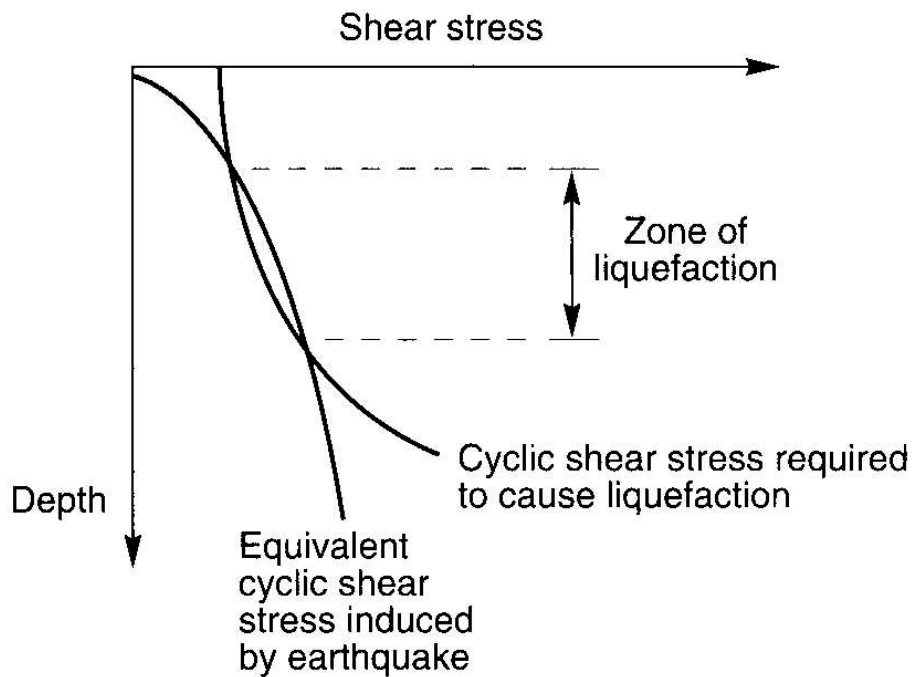


Figure 2-12: Example of Plotting CSR Versus CRR With Depth (After Kramer, 1996)

2.5 Liquefaction Effects

If a soil is susceptible to liquefaction, and the state of soil and loading parameters are such that liquefaction initiates, then it becomes important to consider what the possible effects of the liquefaction may be at the given site. Baska (2002) summarized some of the more significant effects of liquefaction as *alteration of ground motion, ground surface settlement, loss of bearing capacity, increased lateral pressures on walls, flow failures, ground oscillation, and lateral spread.*

2.5.1 Alteration of Ground Motion

As a mass of soil liquefies from earthquake loading, it decreases significantly in stiffness. As a result of this loss in stiffness, the amplitude and frequency content of the ground motion are altered such that much of the high frequency ground motions can be filtered out, thus only allowing the lower frequency waves to continue to the ground surface. This can result in large, rolling displacements that can be particularly damaging to soft structures with low natural frequencies.

2.5.2 Ground Settlement

After porewater pressures dissipate in a liquefied soil, soil particles often rearrange themselves in a denser configuration. This rearrangement, or volumetric strain, leads to soil reconsolidation, or ground settlement. Such settlement can be destructive to concrete or asphalt, and often lifelines buried at shallow depths can be severely damaged or severed, particularly at joints and connections. Figure 2-13 shows an example of liquefaction-induced settlements around a structure following the 1995 Hyogoken-Nanby earthquake in Japan.



Figure 2-13: Settlement Around a Structure in Kobe, Japan Following 1995 Hyogoken-Nanbu Earthquake (Courtesy of EERC, Univ. of Calif.)

2.5.3 Loss of Bearing Capacity

If the steady state strength of a liquefied soil is significantly smaller than the initial strength of the soil, then structures that are founded on that soil may experience bearing capacity failure. Such was the case for several residential structures that failed in bearing capacity following the 1964 Niigata earthquake in Japan, shown in Figure 2-14. Another effect that is related to loss of bearing capacity is the surfacing of lightweight buried structures such as gasoline storage tanks that are more buoyant than the liquefied soil in which they are buried.



Figure 2-14: Bearing Capacity Failures Following 1964 Niigata, Japan Earthquake (Courtesy of EERC, Univ. of Calif.)

2.5.4 Increased Lateral Pressure on Walls

Because increased pore water pressures in liquefied soils often cause the ground water levels to go rushing towards the ground surface, retaining walls with such soils in their backfill will experience a large increase in static lateral pressures due to the hydrostatic force. This force coupled with inertial earthquake loads is often sufficient to cause large displacements or even failures in these walls. This type of behavior is often seen in quay walls in ports or harbors that are subjected to earthquake loading, and was widely observed following the 1995 Hyogoken-Nanbu earthquake near Kobe, Japan. Large displacements or failure can also result if the soil located at the toe of a retaining wall liquefies because many retaining walls rely on that soil to provide passive and bearing resistance to overcome failure in overturning or sliding.



Figure 2-15: Graben Formed Behind a Displaced Quay Wall in Kobe, Japan Following 1995 Hyogoken-Nanbu Earthquake (Courtesy of NISEE, Univ. of Calif.)

2.5.5 Flow Failures

As already mentioned, flow failures often constitute the most dangerous and serious effects resulting from liquefaction. There is often little or no warning that a flow failure will occur because the loss of soil strength is so sudden once the effective stress path of a soil reaches the FSL. Because static shear stresses must already exist to provide the driving force for a flow failure, almost all such failures occur on steeply sloping ground; directly at the margin of a river, channel, or ocean (also called the “slump zone”); and beneath significant fills such as a dam or

large embankment. Once a flow failure initiates, large masses of fluid-like soil can “flow” at velocities approaching several meters per second. Such a flow will destroy most structures in its path and deposit significant volumes of soil once flow equilibrium has been reached. Flow failure was associated with the 1971 upslope failure of the Lower San Fernando Dam, shown in Figure 2-16, after which the dam was nearly breached. Such a catastrophic event would have likely left thousands dead in the various towns located in the valley downstream of the dam.



Figure 2-16: Portion of Lower San Fernando Dam That Experienced Flow Liquefaction Following 1971 San Fernando Earthquake (Courtesy of EERC, Univ. of Calif.)

2.5.6 Ground Oscillation

Without the presence of static shear stresses to drive flow failures (i.e. on level ground), horizontal deformations can still develop as a result of soil liquefaction and cyclic loading. As a soil on level ground liquefies and cyclic loading continues, large cyclic strains can produce large cyclic displacement of the ground surface. This effect, termed *ground oscillation*, generally results in relatively small permanent deformations, but can still cause significant damage to pavements, structures, pile foundations, and buried pipelines.

2.5.7 Lateral Spread

Lateral spread refers to the uni-directional movement of liquefied soil due to the presence of small existing static shear stresses in the soil and cyclic earthquake loading. Lateral spread can occur on gently sloping ground or near a free-face, and can be a major engineering concern because critical and expensive infrastructure is often located in these areas. Lateral spread demolished port facilities in Port-au-Prince, Haiti following the deadly earthquake in January of 2010 (shown in Figure 2-17). Due to this damage, delivery of humanitarian relief sent from other countries was significantly delayed.

2.6 Chapter Summary

Liquefaction is the deformation of soil resulting from a loss of effective strength due to excess pore water pressures caused by the cyclic or monotonic disturbance of the soil under undrained conditions.

In order for a soil to be susceptible to liquefaction, certain criteria must be met. These criteria include historic, geologic, compositional, and state. Generally speaking, a soil must be

cohesionless and saturated to be susceptible to liquefaction. Liquefaction susceptibility increases directly with soil uniformity and static shear stress, and indirectly with fines content, angularity, age, overconsolidation, and density.



Figure 2-17: Lateral Spread at the Port in Port-au-Prince, Haiti Following the 2010 Earthquake (Courtesy of EERI)

If a soil is susceptible to liquefaction, and if it is exposed to an undrained disturbance sufficiently powerful and/or long enough, liquefaction can be initiated. Once initiated, there are two general types of soil liquefaction that could occur: flow liquefaction and/or cyclic mobility. Flow liquefaction involves a soil's rapid loss of strength and development of its steady state

strength due to large strain deformations initiated by cyclic or monotonic loading and further driven by static shear stresses in the soil. Cyclic mobility involves the incremental straining and loss of effective strength of a soil due to cyclic loading and can result in large cumulative strains. However, catastrophic flows will not develop during cyclic mobility due to the process of phase transformation during which a liquefied soil dilates upon further straining and begins to regain strength. Typically, only very loose soils and/or those with high existing static shear stresses are prone to flow liquefaction. Both loose and medium-dense soils on nearly any ground/slope configuration can be prone to cyclic mobility. It is convenient to use p' - q diagrams to evaluate whether or not a soil will be susceptible to flow liquefaction by comparing its static shear strength with its estimated steady state strength. If the static shear stress is greater than the steady state strength, then the soil is likely prone to catastrophic flow failure, which will be initiated when the effective stress path reaches the flow liquefaction surface. If the static shear stress is less than the estimated steady state strength, then the soil is not likely prone to catastrophic flow failure, but may be prone to cyclic mobility. It is therefore important to accurately estimate the steady state strength of a soil. The use of in-situ residual strength relationships and residual strength ratios are the most commonly used procedures to make such estimations in engineering practice today. The potential for liquefaction initiation of a given soil is most commonly evaluated today by using simplified liquefaction triggering procedures such as Youd et al. (2001), Cetin et al. (2004), and Idriss and Boulanger (2008). The potential for liquefaction triggering is commonly reported as a factor of safety, which is calculated by dividing the cyclic resistance ratio (CRR) by the cyclic stress ratio (CSR). A factor of safety less than or equal to unity suggests that the soil will likely liquefy if subjected to the level of earthquake loading used in the analysis.

If initiated, it is important to evaluate the possible effects of liquefaction at the given site. The occurrence of liquefaction can result in alteration of ground motion, ground surface settlement, loss of bearing capacity, increased lateral pressures on walls, flow failures, ground oscillation, and lateral spread.

3 REVIEW OF LATERAL SPREAD

3.1 Introduction

Lateral spread is a term commonly used to describe the permanent deformation of sloping ground that occurs during earthquake shaking as a result of soil liquefaction. Its effects on structures can be devastating because, unlike flow liquefaction, it can occur in both loose and medium-dense liquefied soils. Deformations can range from millimeters to several meters, with the greatest displacements usually occurring near free-faces such as at quay wall or the margin of a river. Bridges spanning bodies of water with underlying soils prone to liquefaction, as well as pile foundations placed through liquefiable layers are particularly at risk of sustaining damage due to lateral spread.

This chapter will describe the theory and mechanics of lateral spread, as well as some of the common methods that engineers currently use to estimate lateral spread displacements. When reviewing this chapter, it is important that the reader bears in mind that lateral spread results directly from liquefaction. Therefore, if the soils at a given site do not liquefy, then they will probably not experience lateral spread.

3.2 Understanding Lateral Spread

Lateral spread has historically been a major contributor to earthquake losses throughout the world. Lateral spread was partly responsible for the shearing of water lines that prevented

firefighters from battling the ravaging fires following the Great 1906 San Francisco earthquake. Port and coastal facilities near the Prince William Sound were severely damaged, and roads and bridges for hundreds of square kilometers were moderately to severely disrupted as a result of lateral spread from the 1964 $M_w = 9.2$ earthquake. During that same year, parts of Niigata, Japan that were built over reclaimed river channels experienced lateral spread displacements over 8 meters during a $M_w = 7.5$ quake. More recently, lateral spreads during the 1989 Loma Prieta earthquake ($M_w = 7.0$) caused significant displacements along the entire 150 to 300 meter wide spit at Moss Landing by Monterey Bay that nearly resulted in the collapse of the \$6 million Moss Landing Marine Laboratory that was under construction at the time. Finally, lateral spreads during the 1995 Hyogoken-Nanbu earthquake in Japan left the port facilities of the city of Kobe severely damaged. Quay walls had displaced several meters, cranes were toppled, and rails were misaligned. The disaster left thousands of citizens unemployed and/or homeless, and ultimately had a significant effect on the local and regional economy because port business was forced to go elsewhere. Much of that business never returned.

A schematic sketch demonstrating a lateral spread is presented in Figure 3-1.

3.2.1 Experimental Studies of Lateral Spread

In order to better understand the phenomenon of lateral spread and the mechanics behind it, researchers have performed several types of laboratory experiments. Because lateral spread is a very complicated process, each of these studies has only been able to provide limited, but valuable insights into the process of lateral spread and the characteristics that govern the magnitude of horizontal deformations it can produce.

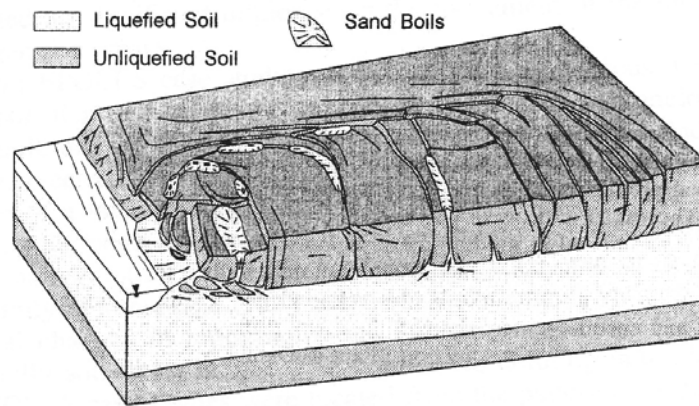


Figure 3-1: Schematic Depiction of Lateral Spread Resulting From Soil Liquefaction (After Varnes, 1978)

3.2.1.1 Shake Table Studies

Shake tables have been a useful tool in performing earthquake engineering studies during the last 60 years. Shake tables can range in length from as small as a few feet to as large as several meters. For experiments involving lateral spread, tests have been performed on tables as large as six meters in length.

Miyajima et al. (1991) performed nine tests on a small shake table with layered sand specimens of varying thicknesses (15, 17, and 19 cm) and slopes (2, 4, and 6 percent). Using 16 colored markers on the surface of the sand layers, the effects of specific gravity, uniformity, void ratio, particle size, permeability, slope, and layer thickness on ground surface displacements and velocity of deformations were measured. Researchers observed that average surface displacements were most closely correlated to the product of sand layer thickness and slope angle.

Sasaki et al. (1991) performed eight tests with tri-layered soil specimens that each consisted of a well-compacted sand for the base, a middle layer composed of a loose sand placed by wet pluviation, and an upper layer of dense lead shot or gravel. The specimen for each test was very well instrumented with tell-tales, accelerometers, pore-pressure transducers, and LVDTs. Base shaking acceleration was gradually accelerated during the test. During the testing, researchers observed that the greatest strains occurred at or near the bottom of the liquefied layer. Also, they noticed that the greatest displacements occurred in the middle of the specimen, but probably due to boundary effects. Finally, it was noted that displacements only occurred during the application of base shaking.

3.2.1.2 Centrifuge Studies

Many centrifuge studies have been performed to better-understand the mechanics of lateral spread. These types of studies have a distinct advantage over shake table tests in that prototype-level vertical stresses can be produced on a small model. However, scaling effects can be a significant concern for centrifuge studies.

A consortium of research institutions conducted a centrifuge-based study of liquefaction during the 1990s. The study was called Verification of Liquefaction Analysis by Centrifuge Studies (VELACS) and was used to observe the occurrence of liquefaction and to validate predictive methodologies developed prior to 1990. The tests were performed at Rensselaer Polytechnic Institute, California Institute of Technology, and the University of California at Davis. Of the nine model geometries planned for testing, model #2 best suited the conditions needed for lateral spread. The results of the testing showed that even though the three institutions had dissimilarities in loading conditions, all obtained fairly similar ground surface displacements, rates of pore pressure buildup, and profiles of lateral displacement versus time.

These results suggested that the lateral spread displacements may be more of a function of the soil and its configuration than of the loading conditions themselves. It was also noted that spikes in accelerations occurred in the liquefied soil when the direction of horizontal shaking was in the upslope direction.

Balakrishnan et al. (1997) conducted a series of centrifuge studies to evaluate methods of liquefaction remediation at bridge sites in California. The fifth series of tests in the study (BAM05) best represented the conditions for lateral spread. The test specimens were subjected to replications of six different recorded ground motions including one from the 1995 Hyogoken-Nanbu earthquake. The test specimens were composed of dense sand with an overlying layer of loose sand and a surficial layer of overconsolidated clay. During the testing, it was observed that much of the high frequency content from ground motions was being filtered out by the liquefied layer. It was also observed that downward spikes in pore pressure corresponded in time with upward spikes in ground surface acceleration.

Toboada-Urtuzuastegui and Dobry (1998) conducted a centrifuge study which involved 11 tests in loose sands. The researchers were able to provide new insight into lateral spread by minimizing boundary effects by using a new container that was very flexible. As a result, some fascinating observations were made. First, researchers observed that with increasing slope, pore pressures tended to be more varied and lower on average than with flatter slopes. Second, it was noted that as the ground motion accelerations were increased, the time to soil liquefaction decreased. Third, it was observed that as the frequency of the loading decreased, the time to soil liquefaction decreased. Finally, as in the BAM05 tests, it was noted that downward spikes in pore pressure corresponded with strain deformations in the test specimens. Researchers

concluded that these spikes resulted from phase transformation and dilation of the liquefied soil during various increments of strain.

Boulangier et al. (2003) performed a series of centrifuge tests to model the effects of various soil-pile configurations on pile response during lateral spread loading. Their tests revealed that it is possible for a water film to develop between the liquefied layer and the non-liquefied soil crust if the crust is composed of a relatively impermeable material such as clay. The water film appeared to govern the large lateral deformations measured in the soil, and much of which occurred after the significant ground motions ceased. Malvick et al. (2006) also observed and reported the same water film phenomenon in the centrifuge tests that were performed as part of their study.

3.2.1.3 Other Experimental Studies

Experiments using undrained torsional tests (Yasuda et al., 1994; Shamoto et al., 1997) and undrained triaxial tests (Nakase et al., 1997) were performed with sands to study post-liquefaction deformation characteristics. The experiments confirmed that soils tend to experience phase transformation and regain shear strength if strained sufficiently. However, the point at which phase transformation begins (i.e. when the soil reaches the QSS) greatly depends on the initial density and previous strain history of the soil.

Wu (2002) conducted studies with a cyclic direct simple shear apparatus on specimens of Monterey 0/30 sand in undrained loading. Tests representing soils located in both level and sloping ground were performed. Wu generally observed that lower pore pressure ratios were induced with sloping ground conditions than with level ground conditions. Wu also observed that some specimens exhibited cyclic mobility behavior when loaded in one direction, but exhibited flow liquefaction behavior when loaded in another direction. This observation suggests that

directivity of ground motion can affect the liquefaction behavior of a soil, particularly if the ground motion directivity is larger in the downslope direction or in the direction of the free face. Wu also noted a general inverse relationship between horizontal strain deformations and volumetric strain deformations.

3.2.2 Summary Lateral Spread Theory

Lateral spread can occur when soil located in sloping ground or adjacent to a free face liquefies at relatively shallow depths during cyclic loading. The deformations due cyclic mobility in a lateral spread appear to occur only while transient loading is taking place. However, the development of a water film between an impermeable non-liquefied soil crust and the liquefied soil could potentially allow for significant deformations following transient loading. The magnitude of the permanent lateral spread deformation appears to be strongly dependent on the initial density of the liquefiable soil and its previous strain history. Experimental studies of lateral spread also suggest that the magnitude of lateral deformations increases with the thickness of the liquefiable layer, the ground slope angle, and duration of shaking. Furthermore, because the studies suggest that low frequency and high acceleration loading decreases the time to liquefaction initiation, such ground motion characteristics could also cause increased lateral deformations. Ground motion directivity also appears to be significant in that ground deformations increase when the direction of horizontal loading is parallel with the slope or in the direction of the free face.

When lateral spread initiates, there appears to be a region within the liquefied soil where the excess pore pressure ratio is approximately equal to unity. With continued strain, this zone often begins to dilate and decrease in pore pressure due to phase transformation. Pore pressures

continue to decrease as straining continues, but may ultimately increase to achieve equilibrium when straining ceases.

3.3 Analytical and Empirical Methods for Predicting Lateral Displacements

Researchers have developed several methods of analyses to compute the permanent deformations resulting from lateral spread during earthquake loading. These different methods of analyses can be categorized into two general types: *Analytical Methods* and *Empirical Methods*.

3.3.1 Analytical Methods

Analytical methods are those developed from our current understanding of soil mechanics and science. They generally are closed-form mathematical models. There are several different types of analytical models developed for estimating permanent lateral spread displacements. For the purpose of this dissertation, analytical methods will briefly be categorized and summarized as follows: the *Numerical Model*, the *Elastic Beam Model*, and the *Newmark Sliding Block Analysis*.

The numerical model works by transforming the soil profile of interest into two- or three-dimensional mesh of nodes and elements, and solving for either the forces or displacements acting on those elements. There are generally two types of numerical models: finite element models and finite difference models. Finite element models discretize the physical continuum of the system, and a system of equations relating nodal displacements to nodal forces is solved directly. Finite difference discretizes a series of governing differential equations and replaces continuous derivatives by the ratio of changes in the variable of interest over a small but finite increment. Numerical models generally can allow for complex conditions such as topography,

pore pressure distribution, and strain effects on shear wave modulus and damping to be taken into consideration. In order to perform a numerical model, a reliable constitutive relationship must be utilized, which can be quite challenging considering the large amount of uncertainty associated with the stress-strain behavior of liquefied soil. Because numerical models generally must rely on computers to perform numerous calculations, their practical use only became a reality during the late 1970s. Early finite element models (Zienkiewicz et al., 1978; Prevost, 1981; Zienkiewicz and Shiomi, 1984; Finn et al., 1986; Shiomi et al., 1987) progressively produced more accurate results, taking into account increasingly more of the governing mechanics behind soil liquefaction. Modern numerical models (Gu et al., 1994; Yang, 2000; Yang et al., 2003; Arduino et al., 2006) have become quite advanced. In general, numerical models comprise much of the research in earthquake engineering today, and models continue to advance and become more user-friendly as technology and constitutive relationships improve. Due to their flexibility and robustness, numerical models will likely become a widely-used tool in the future of geotechnical earthquake engineering.

Another analytical method was developed originally by Japanese researchers and is called the *elastic beam model*. The elastic beam model assumes that the unsaturated surficial soil behaves like an elastic beam supported on a fluid, which is the liquefied soil layer. This approach was first proposed by Hamada et al. (1987), but was not pursued further by Hamada himself. Instead, the co-authors of the publication developed the actual methodology a few years later. This method usually assumes no friction between the surficial layer and the liquefied layer, and can involve the minimization of potential energy in order to estimate the lateral displacements. These models were researched and developed predominantly during the early 1990s (Towhata et al., 1991, 1992; Yasuda et al., 1991), but have since been largely abandoned.

The *Newmark sliding block analysis* (Newmark, 1965) differs from other analytical methods in that it is a discrete system rather than a continuum analysis. This model consists of a frictional block on a sliding plane which, when acted upon by an external force of sufficient size, will overcome the frictional resistance and cause the slope to slide. The model was originally developed to replicate seismic slope failures, but has since been adapted to other applications such as lateral spread. This type of lateral spread model was researched quite heavily during the 1990s, and several different predictive models came about as a result (Dobry and Baziar, 1991; Byrne, 1991; Byrne et al., 1992; Baziar et al., 1992; Tobaoda et al., 1996). More recently, Olson and Johnson (2008) presented a methodology that incorporates residual shear strength ratios with Newmark sliding block time history analysis to compute lateral spread displacements of embankments and slopes. Many other researchers such as Saygili and Rathje (2008) and Bray and Travararou (2007) have presented simplified empirical models for seismic slope displacements that were developed from multiple Newmark sliding block analyses. While these models are relatively convenient to use, it is important that they only be used within the bounds for which they were developed in order to avoid extrapolation due to their empirical nature. As such, it may not be appropriate to apply such models to the case where significant soil softening and porewater pressure effects (i.e. liquefaction) could significantly affect the horizontal strain behavior of a seismically-loaded slope or embankment.

3.3.2 Empirical Methods

Empirical multi-linear regression (MLR) methods involve the use of lateral spread case histories in order to develop statistical relationships between lateral deformations and some measurable soil parameter (e.g. SPT or CPT resistance, ground slope, M_w , R , etc.). The models often do not involve direct consideration of soil mechanics, but are usually based on linear

regression and identifying model parameters such that the prediction error is minimized. The assumption behind such an approach is that the model parameters selected in order to minimize error in linear regression should also be governing parameters in the complex soil mechanics. Though this assumption is not always true, empirical methods have been used with databases of lateral spread case histories to develop models for prediction of deformations that have proven to be fairly accurate, often predicting values within a factor of two of the observed displacements.

The development of an empirical MLR model should clearly state the conditions and assumptions used in the consideration of the lateral spread case histories. Use of inconsistent data during model calibration can not only result in increased error calculated during linear regression, but can also result in the application of the final regression model in locations and conditions where its use should not be warranted. Nearly all predictive models include a range of input parameter values for which the application of the models is considered to be appropriate.

Empirical models tend to be used quite heavily in engineering practice for a few reasons. First, they are considered relatively convenient because they are usually expressed as a simple algebraic equation. Such an equation could easily be applied in any standard spreadsheet, thus providing a quick solution to the problem. Second, a complex understanding of soil mechanics is often not required to use an empirical model. Though such knowledge would likely help in the interpretation of the model's results, it often is not necessary because input parameters can easily be compared with recommended input parameters, thus indicating the relative validity of the results. Finally, an empirical model can be calibrated to the liquefiable soils within a certain region. Because many practicing engineers generally limit the scope of their practice to defined regions, it is logical that they would be attracted to models calibrated for the regions in which they work.

3.3.3 Comparison of Analytical and Empirical Methods

In order to interpret computed lateral spread displacements, it is important to understand the fundamental strengths and weaknesses of both analytical and numerical methods. By understanding these strengths and weaknesses, the correct application of these various approaches may become better understood.

Analytical models have represented certain aspects of lateral spread well. The sliding block model is consistent with observations that the overlying surficial soil often displaces as a coherent block. The models also tend to show the movement of soil in the downslope direction, which is what is commonly observed in the field. Both the elastic beam model and the sliding block model correctly show that most displacements typically occur during transient loading. Both have also been used to accurately compute the maximum displacements from several past historical lateral spread case histories. The numerical model is theoretically sound and has been shown to produce reasonable results when the input parameters from the materials being analyzed were shown to be accurate and their constitutive behavior was relatively well understood.

However, analytical methods also have shortcomings. The sliding block model ultimately attempts to oversimplify a very complex process. The failure surface in a liquefied layer of spread soil usually cannot be accurately represented by a horizontal linear plane, especially when modern research and field data have suggested that shear strain is distributed throughout the entire profile of the liquefied soil (e.g. Holzer and Youd, 2007). In addition, the sliding block model can fail to capture the dynamic processes that lead up to the occurrence of liquefaction, and it often attempts to use simplified rigid-perfectly plastic behavior to represent the non-linear stress-strain characteristics of liquefied soils. The elastic beam method attempts to model the

surficial soil by assuming that it is a continuous elastic beam. However, studies of actual lateral spreads have shown that this assumption is not valid because the surficial soil in a lateral spread is often quite fissured and fractured. Because of these fissures and fractures, the elastic and shear moduli of the soil can vary quite significantly. Also, like the sliding block method, the elastic beam method tends to oversimplify the attributes and characteristics of the liquefied subsurface by assuming that it behaves as a homogenous viscous fluid. As a result, the computed results of everything except the maximum displacements in a lateral spread are usually prone to significant errors. Finally, numerical methods are often complex, and most practicing engineers are still not comfortable either using them or interpreting their results. While increasingly user-friendly computer applications are beginning to make their way to the commercial market, they are typically quite expensive and still limited in the accuracy of their computed lateral displacements by the constitutive models that they utilize. With that said, the development of more accurate constitutive models and the continued development of more user-friendly computer applications will likely make the numerical model the preferred means to predict lateral spread displacements in the future.

Empirical methods have proven very useful in the absence of consistent and reliable analytical procedures. Due to their ease of use, they have generally been considered the preferred method for predicting lateral spread displacements for the past two decades. Also, with major earthquakes and new lateral spread case histories occurring throughout the world each year, existing empirical lateral spread databases can always be updated and improved.

However, like analytical methods, empirical methods also have shortcomings. Every site condition should be consistent with the equation calibration conditions. This can be challenging, especially considering that many lateral spread case histories are from earthquakes that occurred

several decades ago and therefore may be poorly documented, leaving researchers no choice but to make assumptions in order to fully-develop the case history. Most empirical models consist of a complex algebraic equation and are often treated by users as “black boxes” that receive input and simply return a computed value. Most of the methods do not make any consideration of theoretical soil mechanics, and many do not consider the frequency content or duration of a ground motion— two important aspects of an earthquake motion (Kramer, 1996). Also, no empirical model considers every variable known to affect lateral spread displacements. The manner in which key variables are chosen is often one of trial and error, mixing and matching different combinations of variables in order to maximize the linear regression coefficient and to minimize standard error. Finally, nearly all empirical models only consider a single combination of earthquake magnitude and distance in their lateral spread displacement calculations. This implies that engineers must select a single scenario earthquake with which they must use to characterize the entire lateral spread hazard. Such a deterministic approach is likely to provide inconsistent predictive displacement values, particularly as design standards continue to move towards probabilistic and performance-based approaches.

In comparison, analytical methods can potentially provide better accuracy when dealing with general random cases of lateral spread or with cases in which the properties of the soil are well known. If the lateral spread cases of interest are confined to a region in which an empirically-based method was calibrated, empirical methods may produce better results. Ideally, the method of choice for predicting lateral spread deformations would be neither completely analytical nor completely empirical, but rather a combination of both (i.e. semi-empirical). This method would be based on solid soil mechanics and experimentation in order to define the governing variables to use in the predictive model, and then would be calibrated against lateral

spread case histories in order to determine the variable coefficients and to manipulate the equation such that the standard error is minimized.

3.4 Deterministic Procedures for Estimation of Displacements Using Empirical Models

A few of the earlier and pioneering deterministic empirical MLR models for estimating lateral spread displacements will first be presented. Following these, a few of the more modern empirical procedures will be briefly presented. Finally, three empirical MLR models will be presented in greater detail.

3.4.1 Early Empirical MLR Procedures

Many early empirical MLR models are not commonly used among engineers in practice today, though they laid the foundation for many of the modern empirical and semi-empirical MLR lateral spread models.

One of the first recognized empirical procedures for computing horizontal deformations from lateral spread was presented by Hamada et al. (1987). The procedure considered the effects of various geotechnical and topographic variables on permanent ground displacements observed in uniform sands from the 1964 Niigata, 1971 Sand Fernando, and 1983 Nihonkai-Chubu earthquakes. Hamada et al. observed that the variables that best-correlated with observed deformations were the thickness of the liquefied layer and the slope of the ground. This very simple model produced reasonable results when compared with displacements measured from the three studied earthquakes. However, when compared against measured lateral spread displacements from other earthquakes, the computed values showed significant errors. It became

clear that there were other significant variables - most notably the strength of the soil - that the simplified procedure failed to take into account.

Youd and Perkins (1987) developed a procedure that used an index number that served two purposes: to characterize the liquefaction potential of a given site, and to estimate the amount of lateral spread displacements that could occur on wide active flood plains, deltas, or other areas of gently-sloping Late Holocene fluvial deposits. This index was called the Liquefaction Severity Index (LSI). The procedure was developed from observed lateral spread displacements in the western U.S., and became the empirical lateral spread model to incorporate the use of seismic loading parameters (i.e., source-to-site distance and earthquake magnitude). The procedure generally provided a more accurate estimate for lateral spread deformations in the western U.S. than did the Hamada et al. (1987) procedure, but there were still significant errors present in the results. These errors were most likely due to the procedure's failure to take into account any of the site-specific properties of the soil.

Bartlett and Youd (1992, 1995) incorporated MLR techniques to develop an empirical lateral spread displacement predictive equation using a relatively large database of geological topographical, geotechnical, and seismological data from sites of known lateral spread displacements. The database included 448 horizontal ground displacement values from seven different earthquakes. The predictive equation of Bartlett and Youd became widely accepted in engineering practice and was considered by many to be the most commonly used procedure for the estimation of permanent lateral spread displacements. One of the most significant contributions from the Bartlett and Youd procedure is the improvement in the linear regression that is achieved by considering ground slope lateral spread case histories and free-face lateral spread case histories separately. Subsequent incorporation of case histories from earthquakes in

the U.S. allowed peak ground acceleration and duration of strong ground shaking to be included in their predictive equations. However, the lack of recorded ground motions in the database meant that attenuation relationships were needed to compute the ground motion values required for regression, thus likely adding additional variability to the problem. As such, Bartlett and Youd found that the model had a better fit when characterizing the seismic loading with just moment magnitude, M and source-to-site distance, R . Finally, while most of the case histories compiled by Bartlett and Youd were for sites located less than 30 kilometers from the seismic source, they incorporated 19 liquefaction case histories from Ambraseys (1988) to their database in order to extend their model to greater distances. However, because Ambraseys did not compile site and subsurface data, Bartlett and Youd had to approximate the values of the required variables using averaged values from their database.

Rauch and Martin (2000) developed a MLR procedure for computing average displacements from lateral spreads. Their model, termed EPOLLS (Empirical Prediction Of Liquefaction-induced Lateral Spread), was unique in that it was actually comprised of three separate parts: regional, site, and geotechnical analyses. The parts defined the level of accuracy achievable with the model, with regional-EPOLLS being the least accurate and geotechnical-EPOLLS being the most accurate. An engineer could therefore identify the model that best-suited the available site data and make the lateral spread displacement prediction accordingly. The EPOLLS model incorporated lateral spread data from earthquakes dating from 1906 to 1994 and that occurred in the western U.S., Japan, Costa Rica, and the Philippines. Due to the large variety of lateral spreads in the database and the fact that averaged displacement vectors needed to be developed for complex spreads, the model appears to produce results with less accuracy

than that of other empirical models. The EPOLLS' most accurate model (i.e. geotechnical-EPOLLS) yields a regression coefficient of only 70%.

3.4.2 Modern Empirical MLR Procedures

Zhang et al. (2004) developed a semi-empirical lateral spread model to be used directly with in-situ SPT or CPT field data and the results of a liquefaction triggering analysis. The model correlates factor of safety against liquefaction and relative density to horizontal cyclic shear strain levels based on previous research published by Ishihara and Yoshimine (1992) and Seed (1979), which are then cumulatively used to estimate a permanent lateral spread displacement. Like other empirical approaches, the model requires the user to specify whether the site geometry is gently sloping or a free-face. The model was calibrated against selected observed lateral spreads in California, Alaska, and Japan. Because the model is not purely based on regression statistics, but also incorporates laboratory-based cyclic shear strain theory, it is considered to be semi-empirical. While the database for the SPT-based model appears to be large and sufficient for development of such a model, the database for the CPT-based model is surprisingly small and warrants careful consideration and engineering judgment in the evaluation of the computed results. Zhang et al. (2004) provide the user with a range of acceptable values for their model coefficients, but they do not provide any indication of the model uncertainty, which would be necessary for incorporation into a probabilistic framework.

Zhang and Zhao (2005) developed an empirical MLR model that attempts to reduce the scatter in their lateral spread case history database by incorporating the earthquake magnitude and source-to-site distance parameters into the computation of a pseudo-displacement parameter and a faulting mechanism parameter. The model appears to be the first of its kind to consider faulting mechanism (i.e., strike-slip/normal, reverse/thrust, subduction interface, subduction

intraslab) in the computation of lateral spread displacements. Two separate models were developed: one incorporating a Japanese attenuation model (Takahashi et al., 2004), and one incorporating American attenuation models (Sadigh et al., 1997 and Youngs et al., 1997). Though the models appear to accurately compute lateral displacements from the 1997 Kocaeli, Turkey earthquake, the use of a single modification factor to summarize the very complex behavior of non-linear soil response is questionable.

Faris et al. (2006) developed a semi-empirical model similar to the Zhang et al. (2004) model in that it is a cumulative strain-based model, but different in that it is based on the shear strain potential curves developed by Wu (2002) and incorporates a new parameter called the “Displacement Potential Index” (DPI). Faris et al. used a Bayesian statistical updating approach with their lateral spread displacement database to develop the coefficients for their final predictive model. This Bayesian-based approach allowed them to consider not only uncertainty in the strain data itself, but also in the back-analyses of field case histories. The Faris et al. (2006) model differs from other empirical lateral spread models in that it does not define site geometry as either “free-face” or “ground-slope”, but rather uses a universal variable “ α ,” defined as the ratio of the shear stress in the soil to the effective vertical stress, to characterize the site geometry. Faris et al. did not provide any indication of acceptable bounds for the parameters of their semi-empirical model, and they did not formally indicate the uncertainty of their statistical model, thus disqualifying its incorporation into a more advanced probabilistic framework.

3.4.3 Youd et al. (2002) Procedure

Youd et al. (2002) presented revisions of the original Bartlett and Youd (1992, 1995) empirical equations developed for predicting lateral spread displacements. The original procedure incorporated 448 displacement values compiled from 7 different earthquakes that occurred either in Japan or the western United States. The database of displacements was divided into two general categories: free-face displacements and ground-slope displacements. Standard linear regression was used to determine the combination of variables that maximized the regression coefficient. Youd et al. (2002) made the following updates to the original procedure: erroneous displacement values were corrected; cases that were determined not to be lateral spread were removed; additional case histories from the earthquakes at Borah Peak, Loma Prieta, Northridge, and Kobe were added to the database; the mean grain size parameter was weighted so that it would not affect the resulting displacements as significantly; a cap was placed on the fines content; and a term to accommodate near-fault conditions was added. The Youd et al. procedure is arguably the most widely used and accepted procedure for predicting lateral spread displacements in engineering practice today.

The Youd et al. (2002) procedure, like the earlier Bartlett and Youd procedure, requires the user to characterize the site geometry as either “Free-Face” or “Ground Slope.” Figure 3-2 below uses a simplified geometry to demonstrate this site geometry characterization.

Once the site geometry is classified, the estimated permanent lateral spread displacement can be computed respectively for the free-face case or the ground slope case as:

$$\log D_{H-FF} = b_o + b_{off} + b_1 M + b_2 \log R^* + b_3 R + b_4 \log W + b_6 \log T_{15} + b_7 \log(100 - F_{15}) + b_8 \log(D50_{15} + 0.1) \quad (3-1)$$

$$\log D_{H-GS} = b_o + b_1 M + b_2 \log R^* + b_3 R + b_5 \log S + b_6 \log T_{15} + b_7 \log(100 - F_{15}) + b_8 \log(D50_{15} + 0.1) \quad (3-2)$$

where M is the earthquake moment magnitude, R is the closest horizontal distance from the site to the surface projection of the source, W is the free-face ratio in percent, S is the ground slope gradient in percent, T_{15} is the cumulative thickness of all saturated soil layers with $(N_1)_{60}$ values less than 15 blows/foot, F_{15} is the average fines content in percent from all saturated soil layers with $(N_1)_{60}$ values less than 15 blows/foot, and $D50_{15}$ is the average mean grain size diameter from all saturated soil layers with $(N_1)_{60}$ values less than 15 blows/foot. Regression coefficients are provided in Table 3-1. R^* is computed as:

$$R^* = R + 10^{(0.89M - 5.64)} \quad (3-3)$$

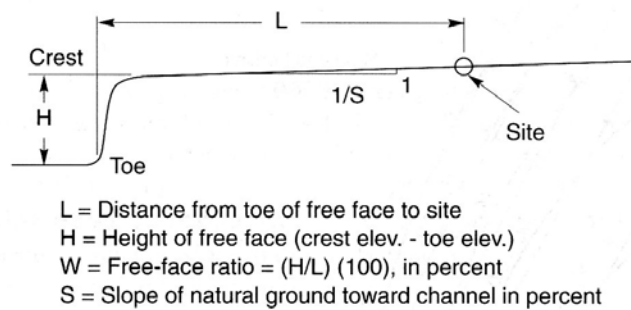


Figure 3-2: Determination of Site Geometry for Empirical MLR Equation

Table 3-1: Regression Coefficients for the Youd et al. (2002) MLR Model

b_o	b_{off}	b_1	b_2	b_3	b_4	b_5	b_6	b_7	b_8
-16.213	-0.5	1.532	-1.406	-0.012	0.592	0.338	0.54	3.413	-0.795

Upon computing the lateral spread displacement from either Equations (3-1) or (3-2), it is important to compare the model input parameters against the recommended model bounds in order to verify that the user is not extrapolating with the model. Youd et al. (2002) provided such bounds based on the limits in their database, and they are presented below in Table 3-2 and Figure 3-3. Note that the term Z_T is defined as the depth, in meters, from the ground surface to the top of the liquefiable layer.

Table 3-2: Recommended Range of Parameters for the Youd et al. (2002) Procedure

Variable	Description	Range
M	Moment magnitude of earthquake	6.0 to 8.0
R (km)	Closest horizontal distance from the site to the surface projection of the source	0.2 to 100 km
W (%)	Free face ratio (height of free face/distance from the free face to the point of displacement in percent)	1 to 20 percent
S (%)	Ground slope in percent	0.1 to 6 percent
T_{15} (m)	Cumulative thickness in meters of saturated soil with an SPT resistance less than 15	1 to 15 m
Z_T (m)	Depth in meters from ground surface to top of liquefied layer	1 to 10 m

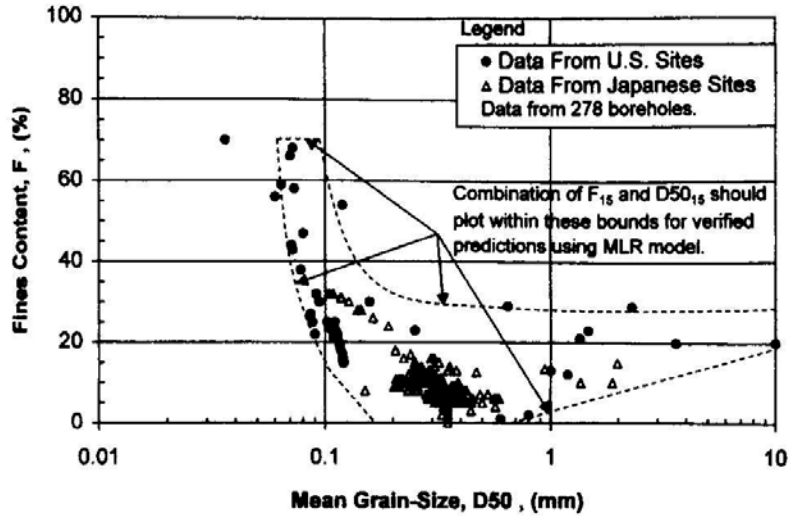


Figure 3-3: Compiled Grain-Size Data With Ranges of F_{15} and $D50_{15}$ for Use With the Youd et al. (2002) Procedure (After Youd et al., 2002)

3.4.4 Bardet et al. (2002) Procedure

Bardet et al. (2002) developed a four-parameter empirical MLR model for estimating displacements due to lateral spread. The model was developed for use over relatively large areas and was intended for the prediction of large-scale lateral displacements that could significantly damage or destroy lifeline networks. The Bardet et al. (2002) procedure was termed FFGS4 (Free-Face, Ground-Slope, # of parameters) and is divided into two data sets: complete data for all ranges of displacement amplitude (Data Set A), and data limited to displacement amplitudes smaller than 2 meters (Data Set B). However, because the linear regression analysis provided a nearly identical regression coefficient for both amplitudes of displacement, the coefficients for from Data Set B will not be summarized in this dissertation. An attractive feature of the FFGS4 procedure for engineers is that it allows them to compute displacements without the challenge of estimating the average fines content or mean grain size for the susceptible soil layers across the

site. With that being said, the regression coefficient for the four-parameter procedure is only 64.25%, as opposed to 83.6% for the six-parameter Youd et al. (2002) procedure. Therefore the accuracy of the predictions is significantly affected by the removal of the average fines content and mean grain size parameters from the model.

The Bardet et al. (2002) procedure, like the Youd et al. (2002) procedure, requires the user to characterize the site geometry as either “Free-Face” or “Ground Slope” as described in Figure 3-2. Once the site geometry is classified, the estimated permanent lateral spread displacement can be computed respectively for the free-face case or the ground slope case as:

$$\log(D_{H-FF} + 0.01) = b_o + b_{off} + b_1M + b_2 \log R + b_3R + b_4 \log W + b_6 \log T_{15} \quad (3-4)$$

$$\log(D_{H-GS} + 0.01) = b_o + b_1M + b_2 \log R + b_3R + b_5 \log S + b_6 \log T_{15} \quad (3-5)$$

where M is the earthquake moment magnitude, R is the source-to-site distance in kilometers, W is the free-face ratio in percent, S is the ground slope gradient in percent, and T_{15} is the cumulative thickness of all saturated soil layers with $(N_1)_{60}$ values less than 15 blows/foot. Regression coefficients for use in Equations (3-4) and (3-5) are given below in Table 3-3. Recommended bounds for the FFGS4 model parameters are summarized in Table 3-4.

Table 3-3: Regression Coefficients for the Bardet et al. (2002) FFGS4 Model

b_o	b_{off}	b_1	b_2	b_3	b_4	b_5	b_6
-6.815	-0.465	1.017	-0.278	-0.026	0.497	0.454	0.558

Table 3-4: Recommended Range of Parameters for the Bardet et al. (2002) FFGS4 Model

Variable	Description	Range
D (m)	Displacement in meters calculated by procedure	0 to 10.15 m
M	Moment magnitude of earthquake	6.4 to 9.2
R (km)	Closest horizontal distance from the site to the surface projection of the source	0.2 to 100 km
W (%)	Free face ratio (height of free face/distance to the free face from the point of displacement in percent)	1.64 to 55.68 percent
S (%)	Ground slope in percent	0.05 to 5.9 percent
T_{15} (m)	Cumulative thickness in meters of saturated soil with an SPT resistance less than 15	1 to 15 m

3.4.5 Baska (2002) Procedure

Baska (2002) and Kramer et al. (2007) presented a semi-empirical procedure for the estimation of lateral spread displacement that is consistent with the known mechanics of liquefiable soil, but was calibrated against a database of lateral spread case histories from the field. Baska incorporated a constitutive model that accounts for the many of the important characteristics of liquefiable soils, and implemented it within a nonlinear one-dimensional site response analysis program to compute the strains induced in several different soil columns by a large suite of ground motions. The site response program was then used to develop a database of “virtual” lateral spreads using thousands of combinations of slope geometries, material properties, and time histories, from which the basic form of the model was regressed. The actual regression coefficients for the model were then developed by calibrating the model against a large set of lateral spread case histories from the field. The resulting semi-empirical model is

therefore consistent with many of the known mechanical behaviors of liquefiable soil, but is also calibrated against a large set of available field data.

Unlike the Youd et al. (2002) and the Bardet et al. (2002) procedures, the Baska (2002) procedure does not utilize the T_{15} parameter to characterize the thickness of the soils susceptible to lateral spread. Rather, the model computes a cumulative effective thickness of the laterally spread soils, T^* which can be computed respectively for the ground slope case and the free-face cases as:

$$T_{gs}^* = 2.586 \sum_{i=1}^n t_i \cdot \exp \left[-0.05 \cdot (N_{1,60,cs})_i - 0.04 \cdot z_i \right] / \left[1 + (PI_i/5.5)^8 \right] \quad (3-6)$$

$$T_{ff}^* = 5.474 \sum_{i=1}^n t_i \cdot \exp \left[-0.08 \cdot (N_{1,60,cs})_i - 0.10 \cdot z_i \right] / \left[1 + (PI_i/5.5)^8 \right] \quad (3-7)$$

where n is the number of sublayers in the soil profile, t_i is the thickness in meters of sublayer i (recommended to be no larger than 1.5 meters), $(N_{1,60,cs})_i$ is the corrected clean sand-equivalent SPT blowcount for sublayer i (computed using Equation (2-4)), z_i is the depth in meters of the midpoint of sublayer i , and PI_i is the plasticity index for sublayer i (if applicable).

After computing the effective thickness of the laterally spread soil for either the free-face or ground slope case, the median permanent lateral spread displacement can be computed as:

$$\hat{D}_H = \begin{cases} 0 & \text{for } \sqrt{D_H} \leq 0 \\ \left(\sqrt{D_H}\right)^2 & \text{for } \sqrt{D_H} > 0 \end{cases} \quad (3-8)$$

$$\sqrt{D_H} = \frac{\beta_1 + \beta_2 T_{gs}^* + \beta_3 T_{ff}^* + 1.231M - 1.151 \log R^* - 0.01R + \beta_4 \sqrt{S} + \beta_5 \log W}{1 + 0.0223(\beta_2/T_{gs}^*)^2 + 0.0125(\beta_3/T_{ff}^*)^2} \quad (3-9)$$

$$R^* = R + 10^{(0.89M - 5.64)} \quad (3-10)$$

where M is the earthquake moment magnitude, R is the source-to-site distance in kilometers to the epicenter of the earthquake, S is the ground slope gradient in percent, and W is the free-face ratio in percent. Regression coefficients for the Baska (2002) model are provided in Table 3-5. Recommended bounds for the model parameters are summarized in Table 3-6.

Table 3-5: Regression Coefficients for Baska (2002) Model

Model	β_1	β_2	β_3	β_4	β_5
Ground Slope	-7.207	0.067	0	0.544	0
Free Face	-7.518	0	0.086	0	1.007

Table 3-6: Recommended Range of Parameters for Baska (2002) Model

Variable	Description	Range
$(N_{1,60-cs})_i$	Corrected clean sand-equivalent SPT blowcount for sublayer computed using Equation (2-1) and Table 2-1	unlimited
z_i	Depth to the midpoint of sublayer in meters	unlimited
t_i	Sublayer thickness in meters	≤ 1 m
T^*	Equivalent thickness of saturated cohesionless soils (clay content ≤ 15 percent) in meters	0 to 20 m
M	Moment magnitude of the earthquake.	6.0 to 8.0
R	Closest horizontal distance from the site to surface projection of the source	0 to 100 km
W	Free face ratio (height of free face/distance to the free face from the point of displacement) in percent	≤ 20 percent
S	Ground slope in percent	0 to 6 percent

3.5 Incorporation of Uncertainty in the Estimation of Lateral Spread Displacements

Deterministic procedures for lateral spread displacements can be very convenient tools for providing quick estimates of lateral spread displacements. However, these procedures were derived from data that is often very scattered at best, and do not account for uncertainty in the estimated displacement value. For this reason, many researchers and professional engineers prefer to incorporate a statistical approach that allows them to consider the variability in lateral spread data and to assign a level of statistical confidence to their estimation.

While Youd et al. (2002) did not formally define the uncertainty of their MLR empirical lateral spread model, they did indicate that approximately 90% of the predicted displacements from the MLR database falls within a factor of two of the actual displacements. However, Bartlett (personal communication, June 2009) indicated that the residual mean square, s^2 for the 2002 updated MLR model is approximately equal to 0.0408. While it is technically correct to

quantify uncertainty for the MLR model by using the Student's t -distribution in conjunction with the residual mean square and the model's covariance matrix, several simplifying assumptions can reasonably be made. First, because there is essentially no difference in the computed statistical probability density between the Student's t -distribution and the Normal distribution for degrees of freedom greater than about 100, and because the Youd et al. (2002) model has almost 450 degrees of freedom, one could justify substituting the Normal distribution for the Student's t -distribution in order to approximate the probability density for the MLR model. In addition, because the covariance matrix produced from the MLR model contains individual covariance values that are relatively low (Bartlett and Youd, 1992), thus suggesting that the parameters are essentially behaving independently from one another, one could reasonably neglect its incorporation in the evaluation of uncertainty. While these assumptions will add slight bias to the estimated standard error of the model, this bias is not considered to be significant in a practical sense, and will result in an overall simplification of the evaluation of uncertainty with the MLR model for the user. Therefore, the standard deviation for log of displacement from the Youd et al. (2002) MLR model can be approximated as $\sigma_{\log D_{H-fj,gs}} \approx \sqrt{0.0408} \approx 0.2020$.

Unlike Youd et al. (2002), Bardet et al. (2002) formally defined the residual mean square, s^2 for the FFGS4 model as 0.0840, as well as reported the model's covariance matrix. However, since the model has over 450 degrees of freedom, and no individual value in the covariance matrix is greater than 5%, it is reasonable to simplify the uncertainty characterization of the FFGS4 model by approximating the standard deviation of the log of displacement as $\sigma_{\log(D+0.01)} \approx \sqrt{0.0840} \approx 0.2898$, which can be used directly with a Normal distribution. Such a simplification in the uncertainty characterization generally introduces bias of about $\pm 3\%$ or less into the estimate of the uncertainty, which would likely be considered negligible by most

practical standards. However, for situations where such bias would not be acceptable, then it would be necessary to incorporate the residual mean square with the Student's t -distribution and the covariance matrix in order to compute a more accurate estimate of the model uncertainty.

Baska (2002) reports his model uncertainty as $\sigma_{\sqrt{D}} = 0.28$, which can be used directly with a Normal distribution. No covariance matrix for the model parameters was reported by Baska, however.

Assuming the simplifying assumptions regarding model uncertainty discussed above are incorporated, the *probability density function* (PDF) for Youd et al. (2002), Bardet et al. (2002), and Baska (2002) empirical models can be approximated by using a Normal (or Gaussian) distribution, which is given by the following equation:

$$f_x(x) = \frac{1}{\sqrt{2\pi}\sigma_x} e^{-\left(\frac{1}{2}\left(\frac{x-\bar{x}}{\sigma_x}\right)^2\right)} \quad (3-11)$$

where \bar{x} is the mean value and σ_x is the standard deviation of the distribution. By plotting this function, one obtains the familiar bell curve. The probability that a random occurrence of x (represented as X) is less than or equal to a known value of x is equal to the sum of the area under the PDF from $-\infty$ to the known value of x . This probability could be cumulatively summed against x to produce the *cumulative density function* (CDF) and can be represented in equation form as:

$$F_x(x) = P[X \leq x] = \int_{-\infty}^x f_x(x) dx \quad (3-12)$$

Equation (3-12) can be approximated numerically by using a closed-form representation of the CDF developed by Abramowitz and Stegun (1965). This approximation can be written as:

$$F_x(x) \approx 1 - f_x(x) [a_1 t + a_2 t^2 + a_3 t^3] \quad (3-13)$$

$$a_1 = 0.4361836 \quad (3-14)$$

$$a_2 = -0.1201676 \quad (3-15)$$

$$a_3 = 0.9372980 \quad (3-16)$$

$$t = \frac{1}{1 + 0.33267x} \quad (3-17)$$

An often-employed methodology in computing probabilities with these relationships is the use of Z -values. The Z -values compose a standard bell curve with zero mean and unit standard deviation for which CDF values are known for each value of Z . These values are often published in charts or tables known as Z -tables, and are often easily attainable from the appendices of any statistical textbook, most spreadsheet programs, or the internet. The user then needs only to transform the parameters in his or her distribution of interest into Z -values in order to be able to incorporate Z -tables. The relationship between Z -values and x -parameters is given as:

$$Z = \frac{X - \bar{x}}{\sigma_x} \quad (3-18)$$

3.5.1 Special Considerations of Baska (2002) Statistical Procedure

Because the Baska (2002) model calculates the square root of the lateral spread displacement, the model allows the possibility of zero displacement to be calculated. However, using such a model also allows negative square root displacement values to be calculated. Such cases indicate either lower loading or greater resistance than that associated with zero displacement and are therefore interpreted as corresponding to zero displacement.

Bray and Travararou (2007) faced a similar situation with their Newmark-type model that predicted seismic slope displacements, and treated it using a mixed discrete-continuous probability distribution. This type of distribution is demonstrated in Figure 3-4. The probabilities of all the square roots of displacements equal to or less than zero are summed to represent a discrete probability, \tilde{p} , of zero displacement. The remaining square roots of displacement that have values greater than zero are represented using a continuous function. The sum of the area under the continuous portion of the curve is equal to $1 - \tilde{p}$ so that the sum of the area under both the discrete and continuous portions is equal to unity. The discrete portion of the PDF, \tilde{p} can be calculated from the CDF as:

$$P[D = 0 | M, R, S, T_{gs,ff}^*] = \tilde{p} = F_z(z_0) = F_z\left(\frac{0 - \sqrt{D}}{\sigma_{\sqrt{D}}}\right) = F_z\left(\frac{-\sqrt{D}}{0.28}\right) \quad (3-19)$$

3.6 Estimating Lateral Spread Displacement Versus Depth

Although all empirical procedures for estimating lateral spread displacements provide an estimate of the total cumulative displacement at the ground surface, most neglect lateral

displacement prediction with depth. Currently, only strain-based semi-empirical models such as Zhang et al. (2004) and Faris et al. (2006) can claim to predict lateral spread displacements with depth. Knowledge of the lateral strain versus depth is essential for accurately computing the pile response to kinematic loading from lateral spread displacements. In particular, accurate estimation of the strain profile through the non-liquefied soil crust can be crucial to the pile response analysis because many researchers have shown that the non-liquefied soil crust typically governs the pile response during kinematic loading (Abdoun et al., 1996; Abdoun et al., 1997; Berrill et al., 1997; Fujii et al., 1998; Horikoshi et al., 1998; Tokimatsu and Asaka, 1998; Singh, 2002; Boulanger et al., 2003).

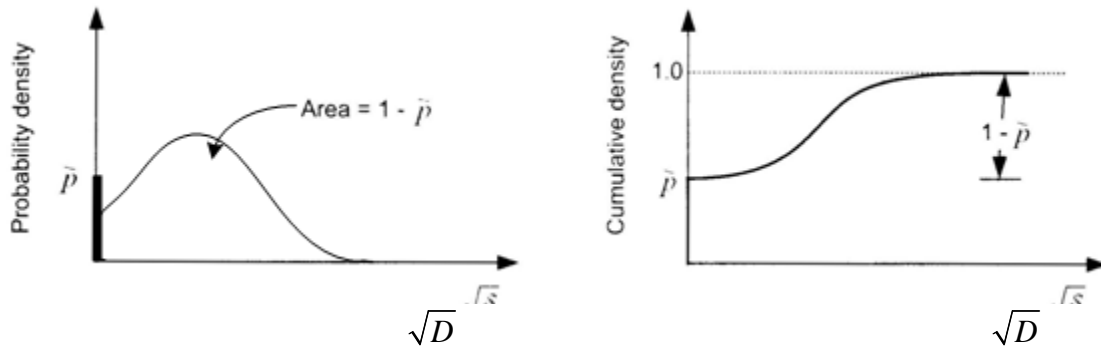


Figure 3-4: Mixed Discrete-Continuous Probability and Cumulative Density Functions

However, despite the critical nature of the problem, lack of both empirical data and knowledge of the mechanics governing lateral spread have forced researchers to develop many simplified assumptions for distributing the predicted surficial lateral spread displacement down

through the rest of the soil profile. These assumptions typically involve distributing the lateral spread displacement through the liquefied soil layer and assuming that the non-liquefied soil crust moves as a coherent block. While such an assumption appears to be an over-simplification of the problem based on the few actual lateral spread strain profiles that researchers have observed (e.g., Holzer and Youd, 2007), this approach appears to produce reasonable pile response results. Previous researchers have recommended linear displacement distributions (Juirnarongrit and Ashford, 2006), quarter-cosine displacement distributions (Cubrinovski and Ishihara, 2004), and half-cosine displacement distributions (Finn and Thavaraj, 2001). One drawback that all of these approaches appear to have in common, however, is that they typically assume that the soil mass behaves as a homogeneous liquefied soil layer, with the exception of the non-liquefied soil crust. Such an assumption erroneously neglects the possible existence of intermediate non-liquefiable soil layers within the liquefied soil mass. Valsamis et al. (2007) developed a model based on many numerical simulations of lateral spreads for estimating displacement versus depth distributions for multi-layered soil systems. Valsamis et al. evaluated one-layer, two-layer, and four-layer liquefied systems, as shown in Figure 3-5.

For a one-layer system (i.e. homogenous liquefied soil), Valsamis et al. (2007) recommend that a sinusoidal displacement distribution be used. For both two-layer systems and four-layer systems, Valsamis et al. recommended that a linear displacement distribution be used. However, investigation of available inclinometer data from actual lateral spreads from the field in layered soil systems such as the Wildlife array (Holzer and Youd, 2007; shown in Figure 3-6) and Moss Landing (Boulanger et al., 1997; shown in Figure 3-7) suggest that sinusoidal displacement distributions are appropriate for even multi-layered systems. Therefore, sinusoidal displacement distributions were incorporated in this study.

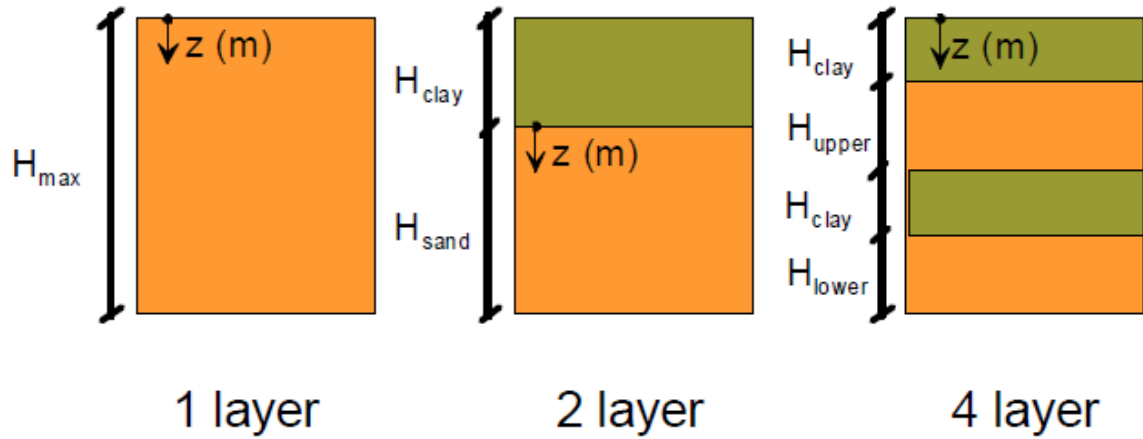


Figure 3-5: Types of Soil Profiles Evaluated Numerically by Valsamis et al. (After Valsamis et al., 2007)

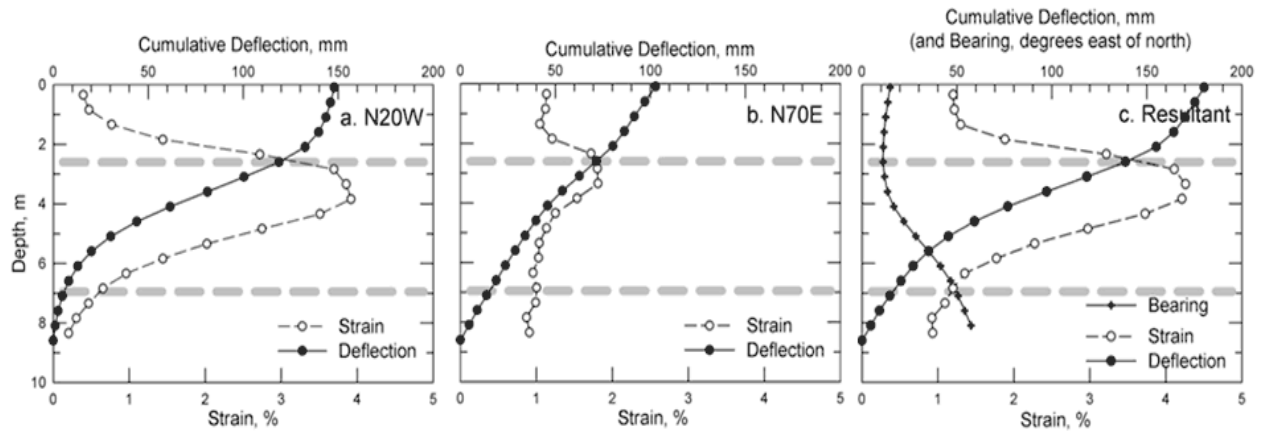


Figure 3-6: Deflection and Strain Profiles at the Wildlife Array (After Holzer and Youd, 2007)

To compute the relative displacements at any relative depth within a given zone of liquefied soil, the sinusoidal displacement distribution can be developed using a half-cosine distribution as:

$$D(z) = D_{bottom} + \cos\left(\pi \cdot \frac{z}{H}\right) \left(\frac{D_{top}}{2}\right) + \left(\frac{D_{top}}{2}\right) \quad (3-20)$$

where D_{bottom} is the total cumulative lateral displacement at the bottom of the liquefied sublayer (equals zero at the bottom of the deepest liquefied layer), z is the relative depth within the liquefied sublayer from the top of the sublayer, H is the total thickness of the liquefied sublayer, and D_{top} is the total cumulative lateral displacement at the top of the liquefied sublayer (equals the total predicted lateral spread displacement at the ground surface).

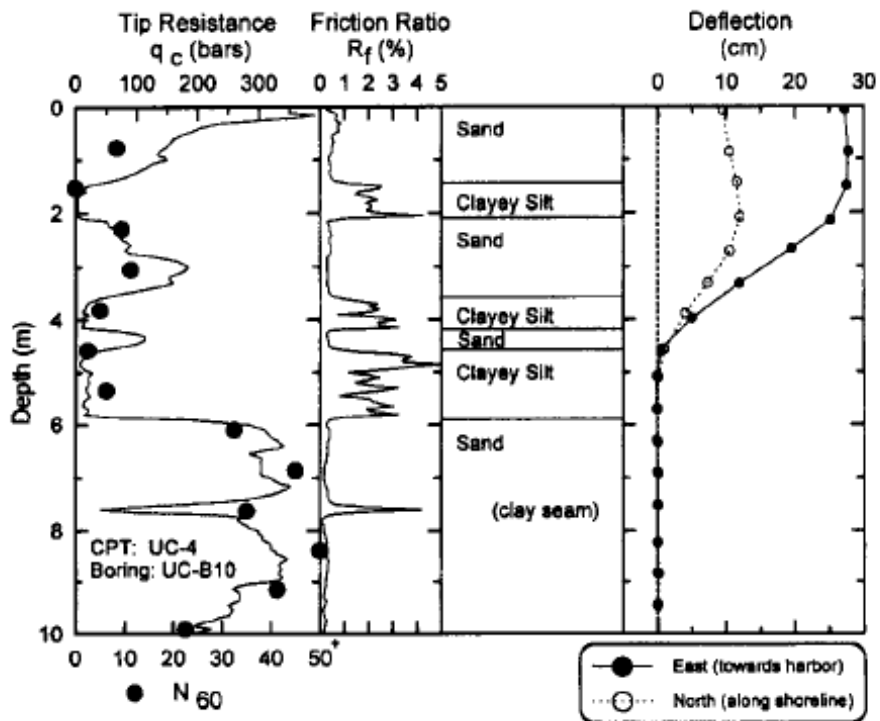


Figure 3-7: Select Deflection Profile From Moss Landing Lateral Spread (After Boulanger et al., 1997)

For a four-layer system, as shown in Figure 3-5, Valsamis et al. (2007) suggest that the relative maximum displacements at the top of the upper and lower liquefiable layers can respectively be estimated as:

$$D_{top,upper} = (1-m)D_{total} \quad (3-21)$$

$$D_{top,lower} = (m)D_{total} \quad (3-22)$$

$$m = \frac{1}{1 + 0.60(H_{upper}/H_{lower})} \quad (3-23)$$

where m is the proportion of the total displacement assigned to the lower liquefied layer, D_{total} is the total predicted lateral spread displacement at the ground surface, and H_{upper} and H_{lower} are the total thicknesses of the upper and lower liquefiable layers, respectively.

Unfortunately, no displacement distribution model for layered liquefied systems larger than four total layers could be found in the literature. Due to a lack of knowledge of such systems, it is reasonable at this time to assume that the total displacement distribution assigned to a given liquefiable layer is proportional to the ratio of the thickness of the liquefiable layer to the cumulative thickness of all the liquefiable layers.

3.7 Depth Limitations When Developing Lateral Spread Displacement Profiles

Observations from both the field and the laboratory suggest that lateral spread is a phenomenon that usually occurs at relatively shallow depths. Intuitively, this makes sense

because it is well known that shear stresses resulting from the presence of a free face or some slope gradient at the ground surface tend to decrease with depth, and lateral spread is known to be a function of shear stress. Therefore, it would make sense that lateral spread hazard generally decreases with depth. The question then becomes: “At what depth can lateral spread displacement typically be neglected?”

The correct response to this question is that it depends on the site-specific dynamic properties and stress history of the soils, the potential ground motions affecting the site, and the site geometry. In some cases where there is an obvious continuous and relatively shallow liquefiable soil layer overlying a dense/stiff non-liquefiable layer, it is easy to identify the maximum depth at which lateral spread displacements would likely occur. However, in other cases it is not quite as simple to identify this depth. For such cases, one could develop a complex numerical model to attempt to predict the maximum depth at which lateral displacements could occur given a design ground motion. This approach is routinely applied in industry on very large and/or critical projects where such knowledge is considered essential to evaluating the performance of the proposed structure or adjacent existing structures. However, for the majority of the projects in industry today, most engineers generally appear comfortable applying simple “rules of thumb” for estimating the maximum depth for consideration of lateral spread displacements.

Youd et al. (2002) indicated that their data showed no lateral spread when the top of the liquefied soil layer (i.e. the top of the first soil layer to be included in the computation of T_{15}) was at a depth greater than 10 meters (approximately 33 feet) below the native ground surface. In addition, Youd (personal communication, 2009) indicated that, based on his experience and observations, lateral spread should rarely occur at depths greater than about 13.7 meters (45 feet)

below the native ground surface for ground slope cases, and at depths greater than about two-times the free-face height below the native ground surface (one free-face height below the slope toe) for free-face cases. Therefore, this study adopts the simplified recommendations made by Youd in developing depth limitations for lateral spread displacement profiles.

3.8 Chapter Summary

Lateral spread is the horizontal deformation of gently sloping or free-faced soil resulting from seismically-induced soil liquefaction. Lateral spread is one of the most common forms of liquefaction-related soil deformation, and most often occurs on gradual slopes or adjacent to free-faces (e.g. bodies of water, quay walls, channels, etc.). Because lateral spread is a product of soil liquefaction, it is important to first evaluate the liquefaction hazard before considering lateral spread itself.

If an engineer determines that site conditions are such that the occurrence of cyclic mobility is probable, then lateral spread should be considered. Lateral spread has caused significant damage to infrastructure bordering bodies of water over the past several decades. Several studies have been conducted by researchers during that time to try and better understand the mechanics of lateral spread and accurately model its occurrence. These studies have been carried out with shake tables and centrifuges, as well as cyclic triaxial, direct simple shear, and torsional shear devices. These studies suggest that lateral spread is strongly correlated with such factors as the slope of the ground, the thickness of the liquefiable layer, and the characteristics of the cyclic loading. These studies have also resulted in the creation of several types of analyses that attempt to predict the displacements resulting from lateral spread, and can be divided into two main categories: analytical analyses and empirical analyses.

Analytical methods include such models as sliding block, elastic beam, and finite element. Empirical methods are generally expressed in the form of multiple-linear regression equations developed from lateral spread case histories. Many engineers prefer empirical methods over analytical methods due to their convenience. However, to be used correctly, empirical lateral spread models should be utilized within the bounds and limitations recommended by the authors of the models.

Several empirical and semi-empirical models for estimating lateral spread displacements were briefly discussed in this dissertation. However, particular attention was paid to the Youd et al. (2002), Bardet et al. (2002), and Baska (2002) empirical models. While these procedures are generally applied in a deterministic manner, it is possible to incorporate estimates of the variance for each model into the analysis, thus accounting for uncertainty in the computation of lateral spread displacements. Such incorporation of uncertainty becomes of prime importance in the performance-based evaluation of lateral spread, which will be discussed later in this dissertation.

While there is generally a large amount of uncertainty involved with the distribution of lateral spread displacements with depth in a given soil profile, a simplified procedure for estimating lateral spread displacements with depth in multi-layered systems was summarized. This procedure can be incorporated with empirical estimation of lateral spread displacements at the ground surface to estimate lateral displacements at various depths within a given soil profile. Such information will be necessary for the computation of kinematic pile response.

Finally, it is generally well known that lateral spread is a phenomenon that occurs in liquefied soils located at relatively shallow depths. However, for many situations, it is necessary to estimate the maximum depth in the soil profile at which lateral spread displacements could be expected to occur. For large, critical, and/or expensive projects in industry today, complex

numerical models are often used to compute this maximum depth. However, for most practical projects, most engineers appear comfortable using simplified rules of thumb to estimate the maximum depth of lateral spread displacement. Following the recommendations of Youd, a maximum depth of 13.7 meters (45 feet) below the native ground surface will be used for ground slope cases, and a maximum depth equal to two-times the free face height below the native ground surface will be used for free face cases.

4 REVIEW OF KINEMATIC PILE RESPONSE ANALYSIS

4.1 Introduction

Since the mid-to-late 1990s, engineers and researchers have developed methodologies to analyze the response of pile and shaft foundation systems to seismically-induced loading from lateral soil movement, or *kinematic loading*. These methodologies were developed in response to severe damage observed to pile/shaft foundations following large earthquakes such as 1964 Niigata, Japan; 1964 Prince William Sound, Alaska; 1989 Loma Prieta, California; 1994 Northridge, California; and 1995 Kobe, Japan. In particular, the massive 1995 earthquake in Kobe, Japan appeared to spark a firestorm of research interest in the topic of kinematic pile response analysis, and many of the modern methods that are utilized in industry today to analyze the kinematic response of piles came about due to this research.

This chapter will briefly present some of the basic background behind the very complex and often controversial topic of kinematic pile response analysis. A brief discussion of the differences between kinematic and inertial loading of piles will be provided. A simplified procedure that is commonly used in engineering practice today to perform kinematic pile response analysis will be presented, and each part of that procedure will be briefly discussed.

4.2 Kinematic Versus Inertial Loading of Piles

When a pile foundation and the structure that it is supporting are shaken by an earthquake event, there are two types of loading which can affect the foundation system:

- 1) Inertial Loading – forces are a result of the accelerated mass of the superstructure and the pile cap transferring dynamic loads to the piles; and
- 2) Kinematic Loading – forces are a result of differential displacements between the pile and the surrounding soil. These differential displacements can occur as a result of wave passage effects or permanent soil deformations such as liquefaction-induced lateral spread displacement.

Figure 4-1 demonstrates how inertial and kinematic loading may interact for a given structure and foundation system.

Studies from case histories (Yoshida and Hamada, 1990; Tokimatsu and Asaka, 1998; Fujii et al., 1998) and small-scale physical models (Abdoun et al., 1996; Adachi et al., 1998; Singh, 2002) suggest that pile and shaft foundations can be critically damaged by either type of loading, or by a combination of both. As such, many researchers such as Boulanger et al. (2007) recommend that both the inertial and kinematic loads should be simultaneously accounted for in the pile response analysis. Boulanger et al. recommend following the methodology developed by Chang et al. (2005), Chang et al. (2006), and Chang (2007) to account for inertial loading in the kinematic pile response analysis. This methodology attempts to modify (i.e. reduce) the peak inertial loads in order to account for the damping effects of liquefaction. According to this methodology, the maximum or peak inertial load in the presence of liquefied soil can be computed as:

$$I_{CC_liq} = C_{CC} \cdot C_{liq} \cdot I_{max_nonliq} \quad (4-1)$$

where I_{max_nonliq} is the maximum or peak inertial load when no liquefied soil is present, C_{CC} is the fraction of the maximum inertial load with liquefaction that occurs at the critical loading cycle (i.e., when the maximum pile bending moments and shear forces occur), and C_{liq} is the ratio of the maximum inertial load with liquefaction versus without liquefaction. Recommended values of C_{CC} and C_{liq} are shown below in Table 4-1, where ZPA is the zero-period acceleration or peak ground acceleration.

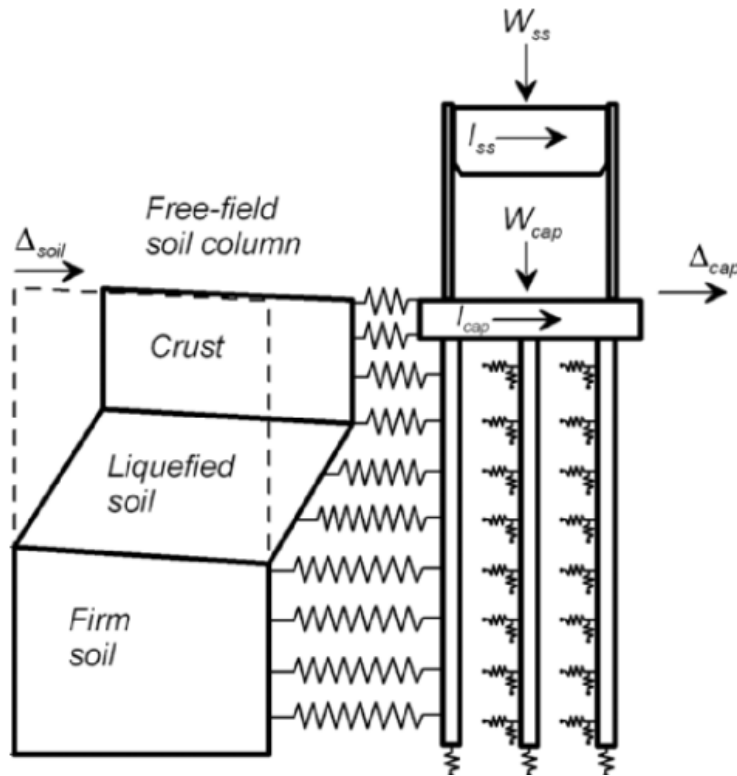


Figure 4-1: Inertial and Kinematic Loading of a Foundation System (After Boulanger et al., 2007)

Table 4-1: Coefficients to Account for Inertial Loading With Kinematic Loading in Liquefied Soil (After Boulanger et al., 2007)

Motion* ($Sa_{T=1s}/ZPA$)	Pile cap		Superstructure	
	C_{liq}	C_{cc}	C_{liq}	C_{cc}
Long period (1.7–2.4)	1.4	0.85	0.75	0.65
Medium period (0.5–1.6)	0.75	0.85	0.55	0.65
Short period (≤ 0.4)	0.35	0.85	0.45	0.65

While much research has demonstrated that a combination of kinematic and inertial loading can be damaging to pile foundations, many engineers feel that coupling the inertial and kinematic response in the same analysis is overly conservative. They cite that such an analysis makes the inherent assumption that peak inertial displacements are occurring in phase with peak kinematic displacements, which they argue is relatively unlikely to occur in reality. In addition, these engineers argue that peak kinematic displacements (i.e., permanent lateral spread displacements) often can occur near the end of the strong ground motion, which is typically after most of the large ground motion pulses have occurred from the earthquake event. Therefore, most pile response analyses performed in industry today consider the kinematic response and the inertial response separately, allowing the design of the pile foundation system to be governed by the more critical of the two responses.

Because this study is specifically concerned with only the kinematic portion of the pile response due to loading from lateral spread displacement, the inertial portion of the pile response will be neglected in this study. However, Juirnarongrit and Ashford (2006) emphasize that a peak combination of inertial and kinematic loads during earthquake shaking may be higher than the response at the end of shaking due to kinematic loading from lateral spread alone, and that for

actual engineering design, an evaluation should be conducted to select the critical design load case and investigate whether a coupled inertial and kinematic response would be applicable to the specific case being analyzed. To aid with this evaluation, both Boulanger et al. (2007) and Tokimatsu et al. (2005) suggest that stiffer structures (i.e., structures whose natural periods are less than the natural period of the liquefied ground) are more likely to be damaged by a combination of inertial and kinematic loading than softer structures.

4.3 Estimation of Lateral Spread Soil Deformations

Estimating the magnitude of seismic-induced soil deformations is a topic that was discussed at length in Chapter 3, and will therefore not be discussed in greater detail here. While it is recognized that there are many methods for estimating permanent lateral spread deformations (e.g., numerical models, Newmark sliding block analyses, empirical models), this study will focus on utilizing empirical models to estimate lateral spread displacements. This selection is in no way intended to minimize the potential effectiveness or appropriateness of other methods for computing permanent ground deformations. The two principal reasons that empirical methods were chosen for this study are: 1) empirical methods are commonly used in engineering practice to predict regional lateral spread displacements, and are therefore familiar to most practicing professionals; and 2) Kramer et al. (2007) demonstrated how a given empirical lateral spread model could be incorporated into a probabilistic hazard integral, thus making its incorporation into a performance-based framework more convenient than other methods for computing lateral spread displacements.

There are some important limitations that must be addressed when using empirical models to estimate permanent lateral spread displacements for use in a pile response analysis.

Empirical lateral spread models are typically intended to be used with soil data representing a generalized average over a relatively large area. The existence of discontinuous or highly heterogeneous soil layering across a given site would likely disqualify the appropriate use of empirical models to compute lateral spread displacements. In addition, the incorporation of lateral spread remediation measures such as passive pin piles or ground improvement (e.g., stone columns or jet grouting) cannot properly be accounted for in the computation of permanent horizontal ground deformations in an empirical lateral spread model. Perhaps the only exception to this observation would be remediation through deep dynamic compaction (DDC) simply because DDC does not incorporate any structural reinforcement and is generally performed over a large area. In general, if lateral spread remediation measures are to be accounted for in the computation of lateral spread displacements, a numerical or Newmark-based approach might be more appropriate because it would be able to account for the presence of the structural reinforcement placed at specific locations in the model. Investigation of such approaches, however, is beyond the scope of this study.

A final consideration in the estimation of soil deformations for kinematic pile response analysis is the potential for liquefaction flow failure to occur in the vicinity of the foundation. This type of failure is almost exclusive to free-faces, steep gradients, or other conditions where considerable shear stresses may exist in the soil. For ground slope conditions with a gradient less than 5% (i.e., 3 degrees), flow failure would not likely occur (Youd, 2005). For all other conditions, however, one may evaluate the possibility of a liquefaction flow failure by performing a simple two-dimensional limit equilibrium stability analysis incorporating residual strengths for the soil layers predicted to liquefy under the design ground motions, and typically incorporating a 20% reduction in the undrained strength for the rest of the soil layers not

predicted to liquefy under the design earthquake ground motions in order to account for effects of cyclic loading (Makdisi and Seed, 1977). A stability factor of safety less than unity would suggest that the post-seismic strength of the native soils would not be sufficient to bear the static shear stresses in the soil due to the steep gradient or presence of the free-face, and large horizontal and vertical deformations would likely result. Currently, there is no widely-accepted procedure for computing the soil deformations from a liquefaction flow failure, and if such a condition is evaluated to be a possibility under the design earthquake loads, then liquefaction remediation methods generally are required in accordance with the standard of engineering practice in the region of interest. Theoretically, one could still perform a kinematic pile response analysis for a flow failure by simply applying a very large horizontal soil deformation on the order of several of meters to the model. However, the large number of uncertainties associated with a liquefaction flow failure and the computation of soil-pile interaction under such conditions would call into question the validity of the results of the analysis. A demonstration of a post-liquefaction limit equilibrium model where flow liquefaction is predicted is shown in Figure 4-2.

4.4 Computing Kinematic Pile Response

Many methodologies have been developed by researchers over the years to analyze the soil-pile interaction effect resulting from a given lateral spread event. These methodologies vary greatly in their approach and complexity, ranging from a simplistic generalization of lateral pressures using limit equilibrium methods (e.g., Ledezma and Bray, 2010; He et al., 2009; Gonzalez et al. 2005; Cubrinovski and Ishihara, 2004; Dobry et al. 2003; Haigh 2002; Haigh and Madabushi 2002; JRA, 2002) to advanced numerical models (e.g., Cheng and Jeremic, 2009;

Lam et al., 2009; Arduino et al., 2006; Yang et al. 2003; Finn and Thavaraj, 2001; Li and Dafalius 2000).

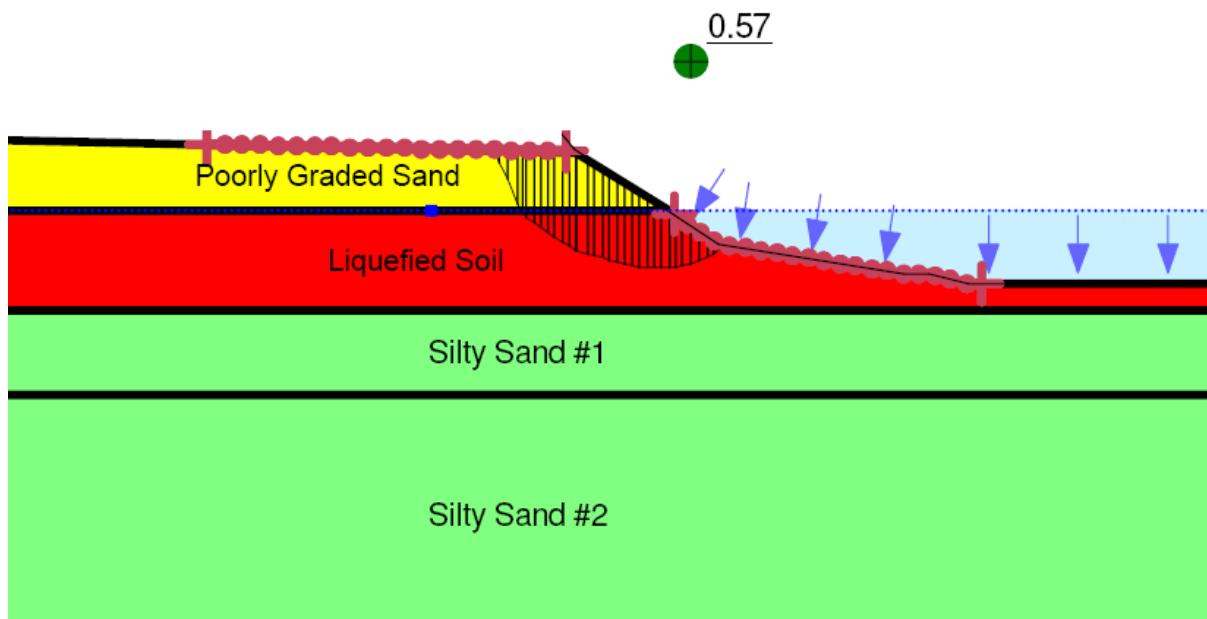


Figure 4-2: Example of a Post-Liquefaction Limit Equilibrium Analysis Evaluating the Potential for Liquefaction Flow Failure

Representation of lateral soil resistance using p-y soil springs in a Beam-on-Winkler Foundation (BWF) method is a popular method among practicing engineers to evaluate both the inertial and the kinematic pile response in liquefied and/or laterally spread soil. As noted by Juirnarongrit and Ashford (2006), this method is often preferred over more simplistic limit equilibrium methods due to its ability to estimate pile displacements. Juirnarongrit and Ashford also note that BWF methods are often preferred over more complex methodologies such as 3D numerical models due to the advanced nature of numerical modeling in general and their inherent

dependency on a reliable constitutive model. Therefore, despite its relative simplicity, the BWF method has repeatedly been demonstrated to provide reasonable representation of the observed inertial and kinematic response of single piles and pile groups in both the laboratory and in the field (Wilson et al., 2000; Tokimatsu et al., 2001; Ashford and Rollins, 2002; Boulanger et al., 2003; Tokimatsu and Suzuki, 2004; Brandenberg, 2005; Rollins et al. 2005; Weaver et al. 2005; Juirnarongrit and Ashford 2006; Brandenberg et al. 2007).

Juirnarongrit and Ashford (2006) presented a simplified procedure to compute the average kinematic response of a pile group using p-y soil springs and the BWF method of analysis. The procedure was based heavily on the work of Mokwa (1999) and Mokwa and Duncan (2003), and it develops an equivalent “single” pile to represent the average soil-pile response behavior of the group and the pile cap. However, Juirnarongrit and Ashford warn that their procedure uses a simplified pseudo-static push over analysis to solve what in reality can be a very complex problem, and caution and engineering judgement should be applied when interpreting the analysis results from their procedure. Furthermore, they recommend that for the design of important and/or critical structures, additional analysis such as numerical modeling should be used for redundancy and to validate the computed results from their simplified procedure.

4.4.1 p-y Analysis Methodology

Juirnarongrit and Ashford (2006) note that BWF procedures are most commonly used by engineers today to evaluate inertial loading of a pile. However, they point out that BWF procedures can also reliably compute the kinematic response of pile loading as well. Reese et al. (2000) originally demonstrated a BWF p-y procedure to analyze the kinematic loading of a pile,

and their approach is well-summarized in Juirnarongrit and Ashford (2006). This approach is demonstrated in Figure 4-3 below.

If the soil mass surrounding the pile is stationary, then the p - y curve for the soil is symmetrical about the p -axis, as shown for curve 1 in Figure 4-3. The pile response for this case can be computed by solving the following differential equation:

$$EI \frac{d^4 y_p}{dz^4} - p y_p = 0 \quad (4-2)$$

where EI is the pile stiffness, p is the soil reaction per unit length of pile, y_p is the pile displacement, and z is the depth.

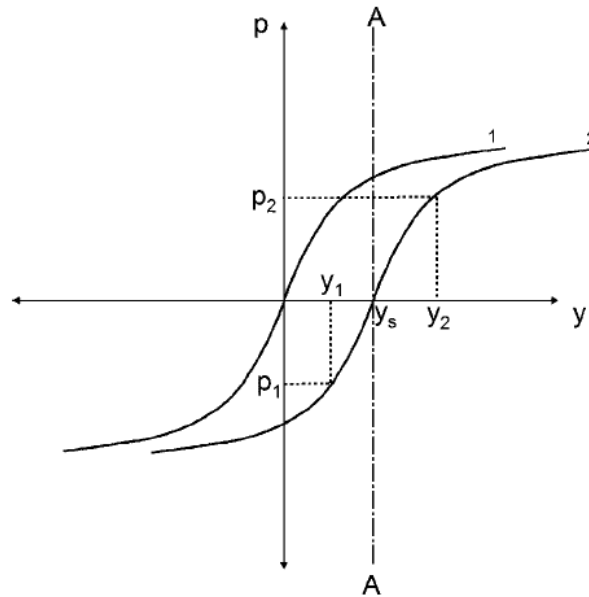


Figure 4-3: Depiction of Procedure for Using p - y Curves to Account for the Kinematic Loading of Piles (After Juirnarongrit and Ashford, 2006; Modified From Reese et al., 2000)

However, if the soil mass moves relative to the pile, then the soil resistance curve (curve 2) is offset by the soil movement. Therefore, if the pile movement, y_p is less than the soil movement, y_s , then the soil applies a driving force (p_1) to the pile. However, if the pile movement is greater than the soil movement, then the soil provides a resistance force (p_2) to the pile. Thus, to compute the response of the pile from kinematic loading using a p-y analysis, the free-field soil movement must be applied as a boundary condition to the Winkler soil springs in the BWF model, as demonstrated in Figure 4-4 .

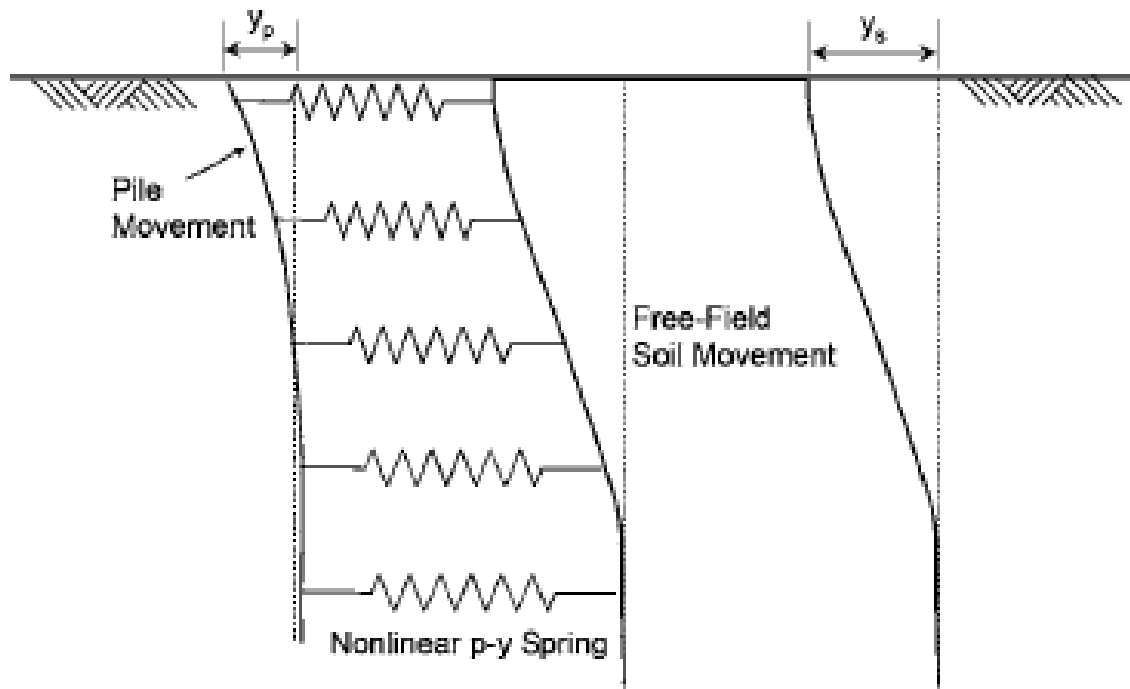


Figure 4-4: p-y Analysis Model for Kinematic Loading (After Juirnarongrit and Ashford, 2006)

The pile response for the p-y soil springs shown in Figure 4-4 can then be computed by solving the following differential equation:

$$EI \frac{d^4 y_p}{dz^4} - p(y_p - y_s) = 0 \quad (4-3)$$

Juirnarongrit and Ashford (2006) note that Equation (4-3) can be solved by using either finite difference or finite element methods. The popular lateral pile response computer software LPILE Plus 5.0 (Ensoft, 2004) incorporates finite difference methods to solve the differential equation. All pile response analyses in this study were performed using LPILE software.

4.4.2 p-y Development for Soil Layering

Because BWF analysis incorporates soil spring models, often called p-y curves, some discussion regarding selection of p-y curves is merited. For a soil layer at a given site, p-y curves can be developed from site-specific lateral load pile tests (e.g., Hales, 2003; Bowles, 2005) by measuring strains in the pile and integrating curvature and slope to obtain pile deflections, y , while also differentiating bending moment and shear force to obtain the distributed soil load or pressure, p . This site-specific approach is diagrammed in Figure 4-5.

Due to the relatively high cost and complex logistics of performing and analyzing site-specific lateral pile load tests, most engineers in practice today choose to use published p-y curve models for various generalized soil types rather than develop site-specific p-y curves. Such curves include Matlock (1970) for soft clay, Reese et al. (1974) for sand, and Reese et al. (1975) for stiff clay beneath the water table. Generalized p-y curves typically require the user to characterize the soil with properties such as friction angle, undrained strength, confining stress,

and p-y modulus. These curves can usually provide a reasonable approximation of the p-y behavior of most soils as long as the user accurately characterizes the properties of the soil.

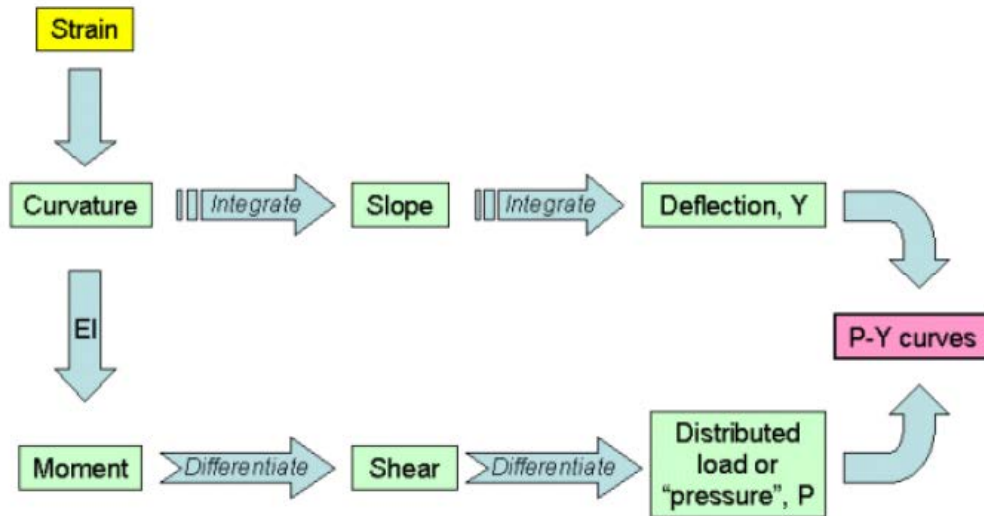


Figure 4-5: Process for Computing Site-Specific p-y Curves From the Measurement of Pile Strain (After Hales, 2003)

Although there is relatively little discord among researchers and engineers regarding p-y behavior of typical soils such as sands and clays, there is considerable uncertainty and disagreement regarding the p-y behavior of liquefied soil. The reason for this uncertainty is due to the complex behavior of liquefied soil and our inability to predict that behavior under variable conditions. Currently, there are three methods commonly used by practicing engineers to model the p-y behavior of liquefied soil. The first method, presented by Wang and Reese (1998), uses the Matlock (1970) p-y model for soft clay to represent the soil resistance behavior of the liquefied soil. With this approach, the soil pressure per unit length of pile can be computed as:

$$p = 0.5 p_u \left[\frac{y}{2.5(\varepsilon_{50})b} \right]^{1/3} \quad (4-4)$$

$$p_u = \min \left\{ \left[3 + \frac{\gamma'}{c} z + \frac{J}{b} z \right] cb, 9cb \right\} \quad (4-5)$$

where y is the relative differential displacement between the pile and soil, p_u is the ultimate soil resistance per unit length of pile, γ' is the average effective unit weight of the soil, z is the depth of interest from the ground surface, c is the shear strength of the soil at depth z (represented by the residual shear strength S_r in the case of liquefied soil), b is the width of the pile, J is a model factor typically equal to 0.5 for soft soils, and ε_{50} is the strain corresponding to one-half the maximum principal stress difference (recommended by Wang and Reese (1998) to be 0.05 for liquefied soil).

The second commonly-used method for computing the p-y behavior of liquefied soil was presented by Rollins et al. (2005) and was developed from full-scale lateral pile load tests in blast-induced liquefied soil. This procedure is recognized for capturing the strain-hardening behavior of medium-dense liquefied soils that is known to occur during phase transformation. As such, this method should only be applied to liquefiable soils with relative densities greater than about 40%. In addition, caution should be applied when using this procedure to model kinematic loading of a pile because it was calibrated against relatively small relative displacements between the soil and pile (i.e. inertial loading). The soil pressure per unit length of pile (kN/m) for this procedure is given as:

$$p = A(By)^C (p_d) \quad (4-6)$$

where $A = 3 \times 10^{-7} (z+1)^{6.05}$, $B = 2.80(z+1)^{0.11}$, $C = 2.85(z+1)^{-0.41}$, $p_d = 3.81(\ln d) + 5.6$, y is the relative displacement between the pile and the soil in millimeters, z is the depth in meters, and d is the diameter or width of the pile in meters.

The third commonly-used method for computing the p-y behavior of liquefied soil is to apply a simple reduction factor (i.e. p-multiplier) to the p-y curve for a non-liquefied sand such as API (1993). Liu and Dobry (1995) performed a series of centrifuge tests with sand and observed p-multipliers of approximately 0.1. Tokimatsu (1999) found that p-multipliers ranging from 0.05 to 0.2 well-represented the observed performance of piles subjected to lateral spread in the field. Wilson (1998) and Wilson et al. (2000) performed a series of centrifuge tests and observed that p-y behavior in liquefied soil was strongly related to the initial relative density of the soil, back-calculating p-multipliers ranging from 0.1 to 0.35 as a result. More recently, Brandenberg (2005) and Brandenberg et al. (2007) correlated p-multipliers with $N_{1,60,CS}$. These p-multipliers range from 0.0 to approximately 0.5. Because the Brandenberg et al. (2007) procedure is widely used among practicing engineers today, it will be the only p-multiplier procedure summarized in this dissertation. According to the Brandenberg et al. procedure, the p-y behavior for a non-liquefied sand can be computed using a modified form of the API (1993) p-y model for sand. According to the modified API (1993) procedure, the governing ultimate soil resistance of the sand must be computed as:

$$p_u = \min \begin{cases} p_{u1} \\ p_{u2} \end{cases} \quad (4-7)$$

where

$$p_{u1} = (c_1 x + c_2 b) \gamma' x \quad (4-8)$$

$$p_{u2} = c_3 b \gamma' x \quad (4-9)$$

$$c_1 = \frac{k_0 \tan \phi \sin \beta}{\tan(\beta - \phi) \cos \alpha} + \frac{\tan^2 \beta \tan \alpha}{\tan(\beta - \phi)} + k_0 \tan \beta (\tan \phi \sin \beta - \tan \alpha) \quad (4-10)$$

$$c_2 = \frac{\tan \beta}{\tan(\beta - \phi)} - \tan^2 \left(45 - \frac{\phi}{2} \right) \quad (4-11)$$

$$c_3 = k_0 \tan \phi \tan^4 \beta + \tan^2 \left(45 - \frac{\phi}{2} \right) \quad (4-12)$$

γ' represents the buoyant unit weight, b is the width or diameter of the pile/shaft, x is the depth below the ground surface, ϕ is the soil friction angle, and $\beta = 45 + \frac{\phi}{2}$. According to Boulanger et al. (2003), k_0 and α are typically assumed to be equal to 0.4 and $\frac{\phi}{2}$, respectively. Once the value of p_u is computed, the soil resistance per unit length of pile for non-liquefied sand can be computed as:

$$p = A(p_u) \tanh \left(\frac{k^* x}{A p_u} y \right) \quad (4-13)$$

$$A = 3 - 0.8 \left(\frac{x}{b} \right) \geq 0.9 \quad (4-14)$$

where y is the relative movement between the soil and the pile/shaft and k^* is the modified subgrade modulus corrected for overburden pressure. According to Boulanger et al. (2003), the modified subgrade modulus can be computed as:

$$k^* = \sqrt{\frac{\sigma'_{ref}}{\sigma'_v}} k \quad (4-15)$$

where k is the initial subgrade modulus recommended by the API (1993) criteria for sand, σ'_v is the vertical effective stress at the depth x , and σ'_{ref} is the reference stress at which k is calibrated (recommended to be 50 kPa or 7.25 psi by Boulanger et al., 2003). Finally, with the computation of the non-liquefied soil resistance p , the liquefied soil resistance can be computed as:

$$p_{liq} = (m_p) p \quad (4-16)$$

where m_p is the p-multiplier and can be obtained from the shaded region shown in Figure 4-6.

While three commonly-used procedures for computing p-y behavior of liquefied soils have been briefly discussed in this dissertation, the obvious question becomes: “Which procedure will be incorporated in this study.” While under certain conditions, the Rollins et al. (2005) dilative p-y procedure may provide an accurate representation of the soil resistance behavior for medium-dense liquefiable soils, the fact that the procedure has not been validated in literature against very large kinematic soil displacements makes its use questionable for this project. The use of the Wang and Reese (1998) procedure in this study is questionable due to the

current disagreement among practicing engineers and researchers regarding the “best” approach to use for estimating the residual strength of a liquefied soil, which can ultimately have an enormous effect on the computed p-y behavior. Therefore, although the Brandenburg et al. (2007) p-multiplier approach does not accurately capture the dilative behavior of medium-dense liquefiable soils and likely over-predicts the soil resistance at small strains, it has been demonstrated repeatedly to provide reasonable results at very large soil strains often representative of lateral spreads. Therefore, the Brandenburg et al. (2007) p-multiplier procedure has been selected to represent the p-y behavior of liquefied soils in this study. However, other p-y models may be substituted into the procedure presented in this study at the discretion of the engineer if deemed more appropriate. In addition, as new p-y models for liquefied soil are developed in the future, they should be compatible with this procedure and may replace the Brandenburg et al. p-multiplier approach if desired.

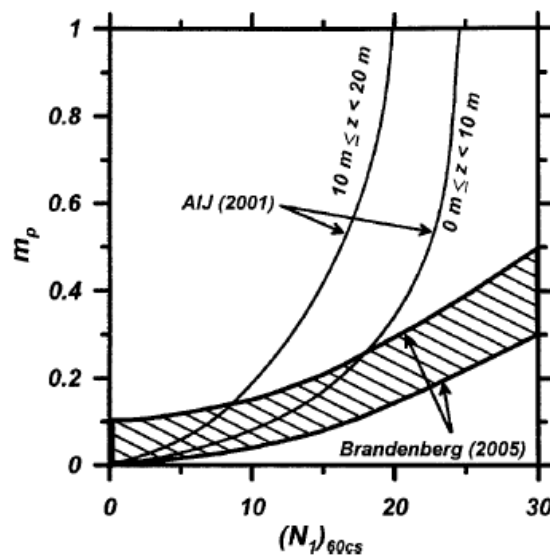


Figure 4-6: Recommended p-Multipliers to Compute p-y Behavior of Liquefied Sand (After Brandenburg et al., 2007)

4.4.3 Equivalent Single Pile for Kinematic Group Response

The procedure presented by Juirnarongrit and Ashford (2006) to model the kinematic pile response of a group as an equivalent “single” pile will now be summarized. As stated earlier, this procedure is based heavily on the work of Mokwa (1999) and Mokwa and Duncan (2003), and is intended to provide the average kinematic response for a single pile in a pile group. The procedure is not able to account for battered piles unless the entire pile group is battered; however, the current engineering standard of practice in most areas appears to neglect the battering of select piles in a pile group in the kinematic pile response analysis in order to be conservative. If it is desired to know the pile response of a particular row of piles, or if complexities such as pile batter or non-typical foundation geometries are desired to be accounted for, then a more sophisticated approach such as a numerical model should be employed by the analyst.

4.4.3.1 Development of the Equivalent Single Pile

Mokwa (1999) suggested that a pile group could be converted to an equivalent single pile by computing the flexural stiffness of a single pile in group, multiplying that stiffness by the number of total piles in the group, and then reducing the p-y soil springs in the model to account for pile group (i.e. pile shadowing) effects. Therefore, the soil spring resistance in the equivalent single pile model can be computed as:

$$p = \sum_{i=1}^N p_i (f_m)_i \quad (4-17)$$

where p_i is the soil spring resistance computed for a single pile, $(f_m)_i$ is the group reduction p-multiplier for the row containing the given pile i , and N is the total number of piles in the group. Several studies have been performed to estimate the group reduction p-multiplier including Brown and Reese (1985), Morrison and Reese (1986), McVay et al. (1994, 1995), Rollins et al. (1998), Ashford and Rollins (2002), and Rollins et al. (2006). For this study, the Rollins et al. (2006) procedure was incorporated for estimating group reduction p-multipliers. According to the Rollins et al. procedure, the group reduction multiplier for a given row in a pile group is computed as:

$$\left. \begin{array}{l} f_m = 0.26 \ln(S/D) + 0.5 \leq 1.0 \\ f_m = 0.52 \ln(S/D) \leq 1.0 \\ f_m = 0.60 \ln(S/D) - 0.25 \leq 1.0 \end{array} \right\} \left\{ \begin{array}{l} \text{Leading Row of Piles} \\ \text{Second Row of Piles} \\ \text{Third and Higher Rows of Piles} \end{array} \right\} \quad (4-18)$$

where S is the uniform center-to-center spacing between the piles, and D is the diameter of the piles.

Figure 4-7 demonstrates the equivalent single pile procedure for a simplified four-pile group geometry. Recommendations regarding the rotational soil spring for the pile cap shown in Figure 4-7 will be summarized in the following section.

The equivalent single pile approach can easily be incorporated into a linear elastic pile response analysis in a software program such as LPILE Plus 5.0. However, it cannot directly be incorporated into a nonlinear pile response analysis because most nonlinear pile response algorithms compute the flexural stiffness of just a single pile. CalTrans (2011) recently published

a guideline for manually incorporating a simplified nonlinear approach into an LPILE Plus 5.0 analysis with an equivalent single pile. The steps presented in that guideline are summarized as:

- 1) Develop a moment-curvature curve for a single pile.
- 2) Scale the moment in the M- ϕ curve by the number of piles in the pile group.
- 3) Determine the yield curvature, ϕ_y , from the M- ϕ plot and calculate the allowable curvature as $\phi_a = 12(\phi_y)$. Extend the M- ϕ curve to point $(\phi_a, 1.1 M_{max})$.
- 4) M-EI values are calculated at several points along the curve using the fact that $EI=M/\phi$. Input these values of M-EI as user-defined moment-stiffness curves in LPILE.

A figure showing an M- ϕ curve and an M-EI curve is shown in Figure 4-8.

4.4.3.2 Resistance of the Pile Cap and Development of the Rotational Soil Spring

The phenomenon of lateral spread has often been observed to cause a rotation in the cap of the pile groups. This rotation is due to the tendency of the back row of piles in the group (i.e. the piles fronting the lateral spread displacements) to be pulled down, while concurrently the leading row of piles are pulled up. Mokwa (1999) and Mokwa and Duncan (2003) theorized that a rotational stiffness coefficient could be developed to describe this observed behavior. According to their work, the rotational stiffness of the pile group can be estimated as:

$$k_{m\theta} = \frac{M}{\theta} \quad (4-19)$$

where M is the restraining moment from the piles that resists rotation, and θ is the angular rotation of the pile head. Juirnarongrit and Ashford (2006) state that the value of $k_{m\theta}$ can be estimated from the ultimate restraining moment M_{ult} and the ultimate angular rotation θ_{ult} if a

linear relationship is assumed between M and θ up to the ultimate restraining moment. This assumption is demonstrated in Figure 4-9.

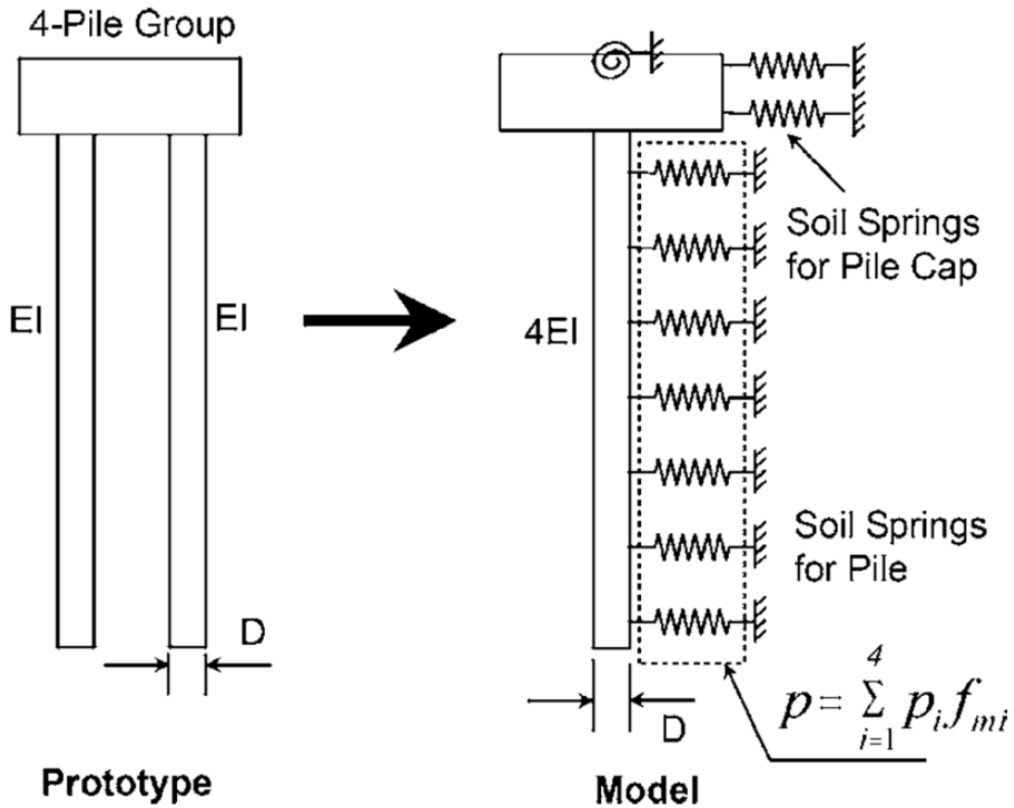


Figure 4-7: Equivalent "Single" Pile for a Simplified Four-Pile Group (After Juirnarongrit and Ashford, 2006)

The ultimate resisting moment from a pile group can be computed as:

$$M_{ult} = \sum_{i=1}^N \left[(Q_s)_i + (Q_p)_i \right] X_i \quad (4-20)$$

where $(Q_s)_i$ is the skin friction resistance for pile i , $(Q_p)_i$ is the end bearing resistance for pile i , X_i is the moment arm for pile i , and N is the total number of piles in the pile group. Note that for upward-moving piles, $(Q_p)_i$ is equal to zero.

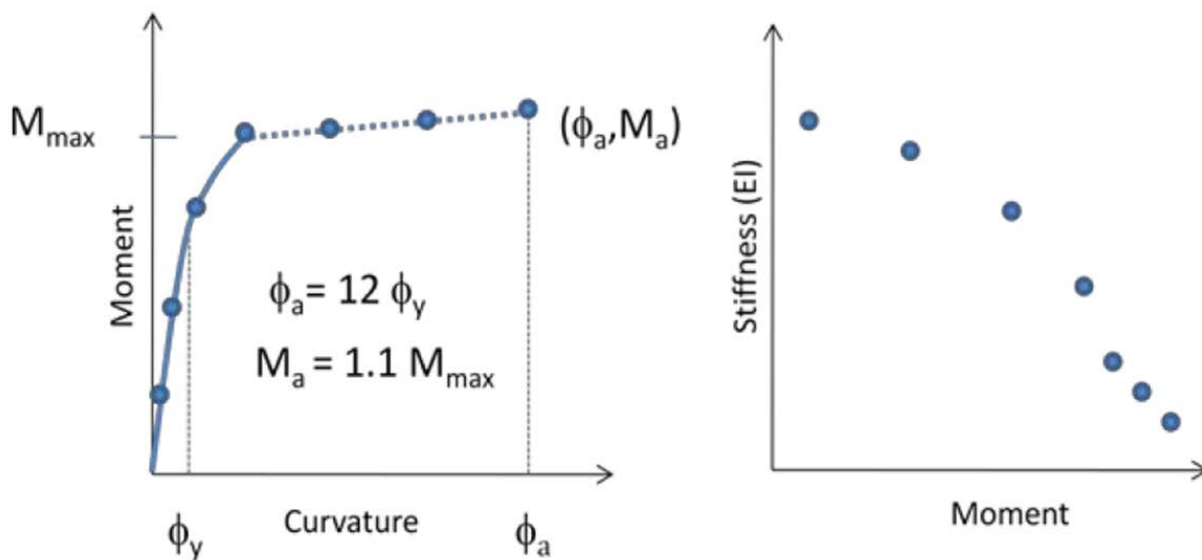


Figure 4-8: Creation of the Equivalent Single Pile M - ϕ Curve for Nonlinear Analysis (After CalTrans, 2011)

In order to estimate $(Q_s)_i$, Juirnarongrit and Ashford (2006) assume that the frictional resistance for an upward-moving pile is the same as for a downward-moving pile. While there have been several methods published for estimating the skin resistance using static pile theory, Juirnarongrit and Ashford recommend using the α -method for cohesive soils (Tomlinson, 1994) and the β -method for cohesionless soils (Esrig and Kirby, 1979).

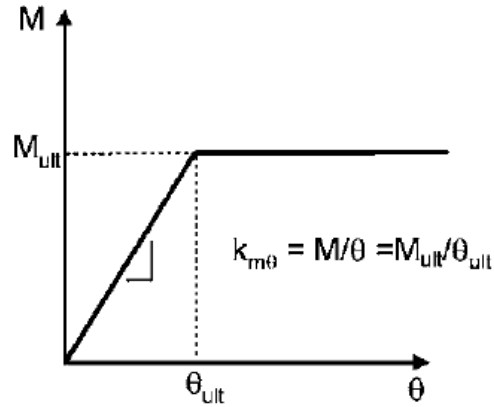


Figure 4-9: Linear Relationship Assumption Between M and θ for the Rotational Stiffness (After Juirnarongrit and Ashford, 2006)

For cohesive soils, there are multiple published methods for estimating α as a function of the undrained strength of the soil, as demonstrated in Figure 4-10. The variation in these published recommendations for α demonstrates the relatively large amount of uncertainty associated with the methodology.

Many consulting engineers today prefer to estimate α via computation for a given soil using the relationship recommended by Kulhawy and Phoon (1993) as:

$$\alpha = \frac{\Psi}{\left(\frac{S_u}{p_a}\right)^{0.5}} \quad (4-21)$$

where Ψ is a factor equal to 0.5 for soil, S_u is the undrained strength of the soil, and p_a is atmospheric pressure in units consistent with the undrained strength. Once α is estimated for all cohesive layers, the total skin resistance for a given pile i in cohesive soil can be computed as:

$$(Q_s)_i = \sum_{j=1}^{N_{layers}} \alpha_j (S_u)_j (A_s)_{j,i} \quad (4-22)$$

where α_j is the alpha factor for soil sublayer j , $(S_u)_j$ is the undrained strength for soil sublayer j , $(A_s)_{j,i}$ is the surface area of pile i in soil sublayer j , and N_{layers} is the total number of cohesive soil sublayers.

For cohesionless soils, the frictional resistance of a pile is computed using the β -method. The β factor is computed as:

$$\beta = K (\tan \delta) \quad (4-23)$$

where δ is the interface friction angle between the soil and the pile and K is the lateral earth pressure coefficient for the soil. K is typically estimated in literature as a function of the at-rest lateral earth pressure K_0 , which is often estimated for cohesionless soils as:

$$K_0 \approx 1 - \sin \phi \quad (4-24)$$

where ϕ is the soil friction angle. Table 4-2 and Table 4-3 present ranges of K and δ , respectively, which are used commonly in engineering design today.

A final consideration in the estimation of skin friction for piles in cohesionless soils is the reduction in the skin resistance due to vertical pile group efficiency effects. Many methods have been published to recommend the capacity efficiency of pile groups (e.g. Feld, 1943; Seiler

and Keeney, 1944; Chellis, 1961; Brand et al., 1972; Liu et al., 1985). A method often used today to compute the group efficiency η in sands was originally presented by Kishida and Meyerhof (1965) and is summarized in Das (2004). This approach suggests that pile group efficiency in sand as it relates to skin resistance is largely a function of the friction angle of the sand and the ratio of the pile diameter to the pile spacing, d/D . Figure 4-11 presents the recommended values for η by Kishida and Meyerhof and was be used to compute the group efficiency of pile groups in sands for this study.

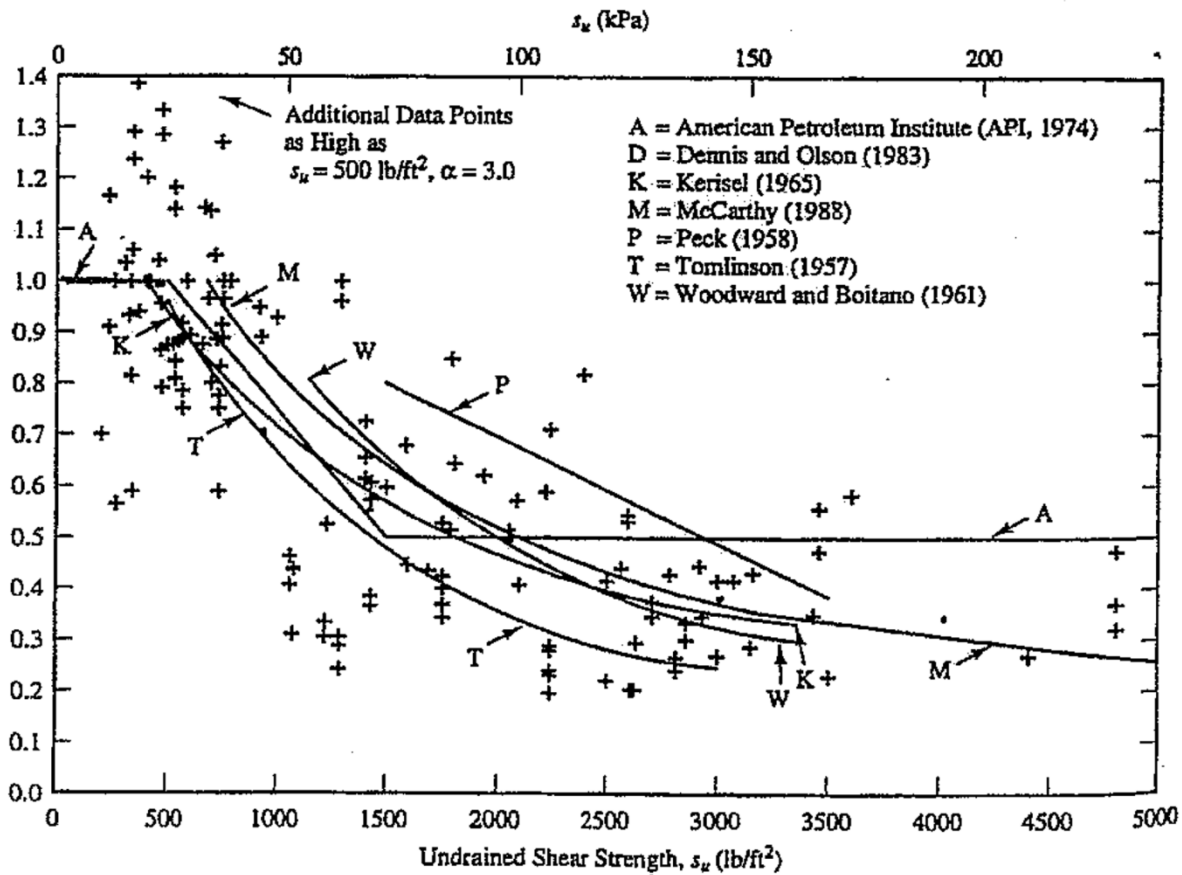


Figure 4-10: Various Published Estimates for α as a Function of Undrained Shear Strength (After Vesic, 1977)

Table 4-2: Recommended Lateral Earth Pressure Coefficients for Use in the β Method (After Kulhawy et al., 1983; Kulhawy, 1991)

Pile type and method of construction	K
Pile-jetted	$(0.5-0.7)K_0$
Pile-small displacement, driven	$(0.7-1.2)K_0$
Pile-large displacement, driven	$(1.0-2.0)K_0$
Drilled shaft-build using dry method with minimal sidewall disturbance and prompt concreting	$(0.9-1.0)K_0$
Drilled shaft-slurry construction with good workmanship	$(0.9-1.0)K_0$
Drilled shaft-slurry construction with poor workmanship	$(0.6-0.7)K_0$
Drilled shaft-casing method below water table	$(0.7-0.9)K_0$

The total skin resistance for a given pile i in cohesionless soil can be computed as:

$$(Q_s)_i = \sum_{j=1}^{N_{layers}} \eta_j \cdot \beta_j (\sigma'_v)_j (A_s)_{j,i} = \sum_{j=1}^{N_{layers}} \eta_j \cdot [K_j \tan \delta_j] (\sigma'_v)_j (A_s)_{j,i} \quad (4-25)$$

where N_{layers} is the total number of cohesionless soil layers in the soil profile, and $(A_s)_{i,j}$ is the surface area of pile i in soil sublayer j .

Estimation of the end bearing resistance for a given pile depends on the type of soil the pile is tipped in. For cohesive soils, the end-bearing resistance can be approximated as:

$$(Q_p)_i = 9(S_u)_i (A_p)_i \quad (4-26)$$

where $(A_p)_i$ is the cross-sectional area for a given pile tip (including the soil plug).

Table 4-3: Recommended Ranges of δ for Various Soil-Pile Interfaces
(After Kulhawy et al., 1983; Kulhawy, 1991)

Pile type	δ
Rough concrete	$1.0\phi'$
Smooth concrete (i.e., precast pile)	$(0.8-1.0)\phi'$
Rough steel (i.e., step-taper pile)	$(0.7-0.9)\phi'$
Smooth steel (i.e., pipe pile or <i>H</i> pile)	$(0.5-0.7)\phi'$
Wood (i.e., timber pile)	$(0.8-0.9)\phi'$
Drilled shaft built using dry method or with temporary casing and good construction techniques	$1.0\phi'$
Drilled shaft built with slurry method (higher values correspond to more careful construction methods)	$(0.8-1.0)\phi'$

For cohesionless soils, the end-bearing resistance can be estimated as:

$$(Q_p)_i = (q_p)_i (A_p)_i \approx [(\sigma'_v)_i (N_q)_i] (A_p)_i \leq 0.5(p_a) \tan(\phi_i) (A_p)_i \quad (4-27)$$

where $(N_q)_i$ is the bearing capacity factor for the end-bearing soil of a given pile. Published values for the bearing capacity factor have varied considerably in literature, as is shown in Figure 4-12.

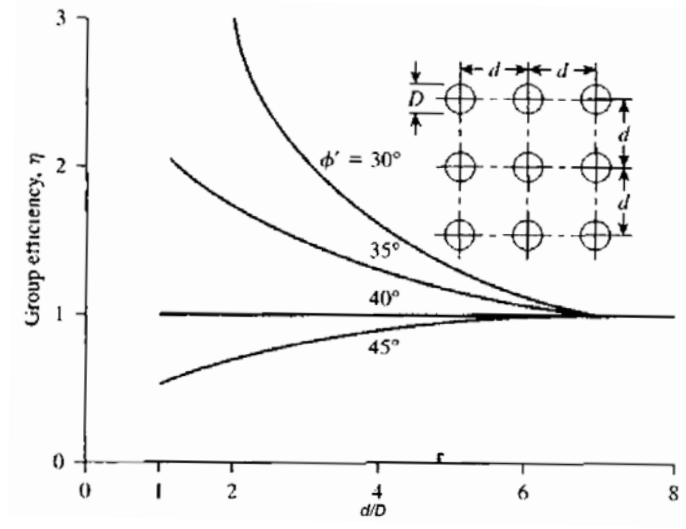


Figure 4-11: Group Efficiency Factor for Use in Computing Skin Resistance of Piles in Sand (After Kishida and Meyerhof, 1965)

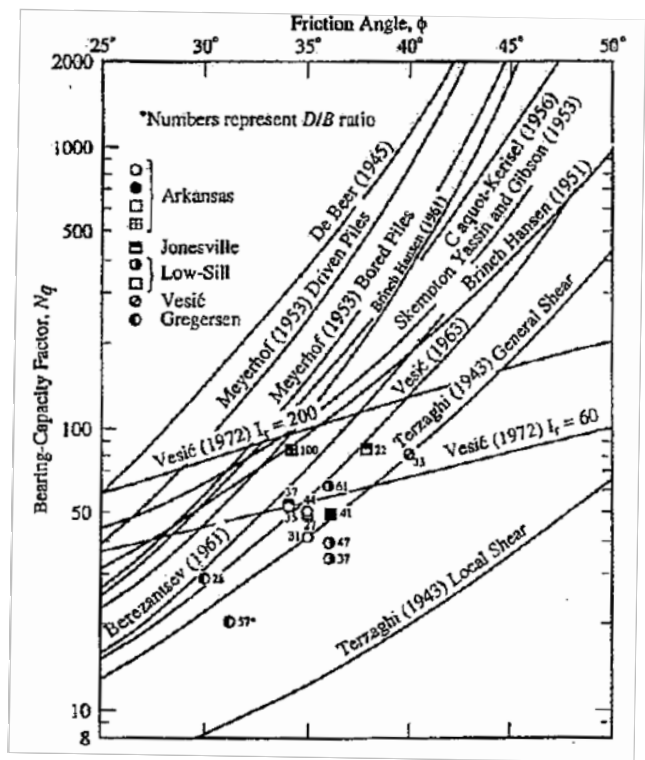


Figure 4-12: Range of Recommended Values for N_q Published in Literature (Adapted From Coyle and Costello, 1981)

A reasonable estimate of N_q for cohesionless soils was provided by Meyerhof (1976) as function of soil friction angle ϕ , and was incorporated in this study. This relationship can be approximated numerically as:

$$N_q \approx 10^{(0.0005\phi^2 + 0.0427\phi + 0.0088)} \quad (4-28)$$

Calculation of X_i in the computation of M_{ult} depends on the chosen datum in the system about which the moments are summed. Juirnarongrit and Ashford (2006) note that for pile groups with three rows or less, it is convenient to sum the moments about the back row of piles (i.e., the pile being pulled down). By doing so, the end-bearing resistance of the downward-moving piles can be neglected because their moment arm is equal to zero. Figure 4-13 demonstrates this concept for a simplified two-row pile group.

Based on Mokwa's approach (Mokwa, 1999), the ultimate angular rotation of the pile cap depends on whether the piles are free to move downward if loaded (i.e. frictional piles), or if they are fixed at their ends (i.e. end-bearing piles). This concept is demonstrated in Figure 4-14.

For the frictional piles, rotation is assumed to occur about the center of the pile cap. Therefore, the ultimate angular rotation of the pile cap is given by Juirnarongrit and Ashford as:

$$\theta_{ult} = \tan^{-1} \left(\frac{2\Delta_{ult}}{S} \right) \quad (4-29)$$

where S is the pile spacing and Δ_{ult} is the relative displacement between the soil and pile required to fully mobilize skin friction along the pile shaft.

For the end-bearing piles, rotation is assumed to occur about the back row of piles in the pile group. Therefore, the ultimate angular rotation of the pile cap is given as:

$$\theta_{ult} = \tan^{-1} \left(\frac{\Delta_{ult}}{S} \right) \quad (4-30)$$

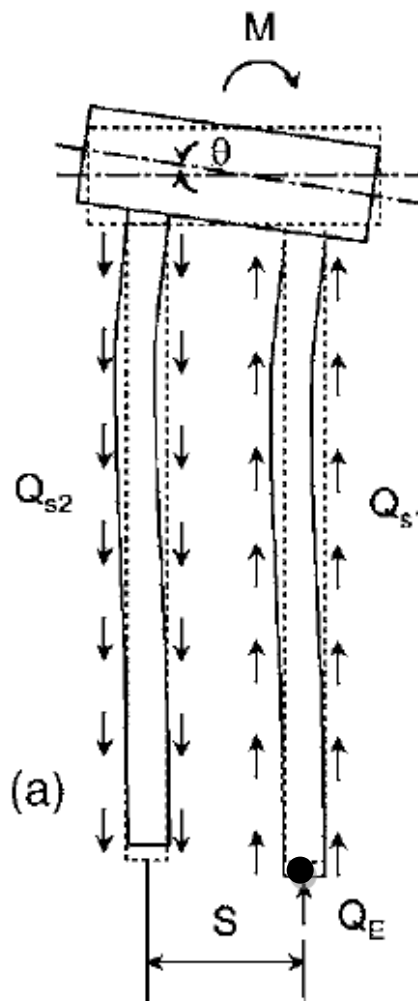


Figure 4-13: Summing the Moments About Downward-Moving Piles (Adapted From Juirnarongrit and Ashford, 2006)

For the purpose of estimating Δ_{ult} , Das (2004) suggested that skin friction along a pile shaft would be fully mobilized when the relative displacement between the pile and the soil was between 5 to 8 millimeters (mm) irrespective of pile diameter and length. Juirnarongrit and Ashford (2006) recommend using a value of 8 mm (0.315 inches or 0.026 feet) for Δ_{ult} based on the results of their study. This study followed the recommendations made by Juirnarongrit and Ashford.

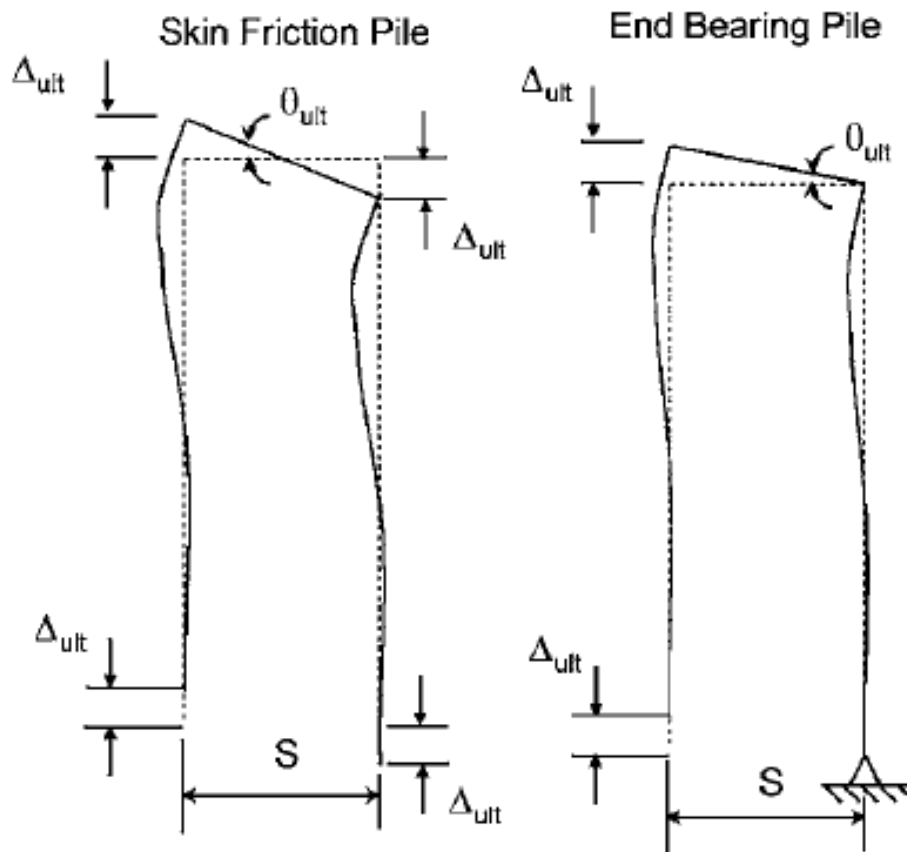


Figure 4-14: Ultimate Angular Rotation of the Pile Cap for Both the Frictional Pile Group and the End-Bearing Pile Group (After Juirnarongrit and Ashford, 2006; Originally Adapted From Mokwa and Duncan, 2003)

4.4.4 Additional Discussion Regarding Kinematic Loading and the Pile Cap

Most lateral spread case histories have shown that the interaction between the pile cap and the non-liquefied soil crust plays a very significant role in the ultimate kinematic response of a given pile group. Under static conditions, soil movement against the pile cap can be represented as a passive pressure distribution against the face of the pile cap. Past research into passive pressures on pile caps under static conditions has shown that full passive pressures are generally developed with relative soil-cap displacements of 1% to 6% of the pile cap height, depending on the type of soil surrounding the pile cap (Duncan and Mokwa, 2001; Rollins and Sparks, 2002). However, additional research with centrifuge testing (Boulanger et al., 2003; Brandenburg et al., 2005) showed that for conditions where the passive failure surface extends into the liquefied zone, the largest passive resistance from the non-liquefied soil crust against the pile cap is achieved at relative displacements ranging from 40% to 100% of the pile cap height. For such conditions, Brandenburg et al. (2005) proposed a relationship to account for this apparent “softening” effect of the non-liquefied crust as:

$$\frac{F_{crust}}{F_{crust,ult}} = \left[\left(\frac{y}{C \cdot H} \right)^{-0.33} + \left(\frac{16 \cdot y}{C \cdot H} \right)^{-1} \right]^{-1} \leq 1 \quad (4-31)$$

where $\frac{F_{crust}}{F_{crust,ult}}$ is the ratio of the “softened” soil resistance divided by the ultimate predicted soil resistance of the non-liquefied soil crust, y is the relative displacement between the soil and the pile, H is the height of the pile cap (in units consistent with y), and C is an empirical curve-fitting constant that controls the curvature of the relationship and ranges between 0.2 to 0.8 for liquefied soil conditions. Equation (4-31) is demonstrated graphically in Figure 4-15.

Brandenberg et al. (2007b) expanded on the findings of Brandenberg et al. (2005) to develop a more comprehensive but complex iterative process for estimating the apparent softening p-y effect in kinematic loading due to soil liquefaction. However, due to its complexity this procedure will not be described in detail in this dissertation.

While accounting for the apparent softening p-y effect of a relatively thin non-liquefied soil crust acting against the pile cap may be appropriate for certain kinematic pile response analyses, it was not accounted for in this study due to relatively large thickness of the non-liquefied soil crusts (i.e. approach embankments) in the case histories presented later in this dissertation.

A final consideration that could significantly alter the soil-pile cap interaction is friction along the sides and base of the pile cap. From their centrifuge studies, Boulanger et al. (2003) and Brandenberg et al. (2005) reported that up to 50% of the total kinematic lateral force exerted on their model pile cap was apparently produced from side and base friction from the soil flowing around the cap. In theory, it would take a relatively small amount of differential displacement between the pile cap and the laterally spread soil to mobilize skin friction on the pile cap.

However, some researchers and consultants hesitate to account for friction along the bottom of the pile cap by arguing that liquefaction-induced soil settlements have often been observed to create a gap between the bottom of the pile cap and the soil. These professionals also point out the possibility that soil beneath the pile cap could become trapped between piles rather than slide along the base of the pile cap. Finally, these researchers and consultants argue that the shallow depth at which most pile caps are located often negates the effects of friction acting on the pile cap due to relatively low confining pressures. Therefore, while it is acknowledged that

cases may exist in practice where skin friction could potentially have a significant effect on the computed kinematic response of the pile group (especially for caps that are geometrically very long in the direction of the lateral spread displacements), such consideration was neglected for pile groups in this study due to the relatively narrow pile caps associated with the case histories in this research, and because such consideration was not recommended in the procedure presented by Juirnarongrit and Ashford (2006).

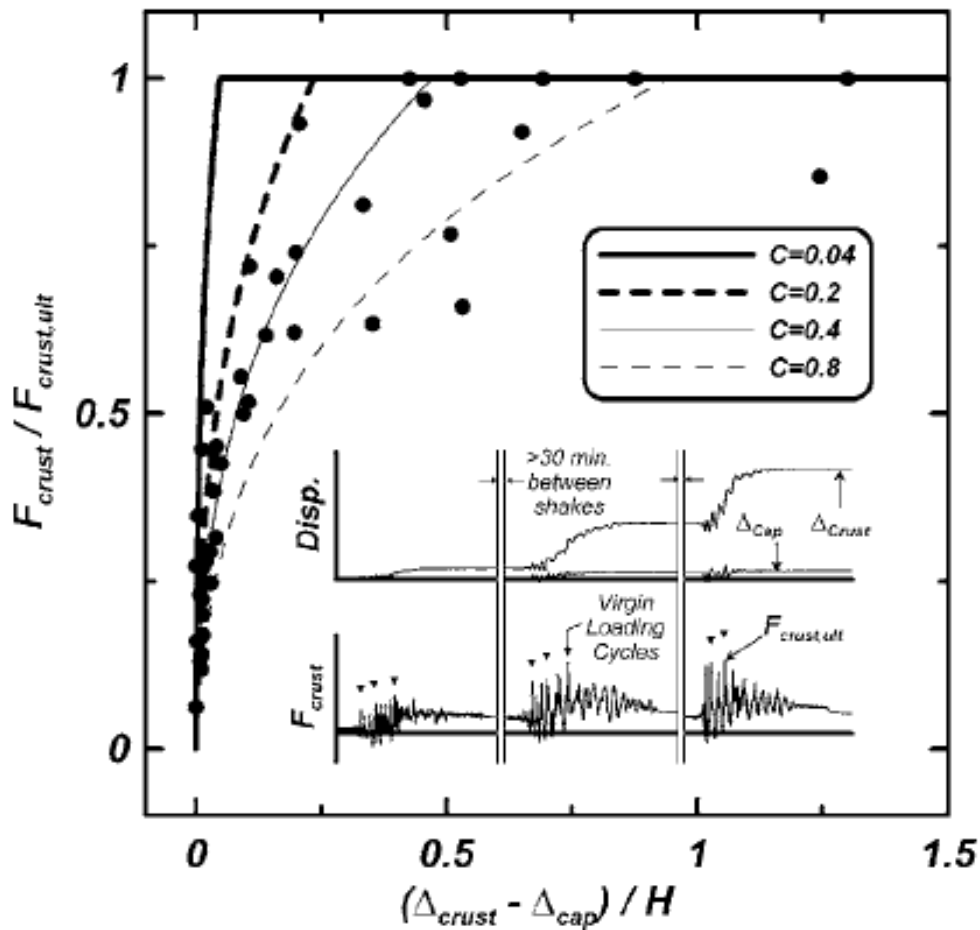


Figure 4-15: Normalized Load-Displacement Curves for Non-Liquefied Crust Over Liquefied Soil From Centrifuge Study (After Brandenburg et al., 2005)

4.5 Chapter Summary

Liquefaction and lateral spread have historically been observed to cause significant damage to deep foundation systems. While such damage has been known to occur for decades, most analysis procedures for engineers to evaluate the kinematic response of deep foundation systems have largely been developed during about the past 15 years.

Current pile response analysis procedures are typically divided between (1) inertial loading, which is caused by the inertial reaction of the mass from the overlying structure being transmitted to the foundation, and (2) kinematic loading, which is caused by a free-field displacement of the soil surrounding the foundation. While some research has shown that a combination of inertial and kinematic loading could provide the most critical scenario for a given structure and its foundation, most engineers prefer to analyze the two scenarios independently and allow the most critical scenario to govern the design. Because the scope of this study is strictly interested in a performance-based procedure for the kinematic response of pile foundations, inertial loading was neglected in this study.

Estimating free-field soil displacements due to lateral spread is commonly performed today using one of three methods: numerical models, Newmark-type sliding block models, or empirical regression equations. This study will incorporate the use of empirical regression equations due to their wide application in engineering practice today and because they have recently been demonstrated to fit within a performance-based framework, thus allowing the development of probabilistic estimations of lateral spread displacements. However, each methodology has its advantages and limitations, and an engineer should be aware of both when applying a given methodology in engineering design. Some common limitations include the inability to account for complex soil geometries and the inability to account for most structural

reinforcement or ground improvement elements. Finally, it is often considered good engineering practice to evaluate the potential for the occurrence of flow liquefaction prior to predicting lateral spread displacements. A simple method for evaluating the potential for flow liquefaction is to perform a two-dimensional limit equilibrium stability analysis that incorporates the estimated residual strengths for the liquefied soils and reduced strengths for the soils not predicted to liquefy. If such an analysis yields a factor of safety equal to unity or less, then the likelihood of flow liquefaction under the design ground motions is considered high, and ground improvement and/or slope stabilization techniques will likely need to be implemented in order to reduce the risk of flow liquefaction occurring.

Given an estimated free-field soil deformation profile, there currently exist several methodologies to analyze the kinematic response of the pile foundation. These methodologies range from simplified limit equilibrium procedures to complex three-dimensional numerical models. A popular method employed by researchers and practicing engineers today is the Beam on Winkler Foundation (BWF) procedure. This procedure incorporates the use of load-displacement soil spring models (commonly referred to as p-y models) in the prediction of the soil-pile interaction. While it is possible to develop site-specific p-y models for the soils at a given site, most engineers in practice today prefer to use generic published p-y models for various soil types. During the past 10 years or so, various p-y models have also been developed to represent liquefied soil. Among these models are residual strength models, strain-hardening models, and p-multiplier (i.e. reduction factor) models. While each of these types of models has its appropriate applications, as well as its strengths and weaknesses, this study incorporated a p-multiplier approach because of its wide use in industry today and because it is generally considered to be a robust approach for considering kinematic loading, particularly when dealing

with relatively large soil deformations. However, an engineer may freely elect to use another p-y model for liquefied soil if deemed more appropriate than the use of p-multipliers.

While it is relatively simple to compute the kinematic response of a single pile, it is a much more complex analysis to compute the kinematic response of a pile group and the pile cap. A published simplified p-y procedure for analysis of an equivalent “single” pile was presented. It should be recognized that this simplified procedure is intended to provide the average pile response for a single pile in the pile group. As such, more sophisticated analyses may be required for complex and/or critical structures in order to validate the results from the simplified procedure.

Many researchers have demonstrated the importance of the pile cap in contributing to the pile response under kinematic loading. Several researchers have demonstrated that such factors as apparent “softening” of the non-liquefied soil crust and friction acting along the sides and bottom of the pile cap can play a significant factor in the kinematic response of a pile group and its cap. These factors should be evaluated for potential significance in the kinematic response of the pile group, and should be accounted for if judged to be significant.

5 PERFORMANCE-BASED EARTHQUAKE ENGINEERING DESIGN

5.1 Introduction

Ever since earthquakes have destroyed man-made buildings, society has turned to engineers to find solutions to make its structures more resilient against earthquake-induced damage. Especially during the 20th century, engineers began making design breakthroughs in helping their structures become more resistant to earthquake damage. The 1920s and 1930s saw the first specific earthquake provisions in building codes in Japan and the United States. These codes were improved upon as engineers and seismologists gained greater understanding regarding the geologic make-up of the earth, plate tectonics, earthquake characteristics, structural response, and soil/structure interaction. In the latter half of the century, research on local site effects, the phenomenon of liquefaction, and probabilistic applications in determining design specifications led to even better earthquake-resistant designs.

As part of this on-going effort to improve seismic design codes, several institutions and researchers are currently developing the idea of Performance-Based Earthquake Engineering (PBEE). PBEE is a revolutionary concept in earthquake resistant design that would ideally help the owner and engineer jointly select a design based on the desired structural performance under common and severe earthquake loading. Such a concept would be a significant step toward the application of the current state of knowledge of earthquake engineering in earthquake-resistant

design, and it would begin moving engineers and owners away from conventional empirically- and deterministically-based decisions.

This chapter will briefly present the basic ideas and philosophies of PBEE, review the concepts of Deterministic and Probabilistic Seismic Hazard Analyses, and introduce the Pacific Earthquake Engineering Research Center's recommended framework for PBEE.

5.2 Basic Philosophy of PBEE

Since the early 1980s, many researchers have analyzed the effects of significant earthquakes and have concluded seismic risks in urban areas are increasing and are far from socio-economically acceptable levels. These researchers believe that the key to correcting this problem is to develop more reliable seismic standards and code provisions than those currently available, and to implement these codes in the engineering of new structures and upgrading of older structures (Bertero and Bertero, 2004). This belief led to the development of PBEE, which was first formally proposed by SEAOC Vision 2000 Committee in 1995 in its report entitled "Performance-Based Seismic Engineering of Buildings" (Bertero and Bertero, 2004).

Since that time, researchers have been working to further develop the idea of PBEE, creating simple but reliable procedures for its practical application and guidelines by which it could be implemented into building codes. As a result, PBEE is continuously evolving into a well-structured framework that implies design, evaluation, construction, monitoring the function and maintenance of engineered facilities whose performance under common and extreme loads responds to the diverse needs and objectives of owners, users, and society (Krawinkler and Miranda, 2004). However, there are still many legal and professional barriers that will need to be

overcome in order to prove PBEE as a safe, simple, and reliable methodology to be applied in the field of Earthquake Engineering.

PBEE is founded on the idea that uncertainty in engineering design can be quantified and used in predicting performance such that engineers and owners together can make intelligent and informed trade-offs based on life-cycle considerations rather than construction costs alone (Krawinkler and Miranda, 2004). For example, if an owner would like a building to be fully operational immediately following a major earthquake, then engineers could design the building to a higher performance level than that required for life-safety. Owners therefore would have options for maximizing the return of their investment by designing for greater levels of performance for their buildings beyond the minimum life-safety requirements imposed by society if they so desired (Krawinkler and Miranda, 2004). PBEE could also be very beneficial in that minimum levels of performance beyond life-safety could be mandated for critical structures such as hospitals, storage facilities for hazardous waste, or nuclear facilities.

In order to predict the likely performance of a structure subjected to a wide range of earthquake loading scenarios, engineers must consider the entire range of possible earthquake hazards and their corresponding uncertainties as opposed to focusing on a single scenario earthquake. This means that design procedures that are more firmly rooted in the realistic computation of structural behavior exposed to a realistic distribution of possible earthquake loads must be developed in such a way that they are practical to apply and relatively simple to interpret, and engineers must begin to move away from purely empirical procedures (Krawinkler and Miranda, 2004). This may involve developing new procedures that consider the entire seismic hazard spectrum, or modifying deterministic empirical procedures so that they can be implemented in a performance-based engineering framework.

The implication of PBEE is that damage to a building from earthquake loading is acceptable as long as it does not exceed the level of damage prohibited by society and it proves the most economic solution (Krawinkler and Miranda, 2004). In order to make such an implication work, engineers must not only have procedures that can realistically predict the building response under a given level of earthquake loading, but must also have procedures which can predict the earthquake loading itself. Through the 1970s and 1980s, most engineers developed design ground motions by using observation-based and empirical approaches that are generally considered simplistic by today's standards. Uncertainty in the estimation of these ground motions was typically accounted for by subjectively applying heavy doses of conservatism. However, because PBEE involves moving engineers away from these simplistic and conservative procedures, a seismic hazard analysis that objectively considers the entire seismic hazard spectrum and quantifies the uncertainties involved in the hazard analysis must be incorporated instead. Such a seismic hazard analysis was already being applied by many engineers well before the advent of PBEE. It is called Probabilistic Seismic Hazard Analysis.

5.3 Seismic Hazard Analysis

A key element of seismic design is the ability to quantify the level of demand placed on a structure or foundation. This quantification can be expressed in terms of a design ground motion, which can be characterized by design ground motion parameters (Kramer, 1996). The computation of design ground motion parameters is called a seismic hazard analysis. During the advent of earthquake engineering, little was understood regarding the estimation of earthquake ground motions. However, a substantial amount of data has been collected in the form of ground motion recordings during the past century, and researchers have used this data to develop

empirical predictive relationships to estimate earthquake ground motions. While these predictive relationships were initially quite simplistic, most have evolved into very complex equations developed using advanced statistical regression methods. These ground motion predictive relationships are commonly referred to as attenuation relationships because the amplitude of the predicted ground motion tends to attenuate with increasing source-to-site distance.

5.3.1 Estimating Earthquake Ground Motions Using Attenuation Relationships

Site-specific ground motions can be influenced by the style of faulting, magnitude of the earthquake, and local soil or rock condition. The attenuation relationships used to estimate ground motion from an earthquake source need to consider these effects.

Many attenuation relationships have been developed, particularly during the last 20 years, to estimate the variation of peak ground surface acceleration with earthquake magnitude and distance from the site to the source of an earthquake. Recently, under a Pacific Earthquake Engineering Research (PEER) Center project entitled “Next Generation Attenuation of Ground Motions (NGA),” five separate research teams developed new attenuation relationships for shallow crustal earthquakes in Western North America from a common dataset of ground motions by applying whatever limitations and statistical transformations of the data they felt necessary. These relationships are Abrahamson and Silva (2008), Boore and Atkinson (2008), Campbell and Bozorgnia (2008), Chiou and Youngs (2008), and Idriss (2008).

The NGA predictive relationships were developed from statistical analyses of recorded worldwide earthquakes, including the records from the 1989 Loma Prieta earthquake, the 1992 Landers earthquake, the 1994 Northridge earthquake, the 1995 Kobe earthquake, and more recent important earthquakes that were not included in previous attenuation relationships developed during the 1990s (e.g., 1999 Kocaeli, Turkey earthquake and the 1999 Chi-Chi,

Taiwan earthquake). The attenuation relationships provide geometric mean values of horizontal ground motions associated with one set of parameters: magnitude, distance, site soil conditions, and mechanism of faulting. The uncertainty in the predicted ground motion is taken into consideration by including a standard error in the probabilistic analysis. Though the NGA attenuation relationships were developed specifically for the western United States, they theoretically can be applied to other areas in the world with moderate to high seismicity and crustal faulting regimes because they were developed considering many ground motions from locations throughout the world such as Japan and Turkey. Because the various NGA attenuation relationships are very complex equations, they are simply referenced and are not summarized in detail in this dissertation. For deterministic liquefaction analyses performed in this study, an NGA calculation spreadsheet developed and made available by PEER (Al Atik, 2009) was used to estimate the ground motions from the scenario earthquake event. In addition, for the probabilistic seismic hazard analyses performed as part of this study, all but the Idriss (2008) NGA attenuation models were incorporated and their results were averaged with equal weights. The Idriss (2008) model was not used is because it is only applicable to rock sites.

Attenuation relationships have also been developed to predict ground motions from other faulting regimes such as subduction zones and inter-continental seismic zones. Because the case histories evaluated in this study included significant earthquake hazard contributions from subduction zone sources, including both interface sources (i.e. slip and resulting crustal uplift along the interface between a crustal tectonic plate and an oceanic tectonic plate) and intraplate sources (i.e. very deep events resulting from the bending and breaking of the subducted oceanic crust located in a region known as the Benioff zone), attenuation relationships that accounted for these two types of events were selected for use in this study. These relationships include Youngs

et al. (1997), Atkinson and Boore (2003), and Zhao et al. (2006). To compute the weighted-average ground motions from the subduction zone sources in this study, equal weights were applied to these attenuation relationships.

For references regarding inner-continental attenuation relationships, particularly for the United States, one may refer to the recommendations made by United States Geological Survey (USGS) in the development of the 2008 National Seismic Hazard Maps for the United States (Petersen et al., 2008).

Using attenuation relationships to estimate an earthquake ground motion for use in design can be a significant challenge because the amount of uncertainty associated with all of the potential earthquake sources, their associated recurrence rates, their size, and the significance of their affect on the site of interest can be relatively large. Due to this large amount of uncertainty, engineers originally relied on a conservative methodology to compute ground motion parameters for use in design. This methodology, known as Deterministic Seismic Hazard Analysis, or DSHA, was the standard of practice among engineers for several decades. However, within the past 30 to 40 years, engineers have begun quantifying their uncertainties relating to seismic hazard by using total probability theory in an attempt to produce a more objective and consistent approach to dealing with ground motions. This method is called Probabilistic Seismic Hazard Analysis, or PSHA.

5.3.2 Review of DSHA

As previously stated, DSHA uses a conservative approach to account for the uncertainties in developing design ground motion parameters. This conservatism can be seen in reviewing the process of performing a DSHA, which Reiter (1990) describes as the following four steps:

- 1) *Identify and characterize all earthquake sources capable of producing significant ground motions at the site.* Deterministic source characterization is defined as identifying the geometry of each potential seismic source, the maximum possible earthquake magnitude associated with each source, and the likelihood of rupture for each source. Deterministic characterization of rupture potential essentially involves classifying the source as being either “active” or “inactive.” Differentiation between active and inactive sources can be a very controversial topic due to its subjective nature. Therefore, the definition of an active source often depends on the prescribed methodology or procedure that is being used for design.
- 2) *Select a source-to-site distance for each source zone, typically the shortest distance possible.* There are various definitions of source-to-site distances including epicentral distance, hypocentral distance, and Boore-Joyner distance. One must be careful to use the appropriate distance(s) as recommended by the selected attenuation relationship(s) in the analysis.
- 3) *Select the earthquake scenario that will produce the strongest level of shaking.* By using attenuation relationships, the mean or median value of the ground motion parameter is typically generated based on the given input earthquake magnitude and distance. By comparing the computed results from the each individual seismic source, the deterministic event that computes the largest ground motions can be identified. This event is usually designated as the governing or controlling deterministic event for the site.
- 4) *Formally define the seismic hazard at the site.* This is done by using the computed ground motion parameter from the governing deterministic event identified in Step 3.

Peak acceleration, peak velocity, and response spectrum ordinates are ground motion parameters commonly used to characterize the seismic hazard (Kramer, 1996).

Figure 5-1 schematically shows the procedure outlined in Steps 1-4 above. The DSHA, therefore, produces what is frequently interpreted as a “worst-case scenario” earthquake to attempt to account for the uncertainty involved with earthquake prediction. Though the deterministic procedure is advantageous due to its simplicity and may seem like a sound approach because of its conservatism, many professionals generally cite three critical flaws in its logic. First, a DSHA does not numerically consider either the recurrence rate of the earthquake source or the exposure time (i.e. life-cycle) of the structure. In other words, the analysis does not directly account for the *likelihood* of occurrence of the governing deterministic earthquake during a given time period; it only accounts for the *possibility* of its occurrence. This can be very significant in a city like Seattle, Washington, which has the potential of experiencing significant ground motions from the Seattle fault, a reverse fault that runs directly through the downtown district. If designing for the characteristic earthquake from the Seattle fault, extraordinary measures and cost may be required to design and construct a building to resist such severe levels of ground shaking. Compare this example with San Francisco, California, which experiences significant earthquakes approximately every 100 years due to the presence of very active strike-slip faults including the San Andreas fault. If one considers that the San Andreas fault and the Seattle fault both produce relatively similar magnitudes of earthquakes and are both located relatively near their respective downtown areas, then DSHA logic would lead one to suggest that buildings in Seattle must be constructed to approximately the same seismic standards as those constructed in San Francisco. However, when one considers that the Seattle fault produces a major earthquake nearly every 2,000 years, while the San Andreas fault produces a major

earthquake nearly every century, then such a line of thinking can suddenly seem economically impractical for developers and owners in Seattle because buildings in San Francisco are much more likely to experience a major earthquake during their respective life-cycles.

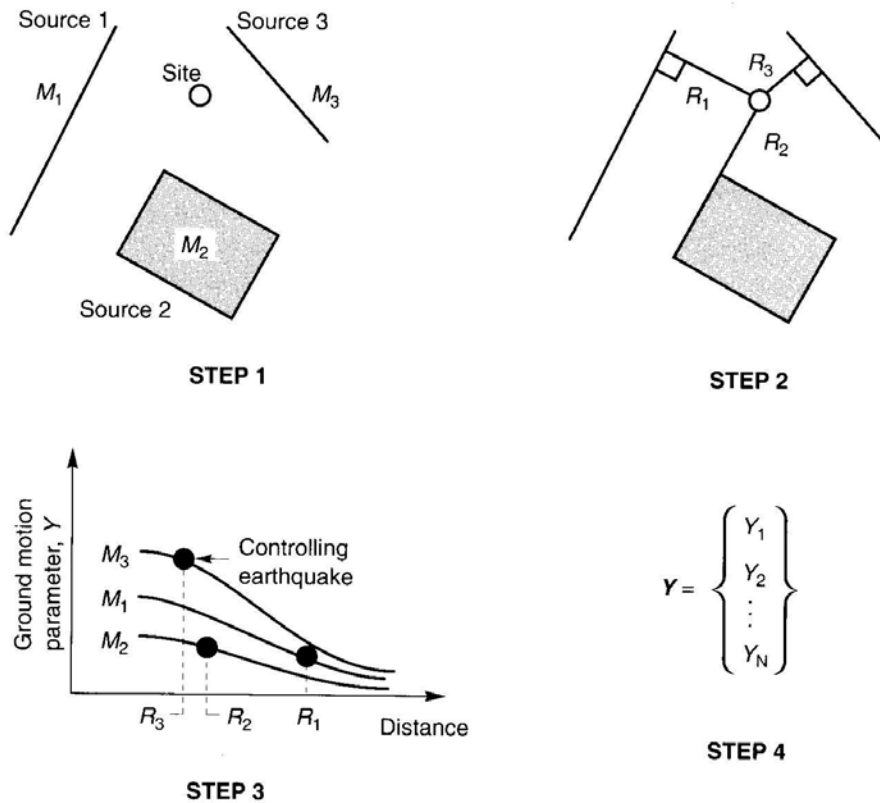


Figure 5-1: Schematic Diagram of DSHA Steps for a Given Site (After Kramer 1996)

The second flaw in DSHA logic is that it is difficult to associate the ground motions computed from a DSHA with the various levels of earthquake design hazard defined in the most of the building codes today. During the last 40 years, a broad spectrum of professionals ranging

from engineers to government officials have defined various levels of earthquake ground motions that are considered appropriate for the design of various structures. These definitions include, but certainly are not limited to *maximum credible earthquake* (MCE), *design basis earthquake* (DBE), *upper basis earthquake* (UBE), *safe shutdown earthquake* (SSE), *maximum probable earthquake* (MPE), *operating basis earthquake* (OBE), and *seismic safe evaluation earthquake* (SSEE) (Committee on Seismic Risk, 1984). While each of these definitions may correspond to the ground motion of a given probability of exceedance computed from a PSHA, it is difficult to objectively define a comparable ground motion from the DSHA. Does one use 1.5 times the median deterministic ground motion to define the MCE, or does one use the median deterministic plus one standard deviation ground motion? How does one appropriately modify the results of the DSHA to develop an appropriate SSE ground motion? Such questions require subjective answers, and often result in discord and disagreement among the various professionals involved in the decision-making process.

A third flaw in DSHA logic is that once an engineer defines a “critical” earthquake scenario, he/she is unable to objectively account for the likelihood of variance in the computed ground motion from the attenuation relationship. How should the engineer handle uncertainty in the ground motion? Should the median computed ground motions be used, or should greater values be used? Certainly there is risk that ground motions larger than the median could be experienced at the site. However, DSHA logic does not account for this risk unless the utilized building code or procedure requires that ground motions greater than the median (e.g., median + 1σ) be used to define the seismic hazard, which may result in a very conservative estimate of the ground motions at the site.

5.3.3 Review of PSHA

To provide a more complete picture of the seismic hazard, a PSHA uses rational principles of mathematics and probability theory to identify, quantify, and combine the uncertainties involved with earthquake prediction. The theory of PSHA has been developed and presented by many researchers over the years (e.g., Cornell, 1968; Cornell, 1971; Merz and Cornell, 1973; McGuire, 2004). The uncertainties that are evaluated and quantified in a PSHA typically include uncertainty in earthquake location, uncertainty in earthquake size, uncertainty in the attenuation relationship(s), and temporal uncertainty.

5.3.3.1 *Uncertainty in Earthquake Location*

Spatial uncertainty is an important aspect to consider in a seismic hazard analysis. The distance between site and earthquake source can contribute greatly to the intensity of shaking felt at a site. Spatial uncertainty is related to the geometry of the earthquake source zones considered in the PSHA. To understand this idea, one must know that there are four basic source geometries: point sources, linear sources, areal sources, and volumetric sources. Point sources can be a single geographical location which can act as an earthquake source, such as a volcano or a small fault. Linear sources are generally well-defined faults where the focal depth along the fault can generally be assumed to be approximately constant. Areal sources generally characterize areas with dense faulting schemes and well-defined faulting planes where an earthquake could occur in many possible locations. Volumetric sources usually characterize areas where the earthquake mechanism is poorly defined or where the faulting network is so dense and complicated that it is difficult to distinguish individual faults. For the purpose of the seismic hazard analysis, source zones may be similar to the actual source, or it may be simplified. For example, a fault that is located at a distance from a site such that the source-to-site distance is approximately the same

for all points along the fault may be modeled as point source. Similarly, an areal source that is shallow enough such that the hypocentral source-to-site distance is approximately the same for all hypocentral depths may be represented as a line source. Finally, a volumetric source that is shallow enough such that the hypocentral source-to-site distance is approximately the same for all hypocentral depths may be represented as a planar source.

Once the source zone is defined, one must consider the spatial distribution of earthquakes in that source zone. Earthquakes are usually assumed to be uniformly distributed within a particular source zone (Kramer, 1996). However, if more detailed data concerning the spatial distribution of earthquakes in a particular source zone is available, then it should be incorporated instead of assuming a uniform distribution. In order to be applied in a PSHA, the spatial distribution must be quantified. Figure 5-2 shows examples of PDFs corresponding to source-to-site distance for various source zones.

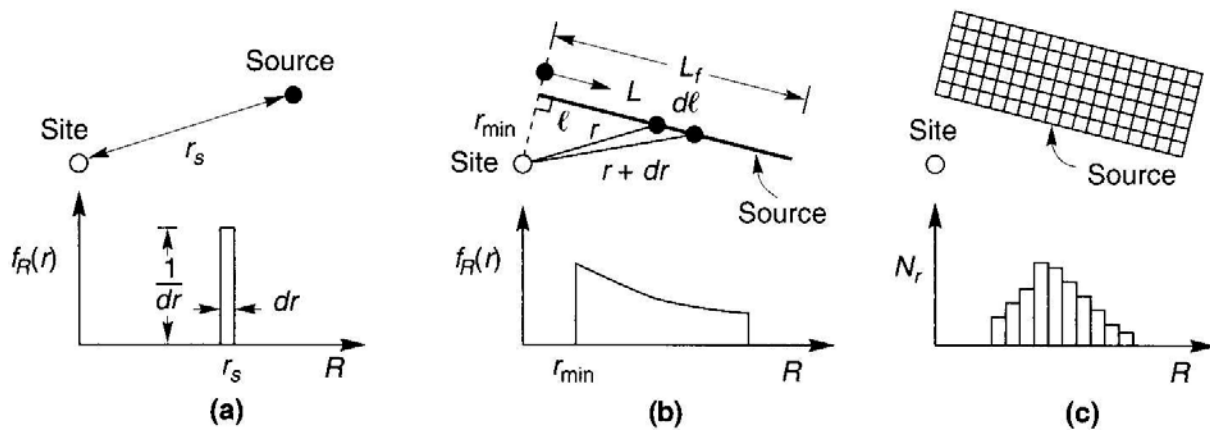


Figure 5-2: Example Probability Density Functions for Source-to-Site Distance for a (a) Point Source, (b) Fault Source, and (c) Area Source (After Kramer, 1996)

Figure 5-2(a) demonstrates that the spatial distribution of earthquakes for a point source is a single source-to-site distance because an earthquake from that source can occur in only one geographic location. However, it becomes more complicated with other source zones. Because the probability that an earthquake will occur on a small segment of the fault between $L = l$ and $L = l + dl$ is the same as the probability that the source-to-site distance will be between $R = r$ and $R = r + dr$, the uniform PDF for the variable R in Figure 5-2(b) can be computed as:

$$f_R(r) = f_L(l) \frac{dl}{dr} = \frac{r}{L_f \sqrt{r^2 - r_{\min}^2}} \quad (5-1)$$

where L_f is the total length of the fault and r_{\min} is the shortest source-to-site distance. In the case of more complicated source zone geometries (i.e. Figure 5-2(c)), $f_R(r)$ can be evaluated by using numerical methods, such as creating a simple histogram.

In the consideration of spatial uncertainty in a PSHA, it is typically assumed that all of the energy associated with the earthquake is released from the hypocenter of the event. While this assumption greatly simplifies the seismic hazard computation, it neglects the actual mechanics of the fault rupture in which the earthquake energy is typically released over the entire rupture surface, not just from the hypocenter. While the large majority of professionals agree that such a level of sophistication is unnecessary in a PSHA, consideration of energy distribution along the fault rupture may be deemed significant for certain types of analyses. For these more sophisticated PSHAs, Der-Kiureghian and Ang (1977) developed a methodology to account for energy distribution along the rupture surface in a PSHA. However, such

sophistication is well beyond the scope of the PSHAs performed in this study, and all earthquake energy is assumed to be released from the hypocenter of the earthquake.

5.3.3.2 Uncertainty in Earthquake Size

To consider the uncertainty in earthquake size, it is important to understand that a particular source zone may produce earthquakes of any size up to a maximum possible earthquake magnitude. This idea can be explained by the elastic rebound theory (Reid, 1911). This theory states that elastic strain energy is stored in rock material near the fault boundary as shear stresses increase on the fault planes that separate the earth's crustal plates, which are in constant motion. When the shear stress approaches the shear strength of the rock that is "locking up" the fault, then the rock breaks and releases the stored strain energy in the form of fault movement and seismic waves. The amount of strain energy released is what determines the size of the earthquake. The elastic rebound theory also suggests that such factors as fault rupture area, normal stresses along the fault plane, and rock shear strength can effectively "cap" the size of the maximum earthquake magnitude that the fault can produce.

Scientists have been able to analyze the distribution of earthquake magnitudes in a given time period and create models that attempt to describe their observations. These models are called recurrence laws. Recurrence laws obtained from past seismicity are assumed appropriate to predict future seismicity in PSHA. There are many recurrence laws that have been developed, particularly in the 1970s (e.g., Merz and Cornell, 1973; Shah et al., 1975; Lomnitz-Adler and Lomnitz, 1979), but there are two particular recurrence laws that have found wide acceptance among practicing engineers and scientists today, namely: the Gutenberg-Richter recurrence law and the Characteristic Earthquake recurrence law.

The Gutenberg-Richter Recurrence Law was originally developed by Gutenberg and Richter (1944) from data gathered from Southern California earthquakes over a period of many years. The recurrence law can be written as:

$$\log \lambda_m = a - bm \quad (5-2)$$

where λ_m is the mean annual rate of exceedance of magnitude m , 10^a is the mean yearly number of earthquakes of magnitude greater than or equal to zero, and b describes the relative likelihood of large and small earthquakes. The reciprocal of λ_m is called the return period of an earthquake exceeding magnitude m , and is often symbolized as T_R . Equation (5-2) above can also be written as:

$$\lambda_m = 10^{a-bm} = e^{\alpha-\beta m} \quad (5-3)$$

where $\alpha = 2.303a$ and $\beta = 2.303b$. Figure 5-3(a) shows the graphical representation of the parameters a and b .

McGuire and Arabasz (1990) demonstrated that a bounded modification of the Gutenberg-Richter recurrence law works well in a PSHA. By eliminating earthquakes smaller than a lower threshold magnitude m_0 , the mean annual rate of exceedance can be written as:

$$\lambda_m = \nu \left(e^{-\beta(m-m_0)} \right) \quad m > m_0 \quad (5-4)$$

where $\nu = \exp(\alpha - \beta m)$. Typically, the lower threshold magnitude is set at values from about 4.0 to 5.0 because magnitudes smaller than that generally cause little significant damage (Kramer, 1996). Upper bounds can also be placed on the magnitudes considered by the modified Gutenberg-Richter recurrence law. If some maximum magnitude, m_{\max} , based on the size of the source is known or can be estimated, then the mean annual rate of exceedance can be expressed as:

$$\lambda_m = \nu \frac{e^{-\beta(m-m_0)} - e^{-\beta(m_{\max}-m_0)}}{1 - e^{-\beta(m_{\max}-m_0)}} \quad m_0 \leq m \leq m_{\max} \quad (5-5)$$

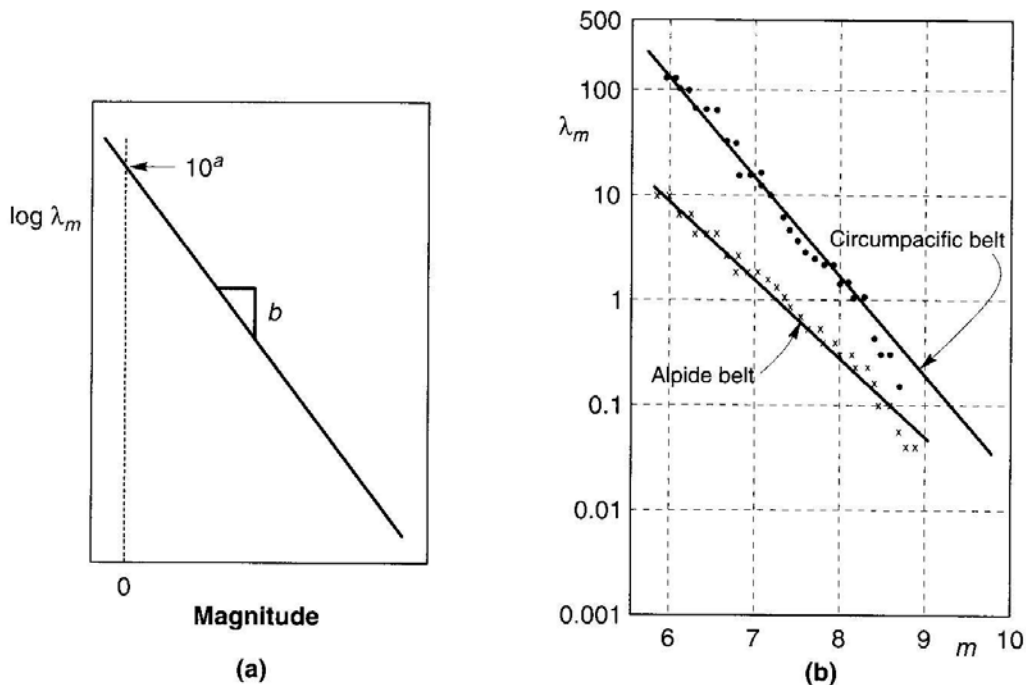


Figure 5-3: (a) Graphical Representation of the Parameters a and b Used in the Gutenberg-Richter Recurrence Law; (b) Gutenberg-Richter Recurrence Law Applied to Two Tectonic Belts (After Kramer, 1996)

This bounded Gutenberg-Richter recurrence law is shown in Equation (5-5) for conditions of constant rate of seismicity, or mean annual rate of exceedance of m_0 . If conditions of constant rate of slip exist instead of constant rate of seismicity, then one may refer to Youngs and Coppersmith (1985) for an appropriate bounded recurrence law. Figure 5-4 shows plots of bounded Gutenberg-Richter recurrence relationships for $m_0 = 4.0$ and $m_{\max} = 6, 7, \text{ and } 8$ constrained by (a) constant rate of seismicity and (b) constant rate of seismic moment (i.e., constant rate of slip because rate of slip is proportional to seismic moment) based on Youngs and Coppersmith (1985).

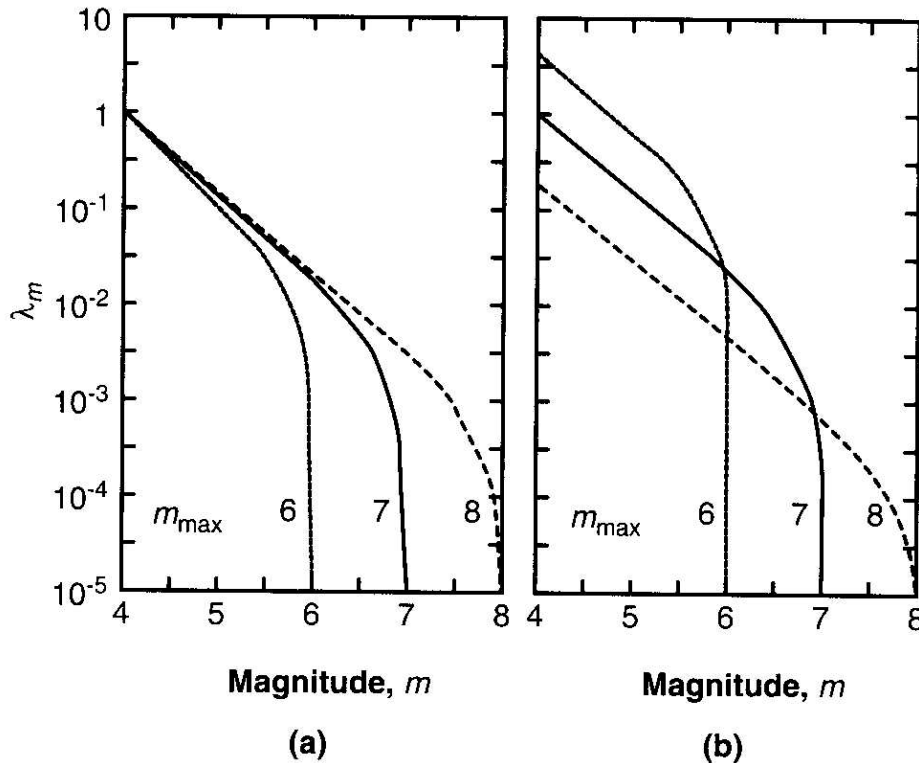


Figure 5-4: Bounded Gutenberg-Richter Recurrence Relationships, Given $m_0 = 4.0$ for (a) Constant Rate of Seismicity, and (b) Constant Rate of Seismic Moment (Based on Youngs and Coppersmith, 1985; After Kramer, 1996)

The probabilistic and cumulative distribution functions for a bounded Gutenberg-Richter recurrence model with upper and lower bounds can be computed respectively as:

$$f_M(m) = \frac{\beta e^{-\beta(m-m_0)}}{1 - e^{-\beta(m_{\max} - m_0)}} \quad (5-6)$$

$$F_M(m) = P[M < m \mid m_0 \leq m \leq m_{\max}] = \frac{1 - e^{-\beta(m-m_0)}}{1 - e^{-\beta(m_{\max} - m_0)}} \quad (5-7)$$

The Characteristic Earthquake Recurrence Laws were developed from paleoseismic studies that suggest that individual points on faults and fault segments tend to move by approximately the same distance in each earthquake. This repetitive earthquake is called the characteristic earthquake and considered to be fault-specific. This theory is supported by geologic evidence that suggests that the characteristic earthquake occurs more frequently along a given fault than would be predicted by extrapolation of the Gutenberg-Richter law (Kramer, 1996). The result is a more complex recurrence law which combines the use of seismicity data to predict the recurrence of lower magnitude earthquakes and geologic data to predict the recurrence of higher magnitude earthquakes. Youngs and Coppersmith (1985) developed such a model, combining an exponential magnitude distribution at lower magnitudes with a uniform distribution near the characteristic earthquake. This model is demonstrated in Figure 5-5. Wesnousky (1994) has suggested that the Characteristic Earthquake recurrence model is likely more appropriate for well-defined faults than the Gutenberg-Richter recurrence model.

For examples of other recurrence models that incorporate the use of a characteristic earthquake, one may refer to Wesnousky et al. (1984), Speidel (1998), Wells (2000), Faccioli et al. (2002), and McGuire et al. (2002).

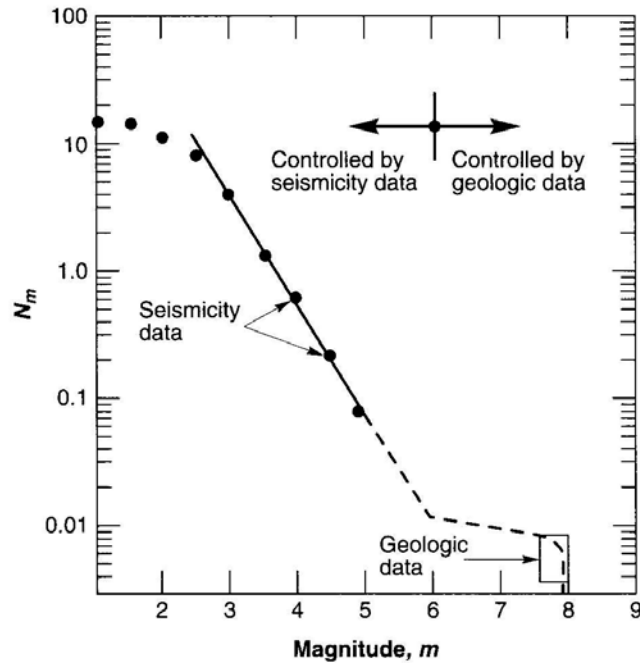


Figure 5-5: Inconsistency of Mean Annual Rate of Exceedance as Determined From Seismicity Data and Geologic Data (After Youngs and Coppersmith, 1985)

5.3.3.3 Uncertainty in the Attenuation Relationships

Because ground motion attenuation relationships are empirically regressed, they have scatter associated with their data. Though least-squares regression is often employed to minimize this scatter, some scatter inherently will remain. This scatter results from randomness in the mechanics of rupture and from variability and heterogeneity of the source, travel path, and site

conditions (Kramer, 1996). Quite often, the standard deviation of the predicted parameter is used to characterize the scatter.

PSHA takes into account the uncertainty in the attenuation relationship data by computing the probability of a ground motion parameter Y exceeding some value of interest, y^* , given certain values of magnitude and distance, m and r . This idea is shown schematically in Figure 5-6, which shows the mean computed values of a given attenuation relationship, the probability distribution function about the mean computed ground motion corresponding to a given magnitude m and distance r , and the probability that the true ground motion given m and r exceeds the value y^* .

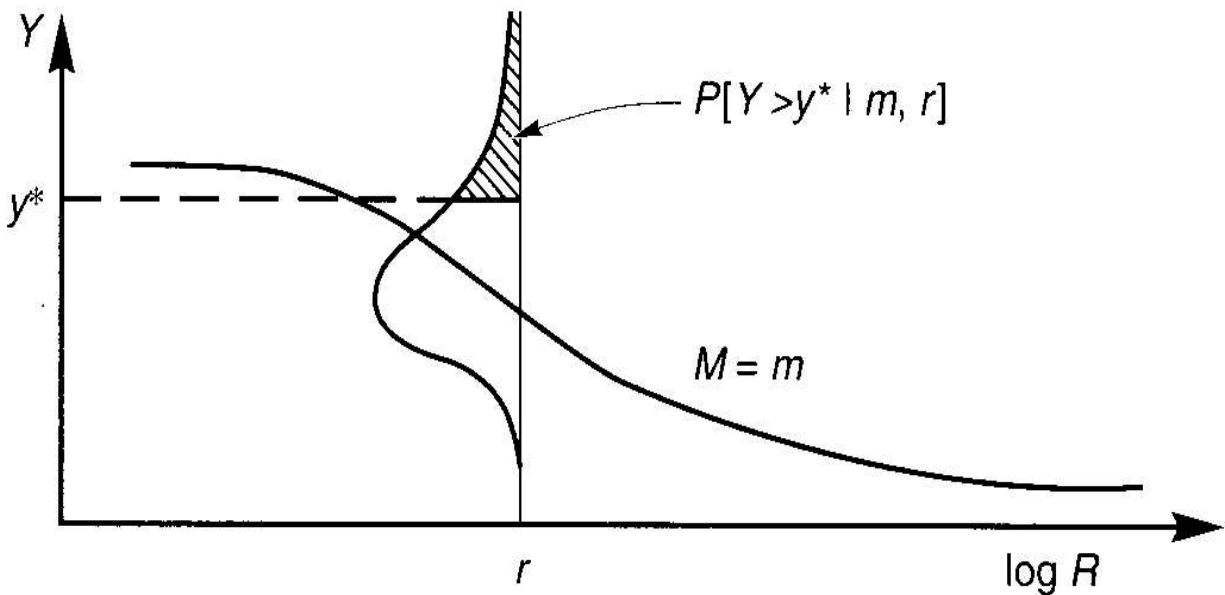


Figure 5-6: Schematic Illustration of Conditional Probability of Exceeding a Particular Value of Ground Motion Parameter for a Given Magnitude and Distance (After Kramer, 1996)

The probability of exceeding some ground motion parameter value y^* can be written as:

$$P[Y > y^* | m, r] = 1 - F_Y(y^*) \quad (5-8)$$

where $F_Y(y^*)$ is the CDF of Y evaluated at y^* . The CDF can be computed using a standard distribution table found in most any statistics textbook, or using a computer program or spreadsheet with probabilistic capabilities. A numerical approximation of the CDF function was also presented in Equation (3-13) in Chapter 3.

5.3.3.4 *Temporal Uncertainty*

The ability to account for temporal uncertainty is an important aspect of a probabilistic seismic hazard analysis and is closely related to uncertainty in earthquake size. Because studies of seismic data have revealed little evidence of temporal patterns in earthquake recurrence, scientists have long assumed that the occurrence of earthquakes is a random process, therefore enabling them to apply simple probabilistic models such as the Poisson probability model to their analyses. However, this assumption appears to contradict the theory of elastic rebound, which states that an earthquake will occur when the accumulating shear stress approaches the shear strength of the rock encountered along the fault plane. The elastic rebound theory suggests that a segment along a fault that has not slipped in a long time will have more elastic strain energy accumulated than another segment along the fault that has recently released its stored strain energy; therefore, the former segment should have a higher probability of experiencing an earthquake than the latter segment. This theory is called the Seismic Gap Theory, and does indeed contradict the idea that earthquake recurrence is a purely random process.

Fortunately, researchers have determined that the use of simple probabilistic procedures for random processes such as the Poisson model is applicable in most seismic hazard analyses. Because the inter-event time for most significant earthquakes is relatively much greater than the time interval being considered in most seismic risk analyses, the error introduced by using probabilistic methods like the Poisson model can typically be considered negligible. Furthermore, Cornell and Winterstein (1986) have investigated the use of Poisson and non-Poissonian models in seismic hazard analysis and have concluded that the use of the Poisson model is valid in most seismic risk analyses, but should not be used when the seismic hazard is governed by a single source for which the time interval since the previous significant event is greater than the average inter-event time and when the source displays strong “characteristic-time” behavior.

Using the Poisson model to characterize temporal uncertainty is therefore considered valid for most practical engineering seismic hazard analysis. The Poisson model provides a way for evaluating the probabilities of events that follow a Poisson process. A Poisson process is a process that satisfies the following properties (Weisstein, 2005):

- 1) The numbers of occurrences of non-overlapping intervals are independent for all intervals.
- 2) The probability of exactly one occurrence in a sufficiently small interval $h \equiv \frac{1}{n}$ is $P = \nu h \equiv \frac{\nu}{n}$, where ν is the probability of one occurrence and n is the number of trials.
- 3) The probability of two or more occurrences in a sufficiently small interval h is essentially zero.

For application in a PSHA, the Poisson probability can be written as follows:

$$P[N = n] = \frac{(\lambda t)^n e^{-\lambda t}}{n!} \quad (5-9)$$

where the random variable N is the number of occurrences of a particular event during a time period of interest, n is the test number of occurrences, t is the time period of interest, and λ is the average rate of occurrence of the event. However, engineers often desire to know the probability that one *or more* significant events will occur during a given time period. This probability can be written as:

$$P[N \geq 1] = P[N = 1] + P[N = 2] + \dots + P[N = \infty] = 1 - P[N = 0] = 1 - e^{-\lambda t} \quad (5-10)$$

Therefore, by obtaining a mean annual rate of exceedance, λ_m , from a recurrence law and combining it with the Poisson model, the probability of occurrence of at least one event in a period of t years can be expressed as:

$$P[N \geq 1] = 1 - e^{-\lambda_m t} \quad (5-11)$$

Likewise, by obtaining a mean annual rate of exceedance λ_{y^*} for any given ground motion parameter y^* and combining it with the Poisson model, the probability of exceeding that ground motion parameter during a period of T years can be expressed as:

$$P[Y_T > y^*] = 1 - e^{-\lambda_{y^*} T} \quad (5-12)$$

While the vast majority of seismic hazard analysis performed today assumes validity of the Poisson model, some instances such as those suggested by Cornell and Winterstein (1986) may exist where a non-Poisson process would be better-suited to represent the temporal uncertainty of the seismic sources in the analysis. If a non-Poissonian process must be used, Kramer (1996) lists several alternative types of models which take into account prior seismicity. These models include nonhomogeneous Poisson models (Vere-Jones and Ozaki, 1982), renewal models (Esteva, 1970; Hagiwara, 1974; Savy et al., 1980; Kiremidjian and Anagnos, 1984; Cornell and Winterstein, 1986; Takahashi et al., 2004; Parsons, 2005), time-predictable models (Anagnos and Kiremidjian, 1984; Kiremidjian et al., 1988; Shanker and Harbindu, 2004), slip-predictable models (Kiremidjian and Anagnos, 1984; Suzuki and Kiremidjian, 1986; Jara and Rosenblueth, 1988), Markov models (Veneziano and Cornell, 1974; Nishioka and Shah, 1980; Thiel and Zsutty, 1987; Rahman and Grigoriu, 1994; Dojcinovsky et al., 1998; Vulpe and Carausu, 2004), semi-Markov models (Patwardhan et al., 1980; Cluff et al., 1980; Coppersmith, 1981; Guagenti-Grandori and Molina, 1984; Kim, 1991; Vulpe and Carausu, 2004), and trigger models (Shlien and Tokosz, 1970; Lai, 1977). The non-Poissonian models listed above are all considered quite advanced and well beyond the scope of this study. Therefore, a Poisson model was assumed valid for all of the PSHAs performed in this study.

5.3.3.5 Steps for Performing a PSHA

The steps for performing a PSHA are similar to the steps for performing a DSHA, but they numerically account for all possible combinations of magnitude and distance, as well as their corresponding uncertainties. Reiter (1990) described the procedure as a four-step process, which is shown schematically in Figure 5-7:

- 1) *Identify and characterize the earthquake sources.* This includes characterizing the probability distribution of potential rupture within each of the sources. A uniform probability distribution of potential rupture is often assumed (i.e. the probability of rupture is the same for every specific point in the source).
- 2) *Characterize the seismicity or temporal distribution of earthquake recurrence by using a recurrence relationship.* Choose an appropriate recurrence law for each earthquake source and assign appropriate parameters for those recurrence laws.
- 3) *Compute the ground motion produced at the site for all possible combinations of earthquake size and location within a source by using a predictive relationship.* The predictive relationship used in a PSHA often comes in the form of an attenuation relationship.
- 4) *Combine the uncertainties in earthquake location, earthquake size, and ground motion parameter prediction.* This step involves the creation of a seismic hazard curve, which is a useful function that plots some ground motion parameter against its mean annual rate of exceedance and will be reviewed in the following section. By utilizing Equation (5-12), seismic hazard curves can be incorporated effectively with the Poisson model to account for temporal uncertainty and to compute the probability that a ground motion parameter will be exceeded during a particular time period. Such information could potentially be valuable to decision-makers, owners, and engineers.

5.3.3.6 *Developing a Seismic Hazard Curve*

Combining the uncertainties in earthquake location, earthquake size, and ground motion parameter prediction in a PSHA involves the creation of a seismic hazard curve. A seismic hazard curve is a function that relates a certain ground motion parameter to its mean annual rate

of exceedance. Such curves can be calculated for each individual earthquake source in a PSHA and then be summed to provide a single function that considers the effects of all possible combinations of magnitude and distance, together with their corresponding uncertainties, from each earthquake source.

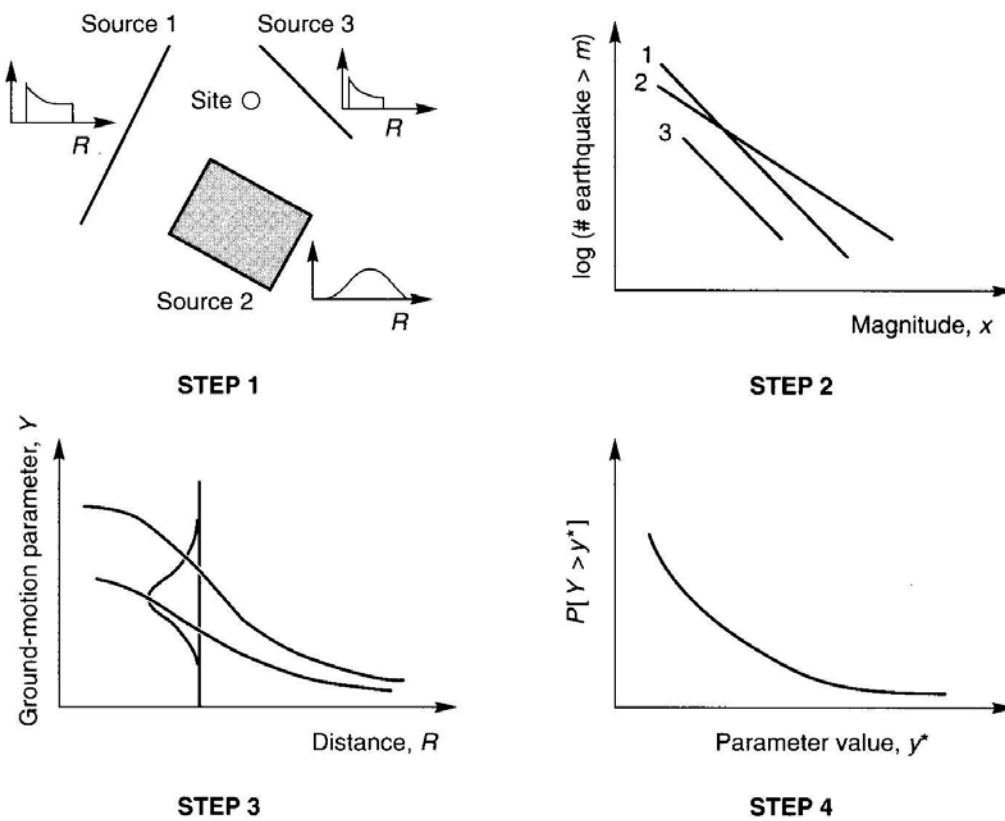


Figure 5-7: Schematic Diagram of the Steps Involved in Completing a PSHA for a Given Site (After Kramer, 1996)

By applying the total probability theorem, the probability that a ground motion parameter Y exceeds the value y^* can be written as:

$$P[Y > y^*] = \iint P[Y > y^* | m, r] f_M(m) f_R(r) dm dr \quad (5-13)$$

where $f_M(m)$ and $f_R(r)$ are the probability density functions for magnitude and distance, respectively. If the site of interest has N_s potential earthquake sources, then Equation (5-13) can be combined with the total average rate of threshold magnitude exceedance ν_i to compute the total average exceedance rate λ_{y^*} , which can be expressed as:

$$\lambda_{y^*} = \sum_{i=1}^{N_s} \nu_i \iint P[Y > y^* | m, r] f_{M_i}(m) f_{R_i}(r) dm dr \quad (5-14)$$

$$\nu_i = e^{\alpha_i - \beta_i m_0} \quad (5-15)$$

where $\alpha = 2.303a$ and $\beta = 2.303b$.

Equation (5-14) can be approximated numerically with the following equation:

$$\lambda_{y^*} \approx \sum_{i=1}^{N_s} \sum_{j=1}^{N_M} \sum_{k=1}^{N_R} \nu_i P[Y > y^* | m_j, r_k] P[M = m_j] P[R = r_k] \quad (5-16)$$

The accuracy of Equation (5-16) improves with increasing values of N_M and N_R . In order to approximate $P[M = m_j]$ and $P[R = r_k]$, Equation (5-16) can be rewritten as:

$$\lambda_{y^*} \approx \sum_{i=1}^{N_s} \sum_{j=1}^{N_M} \sum_{k=1}^{N_R} \nu_i P[Y > y^* | m_j, r_k] f_{M_i}(m_j) f_{R_i}(r_k) \Delta m \Delta r \quad (5-17)$$

$$m_j = m_0 + (j - 0.5) \frac{(m_{\max} - m_0)}{N_M} \quad (5-18)$$

$$r_k = r_{\min} + (k - 0.5) \frac{(r_{\max} - r_{\min})}{N_R} \quad (5-19)$$

$$\Delta m = \frac{(m_{\max} - m_0)}{N_M} \quad (5-20)$$

$$\Delta r = \frac{(r_{\max} - r_{\min})}{N_R} \quad (5-21)$$

A single point on a seismic hazard curve is created when λ_{y^*} is computed. To develop the entire hazard curve, the process must be repeated for all possible values of y^* . Once the desired number of values of λ_{y^*} has been computed, then the points can be connected with a line and the seismic hazard curve is complete.

Figure 5-8 shows an example plot of a seismic hazard curve that has three seismic sources and incorporates peak horizontal acceleration (PHA) as its ground motion parameter. Such a plot is useful for decision-makers because it can be combined with the Poisson model shown in Equation (5-12) to return the probability that some ground motion parameter is exceeded in a given time period. Engineers can also work the equation “backwards” by solving for the value of λ_{y^*} that corresponds with some desired probability of exceedance in a given time period, and then use the seismic hazard curve to obtain the ground motion parameter value

y^* that corresponds with that value of λ_{y^*} . That value of y^* would then become the design ground motion parameter.

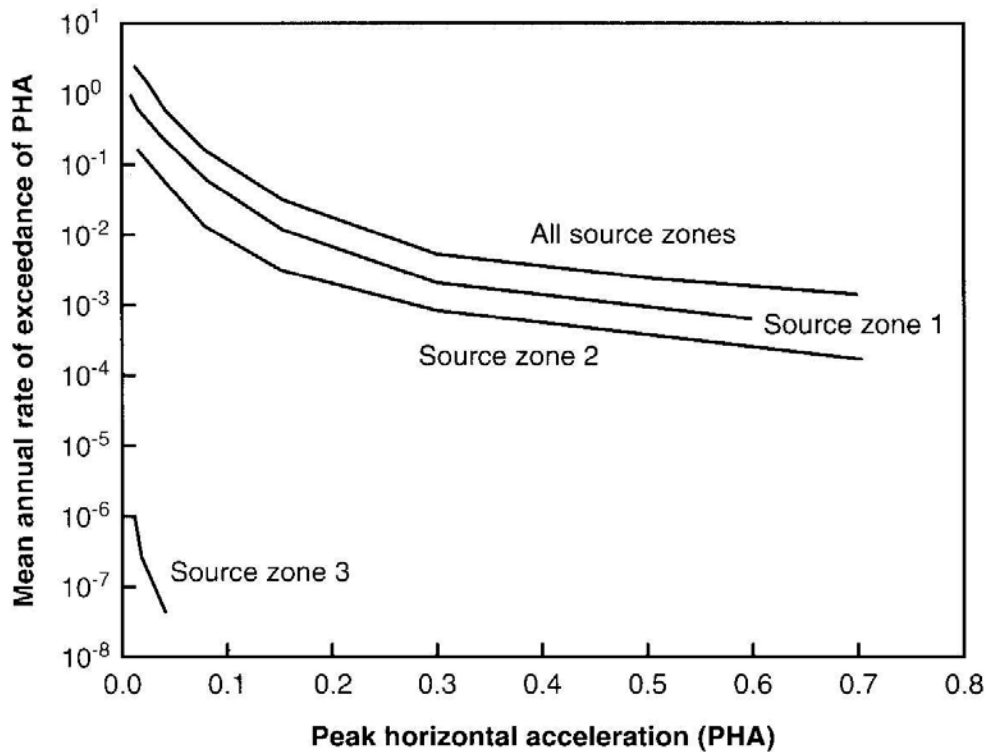


Figure 5-8: Example of Seismic Hazard Curves for the Peak Horizontal Acceleration (PHA) Computed for a Given Site With Three Separate Seismic Sources (After Kramer, 1996)

5.3.3.7 Deaggregation

PSHA involves the summing of individual ground motion parameter values for every possible magnitude and distance combination from each earthquake source in order to obtain a total ground motion hazard value. However, it is often useful for engineers to be able to review

the individual contributions to the total hazard from each combination of magnitude and distance in order to see which combinations carry the greatest influence. To do this, a PSHA must be “deconstructed,” meaning that the total hazard value must be broken up into the individual contributions from each combination of magnitude and distance. This process of deconstructing a PSHA is called *deaggregation*.

The individual contribution to the total hazard from the combination of magnitude m_j and distance r_k can be approximated as:

$$\lambda_{y^*}(m_i, r_k) \approx P[M = m_j] P[R = r_k] \sum_{i=1}^{N_s} v_i P[Y > y^* | m_j, r_k] \quad (5-22)$$

By applying Equation (5-22) to all possible combinations of magnitude and distance, an array of contributory hazard values can be made, the sum of which returns the total hazard value for the ground motion parameter. This data is well represented in graphical form as a deaggregation plot, which is a 3-dimensional plot that considers magnitude, distance, and contribution to the total hazard. Such a plot can often reveal the location and significance of different earthquake sources, and sometimes engineers choose to perform deterministic evaluations of various seismic-related hazards using the mean or modal values of magnitude and/or distance from the deaggregation. Figure 5-9 gives an example of a deaggregation plot for a site in downtown Seattle. The crustal events are mostly from the Seattle fault, which runs in an east-west direction directly through the downtown corridor. The interplate sources and the intraplate sources (or Benioff Zone) come from the Cascadia Subduction Zone, which is located to the west of Seattle.

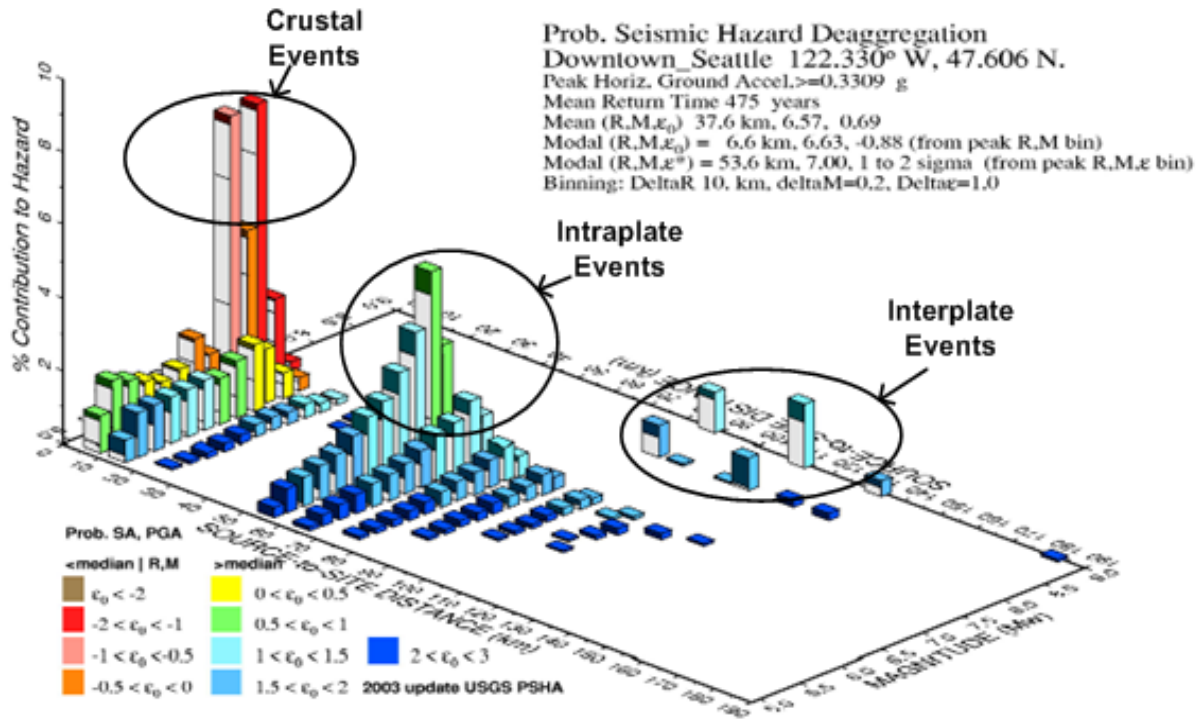


Figure 5-9: Seismic Hazard Deaggregation Plot of the PHA for a Site in Downtown Seattle, WA (Courtesy of Wessel and Smith, USGS, 2002)

5.4 Introduction to PEER PBEE Framework

PBEE provides a methodology that considers the contributions from all hazard levels and incorporates them into a performance evaluation. Such an approach may be preferable over a deterministic design approach, which usually considers a single ground motion hazard level (i.e. a single return period) in earthquake engineering design. In order to consider the probabilistic contributions from all return periods, PBEE must be performed in a probabilistic framework. By doing so, PBEE can ultimately compute the risk associated with earthquake hazard at a given site, which can be expressed in terms of economic loss, fatalities, or other form of loss measurement. The Pacific Earthquake Engineering Research Center (PEER) has developed such

a framework (Cornell and Krawinkler, 2000; Krawinkler, 2002; Deierlein et al., 2003). By utilizing PBEE within the PEER probabilistic framework, risk can effectively be computed as a function of ground shaking through the use of several intermediate variables, which will be defined in the following section.

5.4.1 PEER PBEE Framework Variable Definitions

The variables that comprise the PBEE probabilistic framework developed by PEER are defined as:

- 1) *Intensity Measure, IM* – This variable characterizes the ground motion and could be represented as any one of a number of ground motion parameters (e.g. *PGA*, Arias intensity, etc.). The mean annual rate of exceedance of the *IM*, λ_{IM} , is used in PBEE and must be calculated by means of a PSHA utilizing *IM* as the ground motion parameter of interest.
- 2) *Engineering Demand Parameter, EDP* – This variable shows the effects of the *IM* on the response of a system of interest. Like the *IM*, *EDPs* can also be represented as any one of a number of parameters (e.g. excess pore pressure, *FS_L*, lateral spread displacement, etc.).
- 3) *Damage Measure, DM* – This variable shows the physical effect of the *EDP* as damage to the system of interest. It describes the damage and consequences of damage to a structure or to a component of the structural, nonstructural, or content system (Krawinkler and Miranda, 2004). Kinematic pile response can be considered a *DM*.
- 4) *Decision Variable, DV* – This variable is the quantifiable value on which ultimate performance assessment is based, and can be thought of as the risk associated with the

DM. The *DV* provides information that is very useful for decision-makers and can be represented by such parameters as repair cost, downtime, lives lost, etc.

5.4.2 PEER PBEE Framework Equation

The framework equation developed by PEER to house PBEE is based on the same probabilistic principles that are used in a PSHA calculation. The fundamental equation for this framework can be given as:

$$\lambda_b = \int P[B > b | A] d\lambda_A \quad (5-23)$$

where λ_b is the mean annual rate of exceeding value b , $P[B > b | A]$ is the probability that parameter B exceeds the value b given A , and λ_A is the mean annual rate of exceeding the parameter A . Equation (5-23) returns the single value on the seismic hazard curve corresponding to a value of b .

Substituting the PEER PBEE definitions into Equation (5-23), one can develop a “chain” of system performance as long as a proper order of relations is established (i.e. $IM \rightarrow EDP \rightarrow DM \rightarrow DV$). In other words, one cannot calculate λ_{DM} directly from the IM because DM is dependent on the EDP .

Substituting in the Engineering Demand Parameter and the Intensity Measure, Equation (5-23) can be rewritten using a numerical approximation as:

$$\lambda_{edp} \approx \sum_{i=1}^{N_i} P[EDP > edp | IM = im_i] \Delta\lambda_{IM} \quad (5-24)$$

where $P[EDP > edp | IM = im_i]$ can be computed from a complementary CDF that relates $P[EDP > edp]$ to the IM . This type of CDF is called a fragility curve. An example of a series of fragility curves is presented in Figure 5-10. Equation (5-24) is demonstrated visually in Figure 5-11.

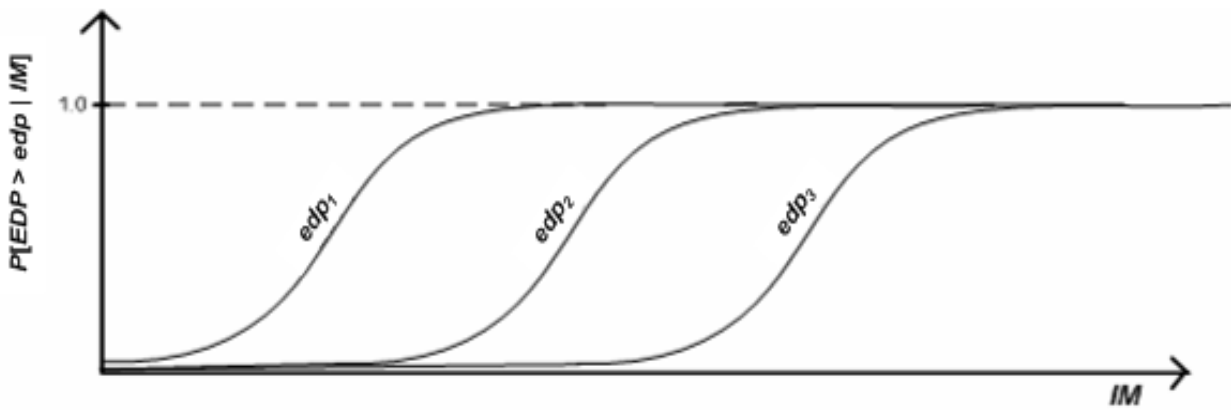


Figure 5-10: Example for Fragility Curves for Some EDP Given Some IM

It is possible to consider all of the PEER PBEE parameters in a single equation to obtain the seismic hazard curve for the DV by utilizing the seismic hazard curve for the IM . This mathematical equation has become well-known in the earthquake engineering community as “PEER’s triple integral.” The equation is given as:

$$\lambda_{DV} = \iiint P[DV | DM] dP[DM | EDP] dP[EDP | IM] d\lambda_{IM} \quad (5-25)$$

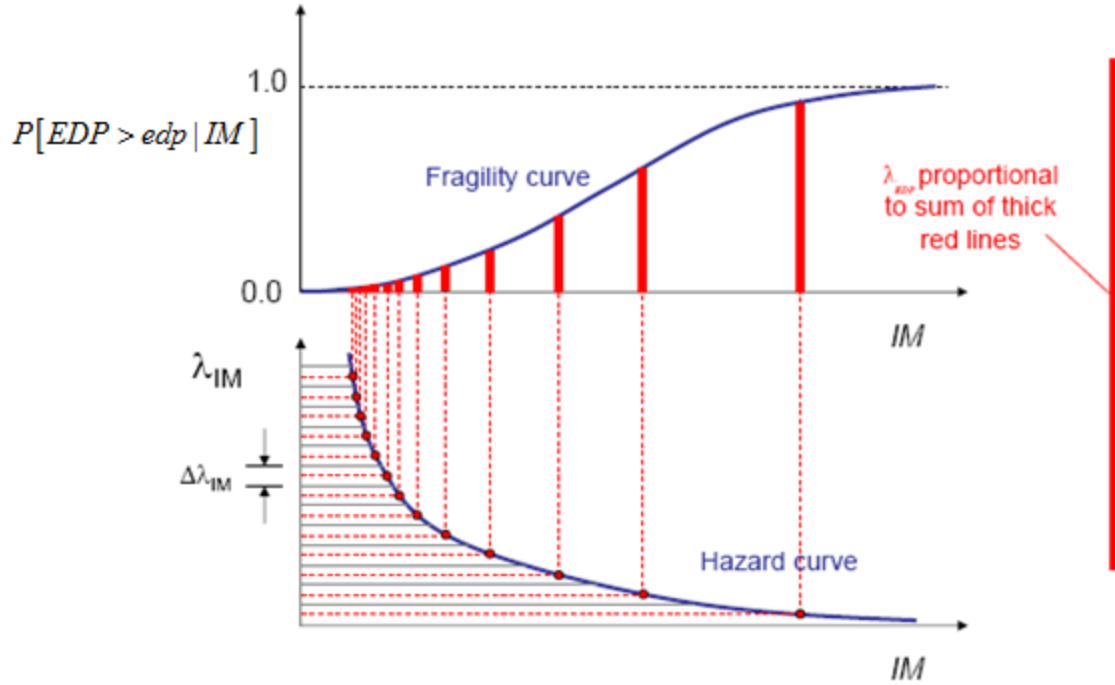


Figure 5-11: Visual Representation of Equation (5-24) (Courtesy of Steven Kramer, From a NEES Presentation in 2005)

Equation (5-25) can be approximated numerically as:

$$\lambda_{DV} \approx \sum_{k=1}^{N_{DM}} \sum_{j=1}^{N_{EDP}} \sum_{i=1}^{N_{IM}} P[DV > dv | DM = dm_k] P[DM = dm_k | EDP = edp_j] P[EDP = edp_j | IM = im_i] \Delta\lambda_{IM} \quad (5-26)$$

where N_{DM} , N_{EDP} , and N_{IM} are the number of increments of DM , EDP , and IM , respectively.

The accuracy of Equation (5-26) increases as N_{DM} , N_{EDP} , and N_{IM} increase.

The final product of Equations (5-25) or (5-26) is the mean annual rate of exceedance of the DV , λ_{DV} . This implies that one could incorporate λ_{DV} with a temporal uncertainty model (i.e.

the Poisson model) to obtain the probability that some value, DV^* , will be exceeded during a given time period. Alternatively, the mean annual rate of exceedance for any other performance parameter short of the DV can be computed as long as a proper chain of parameters is incorporated in the probabilistic analysis. Such information could be extremely valuable to decision-makers and spare the challenge of attempting to base decisions on subjective interpretations of the IM or the EDP alone.

5.5 Chapter Summary

Performance-based earthquake engineering (PBEE) is a relatively recent concept in earthquake resistant design and is founded in the idea that uncertainty in engineering design can be quantified and used in predicting performance such that engineers and owners together can make intelligent and informed trade-offs based on life-cycle considerations rather than construction costs alone. PBEE does not consider a single scenario seismic hazard, but rather considers the contributions from the entire seismic hazard spectrum. Because of this, PBEE must be incorporated within a probabilistic framework.

Seismic hazard analyses are used by engineers to determine design ground motion parameters. There are two basic types of seismic hazard analyses: deterministic seismic hazard analyses (DSHA) and probabilistic seismic hazard analyses (PSHA). A DSHA considers only one combination of magnitude and distance, and it usually accounts for uncertainty by incorporating large amounts conservatism in the analysis (i.e. the worst-case scenario is used in the calculations). A PSHA produces more realistic design parameters by considering the contribution of every possible combination of magnitude and distance from every possible significant earthquake source, together with their respective uncertainties (i.e. uncertainty in

earthquake location, size, and predictive relationship data). PSHAs are often used to develop seismic hazard curves, which relate mean annual probability of exceedance of some ground motion parameter to the ground motion parameter itself. Seismic hazard curves are used in PBEE and can be incorporated with a temporal uncertainty model (e.g. the Poisson model) to predict the probability of the ground motion parameter of interest exceeding a certain value within a certain time frame. The Poisson model is often incorporated with predicting earthquake probabilities because the time between significant earthquake events is relatively large with respect to the time frame being considered in the temporal uncertainty model. PSHAs can also conveniently be broken apart to reveal the individual contribution from each combination of magnitude and distance to the total hazard. This type of analysis is called deaggregation, and deaggregation data and more is available for sites located in the United States from the US Geological Survey.

The Pacific Earthquake Engineering Research Center (PEER) has developed a probabilistic framework to be utilized by PBEE. The framework consists of intermediate variables named the Intensity Measure (*IM*), Engineering Demand Parameter (*EDP*), Damage Measure (*DM*), and Decision Variable (*DV*). These variables are related and can be combined together with their corresponding conditional probabilities to produce hazard curves that correspond to various parts of the system, which can then be used in risk analysis by engineers and owners to make informed design decisions based on likely structural performance, not just construction costs.

6 PERFORMANCE-BASED KINEMATIC PILE RESPONSE

6.1 Introduction

Using the principles presented in the previous chapters regarding liquefaction triggering, lateral spread, kinematic pile response analysis, and performance-based earthquake engineering, a new performance-based procedure for the evaluation of the kinematic pile response due to lateral spread will be presented in this chapter. This procedure does not represent a new stand-alone “model,” but rather a systematic application of previously-published methods and procedures applied in the performance-based probabilistic framework developed by PEER. This procedure is intended to provide engineers with a new analytical tool in their evaluation of risk and the probability of foundation failure due to kinematic loading.

This chapter will attempt to present the new performance-based procedure by first stating all of the assumptions made in applying this procedure. The procedure will then be presented logically as a series of steps. Finally, a simple hypothetical demonstration of the procedure will be provided.

6.2 Assumptions of the Procedure

The performance-based procedure presented in this chapter is developed for the analysis of lateral spread in the native soil, which is sometimes referred to as *regional* lateral spread. While it is recognized that seismic slope displacements are closely related to the phenomenon of

lateral spread and that both are capable of inflicting significant damage to foundations due to kinematic loading, the methodologies applied by engineers to estimate deformations from each can be quite different, and it is therefore justifiable that the mechanisms be evaluated separately. With that assumption being stated, the performance-based procedure presented in this chapter is sufficiently robust to be applicable to the evaluation of seismic slope displacements as well as to the evaluation of lateral spread displacements. However, the development of a procedure to estimate performance-based seismic slope displacements for use in the performance-based kinematic pile response procedure is beyond the scope of this study, and only a procedure for the performance-based computation of lateral spread displacements are presented herein.

The procedure developed in this study assumes that kinematic loading due to lateral spread is the primary cause of loading to the foundations. While it is possible to include the addition of other externally-applied loads in the kinematic analysis including inertial loads, drag loads from the free-field soil displacements, and structural bracing loads from the superstructure, no recommendations regarding the evaluation and quantification of the uncertainty of such loads is provided in this study. Therefore, any additional inertial loading considered in the analysis by the user must either be evaluated using a probabilistic/stochastic methodology developed by the user or must be considered as constant parameter that does not vary with the return period of the analysis. Such assumptions are not intended to minimize or de-emphasize the effects that these externally-applied forces can have on the performance of a given foundation system. Rather, they are intended to simplify the analysis and remain consistent with many of the deterministic practices that are commonly applied in industry today. Ultimately, it is left to the user to apply sound engineering judgment in evaluating whether or not to include the effects of externally-

applied forces in the performance-based kinematic pile response procedure presented in this study.

The performance-based procedure developed in this study is applicable only to sites where lateral spread displacements can reasonably be predicted. Conditions where liquefaction flow failure is likely to occur are not valid to be modeled with the procedure presented herein. A simple evaluation of the potential likelihood of a flow failure occurring given the triggering of liquefaction in one or more soil layers can be easily be performed using a post-seismic 2D limit equilibrium slope stability analysis as described in Chapter 3. If the limit equilibrium stability analysis yields a factor of safety equal to unity or less, then it can be assumed that liquefaction flow failure is likely to occur given liquefaction triggering of the soil, and significantly large soil deformations are likely to result. As stated previously, no reliable methodology currently exists for accurately predicting the deformations resulting from a liquefaction flow failure.

6.3 Steps in the Performance-Based Kinematic Pile Response Procedure

The performance-based procedure developed in this study utilizes the probabilistic framework developed by PEER that was summarized in Chapter 5. As such, the Intensity Measure will be defined as a portion of the empirical lateral spread equations which behaves like an attenuation relationship as described by Kramer et al. (2007). The Engineering Demand Parameter will be defined as lateral spread displacement. Finally, the Damage Measure will be defined as kinematic pile response, and can ultimately be defined as pile displacement, shear force in the pile, slope of the pile, or bending moment in the pile. The steps for performing the performance-based kinematic pile response procedure can be summarized as follows:

- 1) Characterize the soils at the site;
- 2) Characterize the geometry/topography of the site;
- 3) Characterize the seismicity of the site;
- 4) Evaluate the potential for flow failure at the site;
- 5) Develop the Intensity Measure for the performance-based procedure;
- 6) Develop fragility curves linking the Intensity Measure to the Engineering Demand Parameter (lateral spread displacement);
- 7) Develop the Engineering Demand Parameter (lateral spread displacement) for the performance-based procedure;
- 8) Develop fragility curves linking the Engineering Demand Parameter to the Damage Measure (kinematic pile response); and
- 9) Develop the Damage Measure (kinematic pile response) for the performance-based procedure.

6.4 Soil Site Characterization

Evaluation of the soils at the site of interest is a critical component of the performance-based kinematic pile response analysis. Because the procedure recommended in this study involves regional lateral spread, it is necessary to identify continuous liquefiable layers upon which non-liquefiable soil may displace laterally due to earthquake ground motion. Ideally, the site characterization would be comprised of several SPT borings and CPT soundings in order to establish the possibility of soil layer continuity. Investigative borings and soundings ideally should comprise a line spread across several hundreds of feet in the direction parallel to the anticipated lateral spread displacements (i.e. in the direction perpendicular to the orientation of

the free face, or parallel to the direction of the gradient of the sloping ground.) In addition, a smaller line of borings and soundings should be performed perpendicular to the fore-mentioned line in order to further establish layer continuity. SPT borings ideally would be performed with mud rotary drilling methods in order to minimize the potential for heaving sands at the bottom of an open boring, which are known to create artificially loose soils and inaccurately low SPT blowcounts. If mud rotary methods are not an option, then it is advisable to maintain a head of water in the boring in order to reduce the likelihood of heaving sands. Accurate measurement of the groundwater elevation is also of critical importance, and the installation of one or more piezometers may be advisable.

Because average shear wave velocity measurements are a required input for both the Cetin et al. (2004) liquefaction triggering procedure and the NGA attenuation relationships for ground motion estimation, it is also advisable to perform some sort of direct measurement of the average shear wave velocity profile at the site within the top 30 meters (100 feet) of the soil profile. There are several different methodologies to perform these measurements and they vary considerably in their complexity, cost, and quality of data produced. For high-resolution shear wave velocity profiles, more advanced techniques of directly measuring the shear wave velocity such as downhole logging, crosshole logging, or suspension logging may be used. If the soils are sufficiently soft/loose, then a seismic CPT could also be used to develop a fairly reliable shear wave velocity profile. If an averaged shear wave velocity profile is acceptable, then surface geophysical methods may provide an easier and more economical solution to measuring the shear wave velocity at the site. Such methods include Spectral Analysis of Surface Waves (SASW), Multichannel Analysis of Surface Waves (MASW), and Refraction of Microtremor Analysis (ReMi). These methods typically involve the placement of a line of geophones (i.e.

specialized equipment for detecting velocity pulses in the soil). A seismic source is typically generated, and the time for the resulting energy pulse to reach each geophone is measured. Analysis of the data results in an average estimate of the shear wave velocity over a specified depth. An example of the MASW technique is shown below in Figure 6-1.

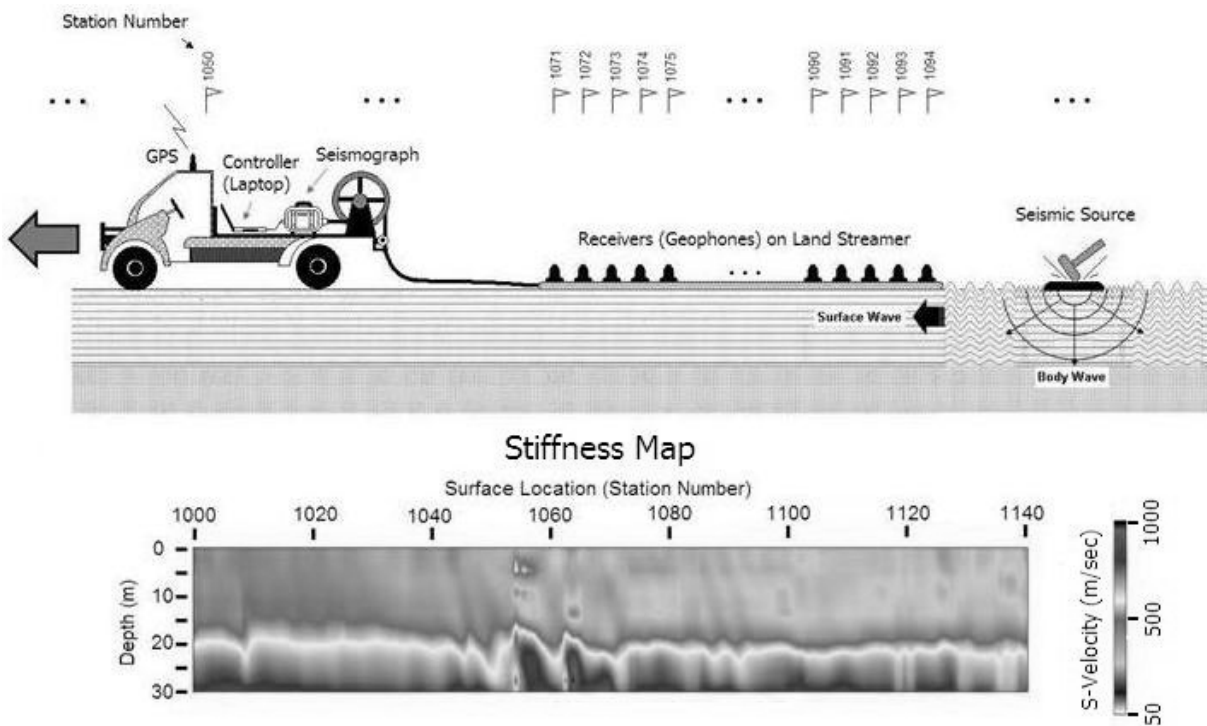


Figure 6-1: MASW Technique and Typical Output for Obtaining an Average Measurement of Shear Wave Velocity at a Given Site (Courtesy of Kansas Geological Survey; After Park Seismic, 2010)

Once all of the soil samples are obtained from the borings, certain laboratory tests should be assigned to various representative samples in order to estimate soil properties that are potentially necessary in the analysis of liquefaction triggering and lateral spread. These tests

include sieve analyses and/or #200 washes to evaluate fines content and grain size distributions, Atterberg limits on fine-grained soil samples to measure liquid limits and soil plasticity, and water content measurements.

Comparison of the SPT borings, CPT soundings, and any available geophysical data should be performed collectively. A convenient way to perform such a comparison is by using a fence diagram, which is simply a 2D layout of the various borings and soundings plotted according to elevation. Such a plot may assist the engineer in identifying continuous soil layers present at the site of interest. Each layer identified as being continuous should have its various soil properties including SPT blowcounts, grain size distribution, fines content, Atterberg limits, and moisture contents averaged across the layer in order to develop a generalized soil profile to represent the site. While it may be easy to provide such written guidance on the development of a generalized soil profile for a site, the practical application of such development can often be quite difficult and subjective. The ability to identify continuous soil layers and develop a representative and accurate generalized soil profile for modeling truly is an art which requires patient practice until mastery and reputability are achieved.

In the event that significant soil continuity does not exist at the site, then it is not likely that regional lateral spread will occur and the performance-based kinematic pile response procedure is considered to be complete. However, other potential hazards to the foundation may still need to be considered such as localized seismic slope displacements, inertial loading and other soil-structure-interaction effects due to the seismic response of the superstructure, and kinematic loading on the piles due to wave passage effects and soil impedance. The elaboration on such hazards, however, is beyond the scope of the current study.

6.5 Characterization of Site Geometry/Topography

Characterization of site geometry is a critical part of performing any lateral spread analysis. If using empirical MLR lateral spread procedures to estimate displacements, it is typically necessary to characterize the site as having either a “free-face” condition or a “ground-slope” condition. A free-face condition is generally recognized as a distinct break in the slope or the topography. A simple graphical representation of a free-face is shown in Figure 3-2. Examples free-face conditions include river channels, quay walls, and man-made excavations. A ground-slope condition is generally recognized as the average regional slope gradient across the site of interest. History has demonstrated that even very shallow gradients can be susceptible to lateral spread displacements.

Scenarios often arise where it may be difficult to determine whether a particular site should be treated as a free-face condition or as a ground-slope condition. These cases reiterate the fact that nature rarely produces clear-cut scenarios to be used in engineering design, and thus subjective reasoning and engineering judgment typically must be applied. While some published empirical lateral spread models were developed to allow the user to model a combined free-face/ground-slope condition (e.g., Rauch and Martin, 2000; Faris et al., 2006), most models require either a free-face or a ground-slope designation. A reasonable approach is to perform the analysis twice using both the free-face and the ground-slope geometries. Upon comparing the computed displacements, engineering judgment should be applied in selecting which condition would be most appropriate to incorporate into design.

6.6 Characterization of Site Seismicity

A critical component of the performance-based kinematic pile response procedure is the characterization of seismicity and liquefaction potential at the site. Evaluation of the seismicity for the performance-based procedure consists of estimating the seismic hazard curve for the Peak Ground Acceleration. Evaluation of the PGA ground motion parameter can be performed by either a 1) site-specific PSHA, or 2) reliance on seismic hazard results developed as part of the National Seismic Hazard Mapping Project (NSHMP) of the United States Geological Survey (USGS). Note that the latter option can only be performed for sites located within the boundaries of the United States. Either option requires that the seismic hazard curve for the PGA be defined and corresponding deaggregation results be tabulated. In order to adequately define the seismic hazard curve for most performance-based engineering applications, PGA values and corresponding deaggregations should be developed for at least seven return periods: 108 years (50% probability of exceedance in 50 years), 225 years (20% probability of exceedance in 50 years), 475 years (10% probability of exceedance in 50 years), 975 years (5% probability of exceedance in 50 years), 2475 years (2% probability of exceedance in 50 years), 4975 years (1% probability of exceedance in 50 years), and 10000 years (<1% probability of exceedance in 50 years). Intermediate values on the seismic hazard curve can generally be log-linearly interpolated from these results with relatively small amounts of error.

6.6.1 Site-Specific PSHA

A site-specific PSHA involves not only the characterization of the soils at the site of interest, but it also requires development of the seismic source model to use in the PSHA. The seismic source model is the collection of potentially significant seismic sources and their

corresponding geometries, magnitude characteristics, and recurrence rates for those sources. Part of the development of the seismic source model includes consideration of uncertainties due to random occurrence, and uncertainties due to a lack of knowledge of the seismic sources and their associated behavior/characteristics. These uncertainties are generally defined as *aleatory uncertainty* and *epistemic uncertainty*, respectively. While aleatory uncertainty is usually handled by the hazard integral itself of the PSHA, epistemic uncertainty is typically handled using a logic-tree approach. Such an approach recognizes that there are several possibilities associated with a given seismic source's geometry, recurrence patterns, and which attenuation relationship(s) may best represent the ground motions produced by the source. Each possible combination of uncertainties comprises a "branch" on the logic tree. Each branch is assigned a corresponding weight or probability of occurrence. At any given level within the logic tree, the sum of the branches must equal unity. An example of a logic tree is presented below in Figure 6-2.

While a seismic source model and its associated logic tree can be built "from scratch," the process is widely recognized to be quite complex, and only a relatively small circle of professionals today is generally considered reputable in the development of such models due to the subjective reasoning required to characterize the epistemic uncertainty and to form the logic tree. As such, a few of these reputable professionals have developed and maintain active libraries of seismic source models which can be licensed to other practicing professionals for use in a PSHA. A popular commercial software package for performing seismic hazard analysis currently available for such licensing is called EZ-FRISK (Risk Engineering, 2010). While EZ-FRISK was used to perform all of the PSHAs associated with this study, it is recognized that a wide variety of other similar software are available for use in engineering design.

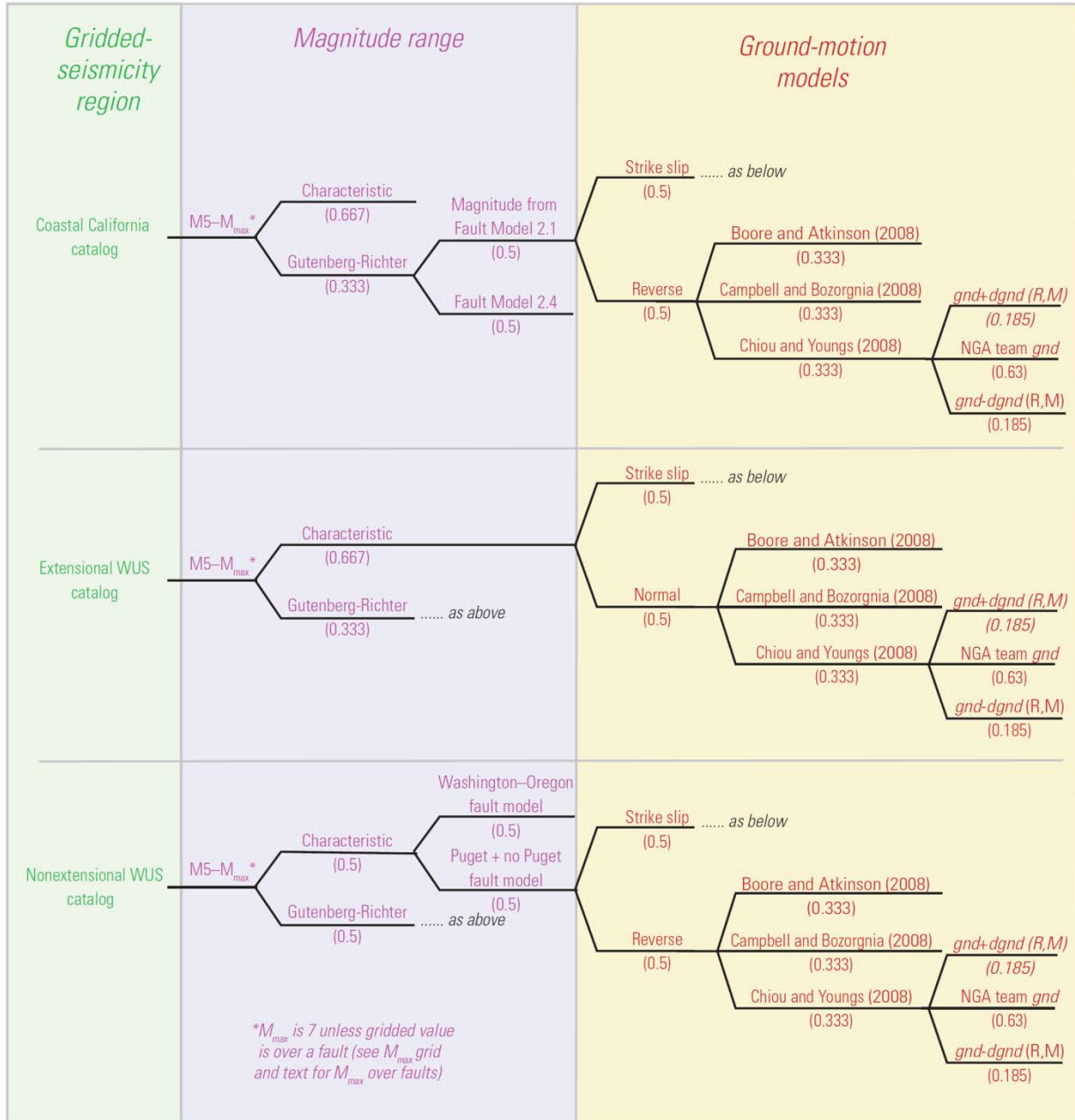


Figure 6-2: Example of a Logic Tree for Seismic Hazard Analysis of Gridded Seismic Sources in the Western United States (After Petersen et al., 2008)

A site-specific PSHA may simply consist of the use of attenuation relationships with the probabilistic hazard integrals associated with a PSHA, or it may also involve more advanced

consideration of the site-specific soil amplification effects if local soil conditions warrant such consideration. This type of analysis is known as a *site response analysis*, and is generally only used in cases associated with critical and/or sensitive structures underlain by significant amounts of very soft soils or soils susceptible to liquefaction. Further discussion on the topic of site response analysis is beyond the scope of this study, but one may refer to Kramer (1996) and Stewart and Kwok (2008) for more information on current methods and recommendations regarding this type of analysis. However, regardless of whether or not a site response analysis is incorporated into the site-specific PSHA, consideration of such things as soil amplification effects, basin effects, and near-source/directivity effects should be properly given. Most recently-developed attenuation relationships such as the NGA relationships attempt to account for soil amplification and basin effects by incorporating such parameters as average shear wave velocity of the soil and depth to bedrock.

6.6.2 USGS National Seismic Hazard Mapping Project

In the absence of software for performing site-specific consideration of probabilistic ground motions, an engineer may use probabilistic ground motion data made available to the public by the USGS for sites located within the United States and its territories. Because designing structures that are resistant to earthquake loading is the country's first and most effective defense against an earthquake catastrophe, the USGS has prepared a collection of maps and data that reflect the current state of knowledge of earthquake shaking hazards for the United States. The information from these maps is often utilized by engineers in the design buildings, bridges, highways, and utilities. The information is also reviewed and used by professional organizations of engineers, as well as by city, county, and state government agencies to develop and update building codes (Brown et al., 1996).

The NSHMP is part of the National Earthquake Hazard Reduction Program (NEHRP). The NSHMP produces design maps, which show zones or contours of different recommended levels of design for earthquake-resistant construction and are based on shaking-hazard maps prepared by USGS scientists and engineers (Brown et al., 1996). A shake map shows the severity of the expected earthquake shaking given a certain level of probability. Shake maps are updated as USGS scientists learn more about the seismicity of the United States. Such updates occurred in 1976, 1996, 2002, and 2008. These updates typically result in significant changes to the seismic design maps included in such building codes as the Uniform Building Code (UBC), International Building Code (IBC), and ASCE 7.

USGS shake maps are developed by contouring given values of spectral acceleration (S_a) at a given return period interpolated from seismic hazard curves, which were developed from a series of PSHAs performed at various gridded points across the country. The PSHAs used for these analyses required characterization of the earthquake sources and development of a robust seismic source model and logic tree (Petersen et al., 2008). The USGS used historical earthquakes, quaternary data, and geodetic data to develop characteristic models for predicting the recurrence of fault sources and areal sources in the United States. Appropriate attenuation relationships were assigned to compute the ground motions from the various seismic sources in the source model. It is known that softer soils tend to amplify surface displacements, and the attenuation relationship uncertainties often account for these local site effects. However, when the local site effects were not accounted for in the attenuation relationship uncertainties, then the attenuation models were adjusted and corrected by performing generalized site response analyses (USGS EHP, 2010).

Much of the information produced by the NSHMP can be conveniently downloaded by the public from the USGS NSHMP website (developed by USGS EHP, 2010, and currently accessible at <http://earthquake.usgs.gov/hazards/>.) The information available to users includes shake maps for spectral accelerations corresponding to various periods of vibration, shake maps incorporating time-dependent recurrence models, earthquake hazard scenario maps, software tools for producing mapped ground motion estimates for specific sites, custom mapping tools for ground motions, interactive deaggregation tools, and various fault maps. Using these interactive mapping tools made available to the public by the USGS, a seismic hazard curve can be developed for a given site and corresponding deaggregations of the seismic hazard can be developed for any site within the United States.

6.6.3 Liquefaction Triggering Analysis

Part of the characterization of the seismicity of the site in the proposed performance-based procedure for the analysis of kinematic pile response is the liquefaction triggering analysis. Deterministic procedures for estimating liquefaction triggering using the Cetin et al. (2004) procedure with a given set of values for magnitude, PGA, average shear wave velocity, and soil SPT blowcounts was presented in Chapter 2. However, values of PGA and magnitude are not considered constant parameters in a performance-based analysis. As such, the performance-based procedure developed by Kramer and Mayfield (2007) for the evaluation of liquefaction triggering is recommended for use in this procedure. According to this procedure, the annual rate of non-exceedance for factor of safety against liquefaction can be computed as:

$$\Lambda_{FS_L^*} = \sum_{j=1}^{N_M} \sum_{i=1}^{N_{a_{\max}}} P[FS_L < FS_L^* | a_{\max_i}, m_j] (\Delta\lambda_{a_{\max_i}, m_j}) \quad (6-1)$$

where N_M and $N_{a_{\max}}$ are the number of magnitude and peak acceleration increments into which the “hazard space” is subdivided; and $\Delta\lambda_{a_{\max},m_j}$ is the incremental mean annual rate of exceedance from the seismic hazard curve of peak ground acceleration a_{\max} corresponding to magnitude m_j . $P[FS_L < FS_L^* | a_{\max}, m_j]$ is the probability of non-exceedance of the factor of safety against liquefaction FS_L^* computed according to Cetin et al. (2004) given the peak ground acceleration a_{\max} and magnitude m_j and is given as:

$$P[FS_L < FS_L^* | a_{\max}, m_j] = \Phi \left[-\frac{(N_1)_{60} (1 + \theta_1 FC) - \theta_2 \ln(CSR_{eq,i} \cdot FS_L^*) - \theta_3 \ln m_j - \theta_4 \ln \left(\frac{\sigma'_{v0}}{p_a} \right) + \theta_5 FC + \theta_6}{\sigma_\epsilon} \right] \quad (6-2)$$

where Φ is the standard normal cumulative distribution function, $(N_1)_{60}$ is the SPT blowcount for a given soil layer corrected for overburden and hammer efficiency, FC is the fines content (in percent) for the given soil layer, $CSR_{eq,i}$ is the cyclic stress ratio incorporating the acceleration a_{\max} as given in Equation (2-14), σ'_{v0} is the initial vertical effective stress, p_a is the atmospheric pressure, θ_1 through θ_6 are regression coefficients dependent on whether one wishes to account for uncertainty in the site investigation, and σ_ϵ is the measure of estimated model and parameter uncertainty. An example of a series of hazard curves for factor of safety against liquefaction initiation is presented in Figure 6-3.

While the Kramer and Mayfield (2007) performance-based procedure for computing liquefaction triggering incorporates the Cetin et al. (2004) procedure for calculating fragility curves (i.e. Equation (6-2)), it would likely be possible to substitute other probabilistic

liquefaction triggering procedures such as Idriss and Boulanger (2010) into the Kramer and Mayfield framework. However, such a substitution would require a separate study to validate the results and is beyond the scope of this present study.

Table 6-1: Probability of Liquefaction Model Coefficients for Cetin et al. (2004)

Include Site Error	θ_1	θ_2	θ_3	θ_4	θ_5	θ_6	σ_ε
Yes	0.004	13.79	29.06	3.82	0.06	15.25	4.21
No	0.004	13.32	29.53	3.70	0.05	16.85	2.70

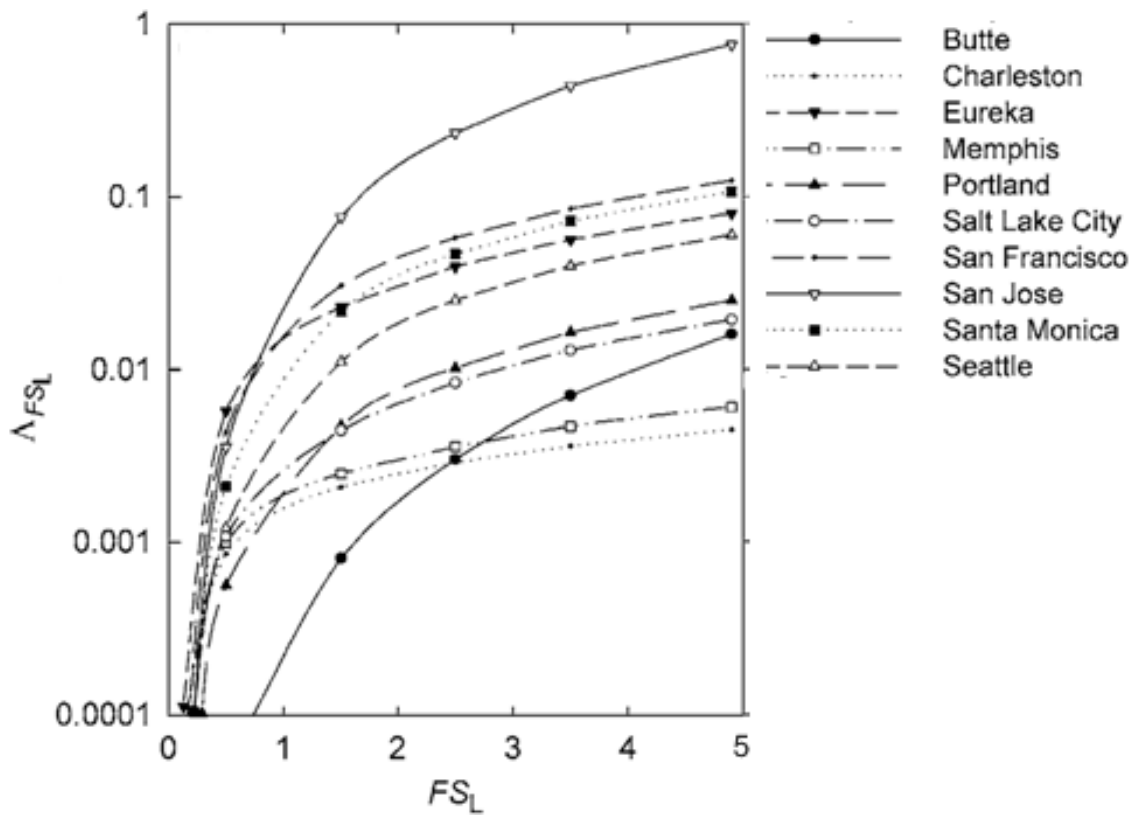


Figure 6-3: Seismic Hazard Curves at a 6-m Depth of a Fictional Soil Profile for the Factor of Safety Against Liquefaction Initiation (Modified From Kramer and Mayfield, 2007)

6.7 Evaluation of Flow Liquefaction

As summarized in Chapter 2, a flow liquefaction failure is a significant and oft-dramatic deformation of soil under static gravity loads due to soil liquefaction. Because of the many complexities and variables involved, there are currently no reliable methodologies recognized for predicting deformations from a flow liquefaction failure. Such a failure therefore contradicts the purpose of performance-based design simply due to the engineer's inability to predict with any amount of certainty the deformations likely to occur during flow. As such, any given soil/geometry/seismic loading combination which produces flow liquefaction cannot validly be evaluated using the performance-based procedure presented in this study.

As suggested in Chapter 4, the most-commonly used method for evaluating the potential for flow failure occurrence is to develop a simple limit equilibrium slope stability model incorporating residual shear strength estimates for the liquefied soil. Engineers typically use residual shear strength correlations with SPT clean sand-corrected blowcounts. Currently, engineers employ either direct shear strength methods such as Seed and Harder (1990) or normalized shear strength methods such as Ledezma and Bray (2010) or Olson and Stark (2002). While normalized shear strength methods appear to be increasing in their popularity and application, one must be aware that such methods may compute erroneously low residual shear strength values for shallow or unconfined liquefied soils. Such low strengths would not be realistic due to the liquefied soil's increased tendency to experience phase transformation and dilation at shallower depths. In addition, excess pore water pressures tend to dissipate much more quickly at shallower depths, thus contributing to greater shear strengths. For such shallow soil conditions, it may be more accurate to use either directly computed residual strengths from Seed and Harder (1990), or even use drained strengths. Currently, no recommendation regarding the

appropriate way to handle the discrepancy between directly-computed residual shear strengths and normalized shear strengths at shallow depths could be located in the published engineering literature. Therefore, one must rely on engineering judgment when making such distinctions in a limit equilibrium analysis.

Because a performance-based analysis typically attempts to consider the risk of failure corresponding to all return periods, consideration of flow failure from various return periods of liquefaction triggering would be appropriate. However, such an analysis would be considered by many to be tedious and unnecessary by many professionals because there is often a governing liquefiable layer that is computed to trigger across most return periods. Therefore, an acceptable approach would be to identify and incorporate the governing liquefiable layer from the performance-based liquefaction triggering analysis into a single post-seismic limit-equilibrium stability analysis. For the limit-equilibrium analysis, methods solving for force equilibrium such as Lowe and Karafiath (1960) may be used, or methods solving for both force and moment equilibrium (i.e. complete equilibrium) such as Spencer (1967) or Morgenstern and Price (1965) may be used. Gerber (2010) recommended that Lowe and Karafiath (1960) may provide a more accurate representation of the factor of safety against stability failure for the post-seismic condition, and that complete equilibrium procedures may tend to under-predict the true factor of safety.

If the results of the post-seismic limit-equilibrium analysis show that the computed factor of safety is less than unity, then flow liquefaction is considered to be a significant risk to the site. If such is the case, then the performance-based procedure for kinematic pile response is terminated and design alternatives for flow liquefaction mitigation should be evaluated. While it is technically possible to evaluate foundation performance for flow liquefaction by simply

applying extremely large horizontal deformations to the soil movement, the results of such an analysis would be questionable at best due to the large amount of uncertainty associated with the behavior of flow liquefaction. As such, the standard of practice in most locations when dealing with flow liquefaction typically involves liquefaction mitigation techniques such as ground improvement.

6.8 Development of the Intensity Measure

Kramer et al. (2007) noted that empirical MLR models for lateral spread are generally comprised of parameters that deal with either 1) site conditions (e.g., liquefiable layer thickness, gradient or free-face ratio, etc.) or 2) seismic loading (e.g., earthquake magnitude and source-to-site distance). Thus, a given empirical lateral spread model can generally be re-written as:

$$\mathcal{D} = \mathcal{L} + \mathcal{S} + \varepsilon \quad (6-3)$$

where \mathcal{D} is the transformed (i.e. log or square-root) lateral spread displacement, \mathcal{L} represents all of the parameters and their corresponding regression coefficients associated with earthquake loading, \mathcal{S} represents all of the parameters and their corresponding regression coefficients associated with site conditions, and ε represents the model uncertainty.

Every empirical lateral spread model that fits within the framework defined by Kramer et al. (2007) will therefore have unique values of \mathcal{L} and \mathcal{S} . For the three empirical lateral spread models incorporated in this study, the value of \mathcal{L} for each model can be given as:

$$\mathcal{L}_{Youd} = 1.532M - 1.406 \log \left(R + 10^{(0.89M - 5.64)} \right) - 0.012R \quad (6-4)$$

$$\mathcal{L}_{\text{Bardet}} = 1.017M - 0.278 \log R - 0.026R \quad (6-5)$$

$$\mathcal{L}_{\text{Baska}} = 1.231M - 1.151 \log \left(R + 10^{(0.89M - 5.64)} \right) - 0.01R \quad (6-6)$$

A plot of the \mathcal{L} parameter for the Youd et al. (2002) model is demonstrated in Figure 6-4, thus showing how the parameter is a function of both earthquake magnitude and distance.

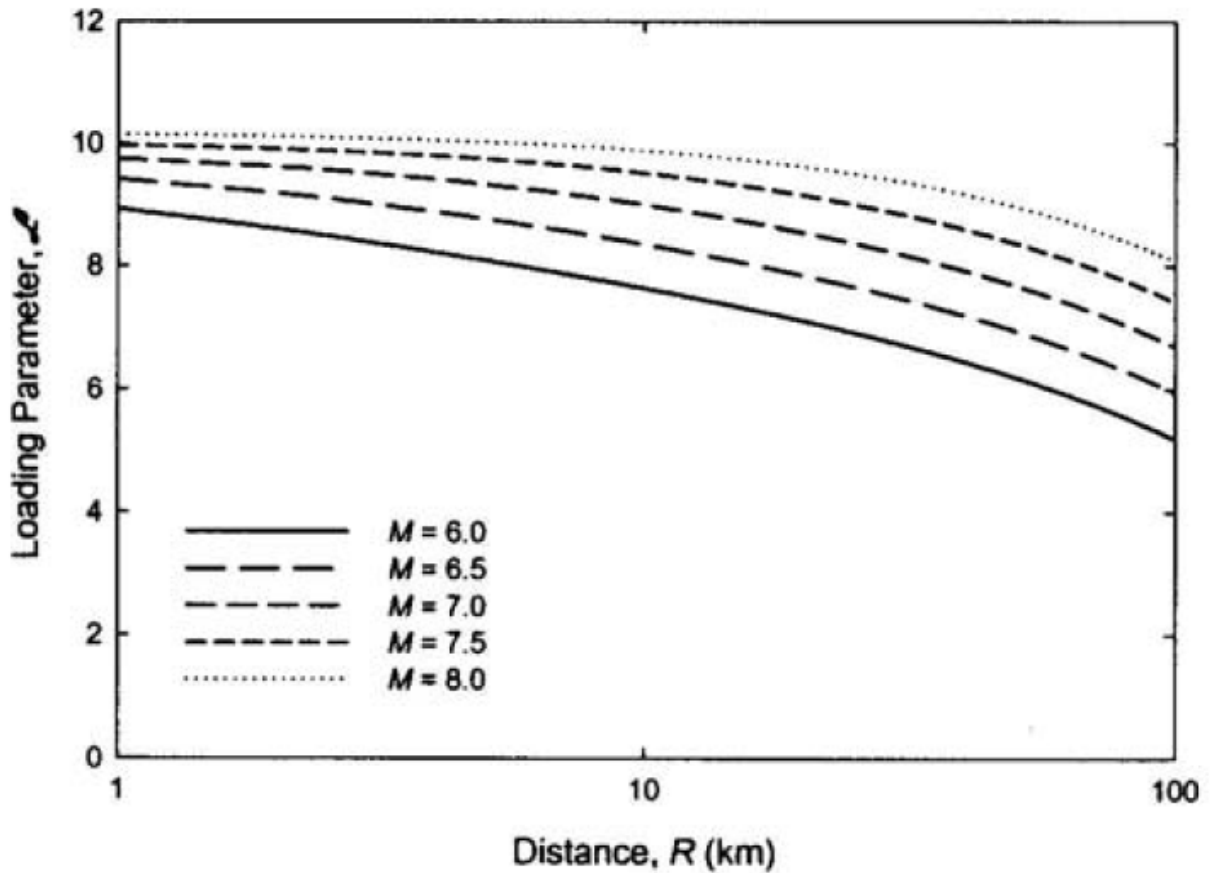


Figure 6-4: \mathcal{L} Parameter for the Youd et al. (2002) Model

As pointed out by Kramer et al. (2007), the \mathcal{L} parameter for a given empirical lateral spread resembles an attenuation relationship. As such, it is possible to use the parameter in a PSHA to develop probabilistic estimates of \mathcal{L} . Because \mathcal{L} represents the earthquake loading in a given empirical lateral spread model, it can be designated as the Intensity Measure in a performance-based analysis according to the methodology presented by Kramer et al. (2007) and Franke (2005).

Development of the seismic hazard curve for a given \mathcal{L} parameter requires that a PSHA be performed using seismic hazard analysis software capable of incorporating user-defined attenuation relationships. The analyses performed in this study used the popular commercial software EZ-FRISK (Risk Engineering, 2010) to develop the seismic hazard curves for the various \mathcal{L} parameters.

If access to seismic hazard software is not available, it is possible to use the magnitude-distance probability distributions from a USGS deaggregation analysis for some other ground motion parameter such as PGA as a proxy to compute the probabilistic estimate for a given \mathcal{L} parameter. If using USGS deaggregation results, this approach can only be performed for sites located within the United States. While the application of this proxy approach for the \mathcal{L} parameter may be used to approximate the value of \mathcal{L} that would otherwise be obtained through a proper PSHA, one should be aware that significant bias could potentially be introduced. For example, Figure 6-5 shows the comparison in the deaggregation plots between the PGA and the \mathcal{L}_{Youd} parameter for a given site. While there is certainly a strong correlation between the two plots, it can easily be seen that the magnitude-distance combinations from the PGA deaggregation can vary significantly from the magnitude-distance combinations from the \mathcal{L}_{Youd} deaggregation.

Therefore, development of the Intensity Measure for the performance-based kinematic pile response procedure involves developing seismic hazard curves and deaggregation plots for \mathcal{L}_{Youd} , \mathcal{L}_{Bardet} , and \mathcal{L}_{Baska} . It is recommended that at least seven return periods be used to define each seismic hazard curve: 108 years, 225 years, 475 years, 975 years, 2475 years, 4975 years, and 10000 years.

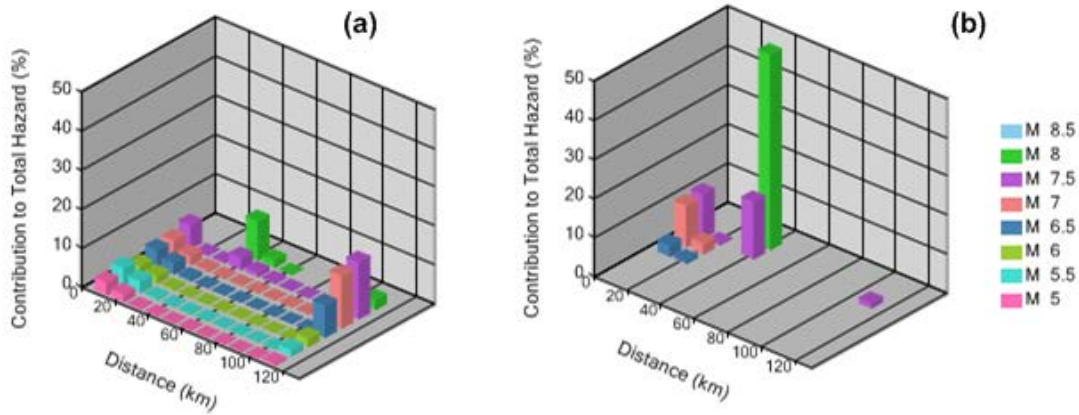


Figure 6-5: Deaggregation Plots for (a) PGA and for (b) \mathcal{L}_{Youd} Parameter for a Site in Costa Rica. Return Period is 475 Years.

6.9 Development of Fragility Functions for Lateral Spread Displacement

Kramer et al. (2007) point out that when re-writing a given empirical lateral spread model to match the format shown in Equation (6-3), the site term \mathcal{S} is treated as a constant value for each site. Like \mathcal{L} , the site parameter \mathcal{S} also varies between empirical lateral spread models. In addition, the parameter also depends on whether the site is characterized as a free-face geometry

or a ground slope geometry. For the three models used in this study, the values of the \mathcal{S} parameter are given as:

$$\begin{aligned} [\mathcal{S}_{Youd}]_{ff} = & -16.713 + 0.592 \log(W) + 0.54 \log(T_{15}) + \\ & 3.414 \log(100 - F_{15}) - 0.795 \log(D50_{15} + 0.1) \end{aligned} \quad (6-7)$$

$$\begin{aligned} [\mathcal{S}_{Youd}]_{gs} = & -16.213 + 0.338 \log(S) + 0.54 \log(T_{15}) + \\ & 3.414 \log(100 - F_{15}) - 0.795 \log(D50_{15} + 0.1) \end{aligned} \quad (6-8)$$

$$[\mathcal{S}_{Bar\ det}]_{ff} = -7.28 + 0.497 \log(W) + 0.558 \log(T_{15}) \quad (6-9)$$

$$[\mathcal{S}_{Bar\ det}]_{gs} = -6.815 + 0.454 \log(S) + 0.558 \log(T_{15}) \quad (6-10)$$

$$[\mathcal{S}_{Baska}]_{ff} = -7.518 + 0.086(T_{ff}^*) + 1.007 \log(W) \quad (6-11)$$

$$[\mathcal{S}_{Baska}]_{gs} = -7.207 + 0.067(T_{gs}^*) + 0.544\sqrt{S} \quad (6-12)$$

While the validity of assuming a constant value of \mathcal{S} for a given site may be argued, such an assumption greatly simplifies the performance-based computation. In addition, variability in the \mathcal{S} parameter is indirectly accounted for in the uncertainty parameter ε for each model. Like \mathcal{S} and \mathcal{L} , the uncertainty parameter ε varies between empirical lateral spread models and is defined as the estimated standard deviation for each empirical lateral spread model as described in

Chapter 3. Therefore, the values of the uncertainty parameter ε for the three models used in this study are given as:

$$\varepsilon_{Youd} = \sigma_{\log D_{H-ff,gs}} \cdot \Phi^{-1}[P] \approx 0.2020 \cdot \Phi^{-1}[P] \quad (6-13)$$

$$\varepsilon_{Bar\ det} = \sigma_{\log(D_{H-ff,gs}+0.01)} \cdot \Phi^{-1}[P] \approx 0.2898 \cdot \Phi^{-1}[P] \quad (6-14)$$

$$\varepsilon_{Baska} = \sigma_{\sqrt{D_H}} \cdot \Phi^{-1}[P] = 0.28 \cdot \Phi^{-1}[P] \quad (6-15)$$

where $\Phi^{-1}[P]$ is defined as the inverse standard cumulative distribution function for a given probability of exceedance P .

Therefore, the final re-written form for each of the three empirical models used in this study following the procedure presented by Kramer et al. (2007) are:

$$\mathcal{D}_{Youd} = \log D_{H-ff,gs} = \mathcal{L}_{Youd} + [\mathcal{S}_{Youd}]_{ff,gs} + \varepsilon_{Youd} \quad (6-16)$$

$$\mathcal{D}_{Bar\ det} = \log(D_{H-ff,gs} + 0.01) = \mathcal{L}_{Bar\ det} + [\mathcal{S}_{Bar\ det}]_{ff,gs} + \varepsilon_{Bar\ det} \quad (6-17)$$

$$\mathcal{D}_{Baska} = \sqrt{D_H} = \frac{\mathcal{L}_{Baska} + [\mathcal{S}_{Baska}]_{ff,gs}}{1 + 0.0223(\beta_2/T_{gs}^*)^2 + 0.0125(\beta_3/T_{ff}^*)^2} + \varepsilon_{Baska} \quad (6-18)$$

Note that the Baska (2002) model is more complicated than the other two models simply due to the fact that the empirical model incorporates a denominator.

By designating the Displacement term in Equation (6-3) (i.e. $\log(D_{H-ff,gs})$, $\log(D_{H-ff,gs} + 0.01)$, or $\sqrt{D_H}$) as the Engineering Demand Parameter, fragility curves must be developed for all possible values of the Displacement term as a function of \mathcal{L} . This can be performed for each empirical model presented in Equations (6-16) through (6-18) by considering the estimated standard deviation for each model given a set of \mathcal{L} and \mathcal{S} . With the empirical models written with the \mathcal{L} and \mathcal{S} format, the Displacement term essentially becomes a linear function of \mathcal{L} with a y-intercept directly proportional or equal to \mathcal{S} . For a given transformed (i.e. log or square-root) lateral spread displacement $DISP^*$, the probability of exceeding that displacement can be computed for various values of \mathcal{L} (i.e. \mathcal{L}_i) as:

$$P[\mathcal{D} > \mathcal{D}^* | \mathcal{L}_i, \mathcal{S}] = 1 - \Phi\left(\frac{\mathcal{D}^* - \mathcal{D}}{\sigma_{\mathcal{D}}}\right) \quad (6-19)$$

where \mathcal{D} is the true transformed lateral spread displacement, \mathcal{L}_i is the lateral spread loading parameter, \mathcal{S} is the given lateral spread site parameter, Φ is the standard normal cumulative distribution function, and $\sigma_{\mathcal{D}}$ is the standard deviation of the transformed lateral spread displacement.

By plotting these probabilities of exceedance against the \mathcal{L} parameter, the fragility curve corresponding to the displacement d (i.e. $EDP_i = d$) is developed. This process is demonstrated graphically with the Youd et al. (2002) model in Figure 6-6. Because this curve only represents

the probability of exceeding one given displacement d , multiple curves must be developed to represent the fragilities for all possible values of d .

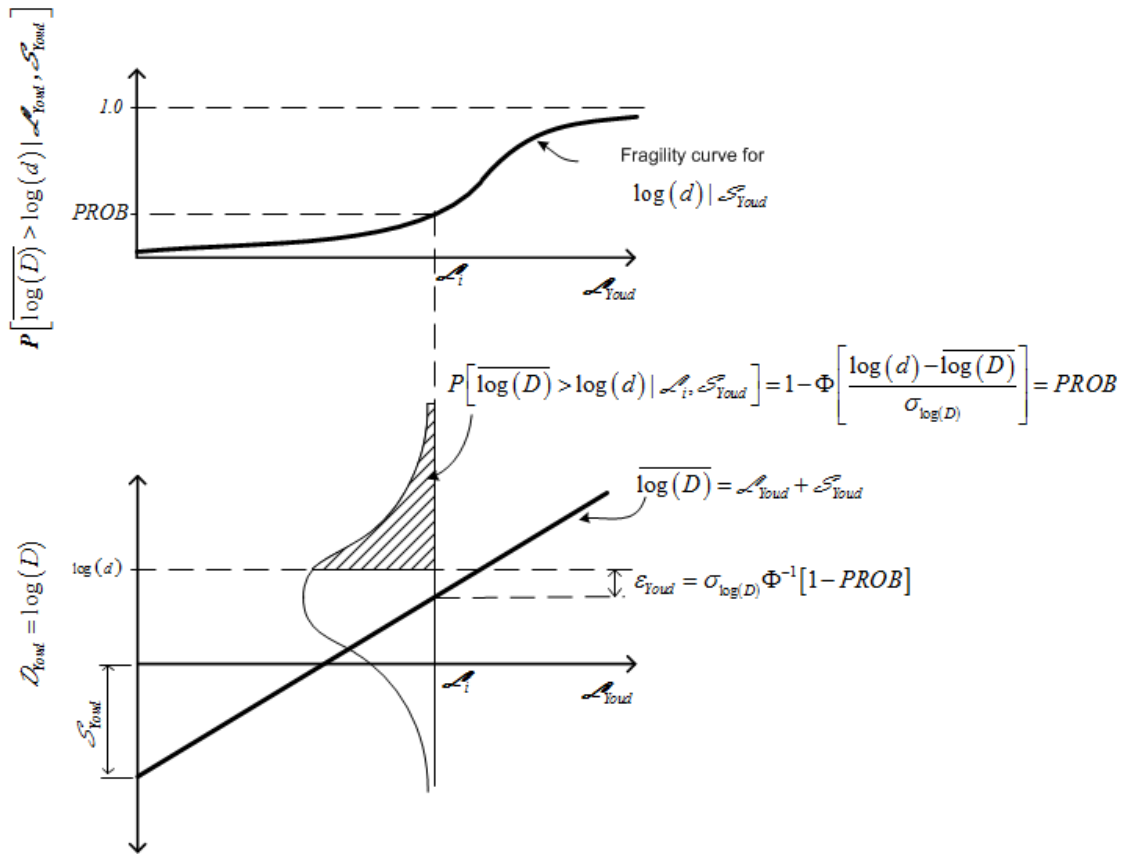


Figure 6-6: Computing the Fragility Curve for $EDP_i = \log(d)$ for the Youd et al. (2002) Empirical Model

6.10 Development of Probabilistic Lateral Spread Displacements

The process to develop a seismic hazard curve for lateral spread displacement at the ground surface is described in both Kramer et al. (2007) and Franke (2005). Once the fragility

curves for the Displacement term are developed for each empirical lateral spread model, they can be convolved with each corresponding seismic hazard curve for the loading parameter \mathcal{L} by utilizing the PEER PBEE framework presented in Chapter 5 to develop the seismic hazard curve for lateral spread displacement at the ground surface for each of the empirical models. Therefore, for a given empirical lateral spread model and assuming that the hazard curve for \mathcal{L} , the fragility curve for a given transformed lateral spread displacement $DISP^*$, and the site-specific value of \mathcal{S} have already been developed, then the steps to developing point $(\lambda_{DISP}, DISP^*)$ on the seismic hazard curve for lateral spread displacement at the ground surface are as follows:

- 1) *Select a value for $\Delta\lambda_{\mathcal{L}}$.* Subdivide the seismic hazard curve for \mathcal{L} into equal segments of length $\Delta\lambda_{\mathcal{L}}$. When selecting $\Delta\lambda_{\mathcal{L}}$, keep in mind that the more segments that exist, the more accurate λ_{DISP} will be.
- 2) *Determine the value of \mathcal{L}_i for each increment $\Delta\lambda_{\mathcal{L}}$.*
- 3) *Calculate $\sum_{i=1}^{N_i} P[DISP > DISP^* | \mathcal{L}_i, \mathcal{S}]$.* From the fragility curve associated with the transformed lateral spread displacement $DISP^*$, determine and sum the probability of exceeding $DISP^*$ for all values of \mathcal{L}_i from Step 2.
- 4) *Calculate the value of λ_{DISP} .* The point $(\lambda_{DISP}, DISP^*)$ on the lateral spread displacement hazard curve is computed by multiplying the sum of the probabilities computed in Step 3 and the value of $\Delta\lambda_{\mathcal{L}}$ determined in Step 1.
- 5) *Convert λ_{DISP} to λ_{D_H} .* Compute the lateral spread hazard curve from the transformed lateral spread hazard curve using the appropriate transformation (i.e. log or square-root).

Figure 5-11 provides a useful visual aid for understanding the concept presented in the four steps above. As previously mentioned, these steps will return a single point on the seismic hazard curve for lateral spread displacement at the ground surface for a single empirical model. In order to develop the entire hazard curve for a given empirical model, the steps must be repeated for multiple values of *DISP**.

Because there are three separate empirical lateral spread models presented in this procedure, the seismic hazard curve for lateral spread displacement at the ground surface should be developed for all three models. A weighted-average scheme can then be applied to develop a seismic hazard curve representative of the three models. For the current study, equal weights are applied to develop the average seismic hazard curve for lateral spread displacement at the ground surface.

The procedure presented by Kramer et al. (2007) and Franke (2005) allow one to develop a seismic hazard curve for the lateral spread displacement at the ground surface. However, the distribution of the lateral displacement versus depth is a critical component to computing the kinematic response of a pile foundation system. Furthermore, as stated in Chapter 3, our current understanding of the distribution of lateral spread displacement versus depth is poor at best, and very few published methods exist to distribute the total lateral spread displacement throughout the soil profile. This study will adopt the recommendations made by Valsamis et al. (2007) as summarized in Chapter 3 for distributing the total estimated lateral spread displacement down through the soil profile. Depth limitations as recommended by Youd (2009) via personal communication and summarized in Chapter 3 will be applied when computing deformations with the Valsamis et al. (2007) procedure. These limitations state that liquefied soils at depths greater than approximately 13.7 meters (45 feet) below the native ground surface or at depths greater

than two-times the height of the native free-face should not significantly contribute to lateral spread displacements for the ground slope case or the free-face case, respectively.

Because liquefaction triggering is a function of the seismic loading, the potential for a given layer of susceptible soil to liquefy should increase proportionally with the seismic loading. Therefore, the consideration of liquefaction triggering should take into account the likelihood of the seismic loading in any performance-based procedure related to soil liquefaction. For this reason, it was recommended as part of Step 3 of the performance-based kinematic pile response procedure that liquefaction triggering be evaluated using the performance-based triggering model presented by Kramer and Mayfield (2007). For a given mean annual rate of exceedance from the seismic hazard curve for lateral spread displacement at the ground surface, the corresponding liquefaction triggering profile can be obtained from the performance-based liquefaction triggering analysis. Using that soil profile in conjunction with the recommended procedure by Valsamis et al. (2007) and the lateral spread depth limitations by Youd (2009), the lateral spread displacement profile versus depth for the given mean annual rate of exceedance can be developed.

While the procedure presented in this chapter relies upon incorporation of empirical lateral spread models in a performance-based framework to develop probabilistic estimates of lateral displacement versus depth, it is recognized that other means could be utilized to develop such displacements. Such means could include incorporation of numerical and/or Newmark-type models. The challenge in applying such models in a performance-based framework, however, is developing fragility relationships between the Intensity Measure and the Engineering Demand Parameter. Kramer (2008) presents two possible ways in which fragility functions could be developed from numerical or Newmark-type models: (1) using a “stripes” approach, and (2)

using a “cloud” approach. With the stripes approach, multiple ground motions are scaled to match given values of the Intensity Measure and run with the model. The variability resulting from the modeling will be evident in the spread of the data at each given Intensity Measure, thus giving a “striped” appearance. With the cloud approach, a wide variety of appropriate and unscaled ground motions are run with the model, and the data produces a “cloud” of points from which regression techniques could estimate median and standard deviation values for the *EDP* given the *IM*. These two methods are demonstrated in Figure 6-7.

Therefore, the performance-based kinematic pile response procedure presented in this study is flexible enough to utilize probabilistic lateral spread displacements computed by means other than those presented in this dissertation, which incorporate probabilistic lateral displacement estimates from empirical models. However, the development and utilization of such means is beyond the scope of this study.

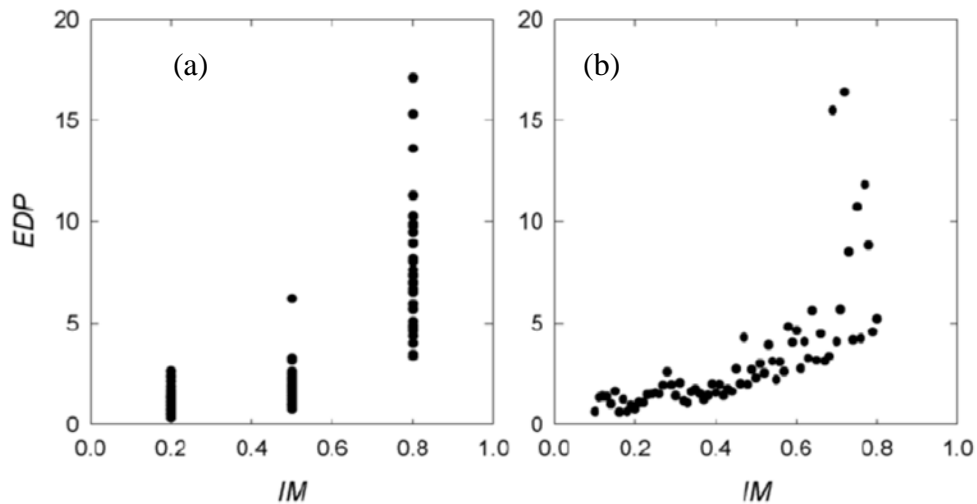


Figure 6-7: Schematic Illustration of the (a) "Stripes" Approach and the (b) "Cloud" Approach to *EDP/IM* Characterization (After Kramer, 2008)

6.11 Development of Fragility Functions for the Kinematic Pile Response

With both the seismic hazard curves for the \mathcal{L} parameter (i.e. the IM) and lateral spread displacement (i.e. the EDP) defined, the seismic hazard curve for the kinematic pile response (i.e. the DM) can be developed if a series of fragility curves relating the EDP and the DM are computed. However, no published method currently exists for directly computing uncertainty in pile response from p-y soil spring methods. Ideally, fragility curves could be computed directly in a probabilistic framework if the incorporated p-y soil spring models provided a formal definition of their model uncertainties. Unfortunately, published p-y soil spring models do not typically provide any indication or definition of their uncertainty. It is therefore currently impossible to directly compute fragility functions for the kinematic pile response using p-y methods.

It is generally recognized that there can be a large amount of uncertainty associated with the soil-pile interaction in a kinematic pile response analysis. Isenhower and Mosher (1996) identified this problem and recommended three potential approaches to estimating this uncertainty: exact methods (e.g., Monte Carlo or Latin Hypercube simulation), first-order second moment (FOSM) methods, and point estimate methods.

Exact methods require that the probability distributions of the random variables in the problem be known or assumed. These distributions are typically assumed to be normally distributed, log-normally distributed, uniformly distributed, or β -distributed. Isenhower and Mosher (1996) point out that exact methods can provide a good estimate of the probability distribution of the dependent variables in a problem; however, such solutions are no better than the assumptions made to develop them, and significant computer time is typically required to develop an adequate estimation of the probability distribution. Exact methods include techniques

such as numerical integration, Monte Carlo simulation, and Latin Hypercube sampling. Many procedures for refining exact methods have been developed, and the topic has become quite extensive. Singh et al. (2007) provide an excellent summary of many of these procedures and provide examples of their application.

FOSM methods are based on a truncated Taylor's series expansion to estimate variance in dependent variables. This type of analysis incorporates multiple iterations of deterministic analyses to estimate the variance of systems with multiple variates. Isenhower and Mosher (1996) point out that the advantage of the FOSM methods is that the method is much simpler mathematically to implement than the exact methods. However, they also point out that FOSM methods are mathematically tedious to perform because derivatives of performance factors with respect to random variables must be evaluated and that the computed values of variance are approximations. In practice, the FOSM methods require $2N+$ deterministic iterations, where N is the number of random variables in the analysis. Partial derivatives are computed using a finite difference expression in which deterministic evaluations of the performance function F are evaluated at the mean plus one standard deviation and the mean minus one standard deviation. This expression is given thus as:

$$\frac{\partial F}{\partial x} = \frac{F(\mu_x + \sigma_x) - F(\mu_x - \sigma_x)}{2\sigma_x} \quad (6-20)$$

where μ_x and σ_x are the mean and standard deviation estimates of random variable x , respectively. Using FOSM methods, the variance for the performance factor omitting terms containing higher-order derivatives is presented by Hahn and Shapiro (1967) as:

$$V[F(x)] = \sum_{i=1}^N \frac{\partial F}{\partial x_i} V[x_i] + 2 \sum_{i=1}^{N-1} \sum_{j=1}^N \left(\frac{\partial F}{\partial x_i} \right) \left(\frac{\partial F}{\partial x_j} \right) \rho_{ij} \quad (6-21)$$

where $V[F(x)]$ is the approximated variance of the performance function $F(x)$ and ρ_{ij} is the correlation coefficient for the terms x_i and x_j . Note that ρ_{ij} is equal to zero for uncorrelated or independent variables.

Point estimate methods (Rosenbluth, 1975) involve computing variance using techniques which do not require the evaluation of partial derivative terms like in FOSM. The methods require 2^N evaluations for problems involving N random variables. Isenhower and Mosher (1996) state that the main advantage of the point estimate methods is that they do not require evaluation of the partial derivatives like in FOSM methods. For models involving a relatively small number of random variables, point estimate methods can provide a reasonable estimate of variance with a manageable number of deterministic calculations. However, as the number of random variables increases, it may not be computationally feasible to perform point estimate methods.

For the case of kinematic pile response, the performance function is the pile response as computed using BWF models with p-y soil springs. A popular method currently for computing soil-pile response using p-y soil springs is the use of the commercial software LPILE (Ensoft, 2004). For the case histories which will be later evaluated in this study, implementation of exact methods using a Monte Carlo simulation approach will be used to estimate the variance of the pile response given a lateral spread displacement profile with depth. Because LPILE does not automatically allow the user to operate in batch mode, multiple simulations can be performed by developing a separate computer code or macro that manually operates LPILE in an iterative

fashion. Such a macro was developed as part of this research and is summarized in Appendix C.

Use of a Monte Carlo simulation to estimate uncertainty in kinematic pile response given a certain level of free-field soil movement requires estimation of the uncertainty of the various input parameters used in the computation of p-y soils springs for each soil layer in the model. In the absence of many soil samples from which these input parameters could be directly measured and their uncertainties computed, one could rely on published values of typical ranges of uncertainties for various soil parameters (e.g. Harr, 1984; Kulhawy, 1992; Lacasse and Nadim, 1997; Duncan, 2000). Table 6-2 shows a series of published coefficients of variation for various soil parameters often used in the computation of p-y soil springs based on the recommendations of Duncan (2000). These coefficients of variation can be used with a normal distribution to estimate the standard deviation of interest given an estimate of the mean.

Therefore, given the lateral spread displacement profile corresponding to a given mean annual rate of exceedance or return period, the resulting mean kinematic pile response and its variance can be estimated at each node in the LPILE model by performing a Monte Carlo simulation. Pile response can be defined as pile displacement, shear force in the pile, bending moment in the pile, and/or curvature of the pile. Figure 6-8 demonstrates a mean pile response and its standard deviation as computed in LPILE with a Monte Carlo simulation.

A numerical challenge in dealing with probabilities of exceedance in pile response is that many of the response values may be positive or negative depending on the direction of the displacements, bending moment, and curvature, or the type (i.e. tension or compression) of the shear force. For negative values of pile response, the probability of interest is not that of exceedance, but rather that of non-exceedance. However, computation of probabilities can be greatly simplified if considering only the absolute value of the pile response. In doing so, the

directional component of the pile response is lost, but amplitude of the response value is retained.

Table 6-2: Coefficients of Variation for Commonly-Used Soil Input Parameters for Many p-y Soil Spring Models (After Duncan, 2000)

Property or in-situ test result	Coefficient of variation, $\frac{S}{x}$
Unit weight (γ)	3-7%
Buoyant unit weight (γ_b)	0-10%
Effective stress friction angle (ϕ)	2-13%
Undrained shear strength (S_u)	13-40%
Soil modulus parameter (k)	30%
Soil strain parameter (ϵ_{50})	30%
SPT blow count (N)	15-45%

Because the Monte Carlo simulation utilizing p-y analysis methods provides mean pile response and its estimated standard deviation at each node in the model, fragility curves must be developed for every node in the model in order to characterize the uncertainty in the pile response across the entire pile. Thus, for a given node in the model, the fragility curve as a function of lateral spread displacement profile $DISP$ can be computed as:

$$P\left[|R| > |R^*| \mid DISP\right] = 1 - \Phi\left(\frac{|R^*| - |\bar{R}| \mid DISP}{S_{R|DISP}}\right) \quad (6-22)$$

where $|R|$ is the absolute value of the pile response (i.e. displacement, bending moment, shear force, or curvature) at the node of interest, $|R^*|$ is the absolute value of the pile response value corresponding to the fragility curve, $DISP$ is the given lateral spread displacement profile, $\overline{|R|} | DISP$ is the absolute value of the mean computed pile response at the node of interest from the Monte Carlo simulation given the lateral spread displacement profile, $S_{R|DISP}$ is the computed standard deviation of the pile response at the node of interest from the Monte Carlo simulation, and Φ is the standard cumulative density function. Equation (6-22) is specific only to the pile response value $|R^*|$, and a family of fragility curves for all possible values of $|R^*|$ must be developed in order adequately characterize the uncertainty in the performance-based pile response analysis. Finally, development of families of fragility curves must be repeated for all nodes in the p-y pile response model.

Because performing a Monte Carlo simulation with a p-y soil spring analysis in LPILE can require a significant effort, Monte Carlo simulations need only be performed for the seven lateral spread displacement profiles developed to define the *EDP* (i.e. at return periods of 108, 225, 475, 975, 2475, 4975, and 100,000 years). With mean pile responses and standard deviations computed at each of these seven return periods, the probability of exceeding $|R^*|$ given a lateral spread displacement profile corresponding to a different return period can be estimated by interpolation for use in Equation (6-22).

6.12 Development of Probabilistic Kinematic Pile Response

With fragility curves developed for the pile response and a series of lateral spread displacement profiles defined across multiple return periods (i.e. the *EDP*), performance-based

estimates of the pile response can now be computed using the probabilistic framework developed by PEER. The base equation for this computation is similar to Equation (5-23) and is given as:

$$\lambda_{|R^*|} = \int P[|R| > |R^*| | DISP](d\lambda_{DISP}) \quad (6-23)$$

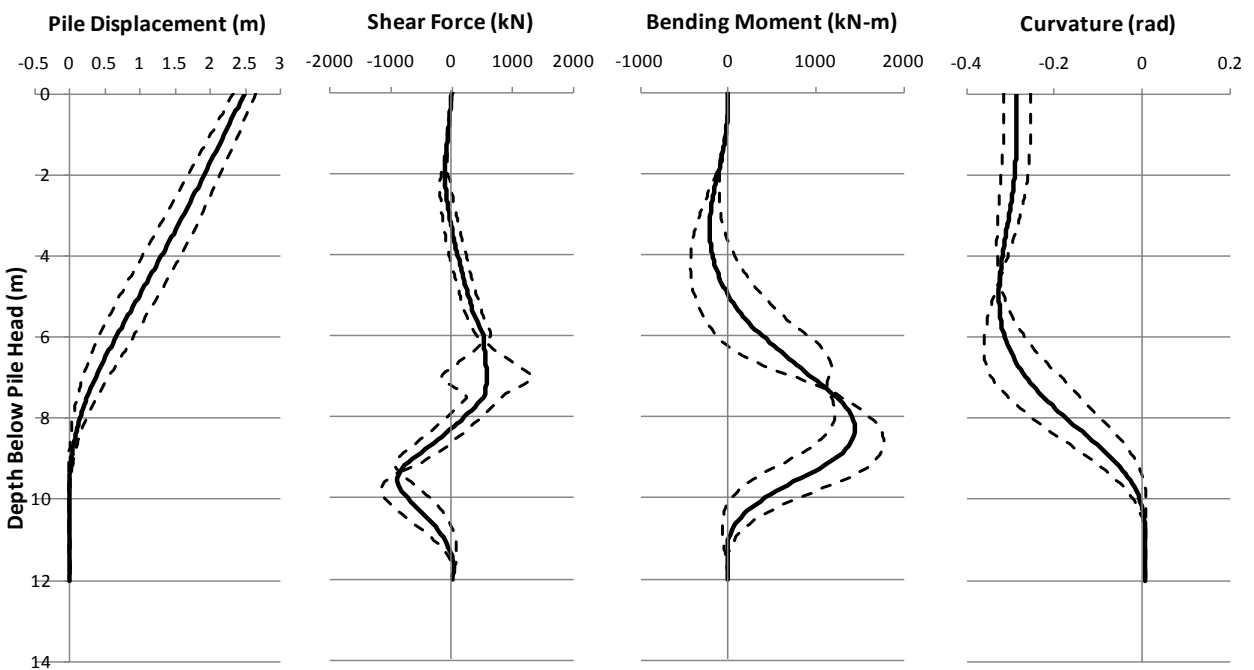


Figure 6-8: Example of Mean Pile Response with +/- 1 Standard Deviation Computed From a Monte Carlo Simulation in LPILE

The steps to computing the mean annual rate of exceedance corresponding to a given value of kinematic pile response $|R^*|$ at a given depth are as follows:

- 1) *Select a node in the pile response model.* Identify the depth of interest along the pile for the analysis.
- 2) *Define the pile response.* Choose displacement, bending moment, shear force, and/or curvature.
- 3) *Select a value for $\Delta\lambda_{DISP}$.* Subdivide the seismic hazard curve for lateral spread displacement $DISP$ at the depth of interest into equal segments of length $\Delta\lambda_{DISP}$. When selecting $\Delta\lambda_{DISP}$, keep in mind that the more segments that exist, the more accurate $\lambda_{|R^*|}$ will be.
- 4) *Determine the lateral spread displacement $DISP$ for each increment $\Delta\lambda_{DISP}$.*
- 5) *Calculate $\sum_{i=1}^{N_i} P[|R| > |R^*| | DISP]$.* From the fragility relationship associated with the given kinematic pile response value $|R^*|$, determine and sum the probability of exceeding $|R^*|$ for all values of $DISP$ from Step 4.
- 6) *Calculate the value of $\lambda_{|R^*|}$.* The point $\left(\lambda_{|R^*|}, |R^*|\right)$ on the kinematic pile response hazard curve is computed by multiplying the sum of the probabilities computed in Step 5 and the value of $\Delta\lambda_{DISP}$ determined in Step 3.
- 7) *Repeat Steps 2 through 6 for all desired depths along the pile.*

Equation (6-23) must be performed for all possible values of $|R^*|$ at all nodes in the pile response model in order to develop the pile response hazard curve at each node along the pile. With these hazard curves, it is possible to develop the pile response profile for a return period of interest by identifying and plotting the pile response value on each hazard curve corresponding to

that return period. This idea is demonstrated visually in Figure 6-9, which shows a seismic hazard curve for lateral pile displacements at the pile head. The bubbles shown in Figure 6-9 are intended to represent the idea that similar hazard curves exist at other depths along the pile, and that those curves can be used to develop pile response profile plots corresponding to a given mean annual rate of exceedance or return period.

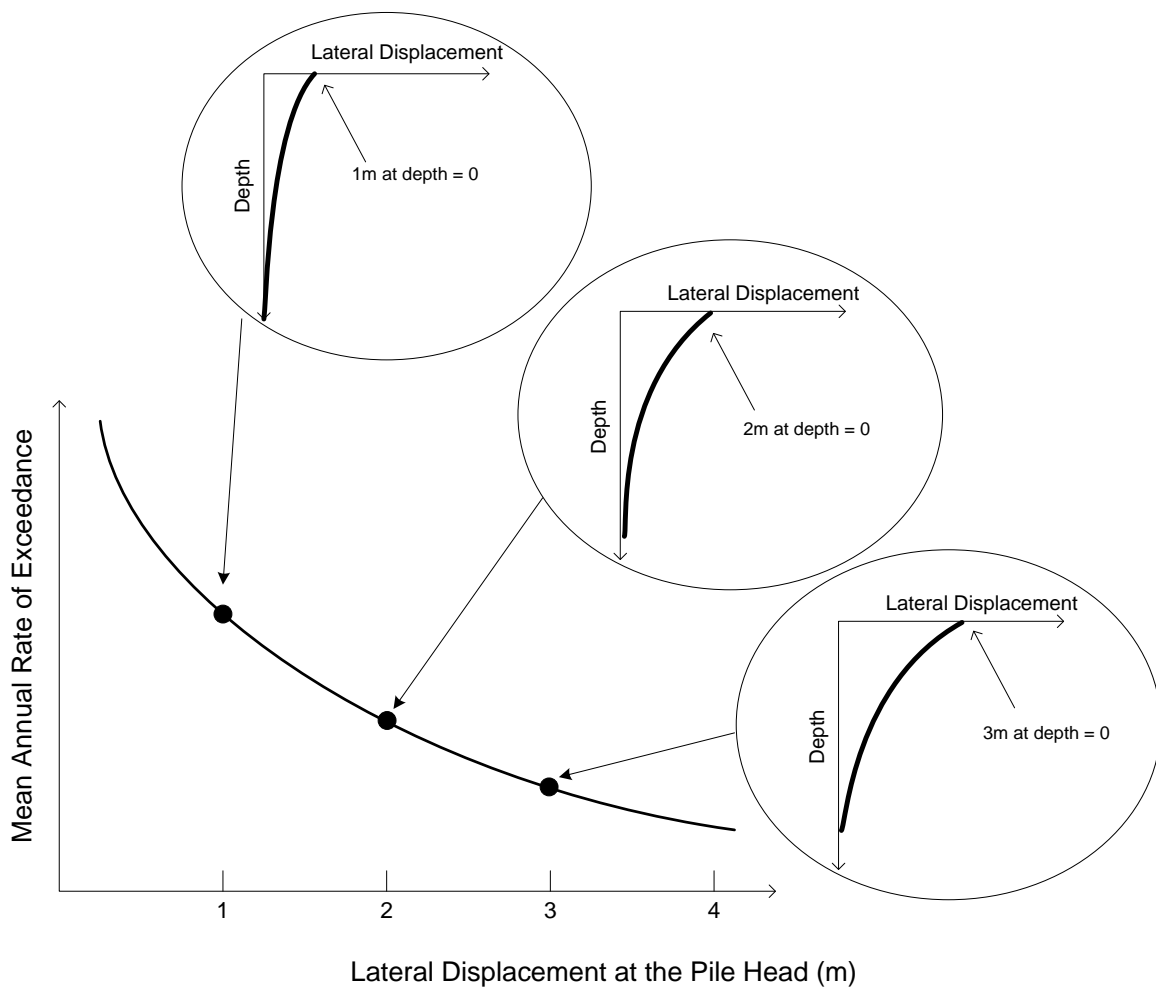


Figure 6-9: Example of Seismic Hazard Curve for Pile Displacement at the Pile Head

6.13 Performance-Based Software Development

While the individual steps of the performance-based pile response procedure described in this chapter may be relatively easy to understand conceptually, they are analytically rigorous and can be difficult to implement for the average engineer. However, much of this difficulty can be minimized if adequate analytical tools are available to the engineer to implement the performance-based procedure. Part of the scope of this study included development of software tools which would enable an engineer to utilize the performance-based pile response procedure in a relatively practical manner. Two pieces of software were developed as part of this study: LPILE MC Simulator, and Performance-based Pile Response Software (PPRS, pronounced “peppers”). Each will be briefly introduced in this section, but more thorough documentation can be found in Appendices C and D of this dissertation.

6.13.1 LPILE MC Simulator

LPILE MC Simulator is a simple but powerful spreadsheet and VBScript macro that was developed to interface with LPILE Plus 5.0 version 5.0.47 in order to perform a basic Monte Carlo simulation with a pile response analysis. Because LPILE does not have the built-in capability to perform a Monte Carlo simulation, the spreadsheet was developed to use keystrokes to imitate an actual user performing the analysis manually. The spreadsheet has the capability to account for pile groups in the analysis of an equivalent single pile, and it can compute and update a rotational stiffness component with each iteration in the Monte Carlo simulation. In addition, the spreadsheet will allow the user to operate LPILE in linear-elastic mode or to incorporate user-defined moment-stiffness curves to perform a nonlinear analysis.

A screenshot of the main worksheet for LPILE MC Simulator is shown in Figure 6-10. Additional information regarding the spreadsheet and a copy of the macro script are provided in Appendix C.

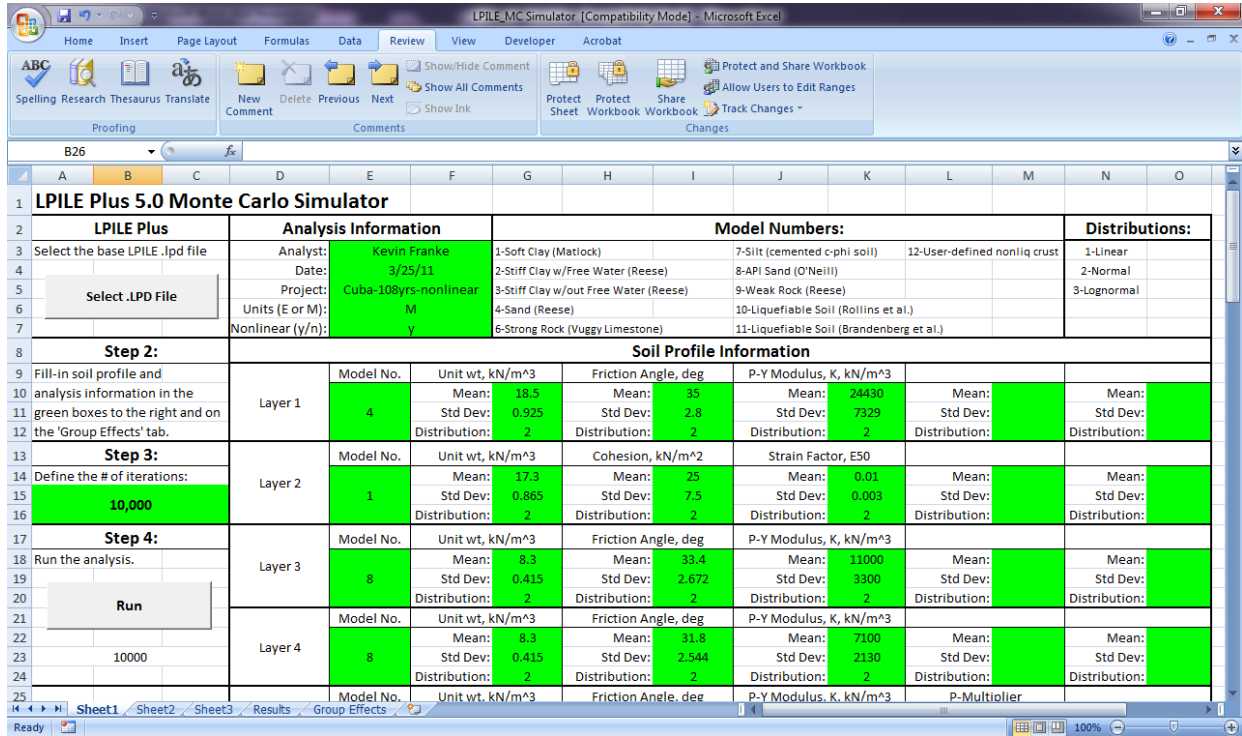


Figure 6-10: Screenshot of LPILE MC Simulator Spreadsheet

6.13.2 Performance-Based Pile Response Software (PPRS)

Performance-based Pile Response Software (PPRS) is a small software tool designed to assist the engineer in performing several of the steps associated with the performance-based kinematic pile response procedure introduced in this chapter. The software helps the engineer

develop the loading parameter, soil profile, site geometry, lateral spread displacement, and probabilistic kinematic pile response.

A screenshot of PPRS is shown in Figure 6-11. Additional information regarding PPRS can be found in Appendix D.

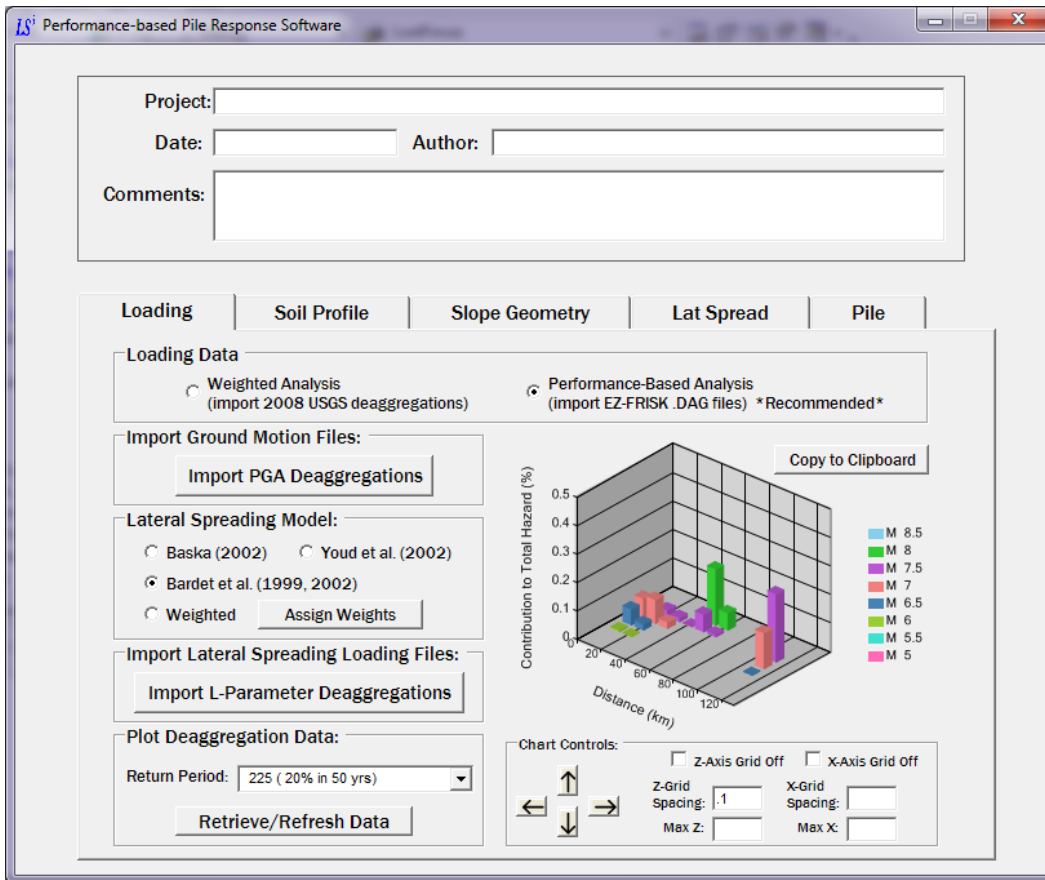


Figure 6-11: Screenshot of PPRS

7 INTRODUCTION TO THE COSTA RICA CASE HISTORIES

7.1 Introduction

Chapters 7 through 12 summarize the development of five lateral spread case histories observed following the 1991 Limon earthquake in Costa Rica. These case histories were developed as part of this study for three principal reasons:

- 1) To demonstrate the performance-based kinematic pile response procedure presented in Chapter 6;
- 2) To evaluate existing deterministic lateral spreading and kinematic pile response analysis procedures and compare the results against the case histories; and
- 3) To provide researchers with a new set of lateral spread/kinematic pile loading case histories to assist in advancing the field of earthquake resistant design.

While a simple generic scenario may have adequately demonstrated the performance-based kinematic pile response procedure, the development of real case histories was judged to be much more valuable and worth the additional effort.

7.2 1991 Limon Earthquake

At 15:57pm local time on April 22, 1991, a large (moment magnitude 7.5) earthquake struck the Limon Province of Costa Rica near the Caribbean Sea. The earthquake killed 53 people, injured another 193 people, and disrupted an estimated 30-percent of the highway

pavement and railways in the region due to fissures, scarps, and soil settlements resulting from liquefaction. (EERI, 1991). While the Limon Province is dominated by a broad plain that gently slopes from the Cordillera de Talamanca to the Caribbean Sea and is dissected by several large and small river valleys that generally broaden as they approach the coast, most of the observed liquefaction appeared to occur in the alluvial and fluvial deposits underlying river floodplains or in deltaic, lagoonal or estuarine deposits that underlie the coastal lowlands. (EERI, 1991; Youd, 1993).

Santana (1992) reported a maximum Modified Mercalli Intensity (MMI) equal to IX in Matina, which is just north of Highway 32 near the Caribbean Sea. Accelerograms were recovered from 14 of the 19 permanent stations deployed by the Earthquake Engineering Laboratory of the University of Costa Rica (Santana, 1991). The closest strong-motion station was located in San Isidro approximately 73 km southwest of the epicenter and located on hard ground. The San Isidro station registered a maximum acceleration of 0.20g horizontal and 0.17g vertical (Santana et al., 1991). The maximum free-field acceleration was recorded in Cartago, which is located on soft ground approximately 94 km to the northwest of the epicenter. The recorded peak horizontal ground acceleration at Cartago was approximately 0.27g. The recorded ground motions indicate that strong shaking ($>0.05g$) occurred for approximately 26.2 seconds. The USGS records the approximate latitudinal and longitudinal coordinates of the epicenter as 9.67° North 83.07° West, and a focal depth of approximately 12.9 kilometers. A shakemap produced by the USGS (2008) is shown in Figure 7-1.

A total of nine bridges in the epicentral region were severely damaged or collapsed as a result of the April 22, 1991 earthquake (Santana, 1992). Minor damage was reported for most other bridges in the region. The damage to these bridges occurred due to both inertial loading

effects during the ground shaking and kinematic loading effects on the foundations due to liquefaction-induced ground displacements. This study identified five of these bridges that sustained damage ranging from severe to minor, and that post-earthquake reconnaissance efforts could identify and measure elements of the seismic bridge performance. The location of these bridges relative to the approximate epicenter of the April 22, 1991 earthquake is shown in Figure 7-2.

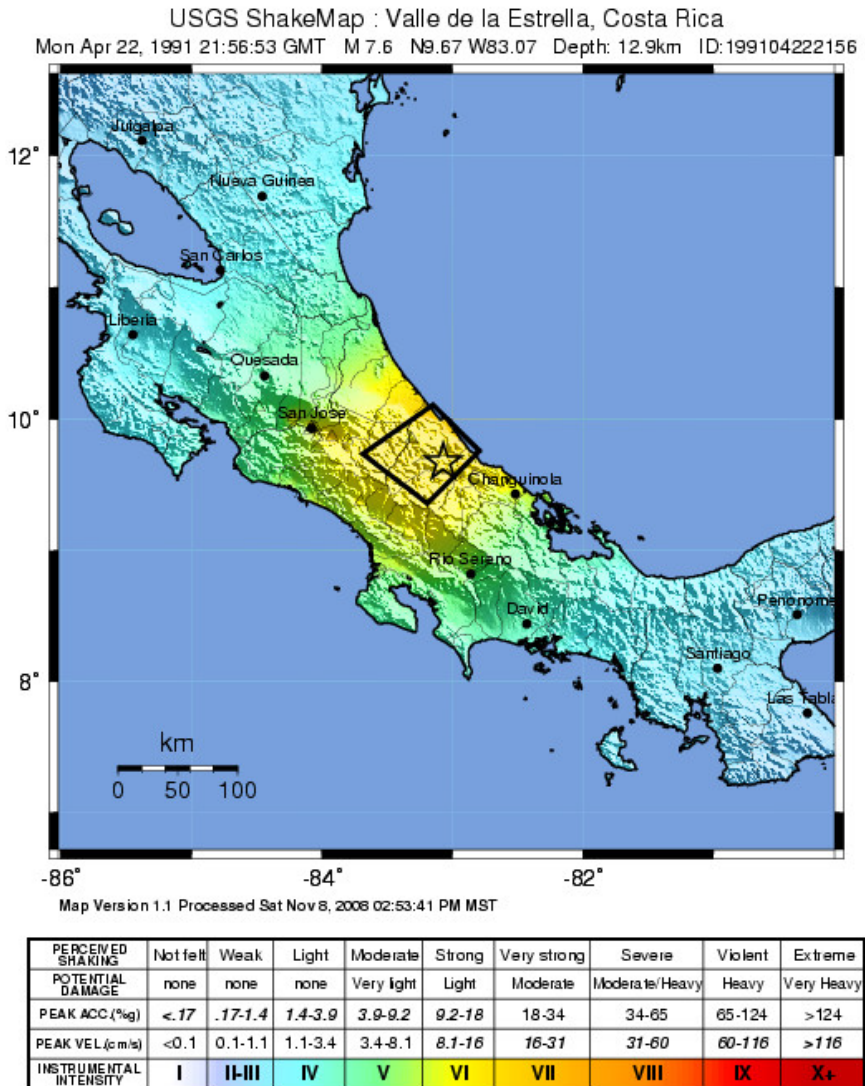


Figure 7-1: Shakemap for April 22, 1991 Costa Rica Earthquake (After USGS, 2008)

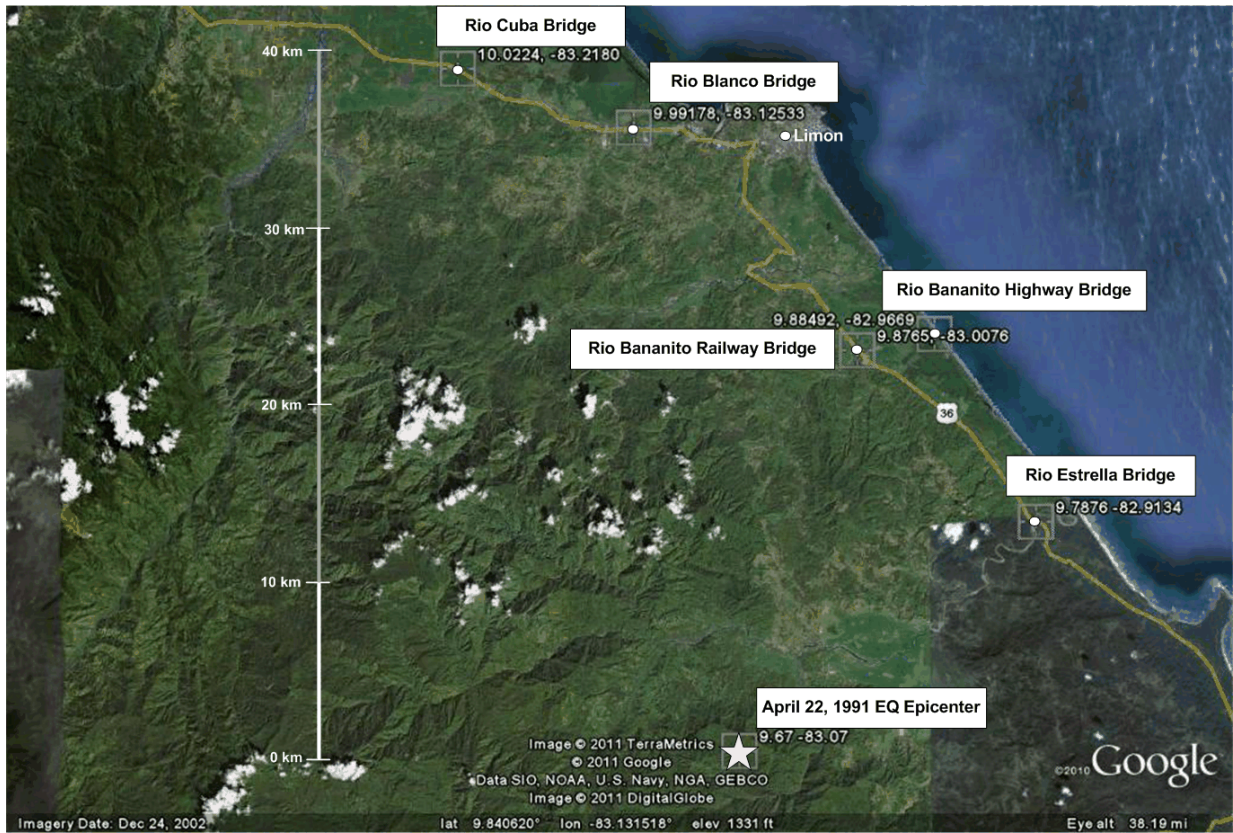


Figure 7-2: Bridge Location Map (Image Courtesy of Google Earth™ 2011)

7.3 Site Investigation

BYU investigators performed a site investigation in Costa Rica which consisted of a preliminary site-reconnaissance and a subsurface investigation performed at the five identified bridge locations. The preliminary site-reconnaissance was performed in April 2009 with the intent of (1) identifying bridges that were capable of being analyzed for kinematic pile response nearly 20 years after the earthquake event, (2) establishing ties with and support from key research institutions and governmental agencies within Costa Rica, and (3) identifying a reputable engineering subconsultant who could perform the geotechnical investigation. All of

these objectives were successfully achieved during the preliminary site-reconnaissance. Five bridges were identified where sufficient bridge performance information and/or free-field soil deformations were either collected during the reconnaissance efforts immediately following the 1991 earthquake event (Youd et al., 1992) or was still visible during the BYU reconnaissance. Critical support was established from the Costa Rica Ministerio de Transporte (Ministry of Transportation), which provided original blueprints and some soil boring information the five identified bridges. In addition, contacts were established with various engineering researchers at the Universidad de Costa Rica. Finally, a reputable engineering subconsultant was identified to perform soil borings at the five identified bridges.

The subsurface investigation was performed one year later in April 2010 by Insuma S.A. Geotechnical Consultants. A total of seven borings ranging in depth from 14 meters to 20 meters were performed at the five identified bridges using a tripod-mounted Standard Penetration Test (SPT) performed in accordance with ASTM D-1586. One more boring was performed in May 2011 by Insuma S.A. Geotechnical Consultants at one of the bridge locations due to some remaining budget flexibility. Representative soil samples were obtaining during SPT tests using a standard split-spoon sampler. Diagrams of the SPT procedure and the hammer/sampling equipment used are shown in Figure 7-3 and Figure 7-4, respectively.

To correct the recorded SPT blowcounts from the field for hammer energy efficiency, the efficiency of the cathead/falling-weight hammer was measured using electronic equipment provided by the Utah Department of Transportation. Hammer efficiency was measured multiple times, and an average efficiency ratio of approximately 87-percent was computed. This value is within the range of reasonable efficiency ratio values reported by Kovacs et al. (1983) for cathead and rope SPT systems.

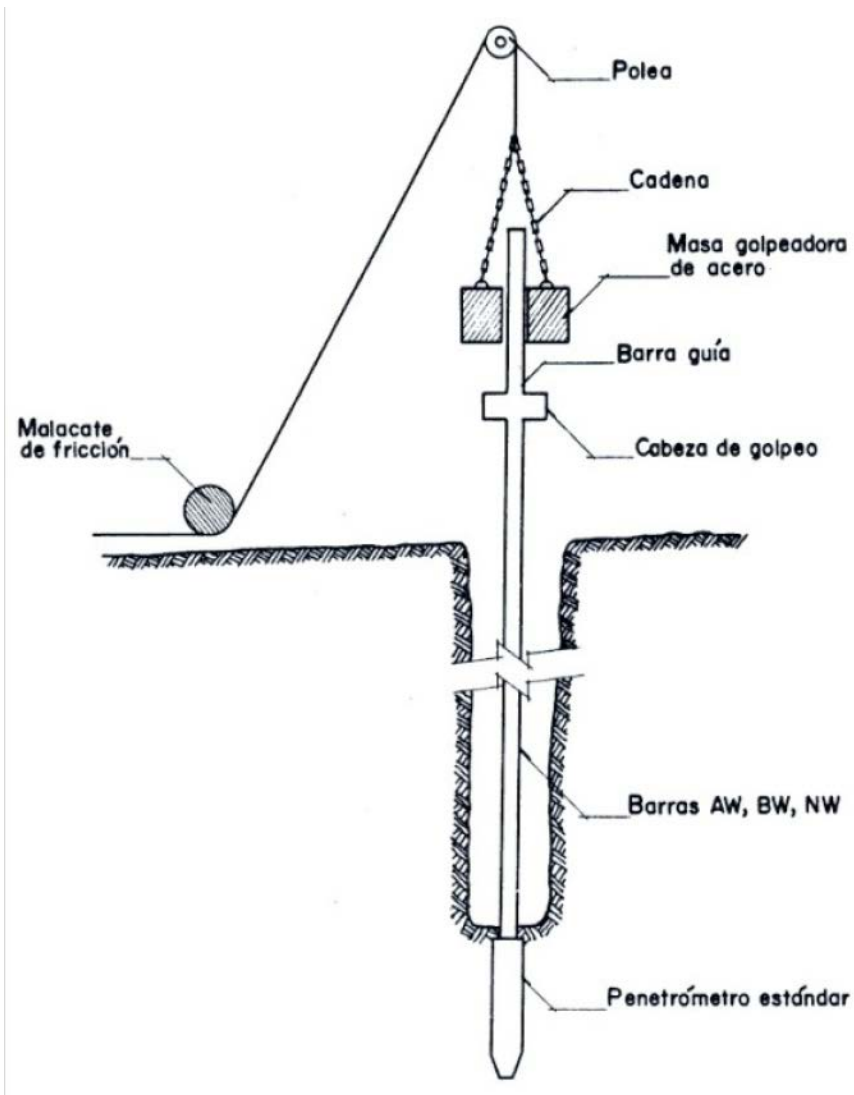


Figure 7-3: Sketch of the Standard Penetration Method (ASTM D-1586) (After Insuma S.A. Geotechnics, 2010 [Appendix A])

Continuous SPT sampling was employed in all eight of the borings that were performed. Retrieved soil samples were returned to the Insuma laboratories for additional evaluation and testing. Laboratory tests performed in this study included particle size analysis, fines measurement using a -200 sieve wash, measurement of natural moisture content, and plasticity evaluation on fine-grained samples using the Atterberg limits. These tests were not performed on

every retrieved soil sample, but were performed at a frequency of one set of tests every 1.5 – 1.75 meters and/or whenever a different type of soil was detected. The boring logs and laboratory test results are found in the Geotechnical Study report prepared by Insuma S.A. Geotechnical Consultants dated July, 2010, which is included as Appendix A of this dissertation.

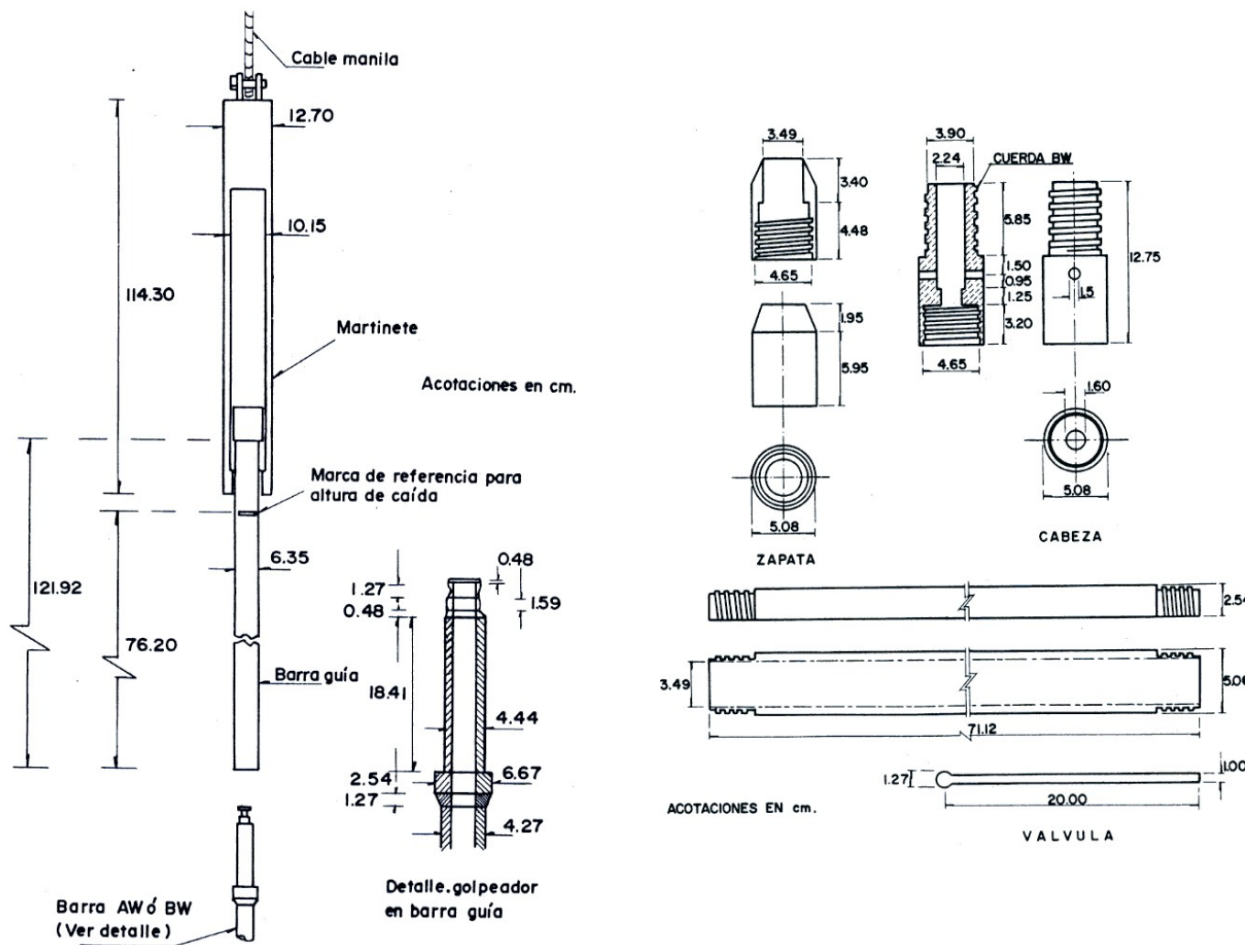


Figure 7-4: Details for the 64 kg (140 lb) Hammer and Split-Spoon Sampler Used in the Field Investigation (After Insuma S.A. Geotechnics, 2010 [Appendix A])

Due to budget and time constraints, BYU investigators did not perform any measurements of shear wave velocity at the five bridge sites in Costa Rica. For simplification, a generalized V_{S30} value equal to 270 m/s (886 ft/s) was assumed for all five bridge sites. This value of shear wave velocity is commonly assumed to represent general soil conditions in engineering design today. Future studies may actually measure the average shear wave velocities at the various bridge sites, resulting in refinement of the computed earthquake ground motions.

8 RIO CUBA BRIDGE

8.1 Introduction

The bridge over the Rio Cuba is a three-span reinforced concrete bridge supporting two lanes of traffic. Each span is approximately 22 meters in length and composed of simply-supported reinforced concrete girders, and the total span of the bridge is nearly 69 meters. The bridge is located along National Route 32 just south of the town of Maravilla. The latitude/longitude coordinates of the bridge are 10.02237° North 83.217967° West. A photo of the east abutment taken from beneath the bridge is shown in Figure 8-1.



Figure 8-1: The East Abutment of the Rio Cuba Bridge

According to bridge plans provided by the Costa Rican Ministry of Transportation, the bridge is founded on a series of 14-inch square reinforced concrete piles. The abutments are supported by two rows of piles (8 piles in the front row, 7 piles in the second row, and 15 piles in total) that are 14 meters in length and spaced at 4.1 diameters in the transverse direction and 2.5 diameters in the longitudinal direction. The dimensions of the pile cap at each abutment is 10.36 meters (transverse) x 1.90 meters (longitudinal) x 2.60 meters (vertical). The two bents are each founded on two 3.60-meter x 4.50 meter pile caps. Each of these pile caps is supported by 20 piles 14-inch x 14-inch (five rows of four piles) that are 10 meters in length and spaced at 2.5 diameters in both the transverse and longitudinal directions. The abutments and the bents are skewed at an angle of 30 degrees to the transverse orientation of the bridge. Finally, the front row of piles at each abutment and bent location are battered at approximately 5V:1H. However, any batter in the piles was neglected in the pile response analysis because the Juirnarongrit and Ashford (2006) pile response procedure does not specify how to account for pile batter in a few of the piles in the group.

8.2 Observed Damage Following the 1991 Earthquake

BYU investigators measured damage still visible from the Rio Cuba Bridge during a preliminary site reconnaissance during April 2009. A rotation of approximately 8.5 degrees was measured at the east abutment (Figure 8-2), and horizontal deformations of 3.35 inches at the bridge deck (Figure 8-3) and 5 inches at the base of the bridge girders were observed (Figure 8-4). A rotation of 6 degrees was measured at the west abutment, and horizontal deformations of 2 inches at the bridge deck and 6 inches at the base of the bridge girders were observed. In addition, each of the three spans of the bridge showed measurable displacements up to 3 inches

towards the river. Unfortunately, the actual amount of lateral spread displacement that occurred at the east abutment of the bridge at the time of the 1991 Limon earthquake is unknown because all evidence of lateral spread in the soil had disappeared by the time of the BYU field investigations in 2009 and 2010.



Figure 8-2: Rotation of the East Abutment at the Rio Cuba Bridge

Evaluation of the piles at each of the abutments showed considerable amounts of cracking and spalling (Figure 8-5), suggesting that bending moments induced by lateral spread approached or exceeded the yield moments for the piles. The backwall of each abutment was lodged against the bottoms of the bridge girders, thus suggesting that lateral spread soil deformations pushed the backwall of each abutment until it made contact with the girders and initiated rotation. Therefore, while the bridge deck appeared to limit the amount of lateral displacement that occurred at each abutment, it likely contributed to the observed rotations at the abutments.



Figure 8-3: Transverse Displacements at the Bridge Deck at the Rio Cuba Bridge



Figure 8-4: Displacement at the Base of the Bridge Girders

Field investigation and subsequent analysis focused on the east abutment of the Rio Cuba Bridge due to the larger rotations that were observed there.



Figure 8-5: Pile Cracking Observed at the East Abutment of the Rio Cuba Bridge

8.3 Soil Site Characterization at the Rio Cuba Bridge

Insuma S.A. Geotechnical Consultants performed a single boring immediately adjacent to the embankment fill at the eastern abutment of the bridge. The boring extended to a depth of 15 meters. The soils encountered in the boring were reported to consist primarily of alluvial deposits alternating between clays, silts, and sands. The clays encountered appeared to have high

plasticity while the silts encountered appeared to have either low or no plasticity. The sands encountered appeared to be fine-grained and varied in fines content from clean to silty. Groundwater was encountered in the boring at a depth of 2.1 meters, which corresponds to an elevation of 8.1 meters. To be conservative and to account for the fact that groundwater levels can fluctuate, groundwater was modeled at a depth of 1.80 meters (EL 7.80 meters) in the subsequent liquefaction and lateral spread analysis. A simple diagram of the soils encountered in the boring performed is shown in Figure 8-6 below. Further details regarding the boring at the Rio Cuba Bridge and the corresponding laboratory test results can be found in the Insuma Geotechnical Report included as Appendix A of this report.

The information from boring P-1 was used to develop a generalized soil profile for the east abutment of the Rio Cuba Bridge. Empirical correlations with SPT blowcounts were averaged to estimate the friction angle of granular soils and non-plastic silts. These correlations include Peck et al. (1974), Hatanaka and Uchida (1996), and Bowles (1977). Relative density of granular soils was estimated using the empirical correlation presented by Kulhawy and Mayne (1990). Corrected soil modulus estimates K^* of the granular soils for use with the API (1993) p-y relationship were estimated using the recommendations presented by Boulanger et al. (2003). Undrained strength of cohesive plastic soils was averaged from empirical correlations including Hara et al. (1971), Kulhawy and Mayne (1990), and Skempton (1957). Assumptions regarding the unit weight of the native soil as well as the strength properties of the embankment fill were made. Liquefied p-multipliers were estimated using Brandenberg et al. (2007). Groundwater was modeled at an elevation of 7.8 meters (i.e. a depth of 6.3 meters from the top of the embankment fill). Table 8-1 summarizes our generalized model of the soil profile at the east abutment of the Rio Cuba Bridge.

Table 8-1: Generalized Soil Profile for the East Abutment at the Rio Cuba Bridge

Top Depth (m)	Top Elevation (m)	Thickness (m)	USCS Soil Class	Friction Angle (deg)	Moist Unit Weight (kN/m ³)	Undrained Strength (kPa)	Relative Density (%)	Corrected Soil Modulus (kN/m ³)	Liquefied p-multiplier
0	14.7	4.5	SM (Fill)	35	18.5	---	62	24,800	NA
4.5	10.2	1.84	ML	---	17.3	25.0	---	---	NA
6.34	8.36	0.92	SW	33	18.1	---	48	11,000	0.14
7.26	7.44	1.84	SM	32	18.1	---	39	7,100	0.09
9.1	5.6	1.38	ML	---	18.1	16.8	---	---	NA
10.48	4.22	1.38	CH	---	18.8	22.1	---	---	NA
11.86	2.84	1.38	ML	---	18.8	38.8	---	---	NA
13.24	1.46	1.38	ML	36	18.1	---	59	15,130	NA
14.62	0.08	1.84	SM	39	18.1	---	77	24,050	NA
16.46	-1.76	1.84	GP	34	18.1	---	53	11,100	0.17
18.3	-3.6	1.38	CH	38	18.8	45.3	---	---	NA

8.4 Characterization of Site Geometry/Topography at the Rio Cuba Bridge

The Rio Cuba is a relatively small river bounded on both sides by a gently sloping floodplain and extensive vegetation. According to elevations shown on the blueprints that were provided by the Costa Rican Ministry of Transportation, the river itself ranges in elevation from about 6.80 meters at the bottom of the river channel to 10.8 meters at the river bank near the bridge abutments. Results from a 2010 BYU survey of the site using Global Positioning System (GPS) equipment provided by the Utah Department of Transportation indicate that the current elevation of the river bank at the bridge is 10.25 meters. According to the bridge blueprints, the roadway elevation across the bridge varied from 14.87 meters at the west abutment to 14.71 meters at the east abutment. From the blueprints, it also appears that the approach embankment was originally constructed at a 2H:1V slope. The elevation of the water in the Rio Cuba was approximately 8.1 meters at the time of our investigation.

Depth (m)	SPT N Value	
0.00 - 0.45	15	Organic soil (Sandy silt with roots, wood)
0.45 - 0.90	9	Brown sandy SILT with soft consistency.
0.90 - 1.35	4	
1.35 - 1.80	2	
1.80 - 2.25	5	Brown well graded clean SAND, loose. ▼
2.25 - 2.70	7	
2.70 - 3.15	12	Gray silty SAND, not plastic, with very loose relative density.
3.15 - 3.60	4	
3.60 - 4.05	2	
4.05 - 4.50	2	
4.50 - 4.95	2	Gray clayey SILT, mixed with a fraction of sand size particles, soft consistency.
4.95 - 5.40	2	
5.40 - 5.85	3	
5.85 - 6.30	2	Gray plastic CLAY, soft consistency.
6.30 - 6.75	4	
6.75 - 7.20	2	
7.20 - 7.65	6	Gray SILT, low plasticity, soft consistency.
7.65 - 8.10	5	
8.10 - 8.55	11	
8.55 - 9.00	17	Gray SILT, not plastic, medium consistency.
9.00 - 9.45	11	
9.45 - 9.90	15	
9.90 - 10.35	22	Gray silty SAND, not plastic with firm to dense relative density.
10.35 - 10.80	24	
10.80 - 11.25	24	
11.25 - 11.70	33	
11.70 - 12.15	23	Mixture of SAND and GRAVEL particles, not plastic, with loose to firm density.
12.15 - 12.60	15	
12.60 - 13.05	10	
13.05 - 13.50	6	
13.50 - 13.95	6	Gray plastic CLAY, mixed with small fraction of sand size particles.
13.95 - 14.40	6	
14.40 - 14.85	10	

Figure 8-6: Boring P-1 Performed at the Rio Cuba Bridge

Because the bridge is surrounded by banana plantations, it is possible that significant modification to the ground surface has been performed throughout the years. While it may be assumed that the site geometry at the time of the 1991 earthquake was the same as was measured during the BYU site survey, it is impossible to know with certainty. However, there appears to be relatively good agreement between the elevations shown on the blueprints and those measured during the BYU site survey. Therefore, this study has relied on the results from the BYU site survey to develop the generalized site geometry used in subsequent lateral spread and pile response analyses, relying on the elevations shown in the blueprints to fill in the gaps as necessary where important topographic information may not have been measured during the BYU site survey.

A sketch of the plan and profile views of the Rio Cuba Bridge as they are shown on the plans provided by the Costa Rican Ministry of Transportation are presented in Figure 8-7. Using the sketch shown in Figure 8-7, a free-face height of 1.8 meters and a free-face ratio of 12-percent were selected to represent the geometry of the native soils at the east abutment.

8.5 Deterministic Pile Response Analysis at the Rio Cuba Bridge

8.5.1 Deterministic Ground Motion Evaluation From the 1991 Earthquake

The Rio Cuba Bridge is located approximately 41 kilometers northwest from the epicenter of the April 22, 1991 earthquake. Assuming an average V_{S30} value of 270 m/s, the average computed median spectral acceleration along with median $\pm 1\sigma$ from the four selected NGA models are shown in Figure 8-8. The median computed PGA and spectral accelerations corresponding to 0.2-second and 1.0-second are 0.150g, 0.313g, and 0.204g, respectively.

8.5.2 Deterministic Liquefaction Evaluation From the 1991 Earthquake

Using the average deterministic ground motions from the NGA equations, the deterministic liquefaction triggering was evaluated at the Rio Cuba Bridge for the M7.6 1991 Limon earthquake using the SPT blowcounts from Boring P-1. The results of the deterministic liquefaction triggering analysis are shown in Figure 8-9. This evaluation included consideration of the Cetin et al. (2004), Idriss and Boulanger (2008), and Youd et al. (2001) simplified procedures. In general, good agreement was observed between the three procedures, suggesting that liquefaction triggered from depths of 3.2 meters to 4.6 meters (EL 7.0m to EL 5.6m) and from depths of 12.5 meters to 13.8 meters (EL -2.3m to EL -3.6m).

8.5.3 Post Earthquake Slope Stability

A simple post earthquake slope stability evaluation was performed for the east bank of the Rio Cuba using SLOPE/W analysis software (GEO-SLOPE, 2010). In evaluating the slope stability, only native soils were considered in the analysis in order to investigate the potential for flow liquefaction failure along the river bank. Such a failure would likely disqualify the use of empirical lateral spread models for computing lateral spread displacements in the native soils along the river bank.

Undrained strengths of fined-grained soils were reduced by 20-percent in accordance with recommendations by Makdisi and Seed (1977). The residual strength ratio S_r/σ' , of the liquefied soil was computed using the Ledezma and Bray (2010) as given in Equation (2-2). Lowe and Karafiath (1960) was used in the limit equilibrium analysis to compute factor of safety.

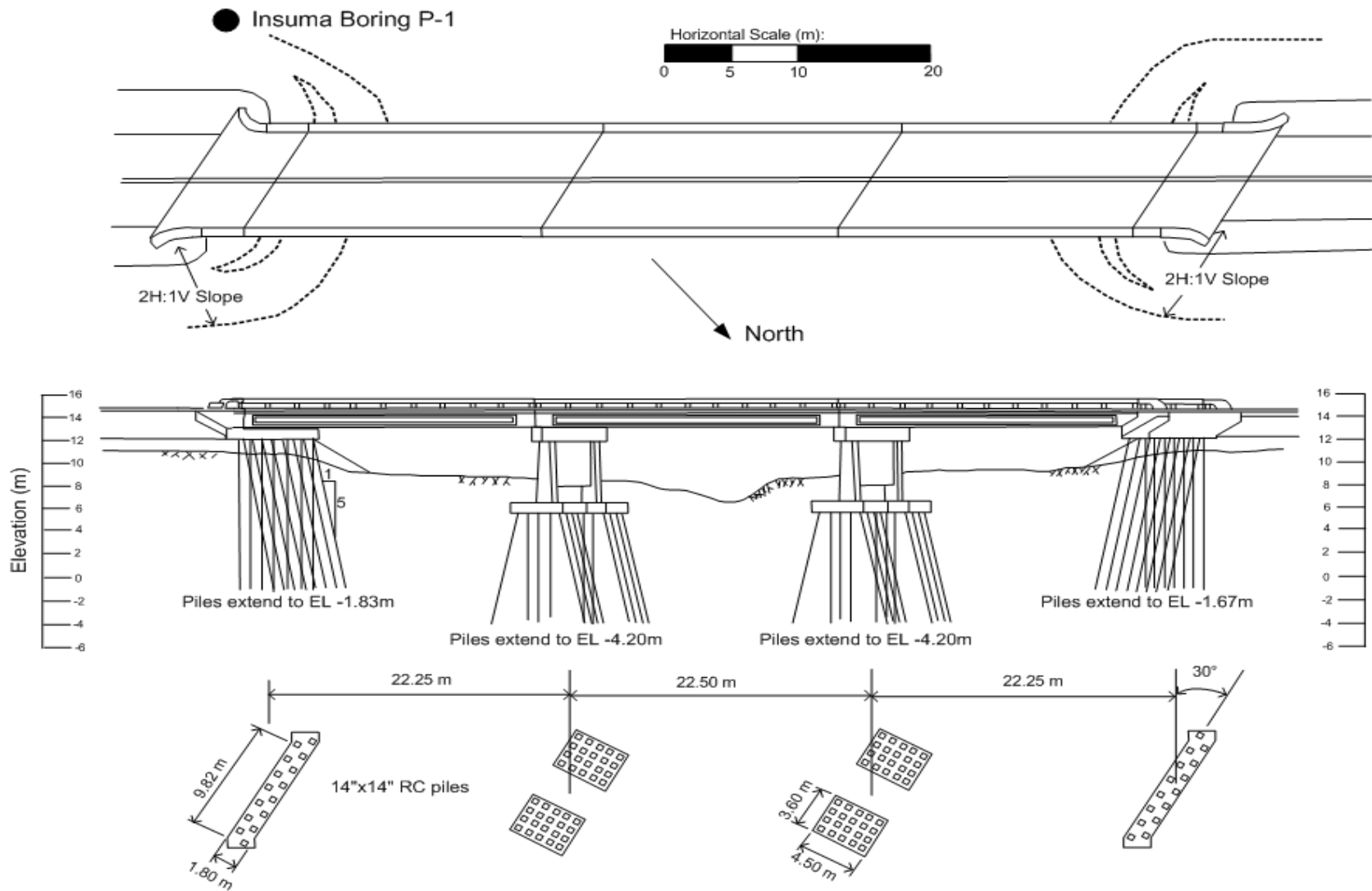


Figure 8-7: Simplified Sketch of the Plan and Profile Views of the Rio Cuba Bridge as Shown on the Bridge Plans Provided by the Costa Rican Ministry of Transportation

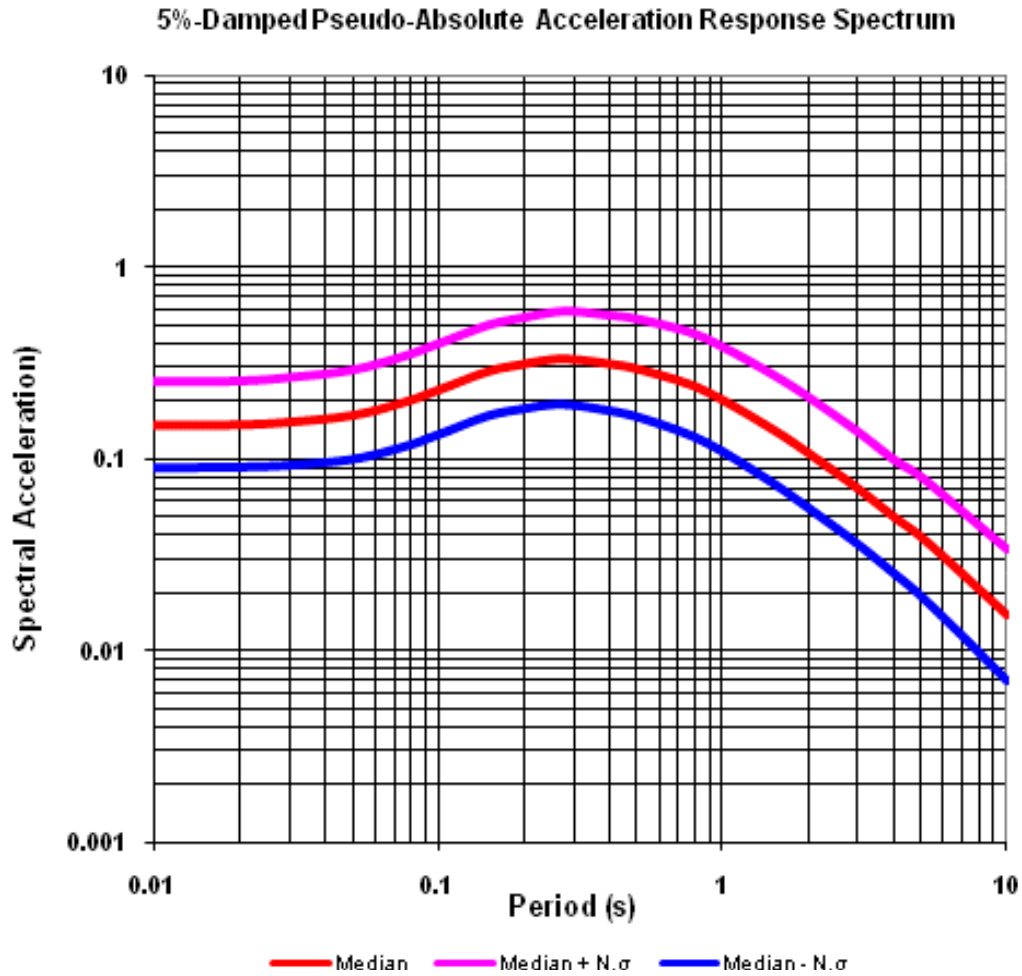


Figure 8-8: Computed Deterministic Response Spectra for the Rio Cuba Bridge From the 1991 Earthquake. $N = 1$

A circular surface search routine was utilized allowing for optimization in order to allow for the possibility of non-linear or log-spiral failure surfaces. A summary output from the post earthquake slope stability evaluation is presented in Figure 8-10. The computed factor of safety was 1.33, which suggests that the risk of a liquefaction flow failure is relatively low at the site.

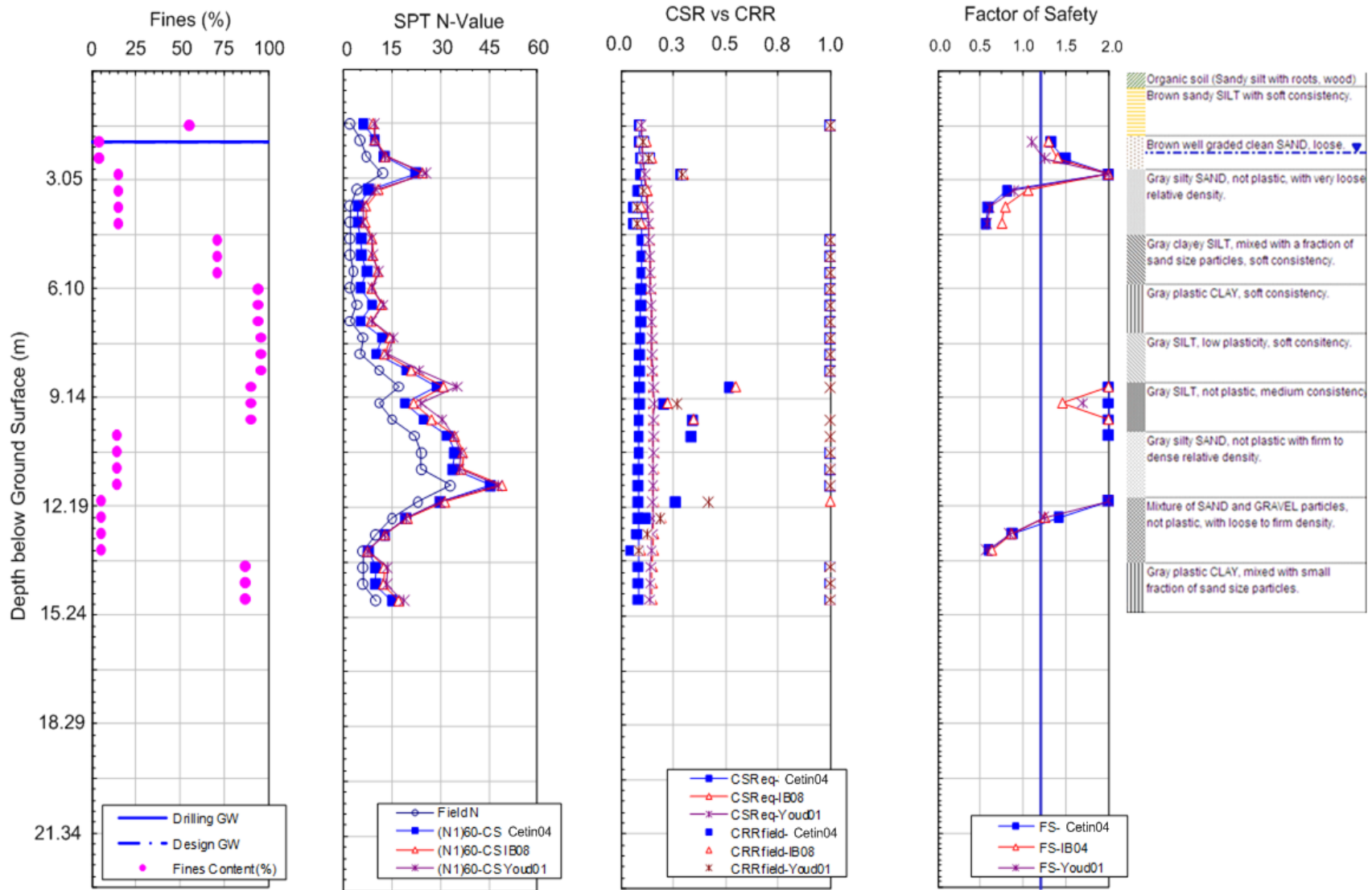


Figure 8-9: Deterministic Liquefaction Triggering Results for the M7.6 1991 Limon Earthquake at the Rio Cuba Bridge

8.5.4 Deterministic Evaluation of Lateral Spread

Empirical evaluation of the free-field soil displacements due to lateral spread was performed using the Youd et al. (2002), Bardet et al. (2002), and Baska (2002) models as presented in Sections 3.4 and 3.5 of this dissertation. This study assumed an earthquake magnitude of 7.6, a source-to-site distance of 41 kilometers, a free-face ratio of 12-percent, and a free-face height of 1.8 meters. The mean grain size diameter for each soil sublayer in the analysis was estimated from the Insuma sieve results, which are available in Appendix A. The median computed lateral spread displacement value and the 95th-percentile confidence interval for each of the three empirical models is shown in Figure 8-11. The average computed median displacement from the three models is 0.27 meter.

The estimated lateral spread displacement profile for the M7.6 1991 Limon earthquake was computed according to the procedure presented in Sections 3.6 and 3.7 of this dissertation in conjunction with the liquefaction triggering profile shown in Figure 8-9. This displacement profile is shown in Figure 8-12.

8.5.5 Pile Response Analysis

With lateral spread displacement profiles, an analysis of the pile response at the east abutment of the Rio Cuba Bridge can be performed using the equivalent single pile procedure summarized in Chapter 4 of this dissertation. However, several assumptions must be made in order to attempt to replicate the pile response that was observed to occur at the Rio Cuba Bridge following the Limon earthquake.

Name: Silt #1 Model: Undrained (Phi=0) Unit Weight: 17.3 kN/m³ Cohesion: 20 kPa B-bar: 0
 Name: Silt #2 Model: Undrained (Phi=0) Unit Weight: 18.1 kN/m³ Cohesion: 13.4 kPa B-bar: 0
 Name: Silt #3 Model: Undrained (Phi=0) Unit Weight: 18.1 kN/m³ Cohesion: 31 kPa B-bar: 0
 Name: Fat Clay #1 Model: Undrained (Phi=0) Unit Weight: 18.8 kN/m³ Cohesion: 17.7 kPa B-bar: 0
 Name: Sand #1 Model: Mohr-Coulomb Unit Weight: 18.1 kN/m³ Cohesion: 0 kPa Phi: 33.4 °
 Name: Liquefied Soil (Sr/Sig') Model: S=f(overburden) Unit Weight: 18.1 kN/m³ Tau/Sigma Ratio: 0.1 Minimum Strength: 3

223

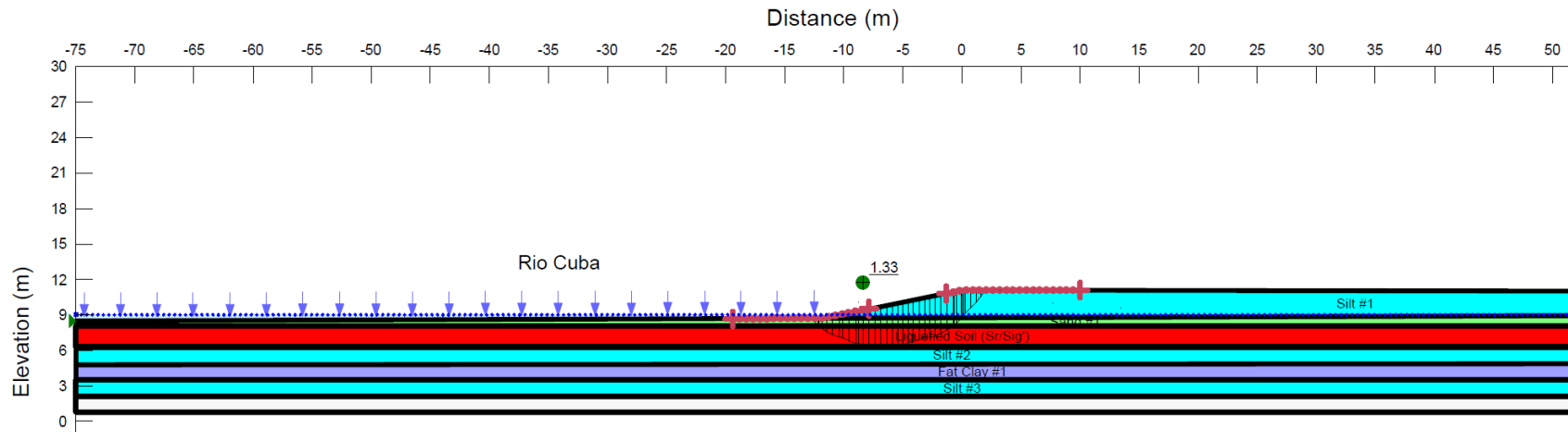


Figure 8-10: Post Earthquake Slope Stability Analysis at the Rio Cuba

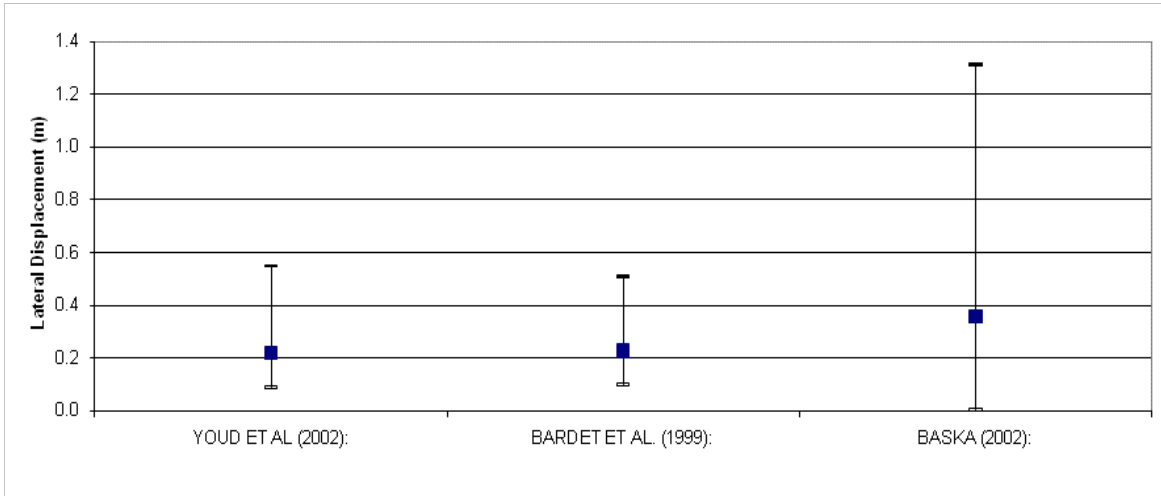


Figure 8-11: Deterministic Median and 95-Percentile Evaluations of Lateral Spread Displacement Using Select Empirical Models for the Rio Cuba Bridge

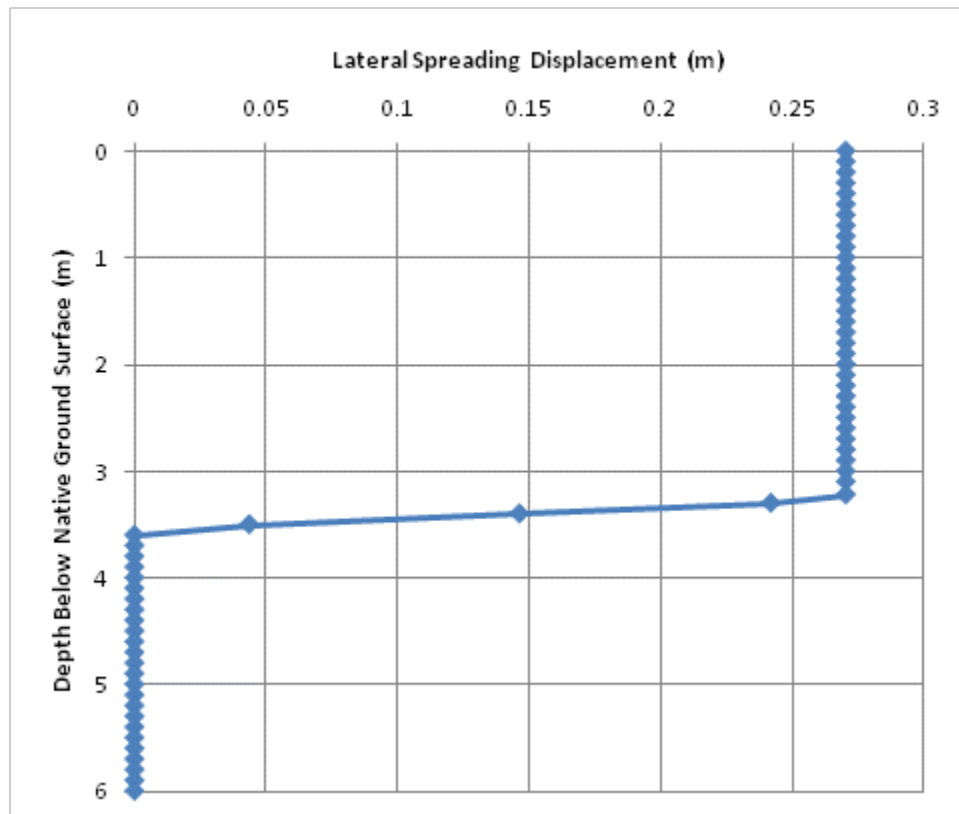


Figure 8-12: Computed Lateral Spread Displacement Profile at the Rio Cuba Bridge for the M7.6 1991 Limon Earthquake

Because the bridge deck did not fall from its supports as a result of the earthquake, the kinematic response of the piles at the abutments was likely significantly affected by the presence of the bridge deck. The presence of the deck would likely act as a supporting strut, thus limiting the amount of lateral deformation at the ground surface. However, brittle foundations such as the reinforced concrete piles supporting the Rio Cuba Bridge would likely not be able to resist very large shear loads and bending moments, and would therefore be susceptible to large deformations and rotation beneath the bridge deck. Such a phenomenon was observed during the BYU reconnaissance in which pile cap rotations were still visible and were measured at 8.5 degrees from vertical. However, had the bridge deck not been in place, it is likely that the piles would have deformed in conjunction with the free-field soil deformations, resulting in greater horizontal displacements and less rotation at the abutments.

Currently, no simplified methodology could be identified in the literature review for predicting when a bridge deck will fall off its supports and no longer act as a reinforcing strut. Such a phenomenon is obviously complex and is dependent on many potential variables including ground motions, foundation stiffness, bridge orientation in relation to the ground motions, bridge/abutment type, connections at the supports, and magnitude of the free-field soil deformations. All of these variables result in significant uncertainty in dealing with the problem. This uncertainty is emphasized by the fact that many other bridges in the Limon earthquake with similar spans, abutment types, foundation stiffness, etc. lost their bridge decks during earthquake shaking and therefore did not have the benefit of a strut load in resisting kinematic loading. Development of a solution to this problem is beyond the scope of this study, but could be a valuable focus for future research. This study only attempted to replicate the pile response that was observed following the Limon earthquake.

To account for the presence of the bridge deck, a lateral resisting load was applied to the head of the pile cap in the LPILE analysis. The load was gradually increased until zero displacement was achieved at the pile head.

Because reinforcing details for the piles were not shown on the bridge plans provided by the Costa Rican Ministry of Transportation, assumptions had to be made regarding the amount and size of rebar in the piles in order to compute their flexural stiffness (i.e. EI). A study was made into many of the available reinforced concrete design standards in practice during 1968 when the bridge was designed, and it was found that most piles in use at the time only incorporated four vertical steel bars for reinforcement. It was assumed that four #4 bars were used in the piles. The resulting initial composite flexural stiffness of a single 14in by 14in pile was computed to be approximately 35,000 kN-m².

The equivalent single pile consists of two sections: the pile cap and the piles. The 1.90m-by-10.36m pile cap comprises the top 2.6 meters of the equivalent single pile. The composite flexural stiffness of the pile cap was computed to be 147,960 MN-m². The second section of the equivalent single pile represents the pile group and was created by multiplying the initial composite flexural stiffness of a single pile by the total number of piles in the pile group (i.e. 15) to develop the initial composite flexural stiffness of the equivalent single pile. This initial composite flexural stiffness was computed to be 525,000 kN-m². A nonlinear moment-stiffness curve was developed to account for yielding of the reinforced concrete piles in accordance with the guidelines presented by CalTrans (2011) as summarized in Section 4.4.3 of this dissertation. The moment-curvature and moment-stiffness curves for the equivalent single pile are presented in Figure 8-13.

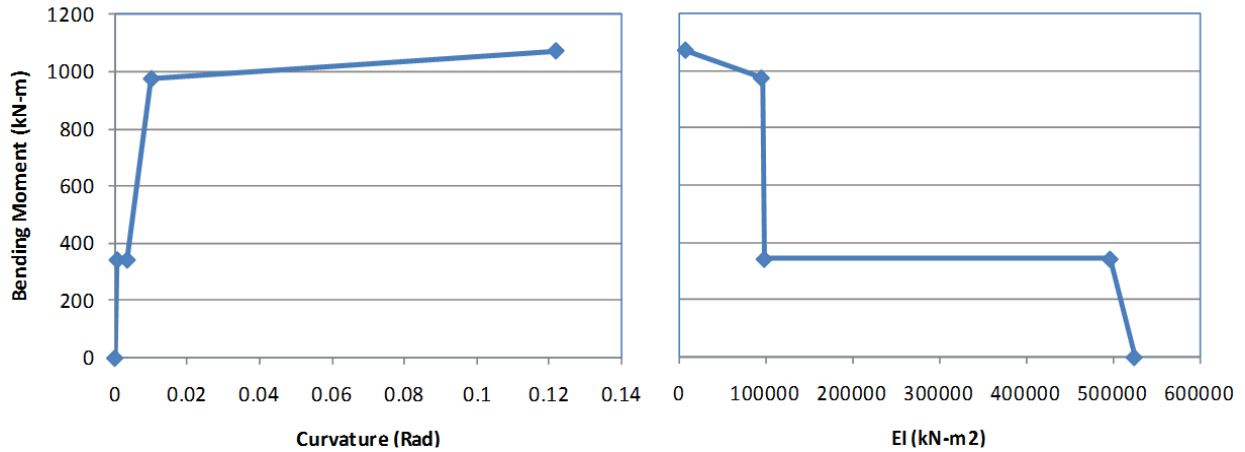


Figure 8-13: Moment-Curvature and Moment-Stiffness Curves for the Rio Cuba Bridge

A p-multiplier for the equivalent pile group to account for the total number of piles in the group and the pile spacing was computed to be 9.73. Rotational stiffness of the equivalent single pile was neglected due to the relative flexibility of the piles and the close pile-to-pile spacing in the direction of the lateral spread (i.e. longitudinal direction). Therefore, the equivalent single pile was modeled with a free-head condition with a lateral load at the head to represent the strut-like behavior of the bridge deck.

Applying the lateral spread deformations shown in Figure 8-12 to the equivalent single pile, the LPILE deterministic pile response from the 1991 Limon earthquake is shown in Figure 8-14.

8.5.6 Summary of Deterministic Results

In general, the deterministic analysis reasonably replicated the response of the pile group to the 1991 earthquake and resulting lateral spread displacements. Using the average lateral spread displacement of 0.27 meter computed from the three empirical models, a rotation of 6.5

degrees was computed for the pile cap. Back-analysis showed that a lateral displacement of 0.35 meter would have produced a pile cap rotation of 8.5 degrees.

If 0.35 meter was the true magnitude of lateral spread displacement following the 1991 Limon earthquake, then all three of the empirical lateral spread models shown in Figure 8-11 reasonably estimated the displacement (i.e. within 31-percent).

8.6 Performance-Based Pile Response Analysis at the Rio Cuba Bridge

8.6.1 Probabilistic Ground Motions

A PSHA was performed at the Rio Cuba Bridge site using EZ-FRISK software and the built-in seismic source model for Central and South America developed by Risk Engineering (see Risk Engineering documentation included in Appendix B). This seismic source model included both area and fault sources.

Attenuation models incorporated into the PSHA included four NGA attenuation models (Abrahamson and Silva, 2008; Chiou and Youngs, 2008; Campbell and Bozorgnia, 2008; and Boore and Atkinson, 2008). These models were assigned to crustal seismic sources, and select attenuation models developed for subduction zones (Youngs et al., 1997; Atkinson and Boore, 2003; and Zhao et al., 2006) were assigned to the subduction seismic sources. Finally, near-source and directivity effects were accounted for in the PSHA by incorporating the fault-normal response spectrum modifications presented by Somerville et al. (1997) and Abrahamson (2000) for all fault sources. A table of the fault sources located within about 100 km of the site is presented in Table 8-2.

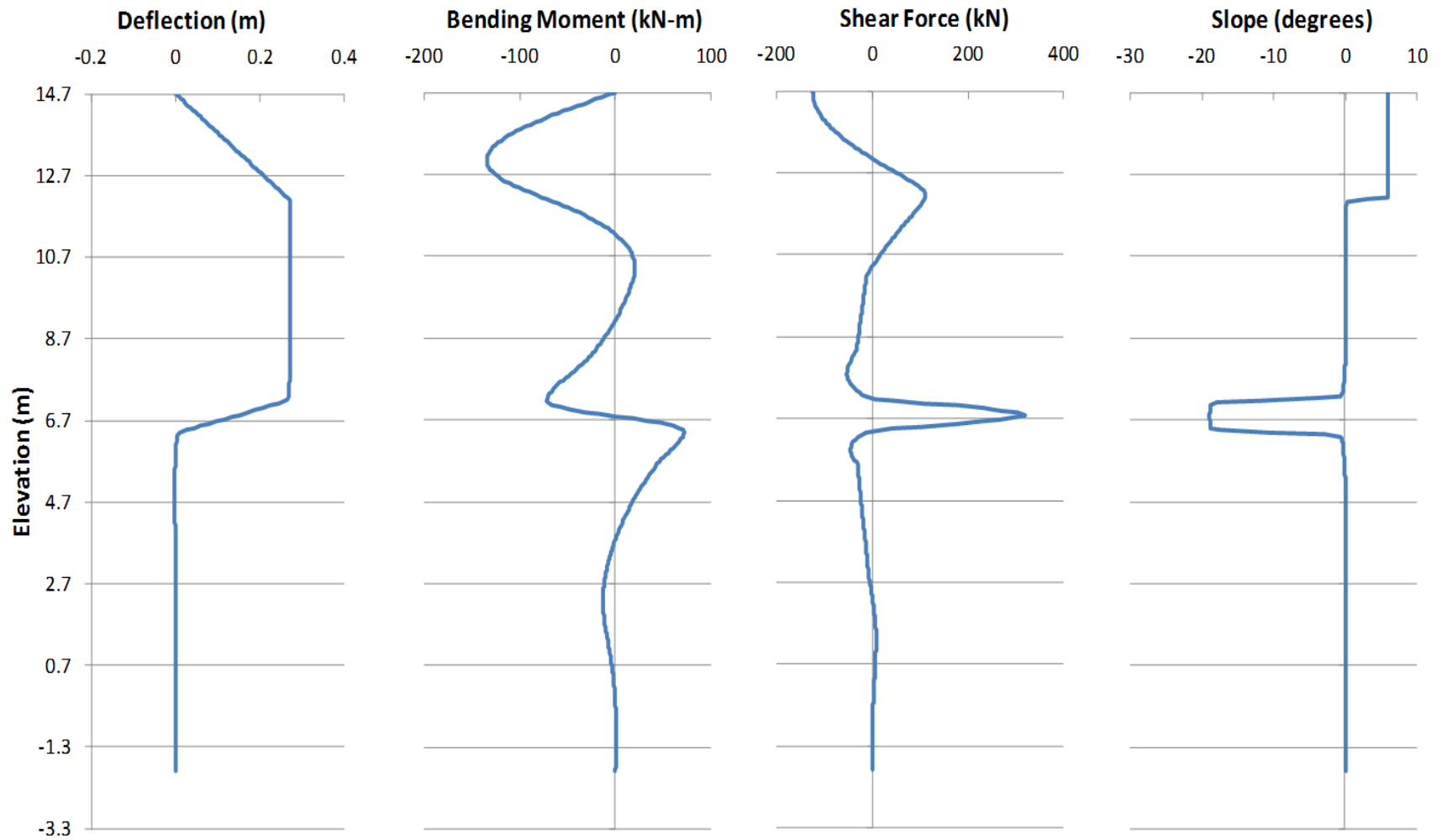


Figure 8-14: Deterministic Computed Pile Response for the Rio Cuba Bridge East Abutment From the 1991 Limon Earthquake

Table 8-2: EZ-FRISK Faults Within About 100 km of the Rio Cuba Bridge

Fault Name	Type	Fault Length (km)	Source to Site Distance (km)	Characteristic Magnitude	Slip Rate (mm/yr)	Recurrence Rate
Limon fault	Reverse	162	8.1	7.8	1.0	---
Panama - North (Caribbean)	Subduction Interface	817	42	8.0	4.0	---
Guapiles fault	Reverse	8	66	6.1	4.0	---
Longitudinal fault	Reverse	42	99	7.4	0.1	---
Longitudinal fault - Costa Rica 2	Reverse	52	99	7.0	0.5	---
Costa Rica	Subduction Intraslab	288	105	7.7	---	0.4958

The seismic hazard curve for the PGA developed from the PSHA is presented in Figure 8-15. The ground motions corresponding 10-percent and 2-percent probabilities of exceedance in 50 years are 0.541g and 0.869g, respectively.

The seismic hazard contributions from the individual sources are shown in Figure 8-16. From Figure 8-16, it appears that the Costa Rica arc and shear zone (area source) and the Costa Rica fault (subduction interface source) govern the probabilistic seismic hazard at most return periods for the PGA. The probabilistic response spectra developed from the PSHA for seven different return periods are shown in Figure 8-17. Finally, simplified deaggregation plots of the PGA are presented in Figure 8-18.

8.6.2 Probabilistic Liquefaction Triggering

Using the probabilistic estimates of a_{max} shown in Figure 8-15 in conjunction with the magnitude/distance deaggregations shown in Figure 8-18, probabilistic estimates of liquefaction triggering were computed with the Kramer and Mayfield (2007) procedure using Equations (6-1)

and (6-2). The performance-based liquefaction triggering computations were performed using the computer program PPRS. The resulting factors of safety against liquefaction triggering for various return periods are shown in Figure 8-19. These factors of safety were computed using the SPT blowcount information from Insuma boring P-1 at the Rio Cuba Bridge. A factor of safety less than or equal to 1.2 was assumed to be liquefiable for this study. Note that for fine-grained soil layers not considered susceptible to liquefaction due to plasticity, a generic factor of safety against liquefaction equal to 2.0 was assigned regardless of return period. A maximum factor of safety equal to 4.0 was assigned to layers with very high resistance to liquefaction triggering. Figure 8-19 shows that for most return periods, liquefaction triggers from depths of about 3.22 meters to 4.60 meters (EL. 6.98m to 5.60m) and from depths of about 12.88 meters to 13.80 meters (EL. -2.68m to -3.6m) below the native ground surface.

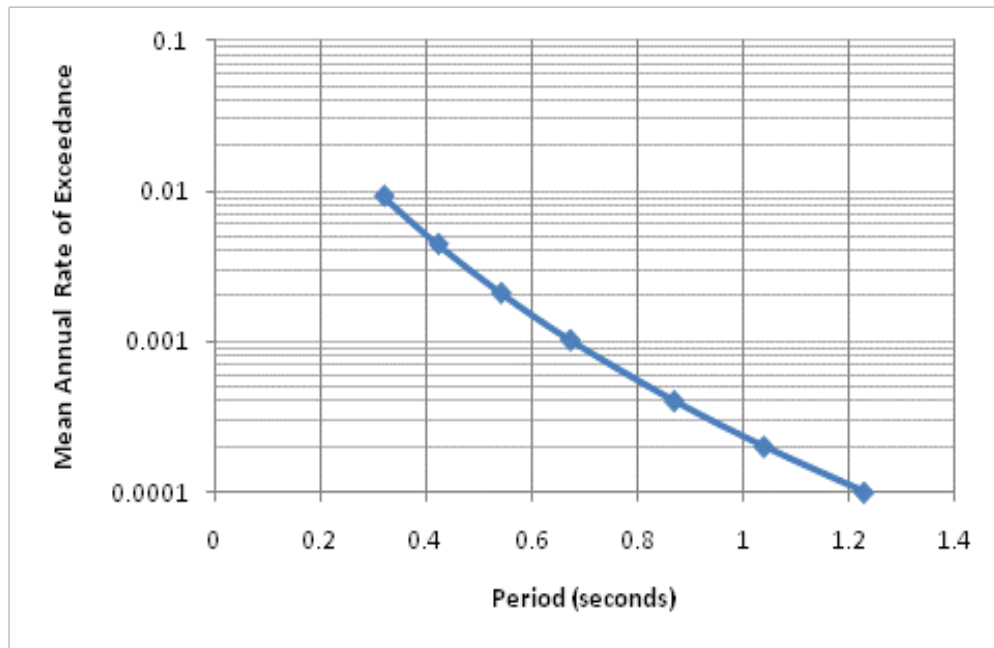


Figure 8-15: Seismic Hazard Curve for the PGA at the Rio Cuba Bridge

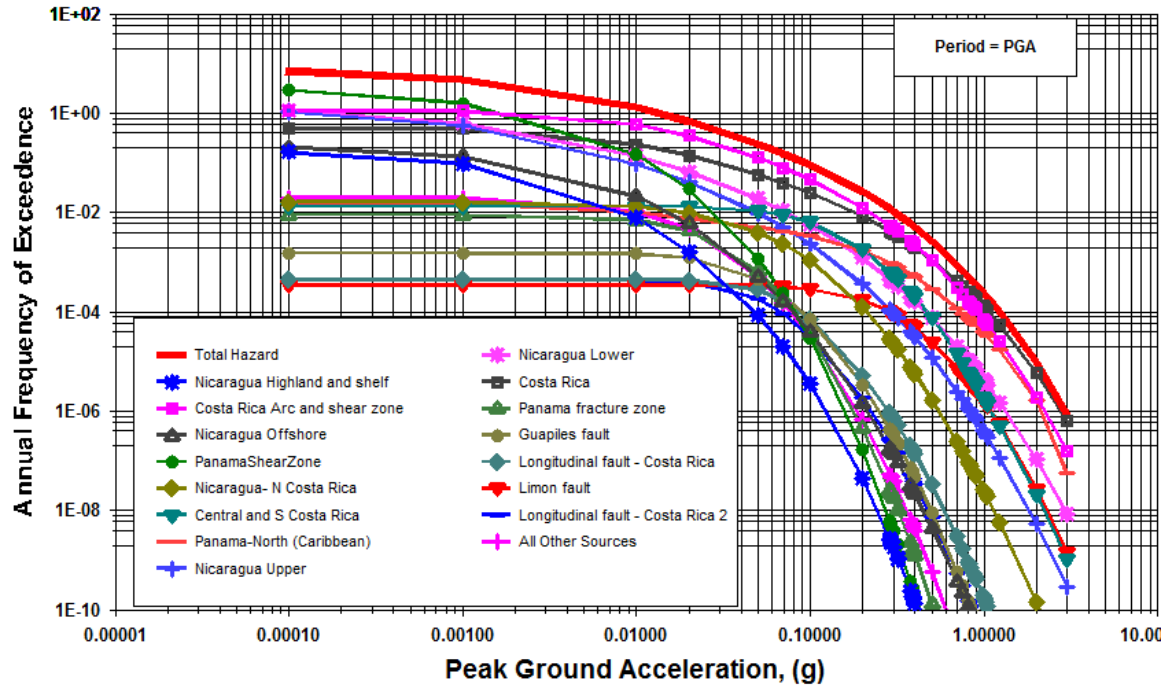


Figure 8-16: Source Contributions to Probabilistic Seismic Hazard for the Rio Cuba Bridge

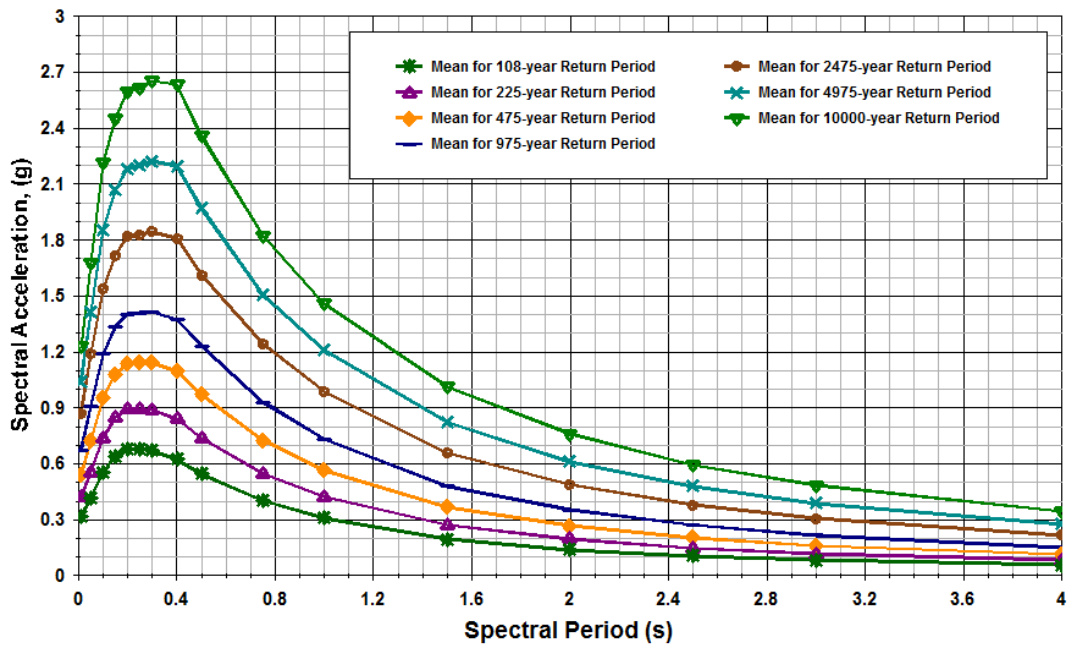


Figure 8-17: Probabilistic Response Spectra (5-Percent Damping) for the Rio Cuba Bridge

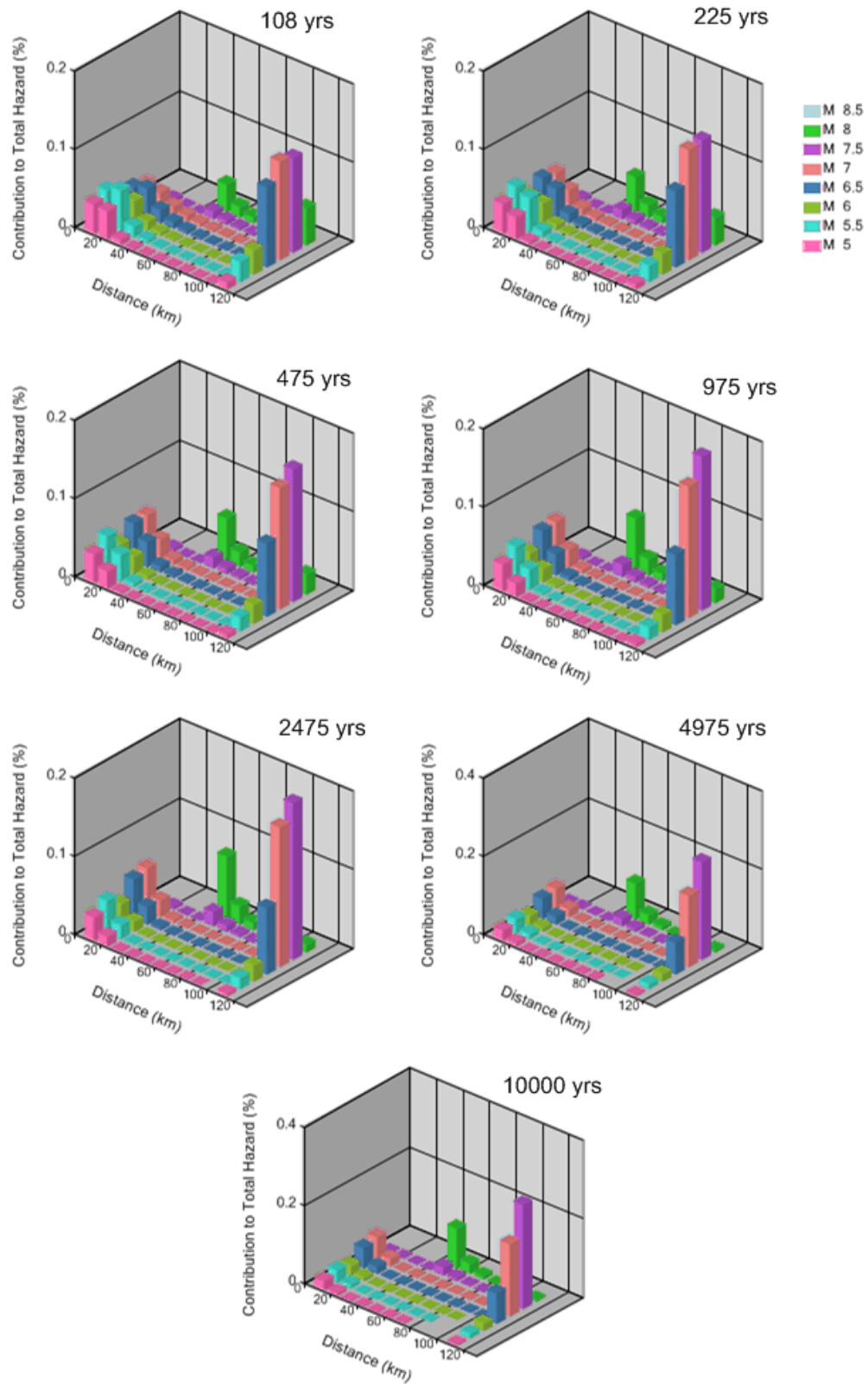


Figure 8-18: Deaggregation Plots for the PGA at the Rio Cuba Bridge

8.6.3 Development of the Loading Parameter, \mathcal{L}

The loading parameter \mathcal{L} , which serves as the intensity measure in the performance-based pile response procedure, was computed using Equations (6-4) through (6-6) from Section 6.8 of this dissertation. The equations were loaded as user-defined attenuation relationships into EZ-FRISK, and the Risk Engineering (2010) seismic source model for Central and South America was used to compute probabilistic estimates for \mathcal{L} . A plot of the hazard curves for \mathcal{L} is presented in Figure 8-20. Note that loading parameter for each model is unique and independent from the other models.

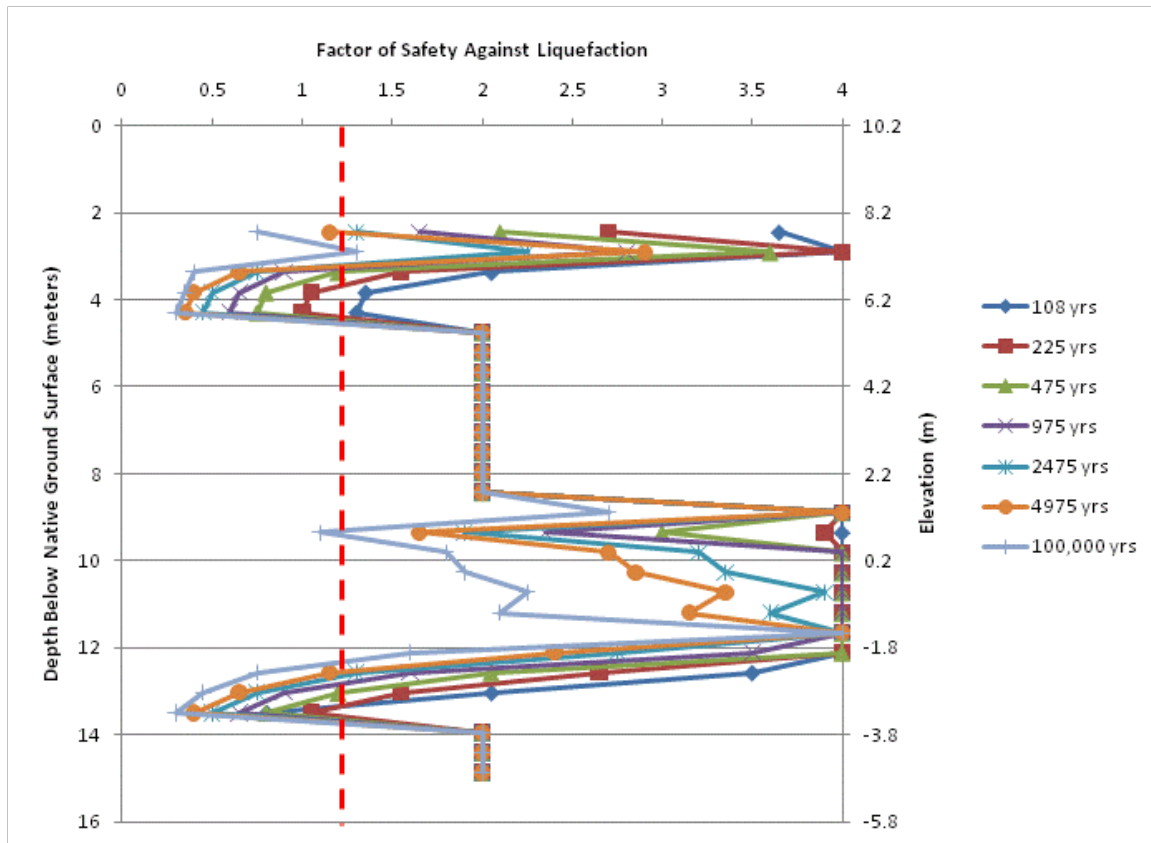


Figure 8-19: Performance-Based Liquefaction Triggering Results for the Rio Cuba Bridge

8.6.4 Development of the Fragility Functions for Lateral Spread Displacement

Fragility curves relating the probability of exceeding a given lateral spread displacement to the loading parameter \mathcal{L} were developed according to the procedure described in Section 6.9. The site parameter \mathcal{S} for the three selected empirical lateral spread models was computed using the soils and SPT blowcounts from Insuma boring P-1 with Equations (6-7), (6-9), and (6-11). A free-face ratio of 12-percent was used with a free-face height of 1.8 meters. Depth limitations as described in Section 3.7 were incorporated. The computed values of \mathcal{S} are shown in Table 8-3.

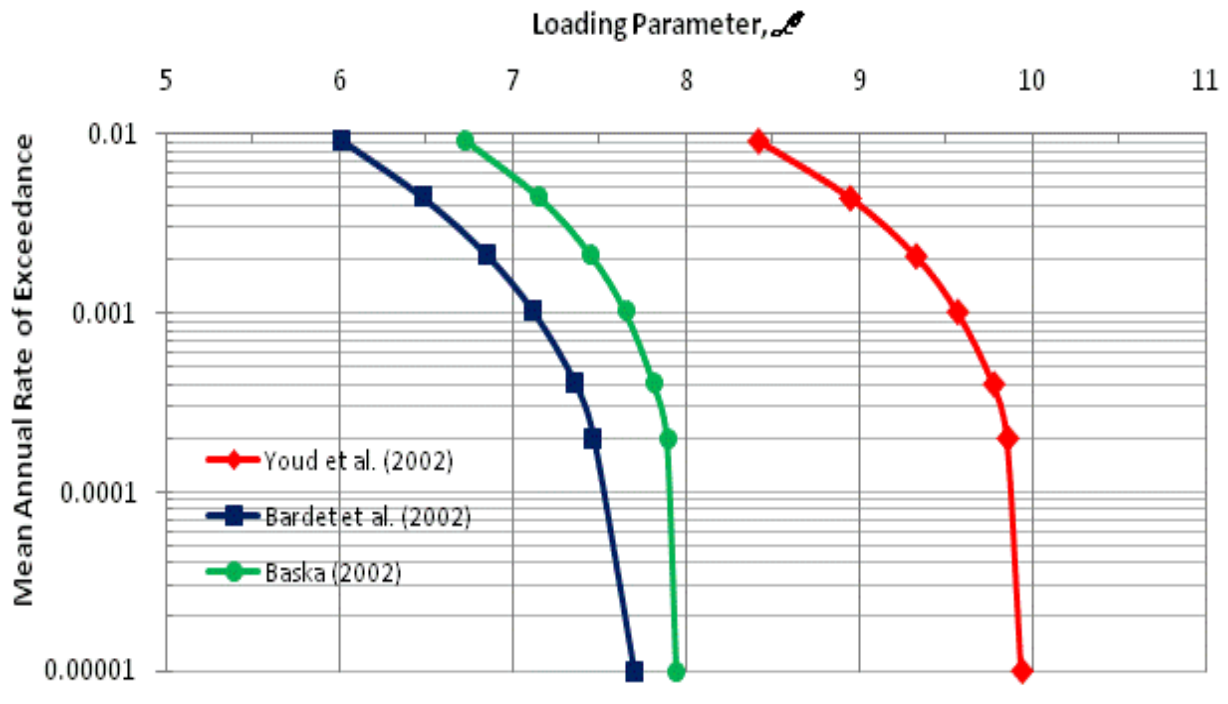


Figure 8-20: Hazard Curves for the Loading Parameter \mathcal{L} for the Rio Cuba Bridge

Table 8-3: Site Parameter \mathcal{S} for the Rio Cuba Bridge

Empirical Lateral Spread Model:	Site Parameter \mathcal{S}
Youd et al. (2002)	-9.367
Bardet et al. (2002)	-6.933
Baska (2002)	-6.351

With \mathcal{S} computed for each empirical lateral spread model, families of lateral spread fragility curves were developed using Equation (6-19). These curves are plotted for lateral spread displacements of 0.1 meter and 1 meter in Figure 8-21.

Values of \mathcal{S} and lateral spread fragility curves were calculated automatically in the computation of probabilistic lateral spread displacements using PPRS software.

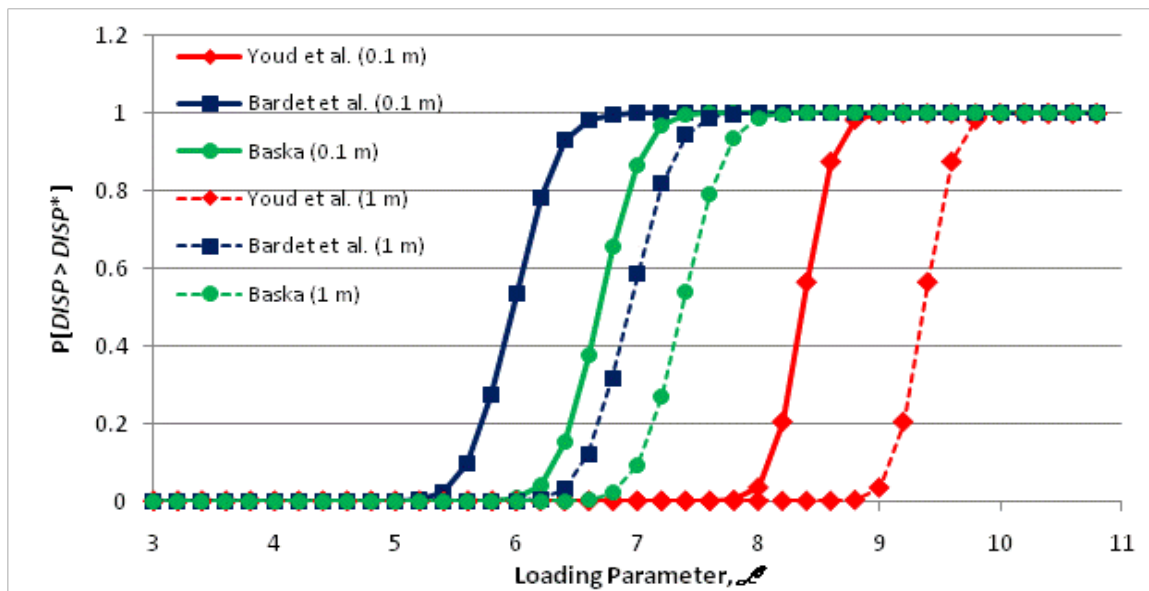


Figure 8-21: Lateral Spread Fragility Curves for $DISP^* = 0.1$ Meter and $DISP^* = 1$ Meter at the Rio Cuba Bridge

8.6.5 Development of Probabilistic Lateral Spread Displacements

Using PPRS software, the lateral spread fragility curves were convolved with the hazard curves for the lateral spread loading parameters \mathcal{L} shown in Figure 8-20 using the steps presented in Section 6.10. The resulting hazard curves for lateral spread displacement at the ground surface are shown in Figure 8-22.

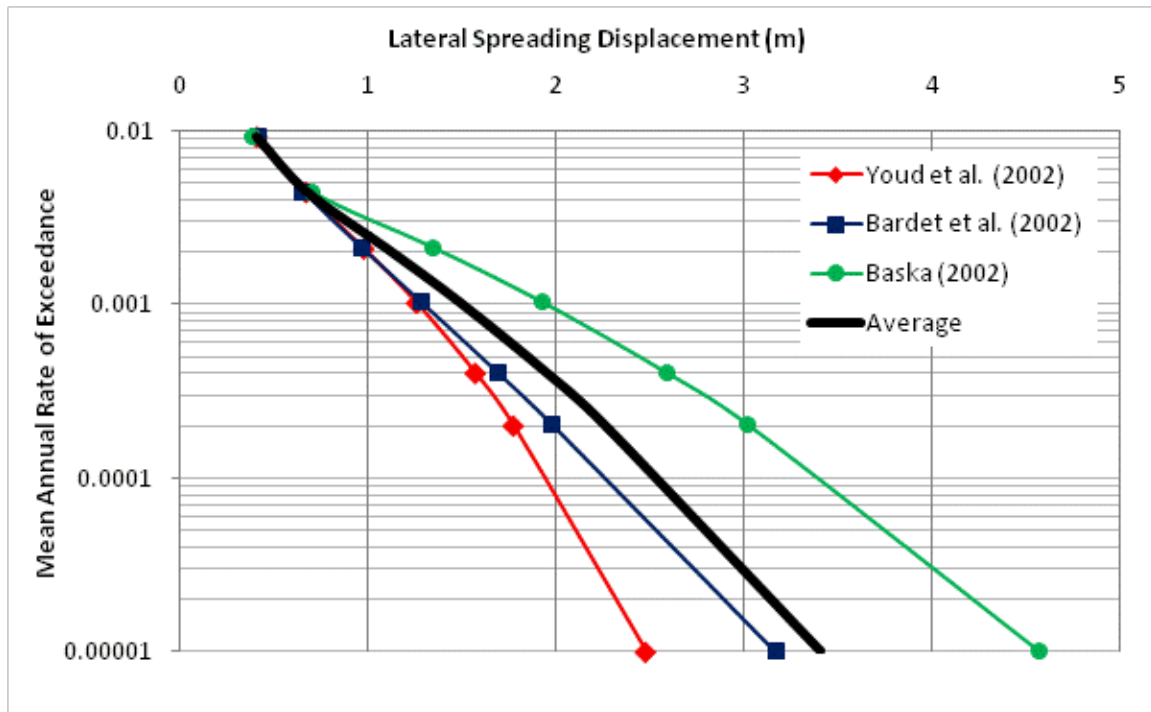


Figure 8-22: Lateral Spread Hazard Curves for the Rio Cuba Bridge

Figure 8-22 shows good agreement in computed probabilistic lateral spread displacements between the three empirical models at higher annual frequencies (i.e. lower return periods); however, the hazard curves tend to diverge at lower annual frequencies (i.e. higher

return periods). The Baska (2002) model appears to compute the largest displacements, and the Youd et al. (2002) appears to compute the smallest displacements. The average displacement hazard curve was computed using equal weights for all three empirical models.

The average computed probabilistic lateral spread displacements were propagated through the soil profile using the recommendations provided in Sections 3.6 and 3.7 in conjunction with the probabilistic liquefaction triggering profiles shown in Figure 8-19. The resulting probabilistic lateral spread displacement profiles are presented in Figure 8-23.

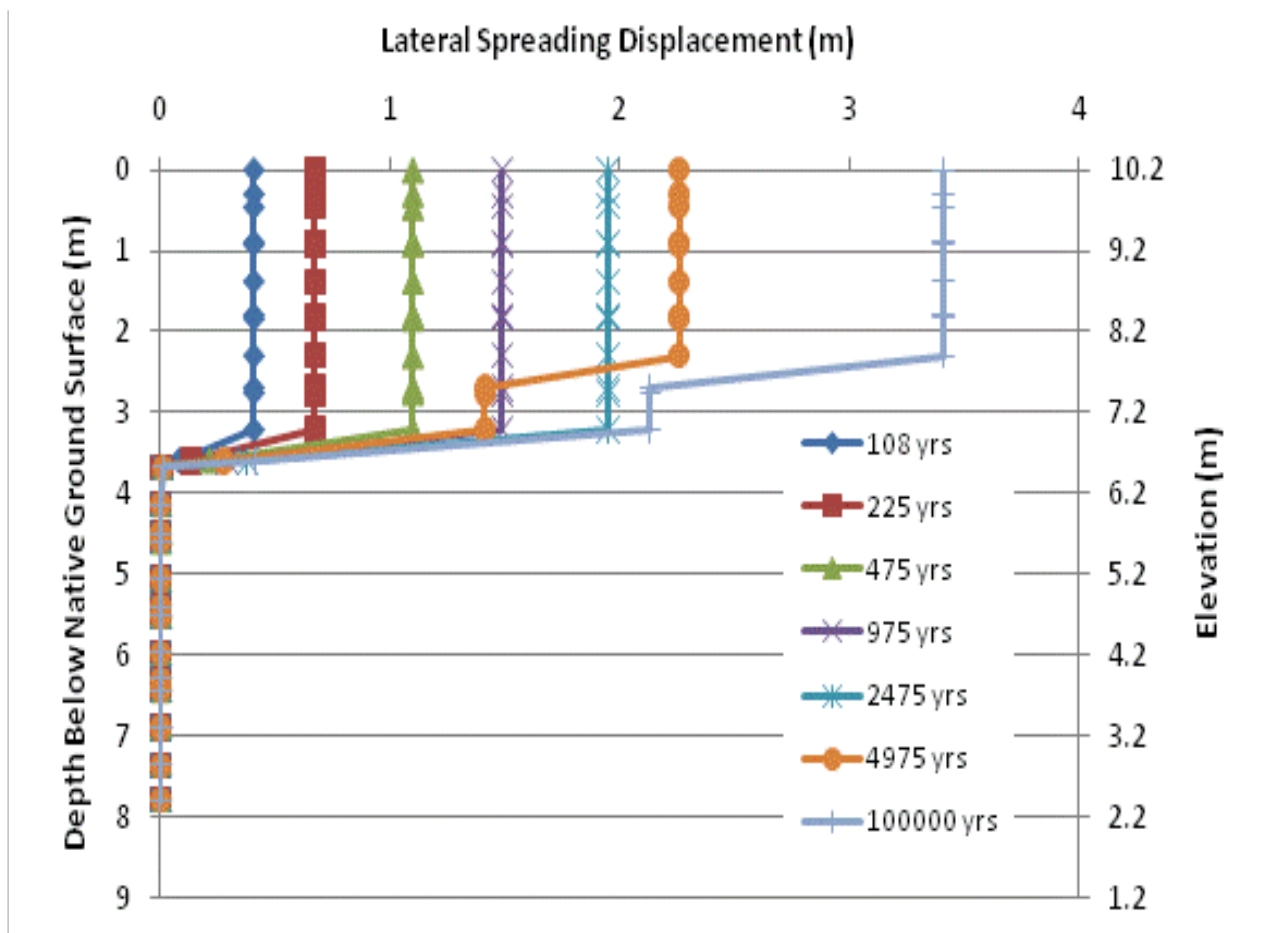


Figure 8-23: Probabilistic Lateral Spread Displacement Profiles for the Rio Cuba Bridge

8.6.6 Development of Fragility Functions for the Kinematic Pile Response

The Monte Carlo procedure described in Section 6.11 was originally intended to be incorporated with the LPILE MC Simulator spreadsheet and LPILE; however, the question of how to properly account for the strut load provided by the bridge deck in a performance-based framework was found to be significant and requires some discussion. The results from the deterministic pile response analysis at the Rio Cuba Bridge demonstrate that the bridge deck played a critical role in the observed performance of the bridge foundations during the kinematic loading of the 1991 Limon earthquake. Had the bridge deck fallen from its supports, the kinematic loading would likely have overwhelmed the foundations, and much larger horizontal deformations would have been observed at the abutment. However, the presence of the bridge deck limited lateral deformations, but caused the foundation and pile cap to rotate beneath the bridge deck.

In a probabilistic framework where earthquake loading and lateral spread displacements are considered from across a wide range of return periods, two critical questions arise when attempting to account for the possible bracing effects of a bridge deck:

- 1) At what return period of ground motion/displacement does the bridge deck fall off its supports?
- 2) How can one adjust the strut load in the probabilistic framework in order to account for the possible variability in the p-y behavior of the soil?

The first question is difficult, if not impossible to answer with simplified analysis techniques. The issue of bridge collapse can be very complex, and is dependent on a large number of variables including the intensity, frequency, and duration of the ground motion; the orientation of the bridge deck; the magnitude of ground displacement at the abutment(s); and the

bridge/support type. To simply attempt to correlate bridge collapse with the magnitude of lateral spread displacement potentially introduces significant error into the analysis. For example, evaluation of the 1991 Limon earthquake shows at least one bridge (Rio Estrella Highway Bridge) which collapsed with very little to no deformations of the foundation and at least one bridge (Rio Bananito Railway Bridge) whose foundation experienced significant deformations but did not collapse. Therefore, any attempt to estimate the return period at which a bridge deck would collapse would likely be better suited for a more sophisticated analysis such as a dynamic finite element/difference model that could account for both soil-structure interaction and dynamic response of the superstructure itself.

The second question deals more with the limitations of the simplified analysis methodology employed in this study. An important aspect of the performance-based evaluation of kinematic pile response is the consideration of variability in the soil-pile interaction. This study proposes a basic Monte Carlo approach in LPILE to estimate the variance of the pile response at various depths along the equivalent single pile. However, addition of a strut load at the head of the equivalent single pile significantly affects the computed pile response. Ideally, the strut load should be modified for each permutation in the Monte Carlo simulation such that the resulting lateral displacement at the pile head is approximately zero. However, there are no known means to program LPILE to automatically alter the applied load such that zero deformation at the pile head is maintained during the parameter randomization of the Monte Carlo simulation. Maintaining a constant strut load in the Monte Carlo simulation is one possible solution to the problem; however, the computed variance in the pile response would be unrealistically high because a constant strut load could either provide too much or too little resistance to kinematic loading for a given permutation. Such unrealistically high variances were

observed during preliminary Monte Carlo simulations with a constant strut load at the Rio Cuba Bridge, resulting in computed coefficients of variation exceeding 300%.

It is apparent that the simplified procedures for computing fragility functions for kinematic pile response as presented in Section 6.11 of this report may not be well-suited for considering additional complex structural phenomenon such as the potential bracing effect from a bridge deck. Such complexity would be better modeled using more sophisticated numerical methods capable of accounting for more of the mechanics and uncertainty associated with the phenomenon. However, the performance-based framework for ultimately computing the probabilistic kinematic pile response as described in Section 6.12 would still be compatible with the resulting fragility functions from such a more sophisticated approach.

For the sake of demonstration, two sets of LPILE analyses were performed at the Rio Cuba Bridge to develop fragility relationships for the kinematic pile response. These two sets of analyses were intended to provide reasonable bounds for the problem by representing the two possible extremes for the kinematic pile response. The first LPILE analysis neglected the presence of a reinforcing bridge deck, thus assuming that the kinematic loading is being resisted solely by the lateral stiffness of the piles themselves. The assumption of no bridge deck is routinely used in engineering practice today because it is considered to be conservative. However, such an assumption inherently defeats the idea of performance-based design because true performance is not necessarily being considered. The results of the first LPILE analysis showed that the computed variance at each node in the pile response was essentially equal to zero, suggesting that the reinforced concrete piles had insufficient stiffness to provide any significant resistance to the lateral spread displacement. Therefore, the performance-based

analysis could be simplified by simply neglecting the variance in the pile response (i.e. $S_{R,DISP} \approx 0$ in Equation (6-22)).

The second LPILE analysis modeled a constant reinforcing strut load at each return period of lateral spread displacement. A constant coefficient of variation equal to 30% was assumed and applied across the entire pile to represent the variability in the kinematic pile response. This approach was used rather than performing a Monte Carlo simulation with a constant strut load in order to maintain more realistic values of the variance in the pile response. However, it is recognized that such a simplified approach should not be applied in actual engineering design; rather, the variance in the kinematic pile response should be computed using more sophisticated methods such as a Monte Carlo simulation coupled with a dynamic numerical model.

8.6.7 Development of Probabilistic Kinematic Pile Response

The probabilistic kinematic pile response was computed for each node in the two LPILE analyses for the Rio Cuba Bridge by convolving the results from the fragility relationships developed in Section 8.6.6 with the probabilistic lateral spread displacement profiles developed in Section 8.6.5. PPRS software was used to apply Equation (6-23) and the steps presented in Section 6.12 for computing probabilistic estimates of displacement, bending moment, shear force, and curvature for all nodes in the pile response model. The resulting probabilistic pile response profiles for the first analysis (i.e. no bridge deck) and the second analysis (i.e. bridge deck) are shown in Figure 8-24 and Figure 8-25, respectively.

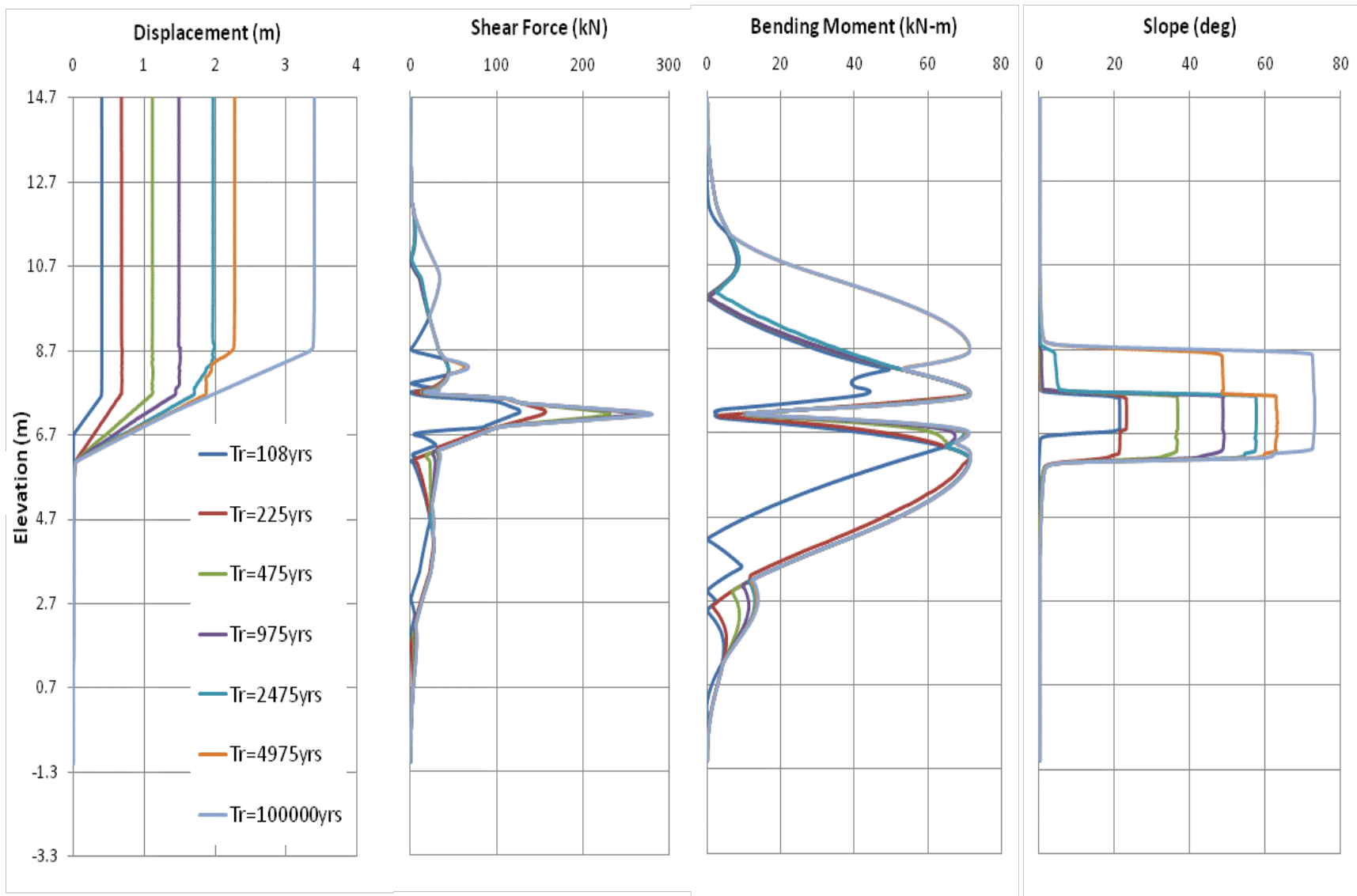


Figure 8-24: Probabilistic Pile Response Curves (Absolute Values) Assuming No Bridge Deck for the Rio Cuba Bridge

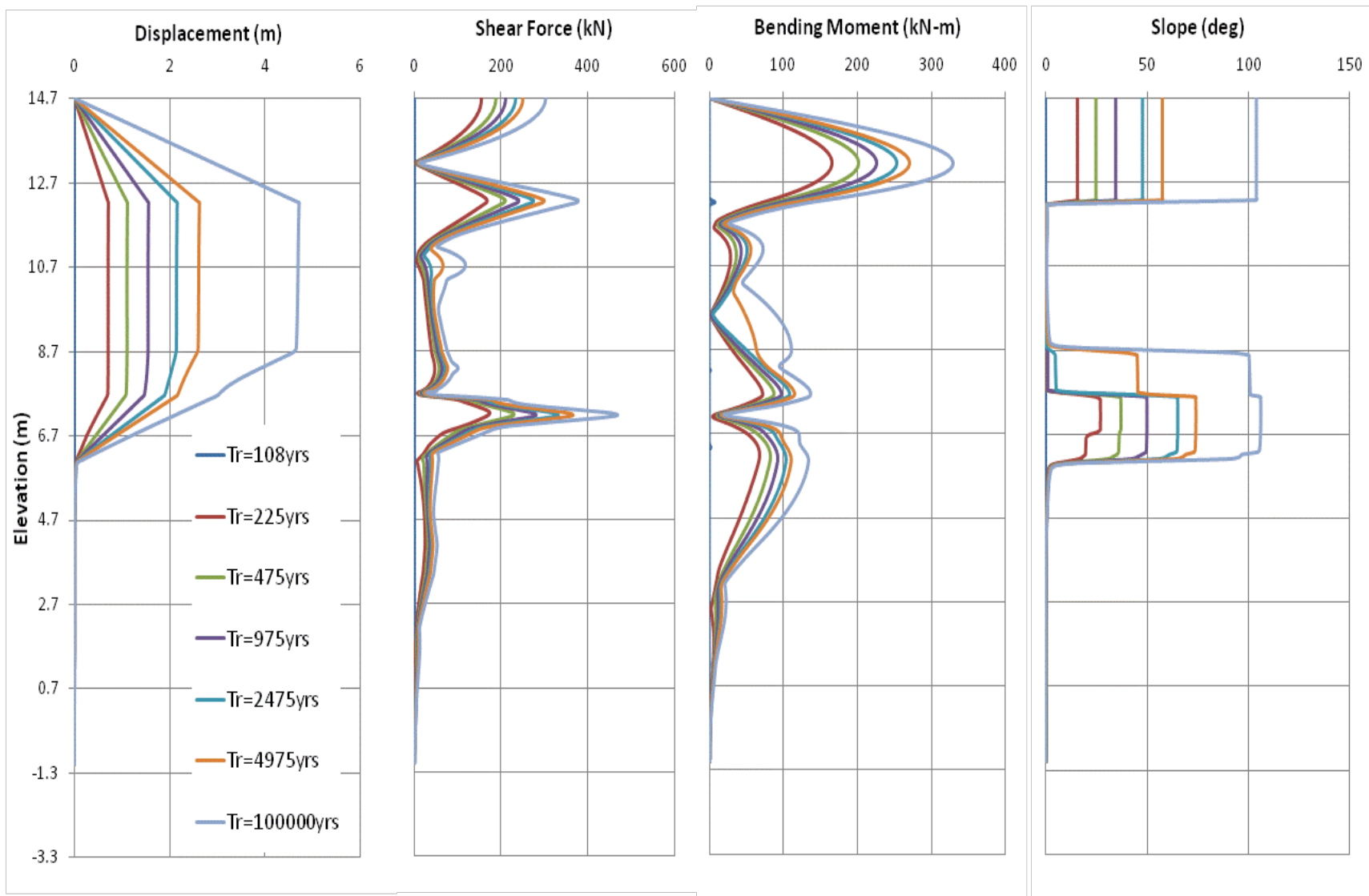


Figure 8-25: Probabilistic Pile Response Curves (Absolute Values) Assuming a Bridge Deck at the Rio Cuba Bridge

8.6.8 Discussion of Results

Thoughtful review of Figure 8-24 and Figure 8-25 reveal a few important observations that deserve discussion. First, the drastically different results from the two performance-based analyses demonstrate the significance that the bridge deck can have in computing the kinematic pile response of a bridge foundation. As performance-based pile response analysis methods become more sophisticated, significant attention should be paid to the estimated dynamic behavior of the bridge deck because it can dramatically affect the performance of the piles in resisting kinematic loading.

The pile response analysis results shown in Figure 8-24, which represent the assumption of no bridge deck, demonstrate that two rows of reinforced concrete piles are generally insufficient to resist any significant amount of kinematic loading. Significant deformations and pile yielding were computed at all return periods. These results suggest that the piles were unable to resist even smallest of ground deformations. In addition, the pile deformation profiles are remarkably similar at each return period to the computed free-field ground deformations shown in Figure 8-23, suggesting that the piles essentially experience the same deformations as the surrounding soils. Ledezma and Bray (2008, 2010) note that such behavior is likely typical of most bridge foundations if the reinforcing effect of the bridge deck is neglected.

The pile response results shown in Figure 8-25 demonstrate the significance that the estimated variance in the soil-pile interaction can have in a performance-based pile response analysis. Using an assumed uniform coefficient of variation of 30% for the pile response produced very large computed probabilistic estimates of the kinematic pile response at return periods greater than about 2,475 years. Therefore, reasonable care should be provided whenever

possible to obtain realistic estimates of the variance in the soil-pile interaction when computing performance-based kinematic pile response.

Finally, when comparing the measured pile cap rotation of 8.5 degrees following the Limon earthquake with the computed performance-based pile response results shown in Figure 8-25, a rotation of 8.5 degrees corresponds with an approximate return period of 125 years (i.e. 45% probability of exceedance in 75 years). Therefore, according to the performance-based analysis, the east abutment of the Rio Cuba Bridge has nearly a two-to-one chance of experiencing a pile cap rotation of at least 8.5 degrees in any given 75 year timeframe if the bridge deck stays in place and the coefficient of variation in the soil-pile interaction is approximately equal to 30% across all depths of the pile group.

9 RIO BLANCO BRIDGE

9.1 Introduction

The bridge over the Rio Blanco is a three-span reinforced concrete bridge supporting two lanes of traffic. The two outside spans are 17 meters in length and the interior span is 22 meters in length. Each span is composed of reinforced concrete girders, and the total span of the bridge is shown to be 59 meters. The bridge is located along National Route 32 just east of the town of Liverpool. The latitude/longitude coordinates of the bridge are 9.9918° North 83.1253° West. A photo of the bridge is presented in Figure 9-1.

According to bridge plans provided by the Costa Rican Ministry of Transportation and dated September 1967, the bridge is founded on a series of 14-inch square reinforced concrete piles. The abutments are supported by two rows of piles (6 piles in the front row, 7 piles in the second row, and 13 piles in total) that are 15 meters in length and spaced at 5-6 diameters in the transverse direction and 3 diameters in the longitudinal direction. The dimensions of the pile cap at each abutment are 12.3 meters (transverse) x 1.90 meters (longitudinal) x 2.60 meters (vertical).

The two bents are each founded on two 4-meter x 5-meter pile caps. Each of these pile caps is supported by 20 14-inch x 14-inch piles (five rows of four piles) that are 11 meters in length and spaced at 2.8 diameters in both the transverse and longitudinal directions. The abutments and the bents are skewed at an angle of 35 degrees to the transverse orientation of the

bridge. Finally, the front row of piles at each abutment and bent location are battered at approximately 5V:1H. However, any batter in the piles was neglected in the pile response analysis because the Juirnarongrit and Ashford (2006) pile response procedure does not specify how to account for pile batter in a few of the piles in the group.



Figure 9-1: The Rio Blanco Bridge

9.2 Observed Damage Following the 1991 Earthquake

BYU investigators measured damage still visible from the Rio Blanco Bridge during a site reconnaissance in May 2011, and observation was focused on the east abutment, which appeared to have sustained the largest amount of damage. A rotation of 10-11.5 degrees was measured at the east abutment. Unfortunately, the actual amount of lateral spread displacement

that occurred at the east abutment of the bridge at the time of the 1991 Limon earthquake is unknown because all evidence of lateral spread in the soil had disappeared by the time of the BYU field investigations in 2009, 2010, and 2011.



Figure 9-2: Rotation of the Pile Cap at the East Abutment of the Rio Blanco Bridge

Evaluation of the piles at each of the abutments showed considerable amounts of cracking and spalling, suggesting that bending moments induced by lateral spread approached or exceeded the yield moments for the piles. The backwall of each abutment was lodged against the bottoms of the bridge girders, thus suggesting that lateral spread soil deformations pushed the backwall of each abutment until it made contact with the girders and initiated rotation. Therefore, while the bridge deck appeared to limit the amount of lateral displacement that occurred at each abutment, it likely contributed to the observed rotations at the abutments.

9.3 Soil Site Characterization at the Rio Blanco Bridge

Insuma S.A. Geotechnical Consultants performed a single boring immediately adjacent to the embankment fill at the eastern abutment of the bridge. The boring extended to a depth of 15 meters. The soils encountered in the boring were reported to consist primarily of alluvial deposits alternating between clays, silts, and sands. The clays encountered appeared to have high plasticity while the silts encountered appeared to have either low or no plasticity. The sands encountered appeared to be fine-grained and varied in fines content from clean to silty/clayey. Groundwater was encountered in the boring at an depth of 4.8 meters, which corresponds to an elevation of 2.2 meters. A simple diagram of the soils encountered in the boring performed is shown in Figure 9-3 below. Further details regarding the boring at the Rio Blanco Bridge and the corresponding laboratory test results can be found in the Insuma Geotechnical Report included as Appendix A of this report.

The information from boring P-1 was used to develop a generalized soil profile for the east abutment of the Rio Blanco Bridge. Empirical correlations with SPT blowcounts were averaged to estimate the friction angle of granular soils and non-plastic silts. These correlations include Peck et al. (1974), Hatanaka and Uchida (1996), and Bowles (1977). Relative density of granular soils was estimated using the empirical correlation presented by Kulhawy and Mayne (1990). Corrected soil modulus estimates K^* of the granular soils for use with the API (1993) p-y relationship were estimated using the recommendations presented by Boulanger et al. (2003). Undrained strength of cohesive plastic soils was averaged from empirical correlations including Hara et al. (1971), Kulhawy and Mayne (1990), and Skempton (1957). Assumptions regarding the unit weight of the native soil as well as the strength properties of the embankment fill were made. Liquefied p-multipliers were estimated using Brandenberg et al. (2007). Groundwater was

modeled at an elevation of 2.2 meters (i.e. a depth of 7.32 meters from the top of the embankment fill). Table 9-1 summarizes our generalized model of the soil profile at the east abutment of the Rio Blanco Bridge.

9.4 Characterization of Site Geometry/Topography at the Rio Blanco Bridge

The Rio Blanco is a relatively small river bounded on both sides by a gently sloping floodplain and extensive vegetation. According to elevations shown on the blueprints that were provided by the Costa Rican Ministry of Transportation, the river channel itself ranges in elevation from about -0.75 meter at the bottom of the river channel to 4.75 meters at the river bank near the eastern bridge abutment. The elevations shown on the blueprints appeared to correspond reasonably well with elevations measured during a BYU GPS site survey in May of 2011. Therefore, the elevations on the blueprints were used for analysis, and elevations measured from the BYU site survey were used as needed to compensate for any missing information. According to the bridge blueprints, the roadway elevation across the bridge varies from 9.52 meters at the east abutment to 9.54 meters at the west abutment. From the blueprints, it also appears that the approach embankment was originally constructed at a 1.5H:1V slope. The elevation of the water in the Rio Blanco was estimated to be 2.2 meters at the time of our investigation. A sketch of the plan and profile views of the Rio Blanco Bridge as they are shown on the plans provided by the Costa Rican Ministry of Transportation is presented in Figure 9-4. Using the sketch shown in Figure 9-4, a free-face height of 5.5 meters and a free-face ratio of 20-percent were selected to represent the geometry of the native soils at the east abutment.

Depth (m)	SPT N Value		
0.00 - 0.45	1	Very sandy brown SILT, mixed with some gravel particles, soft to firm consistency.	
0.45 - 0.90	6		
0.90 - 1.35	11		
1.35 - 1.80	11		
1.80 - 2.25	10	Well graded silty SAND mixed with some gravel, firm relative density.	
2.25 - 2.70	28		
2.70 - 3.15	11		
3.15 - 3.60	11	Gray sandy CLAY or very clayey SAND, mixed with pieces of waste (garbage), with soft consistency.	
3.60 - 4.05	6		
4.05 - 4.50	4		
4.50 - 4.95	4		
4.95 - 5.40	3		
5.40 - 5.85	2		
5.85 - 6.30	3		
6.30 - 6.75	5	Well graded gray SAND, loose.	
6.75 - 7.20	3		
7.20 - 7.65	7		
7.65 - 8.10	10		
8.10 - 8.55	10		Greenish gray silty fine SAND, fines have no plasticity, loose to firm.
8.55 - 9.00	9		
9.00 - 9.45	10		Gray silty SAND mixed with pieces of wood, probably transported by the river.
9.45 - 9.90	12		
9.90 - 10.35	10		
10.35 - 10.80	17		
10.80 - 11.25	21		
11.25 - 11.70	10	Greenish gray very fine silty SAND with very firm to firm relative density.	
11.70 - 12.15	24		
12.15 - 12.60	27		
12.60 - 13.05	24		
13.05 - 13.50	26		
13.50 - 13.95	25		
13.95 - 14.40	35		
14.40 - 14.85	37		

Figure 9-3: Boring P-1 Performed at the Rio Blanco Bridge

Table 9-1: Generalized Soil Profile for the East Abutment at the Rio Blanco Bridge

Top Depth (m)	Top Elevation (m)	Thickness (m)	USCS Soil Class	Friction Angle (deg)	Moist Unit Weight (kN/m ³)	Undrained Strength (kPa)	Relative Density (%)	Corrected Soil Modulus (kN/m ³)	Liquefied p-mult
0	9.52	2.52	SM (Fill)	35	18.5	---	62	24,800	NA
2.52	7.00	1.80	ML (Fill)	---	18.1	38.0	---	---	NA
4.32	5.20	1.35	SW(Fill)	36	18.1	---	63	24,160	NA
5.67	3.85	1.65	CH	---	18.5	24.0	---	---	NA
7.32	2.20	2.40	CH	---	8.7	24.0	---	---	NA
9.72	-0.20	3.15	SW/SM	33	8.3	---	45	10,000	0.12
12.87	-3.35	4.50	SM/ML	38	8.5	---	71	19,300	NA

9.5 Deterministic Pile Response Analysis at the Rio Blanco Bridge

9.5.1 Deterministic Ground Motion Evaluation From the 1991 Earthquake

The Rio Blanco Bridge is located 34.4 kilometers north from the epicenter of the April 22, 1991 earthquake. Assuming an average V_{S30} value of 270 m/s, the average computed median spectral acceleration along with median $\pm 1\sigma$ from the four selected NGA models are shown in Figure 9-5. The median computed PGA is 0.167g.

9.5.2 Deterministic Liquefaction Evaluation From the 1991 Earthquake

Using the average deterministic ground motions from the NGA equations, the deterministic liquefaction triggering was evaluated at the Rio Blanco Bridge using the SPT blowcounts from Insuma Boring P-1. The results of the deterministic liquefaction triggering analysis are shown in Figure 9-6. This evaluation included consideration of the Cetin et al. (2004), Idriss and Boulanger (2008), and Youd et al. (2001) simplified procedures. The results of the analysis suggest that liquefaction triggered from depths of 7.2 meters to 10.4 meters below the ground surface (EL -0.2m to EL -3.4m).

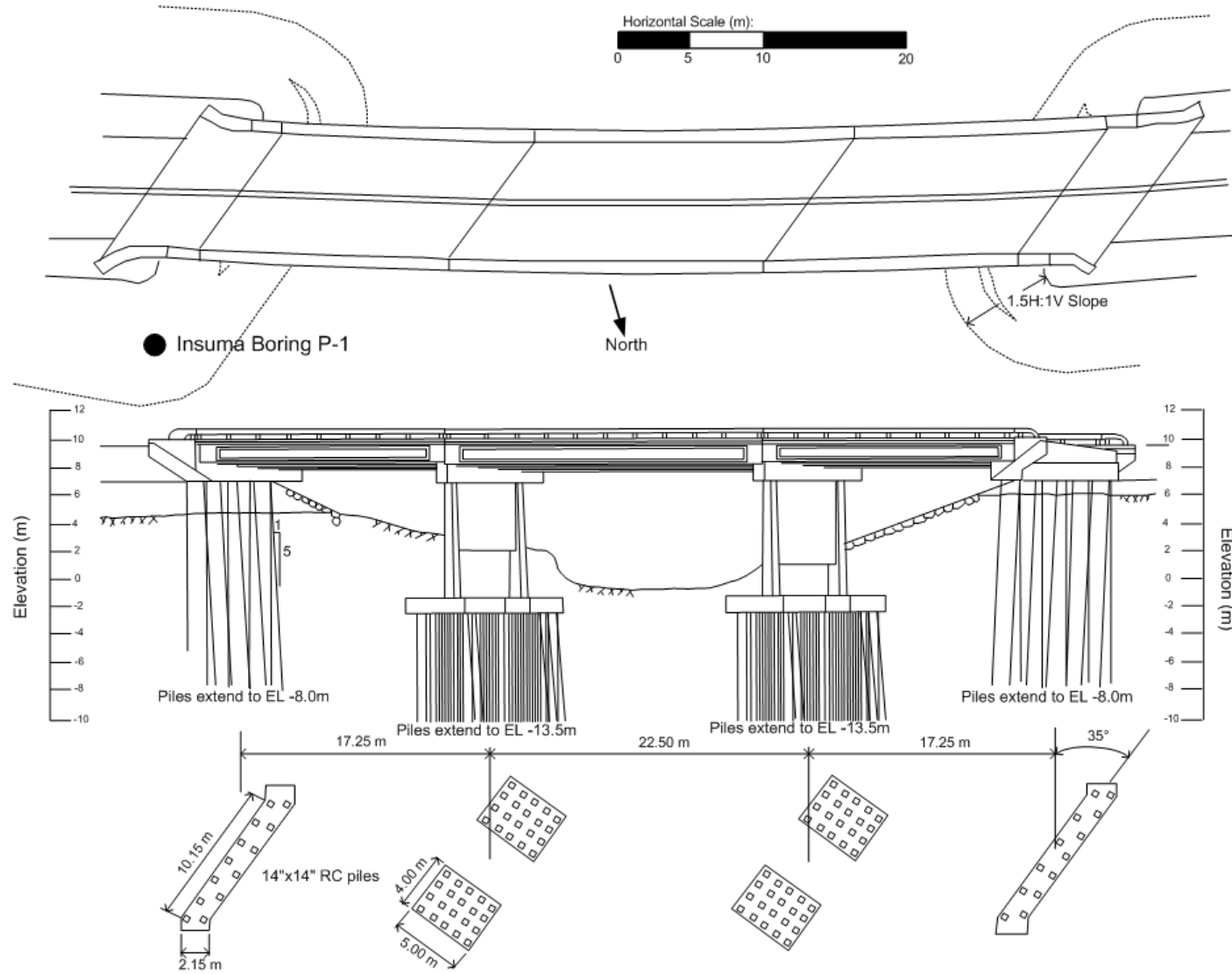


Figure 9-4: Simplified Sketch of the Plan and Profile Views of the Rio Blanco Bridge as Shown on the Bridge Plans

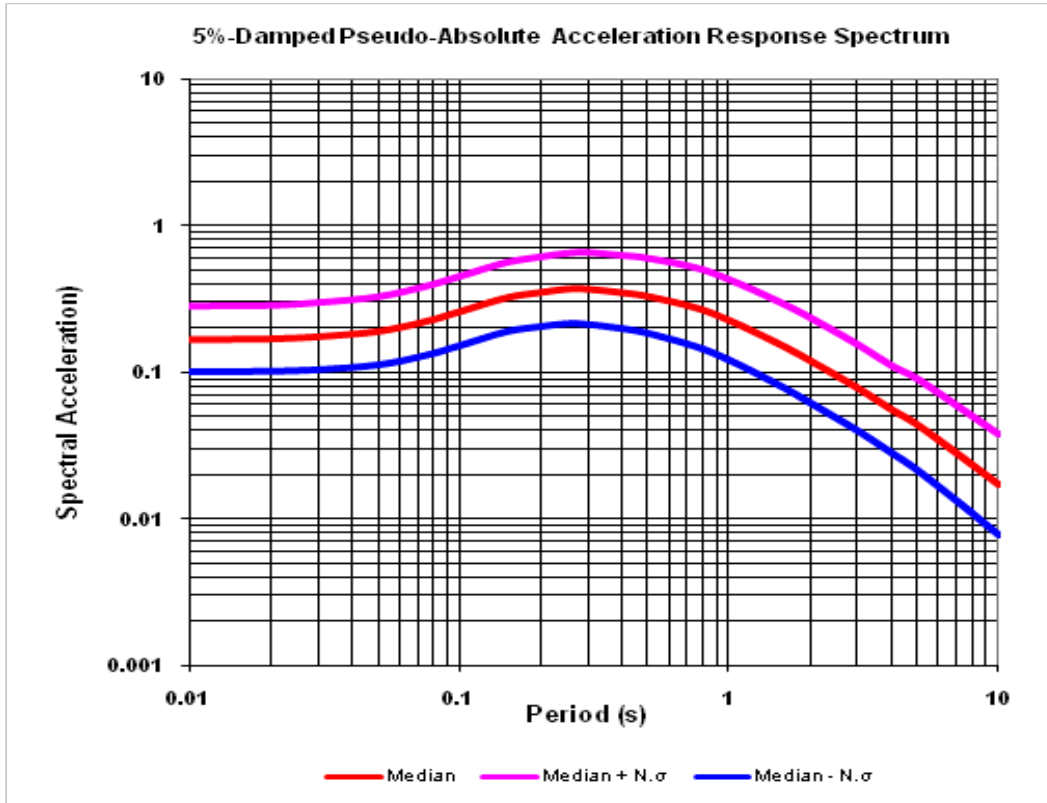


Figure 9-5: Computed Deterministic Response Spectra for the Rio Blanco Bridge From the 1991 Earthquake. N = 1

9.5.3 Post Earthquake Slope Stability

A simple post earthquake slope stability evaluation was performed for the west bank of the Rio Blanco using SLOPE/W analysis software (GEO-SLOPE, 2010) because it is higher and more critical than the east bank. In addition, the pre-bridge geometry of the river bank as indicated on the bridge plans provided by the Costa Rica Ministry of Transportation was used in the analysis to be conservative. In evaluating the slope stability, only native soils were considered in the analysis in order to investigate the potential for flow liquefaction failure along the river bank. Such a failure would likely disqualify the use of empirical lateral spread models

for computing lateral spread displacements in the native soils along the river bank. Undrained strengths of fined-grained soils were reduced by 20-percent in accordance with recommendations by Makdisi and Seed (1977). The residual strength ratio S_r/σ' of the liquefied soil was computed using the Ledezma and Bray (2010) as given in Equation (2-2). Lowe and Karafiath (1960) was used in the limit equilibrium analysis to compute factor of safety. A circular surface search routine was utilized allowing for optimization in order to allow for the possibility of non-linear or log-spiral failure surfaces. A summary output from the post earthquake slope stability evaluation is presented in Figure 9-7. The computed factor of safety was 1.21, which suggests that the risk of a liquefaction flow failure is relatively low at the site.

9.5.4 Deterministic Evaluation of Lateral Spread

Empirical evaluation of the free-field soil displacements due to lateral spread was performed using the Youd et al. (2002), Bardet et al. (2002), and Baska (2002) models as presented in Sections 3.4 and 3.5 of this dissertation. This study assumed an earthquake magnitude of 7.6, a source-to-site distance of 34 kilometers, a free-face ratio of 20-percent, and a free-face height of 5.5 meters. The mean grain size diameter for each soil sublayer in the analysis was estimated from the Insuma sieve results, which are available in Appendix A. The median computed lateral spread displacement value and the 95th-percentile confidence interval for each of the three empirical models is shown in Figure 9-8. The average computed median displacement from the three models is 0.99 meter.

The estimated lateral spread displacement profile was computed in conjunction with the liquefaction triggering profile shown in Figure 9-6. This displacement profile is shown in Figure 9-9.

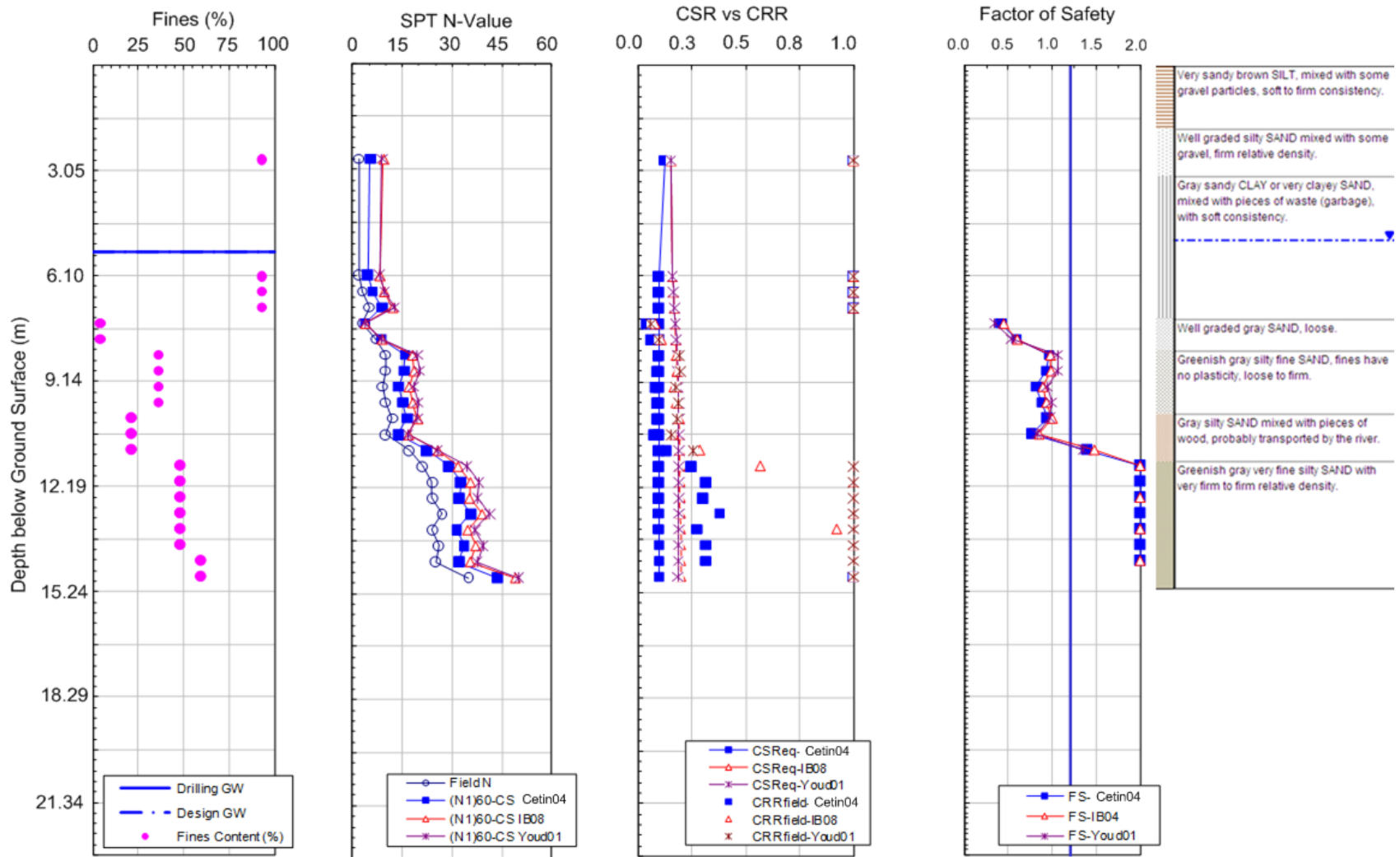


Figure 9-6: Deterministic Liquefaction Triggering Results for the M7.6 1991 Limon Earthquake at the Rio Blanco Bridge

9.5.5 Pile Response Analysis

With lateral spread displacement profiles, an analysis of the pile response at the east abutment of the Rio Blanco Bridge can be performed using the same equivalent single pile procedure used to model the Rio Cuba Bridge in Chapter 8.

Because the bridge deck did not fall from its supports as a result of the earthquake, the kinematic response of the piles at the abutments was likely significantly affected by the presence of the bridge deck. The presence of the deck would likely act as a supporting strut, thus limiting the amount of lateral deformation at the ground surface.

However, like the Rio Cuba Bridge, the relatively brittle foundations supporting the Rio Blanco Bridge would likely not be able to resist very large shear loads and bending moments, and would therefore be susceptible to large deformations and rotation beneath the bridge deck. Such a phenomenon was observed during the BYU reconnaissance in which pile cap rotations were still visible and were measured at 10-11.5 degrees from vertical. However, had the bridge deck not been in place, it is likely that the piles would have deformed in conjunction with the free-field soil deformations, resulting in greater horizontal displacements and less rotation at the abutments.

Because the pile response at the east abutment of the Rio Blanco Bridge appeared to be very similar to the observed pile response at the Rio Cuba Bridge, the pile response analysis at the Rio Blanco Bridge was performed using the same procedure as that used to analyze the Rio Cuba Bridge in Chapter 8. To account for the presence of the bridge deck, a lateral resisting load was applied to the head of the pile cap in the LPILE analysis. The load was gradually increased until zero displacement was achieved at the pile head.

Name: Silt #1 (Seismic) Model: S=f(overburden) Unit Weight: 18.1 kN/m³ Tau/Sigma Ratio: 0.19 Minimum Strength: 30
 Name: Fat Clay #1 Model: Undrained (Phi=0) Unit Weight: 18.8 kN/m³ Cohesion: 17.7 kPa B-bar: 0
 Name: Sand #1 Model: Mohr-Coulomb Unit Weight: 18.1 kN/m³ Cohesion: 0 kPa Phi: 36 °
 Name: Clayey Sand #1 Model: Mohr-Coulomb Unit Weight: 18.5 kN/m³ Cohesion: 2.4 kPa Phi: 34 °
 Name: Silty Sand #1 Model: Mohr-Coulomb Unit Weight: 18.3 kN/m³ Cohesion: 2.4 kPa Phi: 38 °
 Name: Liquefied Soil (Sr/Sig') Model: S=f(overburden) Unit Weight: 18.1 kN/m³ Tau/Sigma Ratio: 0.12 Minimum Strength: 4.8

259

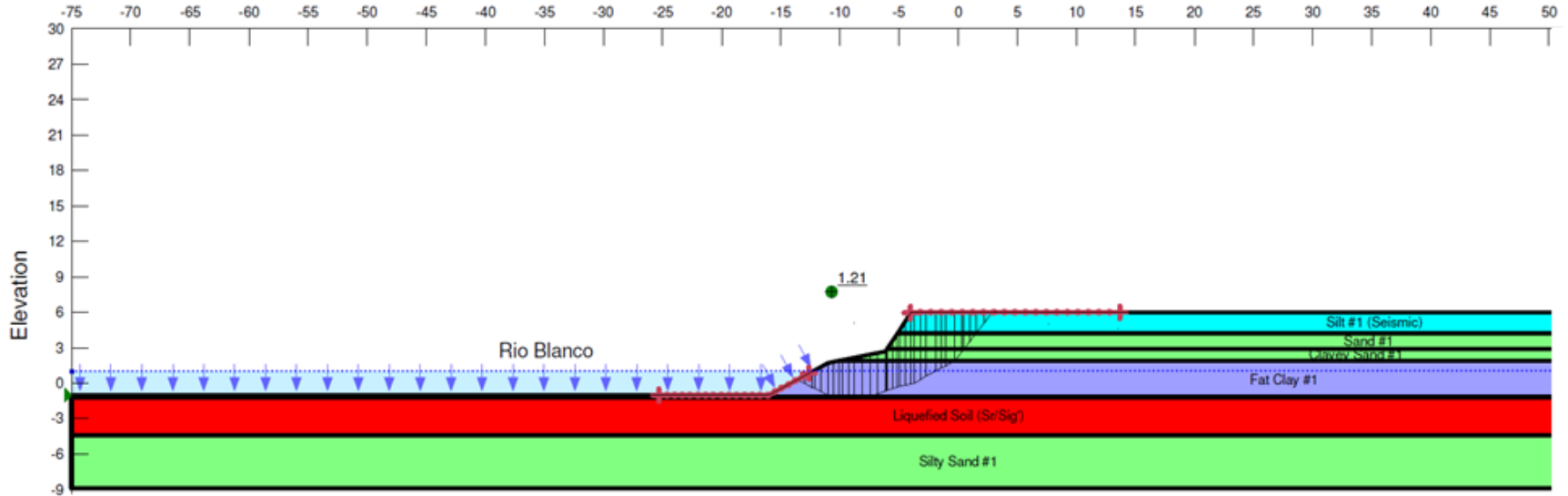


Figure 9-7: Post Earthquake Slope Stability Analysis at the Rio Blanco

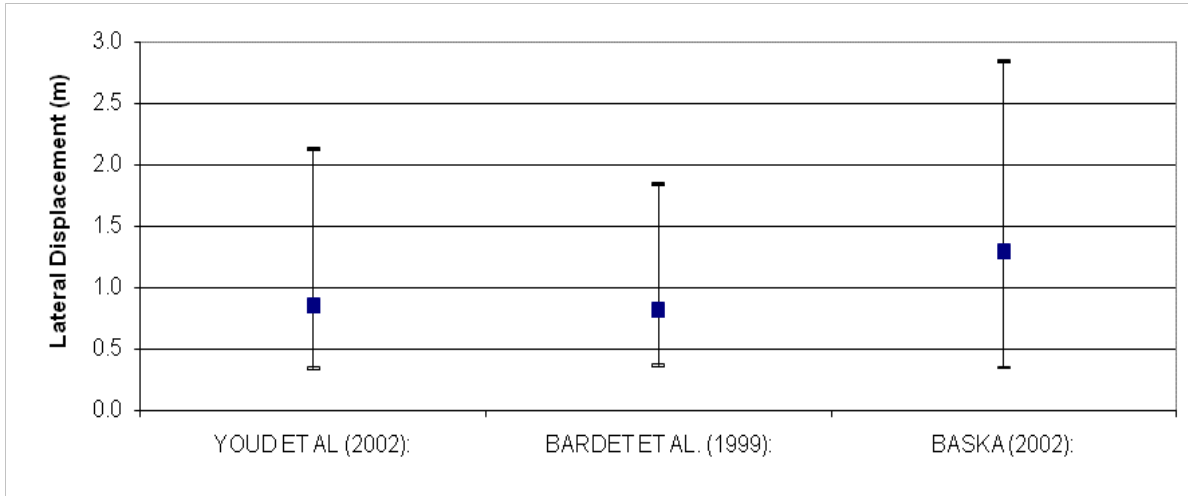


Figure 9-8: Deterministic Median and 95-Percentile Evaluations of Lateral Spread Displacement Using Select Empirical Models for the Rio Blanco Bridge

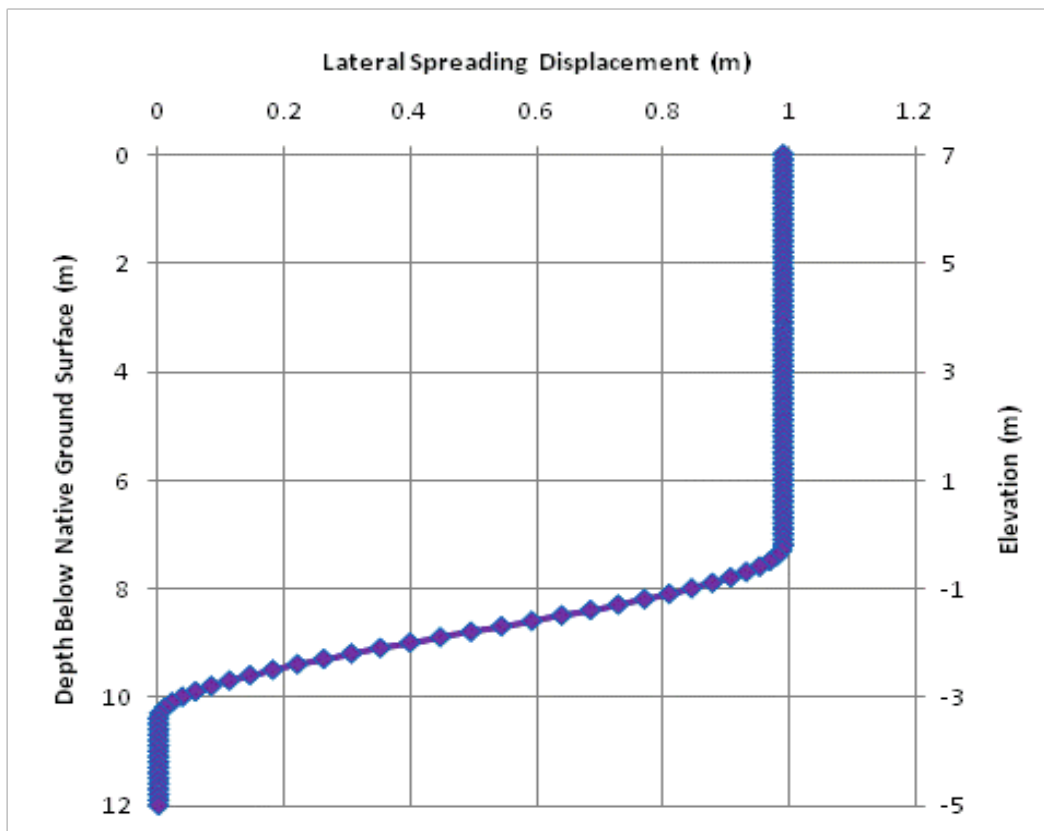


Figure 9-9: Computed Lateral Spread Displacement Profile at the Rio Blanco Bridge for the M7.6 1991 Limon Earthquake

Because reinforcing details for the piles were not shown on the bridge plans provided by the Costa Rican Ministry of Transportation, assumptions had to be made regarding the amount and size of rebar in the piles in order to compute their flexural stiffness (i.e. EI). A study was made into many of the available reinforced concrete design standards in practice during 1968 when the bridge was designed, and it was found that most piles in use at the time only incorporated four vertical steel bars for reinforcement. It was assumed that four #4 bars were used in the piles. The resulting initial composite flexural stiffness of a single 14in by 14in pile was computed to be 35,000 kN-m².

The equivalent single pile consists of two sections: the pile cap and the piles. The 1.90m-by-12.30m pile cap comprises the top 2.6 meters of the equivalent single pile. The composite flexural stiffness of the pile cap was computed to be 175,830 MN-m². The second section of the equivalent single pile represents the pile group and was created by multiplying the initial composite flexural stiffness of a single pile by the total number of piles in the pile group (i.e. 13) to develop the initial composite flexural stiffness of the equivalent single pile. This initial composite flexural stiffness was computed to be 455,000 kN-m². A nonlinear moment-stiffness curve was developed to account for yielding of the reinforced concrete piles in accordance with the guidelines presented by CalTrans (2011) as summarized in Section 4.4.3 of this dissertation. The moment-curvature and moment-stiffness curves for the equivalent single pile are presented in Figure 9-10.

A p-multiplier for the equivalent pile group to account for the total number of piles in the group and the pile spacing was computed to be 9.27. Rotational stiffness of the equivalent single pile was neglected due to the relative flexibility of the piles and the close pile-to-pile spacing in the direction of the lateral spread (i.e. longitudinal direction). Therefore, the equivalent single

pile was modeled with a free-head condition with a lateral load at the head to represent the strut-like behavior of the bridge deck.

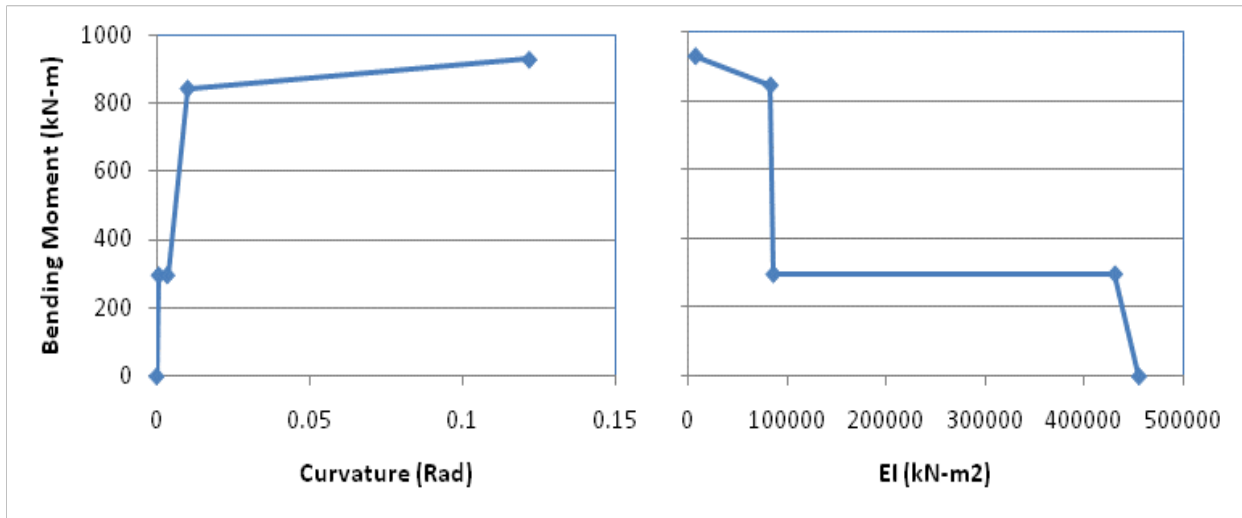


Figure 9-10: Moment-Curvature and Moment-Stiffness Curves for the Rio Blanco Bridge

Applying the lateral spread deformations shown in Figure 9-9 to the equivalent single pile, the LPILE deterministic pile response from the 1991 Limon earthquake is shown in Figure 9-11.

9.5.6 Summary of Deterministic Results

The deterministic pile response results shown in Figure 9-11 suggest that a pile cap rotation of 25 degrees would occur with a lateral spread displacement of 1 meter at the abutment if the bridge deck remained in place. Measurement of the actual pile cap rotation at the east abutment of the Rio Blanco Bridge showed an rotation of 10 to 11.5 degrees. This rotation would

be achieved in the pile response analysis with a lateral spread displacement of 0.45 meter. Such a displacement is within a factor of 2 of the computed median lateral spread displacements from the three empirical models used in this study. The displacement is also located within the 95th-percentile bounds for all three models.

9.6 Performance-Based Pile Response Analysis at the Rio Blanco Bridge

9.6.1 Probabilistic Ground Motions

A PSHA was performed at the Rio Blanco Bridge site using EZ-FRISK software and the built-in seismic source model for Central and South America developed by Risk Engineering (see Risk Engineering documentation included in Appendix B). This seismic source model included both area and fault sources. The four selected NGA attenuation models (Abrahamson and Silva, 2008; Chiou and Youngs, 2008; Campbell and Bozorgnia, 2008; and Boore and Atkinson, 2008) were assigned to crustal seismic sources, and select attenuation models developed for subduction zones (Youngs et al., 1997; Atkinson and Boore, 2003; and Zhao et al., 2006) were assigned to the subduction seismic sources. Finally, near-source and directivity effects were accounted for in the PSHA by incorporating the fault-normal response spectrum modifications presented by Somerville et al. (1997) and Abrahamson (2000) for all fault sources. A table of the fault sources located within about 100 km of the site is presented in Table 9-2.

The seismic hazard curve for the PGA developed from the PSHA is presented in Figure 9-12. The ground motions corresponding 10-percent and 2-percent probabilities of exceedance in 50 years are 0.545g and 0.880g, respectively.

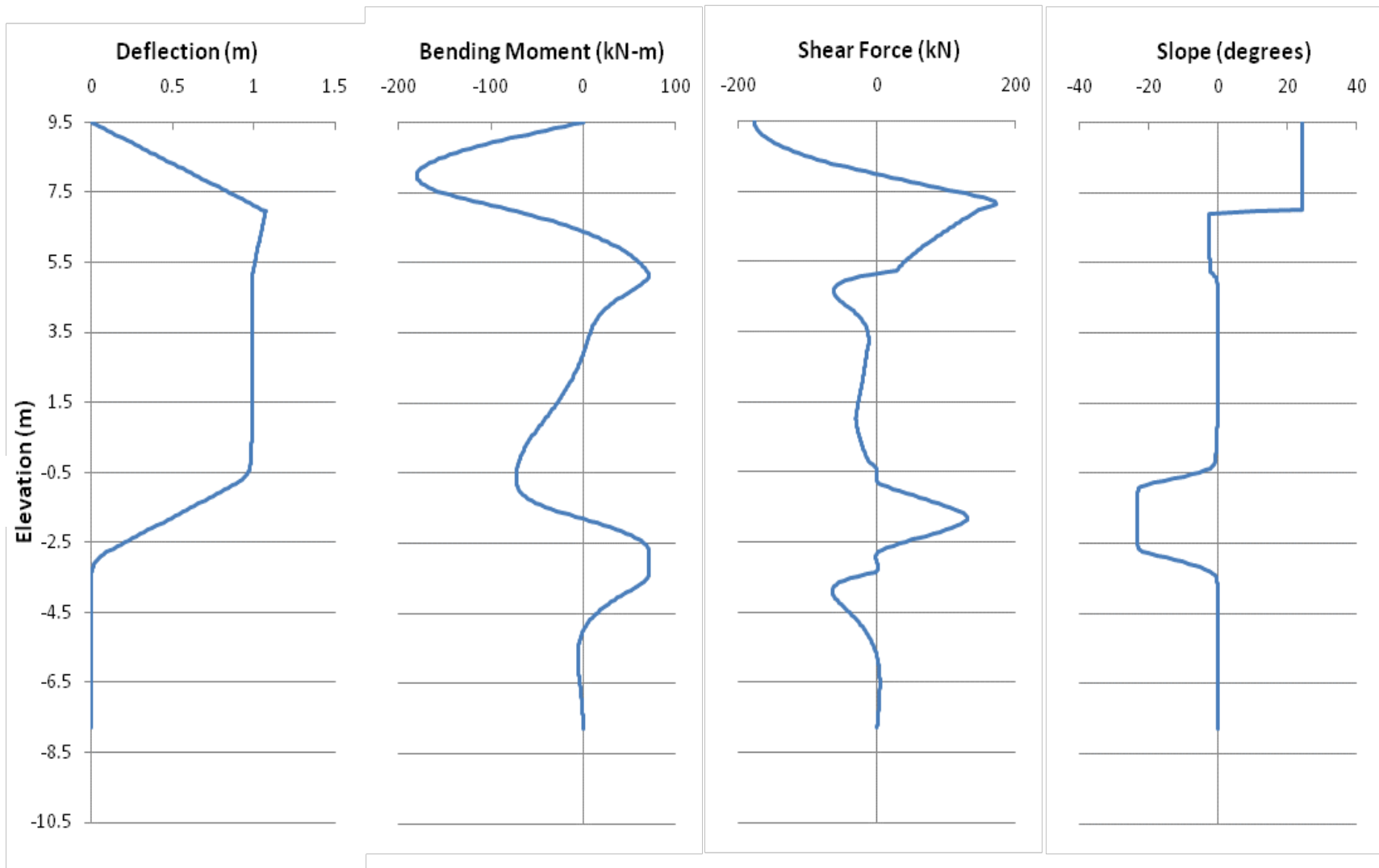


Figure 9-11: Deterministic Computed Pile Response for the Rio Blanco Bridge East Abutment From the 1991 Limon Earthquake

The seismic hazard contributions from the individual sources are shown in Figure 9-13. From Figure 9-13, it appears that the Costa Rica arc and shear zone (area source), the Costa Rica fault (subduction interface source), and the Panama North (Caribbean) fault (subduction interface source) govern the probabilistic seismic hazard at most return periods for the PGA. The probabilistic response spectra developed from the PSHA for seven different return periods are shown in Figure 9-14. Finally, simplified deaggregation plots of the PGA are presented in Figure 9-15.

Table 9-2: EZ-FRISK Faults Within About 100 km of the Rio Blanco Bridge

Fault Name	Type	Source to		Characteristic Magnitude	Slip Rate (mm/yr)	Recurrence Rate
		Fault Length (km)	Site Distance (km)			
Limon fault	Reverse	162	0.2	7.8	1.0	---
Panama - North (Caribbean)	Subduction Interface	817	40	8.0	4.0	---
Guapiles fault	Reverse	8	77	6.1	4.0	---
Longitudinal fault	Reverse	42	103	7.4	0.1	---
Longitudinal fault - Costa Rica 2	Reverse	52	103	7.0	0.5	---
Costa Rica	Subduction Intraslab	288	106	7.7	---	0.4958

9.6.2 Probabilistic Liquefaction Triggering

Using the probabilistic estimates of a_{max} shown in Figure 9-12 in conjunction with the magnitude/distance deaggregations shown in Figure 9-15, probabilistic estimates of liquefaction triggering were computed with the Kramer and Mayfield (2007) procedure using Equations (6-1)

and (6-2). The performance-based liquefaction triggering computations were performed using the computer program PPRS. The resulting factors of safety against liquefaction triggering for various return periods are shown in Figure 9-16. These factors of safety were computed using the SPT blowcount information from Insuma boring P-1 at the Rio Blanco Bridge. A factor of safety less than or equal to 1.2 was assumed to be liquefiable for this study. Note that for fine-grained soil layers not considered susceptible to liquefaction due to plasticity, a generic factor of safety against liquefaction equal to 2.0 was assigned regardless of return period. A maximum factor of safety equal to 4.0 was assigned to layers with very high resistance to liquefaction triggering. Figure 9-16 shows that for return periods greater than about 475 years, liquefaction triggers from depths of about 7.20 meters to 10.35 meters (EL. -0.2m to -3.35m) below the ground surface.

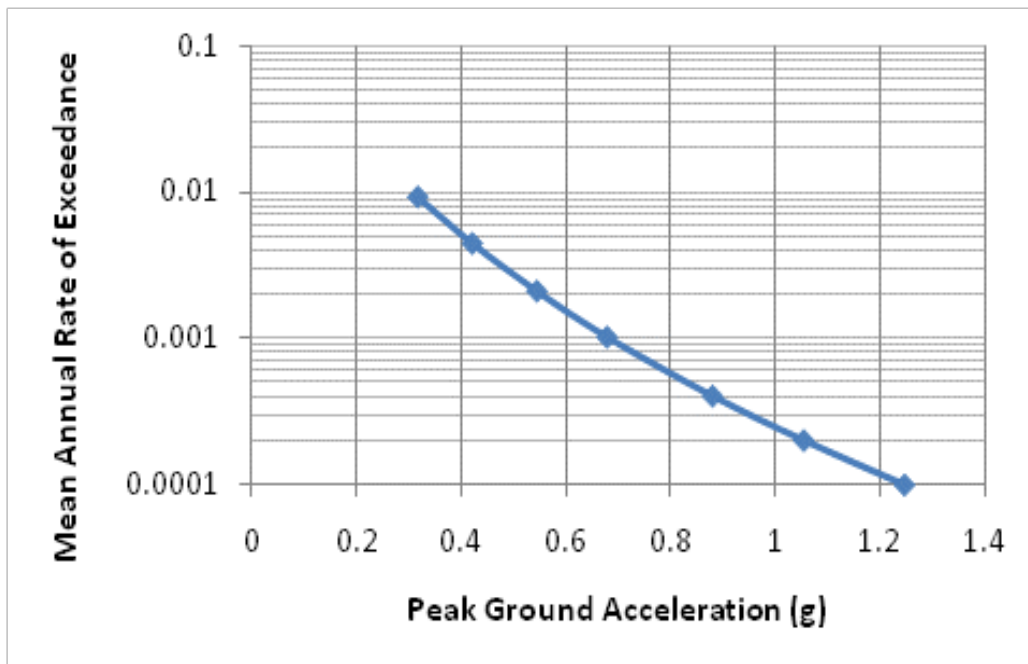


Figure 9-12: Seismic Hazard Curve for the PGA at the Rio Blanco Bridge

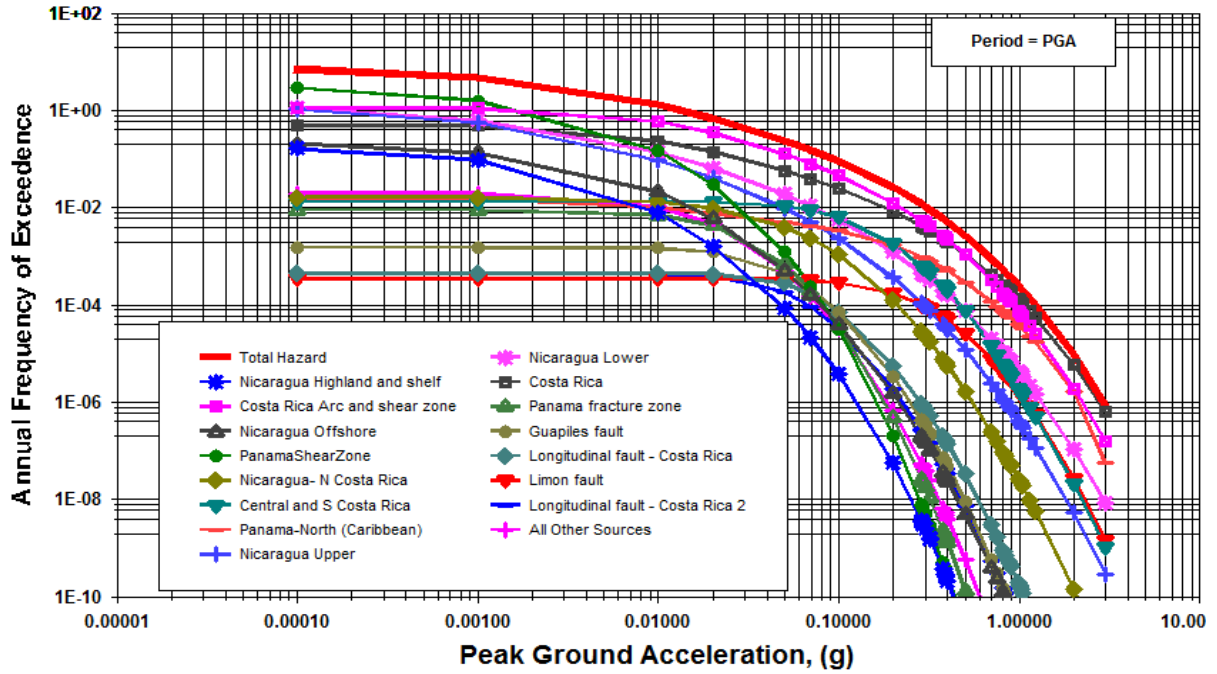


Figure 9-13: Source Contributions to Probabilistic Seismic Hazard at the Rio Blanco Bridge

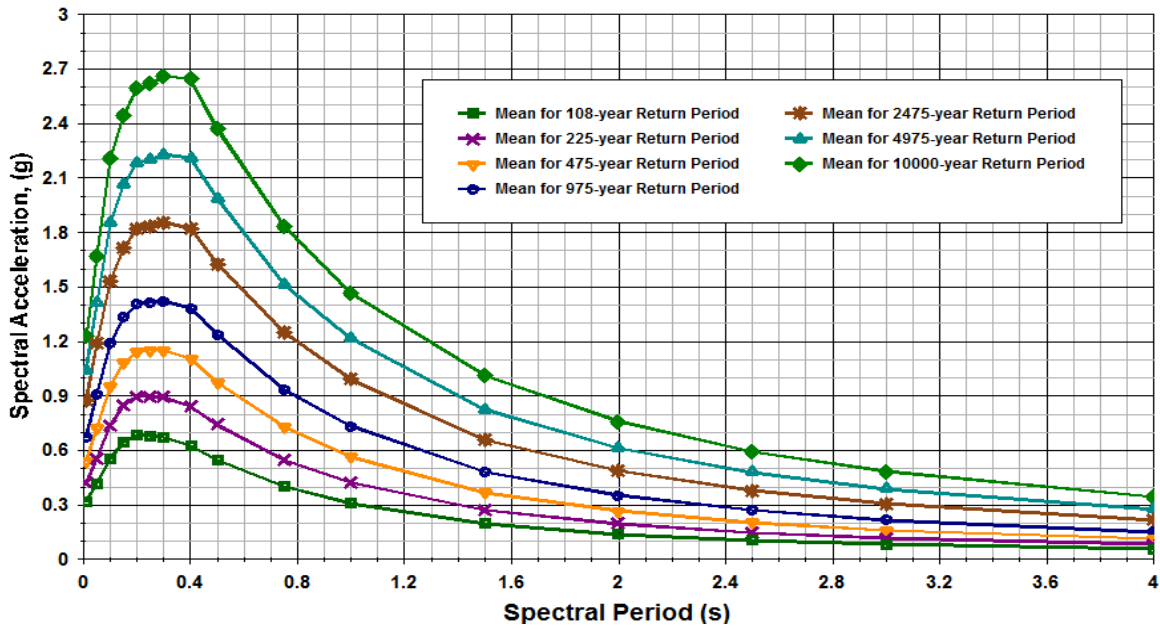


Figure 9-14: Probabilistic Response Spectra (5-Percent Damping) for the Rio Blanco Bridge

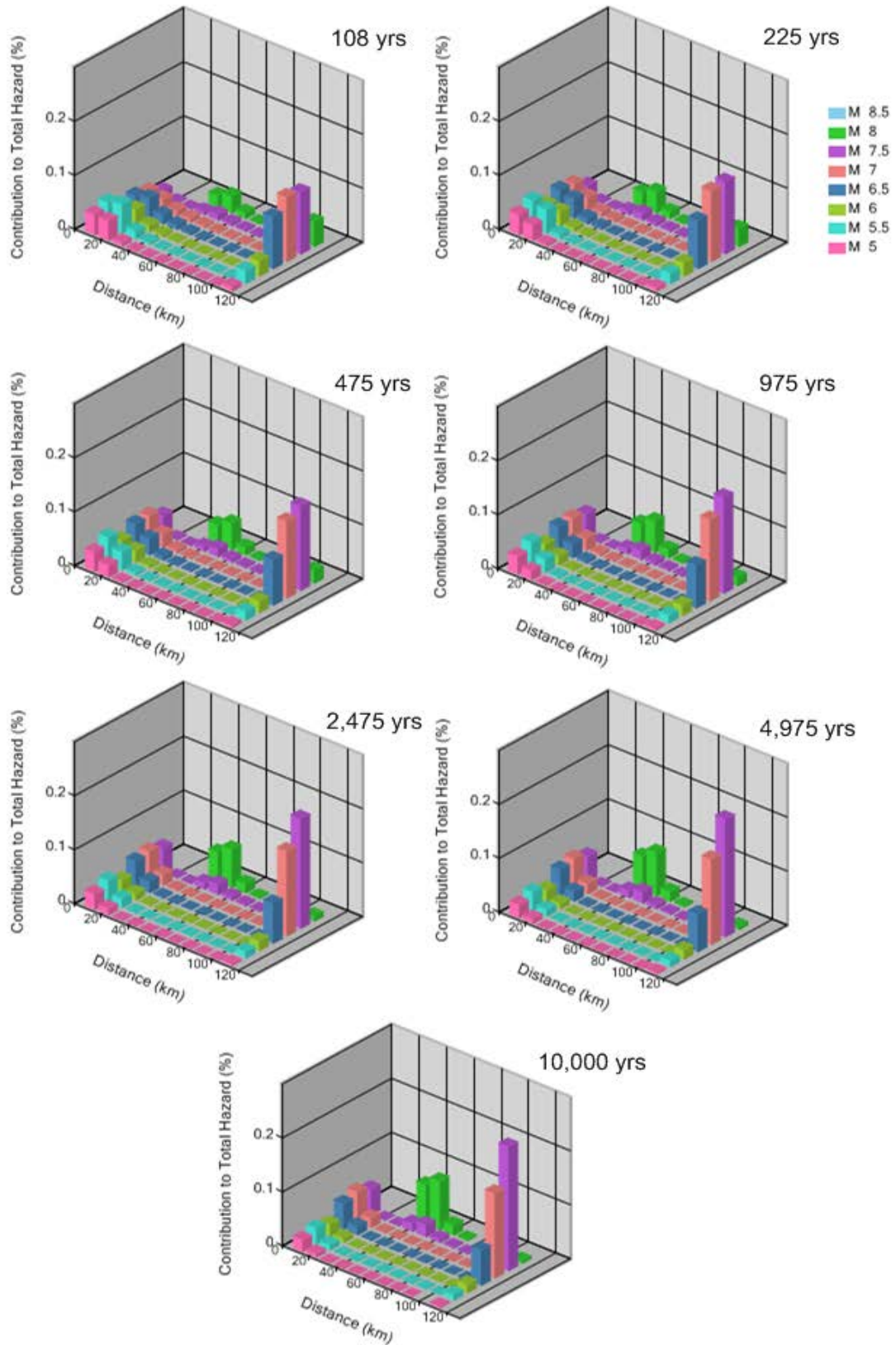


Figure 9-15: Deaggregation Plots for the PGA at the Rio Blanco Bridge

9.6.3 Development of the Loading Parameter, \mathcal{L}

The loading parameter \mathcal{L} , which serves as the intensity measure in the performance-based pile response procedure, was computed using Equations (6-4) through (6-6) from Section 6.8 of this dissertation. The equations were loaded as user-defined attenuation relationships into EZ-FRISK, and the Risk Engineering (2010) seismic source model for Central and South America was used to compute probabilistic estimates for \mathcal{L} . A plot of the hazard curves for \mathcal{L} is presented in Figure 9-17. Note that loading parameter for each model is unique and independent from the other models.

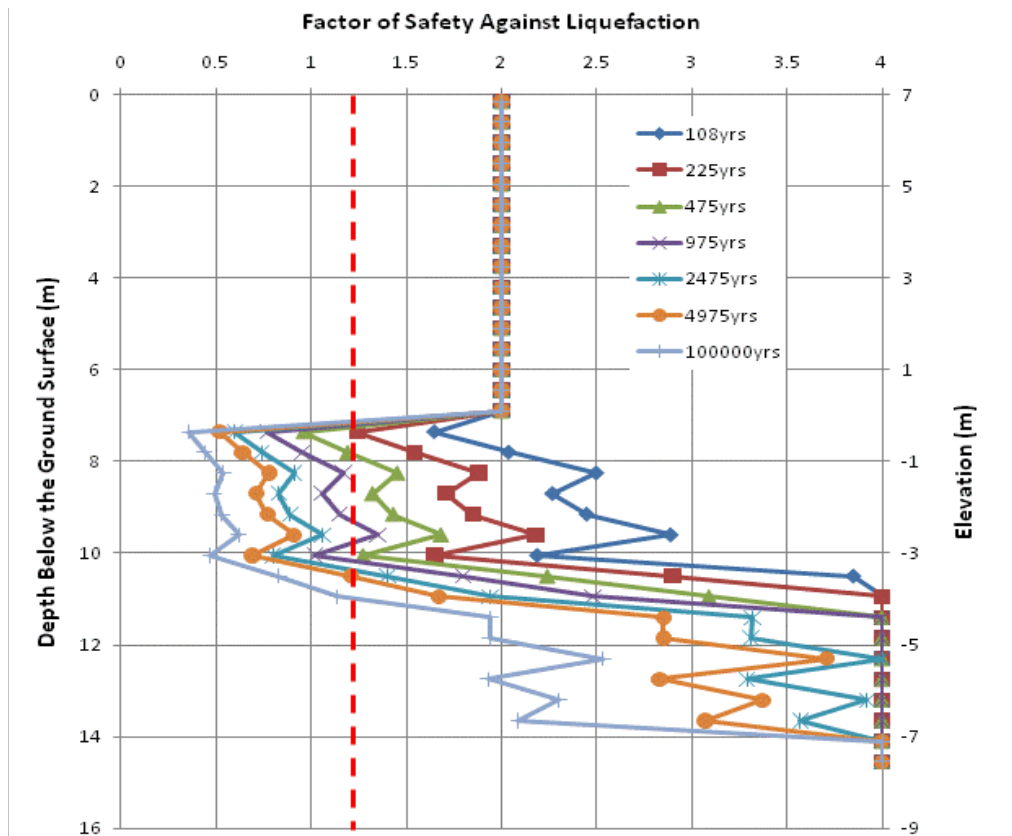


Figure 9-16: Performance-Based Liquefaction Triggering Results for the Rio Blanco Bridge

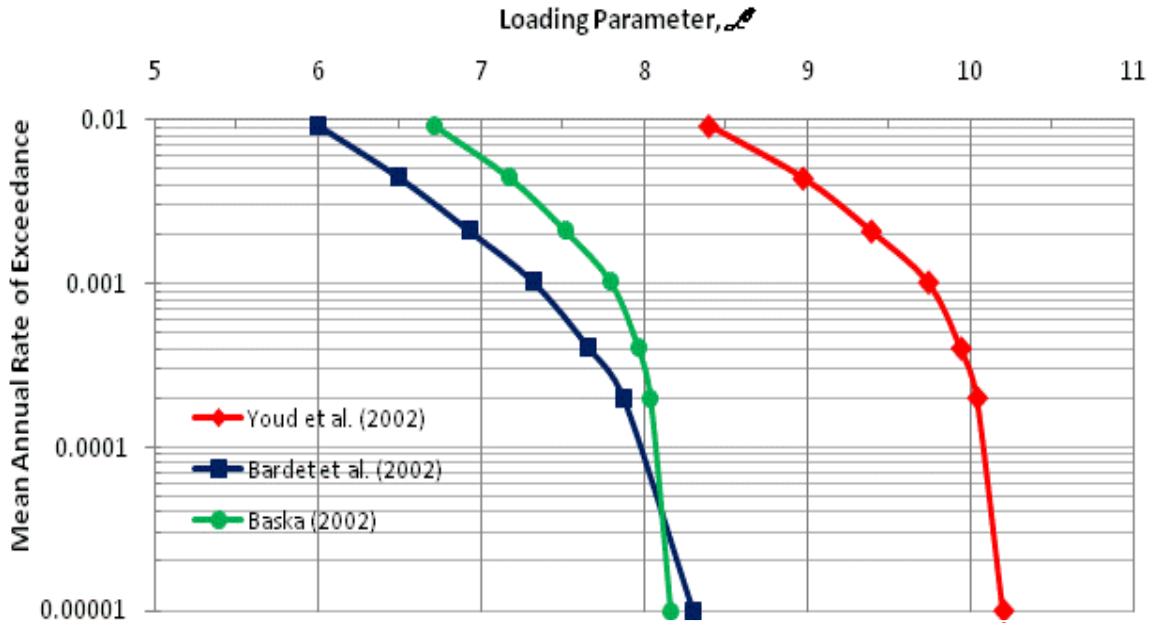


Figure 9-17: Hazard Curves for the Loading Parameter \mathcal{L} for the Rio Blanco Bridge

9.6.4 Development of the Fragility Functions for Lateral Spread Displacement

Fragility curves relating the probability of exceeding a given lateral spread displacement to the loading parameter \mathcal{L} were developed according to the procedure described in Section 6.9. The site parameter \mathcal{S} for the three selected empirical lateral spread models was computed using the soils and SPT blowcounts from Insuma boring P-1 with Equations (6-7), (6-9), and (6-11). A free-face ratio of 20-percent was used with a free-face height of 5.5 meters. Depth limitations as described in Section 3.7 were incorporated. The computed values of \mathcal{S} are shown in Table 9-3.

With \mathcal{S} computed for each empirical lateral spread model, families of lateral spread fragility curves were developed using Equation (6-19). These curves are plotted for lateral spread displacements of 0.1 meter and 1 meter in Figure 9-18.

Table 9-3: Site Parameter \mathcal{S} for the Rio Blanco Bridge

Empirical Lateral Spread Model:	Site Parameter \mathcal{S}
Youd et al. (2002)	-8.948
Bardet et al. (2002)	-6.319
Baska (2002)	-5.952

Values of \mathcal{S} and lateral spread fragility curves were calculated automatically in the computation of probabilistic lateral spread displacements using PPRS software.

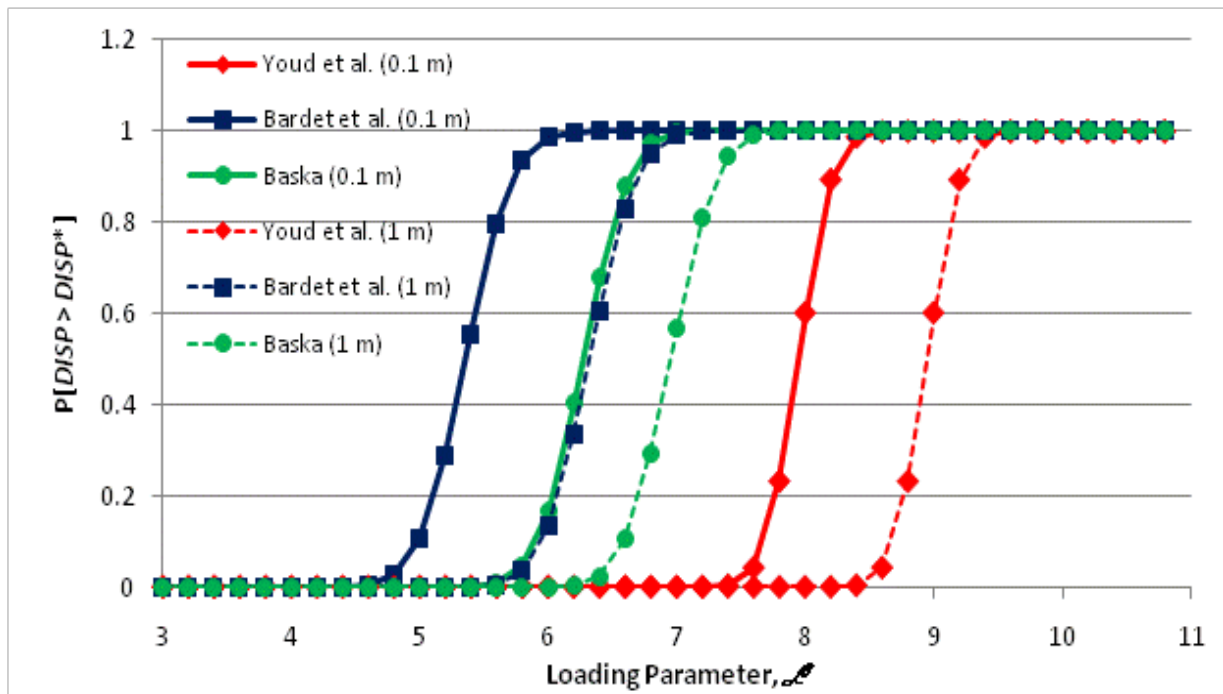


Figure 9-18: Lateral Spread Fragility Curves for $DISP^* = 0.1$ Meter and $DISP^* = 1$ Meter at the Rio Blanco Bridge

9.6.5 Development of Probabilistic Lateral Spread Displacements

Using PPRS software, the lateral spread fragility curves were convolved with the hazard curves for the lateral spread loading parameters \mathcal{L} shown in Figure 9-17 using the steps presented in Section 6.10. The resulting hazard curves for lateral spread displacement at the ground surface are shown in Figure 9-19.

Figure 9-19 shows good agreement in computed probabilistic lateral spread displacements between the Baska (2002) and the Bardet et al. (2002) empirical models at annual frequencies less than 0.0004 (i.e. return period of 2500 years); however, the hazard curves tend to diverge at lower annual frequencies (i.e. higher return periods). The Bardet et al. (2002) model appears to compute the largest displacements and most return periods, and the Youd et al. (2002) appears to compute the smallest displacements. The average displacement hazard curve was computed by weighting the mean annual rates of exceedance using equal weights for all three empirical models.

The average computed probabilistic lateral spread displacements were propagated through the soil profile using the recommendations provided in Sections 3.6 and 3.7 in conjunction with the probabilistic liquefaction triggering profiles shown in Figure 9-16. The resulting probabilistic lateral spread displacement profiles are presented in Figure 9-20.

9.6.6 Development of Fragility Functions for the Kinematic Pile Response

Due to the limitations of the simplified performance-based pile response procedure presented in this dissertation, two sets of LPILE analyses were performed at the Rio Blanco Bridge using the procedure described in Section 8.6.6 for the Rio Cuba Bridge to develop fragility relationships for the kinematic pile response for the purpose of demonstration. These

two sets of analyses were intended to provide reasonable bounds for the problem by representing the two possible extremes for the kinematic pile response. The first LPILE analysis neglected the presence of a reinforcing bridge deck, thus assuming that the kinematic loading is being resisted solely by the lateral stiffness of the piles themselves. The assumption of no bridge deck is routinely used in engineering practice today because it is considered to be conservative. However, such an assumption inherently defeats the idea of performance-based design because true performance is not necessarily being considered. The results of the first LPILE analysis showed that the computed variance at each node in the pile response was essentially equal to zero, suggesting that the reinforced concrete piles had insufficient stiffness to provide any significant resistance to the lateral spread displacement. Therefore, the performance-based analysis could be simplified by simply neglecting the variance in the pile response.

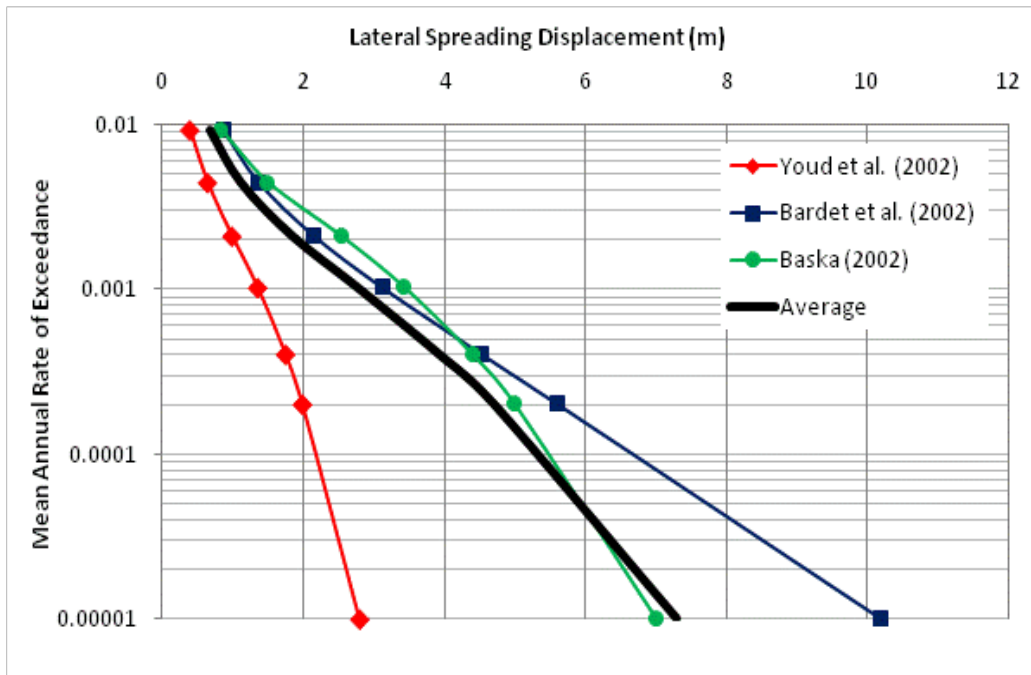


Figure 9-19: Lateral Spread Hazard Curves for the Rio Blanco Bridge

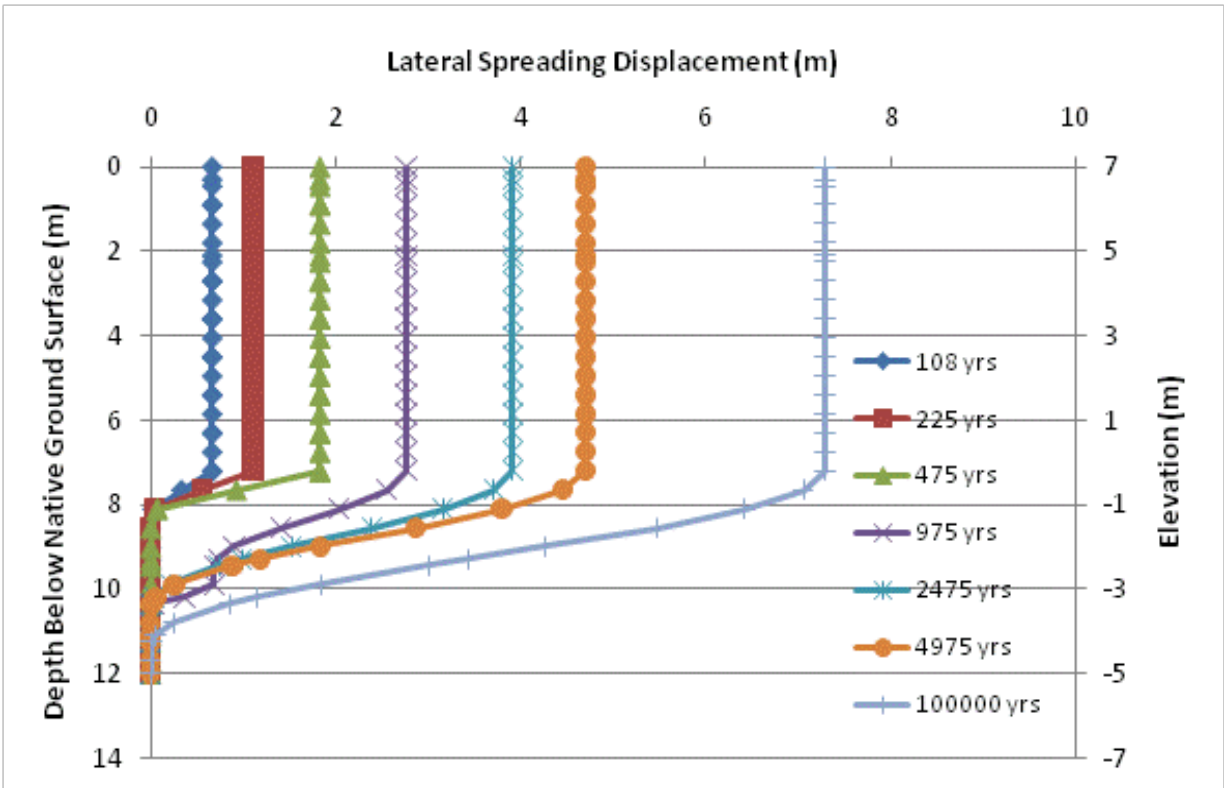


Figure 9-20: Probabilistic Lateral Spread Displacement Profiles for the Rio Blanco Bridge

The second LPILE analysis modeled a constant reinforcing strut load at each return period of lateral spread displacement. A constant coefficient of variation equal to 30% was assumed and applied across the entire pile to represent the variability in the kinematic pile response. This approach was used rather than performing a Monte Carlo simulation with a constant strut load in order to maintain more realistic values of the variance in the pile response. However, it is recognized that such a simplified approach should not be applied in actual engineering design; rather, the variance in the kinematic pile response should be computed using more sophisticated methods such as a Monte Carlo simulation coupled with a dynamic numerical model.

9.6.7 Development of Probabilistic Kinematic Pile Response

The probabilistic kinematic pile response was computed for each node in the two LPILE analyses for the Rio Blanco Bridge by convolving the results from the fragility relationships developed in Section 9.6.6 with the probabilistic lateral spread displacement profiles developed in Section 9.6.5. PPRS software was used to apply Equation (6-23) and the steps presented in Section 6.12 for computing probabilistic estimates of displacement, bending moment, shear force, and curvature for all nodes in the pile response model. The resulting probabilistic pile response profiles for the first analysis (i.e. no bridge deck) and the second analysis (i.e. bridge deck) are shown in Figure 9-21 and Figure 9-22, respectively.

9.6.8 Discussion of Results

The performance-based pile response results for the Rio Blanco Bridge shown in Figure 9-21 and Figure 9-22 are very similar to the pile response results for the Rio Cuba Bridge shown in Figure 8-24 and Figure 8-25, respectfully. The drastically different results from the two performance-based analyses demonstrate the significance that the bridge deck can have in computing the kinematic pile response of a bridge foundation. As performance-based pile response analysis methods become more sophisticated, significant attention should be paid to the estimated dynamic behavior of the bridge deck because it can dramatically affect the performance of the piles in resisting kinematic loading.

The pile response analysis results shown in Figure 9-21, which represent the assumption of no bridge deck, demonstrate that two rows of reinforced concrete piles are generally insufficient to resist any significant amount of kinematic loading. Significant deformations and pile yielding were computed at all return periods. These results suggest that the piles were unable

to resist even smallest of ground deformations. In addition, the pile deformation profiles are remarkably similar at each return period to the computed free-field ground deformations shown in Figure 9-21, suggesting that the piles essentially experience the same deformations as the surrounding soils. Ledezma and Bray (2008, 2010) note that such behavior is likely typical of most bridge foundations if the reinforcing effect of the bridge deck is neglected.

The pile response results shown in Figure 9-22 demonstrate the significance that the estimated variance in the soil-pile interaction can have in a performance-based pile response analysis. Using an assumed uniform coefficient of variation of 30% for the pile response produced very large computed probabilistic estimates of the kinematic pile response at return periods greater than about 975 years. Therefore, reasonable care should be provided whenever possible to obtain realistic estimates of the variance in the soil-pile interaction when computing performance-based kinematic pile response.

Finally, when comparing the measured pile cap rotation of 8.5 degrees following the Limon earthquake with the computed performance-based pile response results shown in Figure 9-22, a rotation of 10-11.5 degrees corresponds with an approximate return period of 111-113 years (i.e. 49% probability of exceedance in 75 years). Therefore, according to the performance-based analysis, the east abutment of the Rio Blanco Bridge has nearly a two-to-one chance of experiencing a pile cap rotation of at least 10 degrees in any given 75 year timeframe if the bridge deck stays in place and the coefficient of variation in the soil-pile interaction is approximately equal to 30% across all depths of the pile group.

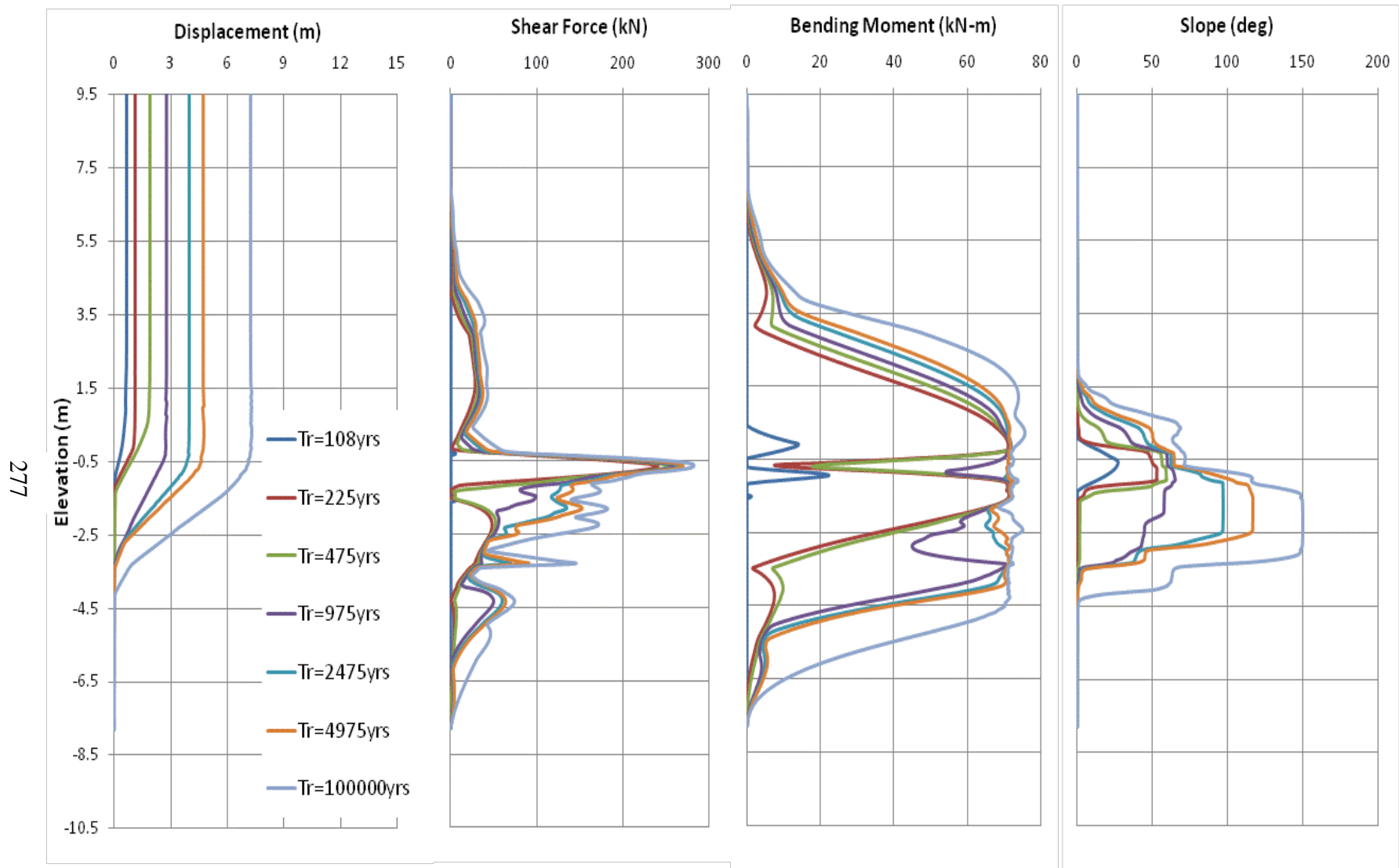


Figure 9-21: Probabilistic Pile Response Curves (Absolute Values) Assuming No Bridge Deck for the Rio Blanco Bridge

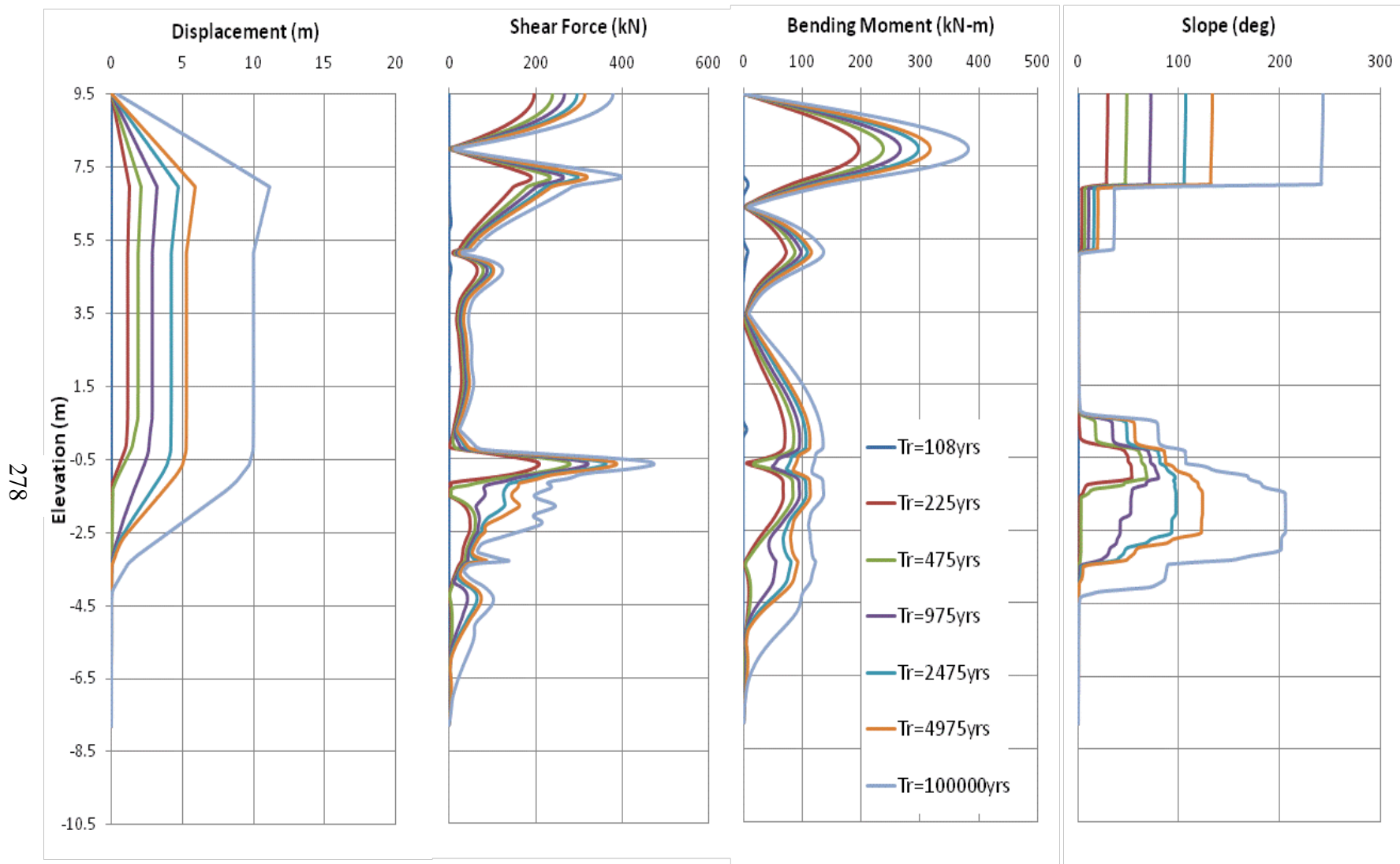


Figure 9-22: Probabilistic Pile Response Curves (Absolute Values) Assuming a Bridge Deck at the Rio Blanco Bridge

10 RIO BANANITO HIGHWAY BRIDGE

10.1 Introduction

The highway bridge over the Rio Bananito was a two-span reinforced concrete bridge supporting two lanes of traffic. The southern span was 28.4 meters in length and the northern span is 25.4 meters in length. The total length of the bridge was 55.3 meters. The bridge was located along National Route 36 just west of the Bananito Beach. The latitude/longitude coordinates of the bridge are 9.8849° North 82.9669° West. Though the bridge collapsed during the 1991 Limon earthquake, it was rebuilt as a three-span bridge with two bents. A photo of the current bridge is presented in Figure 10-1.

According to bridge plans provided by the Costa Rican Ministry of Transportation, the bridge was founded on a series of 14-inch square reinforced concrete piles. The north abutment was supported by two rows of piles (three piles in the front row, three piles in the second row, and six piles in total) that are 15.2 meters in length and spaced at five diameters in the transverse direction and two diameters in the longitudinal direction. The south abutment was supported by two rows of piles (four piles in the front row, five piles in the second row, and nine piles in total) that are 15.2 meters in length and spaced at 2.5-3 diameters in the transverse direction and two diameters in the longitudinal direction. The approximate dimensions of the pile cap and abutment wall at each abutment was 5.66 meters (transverse) x 1.80 meters (longitudinal) x 2.60 meters (vertical).



Figure 10-1: The Current Rio Bananito Highway Bridge

The bent was founded on a 1.64-meter x 5.4-meter pile cap that was supported by ten 14-inch x 14-inch piles (two rows of five piles) that are 11 meters in length and spaced at 2.7 pile diameters in the transverse direction and 2.9 pile diameters in the longitudinal direction. The abutments and the bent were skewed at an angle of 30 degrees to the transverse orientation of the bridge. Finally, the front row of piles at each abutment and bent location were battered at approximately 5V:1H. However, any batter in the piles was neglected in the pile response analysis because the Juirnarongrit and Ashford (2006) pile response procedure does not specify how to account for pile batter in a few of the piles in the group.

10.2 Observed Damage Following the 1991 Earthquake

Significant liquefaction and ground deformation was documented at the Rio Bananito Highway Bridge by Priestley et al. (1991), Youd et al. (1992) and McGuire (1994). During the earthquake, both bridge spans fell from the central pier, with the spans being thrown in the direction of the skew. The central pier did not noticeably settle, tilt or rotate. Both spans were sheared from their seatings on the pier and fell into the river, but there was no indication that they struck or displaced the pier in the process. The bases of both abutments rotated towards the river at the base indicating that the bridge decks initially acted as struts before being thrown into the river. The south abutment was rotated 14 degrees from vertical. Bridge girders on the south still remained on their bearing plates, and the bolts were bent about 1.57 inches but were not sheared off. The piles supporting the abutment were not visible (Figure 10-2). The north abutment was rotated 10 degrees from vertical, and the underside was exposed revealing that five of the six abutment piles were fractured immediately below the pile cap. The orientation of the piles below the break line was documented as erratic (McGuire, 1994).

McGuire (1994) documented the account of a man who lived just west of the south abutment who witnessed the affects of the earthquake at the bridge. During an interview, the man said that he and his family felt minor shaking for about 20 seconds. Major shaking subsequently started, and the family crawled out of the house. The family observed the north span of the bridge fall into the river approximately 30 seconds after the strong shaking began. Following another estimated 30 seconds, the south span of the bridge fell and the southern embankment immediately slid into the river.



Figure 10-2: Rotated Pile Cap at the South Abutment of the Rio Bananito Highway Bridge

Youd et al. (1992) observed that horizontal ground deformation as large as 5 meters toward the river were common across the site. In addition, significant vertical deformations were observed at the southern abutment of the bridge. A length of approximately 43 meters of asphalt surface which paved the south approach to the bridge was shifted and broken into blocks due to lateral earth movements beneath the roadway and settlement in the road base fill. Settlements as large as 2.2 meters were measured in the embankment fill by Youd et al. (1992). A 2-meter high scarp marked the southern margin of ground deformation 43 meters south of the southern bridge abutment (). Nearly no ground disturbance could be seen south of this boundary, while structural elements at the southern bridge abutment were measured to have displaced as much as nearly

4.29 meters (combined horizontal and lateral deformation). Youd et al. (1992) applied three methods to attempt to measure the ground deformations at the southern abutment. The first method involved the use of surveying equipment to measure and document the horizontal and vertical deformations of each asphalt block in the ground failure zone. The resulting measured deformations are shown in Figure 10-4. Using these reported deformations, a scaled simple sketch of both the pre- and post earthquake ground surface profiles was prepared and is presented in Figure 10-5.



Figure 10-3: Liquefaction Deformations at the South Approach Embankment for the Rio Bananito Highway Bridge

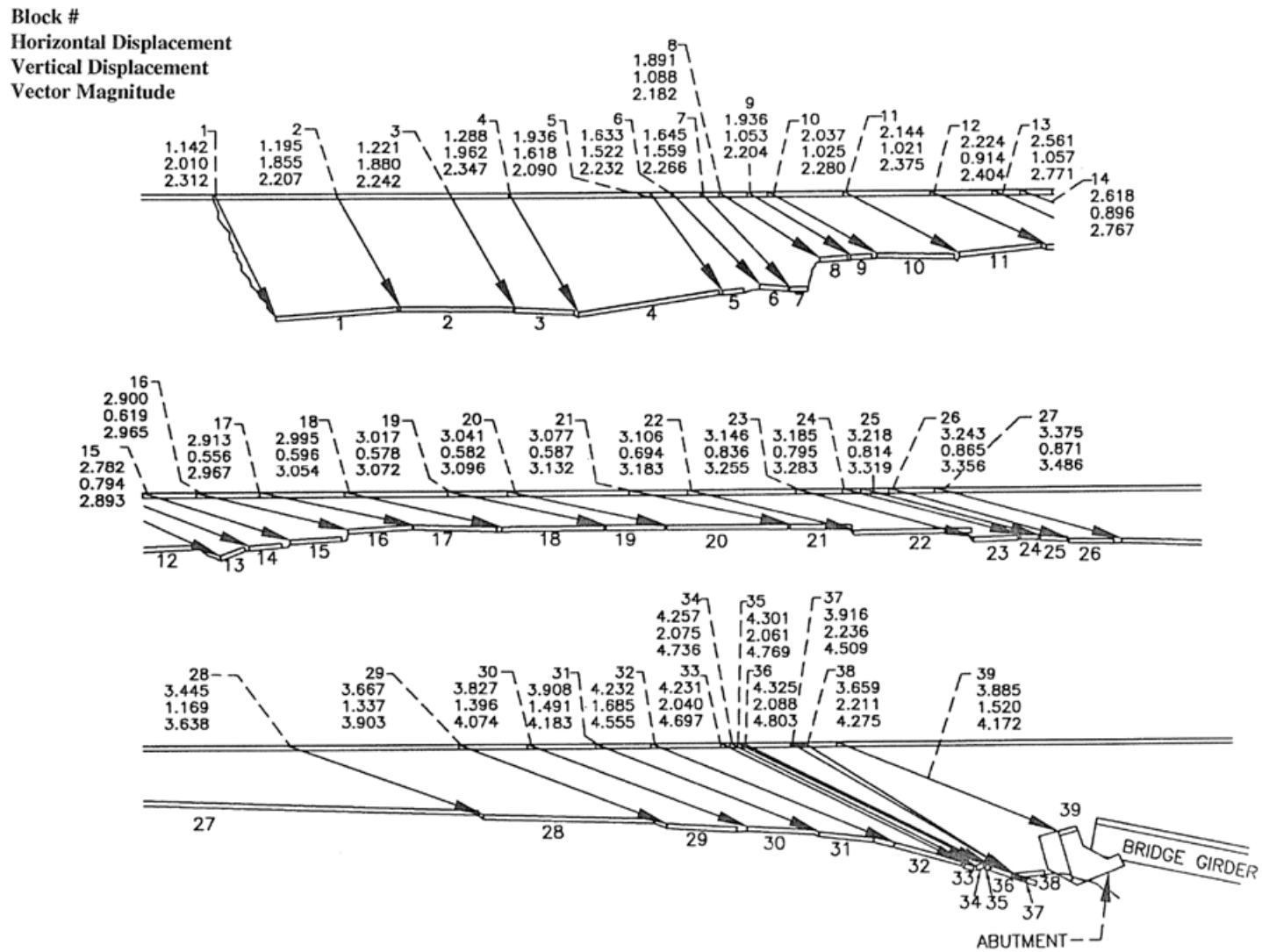


Figure 10-4: Ground Deformations at the South Abutment of the Rio Bananito Highway Bridge as Measured by Youd et al. (1992) (After McGuire, 1994)

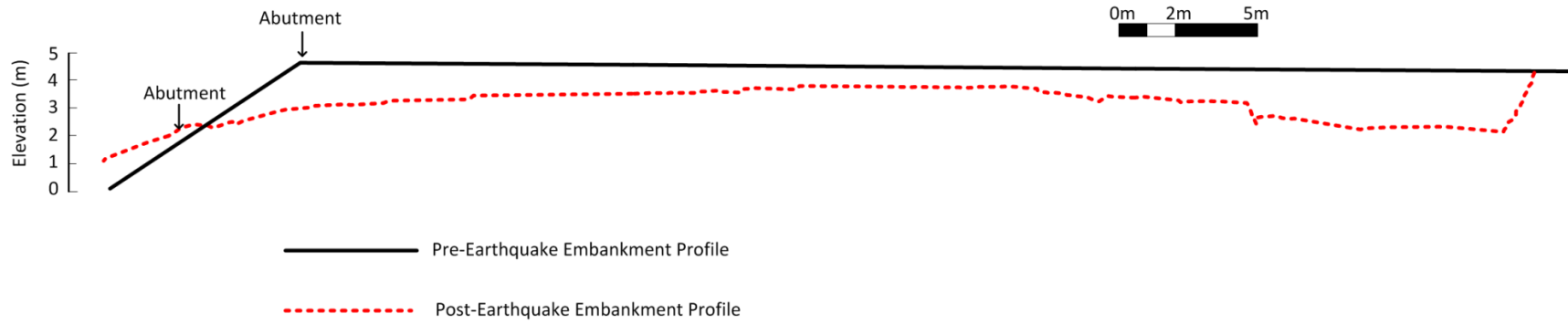


Figure 10-5: Pre- and Post-Earthquake Profile Geometries of the Southern Approach Embankment at the Rio Bananito Highway Bridge

The second method applied by Youd et al. (1992) to measure ground deformations at the south abutment involved the measurement and summation of fissure widths in the ground failure zone. Finally, the third method applied to measure ground deformations at the south abutment involved the surveying the location of the displaced south abutment of the bridge relative to the central pier of bridge, which was assumed to experience no lateral deformations. The resulting measured lateral deformations from these three methods are summarized in Table 10-1.

Table 10-1: Lateral Deformations at the South Abutment of the Rio Bananito Highway Bridge as Measured by Youd et al. (1992) (After McGuire, 1994)

METHOD #	ESTIMATE OF DISPLACEMENT (m)
1 – Summing gaps between pavement blocks	3.885
2 – Summing fissure widths	5.125
3 – Comparing distances with bridge plans	3.417

10.3 Soil Site Characterization at the Rio Bananito Highway Bridge

Insuma S.A. Geotechnical Consultants performed two borings in the vicinity of the southern abutment. Boring P-1 was performed immediately adjacent to the southern abutment and was extended to a depth of 20.25 meters below the ground surface. Boring P-2 was performed about 20 meters to the south of Boring P-1 and was extended to a depth of 20.25 meters. The soils encountered in the borings were reported to consist primarily of varying amounts of surficial embankment fill and alluvial silt and sand deposits. The silts encountered

appeared to have low to no plasticity and would be expected to demonstrate sand-like behavior when loaded cyclically. The sands encountered appeared to be fine-grained and varied in fines content from about 9-percent to 50-percent. Groundwater was encountered in the borings at a depth of 2.0 meters in Boring P-1 and 2.6 meters in Boring P-2, which correspond to estimated elevations of 0.0 meter and 1.64 meters, respectively. Simple diagrams of the soils encountered in the borings performed are shown in Figure 10-6 below. Further details regarding the borings at the Rio Bananito Highway Bridge and the corresponding laboratory test results can be found in the Insuma Geotechnical Report included as Appendix A of this report.

In addition to the borings performed in 2010 by Insuma S.A. Geotechnical Consultants, the Costa Rican Ministry of Transportation provided us with boring logs performed when the bridge was initially being designed. According to the bridge plans for the Rio Bananito Highway Bridge, Boring T-2 was performed at the southern abutment. No detailed surveying information regarding this borings was available, so the ground surface elevation at Boring T-2 was estimated to be 0.6 meter due to its close apparent proximity to the river. Groundwater was encountered in Boring T-2 at an depth of 0.6 meter, which corresponds to an elevation of 0.0 meter. A tabular summary of our interpretation of Boring T-2 is provided in Table 10-2

For the analysis at the southern abutment at the Rio Bananito Highway Bridge, an averaged profile of the SPT blowcounts and fines content was developed. Because Boring P-2 appears to have more embankment fill and denser surficial sands, only Borings P-1 and T-2 were averaged to an elevation of -5.0 meters because it is assumed that these borings better represent the shallow soils at the abutment itself. A plot of the averaged SPT values used for the analysis of the Rio Bananito Highway Bridge is shown in Figure 10-7

a) Boring P-1			b) Boring P-2		
Depth (m)	SPT N Value		SPT N Value		
0.00 - 0.45	4	Brown SAND mixed with organic matter (roots).	36	Brown poorly graded GRAVEL, mixed with some sand and silt, dense.	
0.45 - 0.90	2		39		
0.90 - 1.35	3	Poorly graded gray silty SAND, not plastic fines, loose relative density.	43		
1.35 - 1.80	10		35		
1.80 - 2.25	5		21	Very fine gray SAND, poorly graded, mixed with a fraction of silt size particles, fines are not plastic, loose relative density.	
2.25 - 2.70	2		28		
2.70 - 3.15	1	Fine gray SILT, not plastic, mixed with a fraction of sand size particles, very loose. Presence of wood detected.	17		
3.15 - 3.60	1		8		
3.60 - 4.05	2		8		
4.05 - 4.50	3		7		
4.50 - 4.95	1		6	Fine gray SILT, not plastic, mixed with fraction of sand size particles, loose to firm	
4.95 - 5.40	3		6		
5.40 - 5.85	4	Gray, very silty SAND and/or sandy SILT, fines are not plastic, very loose to loose relative density.	12		
5.85 - 6.30	4		28	Very fine gray silty SAND, fines are not plastic, firm to very firm relative density, some seashells are observed.	
6.30 - 6.75	12		16		
6.75 - 7.20	*		24		
7.20 - 7.65	*		23		
7.65 - 8.10	23	Fine gray SILT, not plastic, mixed with a fraction of sand size particles, firm.	19		
8.10 - 8.55	18		25		
8.55 - 9.00	14		22		
9.00 - 9.45	12	Very fine gray silty SAND, fines are not plastic, firm relative density.	13		
9.45 - 9.90	24		21		
9.90 - 10.35	15		23		
10.35 - 10.80	28	Greenish gray very sandy SILT and/or very silty SAND, fines are not plastic, very firm relative density.	31	Very fine greenish gray silty SAND, fines are not plastic, some seashells observed, relative density between firm and dense.	
10.80 - 11.25	9		23		
11.25 - 11.70	20		23		
11.70 - 12.15	22		18		
12.15 - 12.60	25		11		
12.60 - 13.05	12	Very fine gray silty SAND, with green spots, fines are not plastic, relative density varies between firm and very firm.	19		
13.05 - 13.50	21		23		
13.50 - 13.95	13		30		
13.95 - 14.40	11		22		
14.40 - 14.85	22		24	Greenish gray very sandy SILT, fines are not plastic, firm to dense relative density.	
14.85 - 15.30	10		32		
15.30 - 15.75	24		18		
15.75 - 16.20	20		23		
16.20 - 16.65	14		23		
16.65 - 17.10	21		17		
17.10 - 17.55	18		26		
17.55 - 18.00	19		14		
18.00 - 18.45	13		16		
18.45 - 18.90	13		16		
18.90 - 19.35	14		18		
19.35 - 19.80	15		22		
19.80 - 20.25	15		20		

Figure 10-6: (a) Boring P-1 and (b) Boring P-2 Performed at the Rio Bananito Highway Bridge

Table 10-2: Tabular Summary of Boring T-2 at the South Abutment of the Rio Bananito Highway Bridge

Depth (m)	SPT N Value	Estimated Fines Content (%)	USCS Soil Class
0.15	0	80	Silt with Sand (ML)
0.61	0	80	
1.07	0	80	
1.52	0	80	
1.98	0	80	
2.44	0	80	
2.90	0	80	
3.35	4	80	
3.81	4	80	
4.27	4	80	
4.72	2	25	Silty Sand (SM)
5.18	2	25	
5.64	8	25	
6.10	20	25	
6.55	20	25	
7.01	20	25	
7.47	12	25	
7.92	12	25	
8.38	13	25	
8.84	17	25	
9.30	30	25	Silty Sand (SM) / Sandy Silt (ML)
9.75	8	25	
10.21	13	25	
10.67	15	50	
11.13	13	50	
11.58	25	50	
12.04	15	50	
12.50	15	50	
12.95	20	50	
13.41	15	50	
13.87	20	50	
14.33	20	50	
14.78	18	50	
15.24	18	50	
15.70	30	50	
16.15	14	50	
16.61	6	50	
17.07	6	50	
17.53	8	50	
17.98	3	50	

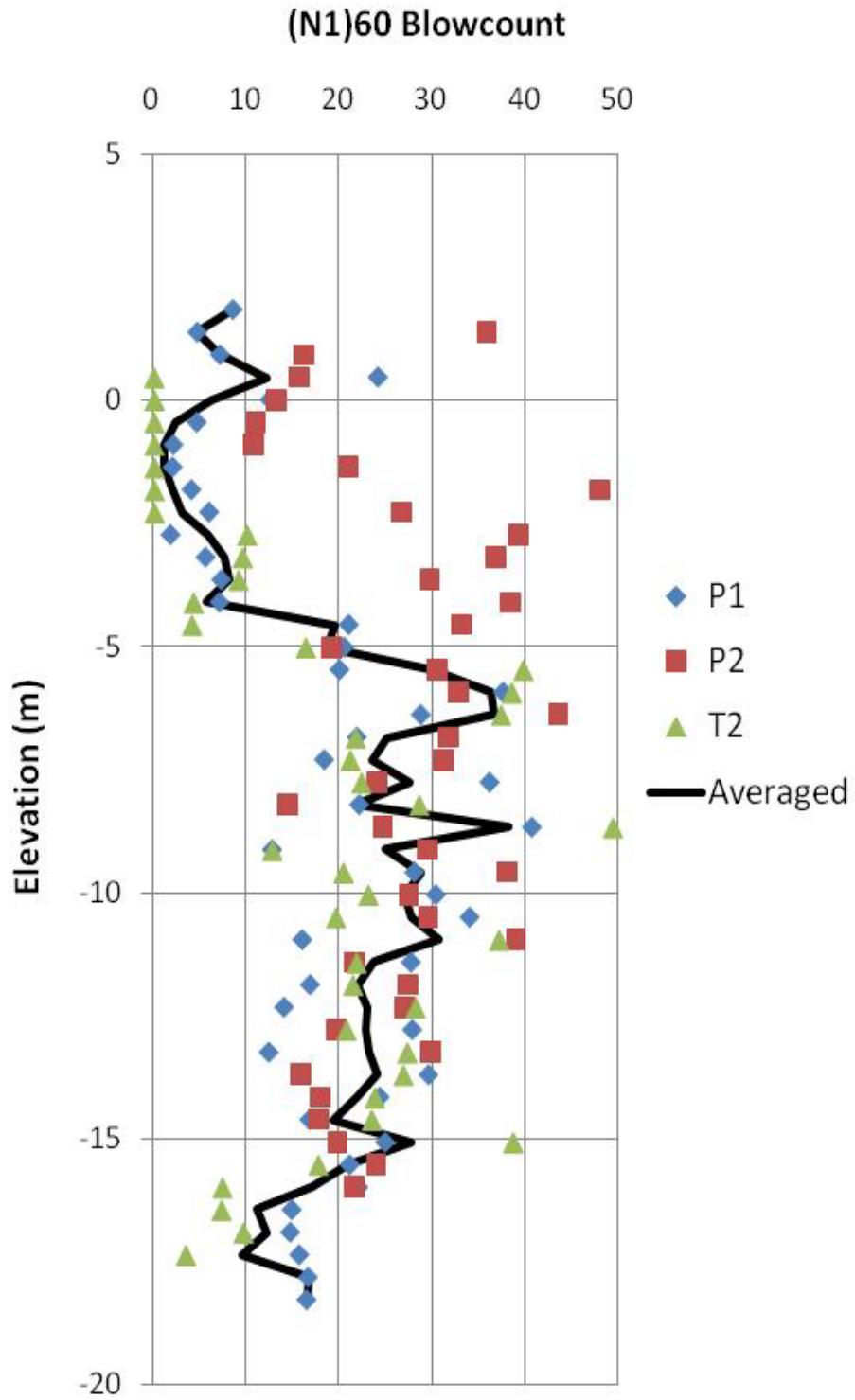


Figure 10-7: Averaged SPT Blowcounts for the Southern Abutment at the Rio Bananito Highway Bridge

The information from Borings P-1, P-2, and T-2 was used to develop a generalized soil profile for the southern abutment of the Rio Bananito Highway Bridge. Empirical correlations with SPT blowcounts were averaged to estimate the friction angle of granular soils and non-plastic silts. These correlations include Peck et al. (1974), Hatanaka and Uchida (1996), and Bowles (1977). Relative density of granular soils was estimated using the empirical correlation presented by Kulhawy and Mayne (1990). Corrected soil modulus estimates K^* of the granular soils for use with the API (1993) p-y relationship were estimated using the recommendations presented by Boulanger et al. (2003). Undrained strength of cohesive plastic soils was averaged from empirical correlations including Hara et al. (1971), Kulhawy and Mayne (1990), and Skempton (1957). Assumptions regarding the unit weight of the native soil as well as the strength properties of the embankment fill were made. Groundwater was modeled at an elevation of 0.0 meter (i.e. an estimated depth of 4.50 meters from the top of the embankment). Table 10-3 summarizes the generalized model of the soil profile at the south abutment of the Rio Bananito Highway Bridge.

Table 10-3: Generalized Soil Profile for the South Abutment at the Rio Bananito Highway Bridge

Top Depth (m)	Top Elevation (m)	Thickness (m)	USCS Soil Class	Friction Angle (deg)	Moist Unit Weight (kN/m ³)	Undrained Strength (kPa)	Relative Density (%)	Corrected Soil Modulus (kN/m ³)	Liquefied p-mult
0	4.50	4.00	SM (Fill)	35	18.5	---	62	24,800	NA
4.00	0.50	0.50	ML	31	18.06	---	40	9,900	NA
4.50	0.00	3.20	ML	31	8.25	---	40	9,900	0.1
7.70	-3.20	0.90	SM	31	8.25	---	40	8,400	0.1
8.60	-4.10	4.40	SM	36	9.04	---	68	18,600	NA
13.00	-8.50	6.30	SM	38	9.04	---	76	18,900	NA
19.30	-14.80	3.60	SM	33	8.44	---	50	7,900	0.16

10.4 Characterization of Site Geometry/Topography at the Rio Bananito Highway Bridge

The Rio Bananito is a moderately-sized river bounded on both sides by a gently sloping floodplain and extensive vegetation. According to elevations shown on the bridge plans provided by the Costa Rican Ministry of Transportation, the river channel itself ranges in elevation from about -3.0 meters at the bottom of the river channel to 0.5 meter at the river bank near both the north and south abutments. These elevations corresponded reasonably well with the ground surface elevations measured with GPS equipment by the BYU reconnaissance team in 2010. According to the bridge plans, the roadway elevation across the bridge is 4.50 meters. From the bridge plans, it also appears that the berm at the spillslope and the approach embankment were originally constructed at a 1.5H:1V slope. The elevation of the water in the Rio Bananito was measured at 0.0 meters at the time of our investigation. A sketch of the Rio Bananito Highway Bridge as originally presented by Priestley et al. (1991) is shown in Figure 10-8. An elevation contour sketch of the bridge based on the 2010 BYU GPS survey is presented in Figure 10-9.

10.5 Deterministic Pile Response Analysis at the Rio Bananito Highway Bridge

10.5.1 Deterministic Ground Motion Evaluation From the 1991 Earthquake

The Rio Bananito Highway Bridge is located 25 kilometers north from the epicenter of the April 22, 1991 earthquake. Assuming an average V_{s30} value of 270 m/s, the average computed median spectral accelerations and median $\pm 1\sigma$ spectral accelerations from the four selected NGA models are shown in Figure 10-10. The median computed PGA and spectral accelerations corresponding to 0.2-second and 1.0-second are 0.213g, 0.445g, and 0.290g.

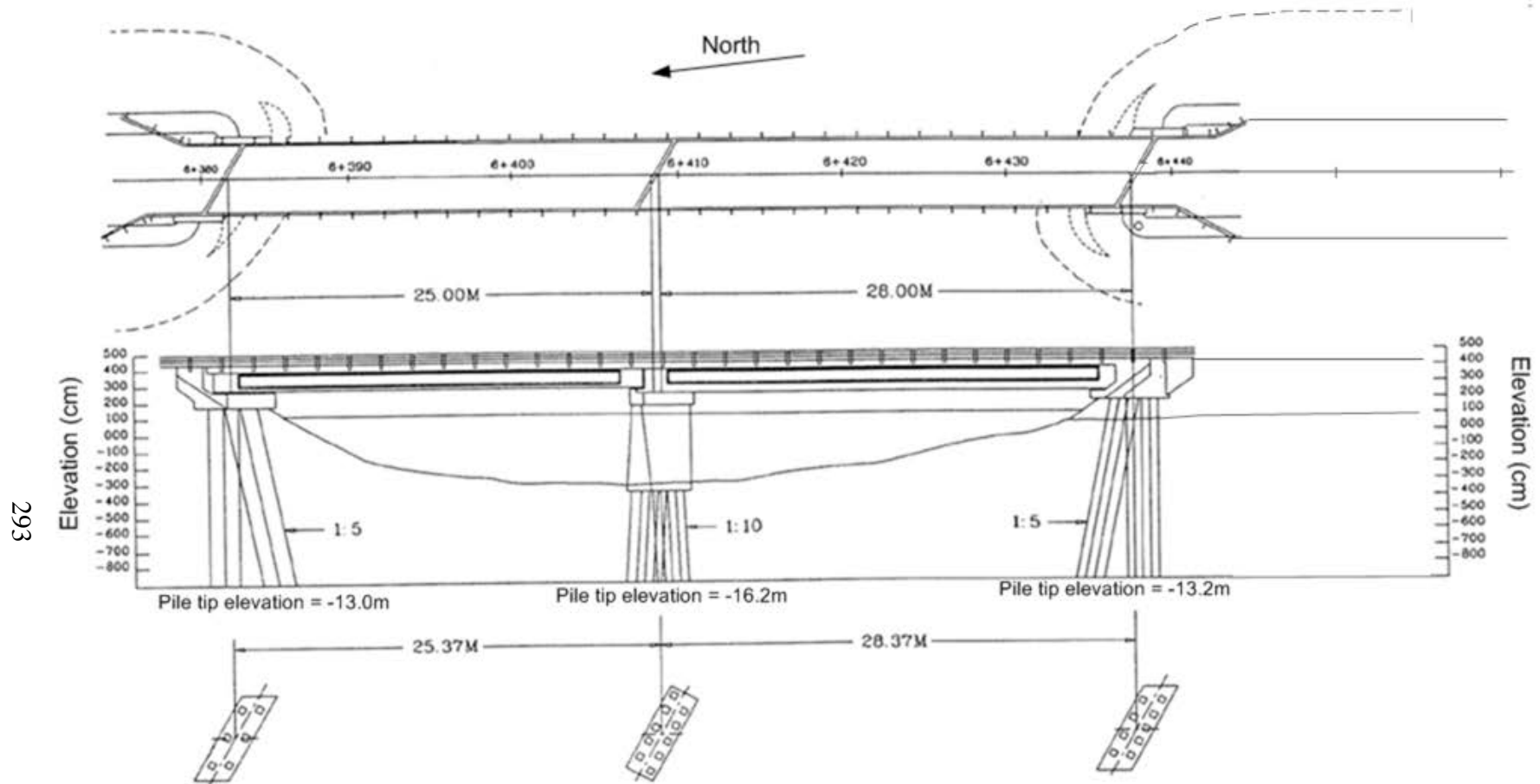


Figure 10-8: Simplified Sketch of the Plan and Profile Views of the Rio Bananito Highway Bridge (After Priestley et al, 1991; McGuire, 1994)

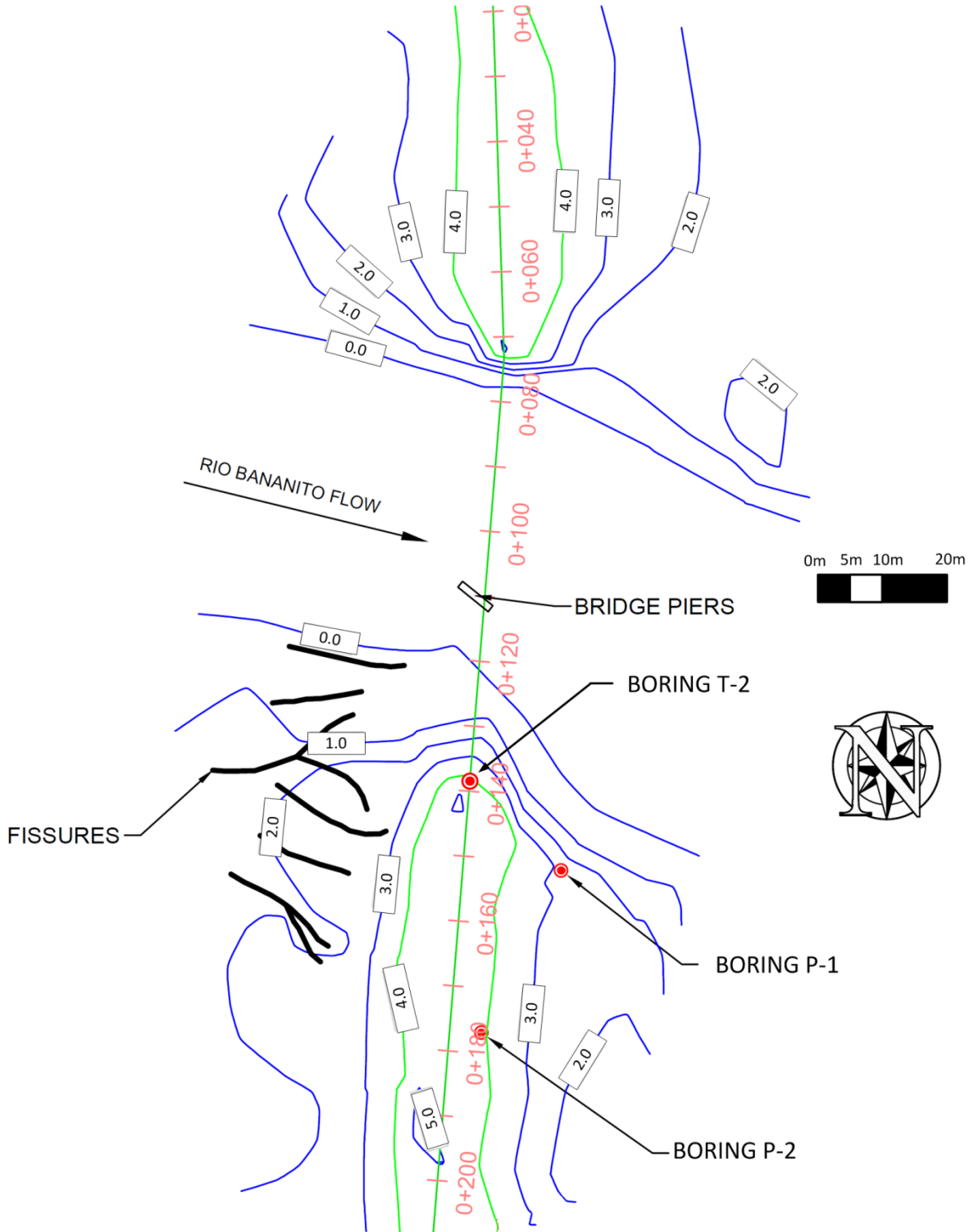


Figure 10-9: Contour Sketch of the Rio Bananito Highway Bridge

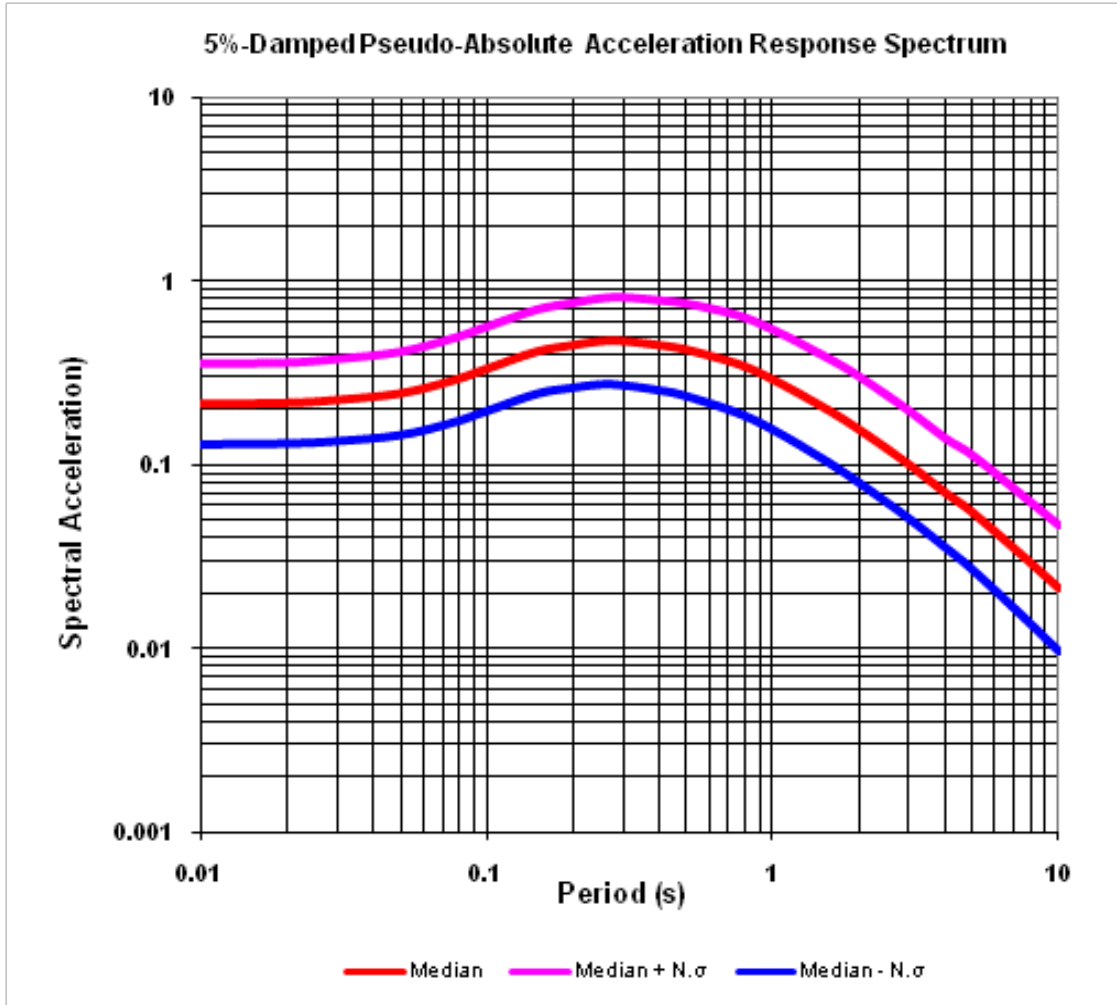


Figure 10-10: Computed Deterministic Response Spectra for the Rio Bananito Highway Bridge From the 1991 Earthquake. N = 1

10.5.2 Deterministic Liquefaction Evaluation From the 1991 Earthquake

Using the average deterministic ground motions from the NGA equations, the deterministic liquefaction triggering was evaluated at the Rio Bananito Highway Bridge for the M7.6 1991 Limon earthquake using the SPT blowcounts from both Borings P-1 and P-2.

The results of the deterministic liquefaction triggering analysis are shown in Figure 10-11 and Figure 10-12. This evaluation included consideration of the Cetin et al. (2004), Idriss and Boulanger (2008), and Youd et al. (2001) simplified procedures. In general, good agreement was observed between the three procedures. The results of the analysis at boring P-1 suggest that liquefaction triggered from depths of 2.0 meters to 6.4 meters below the ground surface (EL 0.0m to EL -4.4m). In addition, thin layers of sand are shown to liquefy at about 1.5-meter intervals from depths of about 9.1 meters to 18.3 meters (EL -7.1m to EL -16.3m). The results of the analysis at boring P-2 suggest that liquefaction triggered from depths of 2.6 meters to 5.5 meters below the ground surface (EL 1.6m to EL -1.2m). Though there is a small discrepancy in the elevations of the principle liquefiable layer between Borings P-1 and P-2, it is clear that there is a continuous liquefiable layer near the ground surface that likely governed the observed soil deformations following the 1991 Limon earthquake.

10.5.3 Post Earthquake Slope Stability

A simple post earthquake slope stability evaluation was performed for the south bank of the Rio Bananito Highway using SLOPE/W analysis software (GEO-SLOPE, 2010). In evaluating the slope stability, only native soils were considered in the analysis in order to investigate the potential for flow liquefaction failure along the river bank. Such a failure would likely disqualify the use of empirical lateral spread models for computing lateral spread displacements in the native soils along the river bank.

The residual strength ratio S_r/σ' , of the liquefied soil was computed using both normalized residual strength ratios and uniform residual strengths. Normalized strength ratios were computed using Ledezma and Bray (2010) as given in Equation (2-2).

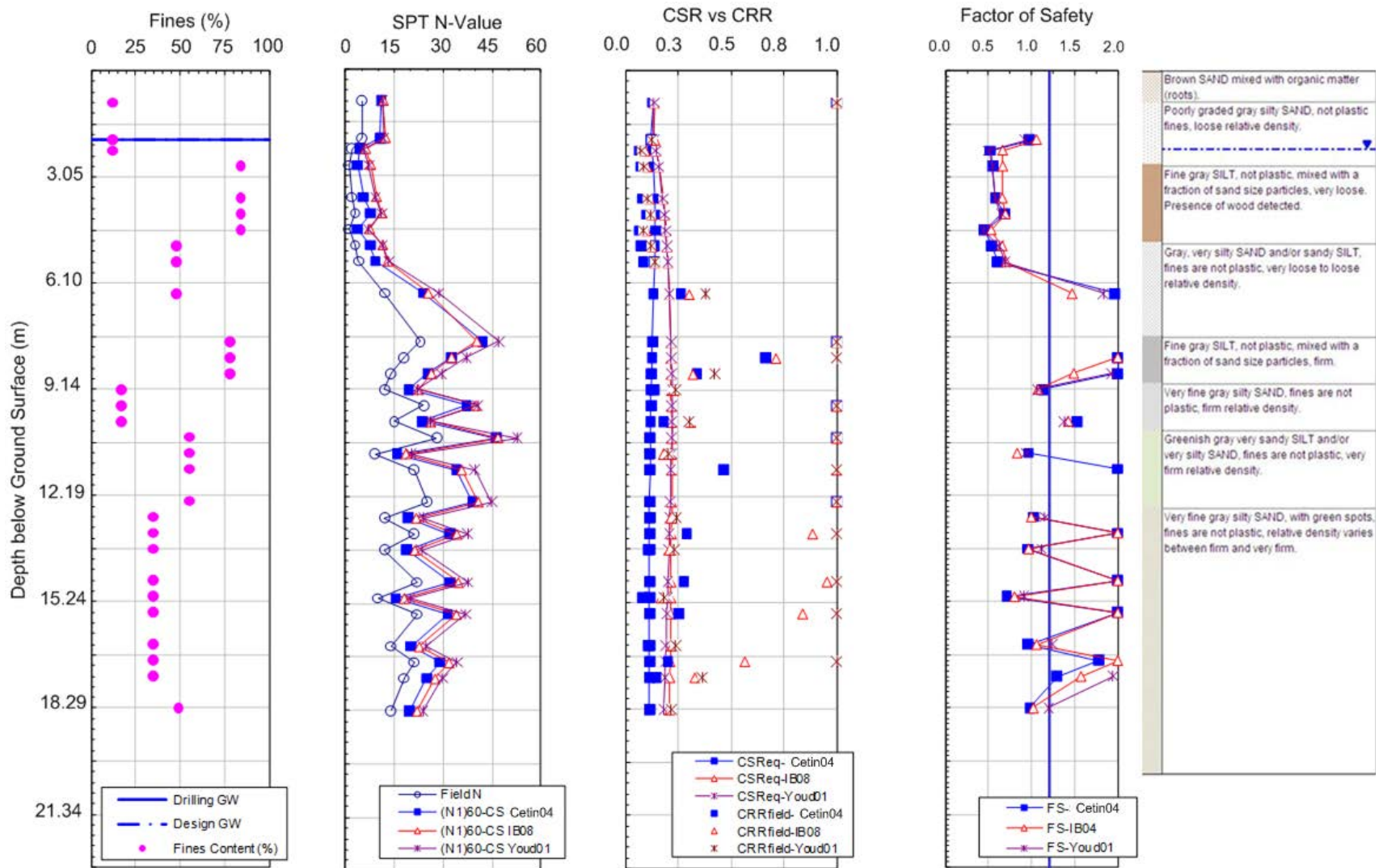


Figure 10-11: Deterministic Liquefaction Triggering Results From Boring P-1 for the M7.6 1991 Limon Earthquake at the Rio Bananito Highway Bridge

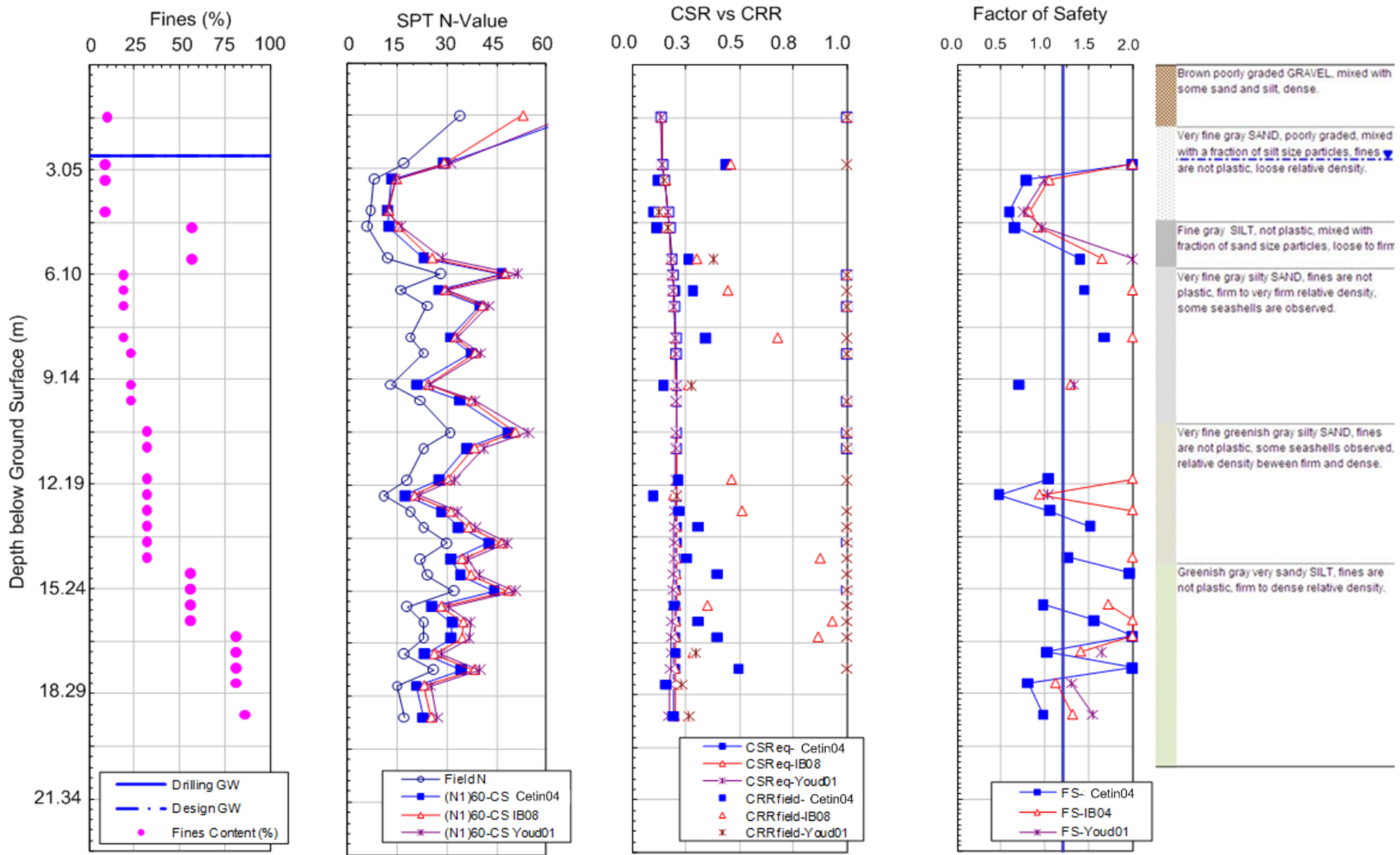


Figure 10-12: Deterministic Liquefaction Triggering Results From Boring P-2 for the M7.6 1991 Limon Earthquake at the Rio Bananito Highway Bridge

Uniform residual strengths were computed using the 33rd-percentile from Seed and Harder (1990) as presented in Figure 2-8. The Lowe and Karafiath (1960) method was used in the limit equilibrium analysis to compute factor of safety. A non-circular surface search routine was utilized allowing for optimization in order to allow for the possibility of non-linear or log-spiral failure surfaces. A summary output from the post earthquake slope stability evaluation is presented in Figure 10-13 and Figure 10-14.

The post-liquefaction factor of safety was computed to be 0.54 and 0.59 using the residual strength ratios and the uniform residual strength, respectively. Because these factors of safety are significantly less than unity, the lateral soil deformations observed at the southern abutment of the Rio Bananito Highway Bridge were likely caused by liquefaction flow failure and not lateral spread. Such a finding would have significant impact on design if the bridge were being evaluated for seismic stability using modern design standards. While engineers currently have many methodologies for lateral soil deformations due to lateral spread, few reliable and practical methodologies currently exist for engineers to estimate displacements due to liquefaction flow failures. Therefore, if liquefaction flow failure is determined to pose a significant threat of occurring, the standard of practice in most locations requires that liquefaction mitigation techniques be implemented to prevent liquefaction from triggering. Such mitigation usually involves the installation of soil ground improvement and/or the implementation of slope stabilization alternatives such as a berm.

Because it is likely that liquefaction flow failure caused the ground deformations and resulting damage to the bridge at the southern abutment, empirical lateral spread displacements were not computed and the Rio Bananito Highway Bridge was not analyzed in the proposed performance-based pile response framework. However, a deterministic pile response analysis

was performed to attempt to replicate the damage that was observed at the southern abutment following the 1991 Limon earthquake.

10.5.3.1 Back-Analysis of Residual Strengths

While flow liquefaction failures are often considered the most dangerous and potentially catastrophic hazard associated with soil liquefaction, there are relatively few well-developed case histories that are available for researchers to study. As such, the soil deformations observed at the southern abutment of the Rio Bananito Highway Bridge following the 1991 Limon earthquake could provide some valuable insight for researchers investigating the phenomenon of liquefaction flow failure.

Using the deformed geometry shown in Figure 10-4, a post-earthquake stability model was built using the same non-liquefied strength parameters and limit equilibrium methods incorporated in the stability models from the previous section. Engineering judgment was required to develop the subsurface layering in the deformed soil mass and the post-seismic geometry at the toe of the failure. The residual strength of the liquefied soil was then incrementally adjusted to identify the strength required to achieve a factor of safety equal to 1.0. Both residual strength ratios and uniform residual strengths were back-analyzed. An averaged SPT blowcount (i.e. $(N_1)_{60}$) of 3.8 with a fines content of 68-percent was computed for the liquefiable soil from the liquefaction triggering analysis. Clean-sand equivalent SPT blowcounts of 7.8 and 9.6 were computed for the Seed and Harder (1990) and Ledezma and Bray (2010) relationships using Equations (2-1) and (2-4), respectively. The resulting stability analyses are presented for residual strength ratios and uniform residual strengths in Figure 10-15 and Figure 10-16, respectively. The computed residual strength ratio and uniform residual strength are 0.3 and 11.4 kPa (238 psf).

A simple evaluation of these preliminary residual strength parameters can be performed by comparing the computed results against published residual strength ranges. The computed uniform residual strength is compared against the strengths as recommended by Seed and Harder (1990). The computed residual strength ratio is compared against a variety of published residual strength ratio relationships as summarized by Ledezma and Bray (2010). These comparisons are presented in Figure 10-17.

Figure 10-17 reveals that the back-analyzed uniform residual strength falls within the recommended range of strengths after Seed and Harder (1990). However, the back-analyzed residual strength ratio falls well above the recommended ranges of current models. This result suggests that existing models for computing residual strength ratios may not be well-suited for computing residual strengths at very shallow depths or in daylighting soil, and that uniform residual strengths may be better-suited for representing liquefied soil under such conditions. Such an observation could have a significant impact on the current standard of engineering practice, and future study may be warranted.

10.5.4 Deterministic Evaluation of Lateral Spread Displacement

Even though the post earthquake slope stability analysis strongly suggests that liquefaction flow failure occurred at the Rio Bananito Highway Bridge, deterministic lateral spread displacements were still computed. Few if any of the case histories in most empirical lateral spread data sets have been checked against liquefaction flow failure (personal communication, T.L. Youd).

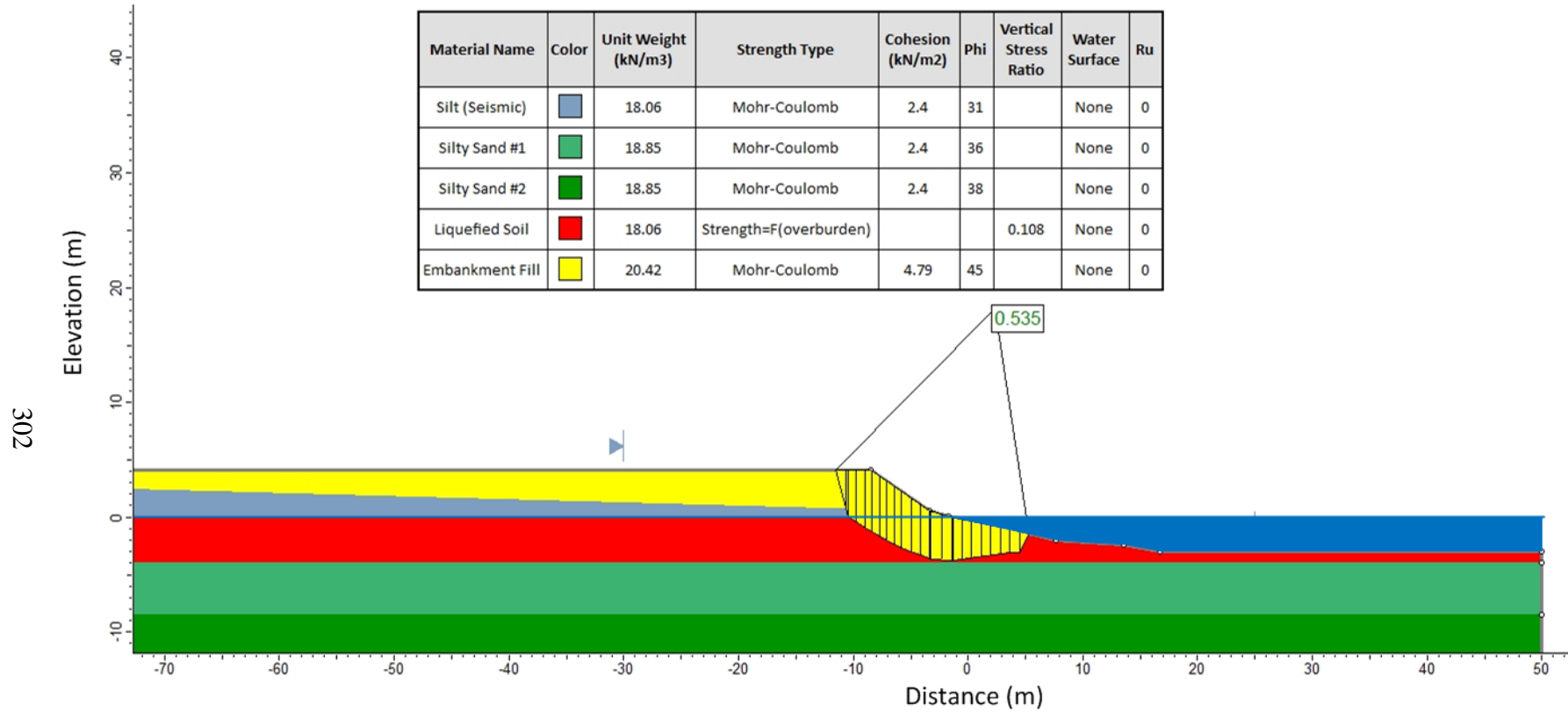


Figure 10-13: Post Earthquake Slope Stability Analysis at the Rio Bananito Highway Computed Using Residual Strength Ratios

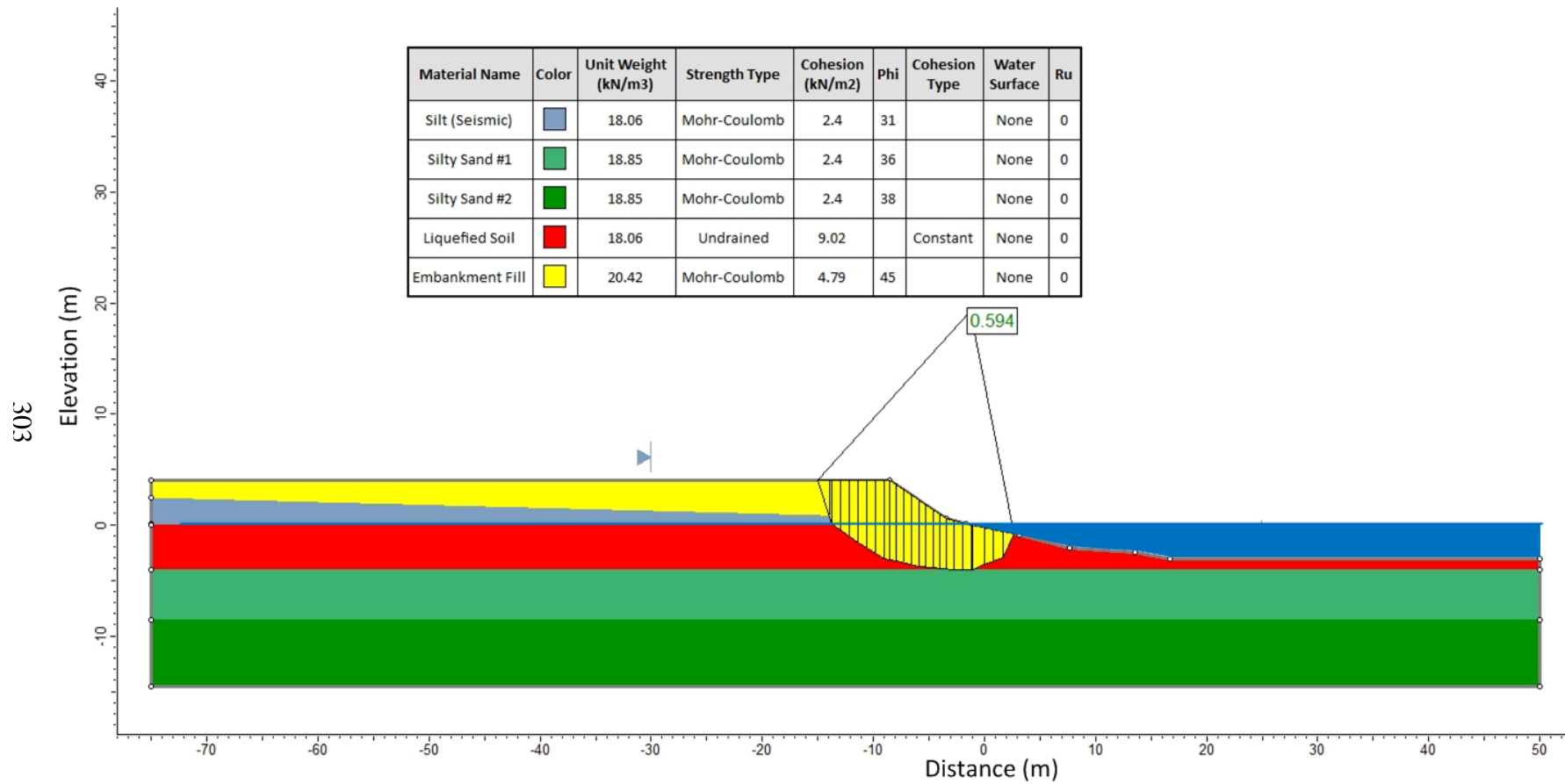


Figure 10-14: Post Earthquake Slope Stability Analysis at the Rio Bananito Highway Computed Using Uniform Residual Strength

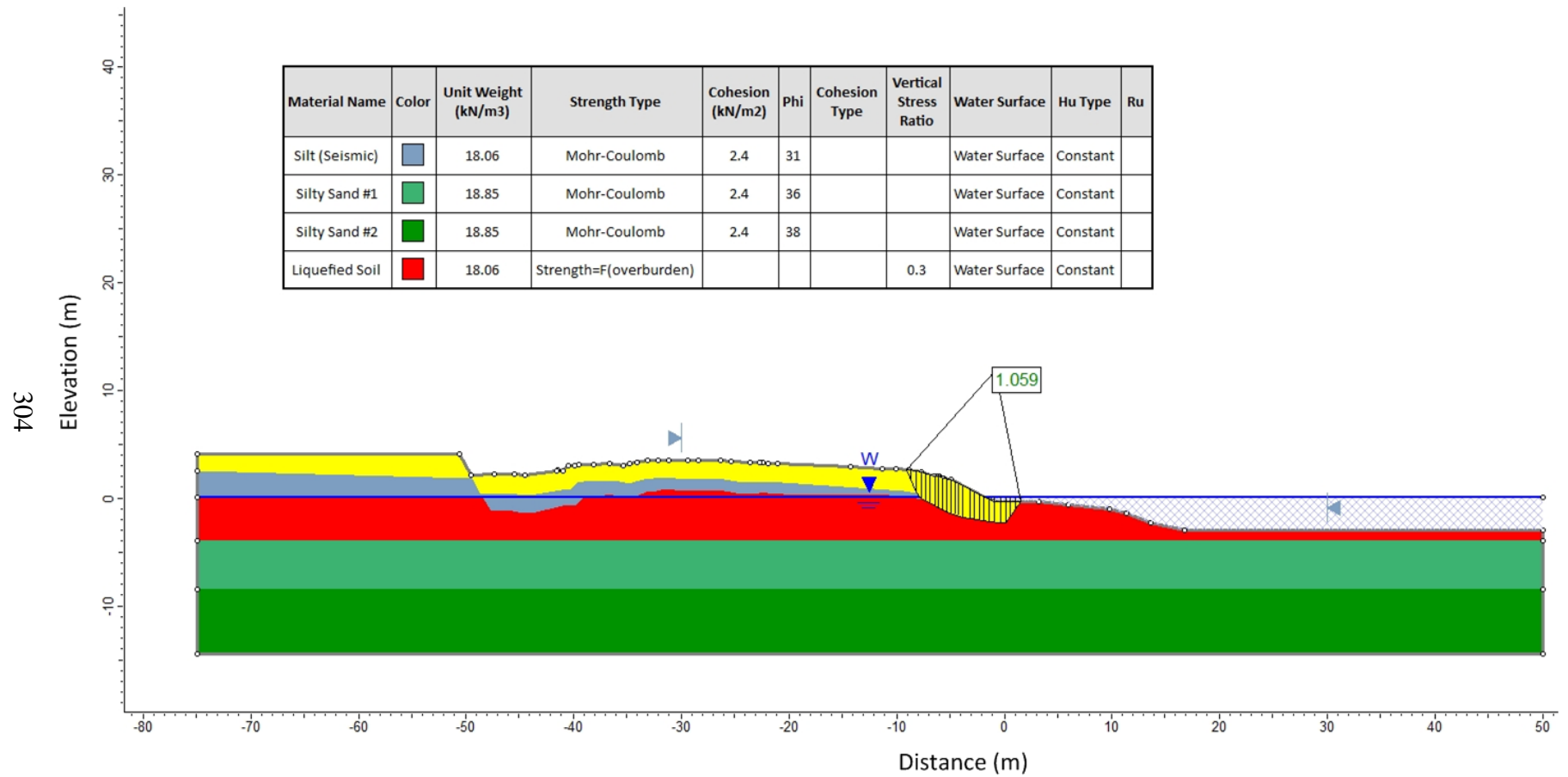


Figure 10-15: Back-Analysis of the Residual Strength Ratio at the Rio Bananito Highway Bridge

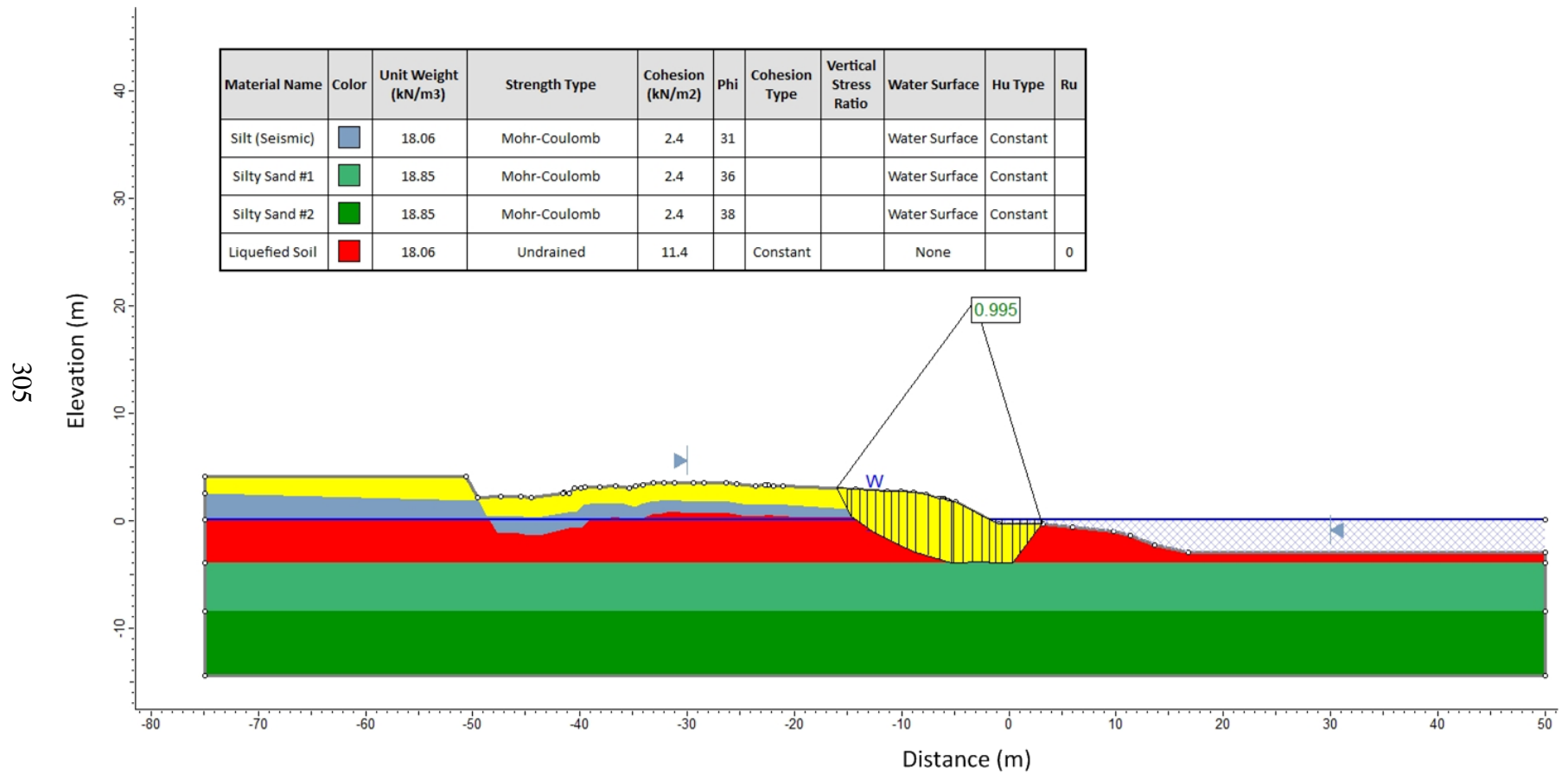


Figure 10-16: Back-Analysis of the Uniform Residual Strength at the Rio Bananito Highway Bridge

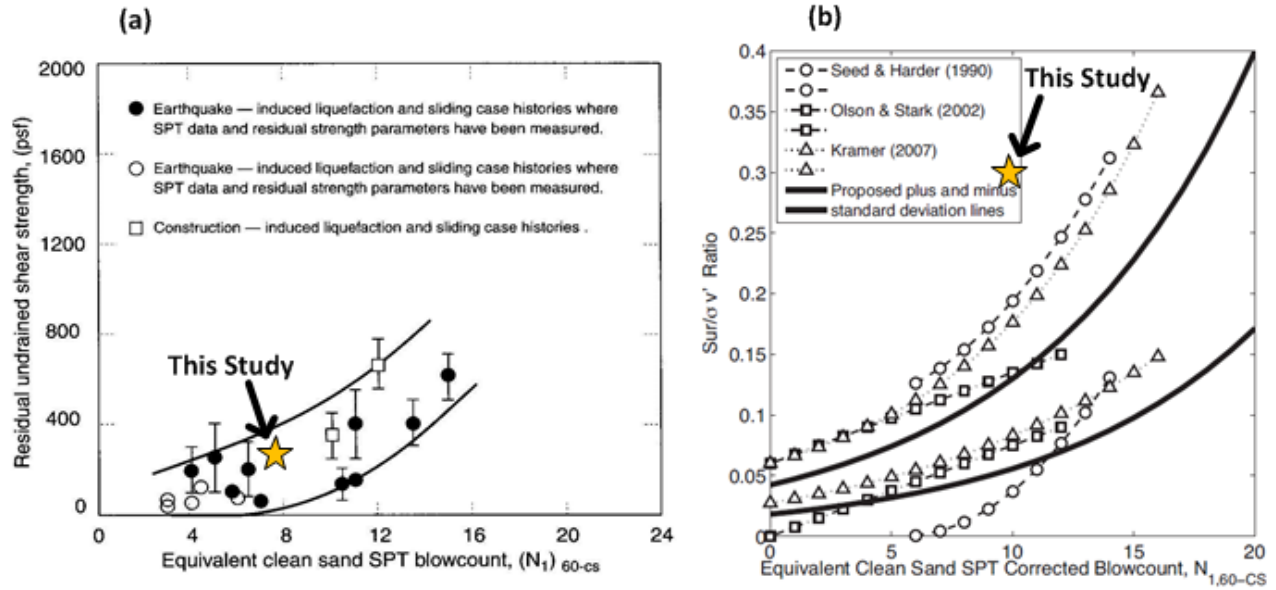


Figure 10-17: Residual Strength Comparisons for (a) Uniform Residual Strength (After Seed and Harder, 1990), and (b) Residual Strength Ratio (After Ledezma and Bray, 2010)

Empirical evaluation of lateral spread displacement was performed using the Youd et al. (2002), Bardet et al. (2002), and Baska (2002) models as presented in Sections 3.4 and 3.5 of this dissertation. This study assumed an earthquake magnitude of 7.6, a source-to-site distance of 25 kilometers, a free-face ratio of 20-percent, and a free-face height of 4.9 meters. The averaged SPT blowcounts shown in Figure 10-7 were used in the analysis. The mean grain size diameter for the generalized boring was estimated from Insuma sieve results for Borings P-1 and P-2, which are available in Appendix A. The median computed lateral spread displacement value and the 95th-percentile confidence interval for each of the three empirical models is shown in Figure 10-18. The average computed median displacement from the three models is 1.80 meters, which is significantly less than the observed displacements near the bridge following the 1991 earthquake.

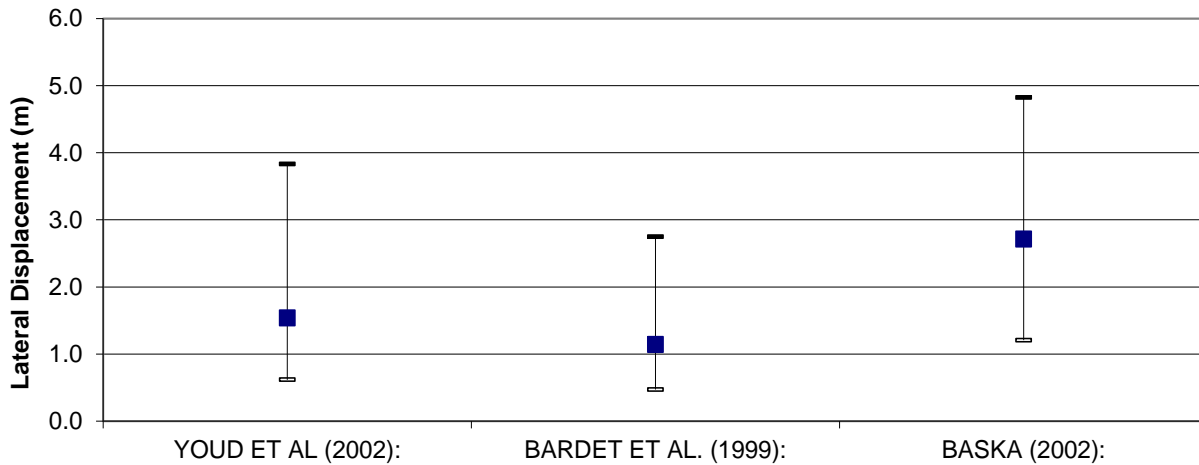


Figure 10-18: Empirically Computed Lateral Spread Displacements at the Southern Abutment of the Rio Bananito Highway Bridge

10.5.5 Pile Response Analysis

To evaluate the deterministic pile response at the southern abutment of the Rio Bananito Highway Bridge, a two-stage analysis was performed. The first stage of the analysis evaluated the initial deformation of the soil in which the bridge deck stayed in place and behaved as a reinforcing strut load. The second stage of the analysis evaluated the final deformation of the soil after the bridge deck fell off its supports.

Because reinforcing details for the piles were not shown on the bridge plans provided by the Costa Rican Ministry of Transportation, assumptions had to be made regarding the amount and size of rebar in the piles in order to compute their flexural stiffness (i.e. EI). A study was made into many of the available reinforced concrete design standards in practice during 1971 when the bridge was designed, and it was found that most piles in use at the time only

incorporated four vertical steel bars for reinforcement. It was assumed that four #4 bars were used in the piles. The resulting initial composite flexural stiffness of a single 14in by 14in pile was computed to be 35,000 kN-m².

The equivalent single pile developed for the pile response analysis consists of two sections: the pile cap and the piles. The 1.80m-by-5.66m pile cap comprises the top 2.6 meters of the equivalent single pile. The composite flexural stiffness of the pile cap was computed to be 72,302 MN-m². The second section of the equivalent single pile represents the pile group and was created by multiplying the initial composite flexural stiffness of a single pile by the total number of piles in the pile group (i.e. 9) to develop the initial composite flexural stiffness of the equivalent single pile. This initial composite flexural stiffness was computed to be 315,000 kN-m². A nonlinear moment-stiffness curve was developed to account for yielding of the reinforced concrete piles in accordance with the guidelines presented by CalTrans (2011) as summarized in Section 4.4.3 of this dissertation. The moment-curvature and moment-stiffness curves for the equivalent single pile are presented in Figure 10-19.

A p-multiplier for the equivalent pile group to account for the total number of piles in the group and the pile spacing was computed to be 4.68 using Rollins et al. (2006). Rotational stiffness of the equivalent single pile was neglected due to the relative flexibility of the piles and the close pile-to-pile spacing in the direction of the lateral spread (i.e. longitudinal direction). Therefore, the equivalent single pile was modeled with a free-head condition with a lateral load at the head to represent the strut-like behavior of the bridge deck for the first stage of the analysis.

In the first stage of the analysis, the magnitude of lateral deformations that caused the pile cap to rotate 14-15 degrees was unknown. Therefore, an iterative procedure was performed in

LPILE in which the magnitude of soil deformation was modified incrementally until a pile cap rotation of 14-15 degrees was achieved. The zone of lateral soil deformation was limited to Elevations 0.0 meters to -4.1 meters and was distributed with depth in accordance with the procedures described in Sections 3.6 and 3.7. The bridge deck was modeled with a lateral load applied to head of the equivalent single pile limiting the pile head deformation to zero. It was found that a pile cap rotation of 14.5 degrees was obtained when a soil displacement of 0.6 meter was applied to the modeled system. The deterministic pile response results from the first stage are shown in Figure 10-20.

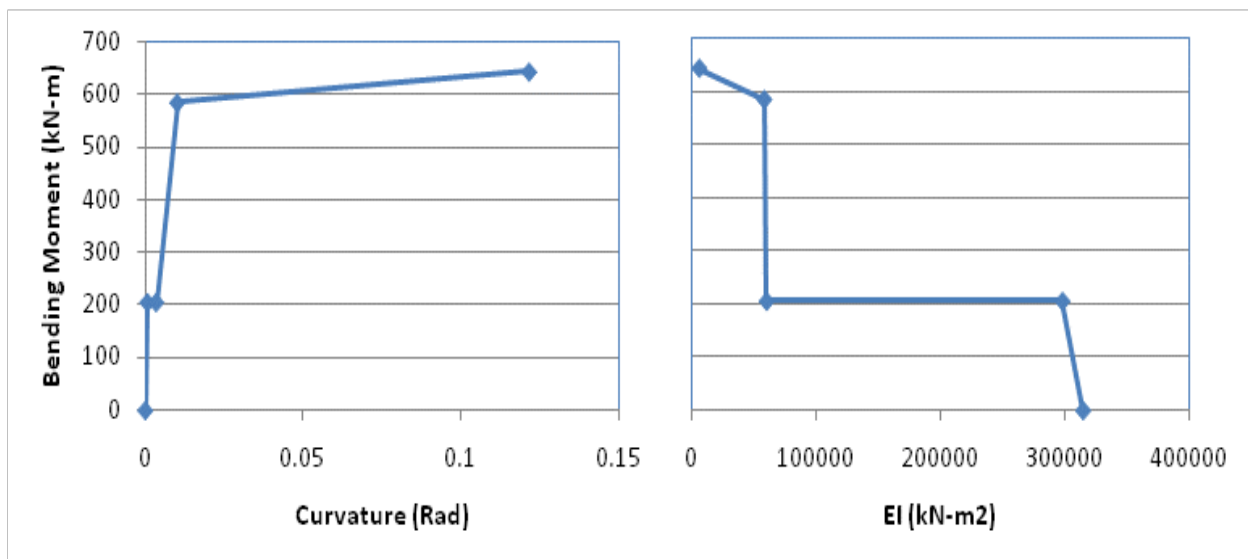


Figure 10-19: Moment-Curvature and Moment-Stiffness Curves for the Rio Bananito Highway Bridge

In the second stage of the analysis, a total of 3.89 meters of additional soil movement was added to the soil movements from the first stage (i.e. 0.6 meter). No additional strut loads were

added to account for the bridge deck falling into the river. Therefore, a total of 4.49 meters of soil movement was applied to the model. The deterministic pile response results from the second stage are shown in Figure 10-21. The computed horizontal displacement at the top of the pile cap at the end of the second stage of analysis was 3.89 meters (as was measured in Method #1 by Youd et al., 1992), and the pile cap rotation was 14.5 degrees. These results match the observed pile response at the southern abutment following the 1991 Limon earthquake.

10.5.6 Summary of Deterministic Results

While the results of this deterministic analysis are simplified in that they do not account for the vertical deformations that occurred at the bridge abutment and are based on back-calculated soil deformations, they demonstrate that modern p-y pile response analysis methodologies can reasonably model the kinematic pile response of even moderately complex systems given adequate information regarding the system itself.

10.6 Probabilistic Analysis at the Rio Bananito Highway Bridge

Because the liquefaction triggering and post earthquake slope stability analyses indicate that liquefaction flow failure likely contributed to the soil deformations at the southern abutment of the Rio Bananito Highway Bridge, no empirical lateral spread displacements were computed for the site. Subsequently, no performance-based lateral spread and pile response analyses were performed. However, for the benefit of potential future research involving the Rio Bananito Highway Bridge case history, probabilistic evaluations of ground motions and liquefaction triggering were performed at the southern abutment of the bridge.

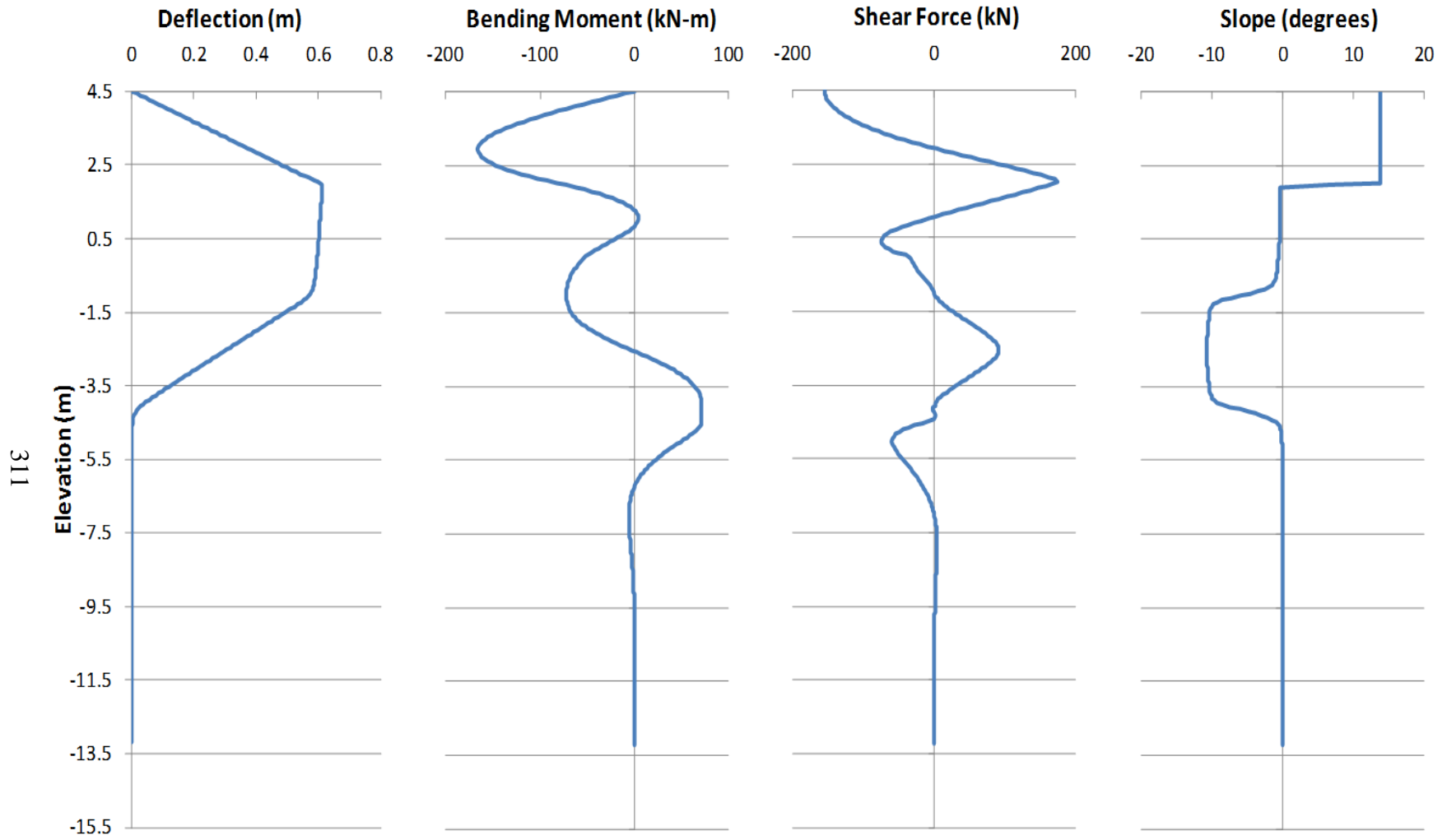


Figure 10-20: Deterministic Computed Pile Response for the Rio Bananito Highway Bridge South Abutment Before Bridge Deck Fell From Its Supports

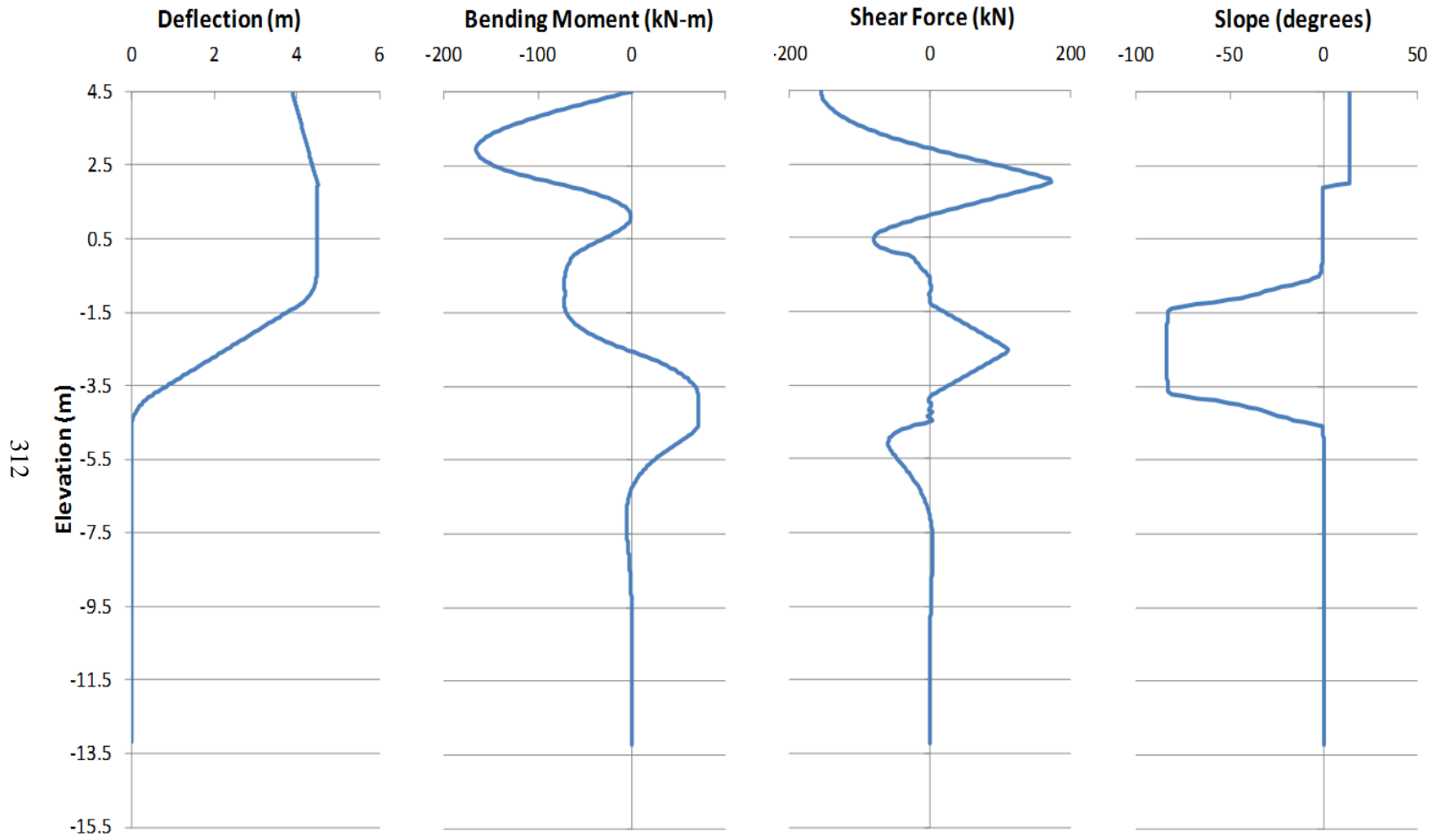


Figure 10-21: Deterministic Computed Pile Response for the Rio Bananito Highway Bridge South Abutment After the Bridge Deck Fell From Its Supports

10.6.1 Probabilistic Ground Motions

A PSHA was performed at the Rio Bananito Highway Bridge site using EZ-FRISK software and the built-in seismic source model for Central and South America developed by Risk Engineering (see Risk Engineering documentation included in Appendix B). This seismic source model included both area and fault sources. The four selected NGA attenuation models (Abrahamson and Silva, 2008; Chiou and Youngs, 2008; Campbell and Bozorgnia, 2008; and Boore and Atkinson, 2008) were assigned to crustal seismic sources, and select attenuation models developed for subduction zones (Youngs et al., 1997; Atkinson and Boore, 2003; and Zhao et al., 2006) were assigned to the subduction seismic sources. Finally, near-source and directivity effects were accounted for in the PSHA by incorporating the fault-normal response spectrum modifications presented by Somerville et al. (1997) and Abrahamson (2000) for all fault sources. A table of the fault sources located within about 100 km of the site is presented in Table 10-4.

Table 10-4: EZ-FRISK Faults Within About 100 km of the Rio Bananito Highway Bridge

Fault Name	Type	Fault Length (km)	Source to Site		Characteristic Magnitude	Slip Rate (mm/yr)	Recurrence Rate
			Distance (km)				
Limon fault	Reverse	162	6.1		7.8	1.0	---
Panama - North (Caribbean)	Subduction Interface	817	34		8.0	4.0	---
Guapiles fault	Reverse	8	97		6.1	4.0	---
Longitudinal fault	Reverse	42	106		7.4	0.1	---
Longitudinal fault - Costa Rica 2	Reverse	52	106		7.0	0.5	---
Costa Rica	Subduction Intraslab	288	106		7.7	---	0.4958

The seismic hazard curve for the PGA developed from the PSHA is presented in Figure 10-22. The ground motions corresponding 10-percent and 2-percent probabilities of exceedance in 50 years (i.e. return periods of 475 and 2,475 years, respectively) are 0.551g and 0.916g, respectively.

The seismic hazard contributions from the individual sources are shown in Figure 10-23. From Figure 10-23, it appears that the Costa Rica arc and shear zone (area source), the Costa Rica fault (subduction interface source), and the Panama North (Caribbean) fault (subduction interface source) govern the probabilistic seismic hazard at most return periods for the PGA. The probabilistic response spectra developed from the PSHA for seven different return periods are shown in Figure 10-24. Finally, simplified deaggregation plots of the PGA are presented in Figure 10-25.

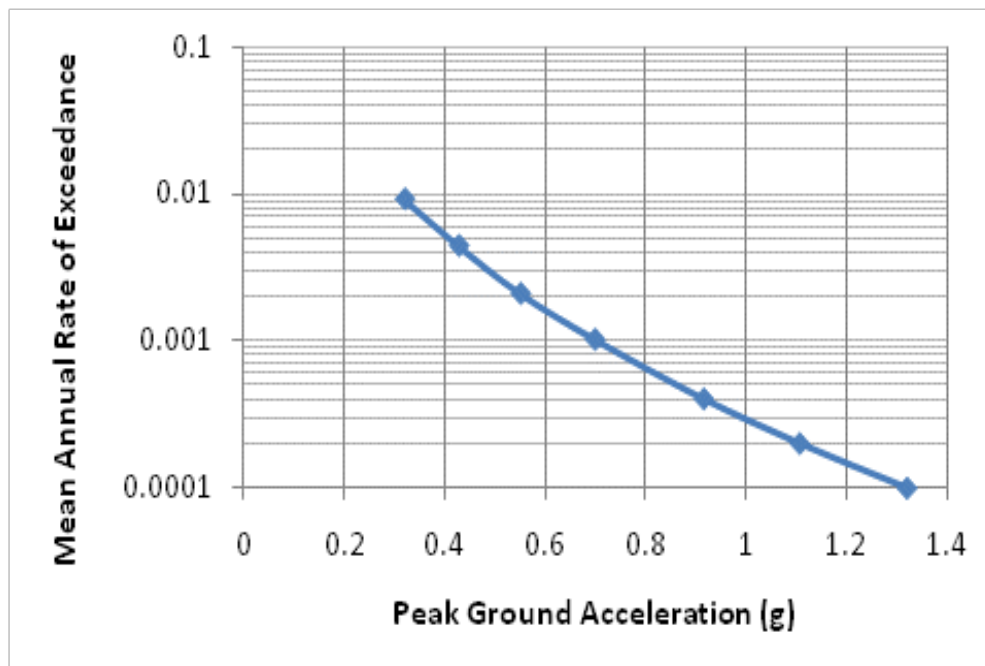


Figure 10-22: Seismic Hazard Curve for the PGA at the Rio Bananito Highway Bridge

10.6.2 Probabilistic Liquefaction Triggering

Using the probabilistic estimates of a_{max} shown in Figure 10-22 in conjunction with the magnitude/distance deaggregations shown in Figure 10-25, probabilistic estimates of liquefaction triggering were computed with the Kramer and Mayfield (2007) procedure using Equations (6-1) and (6-2). The performance-based liquefaction triggering computations were performed using the computer program PPRS. The resulting factors of safety against liquefaction triggering for various return periods are shown in Figure 10-26.

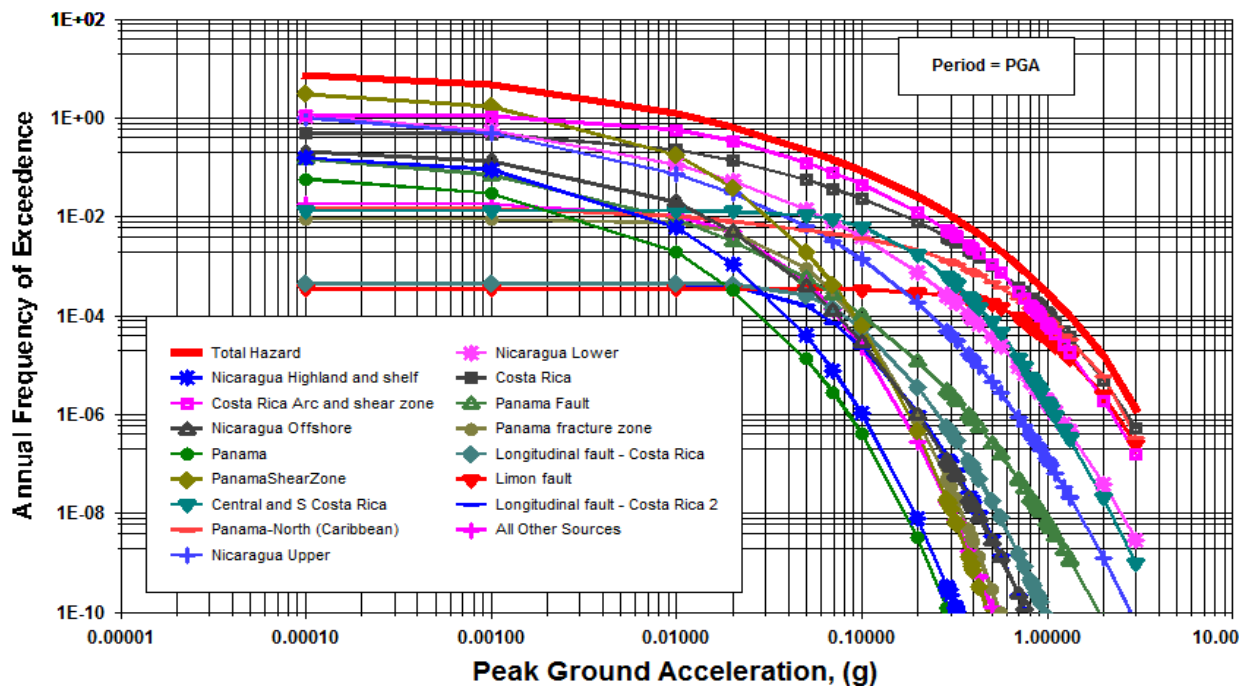


Figure 10-23: Source Contributions to Probabilistic Seismic Hazard for the Rio Bananito Highway Bridge

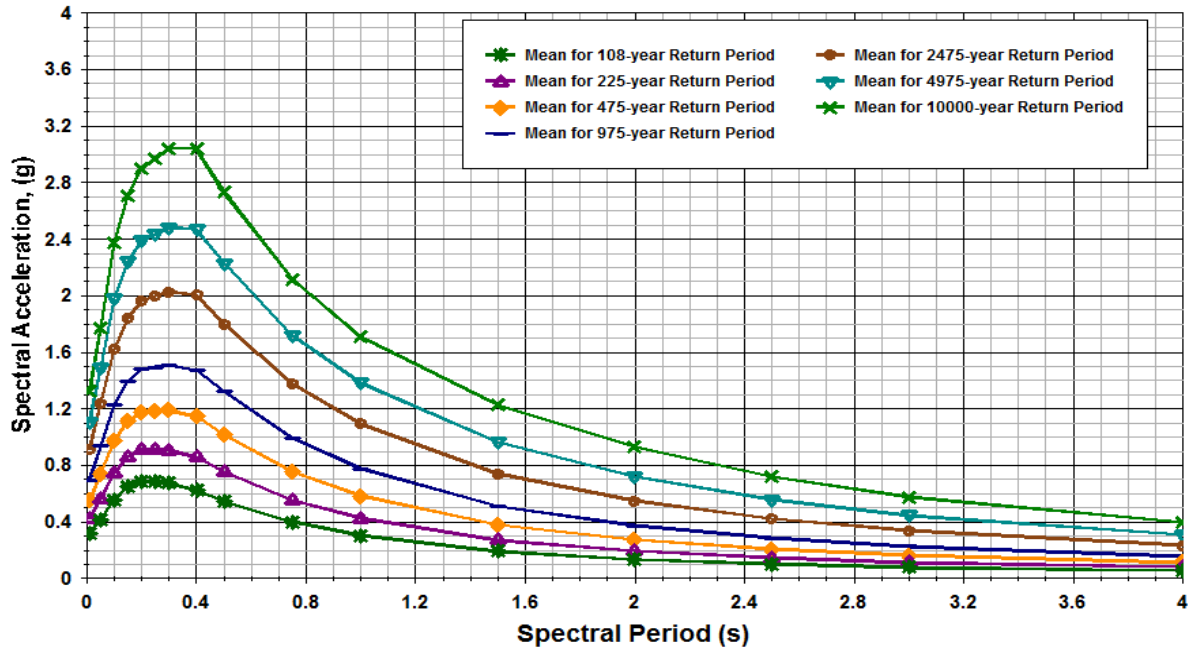


Figure 10-24: Probabilistic Response Spectra (5-Percent Damping) for the Rio Bananito Highway Bridge

The factors of safety shown in Figure 10-26 were computed using the SPT blowcount information from the averaged SPT blowcount profile shown in Figure 10-7. A factor of safety less than or equal to 1.2 was assumed to be liquefiable for this study. Note that for fine-grained soil layers not considered susceptible to liquefaction due to plasticity, a generic factor of safety against liquefaction equal to 2.0 was assigned regardless of return period. A maximum factor of safety equal to 4.0 was assigned to layers with very high resistance to liquefaction triggering. Figure 10-26 shows that for nearly all return periods, liquefaction triggers from depths of about 2.0 meters to 6.1 meters below the ground surface (EL. 0.0m to -4.1m). In addition, for return periods of 475 years and greater, liquefaction appears to trigger below depths of about 18.0 meters below the ground surface (EL. -16.0m).

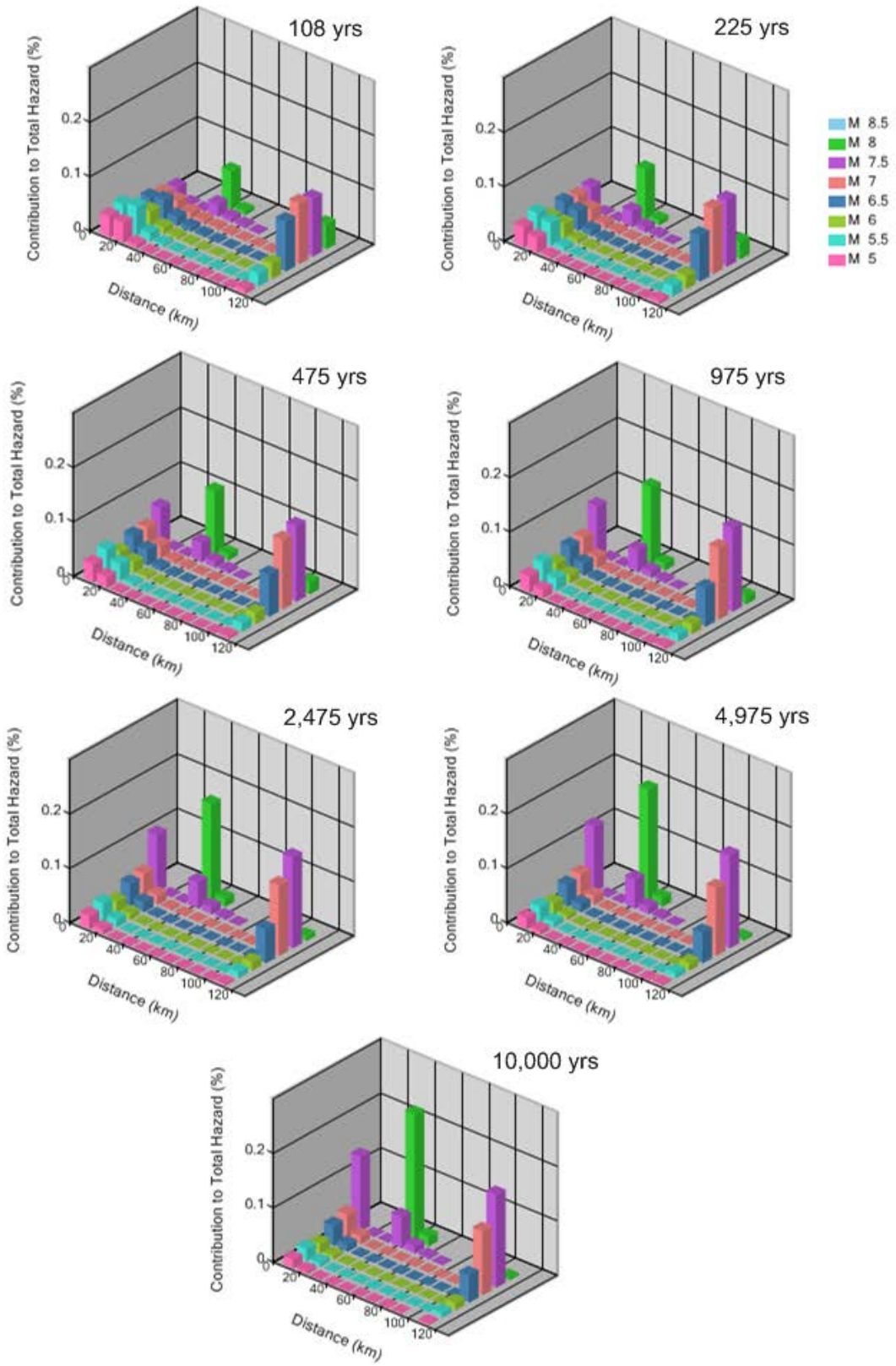


Figure 10-25: Deaggregation Plots for the PGA at the Rio Bananito Highway Bridge

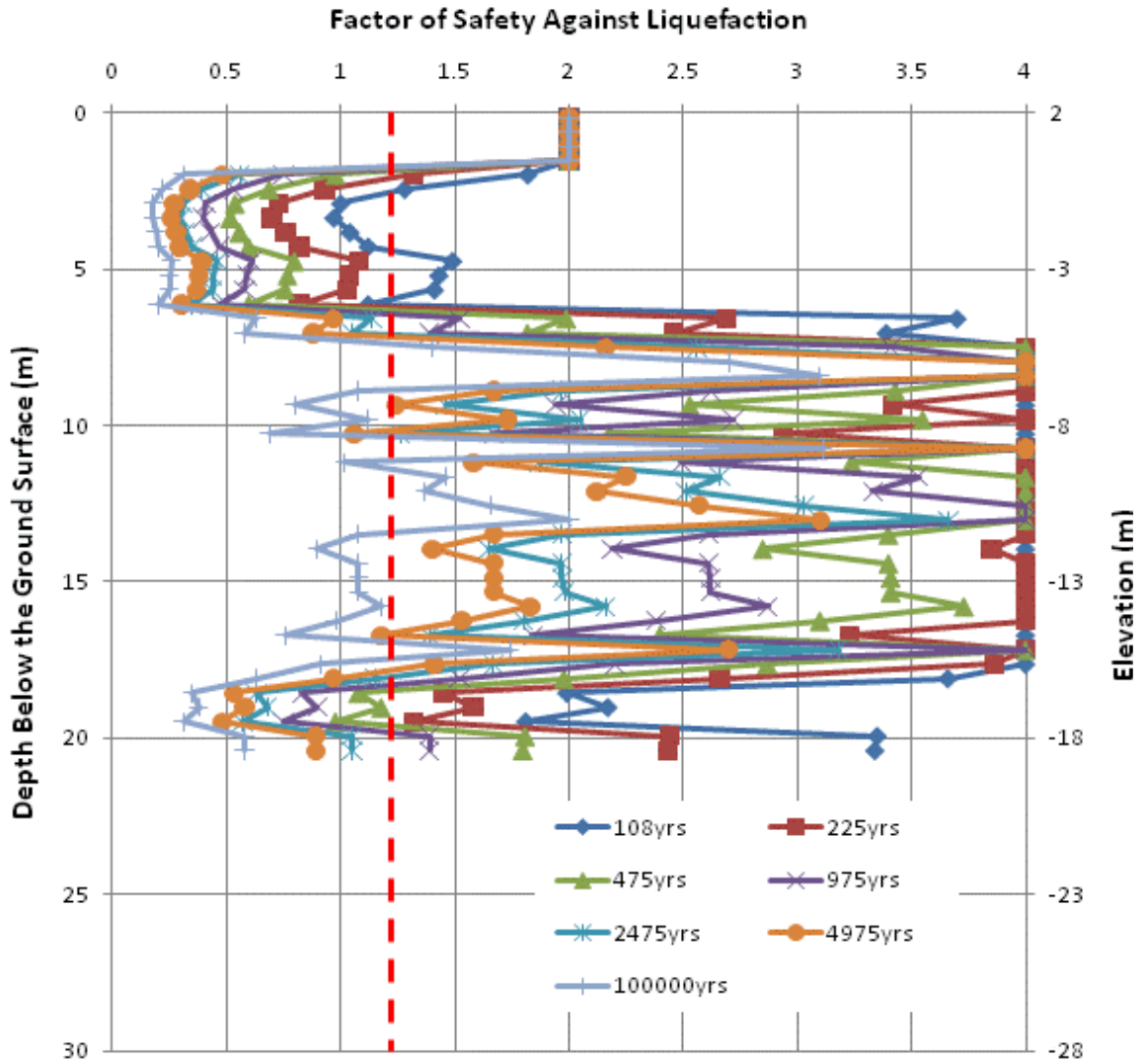


Figure 10-26: Performance-Based Liquefaction Triggering Results for the Rio Bananito Highway Bridge

11 RIO BANANITO RAILWAY BRIDGE

11.1 Introduction

The railway bridge over the Rio Bananito is single-span truss bridge supporting the rail line from Bananito Norte to Bananito Sur. The bridge is located about 15 kilometers upstream from the Rio Bananito Highway Bridge and is the only structure crossing the Rio Bananito upstream from the highway Route 36 at the coast (McGuire, 1994). Today, the bridge is used as both a road and a railway crossing over the Rio Bananito. At the time of the earthquake, the bridge was used primarily for the rail transport of bananas to ports on the east coast of Costa Rica. The latitudinal and longitudinal coordinates for the bridge are 9.8765° North 83.0076° West. A photo of the bridge is presented in Figure 11-1.

According to bridge drawings from the Costa Rica Ministry of Transportation, the bridge was constructed some time prior to 1890. The through-truss bridge is 50 meters in length, and each abutment is founded on two elliptically-shaped caissons that are 1.46 meters by 2.16 meters across the major axes (EERI, 1993). The caissons are constructed of a 12-mm thick steel shell composed of narrow sheet pile segments which were filled with concrete. Details regarding internal reinforcement of the caissons, if any, are unknown. For this study, it was assumed that no internal steel reinforcement was used in the concrete. The results of a dynamic wave equation analysis of a caisson performed by Insuma S.A. during the BYU site reconnaissance in April 2010 (Figure 11-3) suggested that the caissons are 12 meters in length. At the time of the 1991

earthquake, the bridge was simply supported by these caissons and secured with a simple support block as shown in Figure 11-2. The bridge essentially can be modeled as an at-grade crossing because the approach embankment for the rail is relatively small (i.e. <1.5 meters in height).



Figure 11-1: The Rio Bananito Railway Bridge

11.2 Observed Damage Following the 1991 Earthquake

Damage reported at the Rio Bananito Railway Bridge by Priestley et al. (1991) and Youd et al. (1992) following the 1991 Limon earthquake was quite extensive. Significant liquefaction

features such as fissures and sand boils were found parallel to the river bank indicating deformation of the ground in the direction of the river (McGuire, 1994).

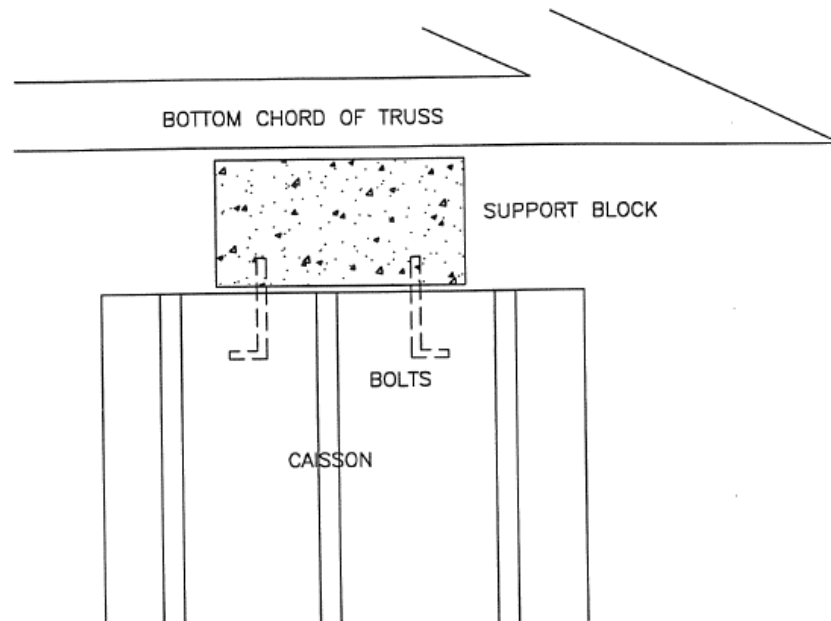


Figure 11-2: Caisson and Support System for the Rio Bananito Railway Bridge (After McGuire, 1994)

Youd et al. (1992) and Priestley et al. (1991) observed that lateral spread displacements at the bridge abutments pushed all four caissons supporting the bridge towards the river. The support blocks from the caisson tops were all sheared, and three of the four caissons lost contact with the bridge truss as shown in Figure 11-4. The downstream caissons rotated more than the upstream caissons, causing the bridge to tilt downward to the east by about 15 degrees. A photo of the tilted bridge is presented in Figure 11-5.

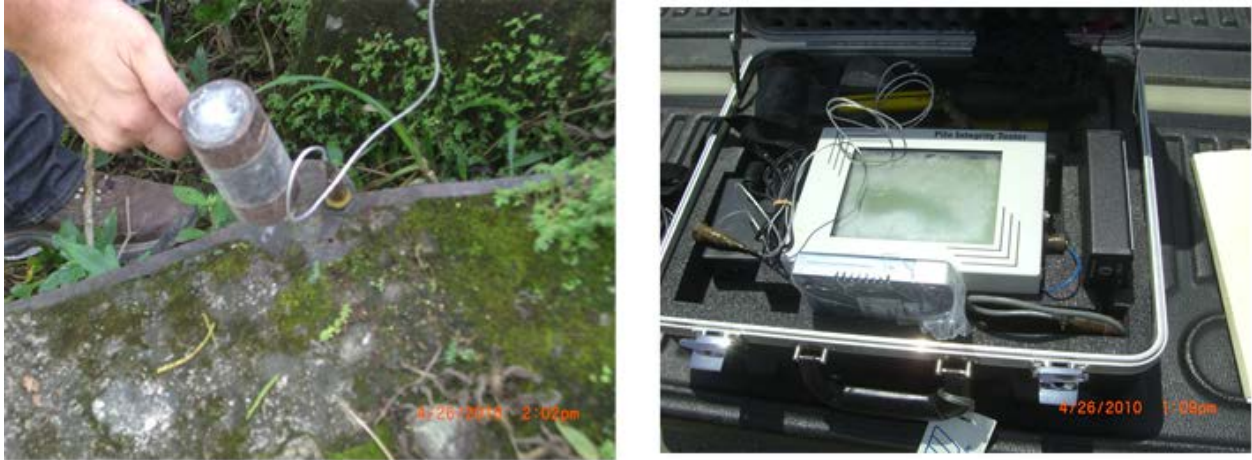


Figure 11-3: Dynamic Wave Equation Analysis Performed at the Rio Bananito Railway Bridge

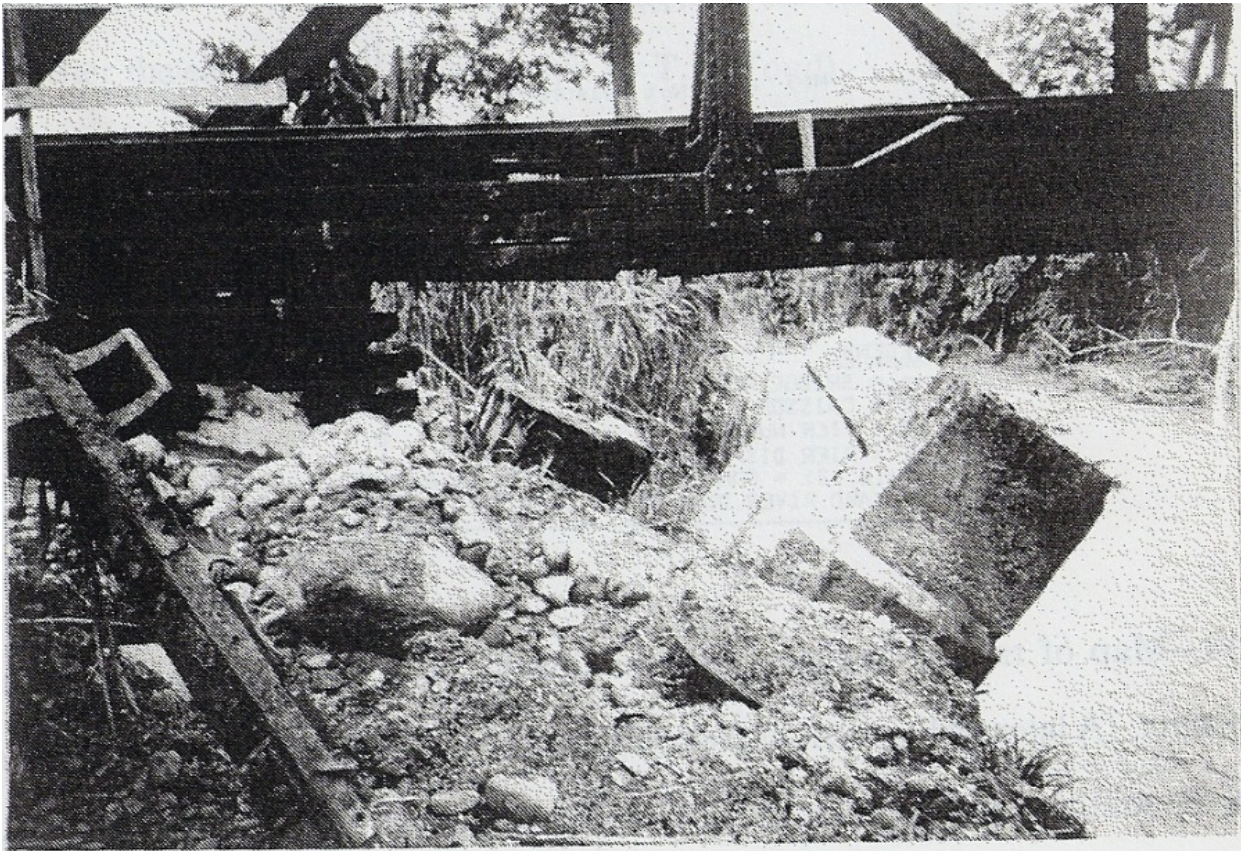


Figure 11-4: Rotated Caissons at the North Abutment of the Rio Bananito Railway Bridge Following the 1991 Limon Earthquake (After Youd, 1993)



Figure 11-5: Damaged Rio Bananito Railway Bridge Following the 1991 Limon Earthquake (After Youd, 1993)

A soccer field located near the north abutment was observed to have lateral spread fissures throughout. The boundaries of the soccer field provided a convenient means to estimate lateral soil deformations for the reconnaissance teams. In addition, the foundations of three houses located near the bridge were cracked and showed fissures running beneath them. The foundation of a house located immediately adjacent to the soccer field was pulled apart by a fissure measured to be 0.378 meter in width. Another house approximately 40 meters south of the bridge was transported northward about 0.5 meter by laterally spread ground. A schematic

plan view of the bridge and the nearby structures at the time of the earthquake is shown in Figure 11-6.

Youd et al. (1992) used three methods to estimate the magnitude of lateral deformations that occurred at the bridge abutments following the 1991 earthquake. Method #1 involved measuring the displaced caissons and retaining walls beneath the abutments relative to their estimated pre-earthquake positions. Method #2 involved summing the fissure widths visible from the ground surface. Method #3 involved comparing the displaced soccer field boundaries with their estimated pre-earthquake positions.

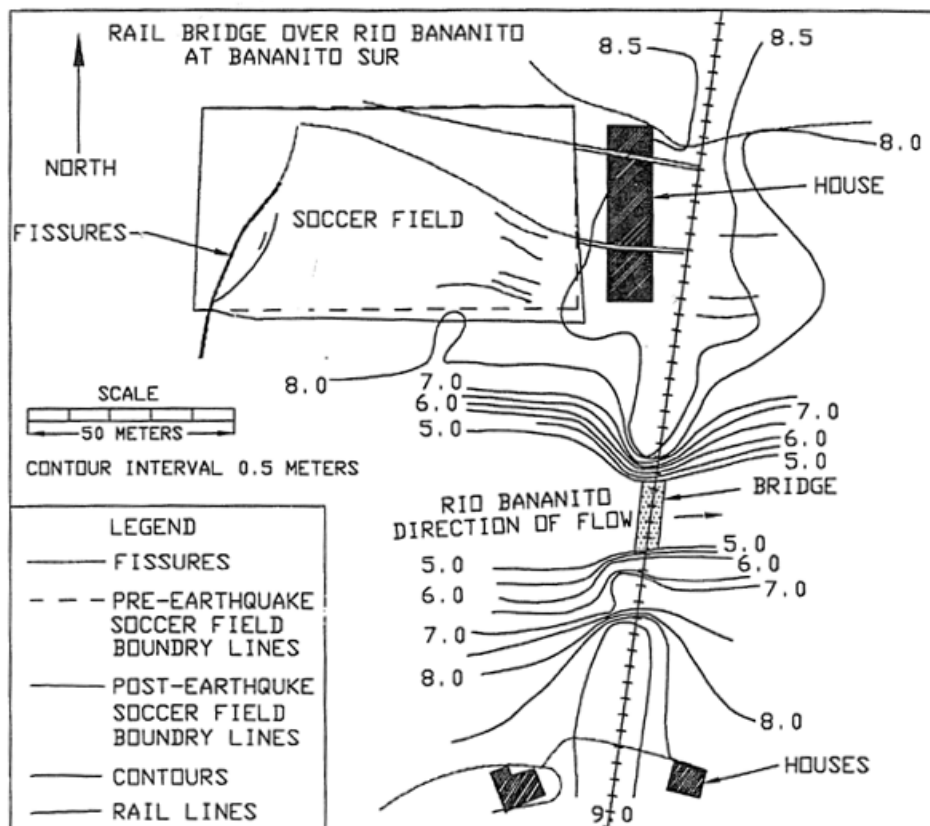


Figure 11-6: Schematic Plan View of the Rio Bananito Railway Bridge and Surrounding Structures at the Time of the 1991 Earthquake (After McGuire, 1994)

The resulting displacements from Method #1 as measured by Youd et al. (1992) and summarized by McGuire (1994) are presented in Table 11-1.

Table 11-1: Measured Displacements From Method #1 (After Youd et al., 1992; McGuire, 1994)

Measured Object		Displacement (m)	Rotation (deg)
North Abutment	Northeast Caisson	4.3	26
	Northwest Caisson	5.7	37
	North Abutment Wall	2.0 – 2.5	---
South Abutment	Southeast Caisson	2.83	19
	Southwest Caisson	1.9	7
	South Abutment Wall	1.0 – 1.5	---

The measured results of Method #2 were summarized in a plan view sketch of both the pre- and post-earthquake positions of the soccer field presented in Figure 11-7.

Finally, Youd et al. (1992) and McGuire (1994) reported that Method #3 indicated cumulative fissure widths measuring 4.171 meters at the north abutment and 0.4-0.8 meter as estimated from photos at the south abutment.

11.3 Soil Site Characterization at the Rio Bananito Railway Bridge

Insuma S.A. Geotechnical Consultants performed two borings in the vicinity of the northern abutment. Boring P-1 was performed 15 meters west from the northern abutment and

was extended to an depth of 14 meters. Boring P-2 was performed about 20 meters to the northwest of Boring P-1 and was extended to an depth of 14 meters.

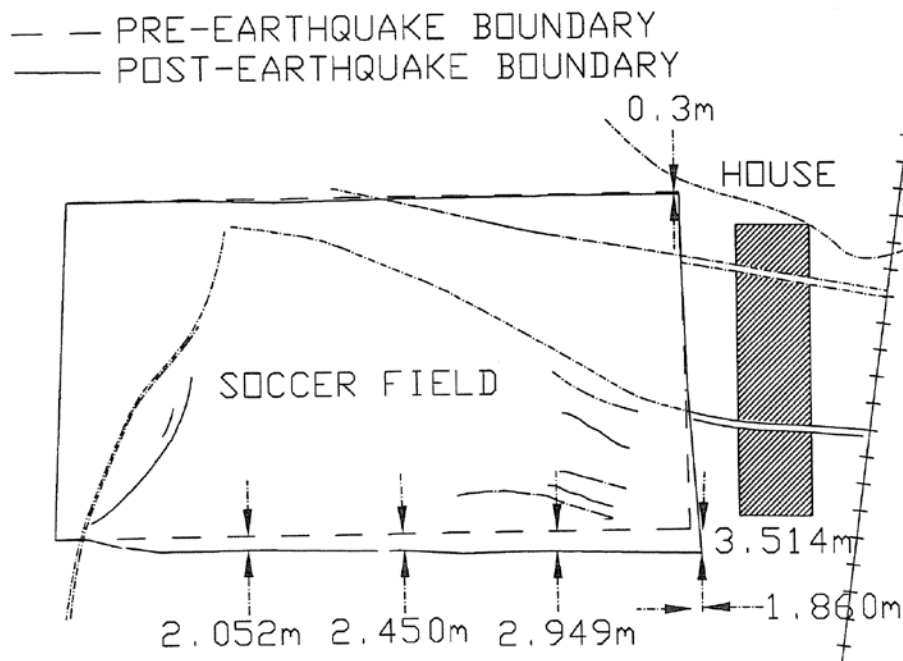


Figure 11-7: Pre- and Post-Earthquake Positions of the Soccer Field Boundaries as Measured in Method #2 (After McGuire, 1994)

The soils encountered in Borings P1 and P2 were reported to consist primarily of very soft to soft clays near the ground surface overlying loose to medium-dense clayey or silty sands. The clays encountered appeared to have medium to high plasticity. The sands encountered appeared to be fine-grained and varied in fines content from about 14-23 percent.

Because absolute elevations were unknown at the time of the BYU site reconnaissance in 2010, elevations relative to a generic value of 100 meters (marking the elevation of the GPS base

station) were used for all of the analyses. The relative elevation of the ground surface at Boring P-1 was measured to be 98.0 meters, and the relative elevation of the ground surface at Boring P-2 was measured to be 99.4 meters. Groundwater was reported by the drillers at a depth of 5.65 meters in Boring P-1 and 6.65 meters in Boring P-2, which correspond to relative elevations of 92.35 meters and 92.75 meters, respectively. It is not unexpected that these relative elevations reported for groundwater appear low because piezometers were not used to obtain a more accurate measurement of the groundwater level and because the native soils represented very low-permeability fat clays. Simple diagrams of the soils encountered in the borings performed are shown in Figure 11-8. Further details regarding the borings at the Rio Bananito Railway Bridge and the corresponding laboratory test results can be found in the Insuma Geotechnical Report included as Appendix A of this report.

For the analysis at the northern abutment at the Rio Bananito Railway Bridge, an averaged profile of the SPT blowcounts was developed. A plot of the averaged SPT values used for the analysis of the Rio Bananito Railway Bridge is shown in Figure 11-9. From Relative Elevation 98 meters to 92 meters, some variability between Borings P-1 and P-2 was observed in the surficial clays. This observation suggests that there are likely some relatively small alluvial deposits of sand scattered throughout the clay layer. Therefore, engineering judgment was applied in modifying the averaged SPT blowcounts in order to better represent a generalized clay layer for modeling purposes.

The information from Borings P-1 and P-2 was used to develop a generalized soil profile for the northern abutment of the Rio Bananito Railway Bridge. Empirical correlations with SPT blowcounts were averaged to estimate the friction angle of granular soils. These correlations include Peck et al. (1974), Hatanaka and Uchida (1996), and Bowles (1977). Relative density of

granular soils was estimated using the empirical correlation presented by Kulhawy and Mayne (1990). Corrected soil modulus estimates K^* of the granular soils for use with the API (1993) p-y relationship were estimated using the recommendations presented by Boulanger et al. (2003). Undrained strength of cohesive plastic soils was averaged from empirical correlations including Hara et al. (1971), Kulhawy and Mayne (1990), and Skempton (1957).

a) Boring P-1			b) Boring P-2		
Depth (m)	SPT N Value		SPT N Value		
0.00 - 0.45	26	Fill that consists in a mixture of GRAVEL and silt.	6	Brown plastic CLAY, medium to high plasticity, very soft to soft consistency.	
0.45 - 0.90	11		2		
0.90 - 1.35	6	3			
1.35 - 1.80	4	3			
1.80 - 2.25	4	3			
2.25 - 2.70	4	3			
2.70 - 3.15	4	3			
3.15 - 3.60	1	Brown plastic CLAY, medium to high plasticity, very soft to soft consistency.	4		
3.60 - 4.05	0		5		
4.05 - 4.50	0		10		
4.50 - 4.95	1		7	Brown clayey SAND, some gravel, loose.	
4.95 - 5.40	2	9			
5.40 - 5.85	3	Greenish gray plastic CLAY, mixed with a fraction of sand size particles, soft.	8	Brown silty SAND, fines with low plasticity, loose relative density.	
5.85 - 6.30	7		13		
6.30 - 6.75	7		19		
6.75 - 7.20	7	Gray or brownish gray clayey SAND, mixed with particles of gravel, fines with medium plasticity, loose to dense relative density.	7	Gray or brownish gray clayey SAND, mixed with particles of gravel, fines with medium plasticity, loose to dense relative density.	
7.20 - 7.65	15		8		
7.65 - 8.10	20		11		
8.10 - 8.55	8		4		
8.55 - 9.00	24		23		
9.00 - 9.45	36		36		
9.45 - 9.90	20		16		
9.90 - 10.35	16		21		
10.35 - 10.80	19	Greenish gray clayey SAND, fines with low to medium plasticity, predominantly medium relative density.	9	Gray or greenish gray silty SAND, fines have no or very little plasticity, medium relative density.	
10.80 - 11.25	21		28		
11.25 - 11.70	25		15		
11.70 - 12.15	23		20		
12.15 - 12.60	6		16		
12.60 - 13.05	17		27		
13.05 - 13.50	24		26		
13.50 - 13.95	18		22		

Figure 11-8: (a) Boring P-1 and (b) Boring P-2 Performed at the Rio Bananito Railway Bridge

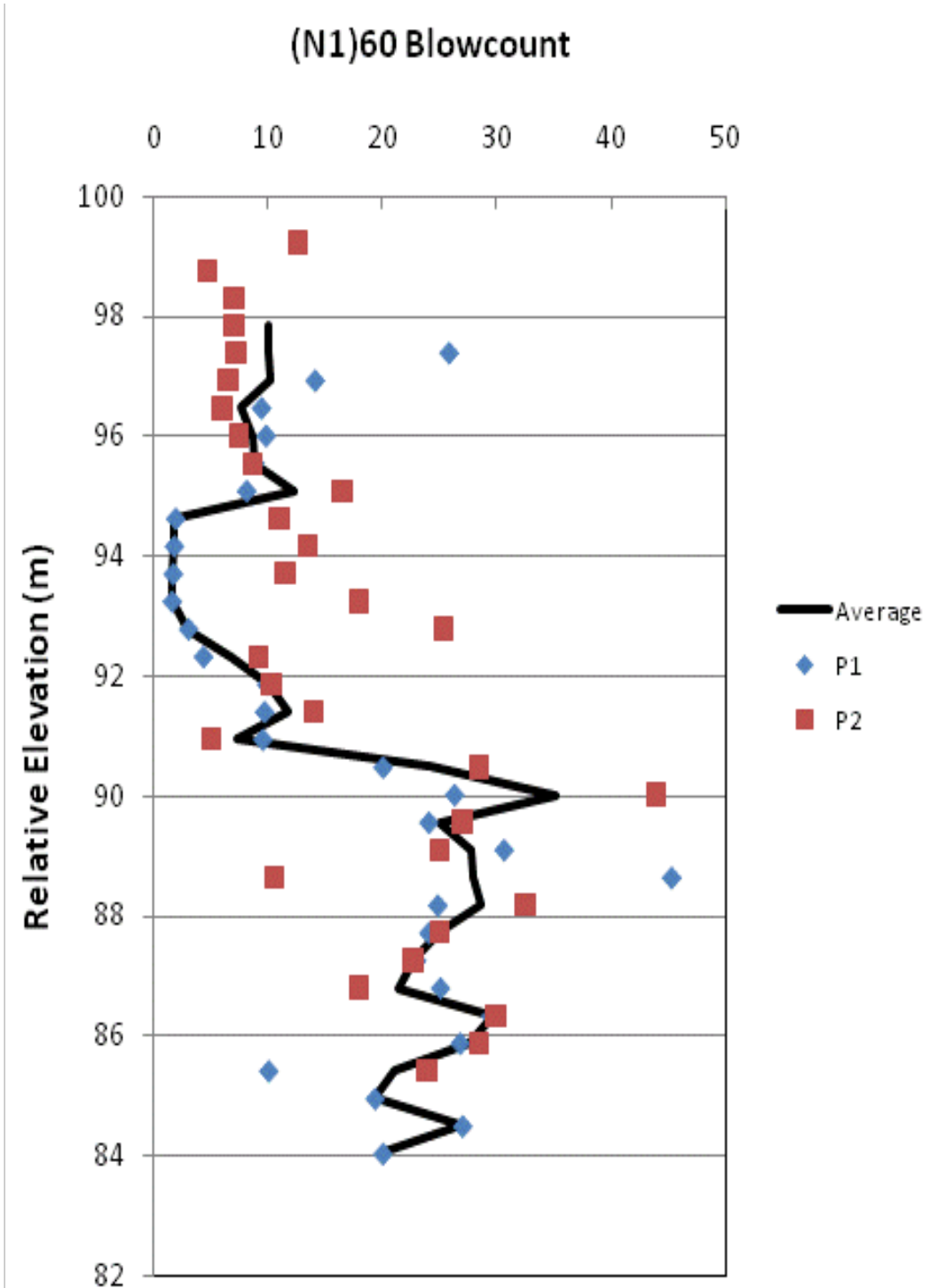


Figure 11-9: Averaged SPT Blowcounts for the North Abutment at the Rio Bananito Railway Bridge

Field measurements of the shear strength of the surficial clays were also performed using simplified tests including the torvane and the pocket penetrometer (Figure 11-10). These field measurements showed remarkably good agreement for the clays between Relative Elevations 93 meters and 96 meters (i.e. up to 3 meters in height above the water level). At relative elevations higher than 96 meters, the field measurements showed greater shear strengths and more variability between the torvane and the pocket penetrometer. This trend could be due to dessication of the near-surface soils and/or increased sand content in the clay. In addition, shear strength parameters using Stress History and Normalized Soil Engineering Properties (SHANSEP) theory (Ladd and Foott, 1974) were estimated by fitting the parameters to the available field measurements and SPT correlations. Greater weight was given to the field measurements due to the reasonably good agreement between the torvane and pocket penetrometer results. The shear strength measurements using the various approaches described above are shown in Figure 11-11. The computed values of S , OCR , and m for the SHANSEP parameters are 0.25, 1.8, and 0.85, respectively. A minimum undrained shear strength value of 20 kPa could be used in conjunction with SHANSEP strength parameters due to the high plasticity of the clay. For simplification, a uniform undrained strength of 27 kPa was used in the LPILE pile response analyses for this study.

Assumptions regarding the unit weight of the native soil as well as the strength properties of the embankment fill were made. Groundwater was modeled at a relative elevation of 93 meters (i.e. an estimated depth of 5.0 meters below the ground surface). Table 11-2 summarizes the resulting generalized model of the soil profile at the north abutment of the Rio Bananito Railway Bridge.



Figure 11-10: Torvane Testing at the Rio Bananito Railway Bridge

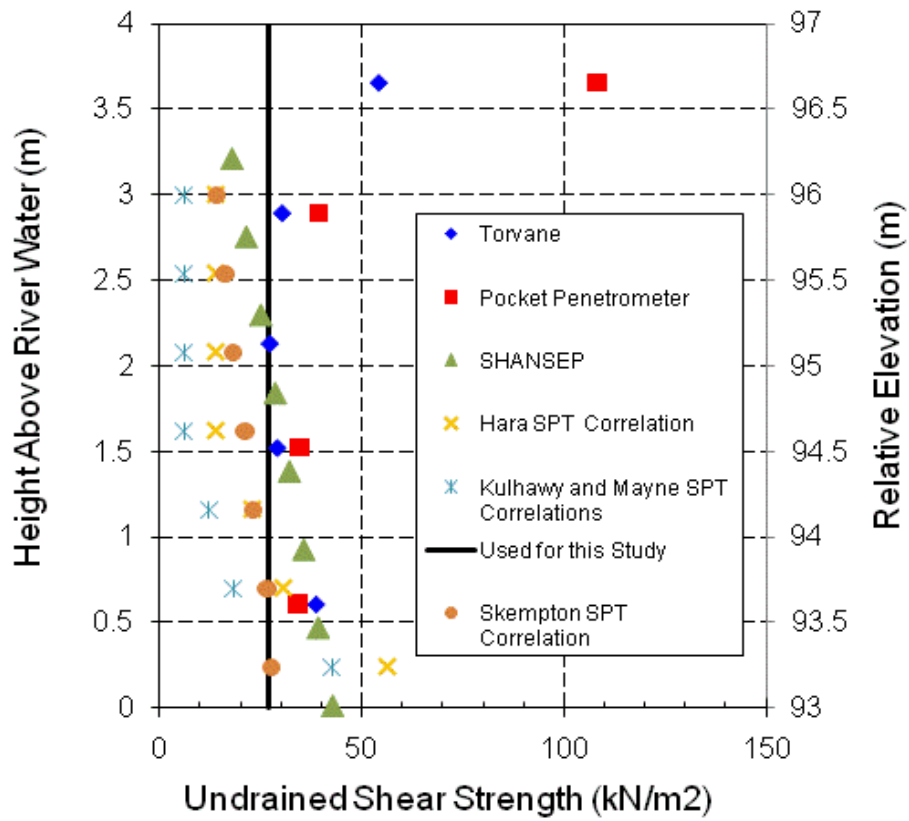


Figure 11-11: Shear Strength Data From the North Abutment at the Rio Bananito Railway Bridge

Table 11-2: Generalized Soil Profile for the North Abutment at the Rio Bananito Railway Bridge

Top Depth (m)	Top Elevation (m)	Thickness (m)	USCS Soil Class	Friction Angle (deg)	Moist Unit Weight (kN/m ³)	Undrained Strength (kPa)	Relative Density (%)	Corrected Soil Modulus (kN/m ³)	Liquefied p-mult
0	98.0	6.0	CH	---	18.85	27	---	---	NA
6.0	92.0	1.4	SC	32	8.25	---	45	8,800	0.12
7.4	90.6	3.7	SC/SM	37	9.00	---	68	16,200	0.43
11.1	86.9	2.8	SC/SM	35	9.00	---	58	11.150	0.28

11.4 Characterization of Site Geometry/Topography at the Rio Bananito Railway Bridge

The surface geometry at the Rio Bananito Railway Bridge is relatively flat in the surrounding river plain, but steep in the river channel itself. According to the results of the GPS site survey performed during the BYU site reconnaissance team in April 2010, the relative ground surface elevation at each abutment is approximately 98 meters. The approximate relative ground surface elevation of the bottom of the river was measured as 91 meters. The slope of the river channel was measured as 1.5H:1V. The relative elevation of the water surface in the Rio Bananito was measured to be 93 meters at the time of the BYU investigation. A sketch of relative elevation contours based on the 2010 BYU GPS survey as well as the locations of the two 2010 Insuma geotechnical borings is presented in Figure 11-12. A sketch of the plan and profile views of the site geometry together with the approximate locations of the caissons is presented in Figure 11-13.

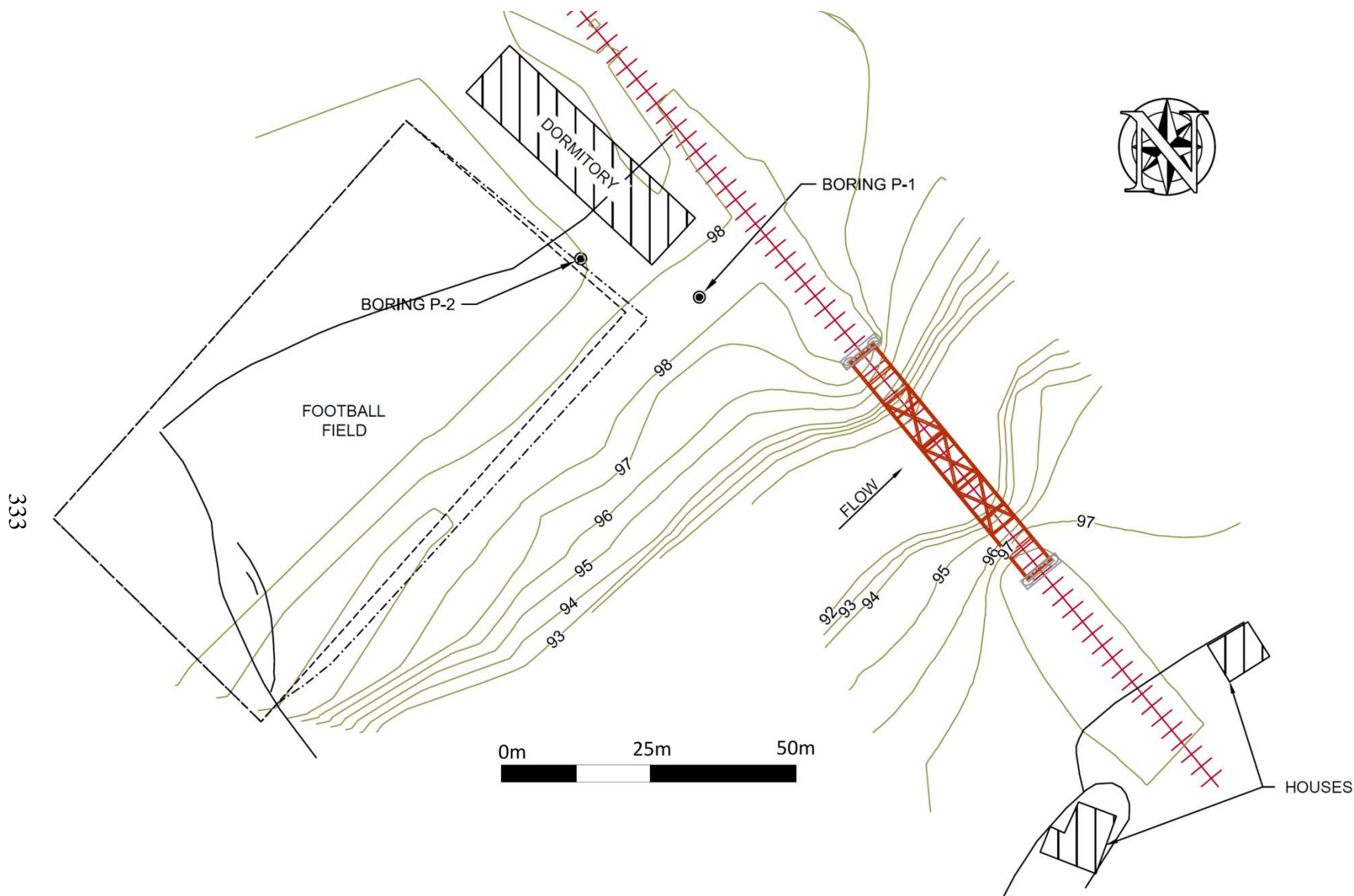


Figure 11-12: Contour Sketch of the Rio Bananito Railway Bridge

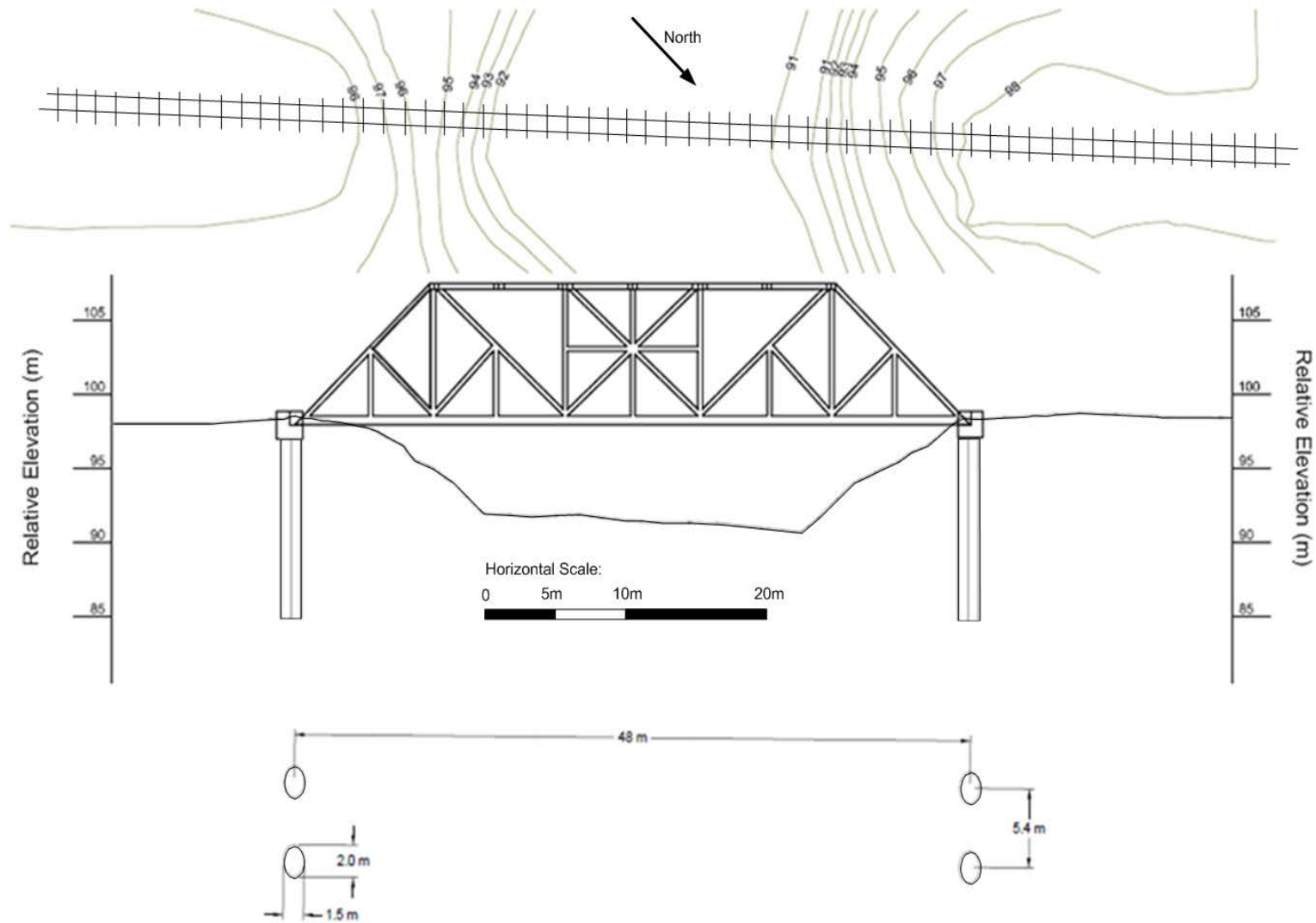


Figure 11-13: Simplified Sketch of the Plan and Profile Views of the Rio Bananito Railway Bridge

11.5 Deterministic Pile Response Analysis at the Rio Bananito Railway Bridge

11.5.1 Deterministic Ground Motion Evaluation From the 1991 Earthquake

The Rio Bananito Railway Bridge is located 22 kilometers north from the epicenter of the April 22, 1991 earthquake. Assuming an average V_{S30} value of 270 m/s, the average computed median spectral acceleration along with median $\pm 1\sigma$ from the four selected NGA models are shown in Figure 11-14. The median computed PGA and spectral accelerations corresponding to 0.2-second and 1.0-second are 0.231g, 0.483g, and 0.318g, respectively.

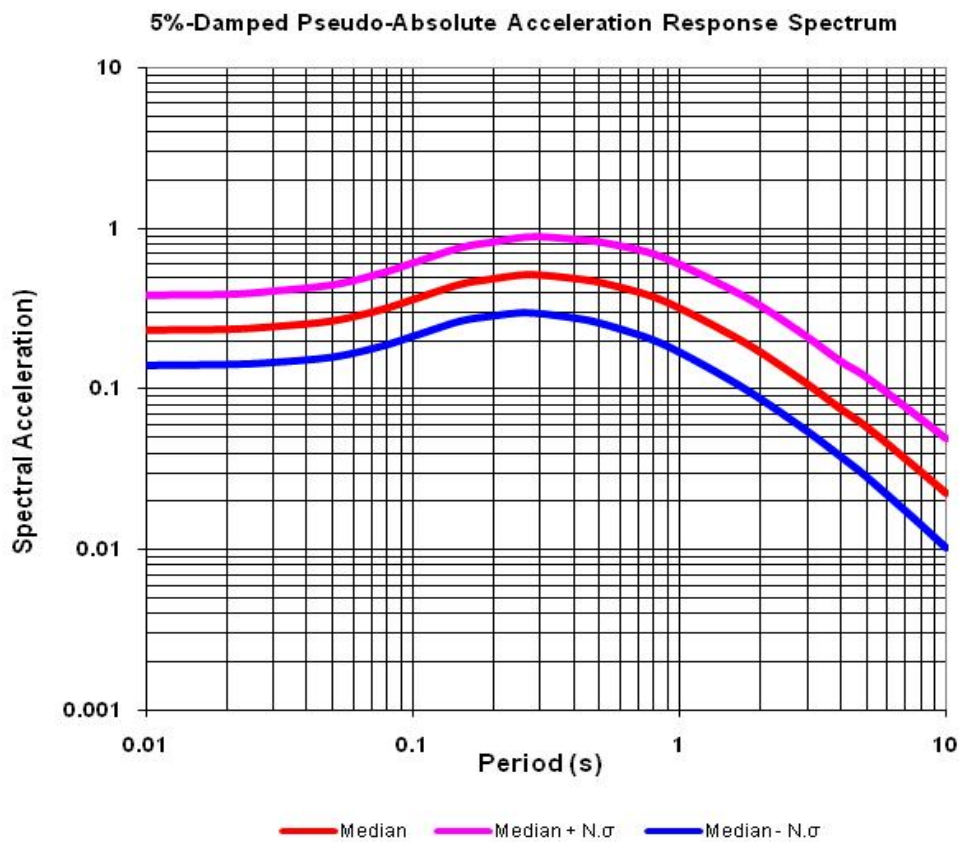


Figure 11-14: Computed Deterministic Response Spectra for the Rio Bananito Railway Bridge From the 1991 Earthquake. $N = 1$

11.5.2 Deterministic Liquefaction Evaluation From the 1991 Earthquake

Using the average deterministic ground motions from the NGA equations, the deterministic liquefaction triggering was evaluated at the Rio Bananito Railway Bridge for the M7.6 1991 Limon earthquake using the SPT blowcounts from both Borings P-1 and P-2. The results of the deterministic liquefaction triggering analysis are shown in Figure 11-15 and Figure 11-16. This evaluation included consideration of the Cetin et al. (2004), Idriss and Boulanger (2008), and Youd et al. (2001) simplified procedures for liquefaction triggering. In general, good agreement was observed between the three procedures. The results of the analysis at Boring P-1 suggest that liquefaction triggers from depths of 6.9 meters to 7.3 meters below the ground surface (R.EL 91.1m to R.EL 90.7m) and from depths of 7.8 meters to 8.2 meters below the ground surface (R.EL 90.2m to R.EL 89.8m). In addition, occasional thin layers of sand are shown to liquefy below depths of about 12.3 meters (R.EL 85.7m). The results of the analysis at Boring P-2 suggest that liquefaction triggers from depths of 7.0 meters to 8.9 meters below the ground surface (R.EL 92.4m to R.EL 90.5m). In addition, occasional thin layers of sand are shown to liquefy below depths of about 10.7 meters (R.EL 88.7m). Though there is a small discrepancy in the elevations of the principle liquefiable layers between Borings P-1 and P-2, it is likely that there is a continuous liquefiable layer near the ground surface that likely governed the observed soil deformations following the 1991 Limon earthquake.

11.5.3 Post Earthquake Slope Stability

A simple post earthquake slope stability evaluation was performed for the north bank of the Rio Bananito Railway using SLOPE/W analysis software (GEO-SLOPE, 2010).

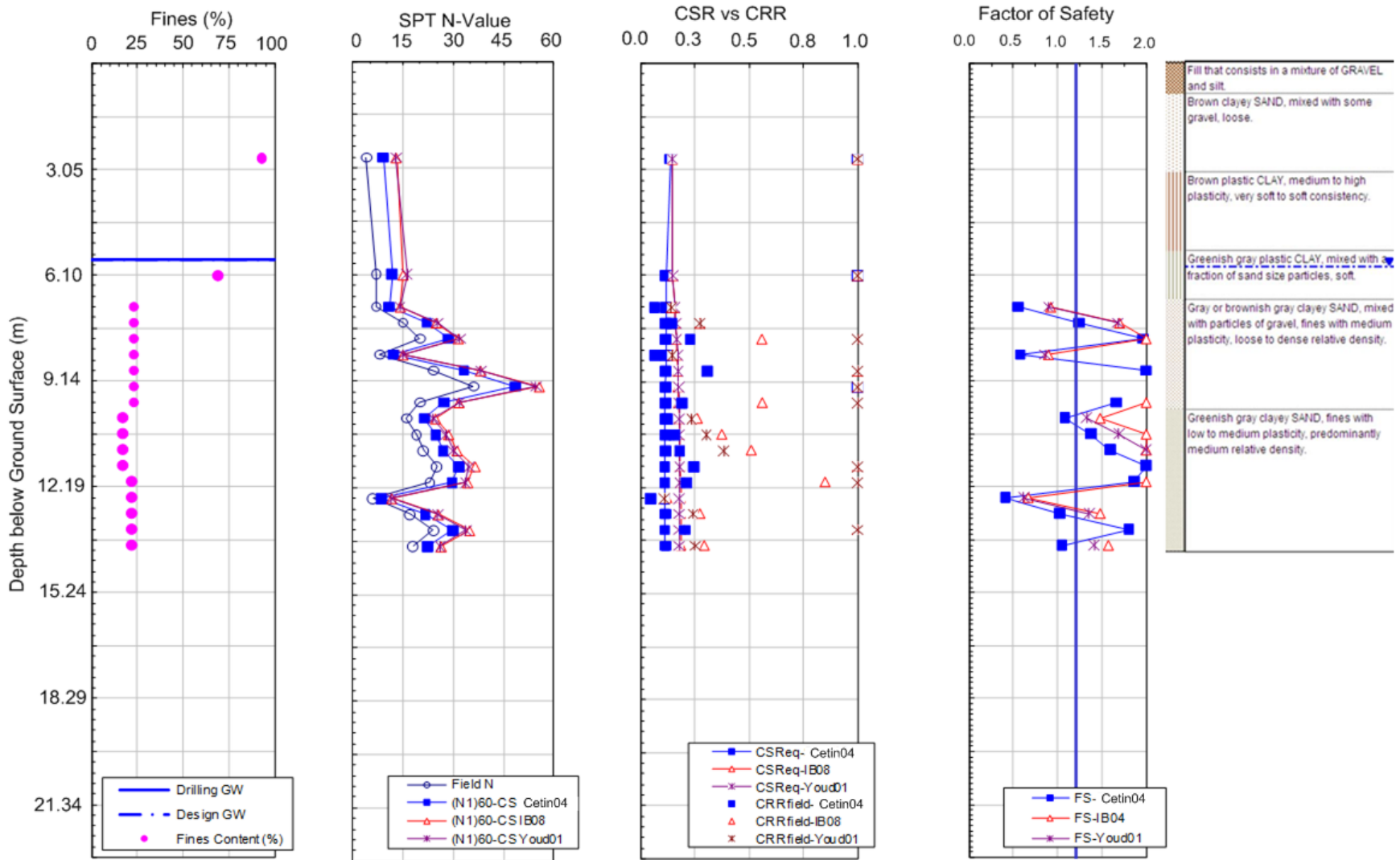


Figure 11-15: Deterministic Liquefaction Triggering Results From Boring P-1 for the M7.6 1991 Limon Earthquake at the Rio Bananito Railway Bridge

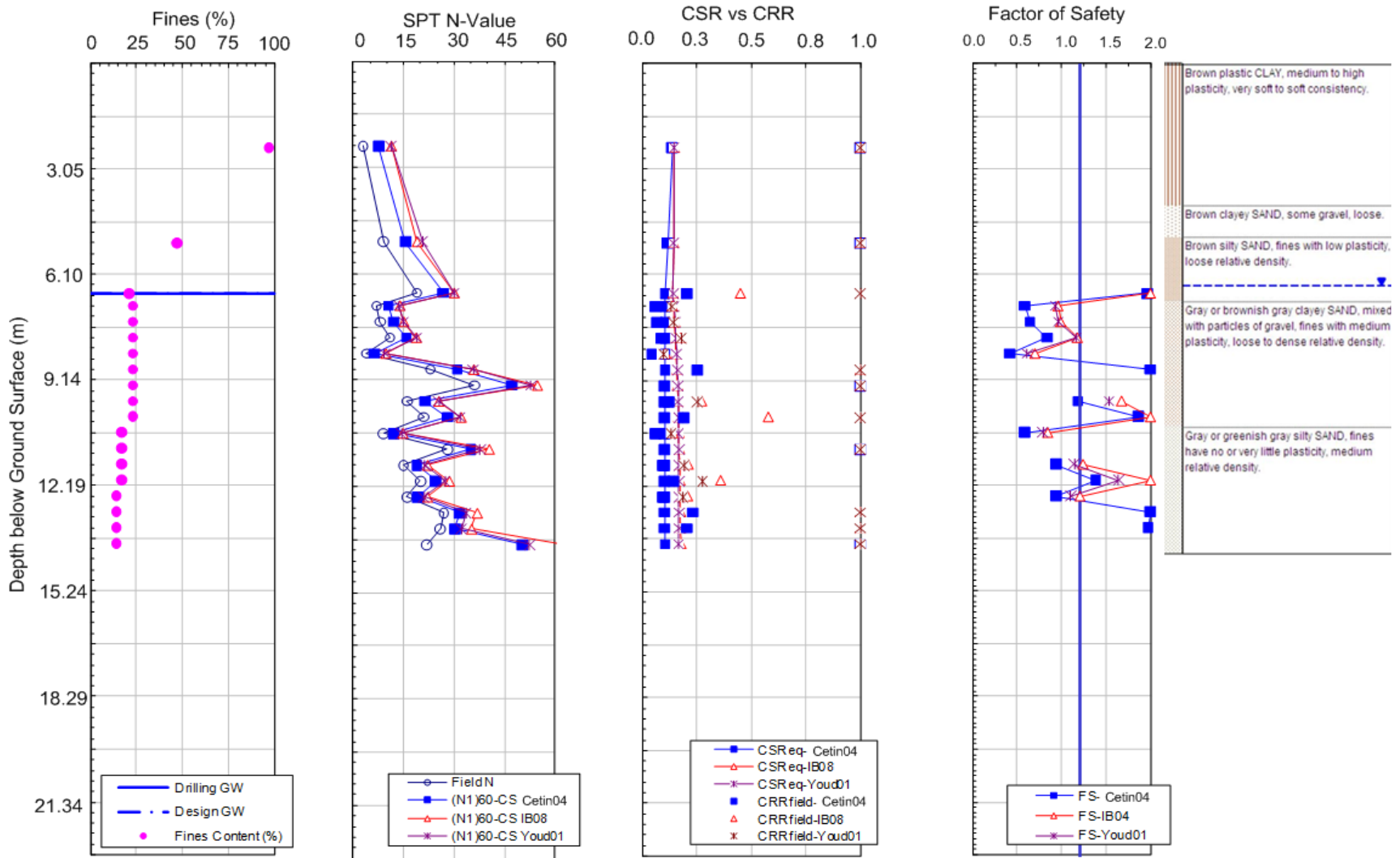


Figure 11-16: Deterministic Liquefaction Triggering Results From Boring P-2 for the M7.6 1991 Limon Earthquake at the Rio Bananito Railway Bridge

In evaluating the slope stability, only native soils were considered in the analysis in order to investigate the potential for flow liquefaction failure along the river bank. Such a failure would likely disqualify the use of empirical lateral spread models for computing lateral spread displacements in the native soils along the river bank.

Undrained strengths of fined-grained soils were reduced by 20-percent in accordance with recommendations by Makdisi and Seed (1977). The residual strength ratio S_r/σ' of the liquefied soil was computed using the Ledezma and Bray (2010) as given in Equation (2-2). Lowe and Karafiath (1960) was used in the limit equilibrium analysis to compute factor of safety. A circular surface search routine was utilized allowing for optimization in order to allow for the possibility of non-linear or log-spiral failure surfaces. A summary output from the post earthquake slope stability evaluation is presented in Figure 11-17. The computed factor of safety was 1.08, which is relatively low and likely would not meet the post-earthquake stability requirements specified by most agencies and organizations. However, because the factor of safety is still greater than 1.0, this study will assume that lateral spread displacements governed the observed soil deformations at the north abutment of Rio Bananito Railway Bridge rather than a liquefaction flow failure.

11.5.4 Deterministic Evaluation of Lateral Spread

Empirical evaluation of the free-field soil displacements due to lateral spread was performed using the Youd et al. (2002), Bardet et al. (2002), and Baska (2002) models. The analysis assumed an earthquake magnitude of 7.6, a source-to-site distance of 22 kilometers, a free-face ratio of 67-percent, and a free-face height of 6 meters. The averaged SPT blowcounts shown in Figure 11-9 were used in the analysis.

Name: Fat Clay #1 (Seismic) Model: S=f(overburden) Unit Weight: 18.3 kN/m³ Tau/Sigma Ratio: 0.33 Minimum Strength: 20
 Name: Clayey Sand #1 Model: Mohr-Coulomb Unit Weight: 18.85 kN/m³ Cohesion: 2.4 kPa Phi: 37 °
 Name: Clayey Sand #2 Model: Mohr-Coulomb Unit Weight: 18.85 kN/m³ Cohesion: 2.4 kPa Phi: 35 °
 Name: Liquefied Soil (Sr/Sig') Model: S=f(overburden) Unit Weight: 18.06 kN/m³ Tau/Sigma Ratio: 0.15 Minimum Strength: 11

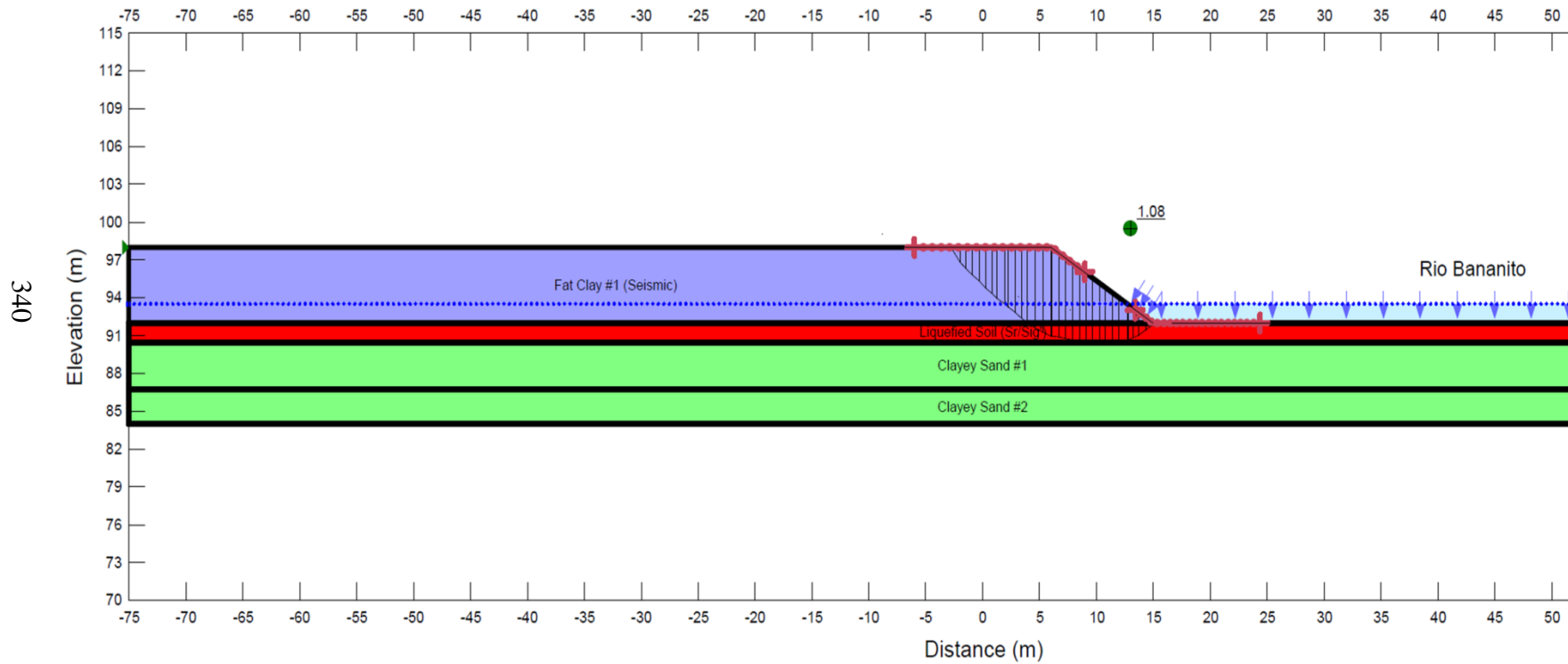


Figure 11-17: Post Earthquake Slope Stability Analysis at the Rio Bananito Railway Bridge

The mean grain size diameter for the generalized boring was estimated from Insuma sieve results for Borings P-1 and P-2. While a free-face ratio of 67-percent is a significant extrapolation beyond the maximum recommended value of 20-percent for the empirical models, the value was used nonetheless in order to properly represent the geometry at the bridge abutment. The median computed lateral spread displacement value and the 95th-percentile confidence interval for each of the three empirical models is shown in Figure 11-18. The average computed median displacement from the three models is 2.63 meters, which is within the range but near the low end of the lateral spread displacements measured by Youd et al. (1992) and reported by McGuire (1994).

Because measured field displacements were available for the Rio Bananito Railway Bridge, a lateral spread surface displacement of 3.85 meters was used for the deterministic evaluation of pile response in this study. The estimated lateral spread displacement profile for the M7.6 1991 Limon earthquake was computed according to the procedure presented in Sections 3.6 and 3.7 of this dissertation in conjunction with the liquefaction triggering profiles shown in Figure 11-15 and Figure 11-16. This displacement profile is shown in Figure 11-19.

11.5.5 Pile Response Analysis

Because the bridge plans for the Rio Bananito Railway Bridge did not contain any details regarding the reinforcing details of the caissons, it was assumed that there was no reinforcing steel in the interior of the caissons for the computation of the initial composite flexural stiffness (i.e. EI). The resulting composite initial flexural stiffness of a single caisson was computed to be 13,312 MN-m². Because the caissons have a non-circular cross-section that is not included in the nonlinear analysis module of LPILE and are comprised of sheet piles instead of a solid steel shell, a linear elastic analysis was used to the kinematic loading behavior of the caissons. A rough

estimate of the yield and plastic moments for a single caisson was computed by analyzing a 2.16m-diameter circular caisson in a nonlinear LPILE piler response analysis. The yield moment for the circular caisson was computed to be 1,300 kN-m and the plastic moment was computed to be 7,900 kN-m. This approach likely over-computed the true yielding and plastic moments slightly due to the elliptical geometry of the actual caisson.

Because each abutment consists of a single row of two independent caissons, the equivalent single pile approach was not used for the kinematic pile response analysis at the Rio Bananito Railway Bridge. Rather, the kinematic pile response for a single caisson was evaluated. Due to the lack of a pile cap or any other stiffening element resisting the rotation of the caisson head, a free-head boundary condition was applied in the model.

Applying the lateral spread deformations shown in Figure 11-19 to a single caisson, the LPILE deterministic pile response from the 1991 Limon earthquake is shown in Figure 11-20.

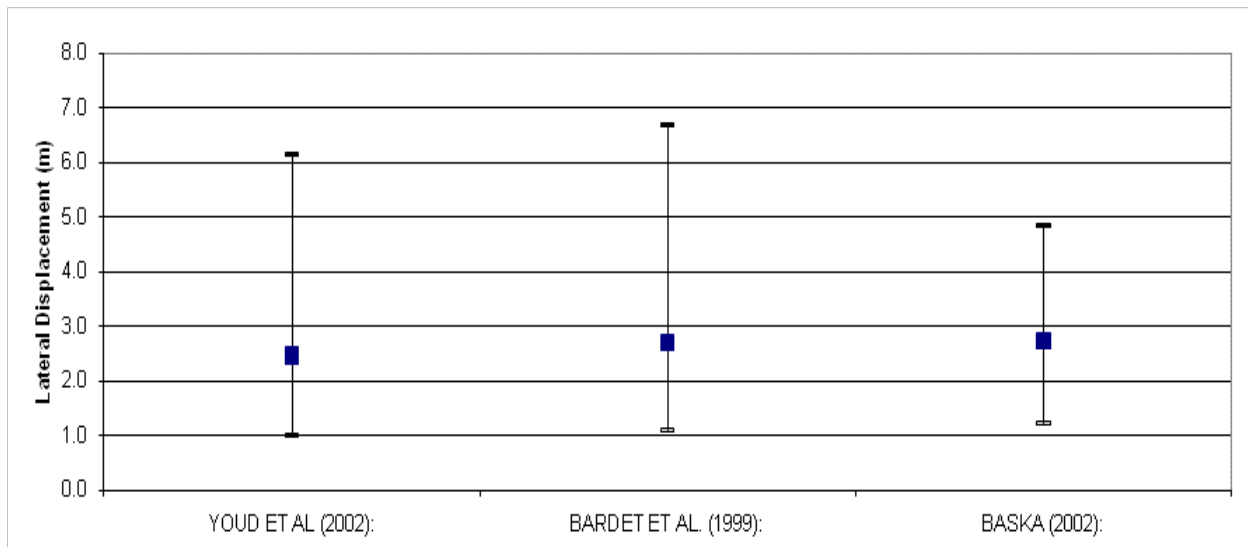


Figure 11-18: Deterministic Median and 95-Percentile Evaluations of Lateral Spread Displacement Using Select Empirical Models for the Rio Bananito Railway Bridge

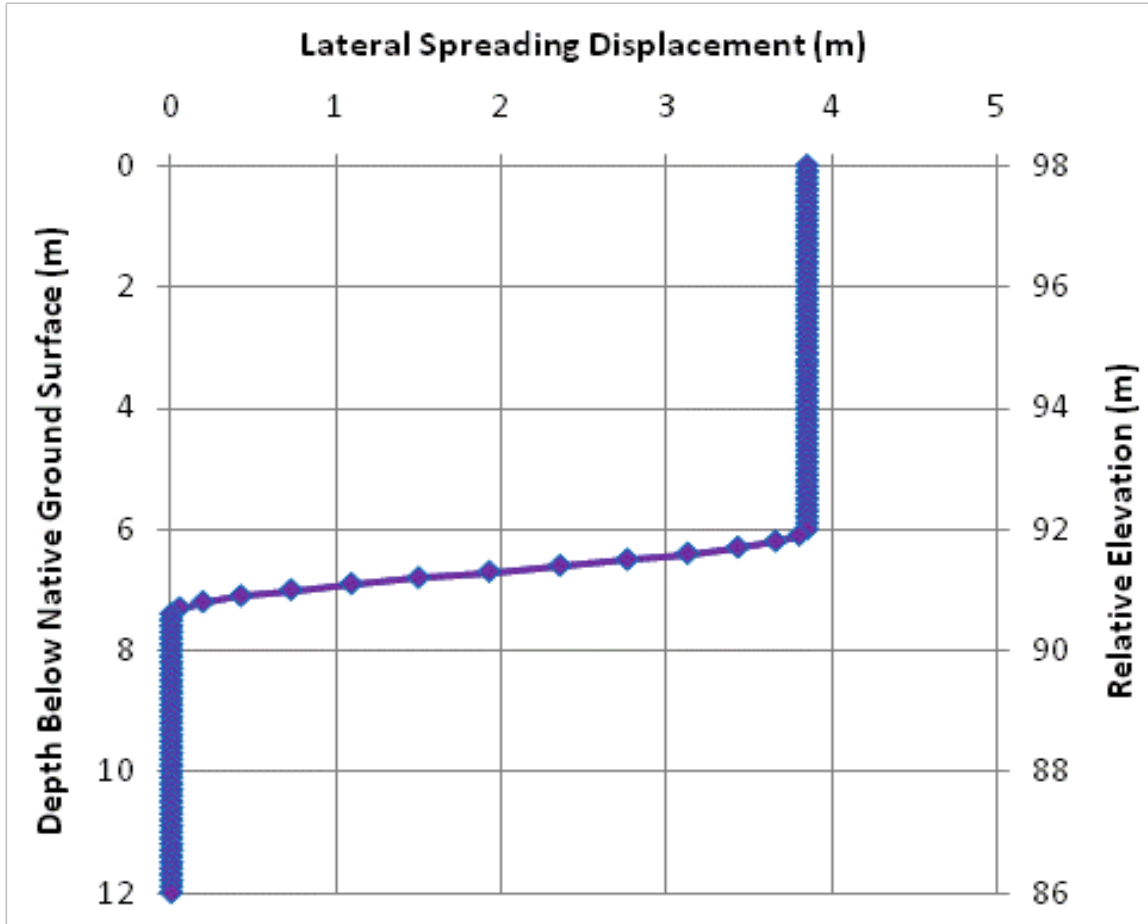


Figure 11-19: Computed Lateral Spread Displacement Profile at the Rio Bananito Railway Bridge for the M7.6 1991 Limon Earthquake

11.5.6 Summary of Deterministic Results

In general, the deterministic analysis reasonably replicated the response of the bridge foundation to the earthquake. Using a surface lateral spread displacement of 3.85 meters, a head displacement of 4.83 meters and a rotation of approximately 30 degrees was computed for the caisson. These values correspond well with the 4.3-5.7 meters of displacement and 26-37 degrees of rotation as measured by Youd et al. (1992) for the caissons at the north abutment.

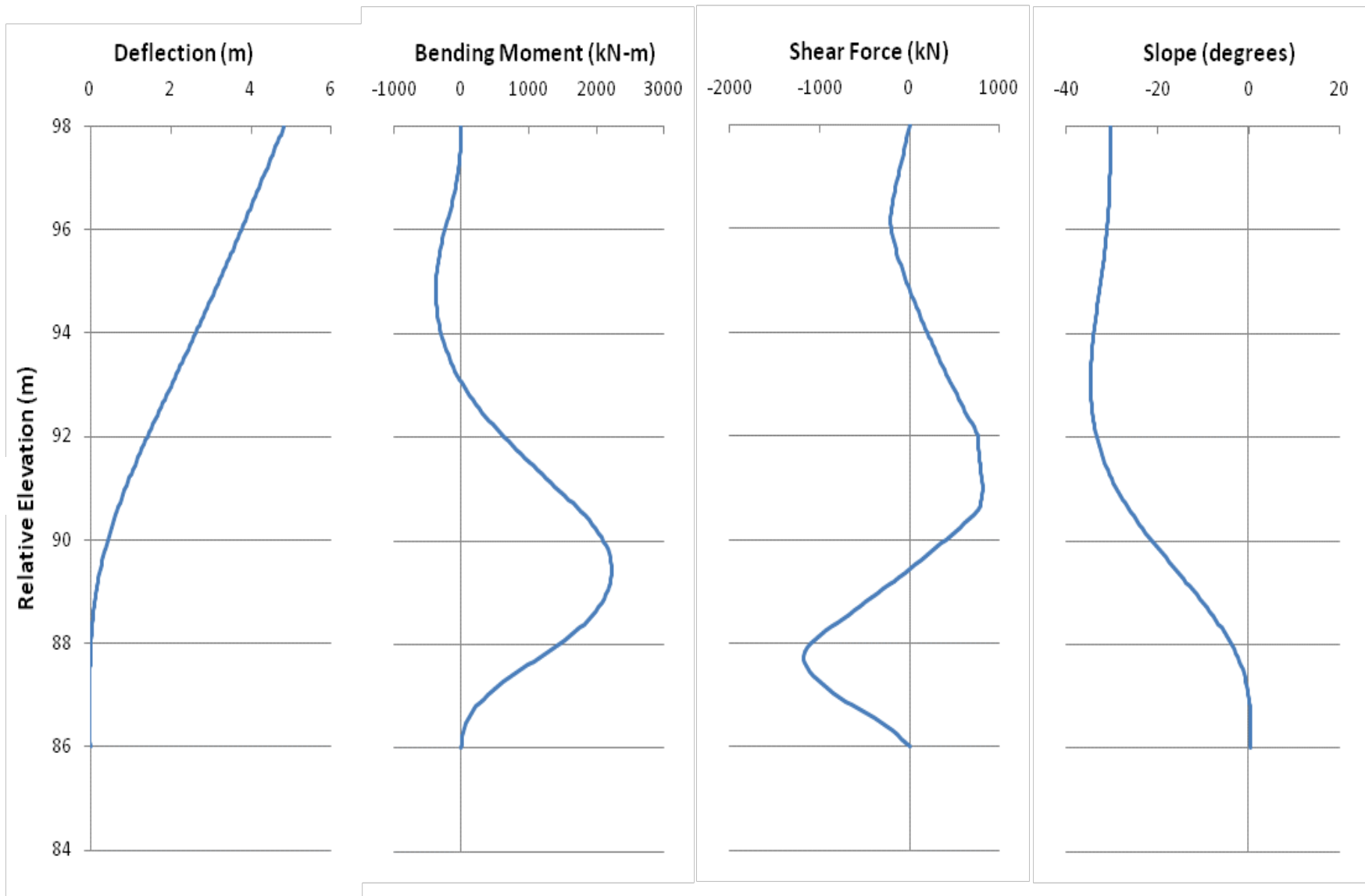


Figure 11-20: Deterministic Computed Pile Response for the Rio Bananito Railway Bridge North Abutment From the 1991 Limon Earthquake

In addition to the good match between the observed and computed caisson displacements/rotations, the results from the dynamic wave equation analysis at the caisson suggest that concrete cracking occurred between depths of 8 to 9 meters below the head of the caisson (i.e. R. EL. 90m-89m), which corresponds well with the relative elevation of maximum computed moment in our analysis. Because the peak bending moment exceeds the computed yield moment of 1,300 kN-m, it is likely that yielding of the caisson occurred resulting in cracking of the concrete.

11.6 Performance-Based Pile Response Analysis at the Rio Bananito Railway Bridge

11.6.1 Probabilistic Ground Motions

A PSHA was performed at the Rio Bananito Railway Bridge site using EZ-FRISK software and the built-in seismic source model for Central and South America developed by Risk Engineering (see Risk Engineering documentation included in Appendix B). This seismic source model included both area and fault sources. The four selected NGA attenuation models (Abrahamson and Silva, 2008; Chiou and Youngs, 2008; Campbell and Bozorgnia, 2008; and Boore and Atkinson, 2008) were assigned to crustal seismic sources, and select attenuation models developed for subduction zones (Youngs et al., 1997; Atkinson and Boore, 2003; and Zhao et al., 2006) were assigned to the subduction seismic sources. Finally, near-source and directivity effects were accounted for in the PSHA by incorporating the fault-normal response spectrum modifications presented by Somerville et al. (1997) and Abrahamson (2000) for all fault sources. A table of the fault sources located within about 100 km of the site is presented in Table 11-3.

Table 11-3: EZ-FRISK Faults Within About 100 km of the Rio Bananito Railway Bridge

Fault Name	Type	Fault Length (km)	Source to Site Distance (km)	Characteristic Magnitude	Slip Rate (mm/yr)	Recurrence Rate
Limon fault	Reverse	162	8.0	7.8	1.0	---
Panama - North (Caribbean)	Subduction Interface	817	35	8.0	4.0	---
Guapiles fault	Reverse	8	93	6.1	4.0	---
Longitudinal fault	Reverse	42	102	7.4	0.1	---
Longitudinal fault - Costa Rica 2	Reverse	52	102	7.0	0.5	---
Costa Rica	Subduction Intraslab	288	105	7.7	---	0.4958

The seismic hazard curve for the PGA developed from the PSHA is presented in Figure 11-21. The ground motions corresponding 10-percent and 2-percent probabilities of exceedance in 50 years (i.e. return periods of 475 and 2475 years, respectively) are 0.557g and 0.916g, respectively.

The seismic hazard contributions from the individual sources are shown in Figure 11-22. From Figure 11-22, it appears that the Costa Rica arc and shear zone (area source), the Costa Rica fault (subduction interface source), and the Panama North (Caribbean) fault (subduction interface source) govern the probabilistic seismic hazard at most return periods for the PGA. The probabilistic response spectra developed from the PSHA for seven different return periods are shown in Figure 11-23. Finally, simplified deaggregation plots of the PGA are presented in Figure 11-24.

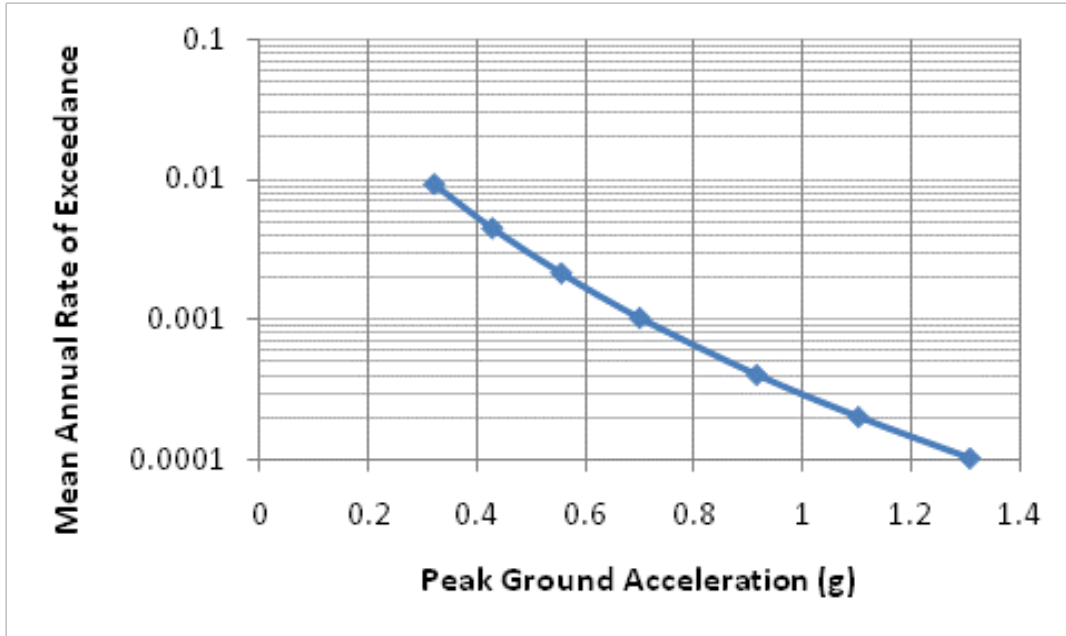


Figure 11-21: Seismic Hazard Curve for the PGA at the Rio Bananito Railway Bridge

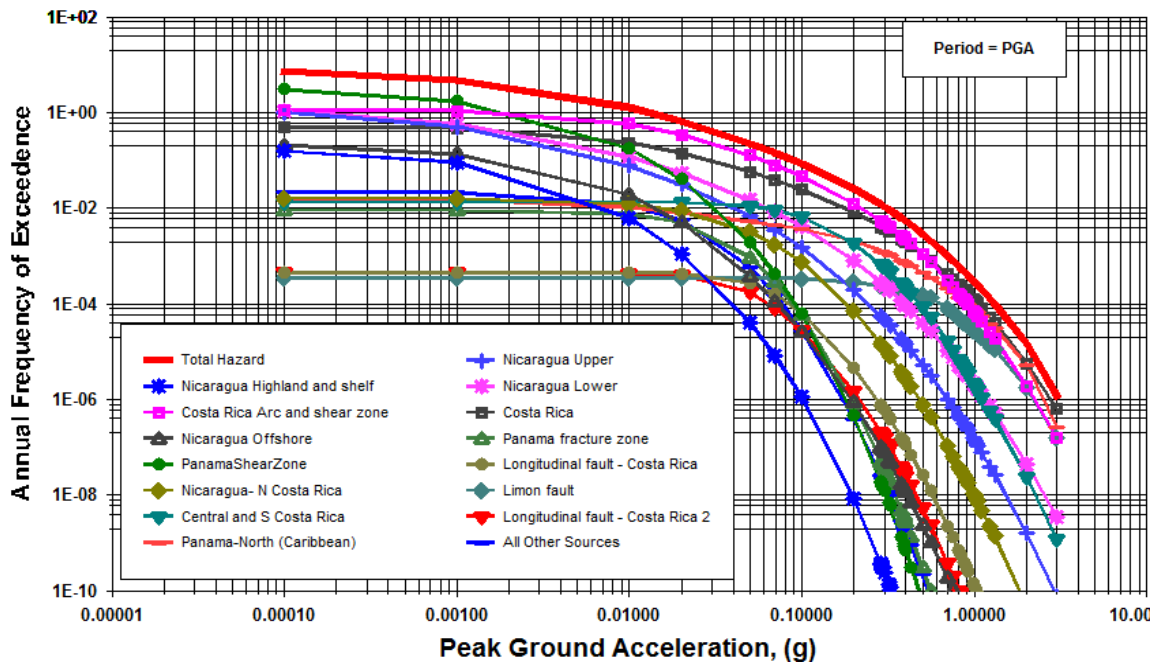


Figure 11-22: Source Contributions to Probabilistic Seismic Hazard for the Rio Bananito Railway Bridge

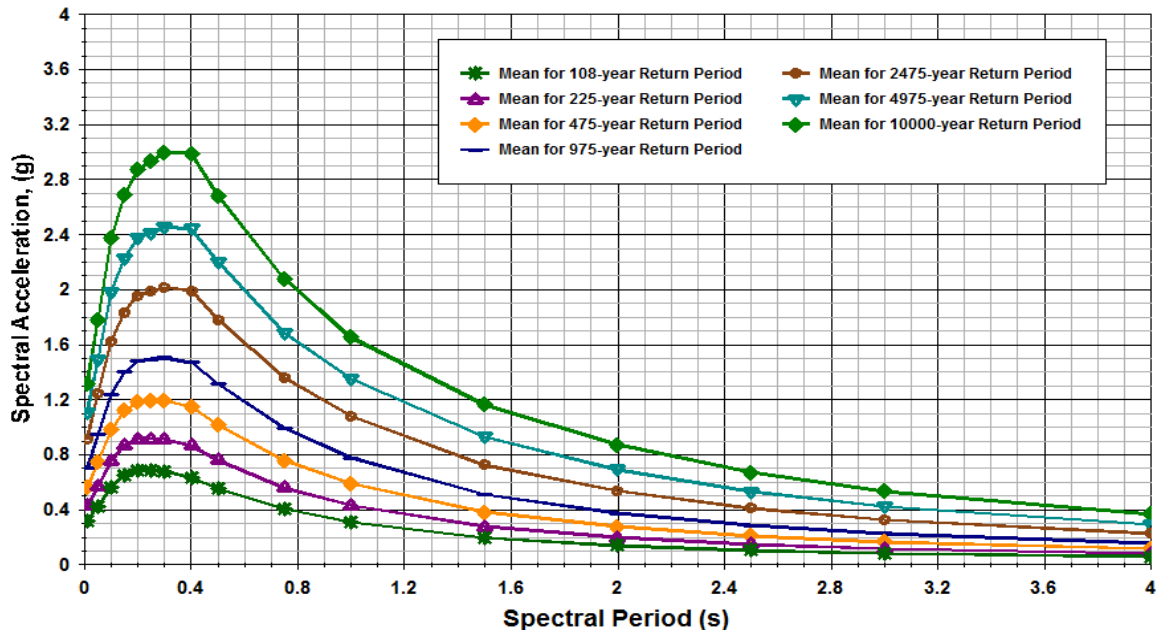


Figure 11-23: Probabilistic Response Spectra (5-Percent Damping) for the Rio Bananito Railway Bridge

11.6.2 Probabilistic Liquefaction Triggering

Using the probabilistic estimates of a_{max} shown in Figure 11-21 in conjunction with the magnitude/distance deaggregations shown in Figure 11-24, probabilistic estimates of liquefaction triggering were computed with the Kramer and Mayfield (2007) procedure using Equations (6-1) and (6-2). The performance-based liquefaction triggering computations were performed using the computer program PPRS. The resulting factors of safety against liquefaction triggering for various return periods are shown in Figure 11-25. These factors of safety were computed using the averaged SPT blowcount information for Rio Bananito Railway Bridge as shown in Figure 11-9. A factor of safety less than or equal to 1.2 was assumed to be liquefiable for this study.

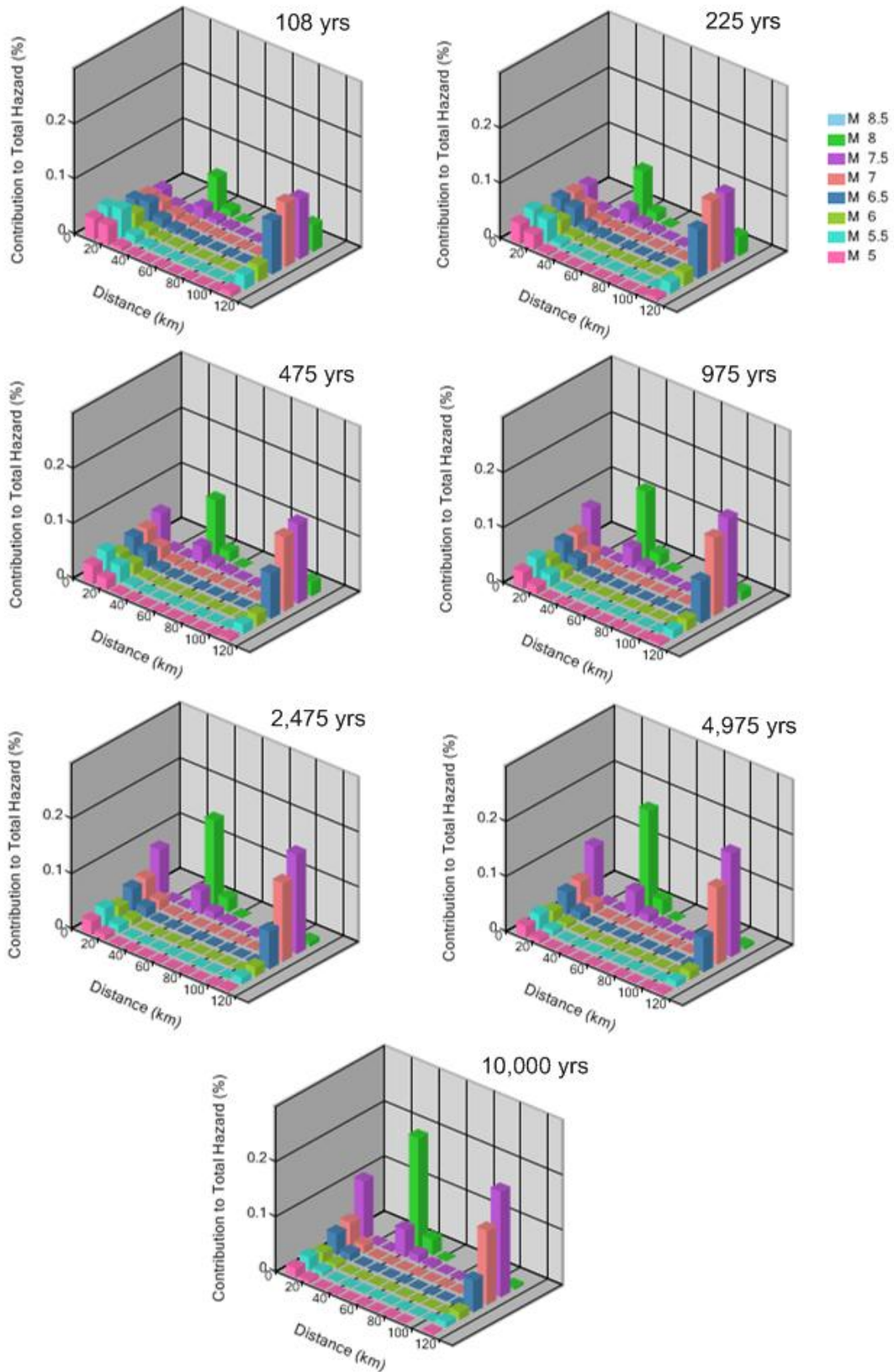


Figure 11-24: Deaggregation Plots for the PGA at the Rio Bananito Railway Bridge

Note that for fine-grained soil layers not considered susceptible to liquefaction due to plasticity, a generic factor of safety against liquefaction equal to 2.0 was assigned regardless of return period. A maximum factor of safety equal to 4.0 was assigned to layers with very high resistance to liquefaction triggering. In general, Figure 11-25 shows that for return periods greater than about 108 years, liquefaction triggers from depths of about 7.0 meters to 8.4 meters (R. EL. 91.0m to 89.6m) below the ground surface. At much higher return periods (i.e. >2,475 years), liquefaction was also computed to trigger in various soil layers below depths of about 11 meters (R. EL 87m).

11.6.3 Development of the Loading Parameter, \mathcal{L}

The loading parameter \mathcal{L} , which serves as the intensity measure in the performance-based pile response procedure, was computed using Equations (6-4) through (6-6) from Section 6.8 of this dissertation. The equations were loaded as user-defined attenuation relationships into EZ-FRISK, and the Risk Engineering (2010) seismic source model for Central and South America was used to compute probabilistic estimates for \mathcal{L} . A plot of the hazard curves for \mathcal{L} is presented in Figure 11-26. Note that loading parameter for each model is unique and independent from the other models. Therefore, the loading parameters should be considered separately and should not be averaged or weighted.

11.6.4 Development of the Fragility Functions for Lateral Spread Displacement

Fragility curves relating the probability of exceeding a given lateral spread displacement to the loading parameter \mathcal{L} were developed according to the procedure described in Section 6.9. The site parameter \mathcal{S} for the three selected empirical lateral spread models was computed using

the soils and the averaged SPT blowcounts shown in Figure 11-9 with Equations (6-7), (6-9), and (6-11). A free-face ratio of 67-percent was used with a free-face height of 7.0 meters. Depth limitations as described in Section 3.7 were incorporated. The computed values of \mathcal{S} are shown in Table 11-4.

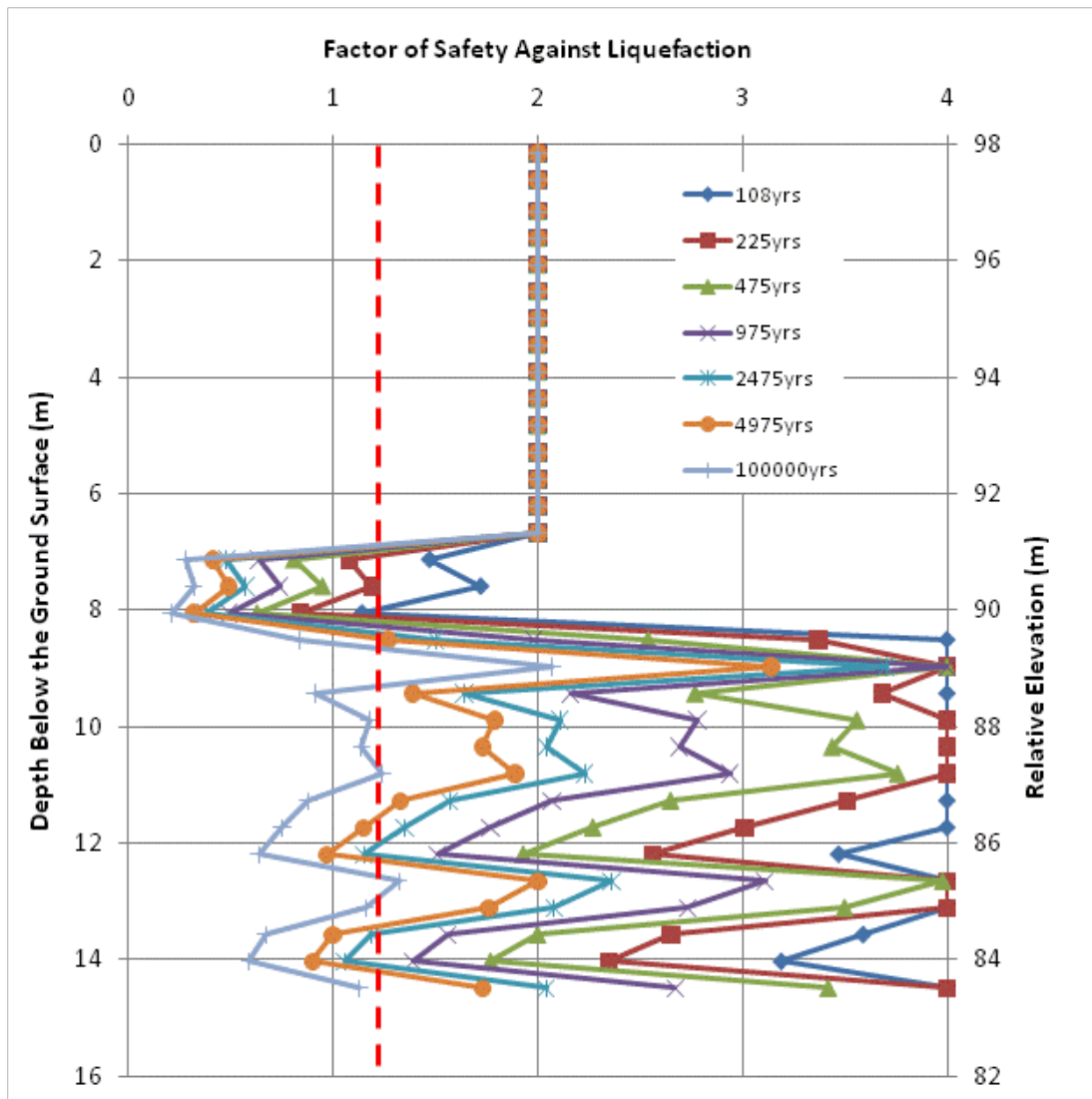


Figure 11-25: Performance-Based Liquefaction Triggering Results for the Rio Bananito Railway Bridge

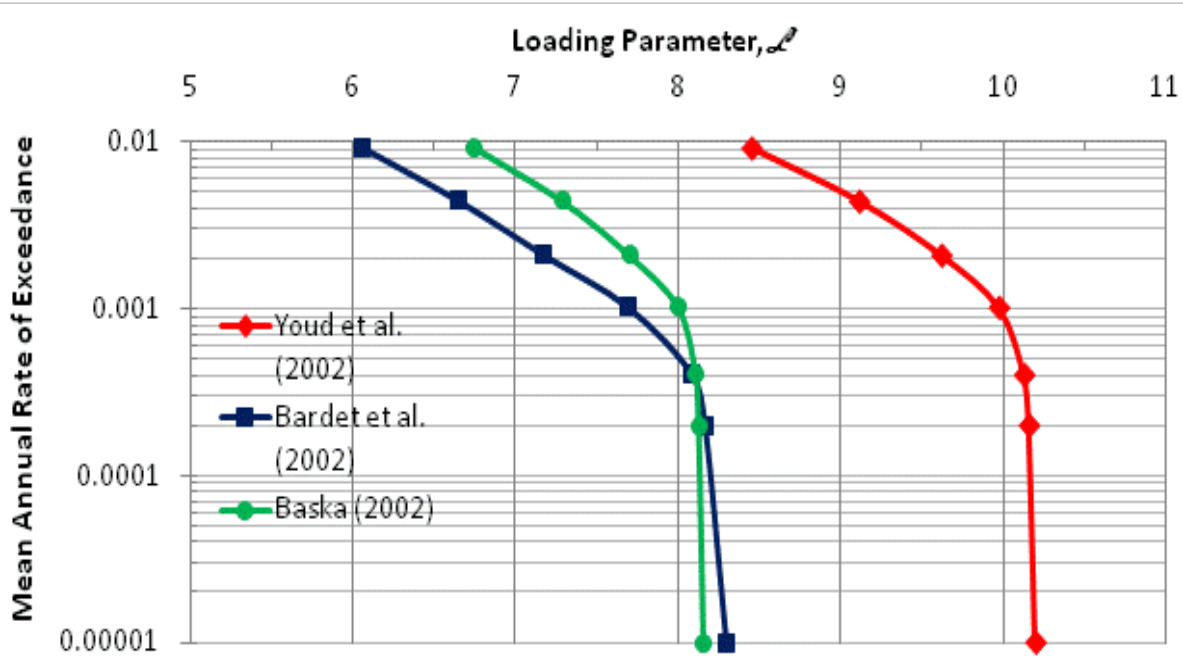


Figure 11-26: Hazard Curves for the Loading Parameter L for the Rio Bananito Railway Bridge

Table 11-4: Site Parameter S for the Rio Bananito Railway Bridge

Empirical Lateral Spread Model:	Site Parameter S
Youd et al. (2002)	-8.801
Bardet et al. (2002)	-6.296
Baska (2002)	-5.671

With S computed for each empirical lateral spread model, families of lateral spread fragility curves were developed using Equation (6-19). These curves are plotted for lateral spread displacements of 0.1 meter and 1 meter in Figure 11-27. Values of S and lateral spread fragility

curves were calculated automatically in the computation of probabilistic lateral spread displacements using PPRS software.

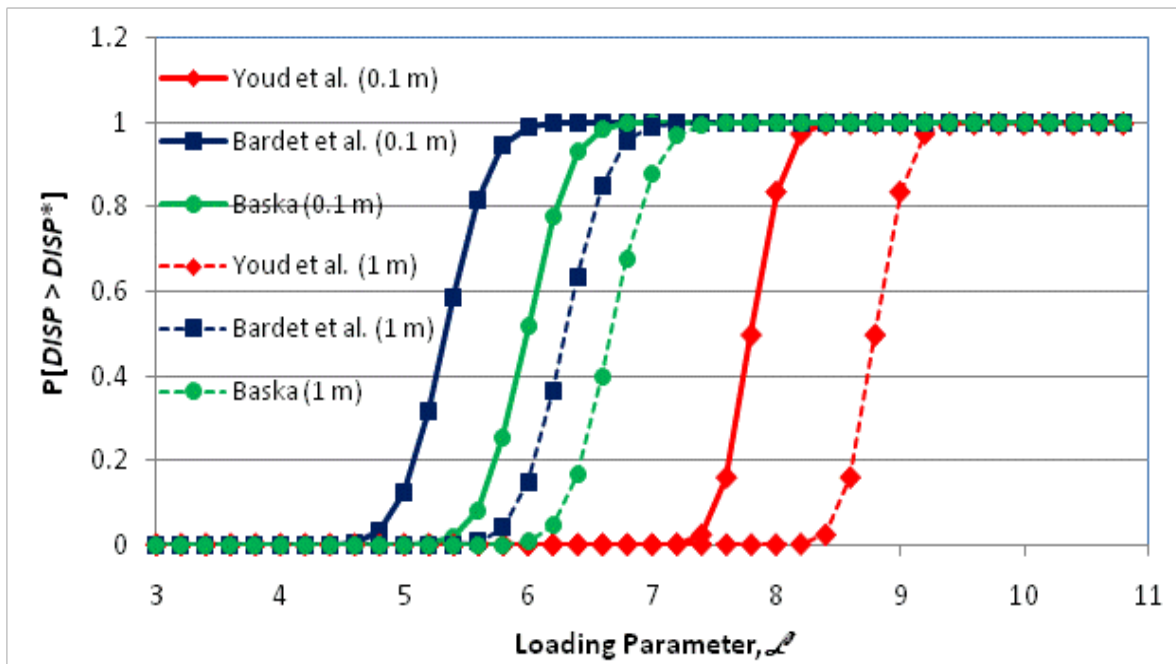


Figure 11-27: Lateral Spread Fragility Curves for $DISP^* = 0.1$ Meter and $DISP^* = 1$ Meter at the Rio Bananito Railway Bridge

11.6.5 Development of Probabilistic Lateral Spread Displacements

Using PPRS software, the lateral spread fragility curves were convolved with the hazard curves for the lateral spread loading parameters \mathcal{L} shown in Figure 9-17 using the steps presented in Section 6.10. The resulting hazard curves for lateral spread displacement at the ground surface are shown in Figure 9-19.

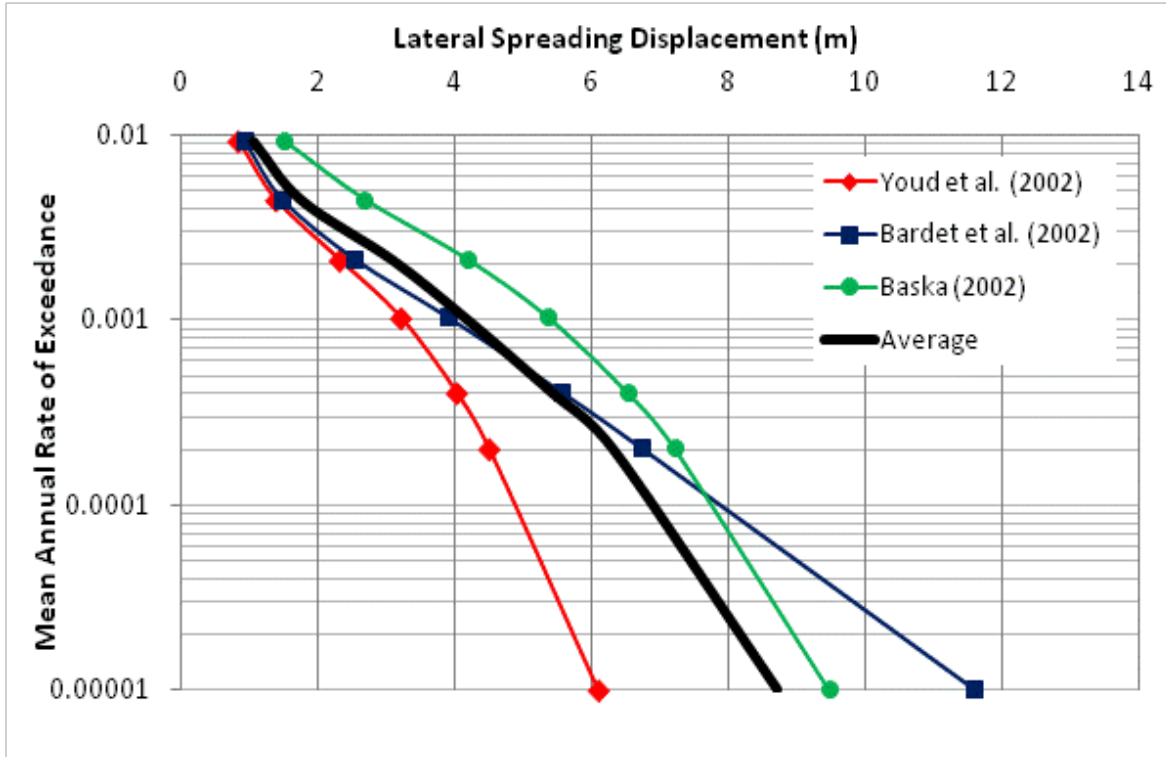


Figure 11-28: Lateral Spread Hazard Curves for the Rio Bananito Railway Bridge

Figure 11-28 shows good agreement in computed probabilistic lateral spread displacements between the Youd et al. (2002) and the Bardet et al. (2002) empirical models at annual frequencies greater than 0.001 (i.e. return periods less than 1000 years); however, the hazard curves tend to diverge at lower annual frequencies (i.e. higher return periods). The Baska et al. (2002) model appears to compute the largest displacements at most return periods, and the Youd et al. (2002) appears to compute the smallest displacements. The average displacement hazard curve was computed by weighting the mean annual rates of exceedance using equal weights for all three empirical models.

The average computed probabilistic lateral spread displacements were propagated through the soil profile using the recommendations provided in Sections 3.6 and 3.7 in

conjunction with the probabilistic liquefaction triggering profiles shown in Figure 11-25. The resulting probabilistic lateral spread displacement profiles are presented in Figure 11-29.

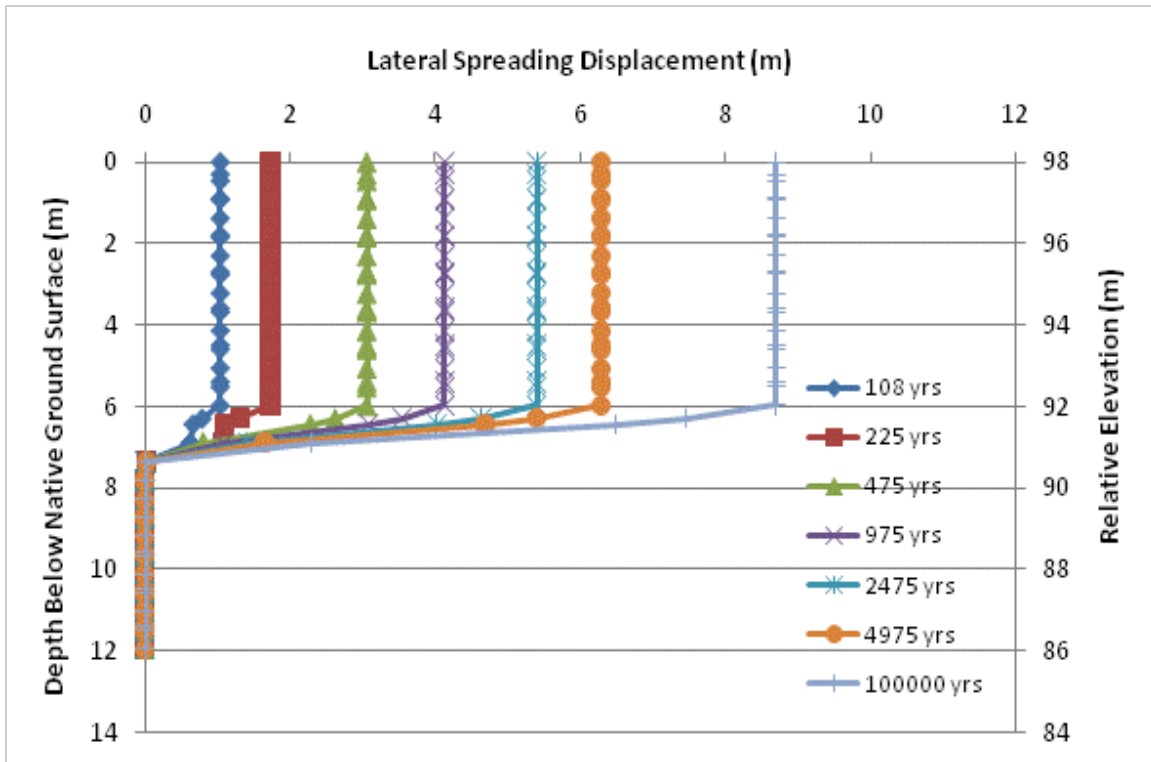


Figure 11-29: Probabilistic Lateral Spread Displacement Profiles for the Rio Bananito Railway Bridge

11.6.6 Development of Fragility Functions for the Kinematic Pile Response

Variance of the kinematic pile response for the lateral spread displacement profiles shown in Figure 11-29 was computed using a Monte Carlo simulation for each return period as described in Section 6.11. Coefficients of variation for the various soil parameters required for

the p-y models in LPILE were estimated from Table 6-2. 10,000 iterations were used for each Monte Carlo simulation, and the spreadsheet/macro LPILE MC Simulator was used to perform the analyses. Kinematic pile response including displacements, bending moments, shear forces, and curvature was computed for each of the seven return periods of lateral spread displacement profiles. Mean values and the standard deviation of the pile response was computed for each node in the pile response analysis. The mean displacements and standard deviations for the pile displacement are shown in Figure 11-30. Similar mean values and standard deviations were also developed for the bending moments, shear forces, and curvature of the caisson.

Using the mean pile response values and their corresponding standard deviations, fragility functions were developed for displacements, bending moments, shear forces, and curvature at each node of the caisson and for each return period using Equation (6-22). The functions were developed using PPRS software and were directly convolved with the lateral spread displacement hazard curves to create performance-based estimates of kinematic pile response.

11.6.7 Development of Probabilistic Kinematic Pile Response

The probabilistic kinematic pile response was computed for each node in the LPILE analysis for the Rio Bananito Railway Bridge by convolving the results from the fragility relationships developed in Section 11.6.6 with the probabilistic lateral spread displacement profiles developed in Section 11.6.5. PPRS software was used to apply Equation (6-23) and the steps presented in Section 6.12 for computing probabilistic estimates of pile displacement, bending moments, shear forces, and curvature for all nodes in the pile response model. The resulting probabilistic pile response profile is shown in Figure 11-31.

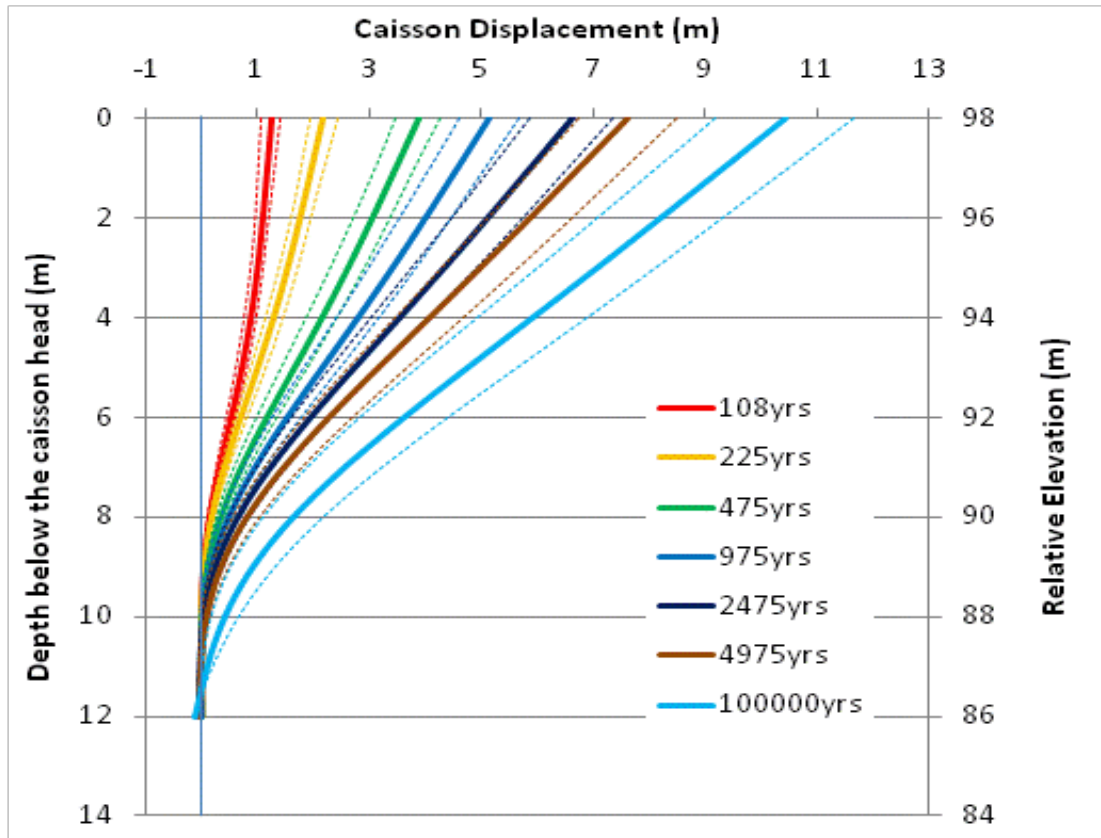


Figure 11-30: Mean Displacements and ± 1 Standard Deviations for a Single Caisson at the Rio Bananito Railway Bridge Computed From a Series of Monte Carlo Simulations

11.6.8 Discussion of Results

The results of performance-based pile response analysis at the Rio Bananito Railway Bridge appear reasonable and demonstrate that it is possible to combine simple pile response analysis procedures which are familiar to most practicing engineers in order to form a relatively sophisticated performance-based procedure. The analysis also demonstrates that it is possible to model the kinematic behavior of relatively large caissons/drilled shafts as long as sufficient information is available to reasonably model the caissons/shafts in the analysis.

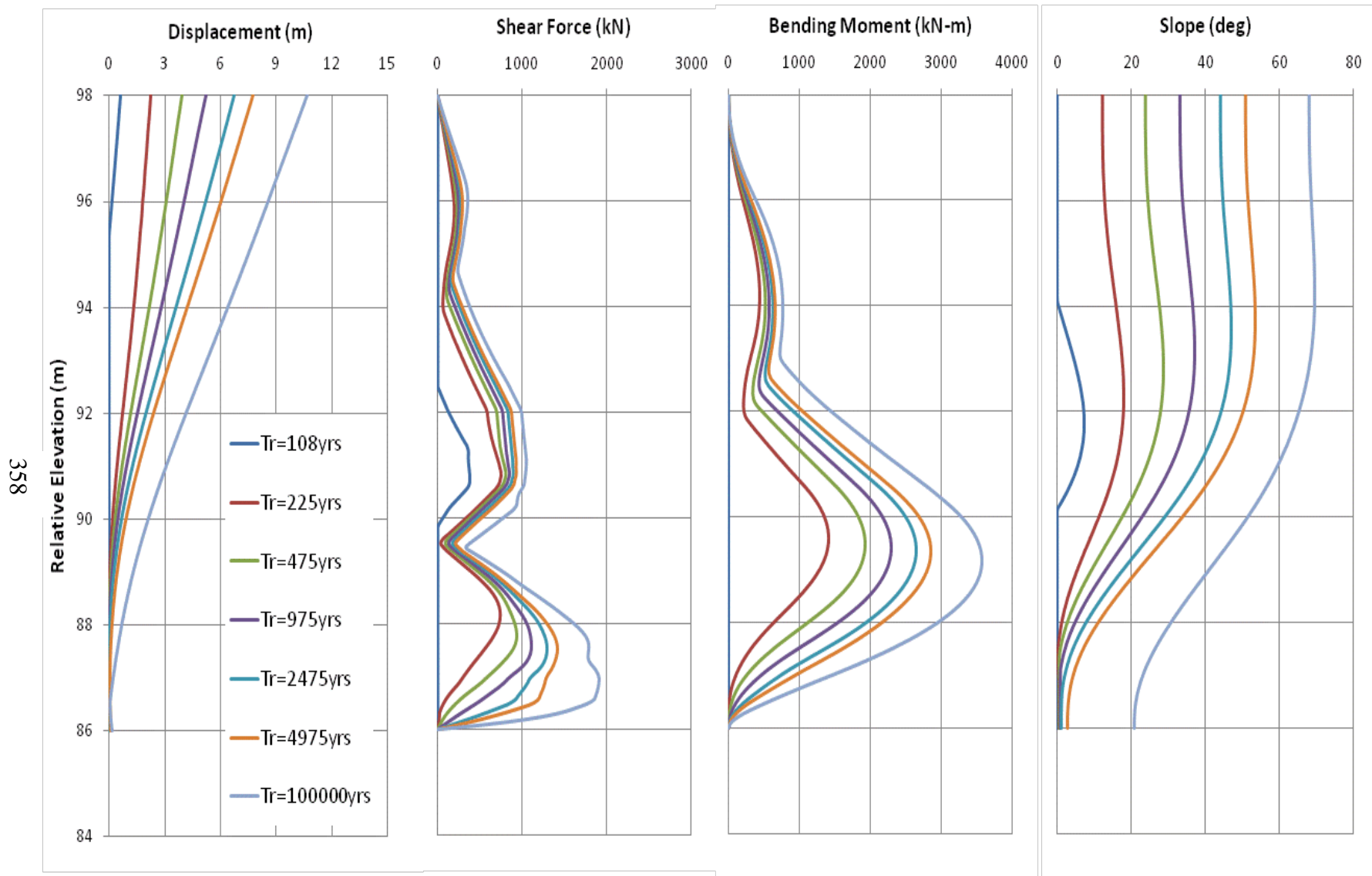


Figure 11-31: Probabilistic Caisson Response Curves (Absolute Values) for the Rio Bananito Railway Bridge

One may note the discrepancy between the various pile responses (i.e. deflection, bending moment, shear, and slope) at the low return period of 108 years. This phenomenon is due to the fact that the pile responses are evaluated independently of one another in the performance-based probabilistic framework and may have different relative coefficients of variation computed from the Monte Carlo simulation. This means that the different forms of pile response should be evaluated independently from one another when considering the results of the analysis. For example, one should not assume that the pile displacement corresponding to a return period of 108 years could be computed by integrating the bending moment corresponding to a return period of 108 years.

According to the results of the performance-based kinematic pile response analysis, caisson head deflections of 4.3 and 5.7 meters correspond to return periods of 600 years and 1,325 years, respectively. Caisson head rotations of 26 and 37 degrees correspond to return periods of 560 years and 1,360 years, respectively. These results agree relatively well with one another, thus suggesting that the true return period corresponding to the observed caisson response following the 1991 Limon earthquake is between 560 and 1,360 years (i.e. probabilities of exceedance of 12.5-percent and 5.4-percent in 75 years, respectively).

12 RIO ESTRELLA HIGHWAY BRIDGE

12.1 Introduction

The highway bridge over the Rio Estrella is a three-span steel and pre-stressed concrete bridge supporting two lanes of traffic. The two southern spans are approximately 75 meters in length and composed of steel trusses. The northern span is approximately 25 meters in length and composed of pre-stressed concrete girders. The total length of the bridge is approximately 178 meters. The bridge is located just north of the Town of Penhurst along National Route 36 and is the southern-most river crossing between Limon and Bribri. The latitude/longitude coordinates of the bridge are approximately 9.78760° North 82.9134° West.

According to bridge plans provided by the Costa Rican Ministry of Transportation and dated April 1971, the bridge is founded on a series of 12BP53 H-piles. The north abutment is supported by two rows of piles (five piles in each row) that are approximately 17.2 meters in length and spaced at 1.5 meters in the transverse direction and 1 meter in the longitudinal direction. The northern bent is founded on two 2.90-meter x 4.94-meter pile caps. Each of these pile caps is supported by fifteen 12BP53 steel piles (three rows of five piles) that are 20 meters in length and spaced at 1 meter in both the transverse and longitudinal directions. The southern bent is founded on two 3.94-meter x 4.94-meter pile caps. Each of these pile caps is supported by twenty 12BP53 steel piles (four rows of five piles) that are 20 meters in length and spaced at 1 meter in both the transverse and longitudinal directions. The southern abutment of the bridge was

designed to be converted into a bent in the event of a bridge expansion and is shown in (). The abutment is founded on two 3.96-meter x 5.96 meter pile caps. Each of these pile caps is supported by 24 12BP53 steel piles (four rows of six piles) that are 20 meters in length and spaced at 1 meter in both the transverse and longitudinal directions. Finally, the front row of piles at each abutment and bent location are battered at approximately 5V:1H. However, any batter in the piles was neglected in the pile response analysis because the Juirnarongrit and Ashford (2006) pile response procedure does not specify how to account for pile batter in a few of the piles in the group.



Figure 12-1: Southern Abutment of the Rio Estrella Bridge

12.2 Observed Damage Following the 1991 Earthquake

Youd et al. (1992) reported that ground shaking from the 1991 Limon earthquake caused the two steel trusses to fall into the Rio Estrella. The south span was reported to have fallen off the southern abutment, collapsing at the central pier by fracture of the two bottom cords immediately adjacent to the central slab pier. The end diagonal was reported to have buckled as the span dropped. Priestley et al. (1991) reported that the northern span pulled off the central pier but was still supported at the northern pier. The pre-tensioned reinforced concrete section at the north end of the bridge did not fall from its supports.

Priestley et al. (1991) reported that the roadway approach leading to the southern abutment of the bridge and the banana plantations on both sides of the embankment were dissected by several large and many small fissures indicative of liquefaction at depths and lateral spread of the surface flood-plain deposits toward the river channel. Fissure widths as large as one to three meters were reported. In addition to fissures, localized slope stability failures of the embankment occurred throughout the approach resulting in graben-like formations in the embankment with up to three meters of slump were reported. Liquefaction-induced settlements of up to 1.5 meters in the soils supporting the embankment were also reported. This value is significantly larger than the 0.2 meter settlements that were observed at the northern abutment. In addition, no fissures were observed in the approach embankment at the northern abutment, and relatively few cracks were reported in the pavement (Priestley et al., 1991).

Youd (1993) estimated that up to 2 meters of lateral spread displacement may have occurred in the vicinity of the southern abutment. Despite these significant ground displacements, the foundation at the southern abutment showed negligible amounts of damage and deformation as shown in Table 12-1 after Youd et al. (1992) and McGuire (1994). The

differences between the measured distances and the distances shown on the bridge plans fall within the range of expected construction error and indicate that no substantial permanent displacement occurred in the foundation elements of the bridge (McGuire, 1994).

Table 12-1: Measured Distances at the Rio Estrella Bridge Following the 1991 Limon Earthquake (After Youd et al., 1992; McGuire, 1994)

<i>Distance between center of bridge seats on:</i>	<i>Plan distance m</i>	<i>Measured post-earthquake distance m</i>
North Abutment and Pier 1	25.00	24.96
Pier 1 and Pier 2	75.00	75.02
Pier 2 and South Abutment	75.00	75.24
North and South Abutments	176.32	176.14

Because the footings/piles at the southern abutment are buried at depth, there is a possibility that small deformations in the footings/piles may have occurred and that the deformations were gradually distributed through the abutment columns from the footings up to the bridge seat in such a way that they were imperceptible at the time of the various reconnaissance missions in the early 1990s. However, such deformations could only be detected by examining and surveying the footings themselves, which would require significant amounts of excavation. Therefore, this study assumed that no significant deformations occurred in the foundation at the southern abutment due to lateral spread during 1991 Limon earthquake.

12.3 Soil Site Characterization at the Rio Bananito Railway Bridge

Insuma S.A. Geotechnical Consultants originally performed a single boring (P-1) adjacent to the southern bridge abutment. Two additional borings (P-2 and P-3) were performed in 2011 to the east of Boring P-1 to evaluate the continuity of the soil layering. Boring P-1 was performed approximately 19 meters south from the southern abutment and was extended to an approximate depth of 20 meters. Boring P-2 was performed about 70 meters to the east of Boring P-1 and was extended to an approximate depth of 12 meters. Boring P-3 was performed about 45 meters to the east of Boring P-1 and was extended to an approximate depth of 11 meters. The soils encountered in the boring were reported to consist primarily of alluvial deposits composed primarily of clayey (i.e. elastic) silts and silty sands. The silts encountered in the boring were generally non-plastic near the ground surface. However, elastic silts with moderate to high plasticity were generally encountered directly beneath the non-plastic silts. The sands encountered appeared to be fine-grained and generally silty. However, a zone of relatively clean sands and gravels was encountered at depths between approximately 4.9 and 10.4 meters.

Elevations measured in 2010 by the BYU reconnaissance team at the southern abutment with GPS equipment generally agreed with the elevations shown on the bridge plans provided by the Costa Rican Ministry of Transportation. The ground surface elevations at Borings P-1, P-2, and P-3 were measured to be approximately 4.3 meters, 4.92 meters, and 4.46 meters, respectively. Groundwater was encountered at depths of 4.9 meters, 4.7 meters, and 4.4 meters in Borings P-1, P-2, and P-3, respectively. These depths correspond to elevations of -0.6, 0.22, and 0.06 meters, respectively. Simple diagrams of the soils encountered in the borings performed are shown in Figure 12-2. Further details regarding the borings at the Rio Estrella Bridge and the corresponding laboratory test results can be found in the Insuma Geotechnical Report included as

Appendix A of this report. An averaged profile of the SPT blowcounts was developed and is shown in Figure 12-3.

The information from Borings P-1, P-2, and P-3 was used to develop a generalized soil profile for the southern abutment of the Rio Estrella Bridge. Empirical correlations with SPT blowcounts were averaged to estimate the friction angle of granular soils. These correlations include Peck et al. (1974), Hatanaka and Uchida (1996), and Bowles (1977). Relative density of granular soils was estimated using the empirical correlation presented by Kulhawy and Mayne (1990). Corrected soil modulus estimates K^* of the granular soils for use with the API (1993) p-y relationship were estimated using the recommendations presented by Boulanger et al. (2003). Undrained strength of cohesive plastic soils was averaged from empirical correlations including Hara et al. (1971), Kulhawy and Mayne (1990), and Skempton (1957). Assumptions regarding the unit weight of the native soil as well as the strength properties of the embankment fill were made. Groundwater was modeled at an elevation of 0.0 meters (i.e. an estimated depth of 4.3 meters below the ground surface). Table 12-2 summarizes the resulting generalized model of the soil profile at the south abutment of the Rio Estrella Bridge.

12.4 Characterization of Site Geometry/Topography at the Rio Estrella Bridge

The Rio Estrella is a relatively wide river bounded on both sides by a gently sloping floodplain with extensive vegetation and banana plantations. According to elevations shown on the blueprints that were provided by the Costa Rican Ministry of Transportation, the river channel itself ranges in elevation from about -1.0 meter in the river channel to approximately 4.0 meters at the river bank near the southern bridge abutment.

a) Boring P-1			b) Boring P-2			c) Boring P-3		
Depth (m)	SPT N Value		SPT N Value		SPT N Value			
0.00 - 0.45	10	Grayish brown or brown very sandy SILT and/or very silty SAND, fines are not plastic	4	Brown or gray very sandy SILT and/or very silty SAND, fines not plastic, very loose to loose relative density	10	Brown or gray very sandy SILT or silty SAND		
0.45 - 0.90	7		2		4			
0.90 - 1.35	6		13		2	Brown clayey SILT, mixed with fraction of sand size particles, low plasticity, very soft to soft consistency.		
1.35 - 1.80	2		8		5			
1.80 - 2.25	2		3	Brown clayey SILT, mixed with fraction of sand size particles, low plasticity, very soft to soft consistency.	2			
2.25 - 2.70	1		4		3			
2.70 - 3.15	1	Brown clayey SILT, mixed with fraction of sand size particles, medium plasticity, soft	4		4			
3.15 - 3.60	1		3		4			
3.60 - 4.05	2		2		2			
4.05 - 4.50	2		4		2			
4.50 - 4.95	2	Gray well graded sandy GRAVEL and/or gravelly SAND, no plasticity, medium.	4		13	Gray well graded sandy GRAVEL and/or gravelly SAND, no plasticity, medium relative density.		
4.95 - 5.40	14		11	Gray well graded sandy GRAVEL and/or gravelly SAND, no plasticity, medium relative density.	13			
5.40 - 5.85	10		11		10			
5.85 - 6.30	16		9		16			
6.30 - 6.75	12		17		15	Gray silty SAND, mixed with not plastic fine and som gravel, relative density varies between very loose and dense.		
6.75 - 7.20	7		13		10			
7.20 - 7.65	10	Gray well graded silty SAND, with some gravel, fines have no plasticity, medium to dense relative density.	15		19			
7.65 - 8.10	10		18	Gray silty SAND, mixed with not plastic fine and som gravel, relative density varies between very loose and dense.	14			
8.10 - 8.55	12		28		13			
8.55 - 9.00	10		27		17	Greenish gray silty GRAVEL with sand, fines are not plastic, medium to dense.		
9.00 - 9.45	28		31		16			
9.45 - 9.90	34		3		21			
9.90 - 10.35	22		4		40			
10.35 - 10.80	24	Greenish gray very fine silty SAND, fines have no plasticity, medium to dense relative density.	5		31			
10.80 - 11.25	19		37	Greenish gray silty GRAVEL with sand, fines are not plastic, dense.				
11.25 - 11.70	19		20					
11.70 - 12.15	24		28					
12.15 - 12.60	17							
12.60 - 13.05	26							
13.05 - 13.50	27							
13.50 - 13.95	35							
13.95 - 14.40	24							
14.40 - 14.85	38							
14.85 - 15.30	35							
15.30 - 15.75	28							
15.75 - 16.20	36							
16.20 - 16.65	36							
16.65 - 17.10	17							
17.10 - 17.55	25							
17.55 - 18.00	21							
18.00 - 18.45	22							
18.45 - 18.90	33							
18.90 - 19.35	32							
19.35 - 19.80	36							
19.80 - 20.25	38							

Figure 12-2: (a) Boring P-1, (b) Boring P-2, and (c) Boring P-3 Performed at the Rio Estrella Bridge

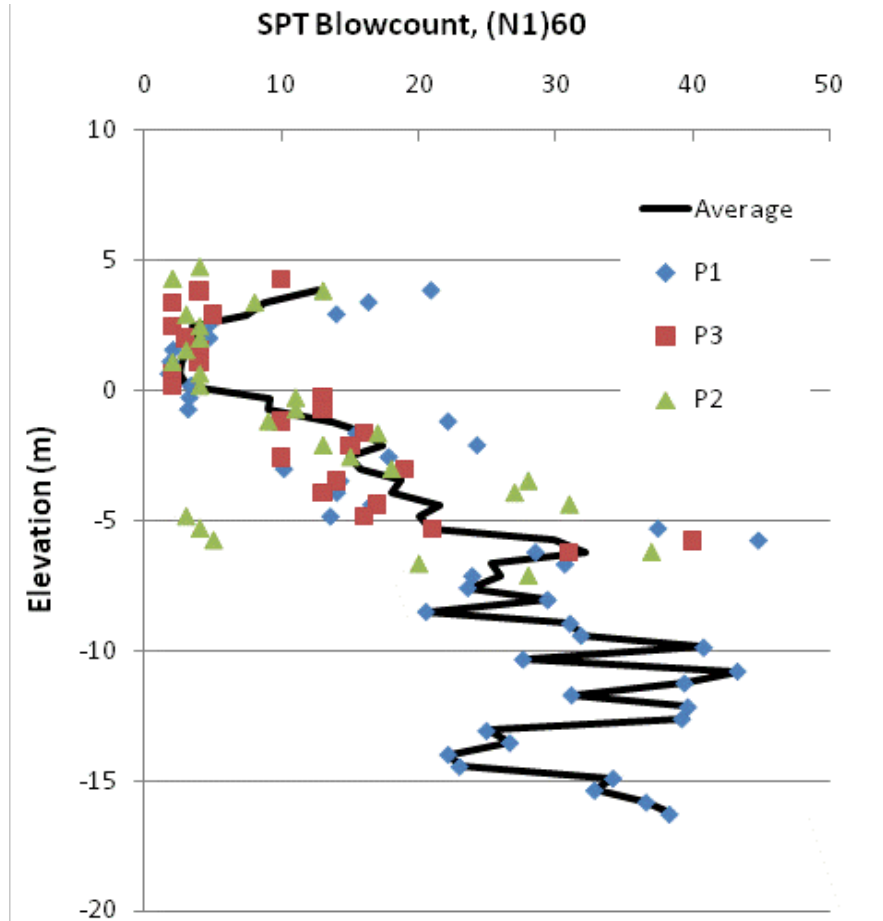


Figure 12-3: Averaged SPT Blowcounts for the South Abutment at the Rio Estrella Bridge

Table 12-2: Generalized Soil Profile for the South Abutment at the Rio Estrella Bridge

Top Depth (m)	Top Elevation (m)	Thickness (m)	USCS Soil Class	Friction Angle (deg)	Unit Weight (kN/m ³)	Undrained Strength (kPa)	Relative Density (%)	Soil Modulus (kN/m ³)	Liquefied p-mult
0	8.9	4.6	SM(Fill)	35	18.5	---	62	24800	---
4.6	4.3	3.0	ML/SM	32	18.1	---	39	7700	---
7.6	1.3	1.3	MH	---	18.8	19	---	---	---
8.9	0.0	2.8	GW	34	8.3	---	53	10300	0.19
11.7	-2.8	2.7	SW-SM	33	8.3	---	48	7700	0.14
14.4	-5.5	0.9	SM	40	8.5	---	77	20000	---
15.3	-6.4	2.3	SM	37	8.5	---	65	13350	0.33
17.6	-9.1	---	SM	39	8.5	---	73	15000	---

However, at the time of the 1991 earthquake, the ground surface elevations measured near the southern abutment did not match the elevations shown on the bridge drawings, indicating that the elevations on the drawings were design elevations which may have changed due to erosion, deposition, or man-made changes in the river geometry. For example, a large trackhoe was excavating a trench approximately 6 meters deep and re-routing river water adjacent to the south-central pier at the time of the 2010 BYU reconnaissance. It is likely that the maintenance of the banana plantations on the south side of the bridge largely contributes to the observed changes in the surface topography. According to the bridge blueprints, the roadway elevation across the bridge is 8.90 meters. From the blueprints, it also appears that the approach embankment was constructed at a 1.5H:1V slope.

A simplified sketch of the profile view of the Rio Estrella Bridge is shown in Figure 12-4. Note that the sketch includes an estimation of the approximate ground surface profile during the 1991 earthquake based on photographic evidence by Youd et al. (1992) and EERI (1993). A plan view sketch showing elevation contours based on the 2010 and 2011 BYU GPS surveys and surveyed boring locations is presented in .

12.5 Deterministic Pile Response Analysis at the Rio Estrella Bridge

12.5.1 Deterministic Ground Motion Evaluation From the 1991 Earthquake

The Rio Estrella Bridge is located approximately 21 kilometers northeast from the epicenter of the April 22, 1991 earthquake. Assuming an average V_{s30} value of 270 m/s, the average computed median spectral accelerations $\pm 1\sigma$ from the four selected NGA models are shown in Figure 12-6. The median computed PGA and spectral accelerations corresponding to 0.2-second and 1.0-second are approximately 0.244g, 0.506g, and 0.334g..

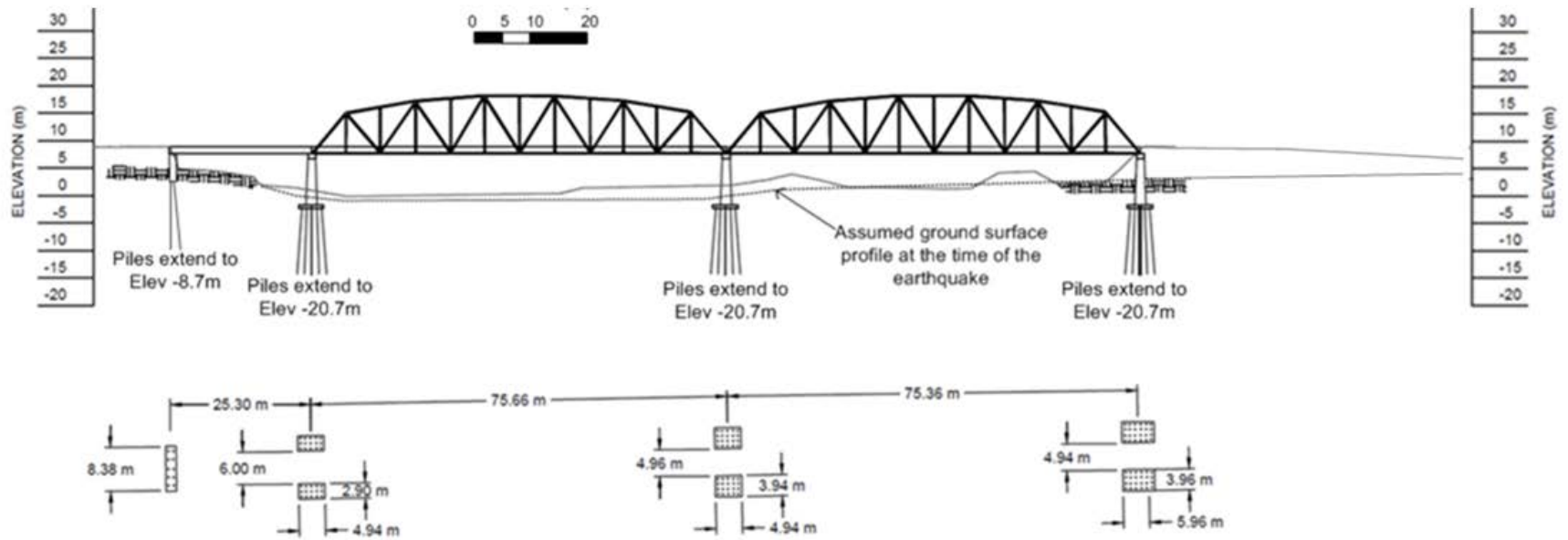


Figure 12-4: Simplified Sketch of the Profile View of the Rio Estrella Bridge

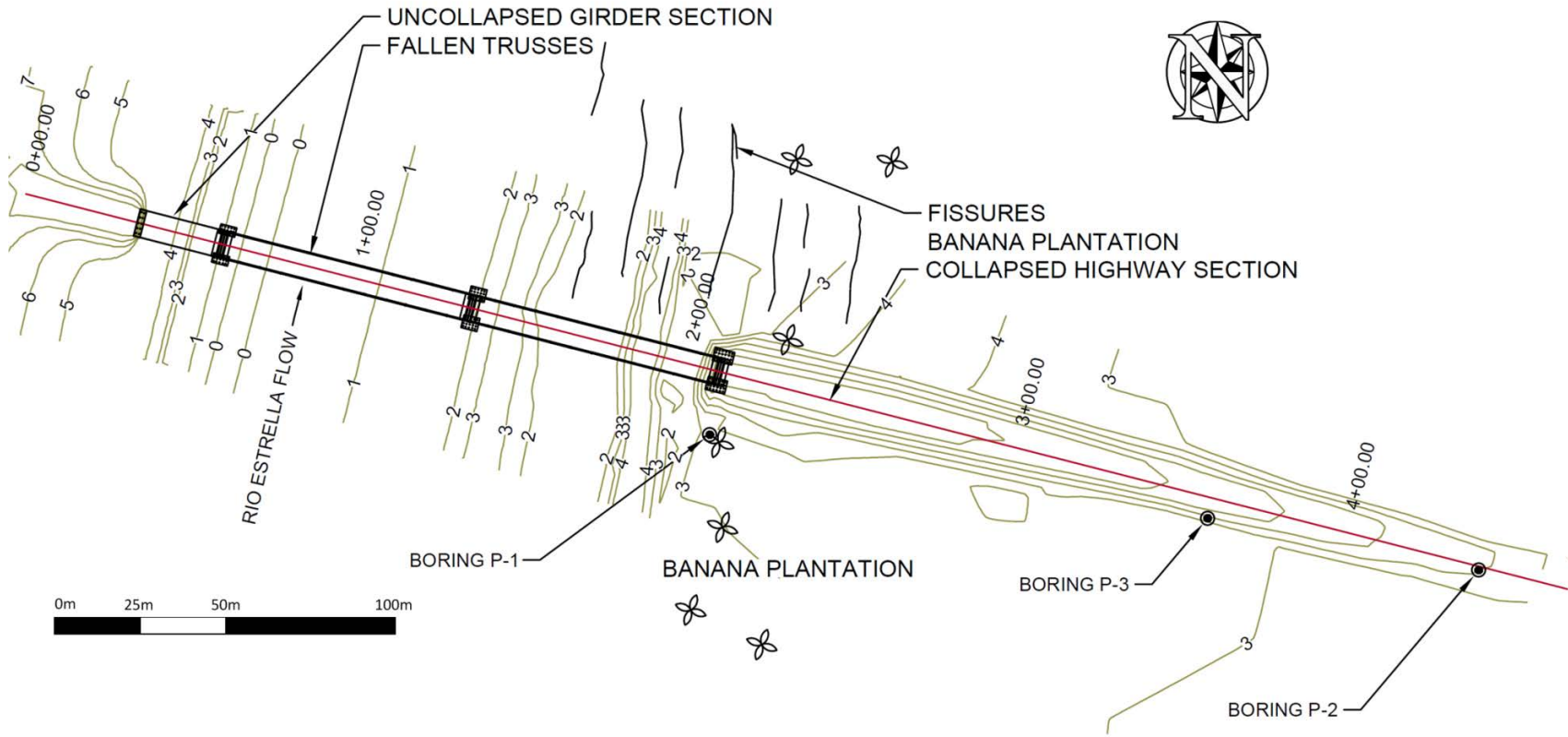


Figure 12-5: Sketch of the Current Elevation Contours and the Insuma Boring Locations at the Rio Estrella Bridge

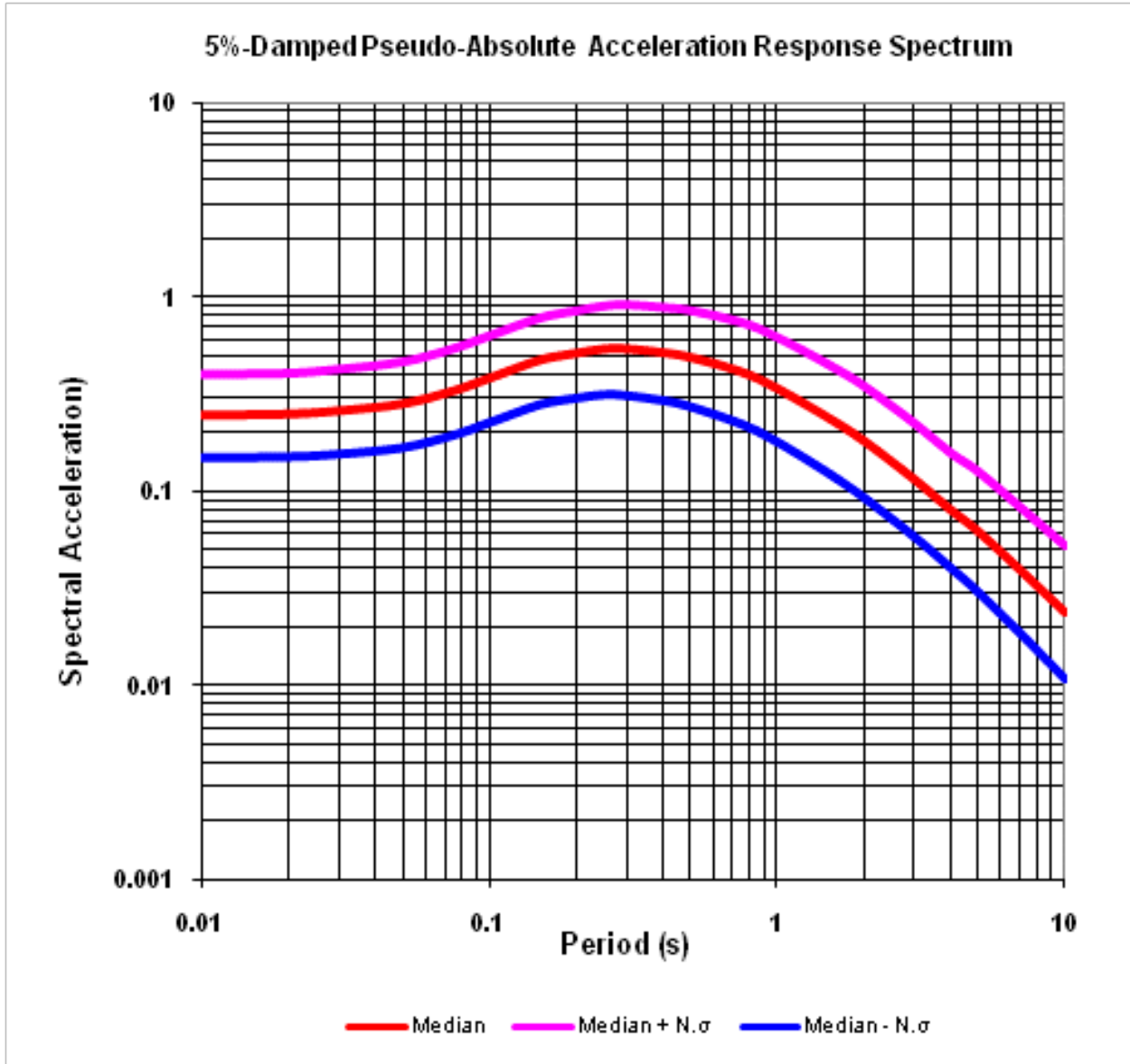


Figure 12-6: Computed Deterministic Response Spectra for the Rio Estrella Bridge From the 1991 Earthquake. N = 1

12.5.2 Deterministic Liquefaction Evaluation From the 1991 Earthquake

Using the average deterministic ground motions from the NGA equations, the deterministic liquefaction triggering was evaluated at the Rio Estrella Bridge for the M7.6 1991

Limon earthquake using the SPT blowcounts from Borings P-1, P-2, and P-3. The results of the deterministic liquefaction triggering analysis are shown in Figure 12-7, Figure 12-8, and Figure 12-9. This evaluation included consideration of the Cetin et al. (2004), Idriss and Boulanger (2008), and Youd et al. (2001) simplified procedures for liquefaction triggering. In general, good agreement was observed between the three procedures. The results of the analysis at Boring P-1 suggest that liquefaction triggers from depths of approximately 5.0 meters to 9.1 meters below the ground surface (EL -0.7m to EL -4.8m). The results of the analysis at Boring P-2 suggest that liquefaction triggers from depths of approximately 4.9 meters to 7.6 meters below the ground surface (EL 0.2m to EL -2.68m). In addition, the analysis shows liquefaction triggering between depths of about 9.3 meters and 10.6 meters below the ground surface (EL -4.38m to EL -5.68). The results of the analysis at Boring P-3 suggest that liquefaction triggers from depths of approximately 4.6 meters to 8.3 meters below the ground surface (EL -0.14m to EL -3.84m).

12.5.2.1 Deterministic Liquefaction Evaluation at the North Abutment

The Costa Rican Ministry of Transportation also provided the BYU reconnaissance team with a boring log numbered T-2 that was performed prior to the bridge construction. Because no lateral spread displacements nor evidence of liquefaction were observed at the north abutment of the bridge following the 1991 Limon earthquake, an additional liquefaction triggering analysis was performed using Boring T-2 for calibration and validation of the analyses at the south abutment. The boring log as provided by the Costa Rican Ministry of Transportation is somewhat antiquated, and no information regarding measured fines contents is reported on the logs. Therefore, fines contents of 90-percent and 25-percent were assumed for the clays/silts and the silty sands, respectively. A summary of Boring T-2 is presented in Table 12-3.

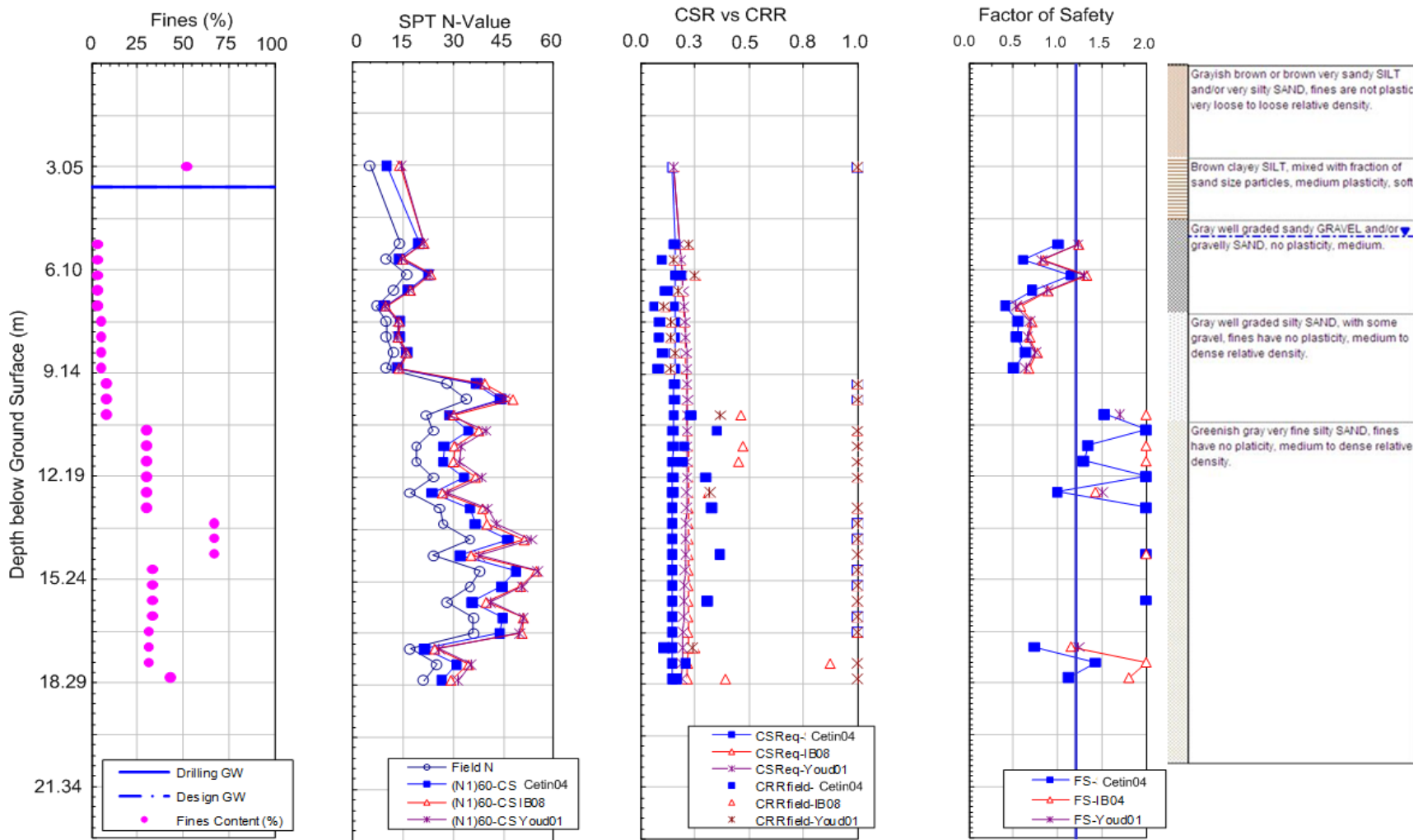


Figure 12-7: Deterministic Liquefaction Triggering Results From Boring P-1 for the M7.6 1991 Limon Earthquake at the Rio Estrella Bridge

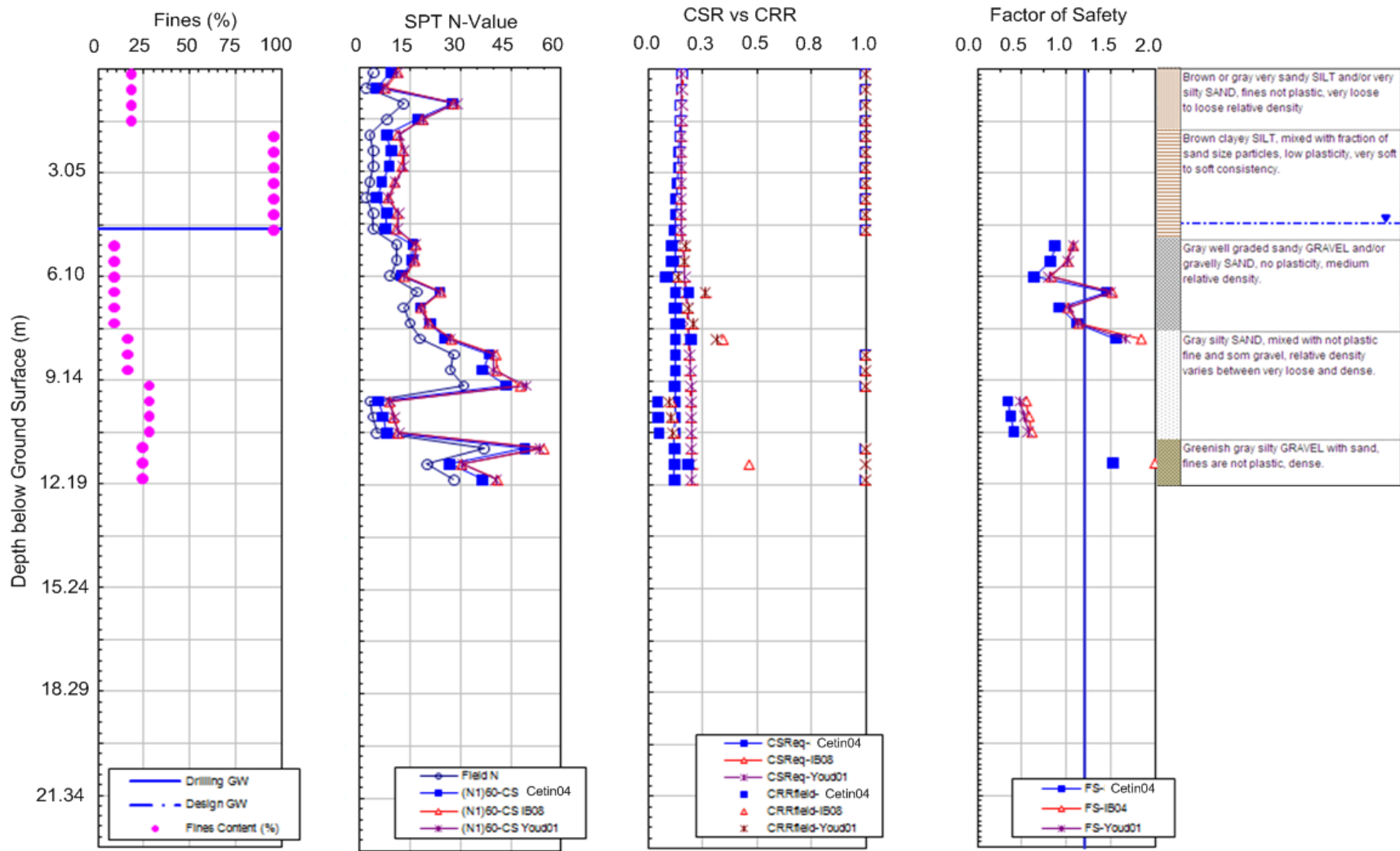


Figure 12-8: Deterministic Liquefaction Triggering Results From Boring P-2 for the M7.6 1991 Limon Earthquake at the Rio Estrella Bridge

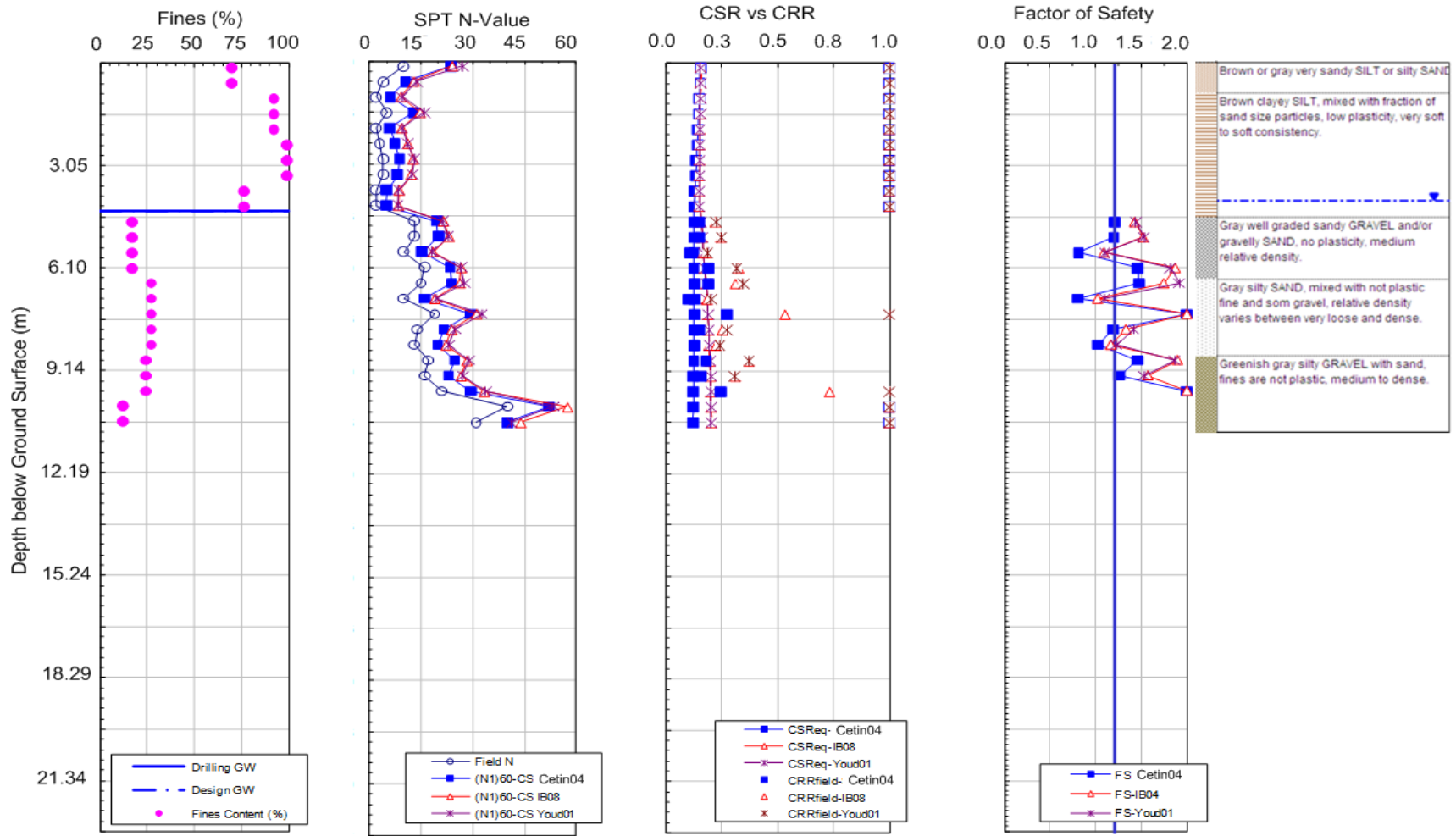


Figure 12-9: Deterministic Liquefaction Triggering Results From Boring P-3 for the M7.6 1991 Limon Earthquake at the Rio Estrella Bridge

Table 12-3: Summary of Boring T-2 at the North Abutment of the Rio Estrella Bridge

Depth (m)	SPT N Value	Estimated Fines Content (%)	USCS Classification
0.15	1	90	ML
0.61	7	90	
1.07	7	90	
1.52	10	90	
1.98	13	90	
2.44	11	90	
2.90	6	90	CL-ML
3.35	5	90	
3.81	8	90	
4.27	26	25	SM
4.72	20	25	
5.18	23	25	
5.64	34	25	
6.10	30	25	
6.55	33	25	
7.01	45	25	
7.47	55	25	
7.92	48	25	

Using the average deterministic ground motions from the NGA equations, the deterministic liquefaction triggering was evaluated using the SPT blowcounts from Boring T-2. A hammer efficiency of 87-percent and a uniform moist unit weight equal to 120 pcf were assumed. Groundwater was assumed at a depth of 3 meters. The results of the deterministic liquefaction triggering analysis are shown in Figure 12-10. This evaluation included consideration of the Cetin et al. (2004), Idriss and Boulanger (2008), and Youd et al. (2001) simplified procedures for liquefaction triggering. In general, no liquefaction triggering was computed at the north abutment of the Rio Estrella Bridge, which confirms the reported observations by Youd et al. (1992) following the 1991 earthquake.

12.5.3 Post Earthquake Slope Stability

Because the southern bridge abutment was located approximately 75 meters from the assumed margin of the Rio Estrella at the time of the 1991 Limon earthquake and the height of the free face was only approximately 5 meters, it is not likely that a liquefaction flow failure occurred in the native soils in southern abutment of the bridge. Therefore, this study assumed that the ground deformations observed following the 1991 earthquake were a result of lateral spread. No post earthquake slope stability analysis was performed for the Rio Estrella Bridge as a result.

12.5.4 Deterministic Evaluation of Lateral Spread

Empirical evaluation of the free-field soil displacements due to lateral spread was performed using the Youd et al. (2002), Bardet et al. (2002), and Baska (2002) models. The analysis assumed an earthquake magnitude of 7.6, a source-to-site distance of 21 kilometers, a free-face ratio of 6-percent, and a free-face height of 4.6 meters. The averaged SPT blowcounts shown in Figure 12-3 were used in the analysis. The mean grain size diameter for the generalized boring was estimated from Insoma sieve results for Borings P-1, P-2, and P-3. The median computed lateral spread displacement value and the 95th-percentile confidence interval for each of the three empirical models is shown in Figure 12-11. The average computed median displacement from the three models is approximately 0.37 meter. This value is significantly less than the reported estimate of 2 meters of lateral spread displacement by Youd (1993). Evaluation of the empirical models showed that a $D_{50_{15}}$ equal to 3.0mm was estimated using the sieve analyses from the liquefiable gravel/sand from Borings P-1, P-2, and P-3. This value of $D_{50_{15}}$ is

quite high, and when coupled with a relatively low free-face ratio results in small computed lateral spread displacements.

Because the empirically computed lateral spread displacements were significantly lower than the estimated observed displacements immediately following the earthquake, a lateral spread displacement value of 2.0 meters was used for the deterministic evaluation of pile response at the Rio Estrella Bridge in this study. The estimated lateral spread displacement profile for the M7.6 1991 Limon earthquake was computed according to the procedure presented in Sections 3.6 and 3.7 of this dissertation in conjunction with the liquefaction triggering profiles shown in Figure 12-7, Figure 12-8, and Figure 12-9. This displacement profile is shown in Figure 12-12.

Due to the relatively complex soil stratigraphy relative to the elevations of the foundation elements at the southern abutment of the Rio Estrella Bridge, one could understandably become confused. A simplified sketch of the generalized soil stratigraphy relative to the foundation elements at the southern abutments is shown in Figure 12-13.

12.5.5 Pile Response Analysis

Because the pile caps are located beneath the top of the liquefied soil layer with columns extending to the bridge abutment, the kinematic loading of the columns was also considered in the analysis. For simplification, the reinforced concrete columns extending from the pile caps to the bridge seat were assumed to be infinitely stiff. The bridge plans provided by the Costa Rican Ministry of Transportation indicated that only about the top 3 meters of the columns were connected with a reinforced concrete diaphragm. The remaining length of the columns remained independent from one another, and laterally spreading soil was free to flow between the columns at these depths.

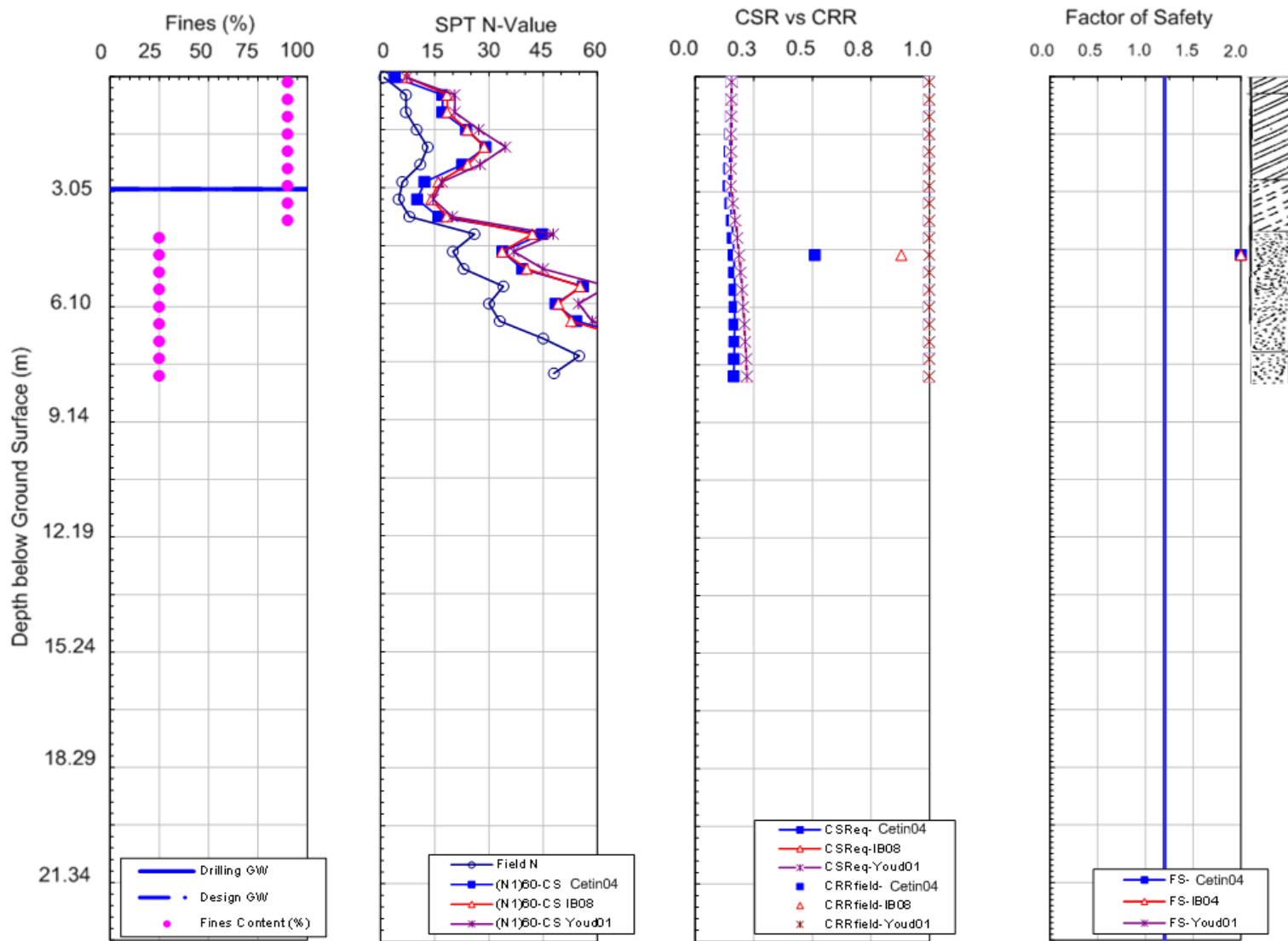


Figure 12-10: Deterministic Liquefaction Triggering Results From Boring T-2 at the North Abutment of the Rio Estrella Bridge

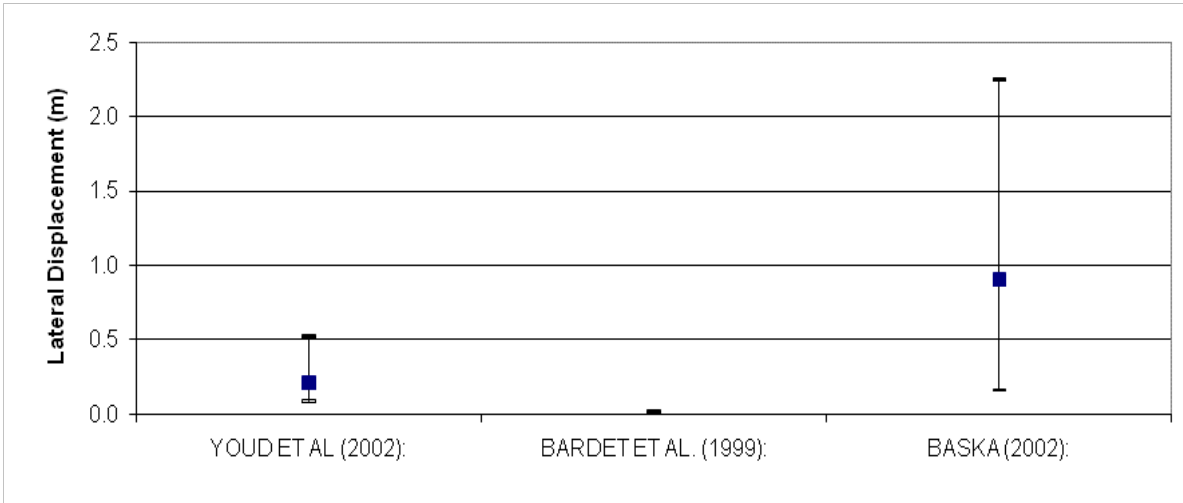


Figure 12-11: Deterministic Median and 95-Percentile Evaluations of Lateral Spread Displacement Using Select Empirical Models for the Rio Estrella Bridge

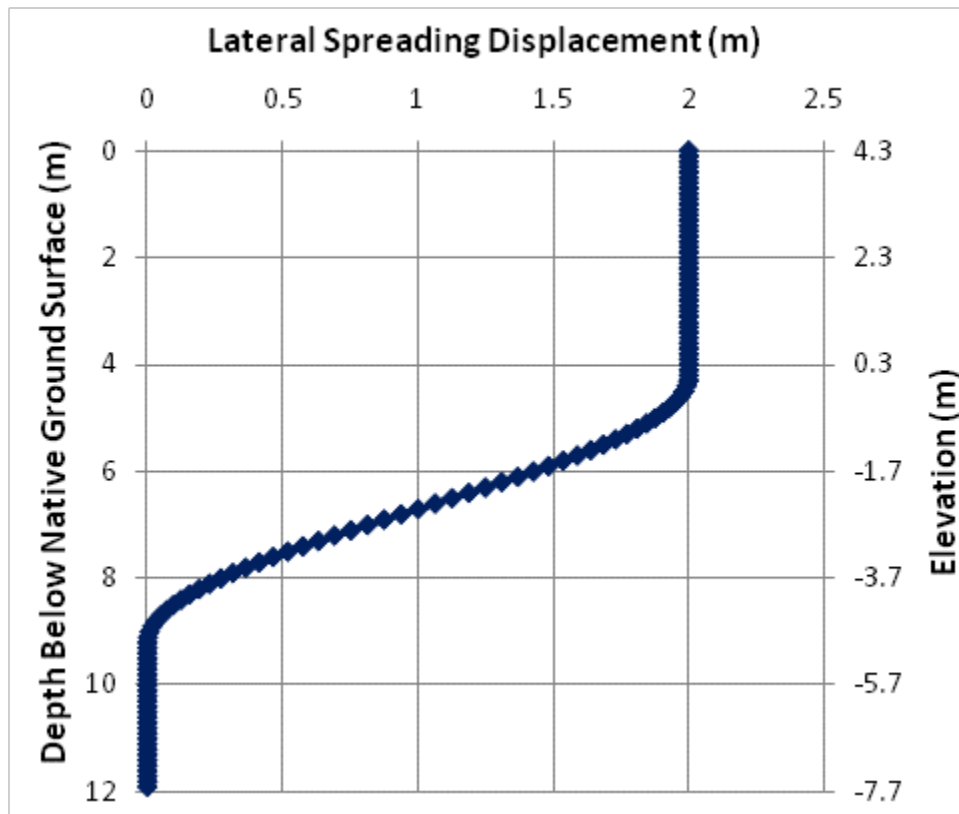


Figure 12-12: Computed Lateral Spread Displacement Profile at the Rio Estrella Bridge for the M7.6 1991 Limon Earthquake

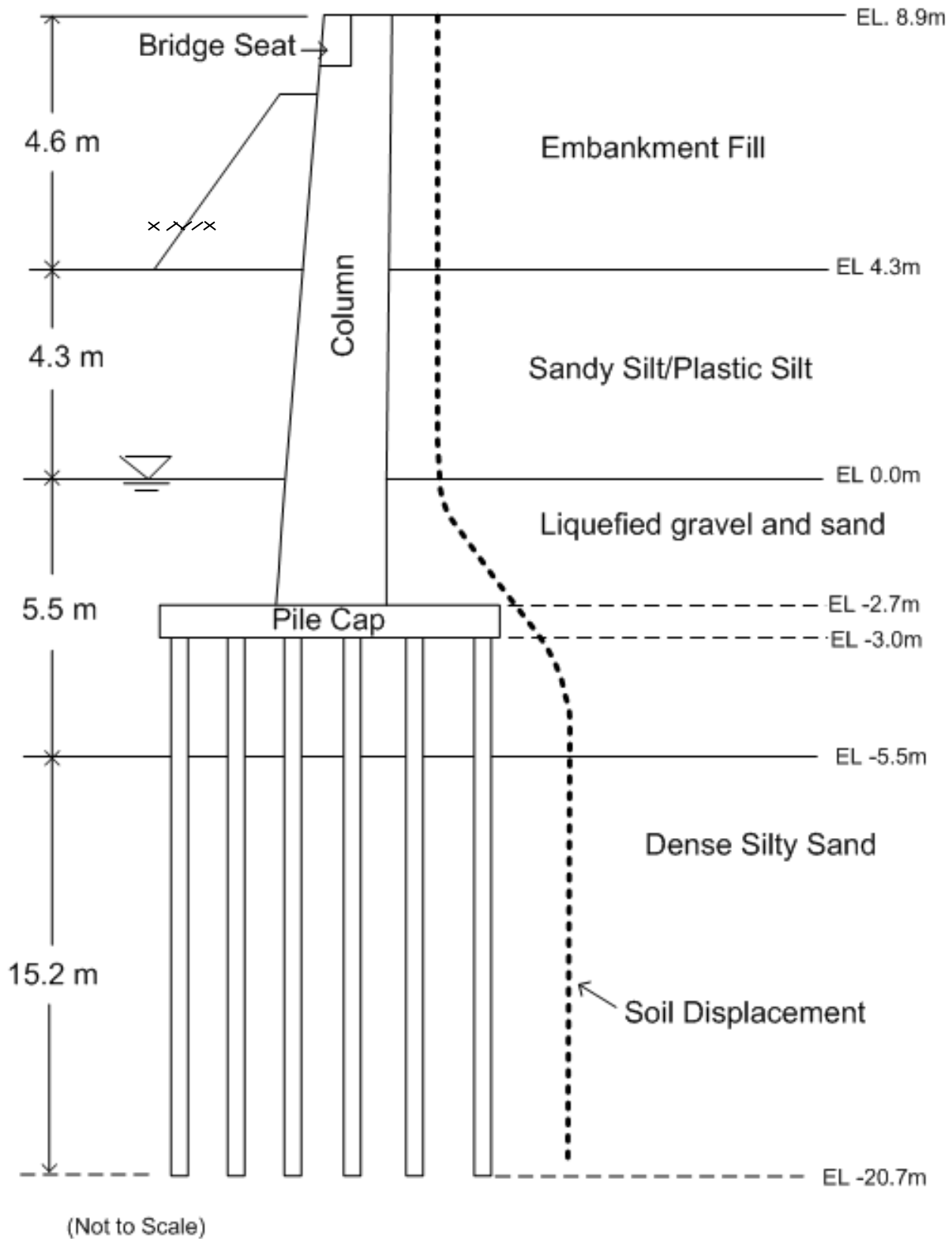


Figure 12-13: Simplified Sketch of the Soil Profile Relative to the Foundation Elements at the Southern Abutment of the Rio Estrella Bridge

To account for the effect of the passive loading applied by the laterally spread non-liquefied crust and the resulting overturning moment on the pile caps, the passive force produced by the non-liquefied soil crust on the columns and abutment wall was computed using Rankine passive pressures. While it is generally accepted that Rankine theory tends to generally underpredict the observed passive load in the field, Brandenberg et al. (2007b) and Brandenberg (2005) cite that the softening effect from the liquefied soil appears to significantly reduce the passive pressures from the non-liquefied crust such that passive pressures computed with Rankine theory may be more accurate than the passive pressures computed with either the Coulomb or log-spiral theories. Therefore, the resulting total horizontal passive force transmitted to the pile caps was computed to be approximately 13,800 kN. Computing the effective moment arm of the horizontal passive force to be approximately 4.08 meters above the tops of the pile caps, the resulting overturning moment on the pile caps was computed to be approximately 56,300 kN-m.

Rotational stiffness of an equivalent single pile cap was computed by summing all of the moments (including the additional moments due to the non-liquefied soil crust and the overburden stress on the pile caps) about the toe of the back row of piles in the pile group as recommended by Juirnarongrit and Ashford (2006) and as summarized in Section 4.4.3.2. The piles were assumed to be fixed-end piles (i.e. only the back row of piles is in compression when rotating the pile cap). As such, the end-bearing forces of the compressed pile on the back row could be neglected. Using the soil properties summarized in Table 12-2 and accounting for the fact that the piles extend from Elevations -3.0m to -20.7m, a total skin resistance of approximately 1500 kN was computed for a single pile. Summing the moments produced by the skin friction about the back row of piles resulted in a moment of approximately 180,780 kN-m.

Taking into account the overturning moment from the non-liquefied soil crust and the moment resulting from the overburden stress on the pile caps (a combined moment approximately equal to 357,400 kN-m), a total overturning moment of 538,180 kN-m was computed for the entire system. For a fixed-end rotation case, this moment results in a total rotational stiffness of approximately 67.274E6 kN-m/rad for the single equivalent pile cap.

Because LPILE version 5.0 Plus does not include a built-in module for the nonlinear pile response analysis of H-piles, a linear-elastic pile response analysis was performed. The resulting composite initial flexural stiffness of a single 12BP53 steel pile was computed to be approximately 40,240 kN-m². The flexural stiffness of the equivalent single pile was computed to be approximately 1609.6 MN-m². Using Rollins et al. (2006) to account for the pile group reduction, a p-multiplier equal to 26.2 was computed for the equivalent single pile. Assuming grade 60 steel for the piles, an approximate yielding moment of 480 kN-m (4248 kip-in) was computed for the strong axis of a single 12BP53 pile.

Applying the lateral spread deformations shown in Figure 12-12 to the equivalent single pile and applying a lateral load of 13,800 kN and a rotational stiffness of 67.274E6 kN-m/rad to the pile head, the LPILE deterministic pile response from the 1991 Limon earthquake was computed and is shown in Figure 12-14.

Examination of Figure 12-14 shows that approximately 0.12 meter of lateral deformation was computed at the pile caps of the abutment resulting in computed bending moments that far exceed the yielding moment of 480 kN-m. Therefore, the pile would likely have yielded early on in the loading process, and the lateral deformations would likely have been larger than 0.12 meter. These results suggest that the computed pile response is much more severe than the actual pile response that occurred during the 1991 Limon earthquake. Several theories could explain the

apparent discrepancy between the computed and observed results. For example, perhaps the severe localized stability failures in the approach embankment disrupted the liquefied soil sufficiently that lateral spread did not occur beneath the footprint of the embankment. Perhaps the piles and pile caps really were damaged due to kinematic loading, but due to the fact that the foundation elements are buried approximately 7 meters beneath the ground surface, the damage is not visually detectable.

This study investigates another possible theory which could explain the discrepancy between the computed and observed pile response at the Rio Estrella Bridge. Because the pile caps at the southern abutment are placed in the middle of the liquefiable soil layer (refer to Figure 12-13), the pile caps and piles would likely experience significantly reduced loading if the majority of the lateral spread displacement was isolated to the top of the liquefiable layer above the pile caps. Such a phenomenon would still apply a kinematic load to the abutment columns and bridge seat, but little kinematic load would be applied to the pile caps and piles themselves. Furthermore, because the width of the abutment columns is far smaller than the width of the pile caps (1.75 meters versus 3.96 meters), then the columns would be more likely to “slice” through the laterally spread soil and attract less kinematic load. However, some mechanism would need to occur to cause the lateral spread to be isolated at the top of the liquefiable layer. One possible mechanism would be the phenomenon of void redistribution and the development of a water film. Void redistribution is a well-documented phenomenon associated with liquefaction, and is perhaps most well known for its purported role in the flow liquefaction failure of the Lower San Fernando Dam following the 1971 San Fernando earthquake (Kramer, 1996). The phenomenon occurs when escaping pore water becomes trapped beneath a low permeability soil cap and is therefore unable to alleviate excess pore pressures. Under these conditions, the individual soil

particles in the liquefied layer can redistribute themselves and consolidate. However, because the pore water is unable to escape, the overlying soil is unable to settle with the consolidated particles in the liquefied soil, thus creating a temporary water film between the non-liquefied soil cap and the liquefied soil. Due to its lack of shear strength, this water film can contribute to significant ground deformations including lateral spread and/or flow failures.

Currently, no analytical methods exist for objectively evaluating the occurrence of void redistribution and the development of a water film in a given soil profile subjected to seismic loading. However, an engineer can recognize an elevated potential for void redistribution and water film development by identifying a continuous liquefiable layer overlain by a continuous low-permeability nonliquefiable cap. Such conditions were encountered in Boring P-1 at the Rio Estrella Bridge in 2010. However, the question of layer continuity was significant and led to the advancement of Borings P-2 and P-3 in 2011. As can be seen in Figure 12-2, the principal soil layers (i.e. low permeability silt cap underlain by loose/saturated sands and gravels) appear to be continuous, thus suggesting an elevated potential for void redistribution and development of a water film in the event of soil liquefaction.

A second deterministic pile response analysis can be performed to evaluate the water film theory. However, lateral deformations would need to be distributed through the liquefied soil and water film in a realistic manner. Unfortunately, no existing procedures to compute such deformations with a water film could be identified at the time of this study. Boulanger et al. (2003) performed a series of centrifuge tests to model lateral spread displacements with a low permeability non-liquefied crust. One of the Boulanger et al. models demonstrated the void redistribution phenomenon and the development of a water film. The relative soil deformations reported in the Boulanger et al. results can be normalized with the thickness of their liquefied

layer and applied to the liquefied soil layer at the Rio Estrella Bridge in order to represent a realistic deformation profile with a water film. These relative deformations are shown in Figure 12-15.

Using the lateral spread distribution shown in Figure 12-15 and a total assumed lateral spread displacement of 2 meters, the deterministic lateral spread displacement profile for the water film was computed as is shown in Figure 12-16.

Using the lateral spread displacement profile shown in Figure 12-16, the deterministic pile response analysis was performed again incorporating the water film assumption. The pile properties and boundary conditions remained unchanged from the previous deterministic analysis described above. Only the soil deformation profile was modified for the analysis. The results of the deterministic water film analysis are shown in Figure 12-17.

12.5.6 Summary of Deterministic Results

The deterministic pile response which assumes that lateral spread displacements were distributed throughout the liquefiable layer at the suggests that pile deformations at the south abutment of the Rio Estrella Bridge should have been larger than what was observed during the post-earthquake reconnaissances of Youd et al. (1992) and Priestley et al. (1991). Figure 12-14 shows that such pile displacements would have been approximately 0.12 meter or greater. In addition, the maximum computed bending moment of approximately 1700 kN-m far exceeds the computed yield moment of approximately 480 kN-m for a single pile, thus suggesting that the piles would have yielded during kinematic loading and that lateral displacements would likely have been larger than 0.12 meter.

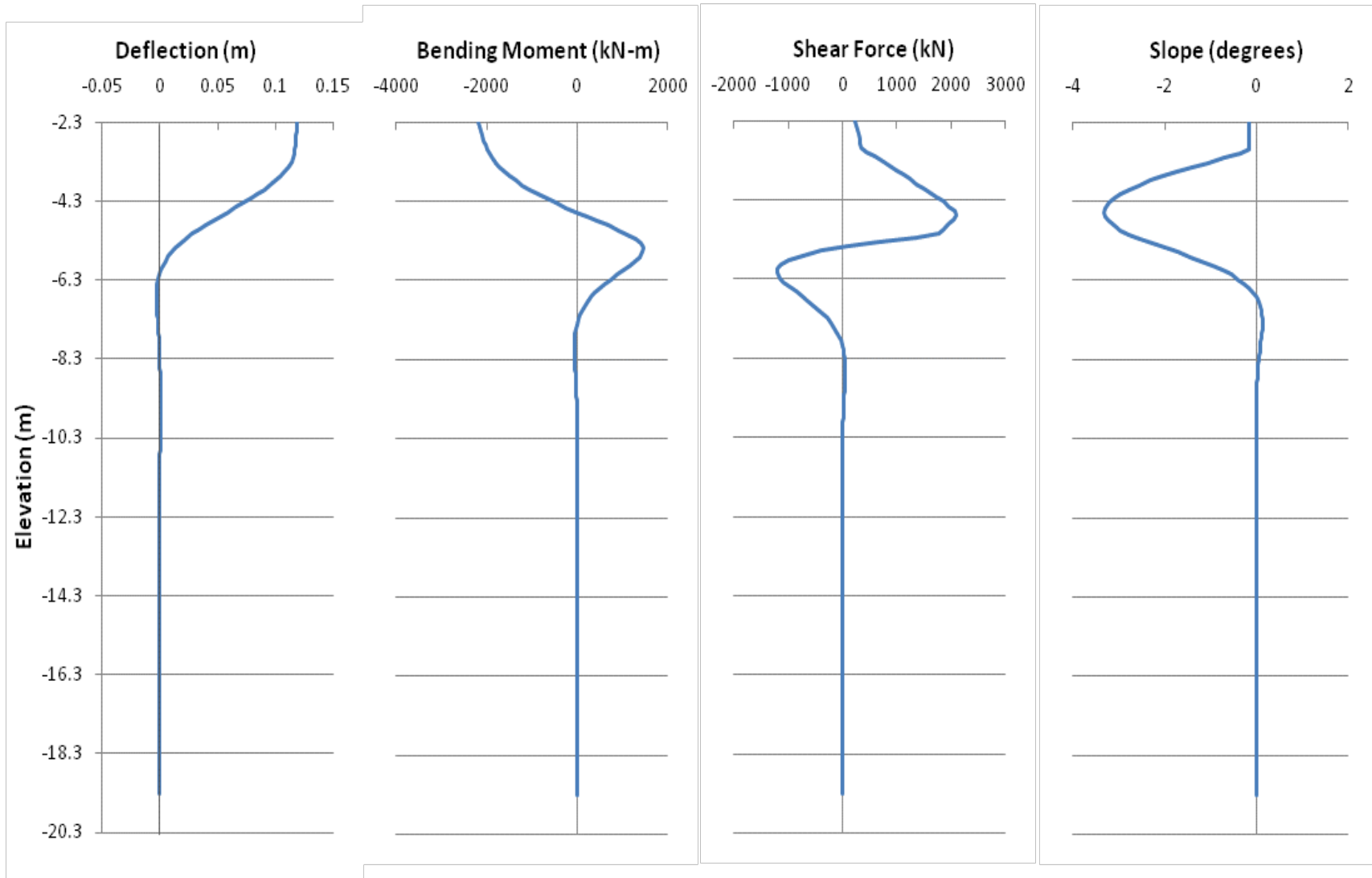


Figure 12-14: Deterministic Computed Pile Response for the Rio Estrella Bridge South Abutment From the 1991 Limon Earthquake

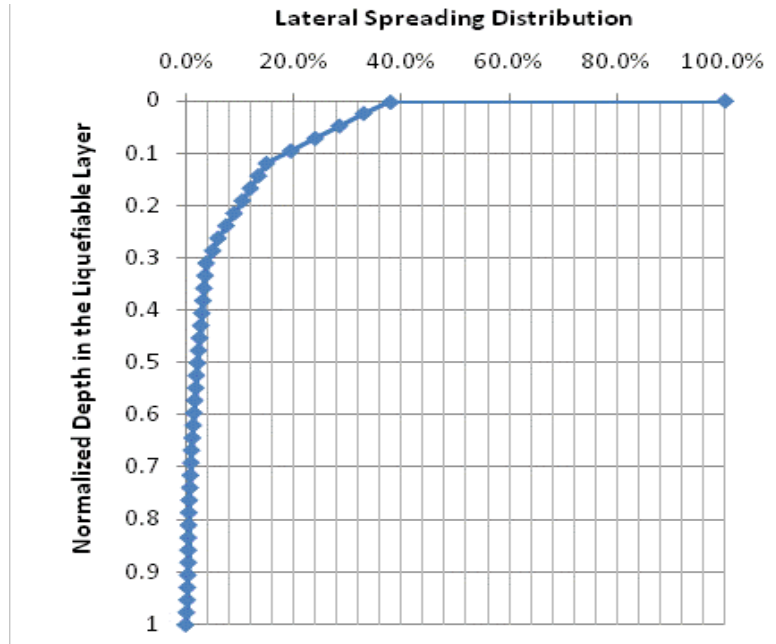


Figure 12-15: Lateral Spread Distribution Versus Normalized Depth in the Liquefiable Layer (After Boulanger et al., 2003)

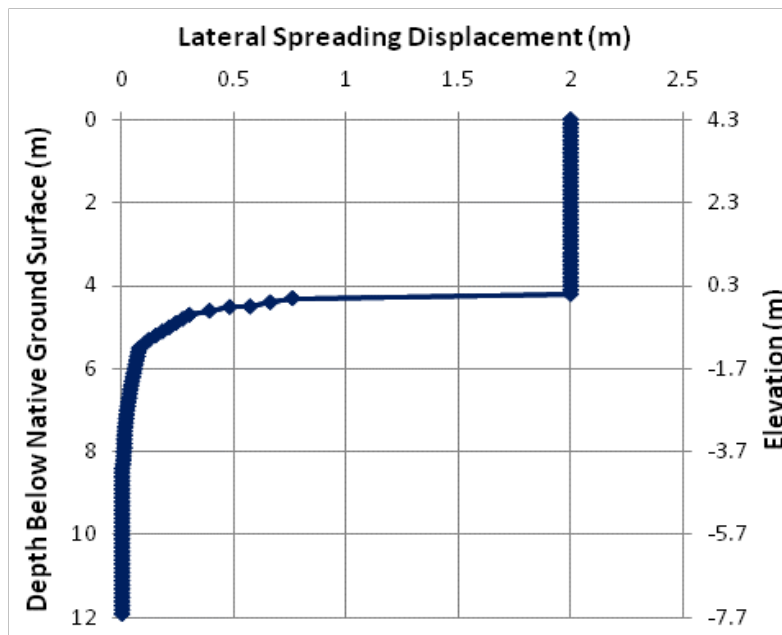


Figure 12-16: Deterministic Lateral Spread Displacement Profile With the Void Redistribution/Water Film Assumption for the Rio Estrella Bridge

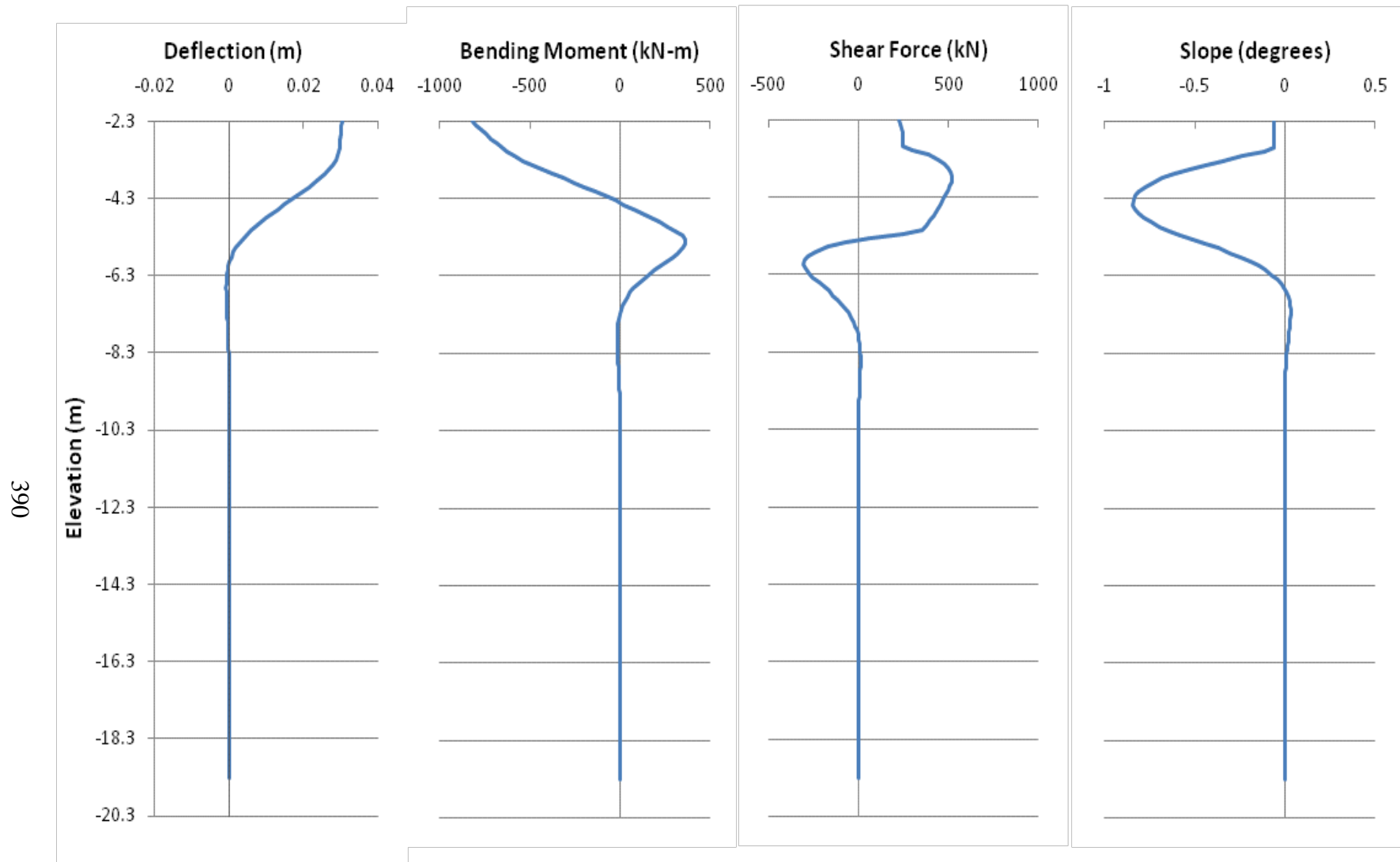


Figure 12-17: Deterministic Pile Response Results With the Void Redistribution/Water Assumption for the Rio Estrella Bridge

Evaluation of the theory that a water film developed due to void redistribution during the 1991 Limon earthquake demonstrates a possible explanation as to why no observable lateral deformations occurred at the southern abutment of the Rio Estrella Bridge. The results of the deterministic pile response analysis with a water film as shown in Figure 12-17 shows a computed lateral displacement of 0.03 meter and a maximum bending moment in the pile of approximately 350 kN-m, which is less than the computed yield moment for a single pile. Such a pile response at the southern abutment would likely be very difficult to detect from the ground surface with traditional surveying equipment. It is noted that the actual maximum bending moment shown in Figure 12-17 is -820 kN-m. However, this value is not likely realistic because it occurs at the connection between the pile cap and the pile. In reality, the connection between the pile cap and the pile would likely yield under such large bending moments, thus allowing for a greater curvature in the pile than is indicated in Figure 12-17, but a substantially smaller bending moment.

While one can not definitively state that void redistribution and the development of a water film was the cause for the apparent lack of damage to the southern abutment of the Rio Estrella Bridge due to the current lack of knowledge regarding the true kinematic response of the piles and pile caps at depth, the phenomenon has been demonstrated to provide a reasonable explanation for the observed performance of the bridge abutment following the 1991 Limon earthquake. Additional investigation into the topic could potentially be of value to the engineering community.

12.6 Performance-Based Pile Response Analysis at the Rio Estrella Bridge

Because the true performance of the piles at the southern abutment of the Rio Estrella Bridge during the 1991 Limon earthquake is not currently known, it would be impractical to use the Rio Estrella Bridge case history for validation of the performance-based kinematic pile response procedure presented in the dissertation. However, the performance-based procedure may still be applied for demonstration purposes if an assumption regarding the lateral spread behavior at the southern abutment is made. For the performance-based analysis, it will be assumed that all liquefaction will result in the development of a water film. In addition, the lateral spread displacement profile for each return period will be computed using the relative lateral spread displacement distribution shown in Figure 12-15.

12.6.1 Probabilistic Ground Motions

A PSHA was performed at the Rio Estrella Bridge site using EZ-FRISK software and the built-in seismic source model for Central and South America developed by Risk Engineering (see Risk Engineering documentation included in Appendix B). This seismic source model included both area and fault sources. The four selected NGA attenuation models (Abrahamson and Silva, 2008; Chiou and Youngs, 2008; Campbell and Bozorgnia, 2008; and Boore and Atkinson, 2008) were assigned to crustal seismic sources, and select attenuation models developed for subduction zones (Youngs et al., 1997; Atkinson and Boore, 2003; and Zhao et al., 2006) were assigned to the subduction seismic sources. Finally, near-source and directivity effects were accounted for in the PSHA by incorporating the fault-normal response spectrum modifications presented by Somerville et al. (1997) and Abrahamson (2000) for all fault sources. A table of the fault sources located within about 100 km of the site is presented in Table 12-4.

Table 12-4: EZ-FRISK Faults Within About 100 km of the Rio Estrella Bridge

Fault Name	Type	Fault Length (km)	Source to Site Distance (km)	Characteristic Magnitude	Slip Rate (mm/yr)	Recurrence Rate
Limon fault	Reverse	162	8.0	7.8	1.0	---
Panama - North (Caribbean)	Subduction Interface	817	32	8.0	4.0	---
Longitudinal fault	Reverse	42	103	7.4	0.1	---
Longitudinal fault - Costa Rica 2	Reverse	52	103	7.0	0.5	---
Costa Rica	Subduction Intraslab	288	103	7.7	---	0.4958
Guapiles fault	Reverse	8	106	6.1	4.0	---

The seismic hazard curve for the PGA developed from the PSHA is presented in Figure 12-18. The ground motions corresponding 10-percent and 2-percent probabilities of exceedance in 50 years (i.e. return periods of 475 and 2475 years, respectively) are 0.568g and 0.938g, respectively.

The seismic hazard contributions from the individual sources are shown in Figure 12-19. From Figure 12-19, it appears that the Costa Rica arc and shear zone (area source), the Costa Rica fault (subduction interface source), and the Panama North (Caribbean) fault (subduction interface source) govern the probabilistic seismic hazard at most return periods for the PGA. The probabilistic response spectra developed from the PSHA for seven different return periods are shown in Figure 12-20. Finally, simplified deaggregation plots of the PGA are presented in Figure 12-21.

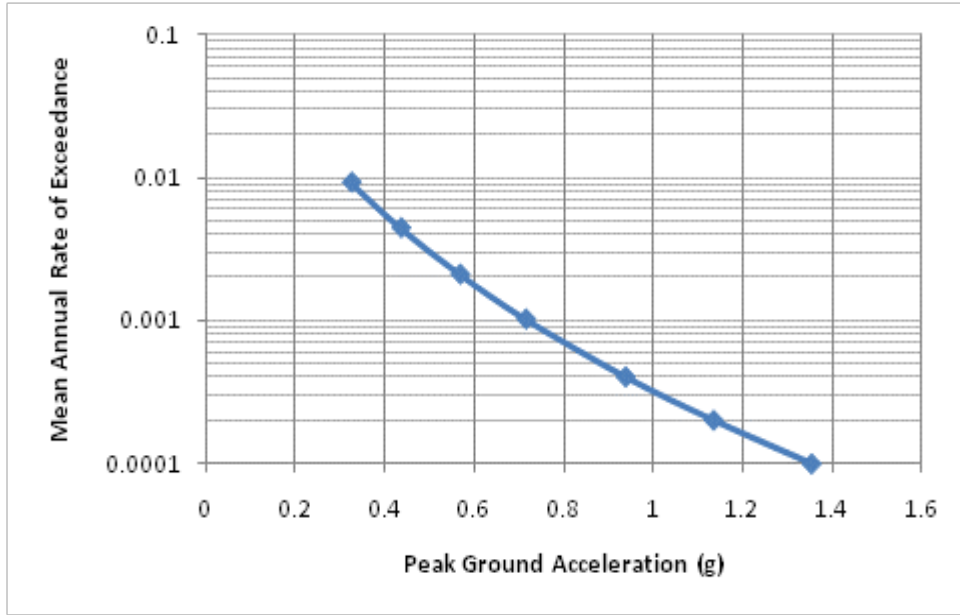


Figure 12-18: Seismic Hazard Curve for the PGA at the Rio Estrella Bridge

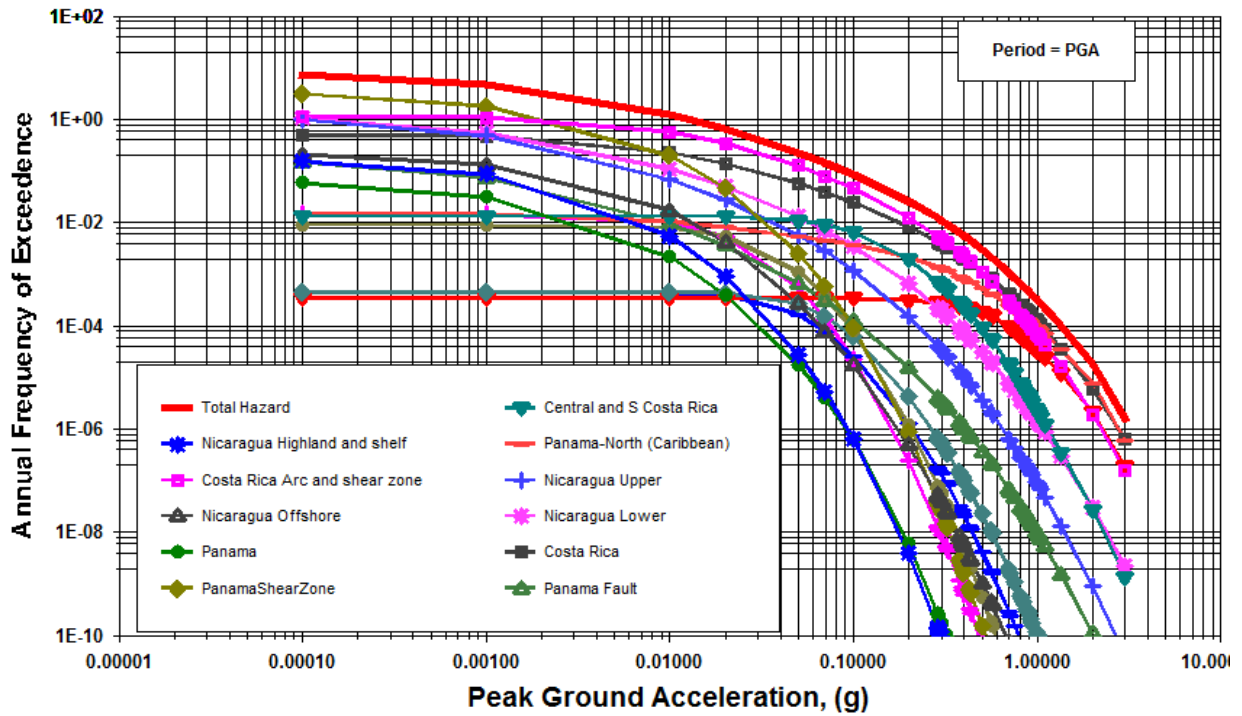


Figure 12-19: Source Contributions to Probabilistic Seismic Hazard for the Rio Estrella Bridge

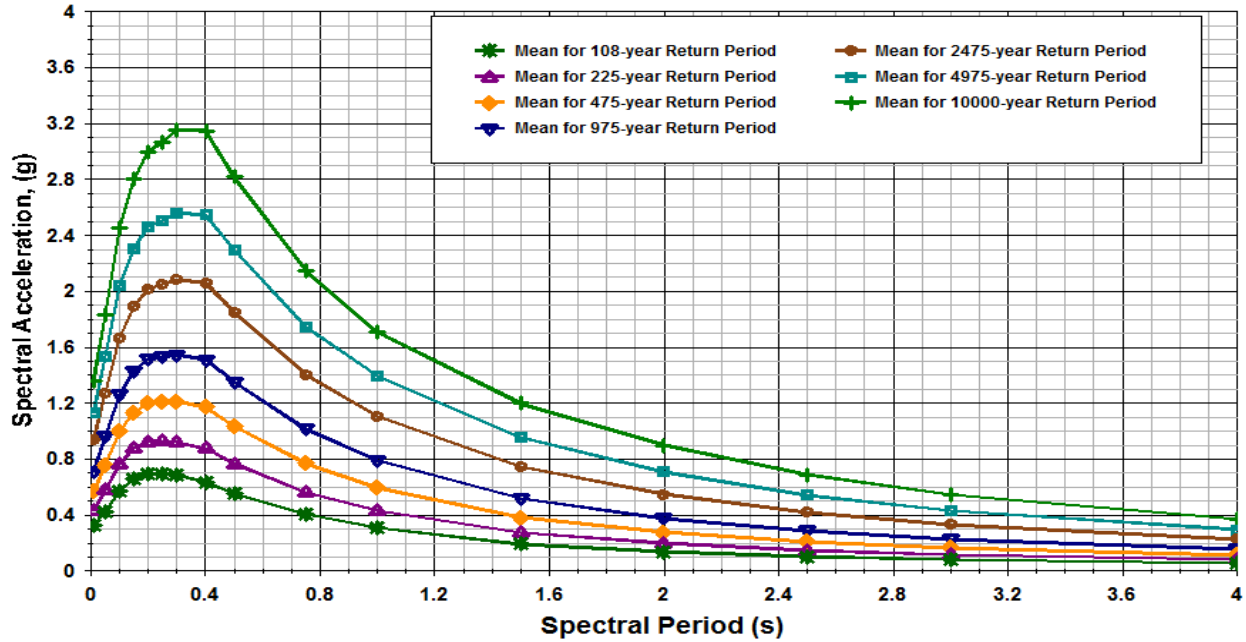


Figure 12-20: Probabilistic Response Spectra (5-Percent Damping) for the Rio Estrella Bridge

12.6.2 Probabilistic Liquefaction Triggering

Using the probabilistic estimates of a_{max} shown in Figure 12-18 in conjunction with the magnitude/distance deaggregations shown in Figure 12-21, probabilistic estimates of liquefaction triggering were computed with the Kramer and Mayfield (2007) procedure using Equations (6-1) and (6-2). The performance-based liquefaction triggering computations were performed using the computer program PPRS. The resulting factors of safety against liquefaction triggering for various return periods are shown in Figure 12-22. These factors of safety were computed using the averaged SPT blowcount information for Rio Estrella Bridge as shown in Figure 12-3. A factor of safety less than or equal to 1.2 was assumed to be liquefiable for this study.

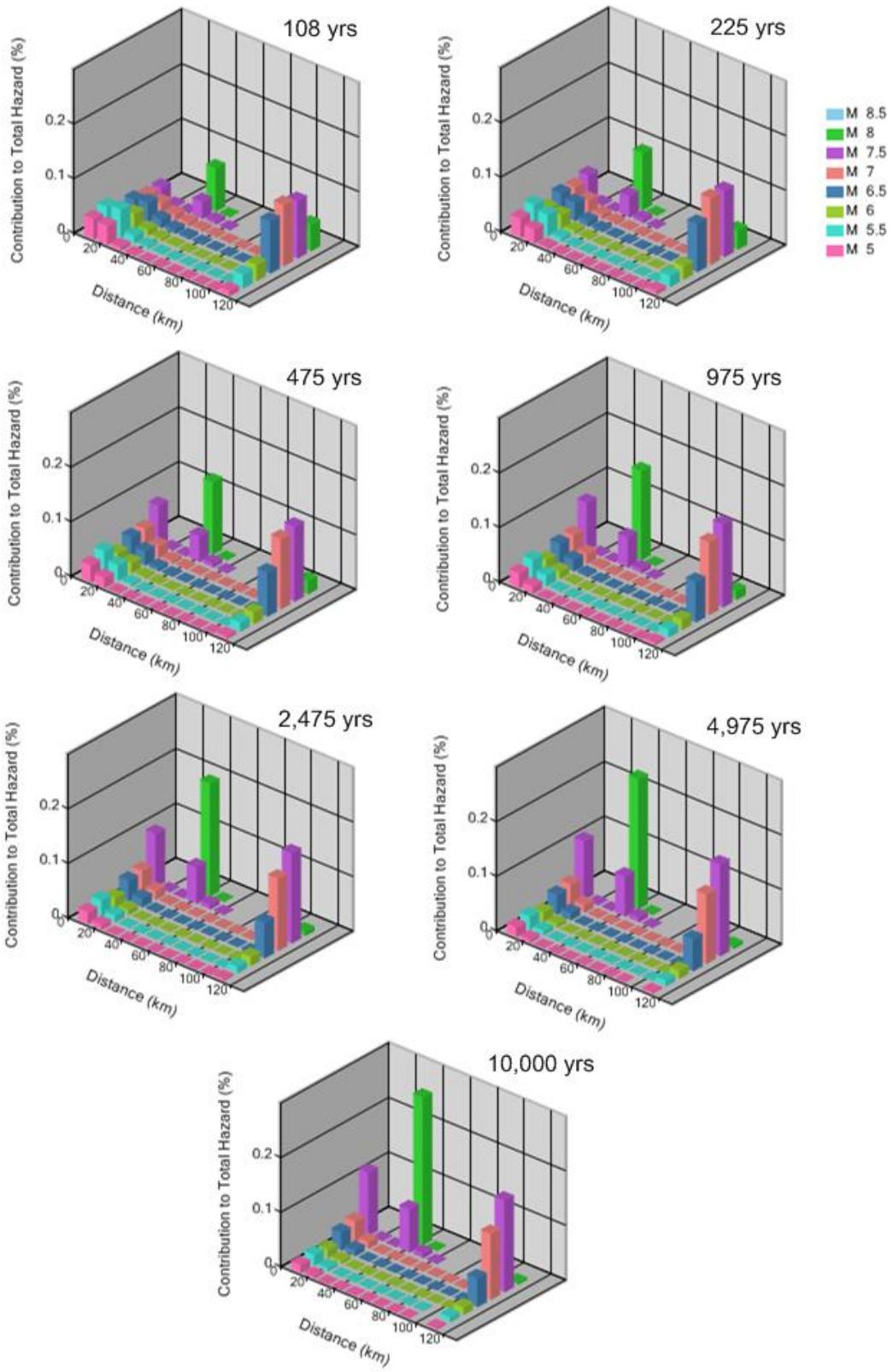


Figure 12-21: Deaggregation Plots for the PGA at the Rio Estrella Bridge

For fine-grained soil layers not considered susceptible to liquefaction due to plasticity, a generic factor of safety against liquefaction equal to 2.0 was assigned regardless of return period. A maximum factor of safety equal to 4.0 was assigned to layers with very high resistance to liquefaction triggering. In general, Figure 12-22 shows that for return periods greater than about 108 years, liquefaction begins triggering at depths below 4.3 meters (EL. 0.0m). The thickness of the liquefiable layer appears to increase with return period.

12.6.3 Development of the Loading Parameter, \mathcal{L}

The loading parameter \mathcal{L} , which serves as the intensity measure in the performance-based pile response procedure, was computed using Equations (6-4) through (6-6) from Section 6.8 of this dissertation. The equations were loaded as user-defined attenuation relationships into EZ-FRISK, and the Risk Engineering (2010) seismic source model for Central and South America was used to compute probabilistic estimates for \mathcal{L} . A plot of the hazard curves for \mathcal{L} is presented in Figure 12-23. Note that the loading parameter for each model is unique and independent from the other models.

12.6.4 Development of the Fragility Functions for Lateral Spread Displacement

Fragility curves relating the probability of exceeding a given lateral spread displacement to the loading parameter \mathcal{L} were developed according to the procedure described in Section 6.9. The site parameter \mathcal{S} for the three selected empirical lateral spread models was computed using the soils and the averaged SPT blowcounts shown in Figure 12-3 with Equations (6-7), (6-9), and (6-11). A free-face ratio of 6-percent was used with a free-face height of 4.6 meters. Depth

limitations as described in Section 3.7 were incorporated. The computed values of \mathcal{S} are shown in Table 12-5.

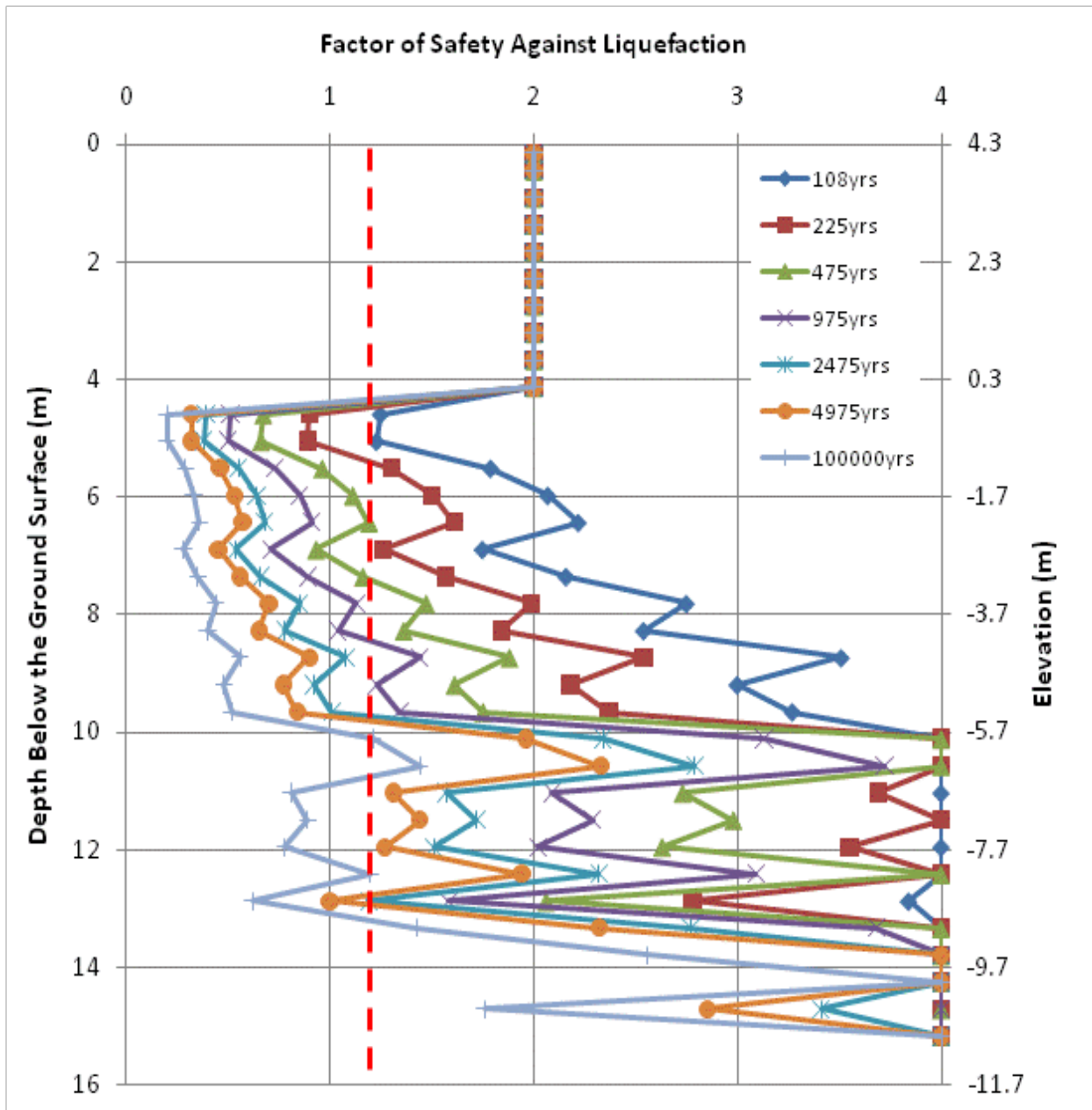


Figure 12-22: Performance-Based Liquefaction Triggering Results for the Rio Estrella Bridge

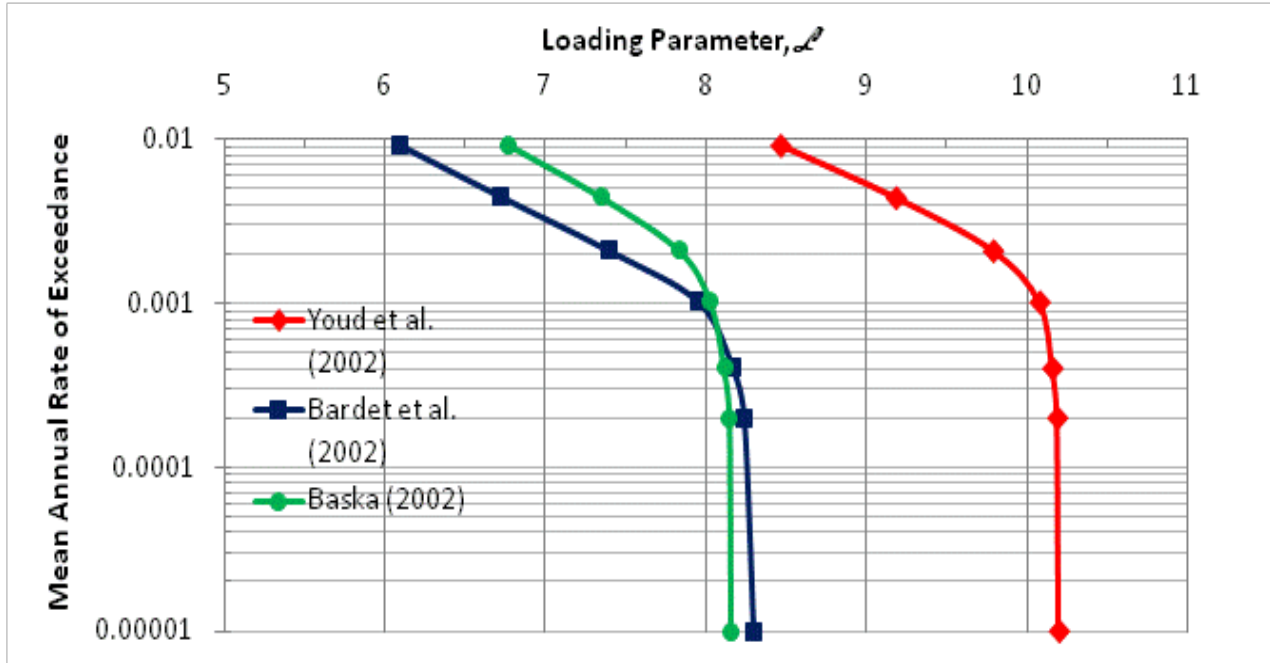


Figure 12-23: Hazard Curves for the Loading Parameter \mathcal{L} for the Rio Estrella Bridge

Table 12-5: Site Parameter \mathcal{S} for the Rio Estrella Bridge

Empirical Lateral Spread Model:	Site Parameter \mathcal{S}
Youd et al. (2002)	-9.912
Bardet et al. (2002)	-6.815
Baska (2002)	-6.430

With \mathcal{S} computed for each empirical lateral spread model, families of lateral spread fragility curves were developed using Equation (6-19). These curves are plotted for lateral spread displacements of 0.1 meter and 1 meter in Figure 12-24. Values of \mathcal{S} and lateral spread fragility

curves were calculated automatically in the computation of probabilistic lateral spread displacements using PPRS software.

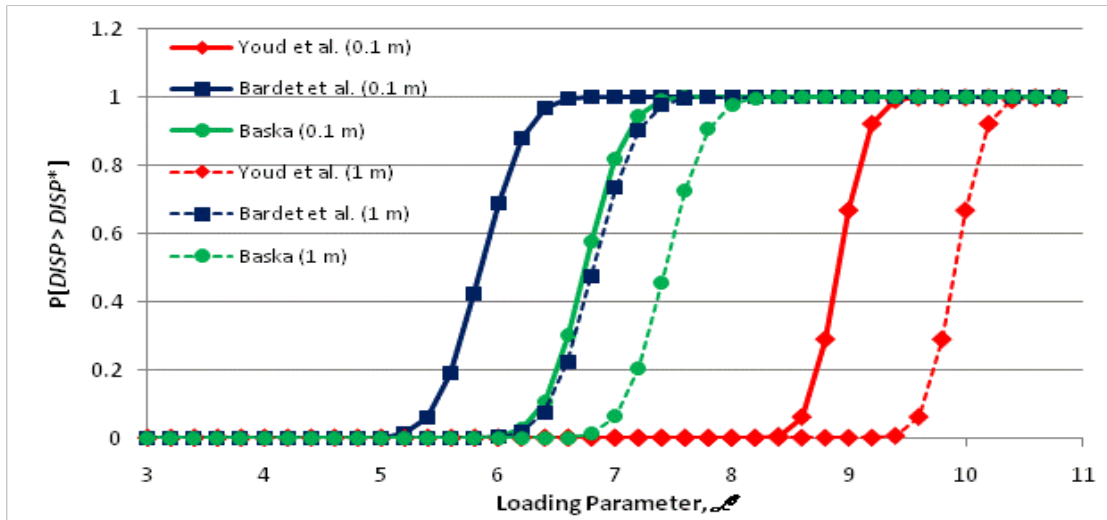


Figure 12-24: Lateral Spread Fragility Curves for $DISP^*=0.1$ Meter and $DISP^*=1$ Meter at the Rio Estrella Bridge

12.6.5 Development of Probabilistic Lateral Spread Displacements

Using PPRS software, the lateral spread fragility curves were convolved with the hazard curves for the lateral spread loading parameters \mathcal{L} shown in Figure 12-23 using the steps presented in Section 6.10. The resulting hazard curves for lateral spread displacement at the ground surface are shown in Figure 12-25.

Figure 12-25 shows good agreement in computed probabilistic lateral spread displacements between the Baska (2002) and the Bardet et al. (2002) empirical models at annual

frequencies greater than 0.001 (i.e. return periods less than 1000 years); however, the hazard curves tend to diverge at lower annual frequencies (i.e. higher return periods). The Bardet et al. (2002) model appears to compute the largest displacements at most return periods, and the Youd et al. (2002) model appears to compute the smallest displacements. The average displacement hazard curve was computed by weighting the mean annual rates of exceedance using equal weights for all three empirical models.

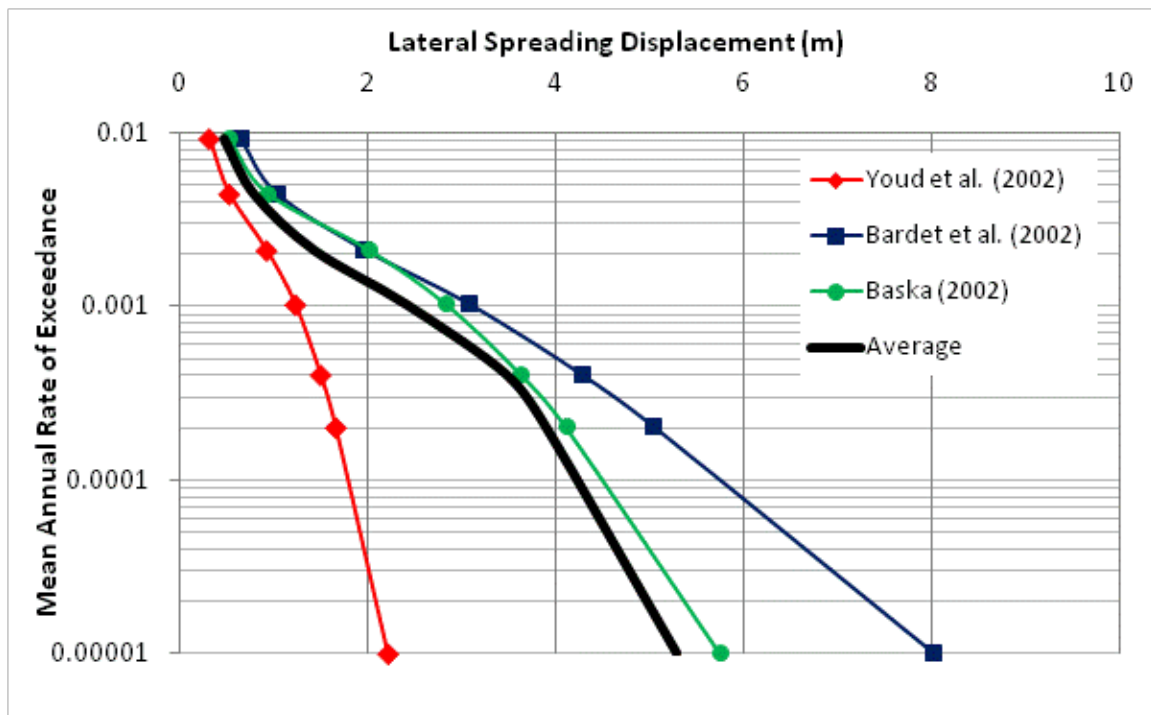


Figure 12-25: Lateral Spread Hazard Curves for the Rio Estrella Bridge

The average computed probabilistic lateral spread displacements were propagated through the soil profile using the Bardet et al. (2003) relative lateral spread displacement

distribution shown in Figure 12-15 in conjunction with the probabilistic liquefaction triggering profiles shown in Figure 12-22. The resulting probabilistic lateral spread displacement profiles are presented in Figure 12-26.

12.6.6 Development of Fragility Functions for the Kinematic Pile Response

Variance of the kinematic pile response for the lateral spread displacement profiles shown in Figure 12-26 was computed using a Monte Carlo simulation for each return period as described in Section 6.11. Coefficients of variation for the various soil parameters required for the p-y models in LPILE were estimated from Table 6-2. In order to account for the variance of the passive force from the overlying non-liquefied soil crust and approach embankment, the resulting overturning moment from the passive force used in computing the rotational stiffness for the equivalent single pile was randomized using a log-normal distribution with a mean value of 357,400 kN-m. The standard deviation of the logarithm of the overturning moment was estimated to be equal to 0.16, which provides an overturning moment approximately equal to 300% the mean overturning moment at a value 3σ . This upper-bound value is intended to approximate the overturning moment that would be computed using log-spiral passive theory. 10,000 iterations were used for each Monte Carlo simulation, and the spreadsheet/macro LPILE MC Simulator was used to perform the analyses. Kinematic pile response including displacements, bending moments, shear forces, and curvature was computed for each of the seven return periods of lateral spread displacement profiles. Mean values and the standard deviation of the pile response was computed for each node in the pile response analysis. The mean displacements and standard deviations for the pile displacement are shown in Figure 12-27. In general, the computed coefficients of variation for the pile displacement ranged from about 4-

percent to 10-percent. Similar mean values and standard deviations were also developed for the bending moments, shear forces, and curvature of the equivalent single pile.

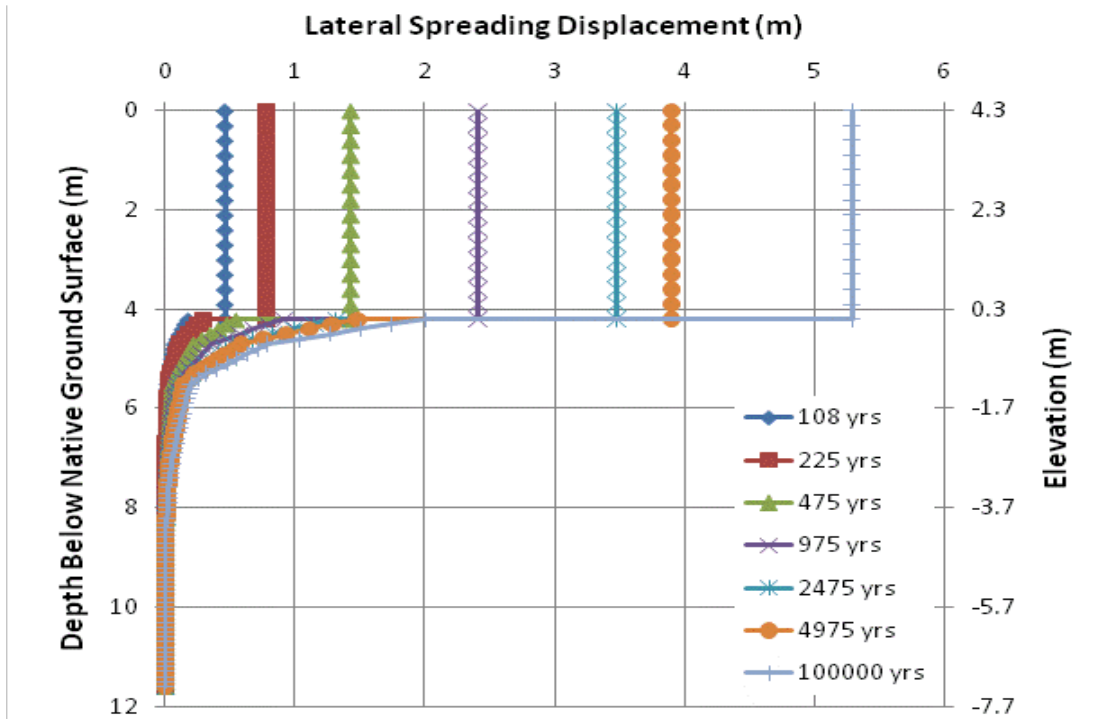


Figure 12-26: Probabilistic Lateral Spread Displacement Profiles for the Rio Estrella Bridge

Using the mean pile response values and their corresponding standard deviations, fragility functions were developed for displacements, bending moments, shear forces, and curvature at each node of the caisson and for each return period using Equation (6-22). The functions were developed using PPRS software and were directly convolved with the lateral spread displacement hazard curves to create performance-based estimates of kinematic pile response.

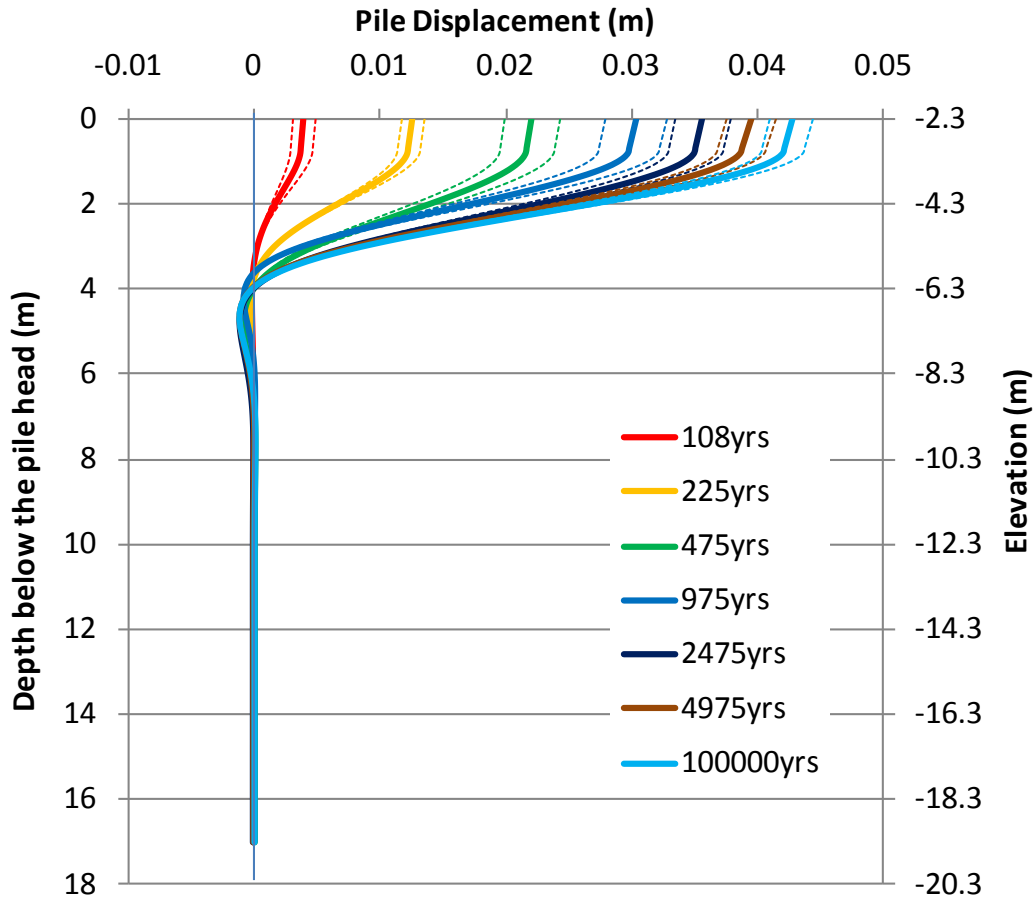


Figure 12-27: Mean Displacements and ± 1 Standard Deviations for the Equivalent Single Pile at the Rio Estrella Bridge Computed From a Series of Monte Carlo Simulations

12.6.7 Development of Probabilistic Kinematic Pile Response

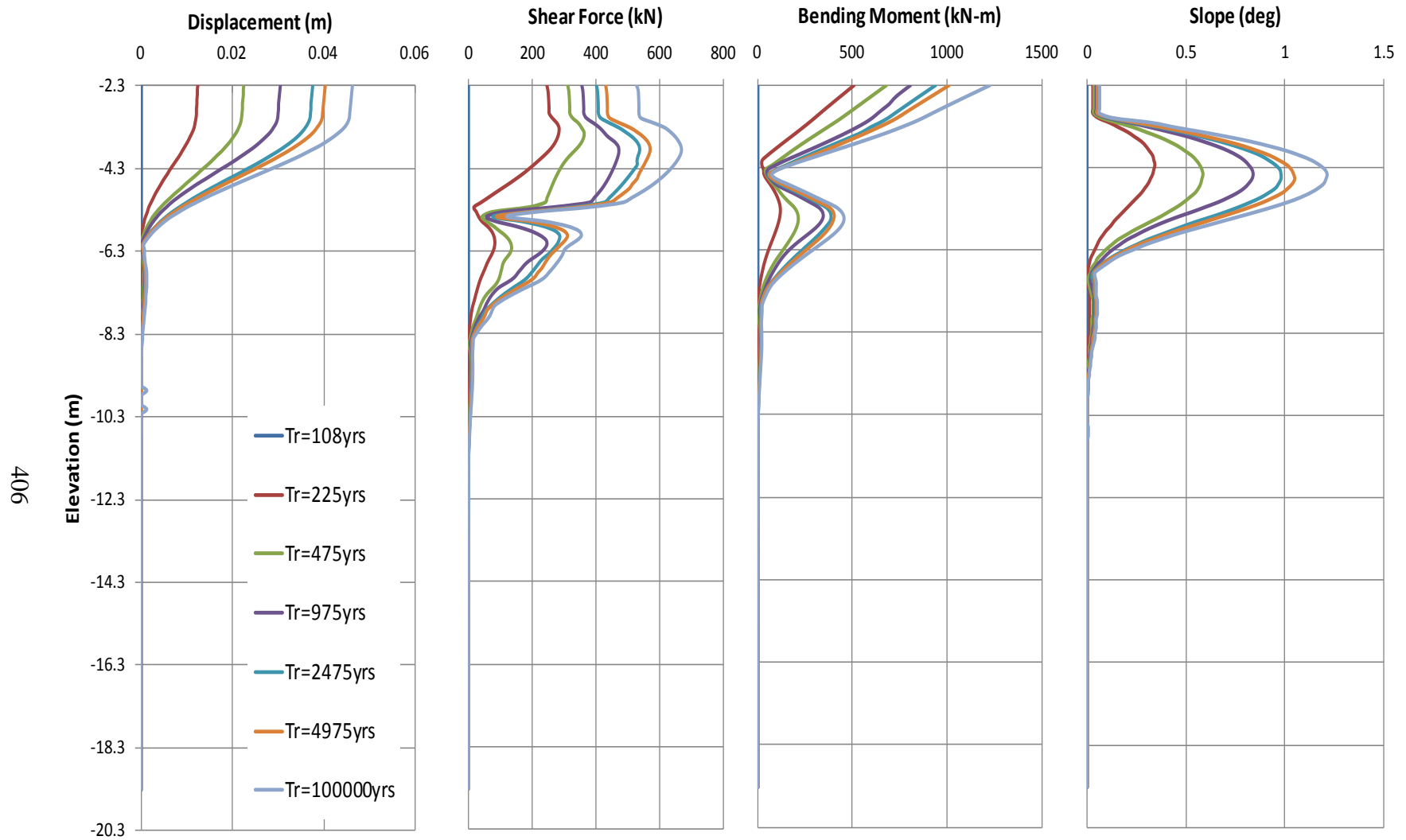
The probabilistic kinematic pile response was computed for each node in the LPILE analysis for the Rio Estrella Bridge by convolving the results from the fragility relationships developed in Section 12.6.6 with the probabilistic lateral spread displacement profiles developed in Section 12.6.5. PPRS software was used to apply Equation (6-23) and the steps presented in Section 6.12 for computing probabilistic estimates of pile displacement, bending moments, shear

forces, and curvature for all nodes in the pile response model. The resulting probabilistic pile response profile is shown in Figure 12-28.

12.6.8 Discussion of Results

The performance-based pile response analysis at the southern abutment of the Rio Estrella Bridge demonstrates that the magnitude of lateral spread displacement likely would have been negligible as long as the majority of that displacement was concentrated near the top of the liquefied layer. One theory that could possibly explain such a concentration is the occurrence of void redistribution and the development of a water film at the top of the liquefiable layer during the 1991 Limon earthquake. The results of this study demonstrate how the development of a water film during ground shaking could have limited the foundation deformations despite significant lateral spread at the ground surface due to the fact that the pile caps would have been located approximately 2.3 meters below the water film. Most of the lateral spread deformations would have loaded the relatively narrow abutment piers rather than the relatively wide pile caps. While it is currently impossible to conclusively state that such a water film developed in conjunction with liquefaction during the 1991 Limon earthquake, the back-calculated analytical evidence and the observed soil stratigraphy support the theory.

The computed deterministic pile response shown in Figure 12-14 showed a peak pile displacement of approximately 0.03 meter, a peak bending moment of approximately 350 kN-m, a peak shear force of approximately 500 kN, and a maximum slope of 0.84 degrees. These values of pile response correspond to return periods of 907, 1046, 1906, and 1012 years and probabilities of exceedance equal to 7.9%, 6.9%, 3.9%, and 7.1% in 75 years, respectively. These return periods also match reasonably well those computed in the performance-based pile response analysis for the Rio Bananito Railway Bridge in Section 11.6.8.



406

Figure 12-28: Probabilistic Pile Response Curves (Absolute Values) for the Rio Estrella Bridge

13 SUMMARY AND CONCLUSIONS

Lateral spread is a term commonly used to describe the permanent deformation of the ground resulting from soil liquefaction due to earthquake shaking. Its effects on infrastructure and critical lifelines can be devastating. This study reviewed and summarized many of the basic mechanics behind liquefaction initiation and subsequent occurrence of lateral spread. In addition, several of the simplified empirical procedures currently used in engineering practice to design for these phenomena were presented and briefly discussed.

This study introduced a new pile response procedure based on the Pacific Earthquake Engineering Research Center's performance-based earthquake engineering framework for computing performance-based kinematic pile response due to lateral spread displacement. Unlike previously published performance-based models for computing kinematic pile response, the procedure presented in this study is not aimed solely at bridge foundations, and has the capability of producing probabilistic estimates of kinematic pile response for any deep foundation system subjected to lateral spread displacements. The procedure utilizes and combines previously published methodologies for evaluating liquefaction triggering, estimating lateral spread displacements, and computing pile response using p-y soil springs with popular analytical software such as LPILE in order to produce probabilistic estimates of kinematic pile response for either single piles or pile groups. The ultimate value of this procedure to engineers and decision makers is that it provides them with a tool to objectively evaluate the risk posed to a given deep foundation system from liquefaction-induced lateral spread.

This study also developed and presented five separate lateral spread case histories involving bridges that were damaged following the April 22, 1991 earthquake which struck the Limon Province in Costa Rica. These case histories were principally developed to demonstrate the performance-based kinematic pile response procedure presented in Chapter 6. While a simple scenario example could have achieved this same purpose, development and incorporation of these case histories were deemed more valuable because the case histories by themselves can potentially shed additional light on the phenomenon of lateral spread and be used by future researchers in their related studies. The magnitude 7.6 earthquake killed 53 people, injured another 193 people, and disrupted an estimated 30-percent of the highway pavement and railways in the region due to fissures, scarps, and soil settlements resulting from liquefaction. As part of this study, a subsurface exploration program was developed to evaluate the soil conditions at each of the five selected bridges, where post-earthquake structural damage was observed to range from minor to severe. As a result, this study will significantly increase the number of available case histories for researchers investigating lateral spread and its effects on bridge structures and their foundations, and should prove to be a valuable addition to the field of earthquake hazard mitigation.

Both probabilistic and deterministic estimates of kinematic pile response for each case history were computed and (where appropriate/available) compared against the observed kinematic pile response from the 1991 earthquake. This study demonstrates that both deterministic and performance-based simplified pile response procedures are capable of reasonably modeling the response of even fairly complex systems for most cases given that sufficient information regarding the forces, mechanisms, and uncertainties involved is available for incorporation into the model.

Several valuable observations were made in the development and analysis of the five Costa Rican lateral spread case histories. These observations include:

- 1) Empirical and simplified procedures for computing liquefaction triggering and lateral spread displacements can produce reasonable results if proper input parameters are used;
- 2) The three empirical lateral spread models applied in this study (Youd et al., 2002; Bardet et al., 2002; and Baska, 2002) each computed lateral spread displacements that matched reasonably well with observed lateral spread displacements following the 1991 Limon earthquake. The three models were generally in good agreement with one another for every case history analyzed, with the Baska (2002) model consistently computing the largest displacements. The models appear to possibly under-predict lateral spread displacements for cases where shear forces in the soil are likely relatively large (e.g., free-face ratios greater than 20-percent) or for cases where void redistribution/water film development may govern the soil deformation behavior.
- 3) Extrapolation of empirical lateral spread models may produce reasonable results, but caution and engineering judgment should be applied in interpreting and utilizing such results;
- 4) Simplified kinematic pile response analysis methods incorporating equivalent single pile procedures appear capable of producing reasonable approximations of the average pile response from a given deterministic event if all of the significant contributing factors to the pile response (e.g. restraining “strut” loads from a bridge deck, etc.) are adequately accounted for;
- 5) Modern procedures for computing kinematic pile response at bridges may not adequately consider the restraining force supplied by the possible presence of the bridge

deck. Results from this study suggest that for rigid abutments, the bridge deck may significantly alter the kinematic pile response by limiting lateral displacements at the head of the pile group and causing the abutment to rotate beneath the bridge deck;

- 6) Both lateral spread displacement in the native soils and seismic slope displacement in an approach embankment can apply significant kinematic loads to the pile foundations of a bridge. Therefore, both modes of ground deformation should be considered in a deterministic analysis, and the governing deformation should drive the pile response model;
- 7) Flow liquefaction failure can impose significant damage to deep foundations and the structures which they support. Therefore, ground improvement or other preventative measures should be incorporated to either mitigate the triggering of liquefaction or to limit its effects if flow failure is determined to be a viable risk.
- 8) Back-calculated residual shear strengths from the Rio Bananito Highway Bridge failure suggest that normalized residual strength ratios may significantly under-predict the available residual shear strength of liquefied soils at shallow depths. However, the back-calculated uniform residual strength fell within the range recommended by Seed and Harder (1990);
- 9) The occurrence of a water film due to particle redistribution during liquefaction can significantly increase the ground deformations resulting from an earthquake. Therefore, if the development of a water film is considered a viability, ground deformations resulting from the design earthquake may be much larger than those computed by traditional analysis methods;

- 10) Due to the observed performance of the foundation beneath the south abutment of the Rio Estrella Bridge and the results of the pile response analyses of this study, it may be possible to significantly limit the deformations and corresponding damage to a given structure if the foundation is placed below the depth where significant soil deformations are occurring due to liquefaction and lateral spread. Few cases would likely exist where such a solution would be considered economical, but for cases where the footings or pile cap must be placed at depth for other design requirements (e.g. scour limitations), no additional ground improvement for liquefaction/lateral spread mitigation may be necessary if an analysis demonstrates that the foundation will be able to resist the anticipated kinematic loads;
- 11) The results from the performance-based kinematic pile response analysis performed at the Rio Bananito Railway Bridge and the Rio Estrella Bridge suggest that the kinematic pile response observed during the 1991 Limon earthquake corresponds to a return period between about 600 years and 1900 years (probabilities of exceedance equal to 8% and 2.6% in 50 years, respectively).

The performance-based kinematic pile response analyses at the Rio Bananito Railway Bridge and at the Rio Estrella Bridge demonstrate how the proposed procedure could be of use to the engineering community. Since modern seismic bridge code such as AASHTO LRFD typically requires engineers to design for the 1,075 return period (i.e. 7-percent probability of exceedance in 75 years), a performance-based kinematic pile response analysis at the northern abutment of the Rio Bananito Railway Bridge would have revealed the kinematic caisson performance associated with a return period of 1,075 years to be unacceptable, and retrofitting of the caissons to improve their seismic performance would likely have been recommended.

However, a similar analysis for the southern abutment of the Rio Estrella Bridge would have revealed acceptable performance of the foundation at the same level of risk, thus requiring no retrofitting of the bridge foundation to resist lateral spread loads.

REFERENCES

- Abdoun, T. H., Dobry, R., O'Rourke, T. D., & Chaudhuri, D. (1996). Centrifuge modeling of seismically-induced lateral deformation during liquefaction and its effects on a pile foundation. *6th Japan - U.S. Workshop on Earthquake Resistant Design of Lifeline Facilities and Countermeasures Against Soil Liquefaction, Report No. NCEER-96-0012*, 525-539. Buffalo, New York: SUNY.
- Abdoun, T., Dobry, R., & O'Rourke, T. D. (1997). Centrifuge and numerical modeling of soil-pile interaction during earthquake induced soil liquefaction and lateral spreading. *Observation and Modeling in Numerical Analysis and Model Tests in Dynamic Soil-Structure Interaction Problems, Geotechnical Special Publication No. 64*, 76-90. New York: ASCE.
- Abrahamson, N. A. (2000). Effects of rupture directivity on probabilistic seismic hazard analysis. *Proceedings, 6th International Conference on Seismic Zonation*. Palm Springs, FL.
- Abrahamson, N. A., & Silva, W. J. (2008). Summary of the Abrahamson & Silva NGA ground-motion relations. *Earthquake Spectra*, 24(1), 67-98.
- Abramowitz, & Stegun. (1965). *Handbook of Mathematical Functions*. Dover Publications (originally published by the National Bureau of Standards, 1964).
- Adachi, N., Miyamoto, Y., & Koyamada, K. (1998, September 25). Shaking table test and lateral loading for pile foundation in saturated sand. *Proceedings, International Conference Centrifuge '98*, 289-294. (T. Kimura, O. Kusakabe, & J. Takemura, Eds.) Tokyo, Japan.
- Al Atik, L. (2009, September). NGA Excel Spreadsheet, Version 1.0. Pacific Earthquake Engineering Research Center; http://peer.berkeley.edu/products/rep_nga_models.html.
- Alarcon-Guzman, A., Leonards, G. A., & Chameau, J. L. (1988). Undrained monotonic and cyclic strength of sands. *Journal of Geotechnical Engineering*, 114(10), 1089-1109.
- Ambraseys, N. (1988). Engineering seismology. *Journal of Earthquake Engineering and Structural Dynamics*, 17, 1-105.
- American Petroleum Institute (API). (1993). *Recommended practice for planning, design, and constructing fixed offshore platforms, API-RP-2A-WSD, 20th Ed.* Washington D.C.: API.

- Anagnos, T., & Kiremidjian, A. S. (1984). Stochastic time-predictable model for earthquake occurrences. *Bulletin of the Seismological Society of America*, 74, 6, 2593-2611.
- Andrus, R. D., Piratheepan, P., Ellis, B. S., Zhang, J., & Hsein Juang, C. (2004). Comparison of liquefaction evaluation methods using penetration-VS relationships. *Soil Dynamics and Earthquake Engineering*, 24(9-10), 713-721.
- Arduino, P., Iankatharan, M., Kramer, S. L., Kutter, B. L., & Shin, H. S. (2006). Experimental and numerical analysis of seismic soil-pile-structure interaction of a two-span bridge. *Proceedings, 8th U.S. National Conference on Earthquake Engineering, Paper No. 504*. San Francisco, CA.
- Ashford, S. A., & Rollins, K. M. (2002). TILT: Treasure Island liquefaction test final report. *Report No. SSRP-2001/17*. Department of Structural Engineering, University of California, San Diego.
- Ashford, S. A., Juirnarongrit, T., Sugano, T., & Hamada, M. (2006). Soil-pile response to blast-induced lateral spreading I: Field Test. *Journal of Geotechnical and Geoenvironmental Engineering*, 132, 2, 152-162. ASCE.
- Atkinson, G. M., & Boore, D. M. (2003). Empirical ground-motion relations for subduction-zone earthquake and their application to Cascadia and other regions. *Bulletin of the Seismological Society of America*, 93, 4, 1703-1729.
- Balakrishnan, A., Kutter, B. L., & Idriss, I. M. (1997). Liquefaction remediation at bridge sites - centrifuge data report for BAM05. *Report No. UCD/CGMDR-91/10*. Center for Geotechnical Modeling, University of California at Davis.
- Bardet, J. P., Tobita, T., Mace, N., & Hu, J. (2002). Regional modeling of liquefaction-induced ground deformation. *Earthquake Spectra*, 18(1), 19-46.
- Bartlett, S. F., & Youd, T. L. (1992). Empirical analysis of horizontal ground displacement generated by liquefaction-induced lateral spread. *Technical Report No. NCEER-92-0021*, 114 pp. Buffalo, New York: National Center for Earthquake Engineering Research, State University of New York.
- Bartlett, S. F., & Youd, T. L. (1995). Empirical prediction of liquefaction-induced lateral spread. *Journal of Geotechnical Engineering*, 121(4), 316-329.
- Baska, D. (2002). An analytical model for prediction of lateral spread displacement. *PhD Dissertation*. Seattle, Washington: University of Washington.
- Baziar, M. H., Dobry, R., & Elgamal, A. W. (1992). Engineering evaluation of permanent ground deformations due to seismically-induced liquefaction. *Technical Report NCEER-92-0007*. Buffalo, New York: National Center for Earthquake Engineering Research, State University of New York.

- Baziar, M. H., Dobry, R., & Elgamel, A. M. (1992). Engineering evaluation of permanent ground deformations due to seismically-induced liquefaction. *Technical Report NCEER-92-0007*. Buffalo, New York: National Center for Earthquake Engineering Research, State University of New York.
- Baziar, M. H., Esna-Ashari, M., & Zadeh, H. S. (2004). Comparison of soil classification methods using CPT results. *Proceedings, 5th International Conference on Case Histories in Geotechnical Earthquake Engineering*. New York, New York.
- Beres, J. (2003). *Teach Yourself Visual Studio.NET 2003 in 21 Days*. Indianapolis: Sams Publishing.
- Berrill, J. B., Christensen, S. A., Keenan, R. J., & Okada, W. (1997). Lateral-spreading loads on a piled bridge foundation. *Seismic Behavior of Ground and Geotechnical Structures*, 173-183. (Seco, & Pinto, Eds.) Balkema, Rotterdam.
- Bertero, R. D., & Bertero, V. V. (2004). Performance-based seismic engineering: Development and application of a comprehensive conceptual approach to the design of buildings. *Chapter 8, Earthquake Engineering: From Engineering Seismology to Performance-Based Engineering*. (Y. Bozorgnia, & V. V. Bertero, Eds.) Boca Raton, FL: CRC Press, LLC.
- Boore, D. M., & Atkinson, G. M. (2008). Ground-motion prediction equations for the average horizontal component of PGA, PGV, and 5%-damped PSA at spectral periods between 0.01 s and 10.0 s. *Earthquake Spectra*, 24(1), 99-138.
- Boulanger, R. W., Chang, D., Brandenburg, S. J., Armstrong, R. J., & Kutter, B. L. (2007). Chapter 12: Seismic design of pile foundations for liquefaction effects. In K. D. Pitilakis, *Earthquake Geotechnical Engineering: 4th International Conference on Earthquake Geotechnical Engineering-Invited Lectures* (pp. 277-302). Springer.
- Boulanger, R. W., Kutter, B. L., Brandenburg, S. J., Singh, P., & Chang, D. (2003). Pile foundations in liquefied and laterally spreading ground during earthquakes: centrifuge experiments and analysis. *Report No. UCD/CGM-03/01*. University of California at Davis.
- Boulanger, R. W., Kutter, B. L., Brandenburg, S. J., Singh, P., & Chang, D. (2003). Pile foundations in liquefied and laterally spreading ground: Centrifuge experiments and analysis. *Report UCD/CGM-03/01*, 205 pp. Davis, California: Center for Geotechnical Modeling, University of California.
- Boulanger, R. W., Mejia, L. H., & Idriss, I. M. (1997). Liquefaction at Moss Landing during Loma Prieta earthquake. *Journal of Geotechnical and Geoenvironmental Engineering*, 123(5), 453-467.
- Bowles, J. E. (1977). *Foundation Analysis and Design*, 750pp. McGraw-Hill.

- Bowles, S. I. (2005). Statnamic load testing and analysis of a drilled shaft in liquefied sand. *MS Thesis*. Provo, Utah: Department of Civil and Environmental Engineering, Brigham Young University.
- Brand, E. W., Muktabhant, C., & Taechathummarak, A. (1972). Load test on small foundations in soft clay. *Proceedings, Performance of Earth and Earth-Supported Structures, 1, 2*, 903-928. ASCE.
- Brandenberg, S. J. (2005). Behavior of pile foundations in liquefied and laterally spreading ground. *PhD Dissertation*. Davis, California: University of California, Davis.
- Brandenberg, S. J., Boulanger, R. W., Kutter, B. L., & Chang, D. (2007a). Static pushover analyses of pile groups in liquefied and laterally spreading ground in centrifuge tests. *Journal of Geotechnical and Geoenvironmental Engineering, 133, 9*, 1055-1066. ASCE.
- Brandenberg, S. J., Boulanger, R. W., Kutter, B. L., & Chang, D. (2007b). Liquefaction-induced softening of load transfer between pile groups and laterally spreading crusts. *Journal of Geotechnical and Geoenvironmental Engineering, 133, 1*, 91-103. ASCE.
- Bray, J. D., & Sancio, R. B. (2006). Assessment of the liquefaction susceptibility of fine-grained soils. *Journal of Geotechnical and Geoenvironmental Engineering, 132(9)*, 1165-1177.
- Bray, J. D., & Travasarou, T. (2007). Simplified procedure for estimating earthquake-induced deviatoric slope displacements. *Journal of Geotechnical and Geoenvironmental Engineering, 133(4)*, 381-392.
- Brown, D. A., & Reese, L. C. (1985). Behavior of a large scale pile group subjected to cyclic lateral loading. *Report to the minerals Management Services*. U.S. Dept. of Interior, Reston, VA.; Dept. of Research, FHWA, Washington D.C.; and U.S. Army Engineer Waterways Experiment Station, Vicksburg, MS.
- Brown, W. M., Perkins, D. M., Leyendecker, E. V., Frankel, A. D., Hendley, J. W., Stauffer, P. H., et al. (1996). Reducing earthquake losses throughout the United States: Hazard maps help save lives and property. *Open File Report FS183-96*. USGS.
- Byrne, P. M. (1991). A model for predicting liquefaction-induced displacement. *Proceedings, 2nd International Conference on Recent Advances in Geotechnical Earthquake and Engineering and Soil Dynamics*, 2, 1027-1035. St. Louis, Missouri.
- Byrne, P. M., Jitno, H., & Salgado, R. (1992). Earthquake-induced displacements of soil-structures systems. *Proceedings, 10th World Conference on Earthquake Engineering, 3*, 1407-1412. Madrid, Spain.
- California Department of Transportation. (2011, February). *Guidelines on foundation loading and deformation due to liquefaction induced lateral spreading*. Retrieved from http://dap3.dot.ca.gov/shake_stable/references/Guidelines%20on%20Foundation%20Loading-Feb%202011.pdf

- Campbell, K. W., & Bozorgnia, Y. (2008). NGA ground motion model for the geometric mean horizontal component of PGA, PGV, PGD and 5% damped linear elastic response spectra for period ranging from 0.01 to 10 s. *Earthquake Spectra*, 24(1), 139-172.
- Carraro, J. A., Bandini, P., & Salgado, R. (2003). Liquefaction resistance of clean and nonplastic silty sand based on cone penetrometer resistance. *Journal of Geotechnical and Geoenvironmental Engineering*, 129(11), 965-976.
- Casagrande, A. (1936, January). Characteristics of cohesionless soils affecting the stability of slopes and earth fills. *Journal of the Boston Society of Civil Engineers*, 257-276.
- Casagrande, A. (1976). Liquefaction and cyclic mobility of sands: a critical review. *Harvard Soil Mechanics Series 88*. Cambridge, Massachusetts: Harvard University.
- Castro, G. (1969). Liquefaction of sands. *PhD Dissertation*. Cambridge, Massachusetts: Harvard University.
- Castro, G., & Poulos, S. J. (1977). Factors affecting liquefaction and cyclic mobility. *Journal of the Geotechnical Engineering Division*, 106(GT6), 501-506.
- Cetin, K. O., Seed, R. B., Der Kiureghian, A., Tokimatsu, K., Harder Jr., L. F., Kayen, R. E., et al. (2004). Standard penetration-based probabilistic and deterministic assessment of seismic soil liquefaction potential. *Journal of Geotechnical and Geoenvironmental Engineering*, 130(12), 1314-1340.
- Chang, D. (2007). Inertial and lateral spreading demands on soil-pile-structure systems in liquefied and laterally spreading ground during earthquakes. *PhD Dissertation*. Davis, California: University of California, Davis.
- Chang, D., Boulanger, R. W., Brandenberg, S. J., & Kutter, B. L. (2006). Dynamic analysis of soil-pile-structure interaction in laterally spreading ground during earthquake shaking. *Seismic Performance and Simulation of Pile Foundations in Liquefied and Laterally Spreading Ground*, GSP 145, 218-229. ASCE.
- Chang, D., Boulanger, R. W., Kutter, B. L., & Brandenberg, S. J. (2005). Experimental observations of inertial and lateral spreading loads on pile groups during earthquakes. *Proceedings, Earthquake Engineering and Soil Dynamics*, GSP 133. ASCE.
- Chellis, R. D. (1961). *Pile Foundations, 2nd Edition*. New York, NY: McGraw-Hill.
- Chen, L., Yuan, X., Zhenzhong, C., Longqing, H., Sun, R., Dong, L., et al. (2009). Liquefaction macrophenomena in the great Wenchuan earthquake. *Earthquake Engineering and Engineering Vibration*, 8(2), 219-229.
- Cheng, Z., & Jeremic, B. (2009, March 15-19). Numerical modeling and simulation of soil lateral spreading against piles. *Proceedings, International Foundation Congress and Equipment Expo, 1*, 183-189. Orlando, FL.

- Chiou, B. S.-J., & Youngs, R. R. (2008). An NGA model for the average horizontal component of peak ground motion and response spectra. *Earthquake Spectra*, 24(1), 173-216.
- Cluff, L. S., Patardhan, A. S., & Coppersmith, K. J. (1980). Estimating the probability occurrences of surface faulting earthquake on the Wasatch fault zone. *Bulletin of the Seismological Society of America*, 70, 5, 1463-1478.
- Coduto, D. P. (2001). *Foundation Design: Principles and Practices*. Upper Saddle River, NJ: Prentice-Hall, Inc.
- Coppersmith, K. J. (1981). Probabilities of earthquake occurrences on the San Andreas fault based on geologic risk. *EOS*, 62, 17, 322.
- Cornell, C. A. (1968). Engineering seismic risk analysis. *Bulletin of the Seismological Society of America*, 58, 5.
- Cornell, C. A. (1971). Probabilistic analysis of damage to structures under seismic loading. *Dynamic Waves in Civil Engineering*. London, England: Interscience.
- Cornell, C. A., & Krawinkler, H. (2000, April). Progress and challenges in seismic performance assessment. *PEER News*, 1-3. Pacific Earthquake Engineering Research Center.
- Cornell, C. A., & Winterstein, S. R. (1986). Applicability of the Poisson earthquake-occurrence model. *Seismic hazard Methodology for the Central and Eastern United States, Report No. NP-4726*. Palo Alto, CA: Electric Power Research Institute.
- Coulter, M., & Migliaccio, L. (1966). Effects of the earthquake of March 27, 1964 at Valdez, Alaska. *Professional Paper 542-C*. Washington, D.C.: U.S. Geological Survey, U.S. Department of the Interior.
- Coyle, H. M., & Costello, R. R. (1981). New design correlations for piles in sand. *Journal of Geotechnical Engineering Division*, 107, GT7, 965-986. ASCE.
- Cubrinovski, M., & Ishihara, K. (2004). Simplified method for analysis of piles undergoing lateral spreading in liquefied soils. *Soils and Foundations*, 44(5), 119-133.
- Das, B. M. (2004). *Principles of Foundation Engineering, 5th Edition*. Pacific Grove, CA: Brooks/Cole-Thomson Learning.
- De Alba, P., Seed, H. B., & Chan, C. K. (1975). Determination of soil liquefaction characteristics by large-scale laboratory tests. *Report No. 75-14*. Berkeley, California: University of California.
- Deierlein, G. G., Krawinkler, H., & Cornell, C. A. (2003). A framework for performance-based earthquake engineering. *Proceedings, 2003 Pacific Conference on Earthquake Engineering*.

- Der-Kiureghian, A., & Ang, A. S. (1977). A fault-rupture model for seismic risk analysis. *Bulletin of the Seismological Society of America*, 67, 4, 1173-1194.
- Dobry, R., & Baziar, M. H. (1991). Evaluation of ground deformation caused by lateral spreading. *Proceedings, 3rd Japan-U.S. Workshop on Earthquake Resistant Design of Lifeline Facilities and Countermeasures for Soil Liquefaction, Technical Report NCEER-91-0001*, 209-223. (O'Rourke, & Hamada, Eds.)
- Dobry, R., & Ladd, R. S. (1980). Discussion to "Soil liquefaction and cyclic mobility evaluation for level ground during earthquakes," by H.B. Seed and "Liquefaction potential: science versus practice," by R.B. Peck. *Journal of Geotechnical Engineering*, 106(GT6), 720-724.
- Dobry, R., Abdoun, T., O'Rourke, T. D., & Goh, S. H. (2003). Single piles in lateral spreads: Field bending moment evaluation. *Journal of Geotechnical and Geoenvironmental Engineering*, 129, 10, 879-889. ASCE.
- Dobry, R., Ladd, R. S., Yokel, F. Y., Chang, R. M., & Powell, D. (1982). Prediction of pore water pressure buildup and liquefaction of sands during earthquake by the cyclic strain method. *NBS Building Science Series 138*, 150 pp. Gaithersburg, Maryland: National Bureau of Standards.
- Dobry, R., Mohamad, R., Dakoulas, P., & Gazetas, G. (1984). Liquefaction evaluation of earth dams - a new approach. *Proceedings, 8th world Conference on Earthquake Engineering*, 3, 333-340.
- Dojcinovsky, D., Mihailov, V., & Jordanovsky, L. J. (1998). Seismic risk analysis based on Markov's process used in modeling seismic occurrences: study case. *Proceedings, 11th European Conference on Earthquake Engineering*.
- Douglas, B. J., Olsen, R. S., & Martin, G. R. (1981). Evaluation of the cone penetrometer test for SPT liquefaction assessment. *Proceedings, In Situ Testing to Evaluate Liquefaction Susceptibility*. New York, New York: ASCE.
- Duncan, J. M. (2000). Factors of safety and reliability in geotechnical engineering. *Journal of Geotechnical and Geoenvironmental Engineering*, 126(4), 307-316.
- Earthquake Engineering Research Institute (EERI). (1991). Costa Rica Earthquake Reconnaissance Report. *Earthquake Spectra*, 7, Sup B, 127 p. EERI.
- Ensoft. (2004). *LPILE Plus 5.0*. developed by Ensoft, Inc.
- Esrig, M. E., & Kirby, R. C. (1979). Advances in general effective stress method for the prediction of axial capacity for driven piles in clay. *Proceedings, 11th Annual Offshore Technology Conference*, 437-449. Houston, Texas.
- Esteva, L. (1970). Seismic risk and seismic design decisions. *Seismic Design and Nuclear Power Plants*. (R. J. Hansen, Ed.) Cambridge, MA: MIT Press.

- Faccioli, E., Paolucci, R., & Pessina, V. (2002). Engineering assessment of seismic hazard and long period ground motions at the Bolu Viaduct site following the November 1999 earthquake. *Journal of Seismology*, 6, 3, 307-327.
- Faris, A. T., Seed, R. B., Kayen, R. E., & Wu, J. (2006). A semi-empirical model for the estimation of maximum horizontal displacement due to liquefaction-induced lateral spreading. *Proceedings, 8th U.S. National Conference on Earthquake Engineering, Paper No. 1323*, 10 pp. San Francisco, California.
- Feld, J. (1943). Friction Pile Foundations. *Discussion, Transactions*, 108. ASCE.
- Finn, W. D. (1991). Assessment of liquefaction potential and post-liquefaction behavior on earthqu structures: Developments 1981-1991 (State-of-the-art paper). *Proceedings, 2nd International Conference on Recent Advances in Geotechnical Engineering and Soil Dynamics*, 3, 1833-1850. St. Louis, Missouri.
- Finn, W. D., & Thavaraj, T. (2001). Deep foundations in liquefiable soils: case histories, centrifuge tests and methods of analysis. *Proceedings, 4th International Conference on Recent Advances in Geotechnical Earthquake Engineering and Soil Dynamics, Paper No. SOAP-1*, 1-11. (S. Prakash, Ed.) Rolla, Missouri: University of Missouri-Rolla.
- Finn, W. D., Bransby, P. L., & Pickering, D. J. (1970). Effect of strain history on liquefaction of sands. *Journal of Soil Mechanics and Foundations Division*, 96(SM6), 1917-1934.
- Finn, W. D., Yogendrakumar, M., Yoshida, M., & Yoshida, N. (1986). TARA-3: A program to compute the response of 2-D embankments and soil-structure interaction systems to seismic loadings. Vancouver, British Columbia: Department of Civil Engineering, University of British Columbia.
- Franke, K. W. (2005). Development of a performance-based model for the prediction of lateral spreading displacements. *MS Thesis*, 276 pp. Seattle, WA: The University of Washington.
- Fujii, S., Iseimoto, N., Satou, Y., Kaneko, O., Funahara, H., Arai, T., et al. (1998). Investigation and analysis of a pile foundation damaged by liquefaction during the 1995 Hyogoken-Nambu earthquake. *Special Issue of Soils and Foundations*, 179-192. Japanese Geotechnical Society.
- GEO-SLOPE International Ltd. (2010). SLOPE/W 2007 software, version 7.17, build 4921.
- Gerber, T. M. (2010, July). Personal Communication.
- Golesorkhi, R. (1989). Factors influencing the computational determination of earthquake-induced shear stresses in sandy soils. *PhD dissertation*. Berkeley, Calif.: Univ. of California, Berkeley.
- Gonzalez, L., Abdoun, T., & Dobry, R. (2005, March 16-19). Effect of soil permeability on centrifuge modeling of pile response to lateral spreading. *Seismic Performance and*

Simulation of Pile Foundations in Liquefied and Laterally Spreading Ground, Proceedings. Davis, California: University of California, Davis.

- Gu, W. H., Morgenstern, N. R., & Robertson, P. K. (1994). Post-earthquake deformation analysis of wildlife site. *Journal of Geotechnical Engineering*, 120(2), 274-289.
- Guagenti-Grandori, E., & Molina, D. (1984). Semi-Markov processes in seismic risk analysis. *Proceedings, International Symposium of Semi-Markov Processes and their Applications.* Brussels, Belgium.
- Gutenberg, B., & Richter, C. F. (1944). Frequency of earthquakes in California. *Bulletin of the Seismological Society of America*, 34, 4, 1985-1988.
- Hagiwara, Y. (1974). Probability of earthquake occurrence as obtained from a Weibull distribution analysis of crustal strain. *Tectonophysics*, 23, 3, 313-318.
- Hahn, G. J., & Shapiro, S. S. (1967). *Statistical Models in Engineering.* John Wiley.
- Haigh, S. K. (2002). Effects of liquefaction on pile foundations in sloping ground. *PhD Dissertation.* Cambridge, England: Cambridge University.
- Haigh, S. K., & Madabhushi, S. P. (2002). Centrifuge modeling of lateral spreading past pile foundations. *Proceedings, International Conference on Physical Modeling in Geotechnics.* St. John's, Newfoundland, Canada.
- Hales, L. J. (2003). Cyclic lateral load testing and analysis of a CISS pile in liquefied sand. *MS Thesis.* Provo, Utah: Department of Civil and Environmental Engineering, Brigham Young University.
- Hamada, M., Towhata, I., Yasuda, S., & Isoyama, R. (1987). Study of permanent ground displacement induced by seismic liquefaction. *Computers and Geotechnics*, 4, 197-220.
- Hanzawa, H., Itoh, Y., & Suzuki, K. (1979). Shear characteristics of a quick sand in the Arabian Gulf. *Soils and Foundations*, 19(4), 1-5.
- Hara, A., Ohata, T., & Niwa, M. (1971). Shear modulus and shear strength of cohesive soils. *Soils & Foundations*, 14, 3, 1-12. Japanese Geotechnical Society.
- Harr, M. E. (1984). Reliability-based design in civil engineering. *1984 Henry M. Shaw Lecture.* Raleigh, NC: Dept. of Civil Engineering, North Carolina State University.
- Hatanaka, M., & Uchida, A. (1996). Empirical correlation between penetration resistance and effective friction of sandy soils. *Soils & Foundations*, 36, 4, 1-9. Japanese Geotechnical Society.
- He, L., Elgamal, A., Abdoun, T., Abe, A., Dobry, R., Hamada, M., et al. (2009). Liquefaction-induced lateral load on pile in a medium Dr sand layer. *Journal of Earthquake Engineering*, 13, 7, 916-938.

- Holzer, T. L., & Youd, T. L. (2007). Liquefaction, ground oscillation, and soil deformation at the Wildlife array, California. *Bulletin of the Seismological Society of America*, 97(3), 961-976.
- Horikoshi, P., Fujiwara, T., & Tateishi, A. (1998, September 23-25). Pile behavior during seismically-induced lateral spreading of liquefied sand. *Centrifuge '98*, 377-382. (T. Kimura, O. Kusakabe, & J. Takemura, Eds.) Tokyo, Japan.
- Idriss, I. M. (1999). An update to the Seed-Idriss simplified procedure for evaluating liquefaction potential. *Proceedings, TRB Workshop on New Approaches to Liquefaction*. Publication No. FHWA-RD-99-165, Federal Highway Administration.
- Idriss, I. M. (2008). An NGA empirical model for estimating the horizontal spectral values generated by shallow crustal earthquakes. *Earthquake Spectra*, 24(1), 217-242.
- Idriss, I. M., & Boulanger, R. W. (2007, March 5-9). Residual shear strength of liquefied soils. *Proceedings, 27th USSSD Annual meeting and Conference, Modernization and Optimization of Existing Dams and Reservoirs*. Philadelphia, Pennsylvania: U.S. Society on Dams.
- Idriss, I. M., & Boulanger, R. W. (2008). *Soil Liquefaction During Earthquakes* (Vols. Monograph MNO-12). Oakland, CA: Earthquake Engineering Research Institute.
- Idriss, I. M., & Boulanger, R. W. (2010, December). SPT-based liquefaction triggering procedures. *Report No. UCD/CGM-10/02*, 136 p. Davis, CA: Center for Geotechnical Modeling, University of California at Davis.
- Isenhower, I. M., & Mosher, R. L. (1996, August 1-3). Evaluation of reliability of pile-supported structures. *Proceedings, Uncertainty in the Geologic Environment: From Theory to Practice*, 666-684. Madison, WI.
- Ishihara, K. (1984). Post-earthquake failure of a tailings dam due to liquefaction of the pond deposit. *Proceedings, International Conference on Case Histories in Geotechnical Engineering. Vol. 3*, pp. 1129-1143. St. Louis, MO: University of Missouri.
- Ishihara, K. (1985). Stability of natural deposits during earthquakes. *Proceedings, 11th International Conference on Soil mechanics and Foundation Engineering, Vol. 1*, pp. 321-376.
- Ishihara, K. (1993). Liquefaction and flow failure during earthquakes. *Geotechnique*, 43(3), 351-415.
- Ishihara, K., & Yoshimine, M. (1992). Evaluation of settlements in sand deposits following liquefaction during earthquakes. *Soils and Foundations*, 21(1), 173-188.
- Ishihara, K., Tatsuoka, F., & Yasuda, S. (1975). Undrained deformation and liquefaction of sand under cyclic stresses. *Soils and Foundations*, 15(1), 16-23.

- Jara, J. M., & Rosenblueth, E. (1988). The Mexico earthquake of September 19, 1985 - probability distribution of times between characteristic subduction earthquakes. *Earthquake Spectra*, 4, 3, 499-529. EERI.
- JRA. (2002, November). *Specifications for Highway Bridges*. Japan: Japan Road Association, Preliminary English version prepared by Public Works Research Institute (PWRI) and Civil Engineering Research Laboratory (CRL).
- Juimarongrit, T., & Ashford, S. A. (2006). Soil-pile response o blast-induced lateral spreading II: Analysis and assessment of the p-y method. *Journal of Geotechnical Engineering*, 132(2), 163-172. ASCE.
- Kayen, R. E., Mitchell, J. K., Seed, R. B., Lodge, A., Nishio, S., & Cotinho, R. (1992). Evaluation of SPT-, CPT-, and shear wave-based methods for liquefaction potential assessment using Loca Prieta data. *Proceedings, 4th U.S.-Japan Workshop on Earthquake Resistant Design of Lifeline Facilities and Countermeasures for Soil Liquefaction*, 1, 177-204.
- Kim, S. G. (1991). An application of a semi-Markov model to seismic risk analysis. *Bulletin of the International Institute of Seismology and Earthquake Engineering*, 25, 23-38.
- Kiremidjian, A. S., & Anagnos, T. (1984). Stochastic slip-predictable model for earthquake occurrences. *Bulletin of the Seismological Society of America*, 74, 739-755.
- Kiremidjian, A. S., Anagnos, T., & Rosenblueth, E. (1988). Time-predictable model for characteristic earthquake events. *Probabilistic Methods in Civil Engineering: Proceedings of the 5th ASCE Specialty Conference*, 245-248. ASCE.
- Kishida, H., & Meyerhof, G. G. (1965). Bearing capacity of pile groups under eccentric load in sand. *Proceedings, 6th International Conference on Soil Mechanics and Foundation Engineering*, 2, 270-274.
- Kovacs, W. D., Salomone, L. A., & Yokel, F. Y. (1983). Comparison of energy measurements in the Standard Penetration Test using the cathead and rope method. *Final Report*, 99 pp. U.S. Nuclear Regulatory Commission.
- Kramer, S. L. (1996). *Geotechnical Earthquake Engineering*. Upper Saddle River, NJ: Prentice Hall, Inc.
- Kramer, S. L. (2005, August). Personal Communication with K. Franke.
- Kramer, S. L. (2008, May 18-22). Performance-based earthquake engineering: opportunities and implications for geotechnical engineering practice. *Proceedings and keynote speech, Geotechnical Earthquake Engineering and Soil Dynamics IV, ASCE GSP 181*. Sacramento, CA: ASCE.
- Kramer, S. L., & Mayfield, R. T. (2007). The return period of soil liquefaction. *The Journal of Geotechnical and Geoenvironmental Engineering*, 133, 7, 1-12. ASCE.

- Kramer, S. L., & Seed, H. B. (1988). Initiation of soil liquefaction under static loading conditions. *Journal of Geotechnical Engineering*, 114(4), 412-430.
- Krawinkler, H. (2002). A general approach to seismic performance assessment. *Proceedings, International Conference on Advances and New Challenges in Earthquake Engineering Research*. Hong Kong, China: ICANCEER.
- Krawinkler, H., & Miranda, E. (2004). Performance-based earthquake engineering. *Chapter 9, Earthquake Engineering: From Seismology to Performance-Based Engineering*. (Y. Bozorgnia, & V. V. Bertero, Eds.) Boca Raton, FL: CRC Press, LLC.
- Krawinkler, H., & Miranda, E. (2004). Performance-Based Earthquake Engineering, appearing as Chapter 9. In Y. Bozorgnia, & V. V. Bertero (Eds.), *Earthquake Engineering: From Seismology to Performance-Based Engineering*. Boca Raton, FL: CRC Press LLC.
- Ku, C. S., Lee, D. H., & Wu, J. H. (2004). Evaluation of soil liquefaction in the Chi-Chi, Taiwan earthquake using CPT. *Soil Dynamics and Earthquake Engineering*, 24(9-10), 659-673.
- Kulhawy, F. H. (1991). Drilled shaft foundations, Chapter 14. *Foundation engineering handbook, 2nd edition*. (H. -Y. Fang, Ed.) New York, NY: Van Nostrand Reinhold.
- Kulhawy, F. H. (1992). On the evaluation of soil properties. *ASCE Geotechnical Special Publication No. 31*, 95-115. ASCE.
- Kulhawy, F. H., & Mayne, P. W. (1990). Manual on Estimating Soil Properties for Foundation Design. *Report No. EL-6800*, 306 p. . Palo Alto, CA: Electric Power Research Institute.
- Kulhawy, F. H., & Phoon, K. K. (1993). Drilled shaft side resistance in clay soil to rock. *Design and Performance of Deep Foundations: Piles and Piers in Soil and Rock, GSP No. 38*, 172-183. ASCE.
- Kulhawy, F. H., Trautmann, C. H., Beech, J. F., O'Rourke, T. D., McGuire, W., Wood, W. A., et al. (1983). Transmission line structure foundations for uplift-compression loading. *Report No. EL-2870*. Palo Alto, CA: Electric Power Research Institute.
- Lacasse, S., & Nadim, F. (1997). Uncertainties in characterizing soil properties. *Publication No. 201*, 49-75. Oslo, Norway: Norwegian Geotechnical Institute.
- Ladd, C. C., & Foott, R. (1974, July). New design procedure for stability of soft clays. *Journal of Geotechnical Engineering Division*, 100, GT7, 763-786. ASCE.
- Ladd, R. S. (1974). Specimen preparation and liquefaction of sands. *Journal of Geotechnical Engineering Division*, 100(GT10), 1180-1184.
- Lai, C. D. (1977). A two-dimensional 'immigration-branching' model with application to earthquake occurrence times and energies. *Journal of Applied Probability*, 14, 464-474.

- Lam, I. P., Arduino, P., & Mackenzie-Helnwein, P. (2009, March 15-19). OPENSEES soil-pile interaction study under lateral spread loading. *Proceedings, International Foundation Congress and Equipment Expo, 1*, 206-213. Orlando, FL.
- Ledezma, C., & Bray, J. D. (2010). Probabilistic performance-based procedure to evaluate pile foundations at sites with liquefaction-induced lateral displacement. *Journal of Geotechnical and Geoenvironmental Engineering*, 136(3), 464-476.
- Li, X. S., & Dafalias, Y. F. (2000). Dilatancy for cohesionless soils. *Geotechnique*, 50, 4, 449-460.
- Liu, J. L., Yuan, Z. L., & Zhang, K. P. (1985). Cap-pile-soil interaction of bored pile groups. *Proceedings, Eleventh International Conference on Soil Mechanics and Foundation Engineering*, 3, 1433-1436. San Francisco, CA.
- Liu, L., & Dobry, R. (1995). Effect of liquefaction on lateral response of piles by centrifuge model tests. *NCEER Bulletin*, 9, 1, 7-11.
- Lomnitz-Adler, J., & Lomnitz, C. (1979). A modified form of the Gutenberg-Richter magnitude-frequency law. *Bulletin of the Seismological Society of America*, 63, 1999-2003.
- Lowe, J., & Karafiath, L. (1960). Stability of earth dams upon drawdown. *Proceedings, 1st PanAm Conference on Soil Mechanics and Foundation Engineering*, 2. Mexico City, Mexico.
- Makdisi, F. I., & Seed, H. B. (1977). A simplified procedure for estimating earthquake-induced deformations in dams and embankments. *Earthquake Engineering Research Center Report UCB/EERC-77/19*, 33 p. University of California, Berkeley.
- Malvick, E. J., Kutter, B. L., Boulanger, R. W., & Kulasingam, R. (2006). Shear localization due to liquefaction-induced void redistribution in a layered infinite slope. *Journal of Geotechnical and Geoenvironmental Engineering*, 132(10), 1293-1303.
- Marchetti, S. (1982). Detection of liquefiable sand layers by means of quasi-static penetration tests. *Proceedings, 2nd European Symposium on Penetration Testing*, 2, 458-482. Amsterdam.
- Martin, G. R. (1992). Evaluation of soil properties for seismic stability analysis of slopes. *Proceedings, Stability and Performance of Slopes and Embankments*, 1, 116-142. Geotechnical Special Publication No. 31, ASCE.
- Matlock, H. (1970). Correlations for design of laterally loaded piles in soft clay. *Proceedings, 2nd Offshore Technology Conference, Paper No. OTC 1204*, 1, 577-594. Houston, Texas.
- McGuire, J. J., Zhao, L., & Jordan, T. H. (2002). Predominance of unilateral rupture for global catalog of large earthquakes. *Bulletin of the Seismological Society of America*, 92, 8, 3309-3317.

- McGuire, J. P. (1994, January 20). Liquefaction induced bridge damage in the Costa Rica earthquake of April 22, 1991. *Master's Thesis*, 91 pp. Brigham Young University.
- McGuire, R. (2004). Seismic hazard and risk analysis. *Second Monograph Series MNO-10*. Earthquake Engineering Research Institute.
- McGuire, R. K., & Arabasz, W. J. (1990). An introduction to probabilistic seismic hazard analysis. *Geotechnical and Environmental Geophysics, 1*, 333-353. (S. H. Ward, Ed.) Society of Exploration Geophysicists.
- McVay, M., Bloomquist, D., Vanderlinde, D., & Clausen, J. (1994). Centrifuge modeling of laterally loaded pile groups in sands. *Geotechnical Testing Journal, 17*, 129-137.
- McVay, M., Casper, R., & Shang, T. (1995). Lateral response of three-row groups in loose to dense sands at 3D and 5D pile spacing. *Journal of Geotechnical Engineering, 121*, 5, 436-441. ASCE.
- Merz, H. L., & Cornell, C. A. (1973). Seismic risk analysis based on quadratic magnitude-frequency law. *Bulletin of the Seismological Society of America, 63*, 6.
- Merz, H., & Cornell, C. A. (1973). Seismic risk based on a quadratic magnitude-frequency law. *Bulletin of Seismological Society of America, 73*, 6, 1949-2006.
- Meyerhof, G. G. (1976). Bearing capacity and settlement of pile foundations. *Journal of the Geotechnical Engineering Division, 102*, GT3, 197-228. ASCE.
- Mitchell, J. K., & Tseng, D. J. (1990). Assessment of liquefaction potential by cone penetration resistance. *Proceedings, H. Bolton Seed Memorial Symposium, 2*, 335-350. Berkeley, California.
- Miyajima, Kitaura, & Ando. (1991). Experiments on liquefaction-induced large ground deformation. *Proceedings, 3rd Japan-U.S. Workshop on earthquake Resistant Design of Liefeline Facilities and Countermeasures for Soil Liquefaction, Technical Report NCEER-91-0001*, 269-292. (O'Rourke, & Hamada, Eds.)
- Mokwa, R. L. (1999). Investigation of the resistance of pile caps to lateral spreading. *PhD Thesis*. Blacksburg, Virginia: Department of Civil Engineering, Virginia Polytechnic Institute and State University.
- Mokwa, R. L., & Duncan, J. M. (2003). Rotational restraint of pile caps during lateral loading. *Journal of Geotechnical and Geoenvironmental Engineering, 129*, 9, 829-837. ASCE.
- Morgenstern, N. R., & Price, V. E. (1965). The analysis of the stability of general slip surfaces. *Geotechnique, 15*, 1, 79-93.
- Morrison, C., & Reese, L. C. (1986). A lateral-load test of full-scale pile group in sand. *GR86-J*. Washington, D.C.: FHWA.

- Moss, R. E., Seed, R. B., Kayen, R. E., Steward, J. P., Der Kiureghian, A., & Cetin, K. O. (2006). CPT-based probabilistic and deterministic assessment of in situ seismic soil liquefaction potential. *Journal of Geotechnical and Geoenvironmental Engineering*, 132(8), 1032-1051.
- Nakase, H., Hiro-oka, A., & Yanagihata, T. (1997). Deformation characteristics of liquefied loose sand by triaxial compression tests. *Proceedings, IS-Nagoya 97, Deformation and Progressive Failure in Geomechanics*, 559-564. (A. Asaoka, T. Adachi, & F. Oka, Eds.) Pergamon, Elsevier Science.
- Newmark, N. (1965). Effects of earthquakes on dams and embankments. *Geotechnique*, 15(2), 139-160.
- Nishioka, T., & Shah, H. C. (1980). Application of the Markov chain on probability of earthquake occurrences. *Proceedings of the Japanese Society of Civil Engineering*, 1, 137-145.
- Obermeier, S. F., & Pond, E. C. (1999). Issues in using liquefaction features for paleoseismic analysis. *Seismological Research Letters*, 70(1), 34-58.
- Ohsaki, Y. (1969). The effects of local soil conditions upon earthquake damage. *Proceedings of Specialty Session 2, 7th International Conferenc on Soil Mechanics and Foundation Engineering*. Mexico City, Mexico.
- Olson, S. M., & Johnson, C. I. (2008). Analyzing liquefaction-induced lateral spreading strength ratios. *Journal of Geotechnical and Geoenvironmental Engineering*, 134(8), 1035-1049.
- Olson, S. M., & Stark, T. D. (2002). Liquefied strength ratio from liquefaction flow failure case histories. *Canadian Geotechnical Journal*, 39(3), 629-647.
- Park Seismic. (2010, October). *MASW.com*. Retrieved from <http://www.masw.com/Whatismasw.html>
- Parsons, T. (2005). Significance of stress transfer in time-dependent earthquake probability calculations. *Journal of geophysical Research. B. Solid Earth*, 110, B5.
- Patwardhan, A. S., Kulkarni, R. B., & Tocher, D. (1980). A semi-Markov model for characterizing recurrence of great earthquakes. *Bulletin of the Seismological Society of America*, 70, 1, 323-347.
- Peck, R. B., Hanson, W. E., & Thornburn, T. H. (1974). *Foundation Engineering*, 514 pp. John Wiley & Sons.
- Petersen, M. D., Frankel, A. D., Harmsen, S. C., Mueller, S. C., Haller, K. M., Wheeler, R. L., et al. (2008). Documentation for the 2008 update of the United States National Seismic Hazard Maps. *USGS Open-File Report 2008-1128*, 128 pp. USGS.

- Poulos, S. J., Castro, G., & France, J. W. (1985). Liquefaction evaluation procedures. *Journal of Geotechnical Engineering*, 111(6), 772-792.
- Poulos, S. J., Castro, G., & France, J. W. (1988). Closure to discussion: liquefaction evaluation procedure. *Journal of Geotechnical Engineering*, 114(2), 251-259.
- Prevost, J. H. (1981). DYNFLOW: A nonlinear transient finite element analysis program. Princeton, New Jersey: Dept. of Civil Engineering, Princeton University.
- Priestley, M. J., Nigam, R. S., Singh, J. P., Youd, T. L., & Rollins, K. M. (1991). Costa Rica Earthquake of April 22, 1991, Reconnaissance Report. *Earthquake Spectra, Supplement B*, 7, 79-90. EERI.
- Pyke, R., Seed, H. B., & Chan, C. K. (1975). Settlement of sands under multi-directional loading. *Journal of Geotechnical Engineering Division*, 101(GT4), 379-398.
- Rahman, S., & Grigoriu, M. (1994). A Markov model for local and global indices in seismic hazard analysis. *NCEER Publication, 1 Vol.* Buffalo, NY: National Center for Earthquake Engineering Research.
- Rauch, A. F., & Martin II, J. R. (2000). EPOLLS model for predicting average displacements on lateral spreads. *Journal of Geotechnical and Geoenvironmental Engineering*, 126(4), 360-371.
- Reese, L. C., Cox, W. R., & Koop, F. D. (1974). Analysis of laterally loaded piles in sand. *Proceedings, 6th Offshore Technology Conference, Paper No. OTC 2090*, 2, 473-483. Houston, Texas.
- Reese, L. C., Cox, W. R., & Koop, F. D. (1975). Field testing and analysis of laterally loaded piles in stiff clay. *Proceedings, 7th Offshore Technology Conference, Paper No. OTC 2312*, 671-690. Houston, Texas.
- Reese, L. C., Wang, S. T., Isenhower, W. M., & Arrellaga, J. A. ((2000)). *Computer program LPILE plus version 4.0 technical manual*. Ensoft, Inc., Austin, Texas.
- Reid, H. F. (1911). The elastic rebound theory of earthquakes. *Bulletin of the Department of Geology*, 6, 413-444. Berkeley, CA: University of California, Berkeley.
- Reiter, L. (1990). *Earthquake Hazard Analysis - Issues and Insights*. New York, NY: Columbia University Press.
- Reyna, F., & Chameau, J. L. (1991). Dilatometer-based liquefaction potential of sites in the Imperial Valley. *Proceedings, 2nd International Conference on Recent Advances in Geotechnical Earthquake Engineering and Soil Dynamics, 1*, 385-392. St. Louis, Missouri.
- Risk Engineering. (2010). EZ-FRISK version 7.43. Boulder, CO.

- Risk, C. O. (1984). Glossary of terms for probabilistic seismic risk and hazard analysis. *Earthquake Spectra*, 1, 1, 33-40. EERI.
- Robertson, P. K., & Campanella, R. G. (1985). Liquefaction potential of sands using the CPT. *Journal of Geotechnical Engineering*, 111(3), 384-403.
- Robertson, P. K., & Campanella, R. G. (1986). Estimating liquefaction potential of sands using the flat dilatometer. *Geotechnical Testing Journal*, 9(1), 38-40.
- Rollins, K. M., Gerber, T. M., Lane, J. D., & Ashford, S. (2005). Lateral resistance of a full-scale pile group in liquefied sand. *Journal of Geotechnical and Geoenvironmental Engineering*, 131, 1, 115-125. ASCE.
- Rollins, K. M., Olsen, K. G., Jensen, D. H., Garrett, B. H., Olsen, R. J., & Egbert, J. J. (2006). Pile spacing effects on lateral pile group behavior: Analysis. *Journal of Geotechnical and Geoenvironmental Engineering*, 132, 10, 1272-1283. ASCE.
- Rollins, K. M., Peterson, K. T., & Weaver, T. J. (1998). Lateral load behavior of full-scale pile group in clay. *Journal of Geotechnical and Geoenvironmental Engineering*, 124, 6, 468-478. ASCE.
- Rosenbluth, E. (1975). Point estimates for probability moments. *Proceedings of the National Academy of Sciences, USA*, 72, 10, 3812-3814.
- Sadigh, K., Chang, C. Y., Egan, J. A., Makdisi, F., & Youngs, R. R. (1997). Attenuation relationships for shallow crustal earthquakes based on California strong-motion data. *Seismological Research Letters*, 68.
- Santana, G. (1991). Reporte preliminar de los registros de aceleraciones obtenidos durante el sismo del 22 de diciembre 1990. Laboratorio de Ingenieria Sismica, Instituto de Investigaciones en Ingenieria, Universidad de Costa Rica.
- Santana, G. (1992, July 19-24). Lessons learned and socio-economic issues arising from recent catastrophic earthquakes. *Proceedings, 10th World Conference on Earthquake Engineering*. Madrid, Spain.
- Santana, G., Vargas, W., Sancho, V., Segura, C., Ramirez, A., & Sibaja, R. (1991). Registro de aceleraciones del terremoto de Limon, 22 de abril de 1991. *Reporte INII 48*, 58-91. Laboratorio de Ingenieria Sismica, Instituto de Investigaciones en Ingenieria, Universidad de Costa Rica.
- Sasaki, Tokaida, Matsumoto, & Saya. (1991). Shake table tests on lateral ground flow induced by soil liquefaction. *Proceedings, 3rd Japan-U.S. Workshop on Earthquake Resistant Design of Lifeline Facilities and Countermeasures for Soil Liquefaction, Technical Report NCEER-91-0001*, 371-385. (O'Rourke, & Hamada, Eds.)
- Savy, H. B., Shah, H. C., & Boore, D. M. (1980). Nonstationary risk model with geophysical input. *Journal of the Structural Division*, 106, ST1, 145-164. ASCE.

- Saygili, G., & Rathje, E. M. (2008). Empirical predictive models for earthquake-induced sliding displacements of slopes. *Journal of Geotechnical and Geoenvironmental Engineering*, 134(6), 790-803.
- Seed, H. B. (1979). Soil liquefaction and cyclic mobility evaluation for level ground during earthquakes. *Journal of Geotechnical Engineering*, 105(2), 201-255.
- Seed, H. B. (1980). Closure to soil liquefaction and cyclic mobility evaluation for level ground during earthquakes. *Journal of Geotechnical Engineering Division*, 106(GT6), 724.
- Seed, H. B. (1986). Design problems in soil liquefaction. *Journal of Geotechnical Engineering*, 113(8), 827-845.
- Seed, H. B., & De Alba, P. (1986). Use of SPT and CPT tests for evaluating the liquefaction resistance of soils. *Proceedings, In Situ '86*. ASCE.
- Seed, H. B., & Idriss, I. M. (1971). Simplified procedure for evaluating soil liquefaction potential. *Journal of Soil Mechanics and Foundations Div.*, 97(SM9), 1249-1273.
- Seed, H. B., & Lee, K. L. (1966). Liquefaction of saturated sands during cyclic loading. *Journal of the Soil Mechanics and Foundations Division*, 92(SM6), 105-134.
- Seed, H. B., & Peacock, W. H. (1971). Test procedures for measuring soil liquefaction characteristics. *Journal of the Soil Mechanics and Foundations Division*, 97(SM8), 1099-1119.
- Seed, H. B., Idriss, I. M., & Arango, I. (1983). Evaluation of liquefaction potential using field performance data. *Journal of Geotechnical Engineering*, 109(3), 458-482.
- Seed, H. B., Tokimatsu, K., Harder, L. F., & Chung, R. M. (1984). The influence of SPT procedures in soil liquefaction resistance evaluations. *Report No. UCB.EERC-84/15*. Berkeley, California: University of California.
- Seed, R. B., & Harder, L. F. (1990). SPT-based analysis of cyclic pore pressure generation and undrained residual strength. *Proceedings, H. Bolton Seed Memorial Symposium*, 2, 351-376. (J. Duncan, Ed.) Berkeley, California: University of California.
- Seiler, J., & Keeney, W. (1944). The efficiency of piles in groups. *Wood Preserving News*, 22, 11.
- Shah, H. C., Mortgat, C. P., Kiremidjian, A. S., & Zsutty, T. C. (1975). A study of seismic risk for Nicaragua, Part I. *Report 11*. Palo Alto, CA: The John A. Blume Earthquake Engineering Center, Stanford University.
- Shamoto, Y., Zhang, J. M., & Goto, S. (1997). Mechanism of large post-liquefaction deformation in saturated sand. *Soils and Foundations*, 37(2), 71-80.

- Shanker, D., & Harbindu, A. (2004). Development of the time- and magnitude-predictable model and prediction of earthquake hazard in the central Himalayas. *Proceedings, 13th World Conference on Earthquake Engineering*. Vancouver, Canada.
- Shiomi, T., Tsukuni, S., Hatanaka, M., Tanaka, Y., Suzuki, Y., & Hirose, T. (1987). Simulation analysis of ground liquefaction induced by earthquake. *Computers and Geotechnics*, 4(4), 221-245.
- Shlien, S., & Tokosz, M. N. (1970). A clustering model for earthquake occurrences. *Bulletin of the Seismological Society of America*, 60, 1765-1787.
- Singh, P. (2002). Behavior of pile in earthquake-induced lateral spreading. *MS Thesis*. University of California, Davis.
- Singh, V. P., Sharad, K. J., & Aditya, T. (2007). *Risk and Reliability Analysis*. Reston, VA: ASCE Press.
- Skempton, A. W. (1957). The planning and design of of new Hong Kong airport. *Proceedings, The Institute of Civil Engineers*, 7, 305-307. London, UK.
- Sladen, J. A., D'Hollander, R. D., & Krahn, J. (1985). The liquefaction of sands: a collapse surface approach. *Canadian Geotechnical Journal*, 22(4), 564-578.
- Somerville, P. G., Smith, N. F., Graves, R. W., & Abrahamson, N. A. (1997). Modification of empirical strong ground motion attenuation relations to include the amplitude and duration effects of rupture directivity. *Seismological Research Letters*, 68, 199-222.
- Speidel, D. H. (1998). Seismicity patterns and the 'characteristic' earthquake in the Central Mississippi Valley, USA . *Engineering Geology*, 50, 1-2, 1-8.
- Spencer, E. (1967). A method of analysis of the stability of embankments assuing parallel inter-slice forces. *Geotechnique*, 17, 1, 11-26.
- Stewart, J. P., & Kwok, A. O. (2008). Nonlinear seismic ground response analysis: Code usage protocols and verification against vertical array data. *Proceedings, Geotechnical Earthquake Engineering and Soils Dynamics IV, ASCE Geotechnical Special Publication No. 181*, 24 pp. (D. Zeng, M. T. Manzari, & D. R. Hiltunen, Eds.) ASCE.
- Stokoe, K. H., Roesset, J. M., Bierschwale, J. G., & Aouad, M. (1988). Liquefaction potential of sands from shear wave velocity. *Proceedings, 9th World conference of Earthquake Engineering*, 3, 213-218. Tokyo, Japan.
- Studio, M. V. (2003). *Microsoft Visual Studio .NET 2003*. Microsoft Corporation.
- Suzuki, S., & Kiremidjian, A. S. (1986). Site hazard analysis methods with empirical and geophysical ground motion models. 88 pp. John A. Blume Earthquake Engineering Center.

- Suzuki, Y., Tokimatsu, K., & Koyamada, K. (2003). Correlation between soil liquefaction during earthquakes and CPT data. *Journal of Structural and Construction Engineering*(571).
- Suzuki, Y., Tokimatsu, K., & Koyamada, K. (2004). Correlation between soil liquefaction during earthquakes and shear wave velocity. *Journal of Structural and Construction Engineering*(578), 67-74.
- Takahashi, T., Saiki, T., Okada, H., Irikura, K., Zhang, J., Zhao, J., et al. (2004). Attenuation models for response spectra derived from Japanese strong-motion records accounting for tectonic source type. *Proceedings, 13th World Conference on Earthquake Engineering, Paper No. 1271*. Canada.
- Takahashi, Y., Der-Kiureghian, A., & Ang, A. S. (2004). Life-cycle cost analysis based on a renewal model of earthquake occurrences. *Earthquake Engineering and Structural Dynamics*, 33, 7, 859-880.
- Thiel, C. C., & Zsutty, T. C. (1987). Earthquake parameters and damage statistics. *Publication by Forell/Elsesser Engineers*, 264 pp.
- Toboada, V. M., Abdoun, T., & Dobry, R. (1996). Prediction of liquefaction-induced lateral spreading by dilatant sliding block model calibrated by centrifuge tests. *Proceedings, 11th World Conference on Earthquake Engineering*, Paper No. 1037. Acapulco, Mexico.
- Toboada-Urtuzuastegui, V. M., & Dobry, R. (1998). Centrifuge modeling of earthquake-induced lateral spreading in sand. *Journal of Geotechnical and Geoenvironmental Engineering*, 124(12), 1195-1206.
- Tokimatsu, K. (1999, June 21-25). Performance of pile foundations in laterally spreading soils. *Proceedings, 2nd International Conference of Earthquake Geotechnical Engineering*, 3, 957-964. (Seco, & P. Pinto, Eds.) Lisbon, Portugal.
- Tokimatsu, K., & Asaka, A. (1998). Effects of liquefaction-induced ground displacements on pile performance in the 1995 Hyogoken-Nambu earthquake. *Soils and Foundations, Special Issue No. 2*, 163-178.
- Tokimatsu, K., & Seed, H. B. (1984). Simplified procedures for the evaluation of settlements in clean sands. *Report N. UCB/GT-84/16*. Berkeley, California: University of California.
- Tokimatsu, K., & Suzuki, H. (2004). Pore water pressure response around pile and its effects on p-y behavior during soil liquefaction. *Soils and Foundations*, 43, 6, 101-110.
- Tokimatsu, K., Kuwayama, S., & Tamura, S. (1991). Liquefaction potential evaluation based on Rayleigh wave investigation and its comparison with field behavior. *Proceedings, 2nd International Conference on Recent Advances in Geotechnical Earthquake Engineering and Soil Dynamics*, 1, 357-364. St. Louis, Missouri.

- Tokimatsu, K., Suzuki, H., & Sato, M. (2005). Effects of inertial and kinematic interaction on seismic behavior of pile with embedded foundation. *Soil Dynamics and Earthquake Engineering*, 25, 753-762.
- Tokimatsu, K., Suzuki, H., & Suzuki, Y. (2001). Backcalculated p-y relation of liquefied soils from large shaking table tests. *Proceedings, 4th International Conference on Recent Advances in Geotechnical Earthquake Engineering and Soil Dynamics, Paper No. 6.24*. (S. Prakash, Ed.) Rolla, Missouri: University of Missouri-Rolla.
- Tokimatsu, K., Suzuki, H., & Suzuki, Y. (2001). Backcalculated p-y relation of liquefied soils from large shaking table tests. *Proceedings, 4th International Conference of Recent Advances in Geotechnical Earthquake Engineering and Soil Dynamics, Paper No. 6.24*. (S. Prakash, Ed.) Rolla, Missouri: University of Missouri, Rolla.
- Tomlinson, M. J. (1994). *Pile design and construction practice, 4th edition*. London, U.K.: E&FN Spon.
- Towhata, I., Sasaki, K., Tokida, K., Matsumoto, H., Tamari, Y., & Yamuda, K. (1992). Prediction of permanent displacement of liquefied ground by means of minimum energy principle. *Soils and Foundations*, 32(3), 97-116.
- Towhata, I., Tokida, K., Tamari, H., Matsumoto, H., & Yamada, L. (1991). Prediction of permanent lateral displacement of liquefied ground by means of variational principle. *Proceedings, 3rd Japan-U.S. Workshop on Earthquake Resistant Design of Lifeline Facilities and Countermeasures for Soil Liquefaction, Technical Report NCEER-91-0001*, 237-251. (O'Rourke, & Hamada, Eds.)
- United States Geologic Survey. (2008, November 8). *Shakemap atlas 199104222156*. Retrieved February 7, 2011, from USGS Shakemap Atlas: <http://earthquake.usgs.gov/earthquakes/shakemap/atlas/shake/199104222156/>
- USGS Earthquake Hazard Program. (2010). *USGS National Seismic Hazard Mapping Project*. (EHP Web Team) Retrieved November 2, 2010, from <http://earthquake.usgs.gov/hazards>
- Valsamis, A., Bouckovalas, G., & Dimitriadi, V. (2007, June). Numerical evaluation of lateral spreading displacements in layered soils. *Proceedings, 4th International Conference on Earthquake Geotechnical Engineering, Paper No. 1644*. Thessaloniki, Greece.
- Varnes, D. J. (1978). Slope movement types and processes. *Landslides - Analysis and Control; Special Report 176*. (R. S. Krizek, Ed.) Washington D.C.: Transportation Research Board.
- Vasquez-Herrera, A., & Dobry, R. (1988). The behavior of undrained contractive sand and its effect on seismic liquefaction flow failures of earth structures. *Report to the U.S. Army Corps of Engineers*, 510 pp. Troy, New York: Rensselaer Polytechnic Institute.
- Vasquez-Herrera, A., Dobry, R., & Baziar, M. H. (1990). Re-evaluation of liquefaction triggering and flow sliding in the Lower San Fernando Dam during the 1971 earthquake.

- Proceedings, 4th U.S. National Conference on Earthquake Engineering*, 783-792. Palm Springs, California.
- Veneziano, D., & Cornell, C. A. (1974). Earthquake models with spatial and temporal memory for engineering seismic risk analysis. *Research Report R74-48*. Cambridge, MA: Department of Civil Engineering, Massachusetts Institute of Technology.
- Vere-Jones, D., & Ozaki, T. (1982). Some examples of statistical estimation applied to earthquake data. I. Cyclic Poisson and self-exciting models. *Annals of the Institute of Statistics and Mathematics*, 34, B, 189-207.
- Vesic, A. S. (1977). Design of Pile Foundations. *National Cooperative Highway Research Program Synthesis of Highway Practice, No. 42*. Washington, D.C.: Transportation Research Board.
- Vulpe, A., & Carausu, A. (2004). Stochastic evaluation of availability for subsystems by Markov and semi-Markov models. *Proceedings, 13th World Conference on Earthquake Engineering*. Vancouver, Canada.
- Wang, S. T., & Reese, L. C. (1998). Design of pile foundations in liquefied soils. *Geotechnical Earthquake Engineering and Soil Dynamics III, Geotechnical Special Pub. No. 75, 2*, 1331-1343. (P. Dakoulas, M. Yegian, & R. Holtz, Eds.) ASCE.
- Weaver, T. J., Ashford, S. A., & Rollins, K. M. (2005). Response of 0.6 m cast-in-steel-shell pile in liquefied soil under lateral loading. *Journal of Geotechnical and Geoenvironmental Engineering*, 131, 1, 94-102. ASCE.
- Weisstein, E. W. (2005). *Poisson process*. (W. W. Resource, Producer) Retrieved from MathWorld: <http://mathworld.wolfram.com/PoissonProcess.html>
- Wells, D. L. (2000). Probabilistic seismic hazard analysis and source characterization for central and eastern North America. *Proceedings, 6th International Conference on Seismic Zonation: Managing Earthquake Risk in the 21st Century*. Oakland, CA: Earthquake Engineering Research Institute.
- Wesnousky, S. G. (1994). The Gutenberg-Richter or Characteristic Earthquake distribution, Which is it? *Bulletin of the Seismological Society of America*, 84, 1940-1959.
- Wesnousky, S. G., Scholz, C. H., Shimazaki, K., & Matsuda, T. (1984). Integration of geological and seismological data for the analysis of seismic hazard: a case study of Japan. *Bulletin of the Seismological Society of America*, 74, 687-708.
- Whitman, R. V. (1971). Resistance of soil to liquefaction and settlement. *Soils and Foundations*, 11(4), 59-68.
- Wilson, D. W. (1998). Soil-pile-superstructure interaction in liquefying sand and soft clay. *PhD Dissertation*. Davis, California: University of California at Davis.

- Wilson, D. W., Boulanger, R. W., & Kutter, M. L. (2000). Observed seismic lateral resistance of liquefying sand. *Journal of Geotechnical and Geoenvironmental Engineering*, 126, 10, 898-906. ASCE.
- Wilson, D. W., Boulanger, R. W., & Kutter, M. L. (2000). Observed seismic lateral resistance of liquefying sand. *Journal of Geotechnical and Geoenvironmental Engineering*, 126(10), 898-906.
- Wong, R. T., Seed, H. B., & Chan, C. K. (1975). Liquefaction of gravelly soil under cyclic loading conditions. *Journal of the Geotechnical Engineering Division*, 101(GT6), 571-583.
- Wu, J. (2002). Liquefaction triggering and post-liquefaction deformation of Monterey 0/30 sand under uni-directional cyclic simple shear loading. *PhD Dissertation*. Berkeley, California: University of California.
- Yang, Z. (2000). Numerical modeling of earthquake site response including dilation and liquefaction. *PhD Dissertation*. Graduate School of Arts and Science, Columbia University.
- Yang, Z., Elgamal, A., & Parra, E. (2003). A computational model for liquefaction and associated shear deformation. *Journal of Geotechnical and Geoenvironmental Engineering*, 129(12).
- Yasuda, S., Masuda, T., Yoshida, N., Kiku, H., Itafuji, S., Mine, K., et al. (1994). Torsional shear and triaxial compression tests on deformation characteristics of sands before and after liquefaction. *Proceedings, 5th U.S.-Japan Workshop on Earthquake Resistant Design of Lifeline Facilities and Countermeasures Against Soil Liquefaction, NCEER-94-0026*, 249-266. Salt Lake City, UT.
- Yasuda, S., Nagase, H., Kiku, H., & Uchida, Y. (1991). A simplified procedure for the analysis of the permanent ground displacement. *Proceedings, 3rd Japan-U.S. Workshop on Earthquake Resistant Design of Lifeline Facilities and Countermeasures for Soil Liquefaction, Technical Report NCEER-91-0001*, 225-236. (O'Rourke, & Hamada, Eds.)
- Yoshida, N., & Hamada, M. (1990). Analysis of damages of foundation piles due to liquefaction-induced permanent ground displacements. *Proceedings, 8th Japan Earthquake Engineering Symposium, 1*, 55-60.
- Youd, T. L. (1984). Recurrence of liquefaction at the same site. *Proceedings, 8th World Conference on Earthquake Engineering, Vol. 3*, pp. 231-238.
- Youd, T. L. (1993, January). Liquefaction, ground failure, and consequent damage during the 22 April 1991 Costa Rica earthquake. *Proceedings, U.S.-Costa Rica Workshop, Costa Rica Earthquakes of 1990-1991, Effects on Soils and Structures, EERI Publication No. 93-A*, 74-95. EERI.

- Youd, T. L. (2005, October). Liquefaction-induced flow, lateral spread, and ground oscillation. *Proceedings, GSA Annual Meeting, Paper No. 110-6*. Salt Lake City, Utah: Geological Society of America.
- Youd, T. L. (2009, June). Personal communication.
- Youd, T. L., & Hoose, S. N. (1977). Liquefaction susceptibility and geologic setting. *Proceedings, 6th World Conference on Earthquake Engineering, Vol. 3*, pp. 2189-2194. New Delhi.
- Youd, T. L., & Perkins, D. M. (1987). Mapping of liquefaction severity index. *Journal of Geotechnical Engineering, 113*(11), 1374-392.
- Youd, T. L., DeDen, D. W., Bray, J. D., Sancio, R. B., Cetin, K. O., & Gerber, T. M. (2009). Zero-displacement lateral spreads, 1999 Kocaeli, Turkey, earthquake. *Journal of Geotechnical and Geoenvironmental Engineering, 135*(1), 46-61.
- Youd, T. L., Hansen, C. M., & Bartlett, S. F. (2002). Revised multilinear regression equations for prediction of lateral spread displacement. *Journal of Geotechnical and Geoenvironmental Engineering, 128, 12*, 1007-1017. ASCE.
- Youd, T. L., Idriss, I. M., Andrus, R. D., Arango, I., Castro, G., Christian, J. T., et al. (2001). Liquefaction resistance of soils; summary report from the 1996 NCEER and 1998 NCEER/NSF workshops on evaluation of liquefaction resistance of soils. *Journal of Geotechnical and Geoenvironmental Engineering, 127*(10), 817-833.
- Youd, T. L., Rollins, K. M., Salazar, A. F., & Wallace, R. M. (1992, July 19-25). Bridge damage caused by liquefaction during the 22 April 1991 Costa Rica earthquake. *Proceedings, 10th World Conference on Earthquake Engineering, 1*, 153-158. Madrid, Spain.
- Youngs, R. R., & Coppersmith, K. J. (1985). Implications of fault slip rates and earthquake recurrence models to probabilistic seismic hazard assessments. *Bulletin of the Seismological Society of America, 75, 4*, 939-964.
- Youngs, R. R., Chiou, S. J., Silva, W. J., & Humphrey, J. R. (1997). Strong ground motion attenuation relationships for subduction zone earthquake. *Seismological Research Letters, 68*(1), 58-73.
- Youngs, R. R., Chiou, S. J., Silva, W. J., & Humphrey, J. R. (1997). Strong ground motion attenuation relationships for subduction zone earthquakes. *Seismological Research Letters, 68, 1*, 58-73.
- Zhang, G., Robertson, P. K., & Brachman, R. W. (2004). Estimating liquefaction-induced lateral displacements using the standard penetration test or cone penetration test. *Journal of Geotechnical and Geoenvironmental Engineering, 130*(8), 861-871.
- Zhang, J., & Zhao, J. X. (2005). Empirical models for estimating liquefaction-induced lateral spread displacement. *Soil Dynamics and Earthquake Engineering, 25*, 439-450.

- Zhao, J. X., Zhang, J., Asano, A., Ohno, Y., Oouchi, T., Takahashi, T., et al. (2006). Attenuation relations of strong ground motion in Japan using site classification based on predominant period. *Bulletin of Seismological Society of America*, 96, 3, 898-913.
- Zienkiewicz, O. C., & Shiomi, T. (1984). Dynamic behavior of saturated porous media: the generalized Biot formulation and its numerical solution. *International Journal for Numerical and Analytical Methods in Geomechanics*, 8, 71-96.
- Zienkiewicz, O. C., Chang, C. T., & Hinton, E. (1978). Non-linear seismic response and liquefaction. *International Journal for Numerical and Analytical Methods in Geomechanics*, 2, 381-404.

APPENDIX A. GEOTECHNICAL STUDY REPORTS

Titles: *Geotechnical Study, Bridges in Limon Province of Limon, Costa Rica, and
Complimentary Geotechnical Study, Rio La Estrella Bridge, Province of Limon,
Costa Rica*

Author: Insuma S.A. Geotechnical Consultants

Dates: June 2010 & June 2011

Pages: A-1 to A-50 & A-51 to A-68



BRIGHAM YOUNG UNIVERSITY

GEOTECHNICAL STUDY

BRIDGES IN LIMÓN
PROVINCE OF LIMÓN, COSTA RICA

INSUMA S.A.
Geotechnical Consultants

July, 2010



San José, July 12th, 2010
2056-10

Prof. Kyle Rollins
Department of Civil and Environmental Engineering
Brigham Young University
Provo, Utah

Dear Prof. Rollins:

We present the results of the Geotechnical Study carried out in several bridge sites of the province of Limón, in Costa Rica. The investigated sites correspond to several bridge structures that suffered damages during the Limón-Telire Earthquake, occurred in April of 1991. The investigated sites are listed below:

- Río Cuba Highway Bridge
- Río Blanco Highway Bridge
- Río Bananito Highway Bridge
- Río Estrella Highway Bridge
- Río Bananito Railroad Bridge

The objective of the investigation was to determine the geotechnical conditions of each of the different sites. This objective was achieved through the execution of field and laboratory tests. This report includes, among other things, the field and laboratory information that was used to determine the soil profile and the physical and mechanical characteristics of the materials.

We hope that this report is to your satisfaction and we are available for any further consultation you may have.

Sincerely,
INSUMA S.A.
Geotechnical Consultants


Ing. José A. Rodríguez Barquero

C: File


Ing. José P. Rodríguez Calderón, MSc.

TABLE OF CONTENTS

TABLE OF CONTENTS	i
1. INTRODUCTION.....	1
2. OBJECTIVES AND SCOPE OF THE STUDY	2
3. EXECUTED WORKS	3
3.1 Field Works	3
3.2 Laboratory Works	5
3.3 Analysis and interpretation	6
4. GEOLOGY OF THE AREA	6
5. RIO CUBA BRIDGE	10
5.1 Location and executed works	10
5.2 Geotechnical profile.....	11
6. RIO BLANCO BRIDGE	14
6.1 Location and executed works	14
6.2 Geotechnical profile.....	15
7. RIO BANANITO HIGHWAY BRIDGE	18
7.1 Location and executed works	18
7.2 Geotechnical profile.....	19
8. RIO BANANITO RAILROAD BRIDGE.....	22
8.1 Location and executed works	22
8.2 Geotechnical profile.....	23
9. RIO ESTRELLA BRIDGE.....	26
9.1 Location and executed works	26
9.2 Geotechnical profile.....	27
10. CONCLUSIONS.....	30

1. INTRODUCTION

Attending the request of Prof. Kyle Rollins from Brigham Young University and as proposed in document C114-10, INSUMA executed a geotechnical study in several bridge sites of the province of Limón, in Costa Rica. The bridge sites that were investigated are indicated in Table 1 and their location is presented in Figure 1.

Table 1: Bridge sites that were investigated in Limón, Costa Rica

Bridge Site	Location	
	Latitude	Longitude
Río Blanco Highway Bridge	9.99178	-83.125333
Río Cuba Highway Bridge	10.02237	-83.217967
Río Bananito Railroad Bridge	9.8765	-83.0076
Río Bananito Highway Bridge	9.88492	-82.966883
Río Estrella Highway Bridge	9.78760	-82.9134



Figure 1: Location of the different sites investigated during the study

The geotechnical study was requested as part of a research investigation being carried out by Prof. Rollins, which is related to the topic of soil liquefaction. Each of the investigated sites have the particular characteristic that they host bridge structures that were damaged during the

occurrence of the Limón-Telire Earthquake, in April of 1991. The damages in the bridges were mainly due to the effects of liquefaction.

The objective of the investigation was to determine the geotechnical characteristics at each of the investigated sites. These characteristics include, among other things, the soil profiles and the physical and mechanical properties of the soil layers present at the subsurface levels. This objective was achieved through the execution of borings and laboratory tests that was analyzed in order to establish the geotechnical profiles and the soil properties. The results of the study are presented in this report, which has been divided into several sections.

Section 1 of the report corresponds to the introduction and it mainly describes the content of the report. The objectives and the scope of the investigation are described in Section 2, while the executed works and the methods followed to carry out the works are explained in Section 3.

In order to make a better interpretation of the geotechnical conditions of the site, it is necessary to have a good understanding of the regional geological conditions. Therefore, Section 4 presents a brief description of the geological framework present at the different sites that have been investigated. Even though these sites are distant from one another, the geological and geomorphological conditions are very similar throughout the region.

Once the geological framework has been established, the results obtained for each particular site are presented. Sections 5 through 9 are related to the specific results and geotechnical conditions detected for each of the investigated bridges. The following information is included for each of these sections: 1) brief description of the bridge site and summary of the works executed at the site, 2) description and properties of the soil layers that appear, and 3) soil profile interpreted from the field and laboratory information.

The specific results for each of the studied bridge sites are followed by Section 10 which corresponds to the conclusions of the investigation. To complement the report, five appendices are included and they correspond to the boring logs for each of the boreholes executed at the different bridge sites.

2. OBJECTIVES AND SCOPE OF THE STUDY

The main objective of the investigation is to determine the geotechnical conditions of each of the 5 bridge sites that were defined previously. In order to achieve this general objective, several specific objectives have been defined. Some of the specific objectives are: to determine the geological conditions of the region, to determine the physical and mechanical properties of the different soil layers that appear at the site, and to elaborate a geotechnical model based on the obtained information and based on INSUMA's interpretation.

In order to achieve the mentioned objectives, field and laboratory works were executed and the geotechnical information required to fulfill the objectives was acquired. A detail of the executed works is included in Section 3 of the report.

The executed investigation was carried out following methods that are currently accepted in geotechnical engineering and that comply both with national and international standards. The field and laboratory tests performed as part of the investigation were executed following procedures defined in the ASTM standards.

The scope of the study has been limited to determining the geotechnical conditions of the site; therefore, it does not include any type of analysis regarding foundation of structures, mathematical modeling and/or other types of analysis such as soil liquefaction. It should be understood that these types of analysis and models will probably be done in latter stages of the research project which is underway.

3. EXECUTED WORKS

The geotechnical investigation was divided into three different phases: 1) Field Works, 2) Laboratory Works, and 3) Analysis and interpretation. A more detailed description of each phase is presented below.

3.1 Field Works

The first activity of this phase of the investigation consisted in visits by engineers José A. Rodríguez Barquero and José P. Rodríguez Calderón from INSUMA. These visits were carried out with Prof. Kyle Rollins from BYU and their objective was to coordinate logistical aspects, see the advance of the field works, coordinate the location of the boreholes and gather the basic geological/geotechnical information of each of the sites.

The second activity of the field works consisted in the execution of the boreholes. This activity was supervised by personnel associated to BYU. The location of the boreholes was selected by Prof. Rollins and most of these drillings were executed in the right margin of each of the rivers, with the exception of the Río Bananito Railroad Bridge whose boreholes were done in the left margin. Table 2 summarizes the boreholes executed in each bridge site, the depth reached in the borehole, and the method of drilling used.

Table 2: Summary of the executed boreholes – Bridges in Limón, Costa Rica

Bridge Site	Quantity of Boreholes	Depth of Borehole	Method of Drilling
Río Cuba Highway Bridge	1	15 m	SPT + Casing
Río Blanco Highway Bridge	1	15 m	SPT + Casing
Río Bananito Highway Bridge	2	20 m 20 m	SPT + Casing
Río Estrella Highway Bridge	1	20 m	SPT + Casing
Río Bananito Railroad Bridge	2	14 m 14 m	SPT + Casing

As indicated in Table 2, the boreholes were executed following the procedure of the standard penetration test (SPT). The drillings were carried out in accordance to standard ASTM D-1586. Given that loose, non-plastic saturated sands were detected at each of the sites it was necessary to use casing to prevent the drillhole from collapsing. Continuous sampling was used in all of the boreholes; hence, it was possible to determine the soil profile down to the investigated depth.

The SPT drilling method is exclusive for soils; therefore, it is not possible to drill through very hard consistency materials (e.g. rocks, boulders or rock masses). This type of drilling procedure has been used worldwide and it consists in driving a split spoon sampler with the use of a hammer. A simple sketch of the drilling procedure is indicated in Figure 2.

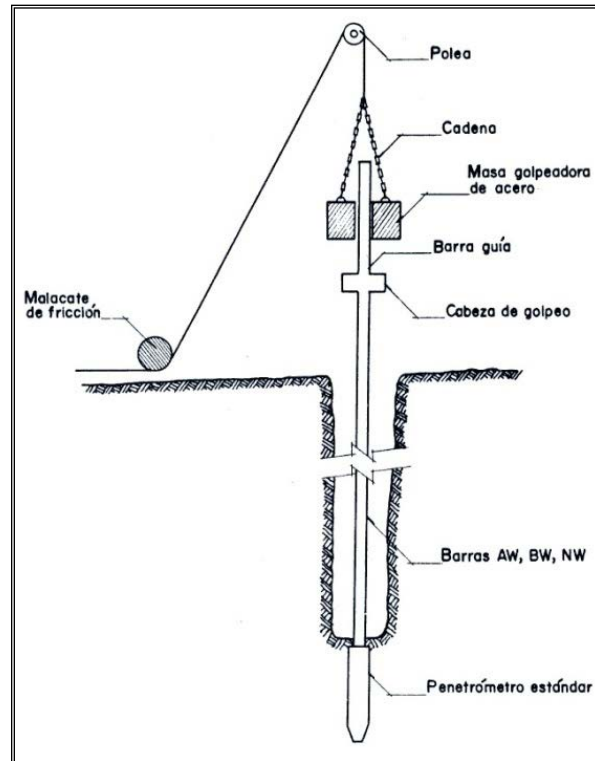


Figure 2: Sketch of the standard penetration test method (ASTM D-1586)

The dimensions of the split spoon sampler, the fall and weight of the hammer, the diameter of the bars and the rest of the materials used in the SPT method are standardized according to the specifications in ASTM D-1586. Figures 3 and 4 present some of the equipment used in the drilling procedure.

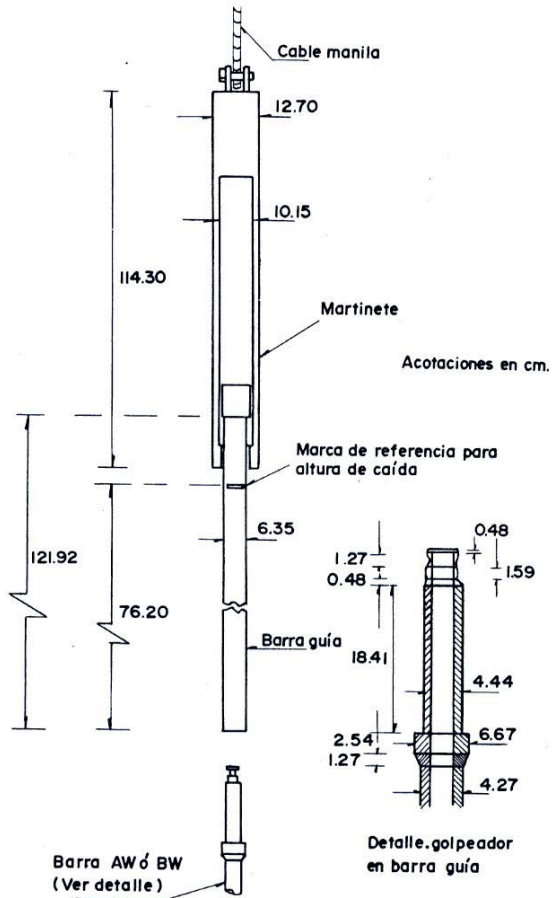


Figure 3: Detail of the 64 kg hammer and the specifications for the fall of the weight

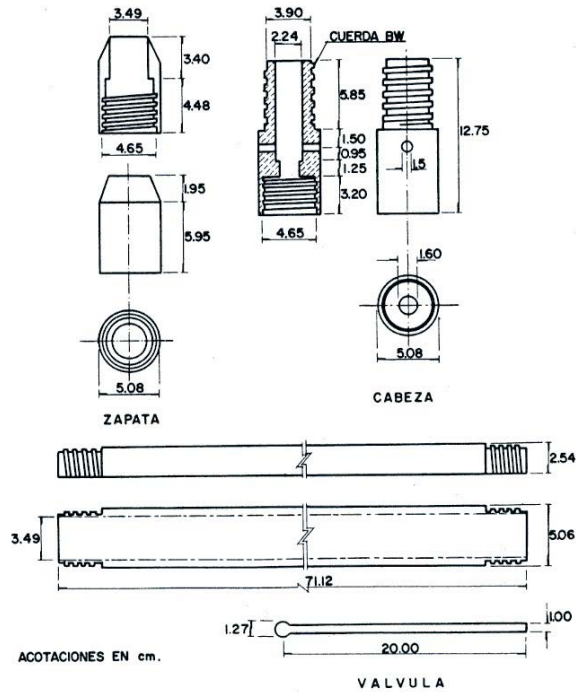


Figure 4: Detail of the standard split spoon sampler

The SPT method allows the correlation of the soil consistency with the N_{SPT} value. This value corresponds to the number of blows required to drive the standard sampler a distance of 0.3 m. In order to be able to define the N_{SPT} value and make it comparable to other investigations, it was necessary to carry out tests in order to determine the efficiency of the SPT drilling rig and its operator. These measurements were carried out directly by BYU personnel and according to the information provided the measured efficiency was higher than 90%; however, these results are not currently available to INSUMA.

The samples collected from the execution of the boreholes were described visually by the foreman of the drilling crew and they were later placed in plastic bags in order to prevent the loss of the natural water content. The samples were later transported to INSUMA's laboratory for the corresponding storage and analysis.

3.2 Laboratory Works

The second phase of the geotechnical study corresponds to the execution of the laboratory works. As indicated, the soil samples collected from the boreholes were transported to INSUMA's laboratory where a visual description was carried out by the laboratory technician. This visual description was executed to all the samples collected from the boreholes.

The visual description was complemented with the execution of the following index property tests:

- Gradation
- Percent washed in 200 Sieve
- Natural water content
- Atterberg limits

These tests were not executed on every sample, but they were carried out with a frequency of every 1.5 – 1.75 m and whenever a different type of soil was detected. All of the tests were carried out following the procedures described in the different ASTM standards. The results obtained from the laboratory tests enabled the classification of the different soil layers with the Unified Soil Classification System.

3.3 Analysis and interpretation

Once all the field and laboratory information was available, it was integrated and analyzed in order to elaborate and present the geotechnical profile of each site. It is important to indicate, as it was described in the scope of the investigation, that this phase of the investigation does not include any type of liquefaction or foundation analysis and/or recommendations. This will probably be done in a later stage of the research project that is being executed.

4. GEOLOGY OF THE AREA

Even though the different bridge sites are distant from one another, the geological conditions of the region are very similar. These geological conditions have a direct influence on the type of materials detected at the different sites, as well as on their mechanical properties and therefore, on the similar geotechnical behavior observed for each of the bridges.

Based on the geological map of Limón (CR2CM-6), scale 1:200.000, the geology of the area consists of Alluvial and coastal deposits (Qal). From the lithological point of view and specifically in the areas near the coast, these deposits are made up of fine sediments with sandy and clayey textures. An extract of Limón's geological map is presented in Figure 5 below. The location of each of the investigated bridge sites is shown in the map.

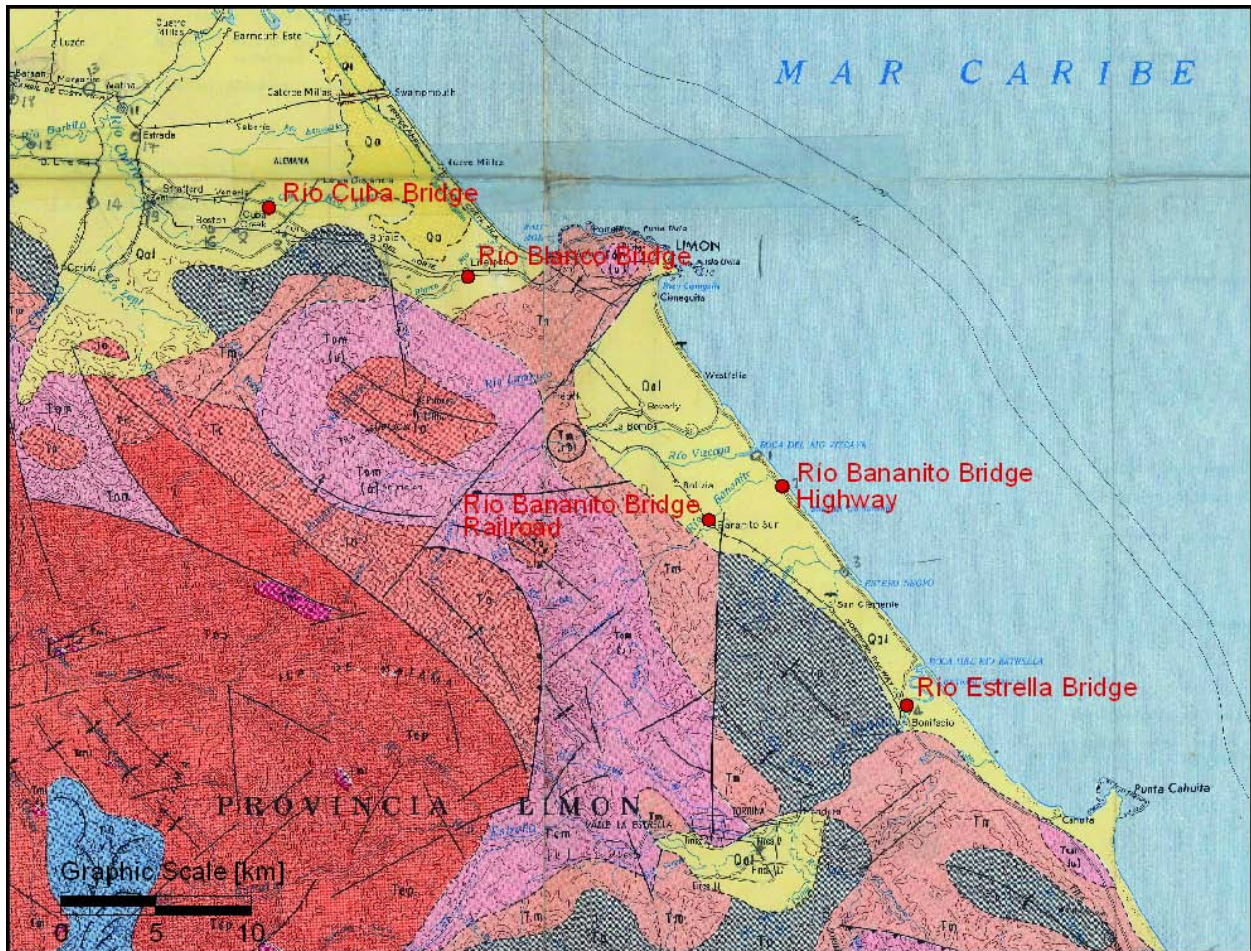


Figure 5: Geologic map of Limón (CR2CM-6) scale 1:200,000

Regarding the map shown in Figure 5, it can be observed that all five of the investigated sites lie within the areas of Alluvial and coastal deposits (Qal) which are indicated in the map with a pale yellow color. This type of geologic formation is located off the Atlantic Coast of the country but it also extends toward the north. Notice that towards the west, the geological formations change and they correspond to volcanic and sedimentary rocks associated to the Cordillera of Talamanca. This other geological formations are represented by the other colors shown in the map of Figure 5.

Regarding the geomorphological conditions of the area, the bridge sites are located in forms of alluvial sedimentation. The origin of this type of geomorphological units is associated with the sedimentation caused by rivers and/or creeks. In some cases, specifically in those areas located near the coast, there is a marine influence related to this soil deposits.

The specific alluvial unit where the bridge sites are located corresponds to the Alluvial Plain of San Carlos and the Atlantic. This unit is divided into two subunits, and the one of interest for this investigation corresponds to the one near the coast, which may have some marine influence in the formation of the soil deposits. One of the main characteristics of this unit consists in the relative flat topography.

From the seismic point of view, within the area of interest there are several active faults that can be the source of important earthquakes. The faults closer to the bridge sites are: Deformed Belt of North Panama – Limón (F2), Siquirres – Matina Fault (F1) and La Estrella Fault (F8). All of these faults are from the Quaternary (relatively recent) and they are considered active. They are indicated in Figure 6 below.



Figure 6: Tectonic map of the province of Limón (Source: Costa Rican Tectonic Atlas)

It is important to clarify that the active and recent faults from the Quaternary are shown in Figure 6 as red lines. The black lines correspond to paleotectonic faults and other geological structures that have not shown activity in the recent geologic past.

With regards to the seismicity of the area, the Limón-Telire earthquake that occurred in April 1991 is a clear example of the seismic potential of the area. For design purposes, the Costa Rican Seismic Code has identified the area as being within Zone III (see Figure 7).

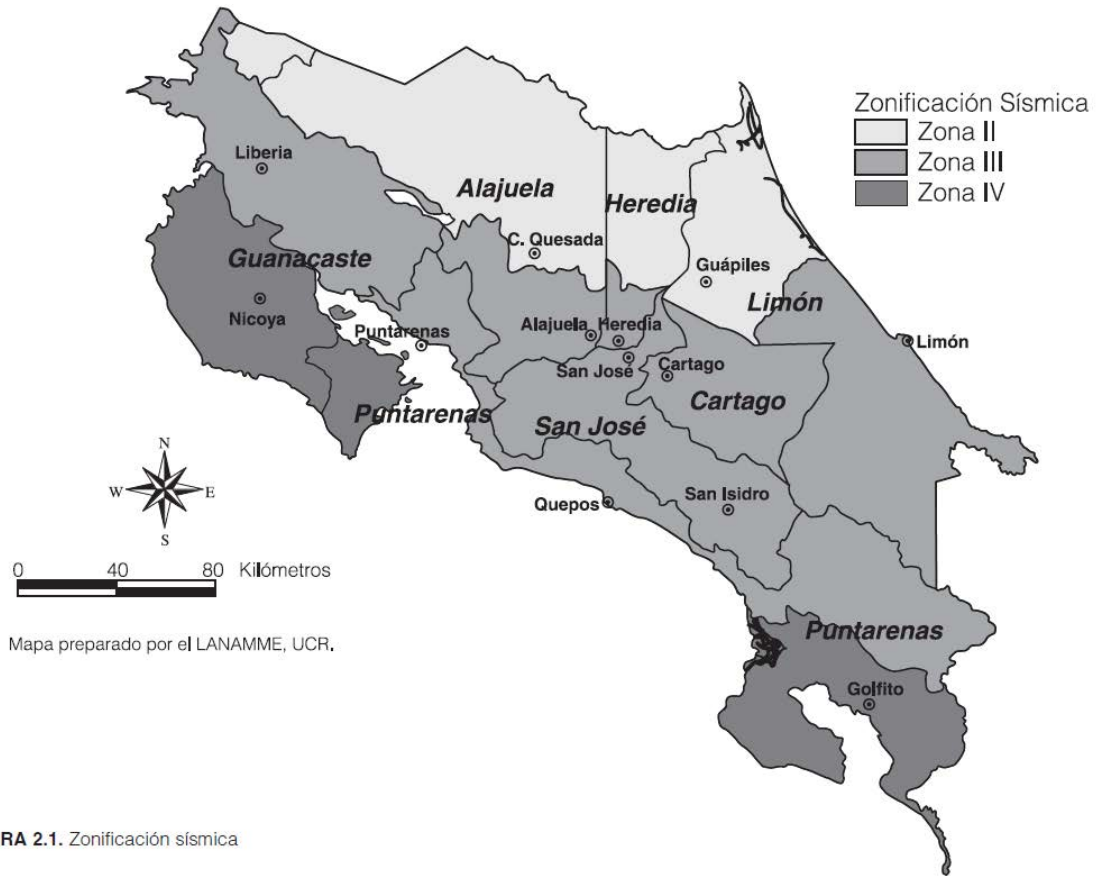


FIGURA 2.1. Zonificación sísmica

Figure 7: Seismic zoning proposed for Costa Rica (Source: Costa Rican Seismic Code 2002)

Within this area and based on the seismic threat studies that have been carried out, the design peak effective acceleration defined by the Costa Rican Seismic Code 2002 is between 0.30 and 0.36g. The peak effective acceleration will depend on the type of soil present at the site (i.e. rock, hard soils, soft soils, etc). With regards to the peak effective accelerations it is important to indicate that these values are for design and that during the Limón-Telire earthquake there were areas where the accelerations measured were higher.

With this brief geological framework of the area, it is possible to proceed with the specific results obtained for each of the investigated bridge sites.

5. RIO CUBA BRIDGE

This chapter includes the results obtained for the Río Cuba Bridge. A brief description of the site and the work executed is presented. This description is followed by a description of the geotechnical profile. The detailed results of the borings and the lab tests are presented in Appendix A, which corresponds to the boring logs.

5.1 Location and executed works

The Río Cuba Bridge is located along national route 32, near the town of Maravilla. From the administrative/political point of view, the bridge site is located in the 7th province Limón, 5th county Matina, 3rd district Carrandí. From the geographical point of view, the site is located at coordinates 10.02237° and -83.217967° . These coordinates can be located in the map Moin, scale 1:50.000, of the Costa Rican Geographical Institute (see Figure 8).

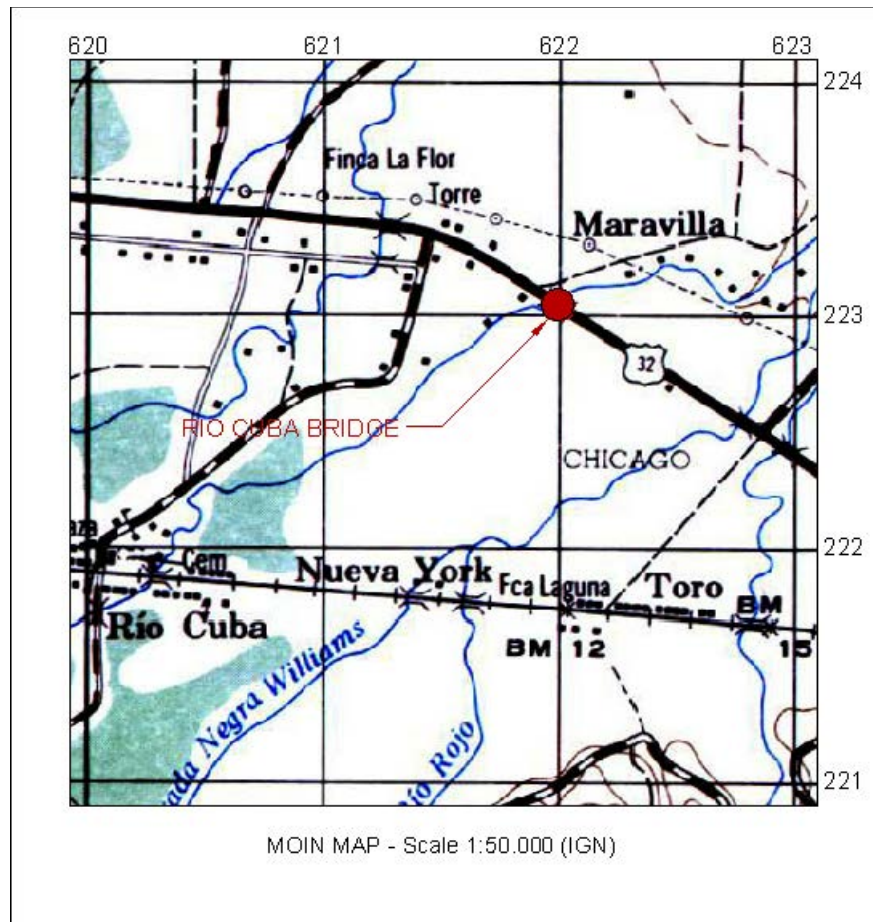


Figure 8: Location of Río Cuba Bridge. The coordinates indicated in the map correspond to North Lambert Projection System which is used locally.

The field work carried out at the Rio Cuba Bridge consisted in one SPT borehole. The location and depth of this borehole is indicated in the Table 2. A photograph of the executed drilling is presented in Photo 1.

Table 3: Location and depth of the executed boreholes – Rio Cuba Bridge

Borehole ID	Date	GPS Coordinates		Borehole Depth [m]
		North	West	
P-1	29-Apr-10	N10 01.327	W83 13.085	15



Photo 1: View of the site where the borehole was executed. The borehole is on the right margin of the river.

As observed in Photo 1 the borehole was executed at the base of the bridge's approach fill. The ground surrounding the area of the borehole is relatively flat and there is some small vegetation. The area is also surrounded by a banana plantation.

5.2 Geotechnical profile

The soil profile detected at the site is typical of this type of alluvial deposits/plains. It consists in sequences and/or alternations of clays, silts and sands. Specifically at this site, the clays detected have a high plasticity, the silts are predominantly not plastic or have very low plasticity, and the sands are clean and/or silty but with no plastic fines. The soil profile interpreted for the site is presented in Figure 9. The detailed profile, which includes the characteristics of each type of soil is included in the boring log of Appendix A.

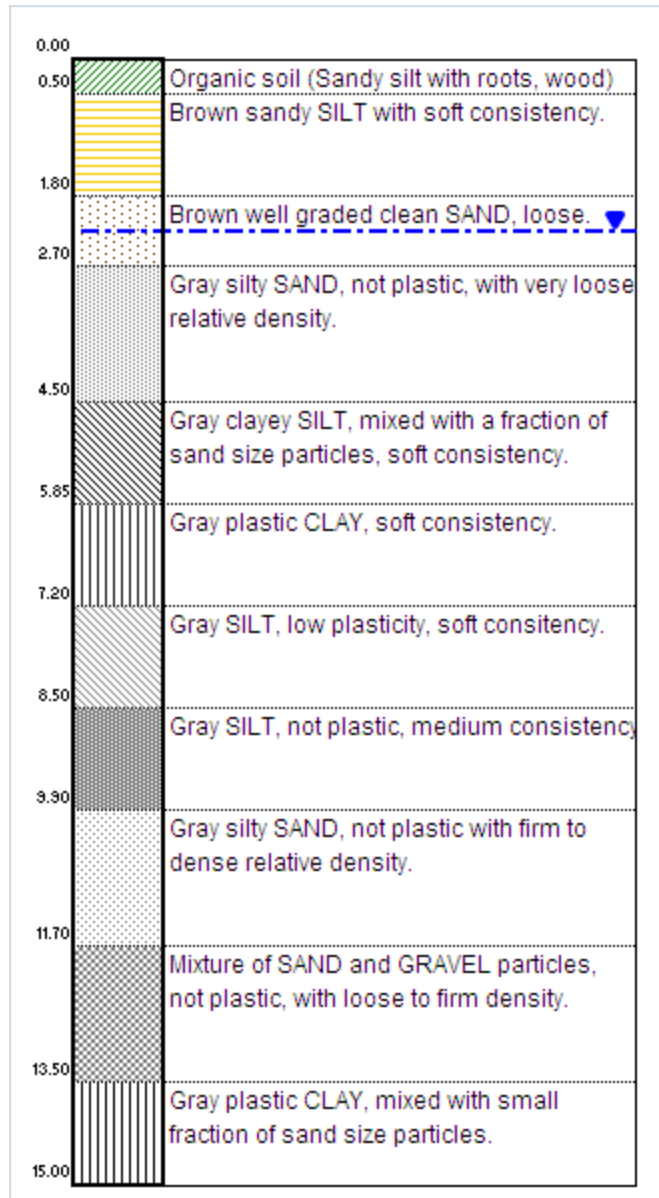


Figure 9: Soil profile detected at the Río Cuba Bridge site

As indicated in the profile above, the phreatic level appears at a depth of 2.10 m below the ground level. In order to complement the soil profile of Figure 9, a summary of the N_{SPT} values obtained in the boreholes is presented in Table 4. This summary includes the same symbol key used to represent the soils of Figure 9. This in order to differentiate the different N_{SPT} values detected for each type of soil. It is important to indicate that these values are the ones measured in the boring and they haven't been corrected.

Table 4: Summary of the N_{SPT} values detected at the Río Cuba Bridge Site

Depth [m]	P-1
0.00 - 0.45	15
0.45 - 0.90	9
0.90 - 1.35	4
1.35 - 1.80	2
1.80 - 2.25	5
2.25 - 2.70	7
2.70 - 3.15	12
3.15 - 3.60	4
3.60 - 4.05	2
4.05 - 4.50	2
4.50 - 4.95	2
4.95 - 5.40	2
5.40 - 5.85	3
5.85 - 6.30	2
6.30 - 6.75	4
6.75 - 7.20	2
7.20 - 7.65	6
7.65 - 8.10	5
8.10 - 8.55	11
8.55 - 9.00	17
9.00 - 9.45	11
9.45 - 9.90	15
9.90 - 10.35	22
10.35 - 10.80	24
10.80 - 11.25	24
11.25 - 11.70	33
11.70 - 12.15	23
12.15 - 12.60	15
12.60 - 13.05	10
13.05 - 13.50	6
13.50 - 13.95	6
13.95 - 14.40	6
14.40 - 14.85	10

Based on the results presented in Table 4, it can be observed that from the surface down to a depth of approximately 8 m the soils that appear have a soft/loose consistency. From depths between 8 – 12 m the materials have a better consistency which again decreases when a clayey layer is detected.

6. RIO BLANCO BRIDGE

This chapter includes the results obtained for the Río Blanco Bridge. A brief description of the site and the work executed is presented. This description is followed by a description of the geotechnical profile. The detailed results of the borings and the lab tests are presented in Appendix B, which corresponds to the boring logs.

6.1 Location and executed works

The Río Blanco Bridge is located along national route 32 near the town of Liverpool. From the administrative/political point of view, the bridge site is located in the 7th province Limón, 1st county Limón, 3rd district Río Blanco. From the geographical point of view, the site is located at coordinates 9.99178° and -83.12533°. These coordinates can be located in the map Río Banano, scale 1:50.000, of the Costa Rican Geographical Institute (see Figure 10).

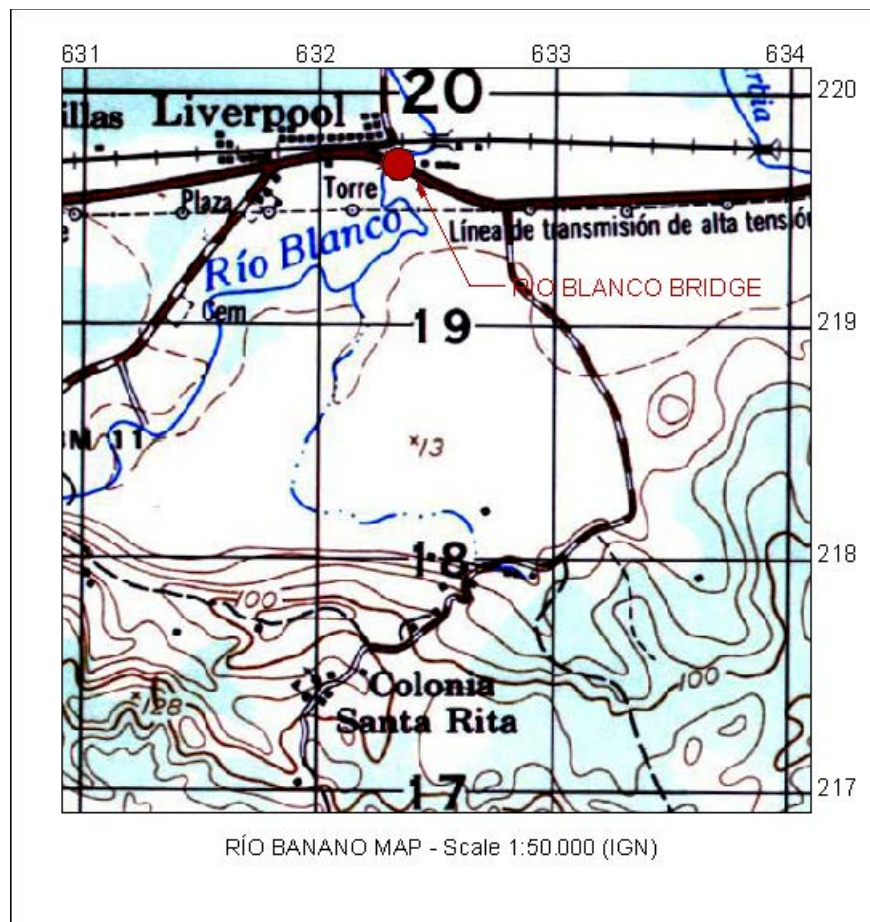


Figure 10: Location of Río Blanco Bridge. The coordinates indicated in the map correspond to North Lambert Projection System which is used locally.

The field work carried out at the Río Blanco Bridge consisted in one SPT borehole. The location and depth of this borehole is indicated in the Table 5. A photograph of the executed drilling is presented in Photo 2.

Table 5: Location and depth of the executed boreholes – Río Blanco Bridge

Borehole ID	Date	GPS Coordinates		Borehole Depth [m]
		North	West	
P-1	28-Apr-10	N9 59.511	W83 07.482	15



Photo 2: View of the site of Río Blanco Bridge where the borehole was executed. The borehole is on the right margin of the river.

As observed in Photo 2 the borehole was executed at the base of the bridge's approach fill. The ground surrounding the area of the borehole is relatively flat and there is some small vegetation.

6.2 Geotechnical profile

The soil profile detected at the site is typical of alluvial transported deposits/plains. The types of soils recovered in the boreholes correspond to clays and silty sands or mixtures of these two materials. A particular characteristic of this site is that at depths between 3 and 7 m there are clays where traces of wood were observed. Furthermore, between 10 and 11 m, sands with pieces of wood also appeared. The pieces of wood that appear at the site are probably transported and deposited by the river. This wood is indicative of the recent soil deposits detected at this site.

The soil profile interpreted for the Río Blanco site is presented in Figure 11. The detailed profile, which includes the laboratory results, is presented in Appendix B.

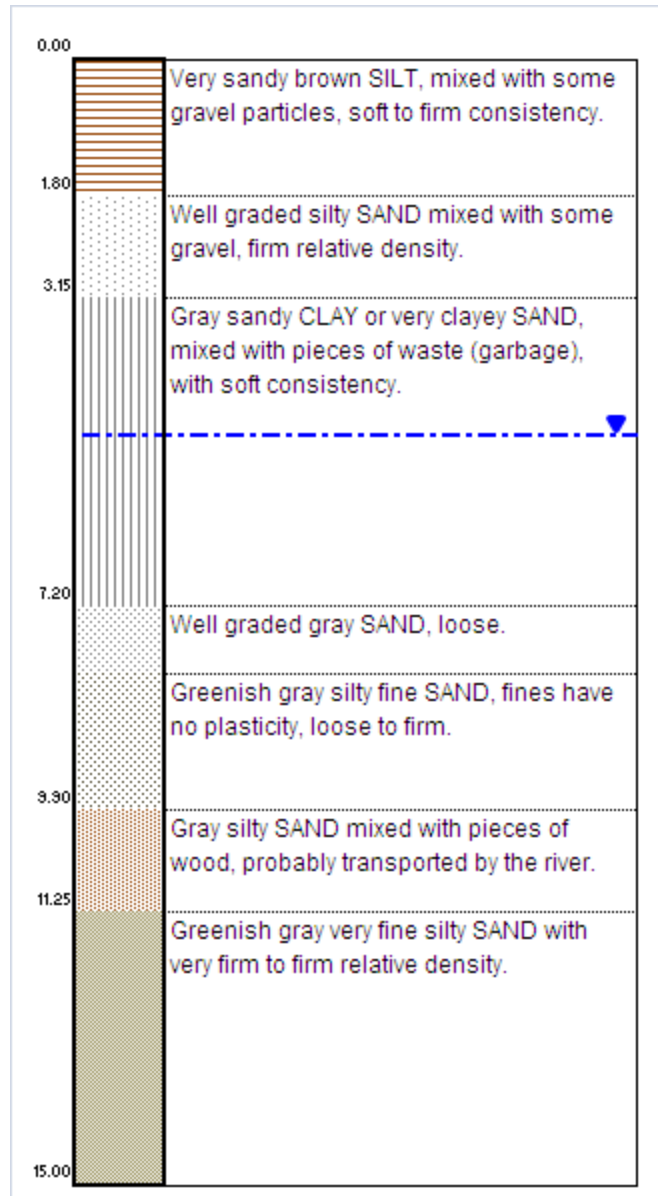


Figure 11: Soil profile detected at the Río Blanco Bridge site

The water table at this site appears at a depth of 4.80 m below the ground level. With regards to the soil profile, it is important to indicate that layer 3 corresponds to a mixture of clays and sands. Based on the laboratory results, this third layer is classified according to the USCS as very sandy CLAY or very clayey SAND.

In order to complement the soil profile of Figure 11, a summary of the N_{SPT} values obtained in the boreholes is presented in Table 6. This summary includes the same symbol key used to represent the soils of Figure 11. This in order to differentiate the different N_{SPT} values detected for each type of soil. It is important to indicate that these values are the ones measured in the boring and they haven't been corrected.

Table 6: Summary of the N_{SPT} values detected at the Río Blanco Bridge Site

Depth [m]	P-1
0.00 - 0.45	1
0.45 - 0.90	6
0.90 - 1.35	11
1.35 - 1.80	11
1.80 - 2.25	10
2.25 - 2.70	28
2.70 - 3.15	11
3.15 - 3.60	11
3.60 - 4.05	6
4.05 - 4.50	4
4.50 - 4.95	4
4.95 - 5.40	3
5.40 - 5.85	2
5.85 - 6.30	3
6.30 - 6.75	5
6.75 - 7.20	3
7.20 - 7.65	7
7.65 - 8.10	10
8.10 - 8.55	10
8.55 - 9.00	9
9.00 - 9.45	10
9.45 - 9.90	12
9.90 - 10.35	10
10.35 - 10.80	17
10.80 - 11.25	21
11.25 - 11.70	10
11.70 - 12.15	24
12.15 - 12.60	27
12.60 - 13.05	24
13.05 - 13.50	26
13.50 - 13.95	25
13.95 - 14.40	35
14.40 - 14.85	37

Based on the results presented in Table 6, it can be observed that soils of soft/loose consistency appear at depths between 3 and 10 m. Towards the end of the borehole, the consistency of the soils considerably improves and the materials that appear are dense silty SANDS.

7. RIO BANANITO HIGHWAY BRIDGE

This chapter includes the results obtained for the Río Bananito Highway Bridge. A brief description of the site and the work executed is presented. This description is followed by a description of the geotechnical profile. The detailed results of the borings and the lab tests are presented in Appendix C, which corresponds to the boring logs.

7.1 Location and executed works

The Río Bananito Highway Bridge is located along national route 36 near Bananito Beach. From the administrative/political point of view, the bridge site is located in the 7th province Limón, 1st county Limón, 2nd district Valle de la Estrella. From the geographical point of view, the site is located at coordinates 9.88492° and -82.966883°. These coordinates can be located in the map San Andrés, scale 1:50.000, of the Costa Rican Geographical Institute (see Figure 12).

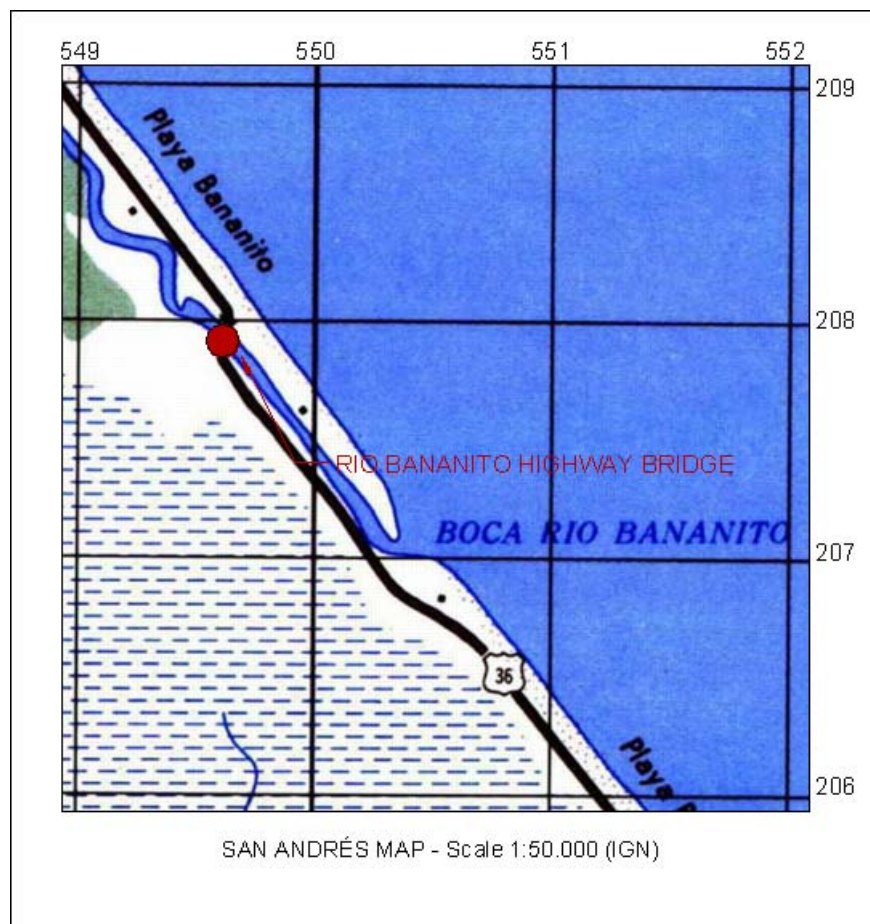


Figure 12: Location of Río Bananito Highway Bridge. The coordinates indicated in the map correspond to Lambert Projection System which is used locally.

The field work carried out at the Rio Bananito Highway Bridge consisted in two SPT boreholes. The location and depth of each borehole is indicated in the Table 7. Photographs of the executed drillings are presented in Photos 3 and 4.

Table 7: Location and depth of the executed boreholes – Rio Bananito Highway Bridge

Borehole ID	Date	GPS Coordinates		Borehole Depth [m]
		North	West	
P-1	23-Apr-10	N9 53.056	W82 58.011	20
P-2	25-Apr-10	N9 53.046	W82 58.012	20



Photo 3: View of the site of borehole P-1 at the Río Bananito Highway Bridge. The borehole is on the right margin of the river.



Photo 4: View of the site of borehole P-2 at the Río Bananito Highway Bridge.

As observed in Photo 3 borehole P-1 was executed practically in the margin of the river. Boreholes P-2 was executed about 20 m from borehole P-1, also on the right margin and following the alignment of route 36.

7.2 Geotechnical profile

The soil profile detected at the site is typical of alluvial transported deposits. The types of soils recovered in the boreholes correspond to silty SANDS and/or very sandy not plastic SILTS. A particular characteristic of this site is in some of the samples there is presence of seashells, which is indicative of the marine influence. This can be expected given the bridges proximity to the coast.

With regards to the soil profile, a sandy or silty poorly graded gravel is detected near the surface in borehole P-2. This material is probably associated to the construction of the road. The soil profile interpreted for the Rio Bananito highway site is presented in Figure 13. The detailed boring logs, which include the laboratory test results, are presented in Appendix C.

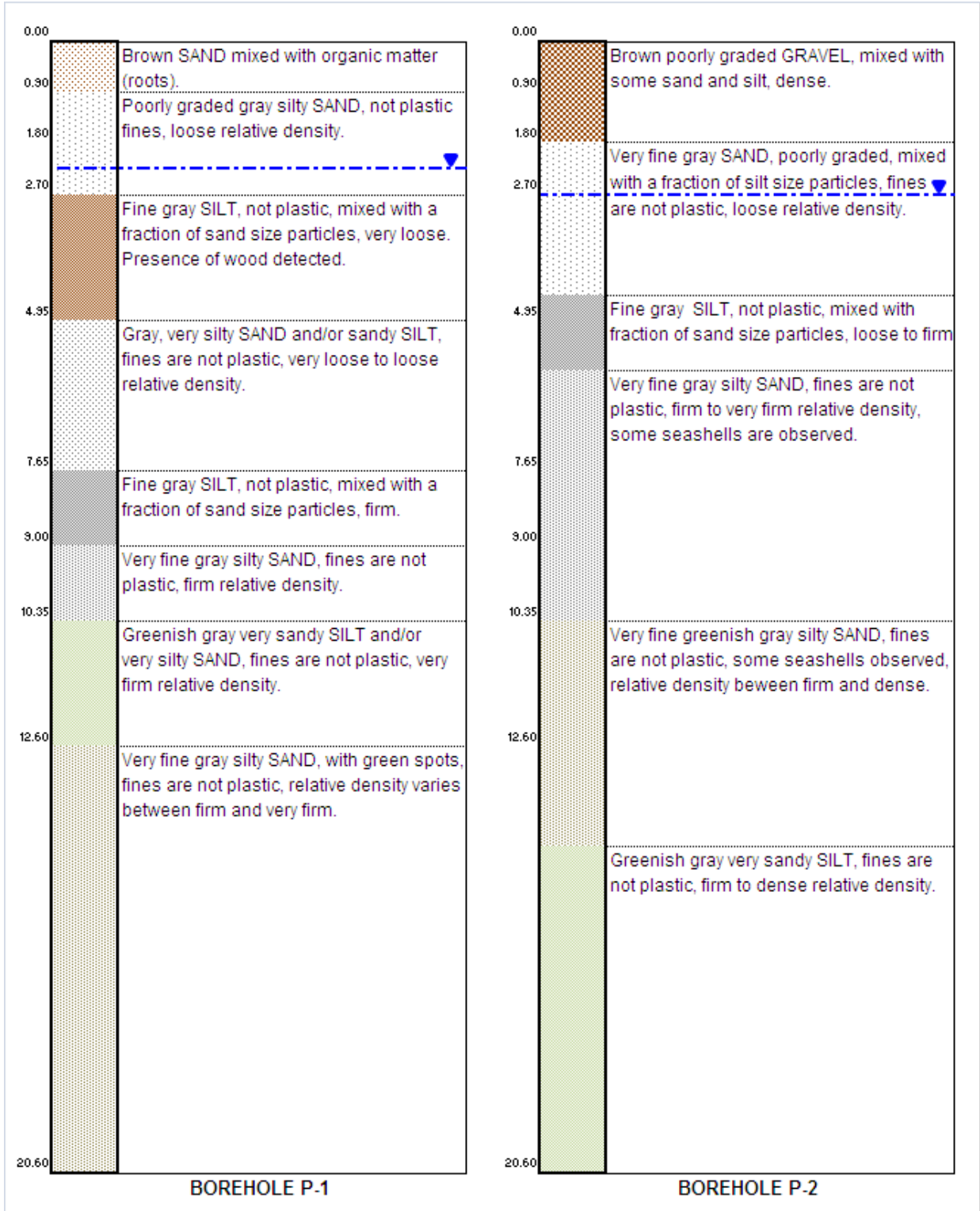


Figure 13: Soil profile detected at the Río Bananito Highway Bridge site

The water table at this site appears at a depth of 2 m below the ground level in P-1 and 2.65 m in boreholes P-2, which is farther away from the river. In order to complement the soil profile of Figure 13, a summary of the N_{SPT} values obtained in the boreholes is presented in Table 8.

Table 8: Summary of the N_{SPT} values detected at the Río Bananito Highway Bridge Site

Depth [m]	P-1	P-2
0.00 - 0.45	4	36
0.45 - 0.90	2	39
0.90 - 1.35	3	43
1.35 - 1.80	10	35
1.80 - 2.25	5	21
2.25 - 2.70	2	28
2.70 - 3.15	1	17
3.15 - 3.60	1	8
3.60 - 4.05	2	8
4.05 - 4.50	3	7
4.50 - 4.95	1	6
4.95 - 5.40	3	6
5.40 - 5.85	4	12
5.85 - 6.30	4	28
6.30 - 6.75	12	16
6.75 - 7.20	*	24
7.20 - 7.65	*	23
7.65 - 8.10	23	19
8.10 - 8.55	18	25
8.55 - 9.00	14	22
9.00 - 9.45	12	13
9.45 - 9.90	24	21
9.90 - 10.35	15	23
10.35 - 10.80	28	31
10.80 - 11.25	9	23
11.25 - 11.70	20	23
11.70 - 12.15	22	18
12.15 - 12.60	25	11
12.60 - 13.05	12	19
13.05 - 13.50	21	23
13.50 - 13.95	13	30
13.95 - 14.40	11	22
14.40 - 14.85	22	24
14.85 - 15.30	10	32
15.30 - 15.75	24	18
15.75 - 16.20	20	23
16.20 - 16.65	14	23
16.65 - 17.10	21	17
17.10 - 17.55	18	26
17.55 - 18.00	19	14
18.00 - 18.45	13	16
18.45 - 18.90	13	16
18.90 - 19.35	14	18
19.35 - 19.80	15	22
19.80 - 20.25	15	20

8. RIO BANANITO RAILROAD BRIDGE

This chapter includes the results obtained for the Río Bananito Railroad Bridge. A brief description of the site and the work executed is presented. This description is followed by a description of the geotechnical profile. The detailed results of the borings and the lab tests are presented in Appendix D, which corresponds to the boring logs.

8.1 Location and executed works

The Río Bananito Railroad Bridge is located near the town of Bananito. Currently this bridge is used by vehicles and occasionally by the train. From the administrative/political point of view, the bridge site is located in the 7th province Limón, 1st county Limón, 4th district Matama. From the geographical point of view, the site is located at coordinates 9.8765° and -83.0076° . These coordinates can be located in the map Río Banano, scale 1:50.000, of the Costa Rican Geographical Institute (see Figure 14).

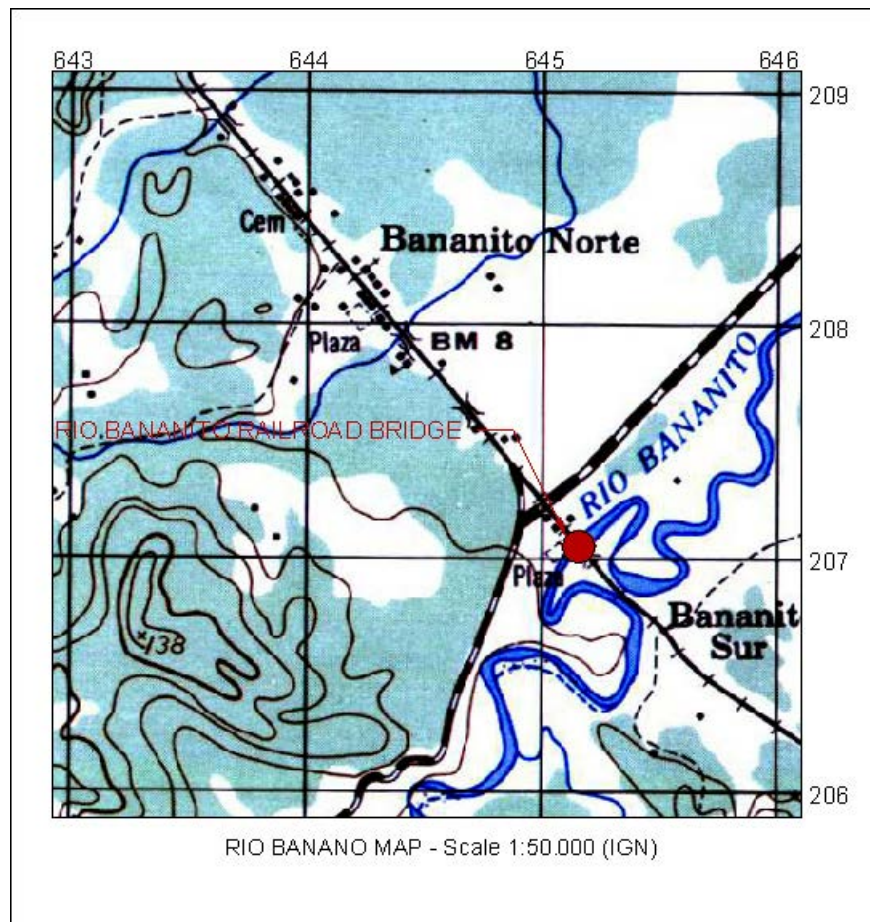


Figure 14: Location of Río Bananito Railroad Bridge. The coordinates indicated in the map correspond to Lambert Projection System which is used locally.

The field work carried out at the Rio Bananito Railroad Bridge consisted in two SPT boreholes. The location and depth of each borehole is indicated in the Table 9. Photographs of the executed drillings are presented in Photos 5 and 6.

Table 9: Location and depth of the executed boreholes – Rio Bananito Railroad Bridge

Borehole ID	Date	GPS Coordinates		Borehole Depth [m]
		North	West	
P-1	20-Apr-10	N9 52.619	W83 00.489	14
P-2	21-Apr-10	N9 52.623	W83 00.498	14



Photo 5: View of the site of borehole P-1 at the Rio Bananito Railroad Bridge. The borehole is on the left margin of the river.



Photo 6: View of the site of borehole P-2 at the Rio Bananito Railroad Bridge. The borehole is about 15 – 20 m apart from P-1.

As observed in Photo 4 and 5, the area where the boreholes were executed is relatively flat. Borehole P-2 was executed next to a pump station as observed in Photo 6.

8.2 Geotechnical profile

The soil profile detected at the site is also characteristics of the type of geologic formation and it consists mainly of two different types of materials: a clayey material near the surface underlain by clayey or silty SANDS. These sands have fines with some plasticity and in general, the relative density varies between loose and medium. On the other hand, the CLAY detected at the site has very soft to soft consistency.

The soil profile interpreted for the Rio Bananito Railroad site is presented in Figure 15. The detailed boring logs, which include the laboratory test results, are presented in Appendix D.

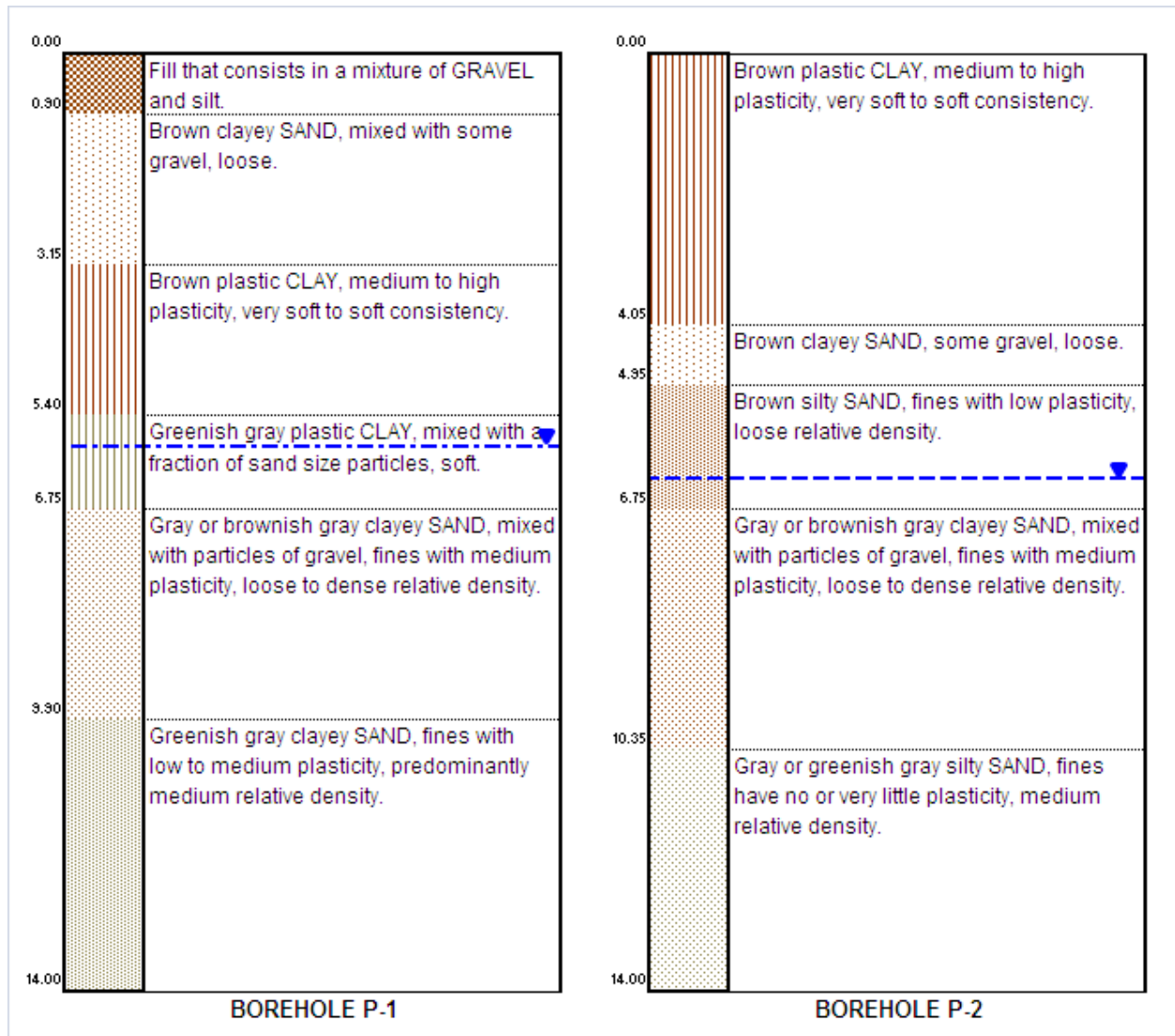


Figure 15: Soil profile detected at the Río Bananito Railroad Bridge site

The water table at this site appears at a depth of 5.65 m below the ground level in P-1 and 6.65 m in borehole P-2, which is farther away from the river. In order to complement the soil profile of Figure 15, a summary of the N_{SPT} values obtained in the boreholes is presented in Table 10.

Table 10: Summary of the N_{SPT} values detected at the Río Bananito Railroad Bridge Site

Depth [m]	P-1	P-2
0.00 - 0.45	26	6
0.45 - 0.90	11	2
0.90 - 1.35	6	3
1.35 - 1.80	4	3
1.80 - 2.25	4	3
2.25 - 2.70	4	3
2.70 - 3.15	4	3
3.15 - 3.60	1	4
3.60 - 4.05	0	5
4.05 - 4.50	0	10
4.50 - 4.95	1	7
4.95 - 5.40	2	9
5.40 - 5.85	3	8
5.85 - 6.30	7	13
6.30 - 6.75	7	19
6.75 - 7.20	7	7
7.20 - 7.65	15	8
7.65 - 8.10	20	11
8.10 - 8.55	8	4
8.55 - 9.00	24	23
9.00 - 9.45	36	36
9.45 - 9.90	20	16
9.90 - 10.35	16	21
10.35 - 10.80	19	9
10.80 - 11.25	21	28
11.25 - 11.70	25	15
11.70 - 12.15	23	20
12.15 - 12.60	6	16
12.60 - 13.05	17	27
13.05 - 13.50	24	26
13.50 - 13.95	18	22

Based on the results presented in Table 10, it is possible to observe that the CLAY layer is deeper near the river (borehole P-1).

9. RIO ESTRELLA BRIDGE

This chapter includes the results obtained for the Río Estrella Bridge. A brief description of the site and the work executed is presented. This description is followed by a description of the geotechnical profile. The detailed results of the borings and the lab tests are presented in Appendix E, which corresponds to the boring logs.

9.1 Location and executed works

The Río Estrella Bridge is located along national route 36 near the town of Penschurt. From the administrative/political point of view, the bridge site is located in the 7th province Limón, 1st county Limón, 2nd district Valle de la Estrella. From the geographical point of view, the site is located at coordinates 9.78760° and -82.9134° . These coordinates can be located in the map Cahuita, scale 1:50.000, of the Costa Rican Geographical Institute (see Figure 16).

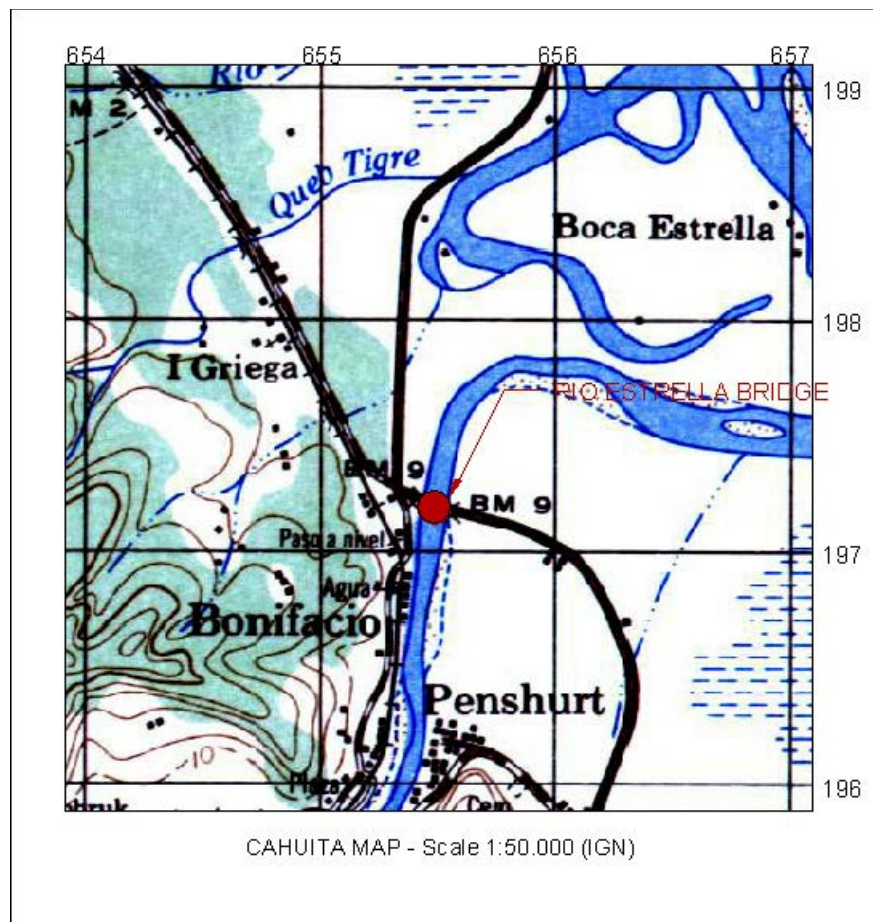


Figure 16: Location of Río Estrella Bridge. The coordinates indicated in the map correspond to Lambert Projection System which is used locally.

The field work carried out at the Rio Estrella Bridge consisted in one SPT borehole. The location and depth of this borehole is indicated in the Table 11. A photograph of the executed drilling is presented in Photo 7.

Table 11: Location and depth of the executed boreholes – Rio Blanco Bridge

Borehole ID	Date	GPS Coordinates		Borehole Depth [m]
		North	West	
P-1	27-Apr-10	N9 47.245	W82 54.816	20



Photo 7: View of the site of Río Estrella Bridge where the borehole was executed. The borehole is on the right margin of the river. Notice the bridge to the right.

As observed in Photo 7 the borehole was executed at the base of the bridge’s approach fill. The borehole is in the vicinity of one of the bridge’s abutments. The ground surrounding the area of the borehole is relatively flat and the vegetation corresponds to a banana plantation.

9.2 Geotechnical profile

The soil profile detected at the site is typical of this type of geological formations. The types of soils recovered in the boreholes correspond to clayey silts and silty sands. Between 4.50 and 7.20 m there is a layer of a coarser alluvial material that consists in very sandy gravels or sands with some gravel particles.

The soil profile interpreted for the Rio Estrella site is presented in Figure 17. The detailed profile, which includes the laboratory results, is presented in Appendix E.

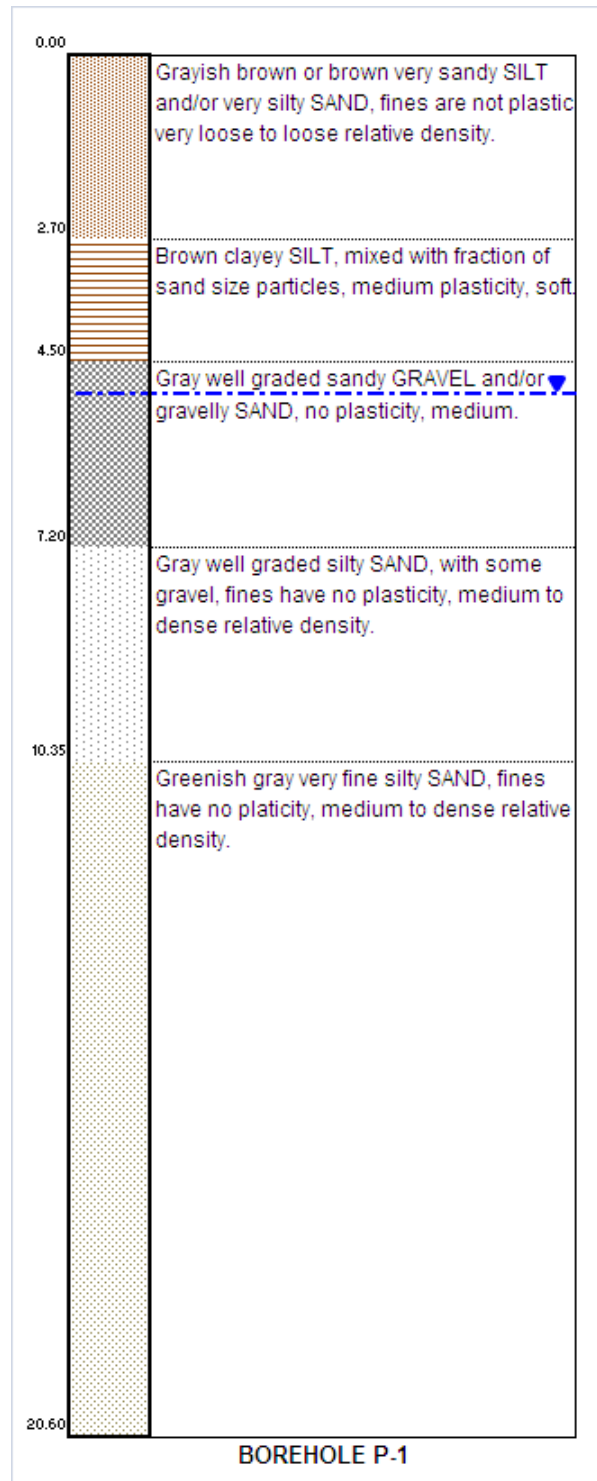


Figure 17: Soil profile detected at the Río Estrella Bridge site

The water table at this site appears at a depth of 4.90 m below the ground level. In order to complement the soil profile of Figure 17, a summary of the N_{SPT} values obtained in the boreholes is presented in Table 12.

Table 12: Summary of the N_{SPT} values detected at the Río Estrella Bridge Site

Depth [m]	P-1
0.00 - 0.45	10
0.45 - 0.90	7
0.90 - 1.35	6
1.35 - 1.80	2
1.80 - 2.25	2
2.25 - 2.70	1
2.70 - 3.15	1
3.15 - 3.60	1
3.60 - 4.05	2
4.05 - 4.50	2
4.50 - 4.95	2
4.95 - 5.40	14
5.40 - 5.85	10
5.85 - 6.30	16
6.30 - 6.75	12
6.75 - 7.20	7
7.20 - 7.65	10
7.65 - 8.10	10
8.10 - 8.55	12
8.55 - 9.00	10
9.00 - 9.45	28
9.45 - 9.90	34
9.90 - 10.35	22
10.35 - 10.80	24
10.80 - 11.25	19
11.25 - 11.70	19
11.70 - 12.15	24
12.15 - 12.60	17
12.60 - 13.05	26
13.05 - 13.50	27
13.50 - 13.95	35
13.95 - 14.40	24
14.40 - 14.85	38
14.85 - 15.30	35
15.30 - 15.75	28
15.75 - 16.20	36
16.20 - 16.65	36
16.65 - 17.10	17
17.10 - 17.55	25
17.55 - 18.00	21
18.00 - 18.45	22
18.45 - 18.90	33
18.90 - 19.35	32
19.35 - 19.80	36
19.80 - 20.25	38

Based on the results presented in Table 12, it can be observed that soils of soft/loose consistency appear at depths between 0 and 9 m. Towards the end of the borehole, the consistency of the soils improves considerably.

10. CONCLUSIONS

The following conclusions can be obtained from the execution of the geotechnical investigation:

- The five bridge sites that were investigated lie within a same geological formation known as Alluvial and coastal deposits, which is characterized by consisting of sediments of clayey, silty and sandy textures. Given the same geological conditions for each site, it can be expected that the sites will be composed of similar soil profiles with a similar geotechnical behavior.
- As indicated in section 4, the bridge sites that were studied, as well as the rest of the Costa Rican territory, is subject to the risk of earthquake. Near the investigated bridge sites there are several active faults and geological structures that can have the potential of producing earthquakes. Proof of the seismicity that can affect the area is the Limón-Telire Earthquake that occurred in April of 1991.
- In all of the five sites, the soil profiles are typical of the geological formation of alluvial and coastal deposits. In general, these soil profiles consist of sequence of clays, silts, sands and mixtures of each of these types of soils. The materials are not consolidated, not cemented and they have a loose/soft consistency near the surface.
- Based on the boreholes and the laboratory tests carried at the different sites, it was possible to determine the physical and mechanical properties of the soils. This information will be helpful for the modeling and interpretation that will be done for the future stages of the research investigation.
- For each investigated site, it was possible to establish that the requirements for liquefaction to occur under a seismic are present (i.e. loose saturated soils, granular not plastic materials, etc). It is important to indicate that a thorough liquefaction analysis was not carried out; however, the precedent of the liquefaction problems that occurred during the Limón-Telire Earthquake is well established.

APPENDIX A

RIO CUBA BRIDGE
BORING LOG



PROJECT: Rio Cuba Bridge	File:
LOCATION: Maravilla, Limón, Costa Rica	CODE:
BOREHOLE: P-1	DATE: 29/04/2010
ELEVATION: m.s.n.m.	DEPTH: 14.85 m
EQUIPMENT: SPT and Casing	DIAMETER: AWJ
DRILLER: V. Murillo	WATER TABLE: 2.1 m

BORING LOG

#	DEPTH (m)		N _{SPT}	% Recovery	N _{SPT}	Symbol	Description	Soil properties						
	From	To						LL	PI	WN (%)	00<#200	USCS		
1	0.00	0.45	15	22			Organic soil (Sandy silt with roots, wood)							
2	0.45	0.90	9	33			Brown sandy SILT with soft consistency.							
3	0.90	1.35	4											
4	1.35	1.80	2											
5	1.80	2.25	5	22			Brown well graded clean SAND, loose.							
6	2.25	2.70	7	89			%Passing: 3/8 = 96; #4=91; #10=82; #40=17;	NP	NP	21.2	4	SW		
7	2.70	3.15	12	67			Gray silty SAND, not plastic, with very loose relative density.							
8	3.15	3.60	4	56										
9	3.60	4.05	2	22										
10	4.05	4.50	2	22			%Passing: 3/8 = 77; #4=73; #10=64; #40=24;	NP	NP	14.8	15	SM		
11	4.50	4.95	2	56			Gray clayey SILT, mixed with a fraction of sand size particles, soft consistency.							
12	4.95	5.40	2	33										
13	5.40	5.85	3	33			%Passing: #40=100;	47	16	62.4	71	ML		
14	5.85	6.30	2	78			Gray plastic CLAY, soft consistency.							
15	6.30	6.75	4	78			%Passing: #40=100;	78	51	66.0	94	CH		
16	6.75	7.20	2	78										
17	7.20	7.65	6	67			Gray SILT, low plasticity, soft consistency.							
18	7.65	8.10	5	89			%Passing: #40=100;	41	15	36.9	96	ML		
19	8.10	8.55	11	89										
20	8.55	9.00	17	33			Gray SILT, not plastic, medium consistency.							
21	9.00	9.45	11	67			%Passing: #40=100;	NP	NP	34.1	90	ML		
22	9.45	9.90	15	78										
23	9.90	10.35	22	89										
24	10.35	10.80	24	67			%Passing: 3/8 = 92; #4=91; #10=88; #40=47;	NP	NP	20.9	14	SM		
25	10.80	11.25	24	67			Gray silty SAND, not plastic with medium to dense relative density.							
26	11.25	11.70	33	78										
27	11.70	12.15	23	78			%Pas: 3/4=72; 3/8=59; #4=45; #10=35; #40=11;	NP	NP	8.7	5	GP		
28	12.15	12.60	15	33			Mixture of SAND and GRAVEL particles, not plastic, with loose to medium density.							
29	12.60	13.05	10	33										
30	13.05	13.50	6	33			%Passing: 3/8 = 78; #4=51; #10=27; #40=2;	NP	NP	8.0	1	SW		
31	13.50	13.95	6	33			%Passing: #10=100; #40=89;	63	35	62.2	87	CH		
32	13.95	14.40	6				Gray plastic CLAY, mixed with small fraction of sand size particles.							
33	14.40	14.85	10				^^^ End of borehole: 14.85 m ^^^							
34														
35														
36														

Observations:

Described by: J.P. Rodríguez	Revised by: J. Rodríguez	Approved by: J. Rodríguez
Date: 15/07/2010	Date: 15/07/2010	Date: 15/07/2010
Signature:	Signature:	Signature:

APPENDIX B

**RIO BLANCO BRIDGE
BORING LOG**



PROJECT:	Río Blanco Bridge	File:	
LOCATION:	Liverpool, Limón, Costa Rica	CODE:	
BOREHOLE:	P-1	DATE:	28/04/2010
ELEVATION:	m.s.n.m.	DEPTH:	14.85 m
EQUIPMENT:	SPT and Casing	DIAMETER:	AWJ
DRILLER:	V. Murillo	WATER TABLE:	4.8 m

BORING LOG

#	DEPTH (m)		N _{SPT}	% Recovery	N _{SPT}	Symbol	Description	Soil properties											
	From	To						LL	PI	WN (%)	0<sup>->#200	SUCS							
1	0.00	0.45	1	56															
2	0.45	0.90	6	33			% Passing: #4=89; #10=83; #40=65;	27	3	24.6	53	ML							
3	0.90	1.35	11	22			Very sandy brown SILT, mixed with some												
4	1.35	1.80	11	33			gravel particles, soft to medium consistency.												
5	1.80	2.25	10	44			% Pas: 3/4=79;3/8=68; #4=54; #10=43; #40=18;	NP	NP	8.7	7	SW-S							
6	2.25	2.70	28	44			Well graded silty SAND mixed with some												
7	2.70	3.15	11	44			gravel, medium relative density.												
8	3.15	3.60	11	22			% Passing: #4=89; #10=81; #40=61;	50	27	25.7	48	SC							
9	3.60	4.05	6	44															
10	4.05	4.50	4	89			Gray sandy CLAY or very clayey SAND,												
11	4.50	4.95	4				mixed with pieces of wood, with soft												
12	4.95	5.40	3				consistency.												
13	5.40	5.85	2																
14	5.85	6.30	3	78															
15	6.30	6.75	5	78			% Passing: #40=100;	53	30	64.8	93	CH							
16	6.75	7.20	3	78															
17	7.20	7.65	7	56			Well graded gray SAND, loose.												
18	7.65	8.10	10	56			% Passing: #4=82; #10=70; #40=31;	NP	NP	25.3	4	SW							
19	8.10	8.55	10	67			Greenish gray silty fine SAND, fines have												
20	8.55	9.00	9	78			no plasticity, loose to medium.												
21	9.00	9.45	10	78			% Passing: #40=100;	NP	NP	36.3	36	SM							
22	9.45	9.90	12	78															
23	9.90	10.35	10	67			Gray silty SAND mixed with pieces of												
24	10.35	10.80	17	44			wood, probably transported by the river.												
25	10.80	11.25	21	56			% Passing: #4=94; #10=89; #40=65;	NP	NP	23.4	21	SM							
26	11.25	11.70	10	33															
27	11.70	12.15	24	44			Greenish gray very fine silty SAND with												
28	12.15	12.60	27	56			medium to dense relative density.												
29	12.60	13.05	24	67			% Passing: #40=100;	NP	NP	25.9	45	SM							
30	13.05	13.50	26	56															
31	13.50	13.95	25	56															
32	13.95	14.40	35	67			% Passing: #40=100;	NP	NP	24.5	59	ML							
33	14.40	14.85	37	56															
34							^^^ End of borehole: 14.85 m ^^^												
35																			
36																			

Observations:

Described by:	J.P. Rodríguez	Revised by:	J. Rodríguez	Approved by:	J. Rodríguez
Date:	15/07/2010	Date:	15/07/2010	Date:	15/07/2010
Signature:		Signature:		Signature:	

APPENDIX C

**RIO BANANITO HIGHWAY BRIDGE
BORING LOGS**



PROJECT:	Bananito River Bridge (Highway)	File:	
LOCATION:	Province of Limón	CODE:	
BOREHOLE:	P-1	DATE:	22/04/2010
ELEVATION:	m.s.n.m.	DEPTH:	20.25 m
EQUIPMENT:	SPT and Casing	DIAMETER:	AWJ
DRILLER:	V. Murillo	WATER TABLE:	2 m

BORING LOG

#	DEPTH (m)		N _{SPT}	% Recovery	N _{SPT}	Symbol	Description	Soil properties						
	From	To						LL	PI	WN (%)	00<#200	SUCS		
1	0.00	0.45	4	89			Brown SAND mixed with organic matter (roots).							
2	0.45	0.90	2	44			Poorly graded gray silty SAND, not plastic							
3	0.90	1.35	3	67			fines, loose relative density.							
4	1.35	1.80	10	67										
5	1.80	2.25	5	56			% Passing: #40=97;	NP	NP	23.1	12	SP-SI		
6	2.25	2.70	2	67										
7	2.70	3.15	1	33										
8	3.15	3.60	1	22			% Passing: #10=100; #40=97;	NP	NP	49.9	84	ML		
9	3.60	4.05	2	1			Fine gray SILT, not plastic, mixed with a fraction of sand size particles, very loose.							
10	4.05	4.50	3	44			Presence of wood detected.							
11	4.50	4.95	1	78										
12	4.95	5.40	3	67										
13	5.40	5.85	4	78			% Passing: #4=100; #10=97; #40=84;	NP	NP	41.1	48	SM		
14	5.85	6.30	4	33			Gray, very silty SAND and/or sandy SILT, fines are not plastic, very loose to loose relative density.							
15	6.30	6.75	12	44										
16	6.75	7.20	*											
17	7.20	7.65	*											
18	7.65	8.10	23	56			% Passing: #40=96;	NP	NP	24.6	78	ML		
19	8.10	8.55	18	78			Fine gray SILT, not plastic, mixed with a fraction of sand size particles, medium.							
20	8.55	9.00	14	44										
21	9.00	9.45	12	56			Very fine gray silty SAND, fines are not plastic, medium relative density.							
22	9.45	9.90	24	56										
23	9.90	10.35	15	44			% Passing: #40=100;	NP	NP	28.4	17	SM		
24	10.35	10.80	28	56										
25	10.80	11.25	9	56			Greenish gray very sandy SILT and/or very silty SAND, fines are not plastic, medium relative density.							
26	11.25	11.70	20	89										
27	11.70	12.15	22	67										
28	12.15	12.60	25	56			% Passing: #40=100;	NP	NP	27.9	55	ML		
29	12.60	13.05	12	56										
30	13.05	13.50	21	56			Very fine gray silty SAND, with green spots, fines are not plastic, relative density medium.							
31	13.50	13.95	13	56										
32	13.95	14.40	11	33										
33	14.40	14.85	22	33										
34	14.85	15.30	10	44			% Passing: #40=100;	NP	NP	31.7	35	SM		
35	15.30	15.75	24	22										
36	15.75	16.20	20	22										

Observations: (*) Washed away during installation of the casing.

Described by:	J.P. Rodríguez	Revised by:	J. Rodríguez	Approved by:	J. Rodríguez
Date:	15/07/2010	Date:	15/07/2010	Date:	15/07/2010
Signature:		Signature:		Signature:	



PROJECT:	Bananito River Bridge (Highway)	File:	
LOCATION:	Province of Limón	CODE:	
BOREHOLE:	P-1 (Continued)	DATE:	22/04/2010
ELEVATION:	m.s.n.m.	DEPTH:	20.25 m
EQUIPMENT:	SPT and Casing	DIAMETER:	AWJ
DRILLER:	V. Murillo	WATER TABLE:	2 m

BORING LOG

#	DEPTH (m)		N _{SPT}	% Recovery	N _{SPT}	Symbol	Description	Soil properties										
	From	To						LL	PI	WN (%)	00<#200 %>	SUCS						
37	16.20	16.65	14	33														
38	16.65	17.10	21	44														
39	17.10	17.55	18	22														
40	17.55	18.00	19	22														
41	18.00	18.45	13	22														
42	18.45	18.90	13	22														
43	18.90	19.35	14	22														
44	19.35	19.80	15	22														
45	19.80	20.25	15	33														
46																		
47																		
48																		
49																		
50																		
51																		
52																		
53																		
54																		
55																		
56																		
57																		
58																		
59																		
60																		
61																		
62																		
63																		
64																		
65																		
66																		
67																		
68																		
69																		
70																		
71																		
72																		

Observations:

Described by:	J.P. Rodríguez	Revised by:	J. Rodríguez	Approved by:	J. Rodríguez
Date:	15/07/2010	Date:	15/07/2010	Date:	15/07/2010
Signature:		Signature:		Signature:	



PROJECT:	Bananito River Bridge (Highway)	File:	
LOCATION:	Province of Limón	CODE:	
BOREHOLE:	P-2	DATE:	24/04/2010
ELEVATION:	m.s.n.m.	DEPTH:	20.25 m
EQUIPMENT:	SPT and Casing	DIAMETER:	AWJ
DRILLER:	V. Murillo	WATER TABLE:	2.65 m

BORING LOG

#	DEPTH (m)		N _{SPT}	% Recovery	N _{SPT}	Symbol	Description	Soil properties					
	From	To						LL	PI	WN (%)	00#>#200 %	SUCS	
1	0.00	0.45	36	67		Brown poorly graded GRAVEL, mixed with some sand and silt, dense.							
2	0.45	0.90	39	56									
3	0.90	1.35	43	78		Brown poorly graded GRAVEL, mixed with some sand and silt, dense.							
4	1.35	1.80	35	67			% Pas: 3/4=68; 3/8=62; #4=48; #10=34; #40=20;	NP	NP	9.2	12	GP-G	
5	1.80	2.25	21	67		Very fine gray SAND, poorly graded, mixed with a fraction of silt size particles, fines are not plastic, loose relative density.							
6	2.25	2.70	28	56									
7	2.70	3.15	17	67		Very fine gray SAND, poorly graded, mixed with a fraction of silt size particles, fines are not plastic, loose relative density.							
8	3.15	3.60	8	67									
9	3.60	4.05	8	56		Very fine gray SAND, poorly graded, mixed with a fraction of silt size particles, fines are not plastic, loose relative density.							
10	4.05	4.50	7	56			% Passing: #40=100;	NP	NP	21.3	9	SP-SI	
11	4.50	4.95	6	67		Fine gray SILT, not plastic, mixed with fraction of sand size particles, loose to medium							
12	4.95	5.40	6	67									
13	5.40	5.85	12	67		Fine gray SILT, not plastic, mixed with fraction of sand size particles, loose to medium							
14	5.85	6.30	28	33			% Passing: #40=100;	NP	NP	39.1	57	ML	
15	6.30	6.75	16	44		Very fine gray silty SAND, fines are not plastic, medium relative density, some seashells are observed.							
16	6.75	7.20	24	33									
17	7.20	7.65	23	33		Very fine gray silty SAND, fines are not plastic, medium relative density, some seashells are observed.							
18	7.65	8.10	19	44			% Passing: #40=100;	NP	NP	25.2	19	SM	
19	8.10	8.55	25	44		Very fine gray silty SAND, fines are not plastic, medium relative density, some seashells are observed.							
20	8.55	9.00	22	56									
21	9.00	9.45	13	67		Very fine gray silty SAND, fines are not plastic, medium relative density, some seashells are observed.							
22	9.45	9.90	21	44			% Passing: #40=100;	NP	NP	29.0	23	SM	
23	9.90	10.35	23	44		Very fine greenish gray silty SAND, fines are not plastic, some seashells observed, relative density medium.							
24	10.35	10.80	31	78									
25	10.80	11.25	23	22		Very fine greenish gray silty SAND, fines are not plastic, some seashells observed, relative density medium.							
26	11.25	11.70	23	67									
27	11.70	12.15	18	56		Very fine greenish gray silty SAND, fines are not plastic, some seashells observed, relative density medium.							
28	12.15	12.60	11	67			% Passing: #40=100;	NP	NP	38.7	32	SM	
29	12.60	13.05	19	56		Very fine greenish gray silty SAND, fines are not plastic, some seashells observed, relative density medium.							
30	13.05	13.50	23	56									
31	13.50	13.95	30	56		Very fine greenish gray silty SAND, fines are not plastic, some seashells observed, relative density medium.							
32	13.95	14.40	22	67									
33	14.40	14.85	24	67		Greenish gray very sandy SILT, fines are not plastic, medium relative density.							
34	14.85	15.30	32	56			% Passing: #40=100;	NP	NP	38.6	56	ML	
35	15.30	15.75	18	44		Greenish gray very sandy SILT, fines are not plastic, medium relative density.							
36	15.75	16.20	23	44									

Observations:

Described by:	J.P. Rodríguez	Revised by:	J. Rodríguez	Approved by:	J. Rodríguez
Date:	15/07/2010	Date:	15/07/2010	Date:	15/07/2010
Signature:		Signature:		Signature:	



PROJECT:	Bananito River Bridge (Highway)	File:	
LOCATION:	Province of Limón	CODE:	
BOREHOLE:	P-2 (Continued)	DATE:	24/04/2010
ELEVATION:	m.s.n.m.	DEPTH:	20.25 m
EQUIPMENT:	SPT and Casing	DIAMETER:	AWJ
DRILLER:	V. Murillo	WATER TABLE:	2.65 m

BORING LOG

#	DEPTH (m)		N _{SPT}	% Recovery	N _{SPT}	Symbol	Description	Soil properties										
	From	To						LL	PI	WN (%)	0.075#200	SUCS						
37	16.20	16.65	23	44														
38	16.65	17.10	17	33														
39	17.10	17.55	26	33														
40	17.55	18.00	14	44														
41	18.00	18.45	16	44														
42	18.45	18.90	16	44														
43	18.90	19.35	18	33														
44	19.35	19.80	22	56														
45	19.80	20.25	20	56														
46																		
47																		
48																		
49																		
50																		
51																		
52																		
53																		
54																		
55																		
56																		
57																		
58																		
59																		
60																		
61																		
62																		
63																		
64																		
65																		
66																		
67																		
68																		
69																		
70																		
71																		
72																		

Observations:

Described by:	J.P. Rodríguez	Revised by:	J. Rodríguez	Approved by:	J. Rodríguez
Date:	15/07/2010	Date:	15/07/2010	Date:	15/07/2010
Signature:		Signature:		Signature:	

APPENDIX D

**RIO BANANITO RAILROAD BRIDGE
BORING LOGS**



PROJECT:	Bananito River Bridge (Railroad)	File:	
LOCATION:	Province of Limón	CODE:	
BOREHOLE:	P-1	DATE:	19/04/2010
ELEVATION:	m.s.n.m.	DEPTH:	13.95 m
EQUIPMENT:	SPT and Casing	DIAMETER:	AWJ
DRILLER:	V. Murillo	WATER TABLE:	5.65 m

BORING LOG

#	DEPTH (m)		N _{SPT}	% Recovery	N _{SPT}	Symbol	Description	Soil properties						
	From	To						LL	PI	WN (%)	00<#200	SUCS		
1	0.00	0.45	26	44			Fill that consists in a mixture of GRAVEL and silt.							
2	0.45	0.90	11	22			Brown clayey SAND, mixed with some gravel, loose. %Pas: 3/4=81; 3/8=77; #4=69; #10=62; #40=52;							
3	0.90	1.35	6	56										
4	1.35	1.80	4	22			%Pas: 3/4=81; 3/8=77; #4=69; #10=62; #40=52;							
5	1.80	2.25	4	22				43	18	21.3	40	SC		
6	2.25	2.70	4	22			%Passing: #4=99; #10=98; #40=96;							
7	2.70	3.15	4	56				62	33	55.2	93	CH		
8	3.15	3.60	1	100			Brown plastic CLAY, medium to high plasticity, very soft to soft consistency. %Passing: #40=100;							
9	3.60	4.05	0	22				64	36	62.2	97	CH		
10	4.05	4.50	0	100			Greenish gray plastic CLAY, mixed with a fraction of sand size particles, soft. %Passing: #40=100;							
11	4.50	4.95	1	78				76	39	36.6	69	CH		
12	4.95	5.40	2	44			Gray or brownish gray clayey SAND, mixed with particles of gravel, fines with medium plasticity, loose to dense relative density. %Pas: 3/4=90; 3/8=84; #4=78; #10=69; #40=40;							
13	5.40	5.85	3	44				36	8	23.4	23	SC		
14	5.85	6.30	7	56			%Pas: 3/4=89; 3/8=73; #4=62; #10=50; #40=27;							
15	6.30	6.75	7	44				42	20	18.0	17	SC		
16	6.75	7.20	7	44			Greenish gray clayey SAND, fines with low to medium plasticity, predominantly medium relative density. %Pas: 3/4=79; 3/8=69; #4=56; #10=44; #40=31;							
17	7.20	7.65	15	56				41	19	19.8	22	SC		
18	7.65	8.10	20	56			^^^ End of borehole: 13.95 m ^^^							
19	8.10	8.55	8	56										
20	8.55	9.00	24	56										
21	9.00	9.45	36	33										
22	9.45	9.90	20	22										
23	9.90	10.35	16	67										
24	10.35	10.80	19	56										
25	10.80	11.25	21	67										
26	11.25	11.70	25	67										
27	11.70	12.15	23	33										
28	12.15	12.60	6	22										
29	12.60	13.05	17	89										
30	13.05	13.50	24	56										
31	13.50	13.95	18	56										
32														
33														
34														
35														
36														

Observations:

Described by:	J.P. Rodríguez	Revised by:	J. Rodríguez	Approved by:	J. Rodríguez
Date:	15/07/2010	Date:	15/07/2010	Date:	15/07/2010
Signature:		Signature:		Signature:	



PROJECT:	Bananito River Bridge (Railroad)	File:	
LOCATION:	Province of Limón	CODE:	
BOREHOLE:	P-2	DATE:	20/04/2010
ELEVATION:	m.s.n.m.	DEPTH:	13.95 m
EQUIPMENT:	SPT and Casing	DIAMETER:	AWJ
DRILLER:	V. Murillo	WATER TABLE:	6.65 m

BORING LOG

#	DEPTH (m)		N _{SPT}	% Recovery	N _{SPT}	Symbol	Description	Soil properties					
	From	To						LL	PI	WN (%)	00<#200	SUCS	
1	0.00	0.45	6	89		Brown plastic CLAY, medium to high plasticity, very soft to soft consistency. %Passing: #40=100;							
2	0.45	0.90	2	67									
3	0.90	1.35	3	67				54	25	50.3	97	CH	
4	1.35	1.80	3	44									
5	1.80	2.25	3	44									
6	2.25	2.70	3	33									
7	2.70	3.15	3	44				55	28	48.2	98	CH	
8	3.15	3.60	4	44									
9	3.60	4.05	5	22									
10	4.05	4.50	10	56		Brown clayey SAND, some gravel, loose. %Passing: #4=86; #10=81; #40=61;							
11	4.50	4.95	7	44				39	14	28.7	47	SC	
12	4.95	5.40	9	22		Brown silty SAND, fines with low plasticity, loose relative density. %Passing: 3/8=97; #4=92; #10=89; #40=48;							
13	5.40	5.85	8	67									
14	5.85	6.30	13	56				32	5	26.8	21	SM	
15	6.30	6.75	19	44		Gray or brownish gray clayey SAND, mixed with particles of gravel, fines with medium plasticity, loose to dense relative density. %Passing: 3/8=83; #4=64; #10=49; #40=31;							
16	6.75	7.20	7	44									
17	7.20	7.65	8	44									
18	7.65	8.10	11										
19	8.10	8.55	4	22									
20	8.55	9.00	23	67		Gray or greenish gray silty SAND, fines have no or very little plasticity, medium relative density. %Passing: 3/8=83; #4=70; #10=52; #40=39;							
21	9.00	9.45	36	56				34	11	16.0	23	SC	
22	9.45	9.90	16	33									
23	9.90	10.35	21	78		Gray or greenish gray silty SAND, fines have no or very little plasticity, medium relative density. %Passing: 3/8=90; #4=61; #10=45; #40=23;							
24	10.35	10.80	9	33									
25	10.80	11.25	28	44				31	8	13.2	17	SM	
26	11.25	11.70	15	33									
27	11.70	12.15	20	33		^^^ End of borehole: 13.95 m ^^^^							
28	12.15	12.60	16	33									
29	12.60	13.05	27	33									
30	13.05	13.50	26	33				NP	NP	13.9	14	SM	
31	13.50	13.95	22	44									
32													
33													
34													
35													
36													

Observations:

Described by:	J.P. Rodríguez	Revised by:	J.P. Rodríguez	Approved by:	J.P. Rodríguez
Date:	15/07/2010	Date:	15/07/2010	Date:	15/07/2010
Signature:		Signature:		Signature:	

APPENDIX E

RIO ESTRELLA BRIDGE
BORING LOG



PROJECT:	Estrella River Bridge	File:	
LOCATION:	Cahuita, province of Limón	CODE:	
BOREHOLE:	P-1	DATE:	26/04/2010
ELEVATION:	m.s.n.m.	DEPTH:	20.25 m
EQUIPMENT:	SPT and Casing	DIAMETER:	AWJ
DRILLER:	V. Murillo	WATER TABLE:	4.9 m

BORING LOG

#	DEPTH (m)		N _{SPT}	% Recovery	N _{SPT}	Symbol	Description	Soil properties						
	From	To						LL	PI	WN (%)	00<#200	SUCS		
1	0.00	0.45	10	44			Grayish brown or brown very sandy SILT and/or very silty SAND, fines are not plastic very loose to loose relative density.							
2	0.45	0.90	7	67										
3	0.90	1.35	6	56										
4	1.35	1.80	2	89										
5	1.80	2.25	2	89										
6	2.25	2.70	1	67										
7	2.70	3.15	1	67										
8	3.15	3.60	1	67										
9	3.60	4.05	2	78										
10	4.05	4.50	2	78										
11	4.50	4.95	2	78										
12	4.95	5.40	14	56										
13	5.40	5.85	10	56										
14	5.85	6.30	16	56										
15	6.30	6.75	12											
16	6.75	7.20	7	33										
17	7.20	7.65	10	33										
18	7.65	8.10	10	44										
19	8.10	8.55	12	22										
20	8.55	9.00	10	44										
21	9.00	9.45	28	44										
22	9.45	9.90	34	44										
23	9.90	10.35	22	67										
24	10.35	10.80	24	56										
25	10.80	11.25	19	67										
26	11.25	11.70	19	56										
27	11.70	12.15	24	56										
28	12.15	12.60	17	33										
29	12.60	13.05	26	89										
30	13.05	13.50	27	33										
31	13.50	13.95	35	56										
32	13.95	14.40	24	33										
33	14.40	14.85	38	67										
34	14.85	15.30	35	44										
35	15.30	15.75	28	33										
36	15.75	16.20	36	44										

Observations:

Described by:	J.P. Rodríguez	Revised by:	J.P. Rodríguez	Approved by:	J.P. Rodríguez
Date:	15/07/2010	Date:	15/07/2010	Date:	15/07/2010
Signature:		Signature:		Signature:	



BORING LOG	PROJECT:	Estrella River Bridge	File:	
	LOCATION:	Cahuíta, province of Limón	CODE:	
	BOREHOLE:	P-1 (Continued)	DATE:	26/04/2010
	ELEVATION:	m.s.n.m.	DEPTH:	20.25 m
	EQUIPMENT:	SPT and Casing	DIAMETER:	AWJ
	DRILLER:	V. Murillo	WATER TABLE:	No hay

#	DEPTH (m)		N _{SPT}	% Recovery	N _{SPT}	Symbol	Description	Soil properties				
	From	To						LL	PI	WN (%)	0.075-#200	SUCS
37	16.20	16.65	36	56	36		% Passing: #40=100;	NP	NP	22.6	31	SM
38	16.65	17.10	17	33	17							
39	17.10	17.55	25	56	25		Greenish gray very fine silty SAND, fines					
40	17.55	18.00	21	22	21		have no plasticity, medium to dense relative					
41	18.00	18.45	22	22	22		density.					
42	18.45	18.90	33	44	33		% Passing: #40=100;	NP	NP	27.8	43	SM
43	18.90	19.35	32	56	32							
44	19.35	19.80	36	44	36							
45	19.80	20.25	38	56	38							
46							^^^ End of borehole: 20.25 m ^^^					
47												
48												
49												
50												
51												
52												
53												
54												
55												
56												
57												
58												
59												
60												
61												
62												
63												
64												
65												
66												
67												
68												
69												
70												
71												
72												

Observations:

Described by:	J.P. Rodríguez	Revised by:	J.P. Rodríguez	Approved by:	J.P. Rodríguez
Date:	15/07/2010	Date:	15/07/2010	Date:	15/07/2010
Signature:		Signature:		Signature:	



BRIGHAM YOUNG UNIVERSITY

COMPLEMENTARY GEOTECHNICAL STUDY

**RÍO LA ESTRELLA BRIDGE
PROVINCE OF LIMÓN, COSTA RICA**

**INSUMA S.A.
Geotechnical Consultants**

June, 2011



San José, June 21st, 2011
2330-11

Prof. Kyle Rollins
Department of Civil and Environmental Engineering
Brigham Young University
Provo, Utah

Dear Prof. Rollins:

We present the results of the Complementary Geotechnical Study carried out in the Río Estrella Highway Bridge, located in the province of Limón, Costa Rica. This site had already been investigated by INSUMA in April of 2010 and the results were presented in report #2056-11. This second investigation complements the results that had been obtained.

The objective of the investigation was to determine the geotechnical conditions of the bridge site at locations farther away from the right margin of the Estrella River. This objective was achieved through the execution of field and laboratory tests. This report includes, among other things, the field and laboratory information that was used to determine the soil profile and the physical and mechanical characteristics of the materials.

The field and laboratory works were under the coordination of Ing. José P. Rodríguez. Furthermore, the field tests were also supervised by David Anderson from BYU.

We hope that this report is to your satisfaction and we are available for any further consultation you may have.

Sincerely,
INSUMA S.A.
Geotechnical Consultants


Ing. José A. Rodríguez Barquero

C: File


Ing. José P. Rodríguez Calderón, MSc.

TABLE OF CONTENTS

TABLE OF CONTENTS	i
1. INTRODUCTION.....	1
2. OBJECTIVES AND SCOPE OF THE STUDY	1
3. EXECUTED WORKS	2
3.1 Field Works	2
3.2 Laboratory Works	4
3.3 Analysis and interpretation	4
4. GEOLOGY OF THE AREA	5
5. RIO ESTRELLA BRIDGE.....	7
5.1 Location and executed works	7
5.2 Geotechnical profile.....	8
6. CONCLUSIONS.....	10

1. INTRODUCTION

Attending the request of Prof. Kyle Rollins from Brigham Young University, INSUMA executed a complementary geotechnical study in the Río Estrella Highway Bridge, located in the province of Limón, Costa Rica. This site had already been investigated by INSUMA in April of 2010 as part of a study that included other bridge sites that suffered liquefaction problems during the 1991 Limón – Telire Earthquake. The results of the first investigation were presented in report #2056-10 and the results of this complementary investigation are presented herein.

The complementary geotechnical study was requested as part of a research investigation being carried out by Prof. Rollins, which is related to the topic of soil liquefaction. The objective of the investigation was to determine the geotechnical characteristics at the Río Estrella Bridge site. These characteristics include, among other things, the soil profile and the physical and mechanical properties of the soil layers present at the subsurface levels.

The objective was achieved through the execution of borings and laboratory tests that were analyzed in order to establish the geotechnical profiles and the soil properties. The results of the study are presented in this report, which has been divided into several sections.

Section 1 of the report corresponds to the introduction and it mainly describes the content of the report. The objectives and the scope of the investigation are described in Section 2, while the executed works and the methods followed to carry out the works are explained in Section 3.

In order to make a better interpretation of the geotechnical conditions of the site, it is necessary to have a good understanding of the regional geological conditions. This information had already been presented in report 2056-10 and is summarized briefly in Section 4.

Once the geological framework has been established, the results obtained for the bridge site are presented. Section 5 corresponds to the specific results and geotechnical conditions detected for the Río Estrella Highway Bridge. The following information is included in this section: 1) brief description of the bridge site and summary of the works executed at the site, 2) description and properties of the soil layers that appear, and 3) soil profile interpreted from the field and laboratory information.

The specific results for the studied bridge site are followed by Section 6 which corresponds to the conclusions of the investigation. The boring logs of each of the executed boreholes are included as an Appendix in this report.

2. OBJECTIVES AND SCOPE OF THE STUDY

The main objective of the investigation is to determine the geotechnical conditions of the Río Estrella Bridge site. In order to achieve this general objective, several specific objectives have been defined. Some of the specific objectives are: to determine the geological conditions of the region, to determine the physical and mechanical properties of the different soil layers that appear at the site, and to elaborate a geotechnical model based on the obtained information and based on INSUMA's interpretation.

In order to achieve the mentioned objectives, field and laboratory works were executed and the geotechnical information required to fulfill the objectives was acquired. A detail of the executed works is included in Section 3 of the report.

The executed investigation was carried out following methods that are currently accepted in geotechnical engineering and that comply both with national and international standards. The field and laboratory tests performed as part of the investigation were executed following procedures defined in the ASTM standards.

The scope of the study has been limited to determining the geotechnical conditions of the site; therefore, it does not include any type of analysis regarding foundation of structures, mathematical modeling and/or other types of analysis such as soil liquefaction. It should be understood that these types of analysis and models will probably be done in latter stages of the research project which is underway.

3. EXECUTED WORKS

The geotechnical investigation was divided into three different phases: 1) Field Works, 2) Laboratory Works, and 3) Analysis and interpretation. A more detailed description of each phase is presented below.

3.1 Field Works

The first activity of this phase of the investigation consisted in the execution of the boreholes. This activity was supervised by personnel associated to BYU, specifically Mr. David Anderson. The location of the boreholes was selected by Mr. Anderson who was assigned by Prof. Rollins to supervise the field works. These drillings were executed in the right margin of the river farther away from the borehole that had been executed in April 2010. Table 1 summarizes the boreholes executed in the bridge site, the depth reached in the borehole, and the method of drilling used.

Table 1: Summary of the executed boreholes – Bridges in Limón, Costa Rica

Bridge Site	Quantity of Boreholes	Depth of Borehole	Method of Drilling
Río Estrella Highway Bridge	2	12 m 11 m	SPT + Casing

As indicated in Table 1, the boreholes were executed following the procedure of the standard penetration test (SPT). The drillings were carried out in accordance to standard ASTM D-1586. Given that loose, non-plastic saturated sands were detected at each of the sites it was necessary to use casing to prevent the drillhole from collapsing. Continuous sampling was used in all of the boreholes; hence, it was possible to determine the soil profile down to the investigated depth.

The SPT drilling method is exclusive for soils; therefore, it is not possible to drill through very hard consistency materials (e.g. rocks, boulders or rock masses). This type of drilling procedure

has been used worldwide and it consists in driving a split spoon sampler with the use of a hammer. A simple sketch of the drilling procedure is indicated in Figure 1.

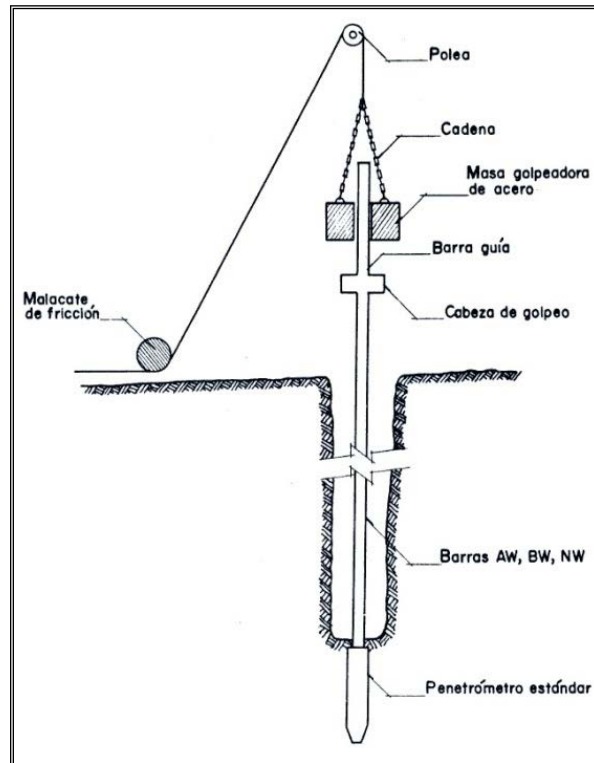


Figure 1: Sketch of the standard penetration test method (ASTM D-1586)

The dimensions of the split spoon sampler, the fall and weight of the hammer, the diameter of the bars and the rest of the materials used in the SPT method are standardized according to the specifications in ASTM D-1586. Figures 2 and 3 present some of the equipment used in the drilling procedure.

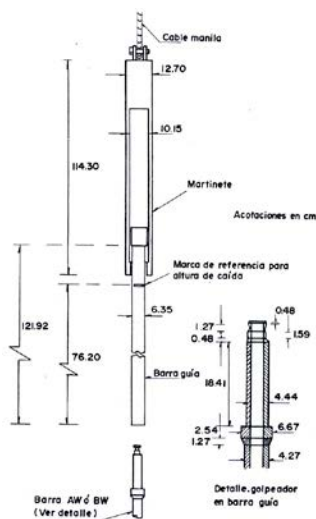


Figure 2: Detail of the 64 kg hammer and the specifications for the fall of the weight

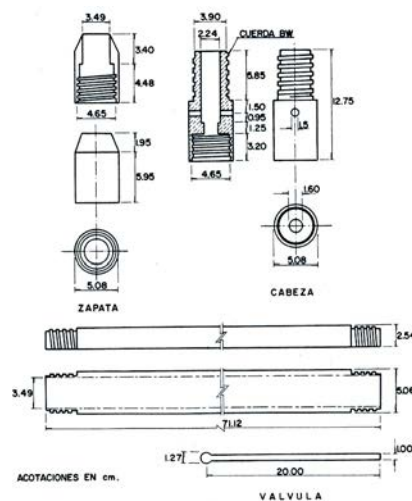


Figure 3: Detail of the standard split spoon sampler

The SPT method allows the correlation of the soil consistency with the N_{SPT} value. This value corresponds to the number of blows required to drive the standard sampler a distance of 0.3 m. In order to be able to define the N_{SPT} value and make it comparable to other investigations, it is necessary to carry out tests in order to determine the efficiency of the SPT drilling rig and its operator.

These measurements were carried out directly by BYU personnel during the investigation of April 2010. The same crew members and the same equipment were used for this complementary study. According to the information provided by BYU, the measured efficiency during the April 2010 investigation campaign was higher than 90%.

The samples collected from the execution of the boreholes were described visually by the foreman of the drilling crew and they were later placed in plastic bags in order to prevent the loss of the natural water content. The samples were later transported to INSUMA's laboratory for the corresponding storage and analysis.

3.2 Laboratory Works

The second phase of the geotechnical study corresponds to the execution of the laboratory works. As indicated, the soil samples collected from the boreholes were transported to INSUMA's laboratory where a visual description was carried out by the laboratory technician. This visual description was executed to all the samples collected from the boreholes.

The visual description was complemented with the execution of the following index property tests:

- Gradation
- Percent washed in 200 Sieve
- Natural water content
- Atterberg limits

These tests were not executed on every sample, but they were carried out with a frequency of every 1.5 – 1.75 m and whenever a different type of soil was detected. All of the tests were carried out following the procedures described in the different ASTM standards. The results obtained from the laboratory tests enabled the classification of the different soil layers with the Unified Soil Classification System.

3.3 Analysis and interpretation

Once all the field and laboratory information was available, it was integrated and analyzed in order to elaborate and present the geotechnical profile of each site. It is important to indicate, as it was described in the scope of the investigation, that this phase of the investigation does not include any type of liquefaction or foundation analysis and/or recommendations. This will probably be done in a later stage of the research project that is being executed.

4. GEOLOGY OF THE AREA

Based on the geological map of Limón (CR2CM-6), scale 1:200.000, the geology of the area consists of Alluvial and coastal deposits (Qal), which is represented by the yellow color. From the lithological point of view and specifically in the areas near the coast, these deposits are made up of fine sediments with sandy and clayey textures. An extract of Limón's geological map is presented in Figure 4 below. The location of the Río Estrella Highway Bridge is shown in the map. The other bridge sites investigated during April 2010 are also indicated.

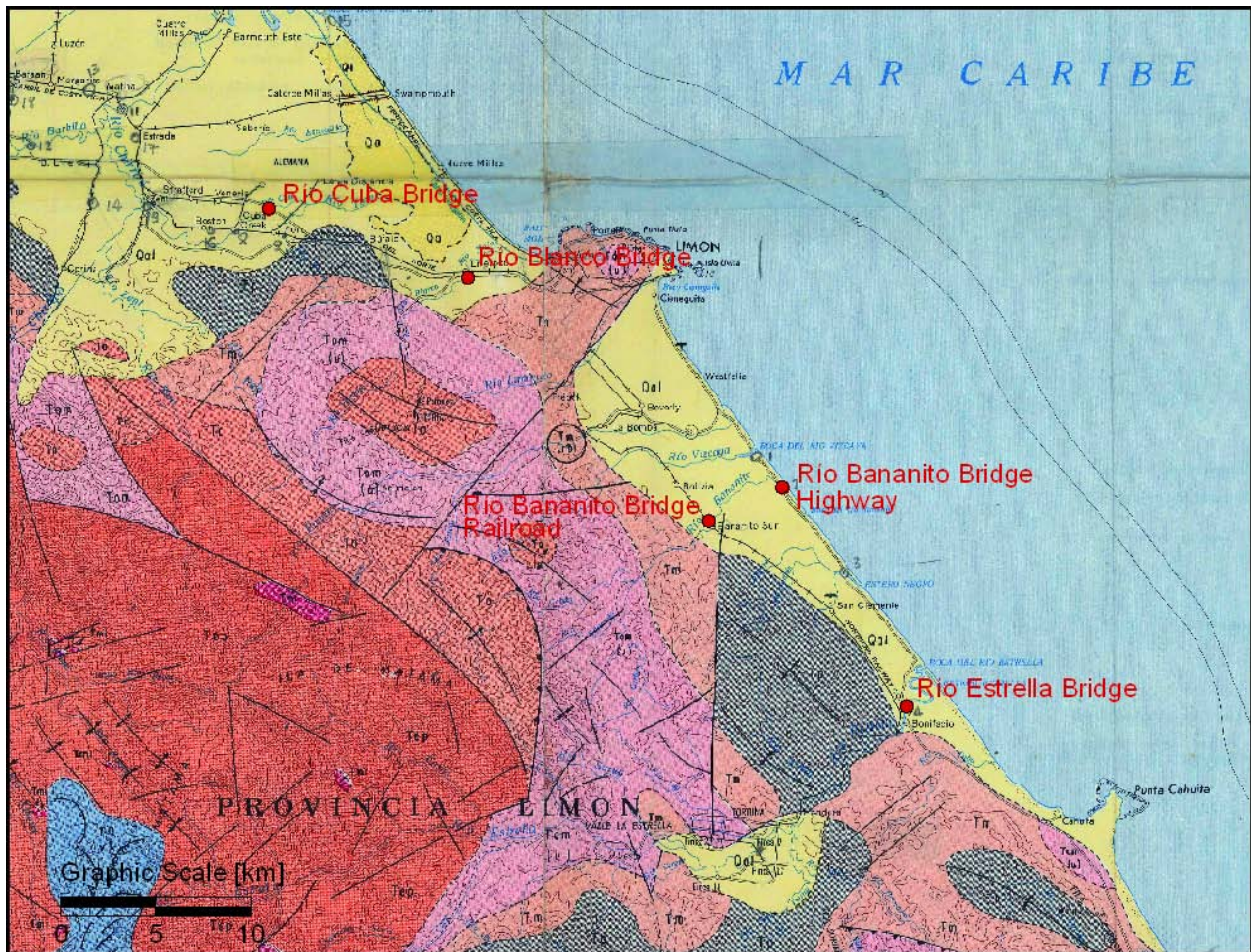


Figure 4: Geologic map of Limón (CR2CM-6) scale 1:200.000

Regarding the map shown in Figure 4, it can be observed that towards the west, the geological formations change and they correspond to volcanic and sedimentary rocks associated to the Cordillera of Talamanca. This other geological formations are represented by the other colors shown in the map of Figure 5.

Regarding the geomorphological conditions of the area, the bridge sites are located in forms of alluvial sedimentation. The origin of this type of geomorphological units is associated with the sedimentation caused by rivers and/or creeks. In some cases, specifically in those areas located near the coast, there is a marine influence related to this soil deposits.

From the seismic point of view, within the area of interest there are several active faults that can be the source of important earthquakes. The faults closer to the bridge sites are: Deformed Belt of North Panama – Limón (F2), Siquirres – Matina Fault (F1) and La Estrella Fault (F8). All of these faults are from the Quaternary (relatively recent) and they are considered active. They are indicated in Figure 5 below.



Figure 5: Tectonic map of the province of Limón (Source: Costa Rican Tectonic Atlas)

It is important to clarify that the active and recent faults from the Quaternary are shown in Figure 6 as red lines. The black lines correspond to paleotectonic faults and other geological structures that have not shown activity in the recent geologic past.

With regards to the seismicity of the area, the Limón-Telire earthquake that occurred in April 1991 is a clear example of the seismic potential of the area. For design purposes, the Costa Rican Seismic Code has identified the area as being within Zone III. Within this area and based on the seismic threat studies that have been carried out, the design peak effective acceleration defined by the Costa Rican Seismic Code 2002 is between 0.30 and 0.36g. The peak effective acceleration will depend on the type of soil present at the site (i.e. rock, hard soils, soft soils, etc). With regards to the peak effective accelerations it is important to indicate that these values are for design and that during the Limón-Telire earthquake there were areas where the accelerations measured were higher.

5. RIO ESTRELLA BRIDGE

This chapter includes the results obtained for the complementary study at the Río Estrella Bridge. A brief description of the site and the work executed is presented. This description is followed by a description of the geotechnical profile. The detailed results of the borings and the lab tests are presented in Appendix A, which corresponds to the boring logs.

5.1 Location and executed works

The Río Estrella Bridge is located along national route 36 near the town of Penshurt. From the administrative/political point of view, the bridge site is located in the 7th province Limón, 1st county Limón, 2nd district Valle de la Estrella. From the geographical point of view, the site is located at coordinates 9.78760° and -82.9134° . These coordinates can be located in the map Cahuita, scale 1:50.000, of the Costa Rican Geographical Institute (see Figure 6).

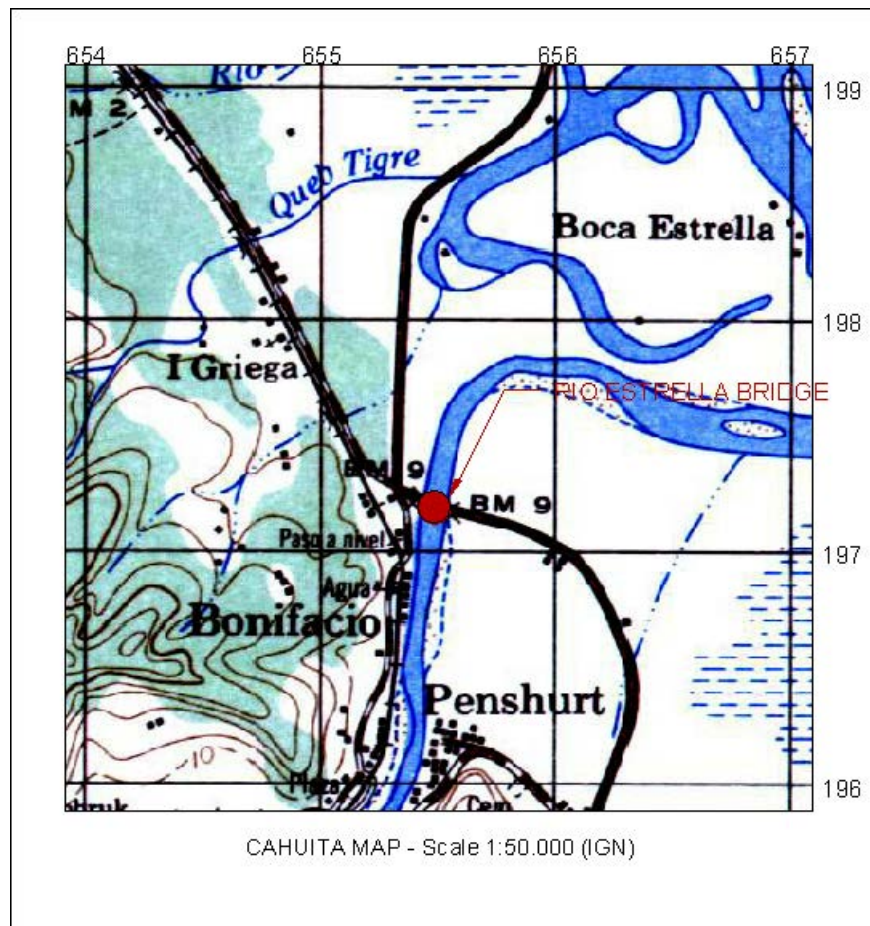


Figure 6: Location of Río Estrella Bridge. The coordinates indicated in the map correspond to Lambert Projection System which is used locally.

The field work carried out at the Río Estrella Bridge consisted in two SPT boreholes. The location and depth of this borehole is indicated in the Table 2. A photograph of the executed drilling is presented in Photo 1.

Table 2: Location and depth of the executed boreholes – Rio Blanco Bridge

Borehole ID	Date	GPS Coordinates		Borehole Depth [m]
		North	West	
P-2	3-May-11	N9 47.238	W82 54.779	12.0
P-3	4-May-11	N9 47.240	W82 54.792	11.0



Photo 1: View of the site of Río Estrella Bridge where one of the boreholes was executed. The borehole is on the right margin of the river and farther away from the river bank.

As observed in Photo 1 the borehole was executed at the base of the bridge's approach fill and in the middle of the existing banana plantation. The ground surrounding the area of the borehole is relatively flat.

5.2 Geotechnical profile

The soil profile detected at the site is typical of this geological formation and it is similar to the soil profile detected during the investigation of April 2010. The following layers were detected in the two new boreholes: 1) brown or grayish brown sandy silt or silty sand, 2) brown silt mixed with a fraction of sand size particles, 3) coarser layer of alluvial material made up of sandy gravels or sand with gravel particles, 4) gray silty sand and 5) greenish gray silty gravel with sand. The soil profile interpreted for the new boreholes of the Río Estrella site is presented in Figure 7. The detailed profile, which includes the laboratory results, is presented in Appendix A.

When comparing the soil profile obtained in the two new boreholes with the one carried out in April 2010 the following comments can be made:

- The layer of coarser alluvial material between 4.50 and 7.20 m appears in all three boreholes
- The very fine greenish gray sand does not appear in the two new boreholes
- A layer of silty gravel with sand appears in the two new boreholes

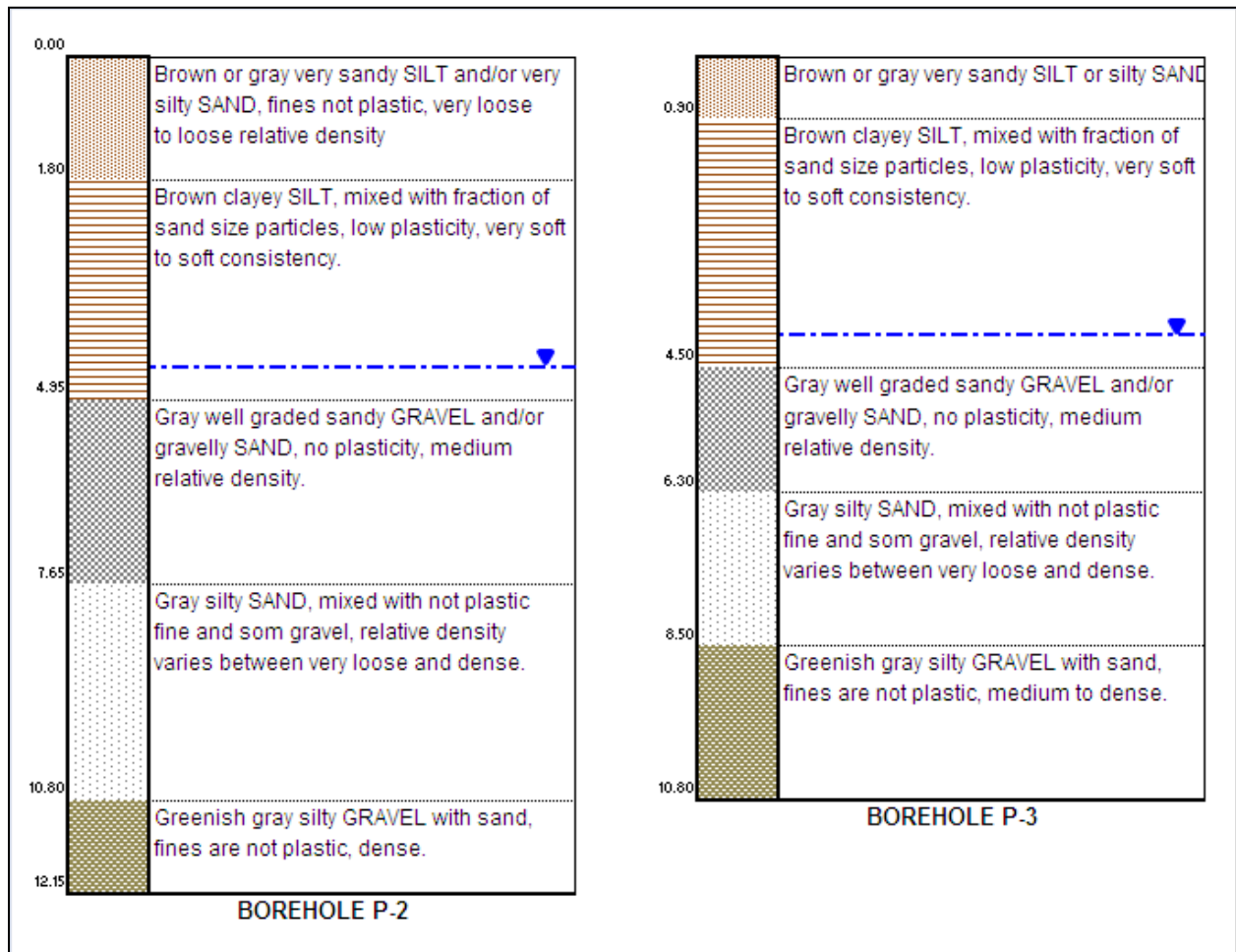


Figure 7: Soil profile detected at the new boreholes of the Río Estrella Bridge site

The water table at this site appears at a depth between 4.40 and 4.70 m below the ground level. In the April 2010 investigation the water table was detected at a depth of 4.90 m. In order to complement the soil profile of Figure 7, a summary of the N_{SPT} values obtained in the boreholes is presented in Table 3.

Table 3: Summary of the N_{SPT} values detected at the new boreholes of Río Estrella Bridge Site

Depth [m]	P-2	P-3
0.00 - 0.45	4	10
0.45 - 0.90	2	4
0.90 - 1.35	13	2
1.35 - 1.80	8	5
1.80 - 2.25	3	2
2.25 - 2.70	4	3
2.70 - 3.15	4	4
3.15 - 3.60	3	4
3.60 - 4.05	2	2
4.05 - 4.50	4	2
4.50 - 4.95	4	13
4.95 - 5.40	11	13
5.40 - 5.85	11	10
5.85 - 6.30	9	16
6.30 - 6.75	17	15
6.75 - 7.20	13	10
7.20 - 7.65	15	19
7.65 - 8.10	18	14
8.10 - 8.55	28	13
8.55 - 9.00	27	17
9.00 - 9.45	31	16
9.45 - 9.90	3	21
9.90 - 10.35	4	40
10.35 - 10.80	5	31
10.80 - 11.25	37	
11.25 - 11.70	20	
11.70 - 12.15	28	

6. CONCLUSIONS

The following conclusions can be obtained from the execution of the geotechnical investigation:

- The Río Estrella Bridge Site lies within a geological formation known as Alluvial and coastal deposits, which is characterized by consisting of transported sediments of clayey, silty and sandy textures.
- As indicated in section 4, the bridge site, as well as the rest of the Costa Rican territory, is subject to the risk of earthquake. Near the investigated bridge sites there are several active faults and geological structures that can have the potential of producing earthquakes. Proof of the seismicity that can affect the area is the Limón-Telire Earthquake that occurred in April of 1991.
- The soil profile detected in the boreholes is typical of the geological formation of alluvial and coastal deposits. In general, these soil profiles consist of sequence of clays, silts, sands and mixtures of each of these types of soils. The materials are not consolidated, not cemented and they have a loose/soft consistency near the surface.

- Based on the boreholes and the laboratory tests carried at the different sites, it was possible to determine the physical and mechanical properties of the soils. This information will be helpful for the modeling and interpretation that will be done for the future stages of the research investigation.
- For each investigated site, it was possible to establish that the requirements for liquefaction to occur under a seismic are present (i.e. loose saturated soils, granular not plastic materials, etc). It is important to indicate that a thorough liquefaction analysis was not carried out; however, the precedent of the liquefaction problems that occurred during the Limón-Telire Earthquake is well established.

APPENDIX A

**RIO ESTRELLA BRIDGE
BORING LOGS**



PROJECT:	Estrella River Bridge	File:	
LOCATION:	Cahuita, province of Limón	CODE:	
BOREHOLE:	P-2	DATE:	03/05/2011
ELEVATION:	m.s.n.m.	DEPTH:	12.15 m
EQUIPMENT:	SPT and Casing	DIAMETER:	AWJ
DRILLER:	V. Murillo	WATER TABLE:	4.7 m

BORING LOG

#	DEPTH (m)		N _{SPT}	% Recovery	N _{SPT}	Symbol	Description	Soil properties						
	From	To						LL	PI	WN (%)	00<sup>->#200	SUCS		
1	0.00	0.45	4	78			Grayish brown or brown very sandy SILT and/or very silty SAND, fines are not plastic very loose to loose relative density.							
2	0.45	0.90	2	33										
3	0.90	1.35	13	22										
4	1.35	1.80	8	89										
5	1.80	2.25	3	67										
6	2.25	2.70	4	44										
7	2.70	3.15	4	33										
8	3.15	3.60	3	67										
9	3.60	4.05	2	67										
10	4.05	4.50	4	67										
11	4.50	4.95	4	67										
12	4.95	5.40	11	67										
13	5.40	5.85	11	67										
14	5.85	6.30	9	67										
15	6.30	6.75	17	67										
16	6.75	7.20	13	56										
17	7.20	7.65	15	44										
18	7.65	8.10	18	44										
19	8.10	8.55	28	44										
20	8.55	9.00	27	22										
21	9.00	9.45	31	22										
22	9.45	9.90	3											
23	9.90	10.35	4											
24	10.35	10.80	5											
25	10.80	11.25	37	33										
26	11.25	11.70	20	33										
27	11.70	12.15	28	44										
28														
29														
30														
31														
32														
33														
34														
35														
36														

Observations:

Described by:	J.P. Rodríguez	Revised by:	J.P. Rodríguez	Approved by:	J. Rodríguez
Date:	21/06/2011	Date:	21/06/2011	Date:	21/06/2011
Signature:		Signature:		Signature:	



BORING LOG	PROJECT: Estrella River Bridge	File:
	LOCATION: Cahuita, province of Limón	CODE:
	BOREHOLE: P-3	DATE: 04/05/2011
	ELEVATION: m.s.n.m.	DEPTH: 10.80 m
	EQUIPMENT: SPT and Casing	DIAMETER: AWJ
	DRILLER: V. Murillo	WATER TABLE: 4.4 m

#	DEPTH (m)		N _{SPT}	% Recovery	N _{SPT}	Symbol	Description	Soil properties						
	From	To						LL	PI	WN (%)	0.075-#200	SUCS		
1	0.00	0.45	10	1			Grayish brown or brown very sandy SILT							
2	0.45	0.90	4	56										
3	0.90	1.35	2	56										
4	1.35	1.80	5	44										
5	1.80	2.25	2	67										
6	2.25	2.70	3	78										
7	2.70	3.15	4	78										
8	3.15	3.60	4	67										
9	3.60	4.05	2	44										
10	4.05	4.50	2	33										
11	4.50	4.95	13	78										
12	4.95	5.40	13	67										
13	5.40	5.85	10	44										
14	5.85	6.30	16	33										
15	6.30	6.75	15	33										
16	6.75	7.20	10	44										
17	7.20	7.65	19	44										
18	7.65	8.10	14	22										
19	8.10	8.55	13	44										
20	8.55	9.00	17											
21	9.00	9.45	16	22										
22	9.45	9.90	21	56										
23	9.90	10.35	40	44										
24	10.35	10.80	31	44										
25							^^^ End of borehole: 10.8 m ^^^							
26														
27														
28														
29														
30														
31														
32														
33														
34														
35														
36														

Observations:

Described by: J.P. Rodríguez	Revised by: J.P. Rodríguez	Approved by: J. Rodríguez
Date: 21/06/2011	Date: 21/06/2011	Date: 21/06/2011
Signature:	Signature:	Signature:

APPENDIX B. PSHA SEISMIC SOURCE MODEL DOCUMENTATION

Title: *Summary of Central and South America Seismic Sources*

Author: Risk Engineering, Inc.

Dates: May 2010

Pages: B-1 to B-14

Summary of Central and South America Seismic Sources

The Central and South American seismic source model includes information for both areal source zones for shallow crustal provinces and fault sources that represent the specific tectonic elements of the region. Fault sources include three types: shallow crustal faults, subduction interface zones, and subduction intraplate zones.

Areal Sources

The areal source zones represent parts of the region with similar tectonic and seismologic characteristics. Definition of the areal source zones was based on examination of spatial patterns of topography, fault locations and kinematics, and historical seismicity. The recurrence model for the areal source zones is based on the historical magnitude frequency distribution for events occurring within the volume of crust defined by the areal source zone boundary and extending from the surface to the base of the shallow crust (~40 km). These events are conservatively assumed to occur on structures within an areal source volume that is commonly much shallower (e.g., 0 to 12 km) than the area of sampled seismicity.

Shallow Crustal Faults

The shallow fault sources, included in the model are primarily from the International Lithosphere Project (ILP) Quaternary fault and fold database. This fault database has been published through a series of open-file reports. ILP reports are available for Argentina, Brazil, Chile and Bolivia, Colombia, Ecuador, Peru, Venezuela, Costa Rica, Panama, and the area around Managua, Nicaragua (see References). The ILP faults included in the model are only those that meet the criteria of having a reported slip rate of >0.2 mm/yr. Slip rates attributed to these line sources are based on the ILP reported rate or a rate determined by other published papers or estimated based on published data from regional geodetic networks. Major crustal faults from other countries not included in the ILP reports (e.g., Motagua and Polochic faults in Guatemala) were added based on other published sources.

Subduction Zones

Regional seismological and geodetic studies indicate that the subduction zones beneath South America and Central America have complex geometries that change along the length of the plate boundary. The geometry of the subduction zone used in the source model is based on analysis of our composite seismicity catalog (see Appendix A) and seismological and geodetic analyses presented in scientific literature (see Reference list). The subduction zone is divided into 10 separate structural segments on the interface portion and 19 separate structural segments on the intraplate portion (Figure 1). The subduction zone segments were defined based on occurrence of large magnitude historical earthquakes, differences in the geometry (strike and dip) of the subducted plate, differences in the age of the subducting plates, and presence of physical asperities such as seamount chains and oceanic fracture zones.

Slip rates along the plate interface zones were estimated taking into consideration the overall plate motion rate, plate-normal component of motion, and amount of seismic

coupling or seismic efficiency along the plate interface. Plate motion rates were derived from published vectors determined by local GPS geodic networks, global plate motion models (e.g., NUVEL 1-A) or GPS-based global plate motion models (obtained through the UNAVCO web-based plate motion calculator).

The maximum earthquake magnitude distribution for the plate interface events is based on two or three potential fault rupture scenarios (characteristic earthquakes) for each subduction zone segment. Factors considered in the analysis of maximum magnitude include: (a) the minimum size of the rupture area based on the maximum historical rupture area for each segment; (b) uncertainties in rupture length and width; (c) presence of physical features on the subducting plate (i.e. fracture zones) that could act as rupture termination points; and (d) the possibility of ruptures larger than historical maximums could occur.

Earthquake recurrence on intraplate sources is modeled as an exponential magnitude distribution. The maximum earthquake magnitude estimates for the intraplate events are based on recorded seismicity, examples from similar tectonic settings, and the physics behind the earthquake generating mechanisms in these environments. The historical magnitude frequency distribution for the intraplate source zone is determined for those events occurring within the volume of crust defined by the map projection of the intraplate zone and extending from the base of the shallow crust (e.g., 40 km) to the maximum depth of recorded earthquakes inferred to be associated with the subducted slab. These events are conservatively assumed to occur along the plane representing the top of the subducted slab.

Magnitude recurrence model parameters are based on a reduction of a catalog of earthquake events from 1530 to 2006.

References

Subduction Zone:

- Barrientos, S. 2005, Giant returns in time: *Nature* 437, p. 329.
- Barrientos, S.E., and Ward, S.N., 1990, The 1960 Chile earthquake: Inversion for slip distribution from surface deformation: *Geophysical Journal International*, v. 103, p. 589-598.
- Beck, S., Barrientos, S., Kausel, E., Reyes, M. 1998. Source characteristics of historic earthquakes along the central Chile subduction zone. *Journal of South American Earth Sciences* Vol. 11, No. 2, pp. 115-129.
- Beck, S.L. and Nishenko, S.P. 1990. Variations in the mode of great earthquake rupture along the central Peru subduction zone. *Geophysical Research Letters*, 17, 1969-1972.
- Bevis, M., et al., 2001, On the strength of interplate coupling and the rate of back arc convergence in the central Andes: An analysis of the interseismic velocity field: *Geochemistry Geophysics Geosystems*, v. 2, 2001GC000198.
- Bradley R. Hackerd, Geoffrey A. Aberse, Robin L. Fergason, (in press), Thermal structure of the Costa Rica – Nicaragua
- Cahill, T., and Isacks, B.L., 1992, Seismicity and shape of the subducted Nazca Plate: *Journal of Geophysical Research*, v. 97, p. 17,503-17,529.
- Cisternas, M., Atwater, B., et al. 2005. Predecessors of the giant 1960 Chile earthquake. *Nature* 437, pp. 404-407.
- CowanCreager, K.C., Chiao, L.Y., et al. 1995. Membrane Strain Rates in the Subducting Plate Beneath South America. *Geophysical Research Letters*, vol. 22, no. 16, pp. 2321-2324.
- DeMets, C. 2001. A new estimate for present-day Cocos-Caribbean plate motion: Implications for slip along the Central American volcanic arc: *Geophysical Research Letters*, v. 28, DOI 10.1029/2001GL013518.
- DeMets, C. 2002. Reply to "Comment on 'A new estimate for Present-day Cocos-Caribbean plate motion: Implications for slip along the Central American volcanic arc' by Marco Guzmán-Speziale and Juan Martín Gómez: *Geophysical Research Letters*, Vol. 29, DOI 10.1029/2002GL015384.
- DeMets, C., and Dixon, T.H., 1999, New kinematic models for Pacific-North America motion from 3 Ma to present, I: Evidence for steady motion and biases in the NUVEL-1A model, *Geophysical Research Letters*, v. 26, p. 1921-1924.

- DeMets, C., Gordon, R., et al. 1990. Current plate motions. *Geophys. J. Int.*, Vol. 101, pp. 425-478.
- DeMets, C., Jansma, E.J. 2000. GPS Constraints on Caribbean-North America plate motion. *Geophysical Research Letters*, Vol. 27, No. 3, pp. 437-440.
- Dewey, J.F. and Lamb, S.H. 1992. Active tectonics of the Andes. *Tectonophysics*, Vol. 205, 79-95.
- Dorbath, L., Cisternas, A., et al. 1990. Assessment of the size of large and great historical earthquakes in Peru. *Bulletin of the Seismological Society of America*, Vol. 80, No. 3, pp. 551-556.
- Dorbath, L., Dorbath, C., Jiménez, E. and Rivera, L., 1991. Seismicity and tectonic deformation in the eastern Cordillera and Sub Andean zone of Central Perú: *Journal of South American Earth Sciences*, v. 4, p. 13-24.
- Geomatrix Consultants, 2004a, Seismicity Update U.S. Department of State New Embassy at the Cardemas Site, Panama City, Panama, Project No. 8734.002, 16p.
- Geomatrix Consultants, 2004b, Seismicity Update U.S. Department of State New Embassy Casa Grande/Casa Chica Compound, Managua, Nicaragua, Project No. 8734.005, 14p.
- Geomatrix Consultants, 2004c, Seismicity Update U.S. Department of State New Embassy Compound, Belmopan, Belize, Project No. 8734.013, 20p.
- Geomatrix Consultants, 2004d, Seismicity Update U.S. Department of State New Embassy Site, Quito, Ecuador, Project No. 8734.015, 14p.
- Grange, F., Cunningham, P., et al. 1984. The configuration of the seismic zone and the downgoing slab in southern Peru. *Geophysical Research Letters*, vol. 11, no. 1, pp. 38-41.
- GSHAP Piloto Report, <http://www.seismo.ethz.ch/gshap/piloto/report.html>, 3/3/06
- Guzmán-Speziale, M., and Meneses-Rocha, J.J., 2000, The North America—Caribbean plate boundary west of the Motagua-Polochic fault system: a fault jog in Southeastern Mexico: *Journal of South American Earth Sciences*, v. 13, p. 459-468.
- Guzman-Speziale, M., Valdes-González, C., et al. 2005. Seismic activity along the Central America volcanic arc: Is it related to subduction of the Cocos plate? *Tectonophysics* 400, pp. 241-254.
- Hackney, R., Götze, H.-J., and Meyer, U., 2005, Topographic, bathymetric and gravity characteristics of convergent margins: *Geotechnologien Science Report No. 5*, Status Seminar, Abstract, p. 30-33.

- Hartzell, S. and Langer, C. 1993. Importance of model parameterization in finite fault inversions: application to the 1974 M_w 8.1 Peru Earthquake. *J. Geophys. Res.*, Vol. 98, 22123-22134.
- Heubeck, C., and Mann, P., 1991, Geologic evaluation of plate kinematic models for the North American—Caribbean plate boundary zone: *Tectonophysics*, v. 191, p. 1-26.
- Johnston, S.T., Thorkelson, D.J. 1996. Cocos-Nazca slab window beneath Central America. *Earth and Planetary Science Letters* 146, pp. 465-475.
- Kley, J., Monaldi, C.R., Salfity, J.A., 1999, Along-strike segmentation of the Andean foreland: causes and consequences: *Tectonophysics*, 259, p. 171-184.
- Klotz, J., Angermann, D., et al. 1999. GPS-derived deformation of the Central Andes including the 1995 Antofagasta $M_w=8.0$ Earthquake. *Pure and Applied Geophysics* 154, 709-730.
- Klotz, J., Khazaradze, G., et al. 2001. Earthquake cycle dominates contemporary crustal deformation in Central and Southern Andes. *Earth and Planetary Science Letters* 193, pp. 437-446.
- Langer, C.J. and Spence, W. 1995. The 1974 Peru earthquake series. *Bull. Seism. Soc. Am.*, Vol. 85, No. 3, pp. 665-687.
- MMI Engineering, 2003, LNG Pipeline and Facility Geologic and Geotechnical Studies. Camisea, Peru, Unpublished consultant report.
- McCaffrey, R. 1997. Short Notes: Statistical Significance of the Seismic Coupling Coefficient. *Bulletin of the Seismological Society of America*, vol. 87, no. 4, pp. 1069-1073.
- Pacheco, J.F., Sykes, L.R., et al. 1993. Nature of Seismic Coupling Along Simple Plate Boundaries of the Subduction Type. *Journal of Geophysical Research*, vol. 98, pp. 14,133-14,159.
- Protti, M., Gündel, F., McNally, K., 1994, The geometry of the Wadati-Benioff zone under southern Central America and its tectonic significance: results from a high-resolution local seismographic network. *Physics of the Earth and Planetary Interiors*, 84, pp. 271-287.
- Quezada, J., Bataille, K., and González, G., 2005, The effect of subduction earthquakes on the coastal configuration of Northern Chile: 6th International Symposium on Andean Geodynamics, Barcelona, Extended Abstracts, p. 578-581.
- Ruegg, J.C., et al., 2002, Interseismic strain accumulation in the south central Chile from GPS measurements, 1996-1999: *Geophysical Research Letters*, v. 29, p. 12-1—12-4.

Tichelaar, B.W., and Ruff, L.J. 1993. Depth of seismic coupling along subduction zones. *Journal of Geophysical Research*, 98, B2, 2017-2037.

Tichelaar, B.W., and Ruff, L.J., 1991, Seismic coupling along the Chilean subduction Zone: *Journal of Geophysical Research*, v. 96, p. 11,997-12,022.

Trenkamp., R. Kellogg J.N., Freymueller J.T., Mora P. H., 2002. Wide plate margin deformation, southern Central America and northwestern South America CASA GPS observations. *South American Earth sciences* 15:157-171.

White, S.M., Trenkamp, R., et al. 2003. Recent crustal deformation and the earthquake cycle along the Ecuador-Columbia subduction zone. *Earth and Planetary Science Letters* 216, pp. 231-242.

Wiens, Douglas, Chilean Patagonia Seismicity (personal communication, 03/04/06).

Upper plate:

Allmendinger R.W., Jordan Teresa E., Kay S.M., Isacks B.L., 1997. The evolution of the Altiplano-Puna Plateau of the Central Andes. *Annu.Rev.Earth Planet Sci.* 25:139-174.

Audemard F.A., 1996, Paleoseismicity studies on the Oca-Ancon fault system, northwestern Venezuela. *Tectonophysics* 259:67-80.

Audemard F.A., Bouquet J.C., Rodriguez J. 1999. Neotectonic and paleoseismicity studies of the Uramaco fault northern Falcon basin, northwestern Venezuela. *Tectonophysics* 308:25-35.

Audemard, F.A., Machette, M.N., Dart, R.L., and Haller, K.M., 2000, Map and Database of Quaternary Faults in Venezuela and its Offshore Regions: U.S. Geological Survey Open-File Report 00-018, 76 p., 1 plate (1:2,000,000 scale).

Bommer, J.J., et al., 2002, The El Salvador earthquakes of January and February 2001: Context, characteristics and implications for seismic risk: *Soil Dynamics and Earthquake Engineering*, v. 22, p. 389-418.

Burkart, B., 1983, Neogene North American—Caribbean Plate boundary across northern Central America: Offset along the polochic fault: *Tectonophysics*, v. 99, p. 251-270.

Cáceres, D., Monterroso, D., and Tavakoli, B., Crustal deformation in northern Central America: *Tectonophysics*, v. 404, p. 119-131.

Cembrano J., Herve F., Lavenu A. 1996, The Liquine Pique fault zone: a long-lived intra-arc fault system in southern Chile. *Tectonophysics* 259:55-66.

- Colleta B., Roure F., De Toni B., Loureiro D., Passalacqua H., 1997, Tectonic inheritance, crustal architecture, and contrasting structural styles in the Venezuelan Andes. *Tectonics* 16(5):777-794.
- Colombo F., Busquets P., Ramos E., Verges J., Ragona D. 2000, Quaternary alluvial terraces in an active tectonic region: the San Juan river valley, Andean Ranges, San Juan Province, Argentina. *Journal of South America Earth Sciences* 13:611-626.
- Corredor F., 2003, Seismic strain rates and distributed continental deformation in the northern Andes and three-dimensional seismotectonics of northwestern South America. *Tectonophysics* 372: 147-166.
- Costa C., 2005. The seismogenic potential for large earthquakes at the southernmost Pampeana flat-slab segment (Argentina) from geologic perspective. 6th International Symposium of Andean Geodynamics, Extended Abstracts: 190-193.
- Costa C. and Vita-Finzi, 1996. Late Holocene faulting in the southeast Sierras Pampeanas of Argentina. *Geology* 24(12):112-1130.
- Costa, C., Machette, M.N, Dart, R.L., Bastias, H.E., Paredes, J.D., Perucca, L.P., Tello, G.I., and Haller, K.M., 2000, Map and Database of Quaternary Faults and Folds in Argentina: U.S. Geological Survey Open-File Report 00-0108, 76 p., 90 p., 1 plate (1:4,000,000 scale).
- Cowan, H., Machette, M.N., Amador, Xavier, Morgan, Karen S., Dart, R.L., and Bradley, Lee-Ann, 2000, Map and Database of Quaternary Faults and Folds in the Vicinity of Managua, Nicaragua: U.S. Geological Survey Open-File Report 00-0437, 61 p., 1 plate (1:750,000 scale).
- Cowan, H., Machette, M.N., Haller, K.M., and Dart, R.L., 1998, Map and database of Quaternary faults and folds in Panama and its offshore regions: U.S. Geological Survey Open-File Report 98-779, 41 p., 1 plate (1:500K scale).
- Deaton, B.C., Burkart, B., 1984, Time of sinistral slip along the Polochic fault of Guatemala: *Tectonophysics*, v. 102, p. 297-313.
- Eguez, Arturo, Alvarado, Alexandra, Yepes, Hugo, Machette, Michael N., Costa, Carlos, and Richard L. Dart, 2003 Database and Map of Quaternary Faults and Folds in Ecuador and its offshore regions: U.S. Geological Survey Open-File Report 03-289, 71 p., 1 plate (1:1,250,000 scale).
- Fernández, M., and Rojas, W., 2000, Faulting, shallow seismicity and seismic hazard analysis for the Costa Rican Central Valley: *Soil Dynamics and Earthquake Engineering*, v. 20, p. 59-73.
- Finch, R.C., and Ritchie, A.W., 1991, The Guayape fault system, Honduras, Central America: *Journal of South American Earth Sciences*, v. 4, p. 43-60.

- Guillaume Backe, Dhont D., Hevouet Y., Gonzales L. 2005. Active tectonic escape of the northwestern Venezuelan Andes. 6th International Symposium of Andean Geodynamics, Extended Abstracts: 86-89.
- Guzmán-Speziale, M., 2001, Active seismic deformation in the grabens of northern Central America and its relationship to the relative motion of the North America—Caribbean plate boundary: *Tectonophysics*, v. 337, p. 39-51.
- Heraül G., Oller J., Baby P., Bonhomme M., Soler P., 1996. Strike-slip faulting, thrusting and related basins in the Cenozoic evolution of the southern branch of the Bolivian orocline. *Tectonophysics* 259:201-212.
- Heubeck C. and Man P., 1991, Geologic evaluation of plate kinematic models for the North American- Caribbean plate boundary zone. *Tectonophysics*, 191:1-26.
- Horton, B., 1999, Erosional control on the geometry and kinematics of thrust belt development in the Central Andes. *Tectonics* 18(6):1292-1304.
- Isacks B., 1988. Uplift of the Central Andean Plateau and Bending of the Bolivian Orocline. *Journal of Geophysical Research*, 93(B4):3211-3231.
- Jordan T. and Allemendinger R.W., 1986. The Sierras Pampeanas of Argentina: A modern analog of Rocky Mountain foreland deformation. *American Journal of Science* 286:737-764.
- Kendrick E., Bevis M., Smalley R., Brooks, B. 2001. An integrated crustal velocity field for the central Andes. *Geochimistry Geophysics Geosystems*, 11p.
- Kiremidjian, A.S., Hareh, C.S., and Sutch, P.L., 1982, Seismic Hazard and Uncertainty Analysis of Honduras: *Soil Dynamics and Earthquake Engineering*, v. 1, p. 83-84.
- Kley J., Gangui A., Kruger D., 1996, Basement-involved blind thrusting in the Eastern Cordillera Oriental, Southern Bolivia: evidence from cross-sectional balancing, gravimetric and magnetotelluric data. *Tectonophysics*, v. 301, p. 75-94.
- Klosko E.R., Hindle D., Kley J., Norabuena E., Dixon T., Liu M., 2002, Comparison of GPS, Seismological, and Geological observations of Andean Mountain Building. *Plate Boundary zones*, P. 123-124.
- Lavenu, A., Thiele, R., Machette, M.N., Dart, R.L., and Haller, K.M., 2000, Map and Database of Quaternary Faults and Folds in Bolivia and Chile: U.S. Geological Survey Open-File Report 00-0283, 38 p., 2 plates.
- Machare, J., Fenton, C.H., Machette, M.N., Lavenu, A., Costa, C., and Dart, R.L., 2003, Database and Map of Quaternary Faults and Folds in Peru and its Offshore Region: U.S. Geological Survey Open-File Report 03-0451, 54 p., 1 plate.

- Mering, C., Huaman-Rodrigo D., Chorowica J., Deffontains, B., Guillande, R., 1996. New Data on the Geodynamics of southern Peru computerized analysis of SPOT and SAR ERS-1 images. *Tectonophysics*, 259, 153-169.
- Montero, W., Denyer, P., Barquero, R., Alvarado, G.E., Cowan, H., Machette, M.N., Haller, K.M., and Dart, R.L., 1998, Map and database of Quaternary faults and folds in Costa Rica and its offshore regions: U.S. Geological Survey Open-File Report 98-481, 63 p., 1 plate (1:750K scale).
- Muñoz, A.V., 1988, Tectonic patterns of the Panama Block deduced from seismicity, gravitational data and earthquake mechanisms: implications to the seismic hazard: *Tectonophysics*, v. 154, p. 253-267.
- Norabuena F., Leffler-Griffin L., Mao A., Dizon T., Stein S., Sacks L.O. Ocola L., Ellis M., 1998, Space Geodetic Observations of Nazca-South America Convergence Across the Central Andes. *Science* 279:358-359.
- Paris, G., Machette, M.N., Dart, R.L., and Haller, K.M., 2000, Map and Database of Quaternary Faults and Folds in Colombia and its Offshore Regions: U.S. Geological Survey Open-File Report 00-248, 61 p., 1 plate (1:2,500,000 scale).
- Perez J.O., Bilham R., Bendick R., Velandia R.J., Hernandez N., Moncayo C., Hoyer M., Kozuch M., 2001, Velocity field across southern Caribbean plate boundary and estimates of Caribbean/South American plate motion using GPS Geodesy 1994-2000. *Geophysical Research Letters*, 28(15): 2987-2990.
- Pratt, T.L., et al., 2003, High-resolution seismic imaging of faults beneath Limón Bay, northern Panama Canal, Republic of Panama: *Tectonophysics*, v. 368. p. 211-227.
- Ramos V., Cegarra M., Cristallini, 1996, Cenozoic tectonics of the High Andes of west-central Argentina (30-36° S latitude). *Tectonophysics*, 259:185-200.
- Ramos V., 1999, Plate tectonic setting of the Andean Cordillera. *Episodes* 22(23):183-190.
- Ramos V.A., Cristallini E.O., Perez D.J., 2003. The Pampean flat-slab of the Central Andes, *Journal of South America Earth Sciences* 15: 59-78.
- Reutter K.J., Scheuber E., Chong G., 1996. The Precordillera fault system of Chuquimata, Northern Chile: evidence for reversals along arc-parallel strike-slip faults. *Tectonophysics*, 259:213-228.
- Roeder D. and Chamberlain R.L., 1995. Eastern Cordillera of Colombia: Jurassic-Neogene crustal evolution, in A. Tankard, R. Suarez, and H.J. Welsinski, *Petroleum basins of South America: AAPG Memoir* 62, 633-645.
- Saadi, Allaoua, Machette, M.N., Haller, K.M., Dart, R.L., Bradley, L.-A., de Souza, A.M.P.D., 2002, Map and Database of Quaternary Faults and Lineaments in

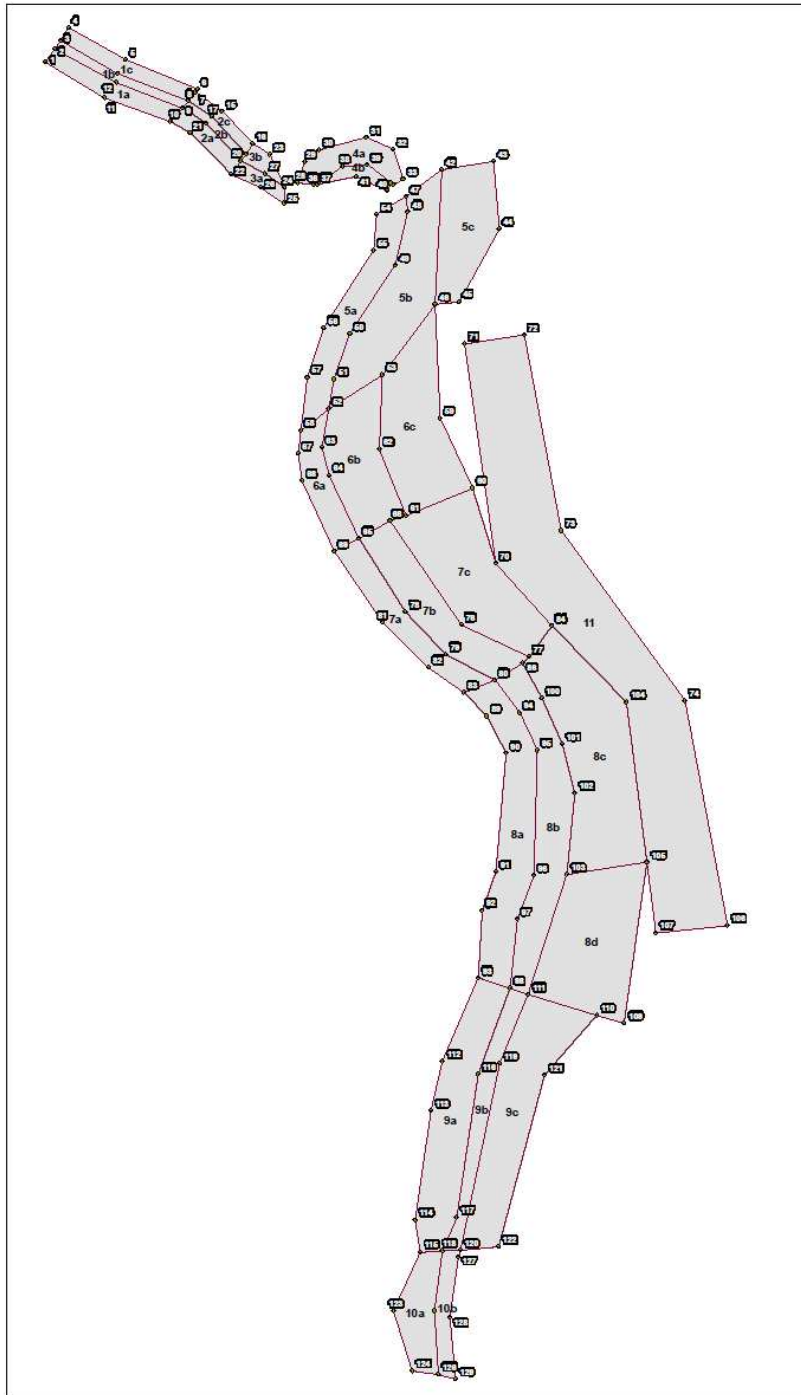
- Brazil: U.S. Geological Survey Open-File Report 02-230, 58 p., 1 plate (1:6,000,000 scale).
- Schwartz, D.P., Lloyd S.C., and Donnelly, T.W., 1979, Quaternary faulting along the Caribbean—North American plate boundary in Central America: *Tectonophysics*, v. 52, p. 431-445.
- Suarez G., Molnar P., Burchfiel B.C., 1983. Seismicity, fault plane solutions, depth of faulting, and active tectonics of the Andes Peru, Ecuador, and Southern Colombia. *Journal of Geophysical Research*, 88(B12):10403-10428.
- Trenkamp R., Mora P. H., Salcedo H. E., Kellog J.N. 2004, Possible rapid strain accumulation rates near Cali, Colombia, determined from GPS measurements (1996-2003). *Earth Sciences Research Journal*, 8:1, 25-33.
- Wells, S.G., et al., 1988, Regional variations in tectonic geomorphology along a segmented convergent plate boundary, Pacific Coast of Costa Rica: *Geomorphology*, v. 1, p. 239-265.
- Wolters, B., 1986, Seismicity and tectonics of southern Central America and adjacent regions with special attention to the surroundings of Panama: *Tectonophysics*, v. 128, p. 21-46.
- Whitman D., Isacks B.L., Kay S.M., 1996. Lithospheric structure and along-strike segmentation of central Andean plateau: seismic Q, magmatism, flexure, topography and tectonics.

Appendix A

The historic earthquake catalog for South and Central America was assembled from a number of sources. Among the agencies and published sources used in the data compilation are (in order of numbers of events):

- GS United States Geological Survey, Denver, Colorado
- ISC International Seismological Centre, Newbury, UK
- GUC Geofísica, Universidad de Chile
- SIS Nicaragua Earthquake Information
- SAT Shepherd and Turner 1992 An earthquakes catalogue for the Caribbean
- RSN Red Sismological Nacional (RSN), ICE-UCR San Jose Costa Rica
- CER CERESIS, Catalog of Earthquakes for South America , 1985
- PDE Preliminary Determination of Epicenter from NEIS/CGS
- GCG Guatemala City, Guatemala
- Department of Defense, U.S.
- OSO OSSO Observatory, Colombia
- SAA Shepherd and Aspinall, 1982
- LAO Large Aperture Seismic Array (LASA), Montana, USA.
- HRV Harvard, Massachusetts, USA
- TRN Trinidad. Trinidad-Tobago
- SAN Santiago, Chile
- HDC Heredia, Cost Rica
- ROT Rothe, J.P. , The Seismicity of the Earth, 1953-1965, UNESCO, 1969
- HRV Harvard Moment Tensor Solutions
- NAO NORSAR, Norway.
- CGS U.S. Coast and Geodetic Survey, Rockville, MD, USA
- SCB San Calixto, Bolivia
- CAR Caracas, Venezuela.
- BRK Berkeley, California, USA
- AMB Ambrayseys, 1994.
- OAE Observatorio Astronómico de Quito, Ecuador
- MOS Moscow, Russia
- PAS Pasadena, California, USA.
- BJI Beijing, China
- USGS United States Geological Survey
- USCGS United States Coast and Geodetic Survey
- PSA Instituto Nacional de Prevención Sísmica (INPRES), San Juan, Argentina
- QUE Quito, Ecuador (also listed as QUI)
- PAL Palisades, New York, USA
- HFS Hagfors, Sweden.
- STL Santa Lucia, Chile
- NEI Preliminary Determination of Epicentres from NEIS/CGS
- G-R Gutenberg and Richter, 'Seismicity of the Earth'
- TOJ Toral, 1992
- G-M Güendel and McNally, 1986
- FIE Gunther Fiedler, Caracas, Venezuela
- SIG Catalog of Significant Earthquakes (Dunbar, Lockridge, Whiteside, 1993)
- SJR San José, Costa Rica
- BCI Bureau Central International de Seismologie, Strasbourg, France.
- SYK Sykes L.R., Earthquake Catalogue. (1963, 1965, 1966)
- IGP Geophysical Institute of Peru
- TAC Tacubaya, México
- SJS Instituto Costarricense de Electricidad, Costa Rica.
- WMR Montero, 1989
- LIM Lima, Peru

Figure 1



APPENDIX C. LPILE MC SIMULATOR

Introduction

While many practicing professionals prefer the convenience and simplicity of Beam on Winkler Foundation (BWF) procedures (i.e. p-y soil spring methods) for computing kinematic and inertial pile response, the methodology is not necessarily well-suited for probabilistic applications due to the apparent lack of published statistical properties of the various p-y models. However, probabilistic applications can still be performed using BWF methods by using iterative statistical procedures (e.g. Monte Carlo simulation) to characterize the uncertainty of the pile response. Such procedures are commonly utilized with other engineering applications to estimate the uncertainty associated with a given problem, and have increasingly become incorporated into many analysis software packages. Unfortunately, the commonly-used BWF software package LPILE does not include any probabilistic applications for the user and can only be directly used in a deterministic manner. Furthermore, because LPILE incorporates a complex series of libraries, it is impossible to the run the program in batch mode (William Isenhower, personal communication, June 2009).

The incorporation of Visual Basic (VB) macros with an Excel spreadsheet and ‘keystroke’ encoding allows one to bypass the limitations presented by the complex library structure of LPILE Plus version 5.0 and effectively perform iterative statistical procedures such as Monte Carlo simulations, point estimate methods, or first-order second moment (FOSM) methods. Keystroke encoding involves the use of encoded keyboard commandments

incorporated directly into the macro in order to perform repetitive computations using a software application.

Instructions for Use

The LPILE MC Simulator spreadsheet uses several worksheets to perform its computations. The majority of the input is entered into the main worksheet, which also controls the number of iterations for the Monte Carlo simulations. A screenshot of the main worksheet is shown in Figure C-1.

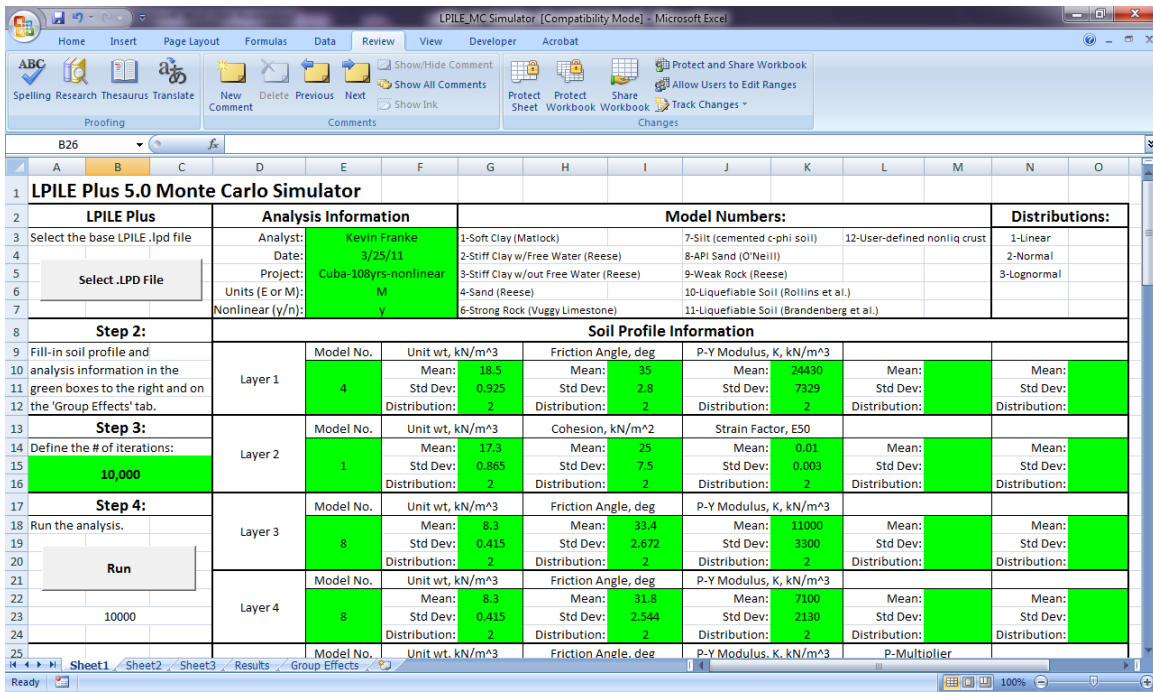


Figure C-1: Screenshot of Main Worksheet for LPILE MC Simulator

The first step to using the spreadsheet is to develop an initial pile response model in LPILE Plus version 5.0 using the mean soil parameter values for all of the p-y soil models. The user then presses the 'Select .lpd File' button and selects the appropriate pile response model. LPILE MC Simulator then loads the file into the spreadsheet, and the user must specify the mean, standard deviation, and probability distribution (i.e. normal, lognormal, or linear-uniform) for all parameters and each soil layer. The user must also clarify whether the initial LPILE pile response model incorporates nonlinear or linear-elastic pile response and the number of iterations desired for the Monte Carlo simulation.

Following data entry on the main worksheet, the user must next define the group behavior on the 'Group Effects' worksheet. The user must first specify whether a pile group or single pile is to be analyzed in the Monte Carlo simulation. If a single pile is specified, nothing on the Group Effects worksheet will be used by the macro and the user may proceed to the Monte Carlo simulations. However, if a pile group is to be analyzed, then the user must also define the pile spacing, number of rows (transverse and longitudinal to the kinematic loading), the type of pile/installation, the fixity behavior of the pile toes, and the strength properties of the soils surrounding the piles. Rollins et al. (2006) is used to compute pile group multipliers for the various rows of piles. A screenshot of the Group Effects worksheet is shown in Figure C-2.

Following data entry on the Group Effects worksheet, the Monte Carlo analysis should be ready to perform. The user must return to the main worksheet in order to run the analysis. It is strongly recommended that all other non-necessary computer applications be closed and the computer be disconnected from the internet if possible in order to reduce the amount of memory allotted to other functions, which could result in errors in the keystroke operation of the Monte Carlo simulation. The user must make sure that the key to operate LPILE Plus version 5.0 is

properly inserted and that the program is able to open and operate smoothly. To begin the Monte Carlo simulation, the user must simply press the “Run” button. Because the macro utilizes keystrokes, the user may not use the computer for any other functions while the Monte Carlo analysis is being performed.

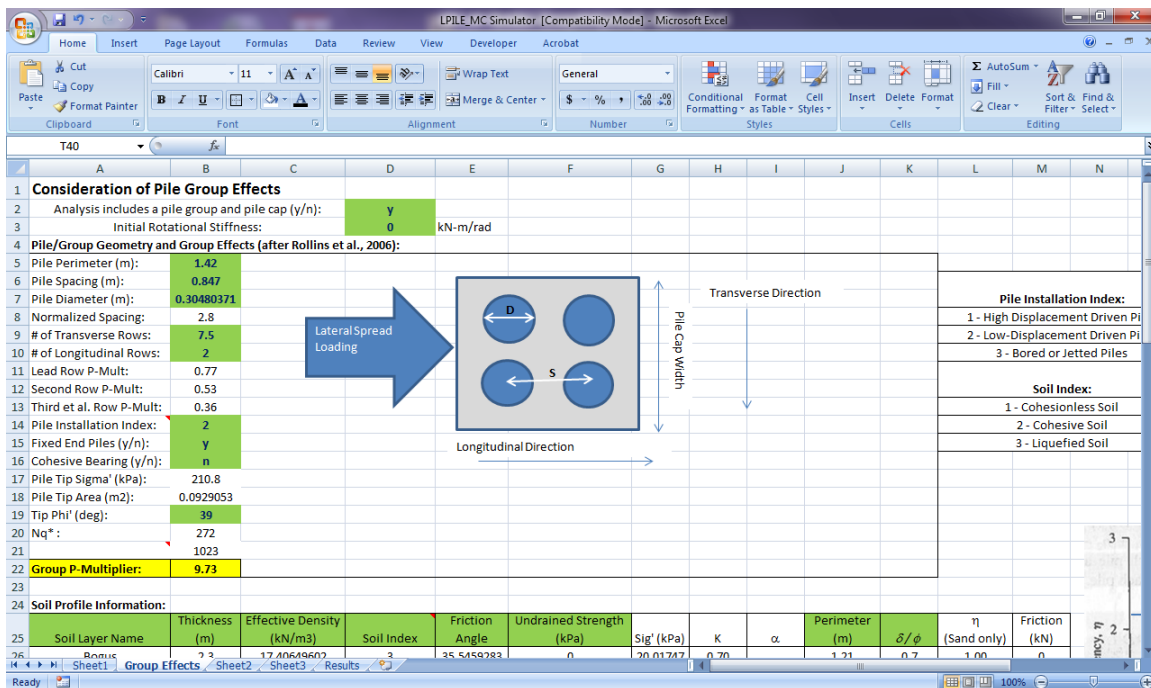


Figure C-2: Screenshot of the Group Effects Worksheet in LPILE MC Simulator

Occasionally, the macro operates faster than the LPILE program can process data. This error usually results in the unanticipated shutdown of LPILE, and the continuing keystrokes of the macro cause the Excel spreadsheet to lock up. The macro incorporates code to distinguish when such errors occur and to not include any potential erroneous results in the Monte Carlo simulation. If such an event occurs, the user simply needs to re-open the LPILE program, close

any file open/close dialog boxes in Excel, quickly select the LPILE program as the active application, and then press ‘Ctrl-Alt-Break’ repeatedly until the macro resumes its normal iterations. Under normal operation, the Monte Carlo simulation should occur at a rate of about one iteration per 1.5 seconds.

Following the completion of the Monte Carlo simulation, the macro will automatically close LPILE and record the computed means and standard deviations for the pile displacement, bending moments, shear forces, and curvature. If considering pile groups, the bending moments and shear forces represent the average values for a single pile in the group. The user may then retrieve the results from the ‘Results’ worksheet. The pile response results can be directly saved into a .txt file for importing as input into the performance-based pile response software PPRS. A screenshot of the ‘Results’ worksheet is shown in Figure C-3.

	A	B	C	D	E	F	G	H	I	J	K
1	Depth(m)	Deflection(m)	Sig_Deflect(m)	Shear(kN)	Sig_Shear(kN)	Moment(kN-m)	Sig_Moment(kN-m)	Slope(rad)	Sig_Slope(rad)		
2	0	0.386673333	5.38919E-05	-2.48889E-09	5.5447E-10	2.68222E-09	3.3393E-09	6.61667E-05	1.96144E-05		
3	0.0553	0.386677	5.33292E-05	0.000739111	6.88931E-05	-2.45333E-07	7.22311E-08	6.61667E-05	1.96144E-05		
4	0.111	0.386680333	5.1984E-05	0.002940089	0.000274559	8.13111E-05	7.63278E-06	6.61667E-05	1.96144E-05		
5	0.166	0.386684333	5.10327E-05	0.006569933	0.000615469	0.000324622	3.04138E-05	6.61667E-05	1.96144E-05		
6	0.221	0.386687667	4.99032E-05	0.011595844	0.001089993	0.000807889	7.5778E-05	6.61667E-05	1.96144E-05		
7	0.277	0.386691667	4.89524E-05	0.017984822	0.001696683	0.001607422	0.000151076	6.61667E-05	1.96144E-05		
8	0.332	0.386695	4.76235E-05	0.025704022	0.002434159	0.002797711	0.00026355	6.61667E-05	1.96144E-05		
9	0.387	0.386698667	4.70567E-05	0.034720489	0.003301146	0.004451511	0.000420446	6.61667E-05	1.96144E-05		
10	0.443	0.386702333	4.55448E-05	0.045001289	0.004296468	0.006639644	0.00062887	0.0000662	1.96619E-05		
11	0.498	0.386706333	4.46019E-05	0.056513444	0.005419061	0.009431156	0.00089585	6.62667E-05	1.96144E-05		
12	0.553	0.386709667	4.32936E-05	0.069227156	0.006664394	0.012893311	0.001228416	6.63333E-05	1.96666E-05		
13	0.609	0.386713333	4.27239E-05	0.083111111	0.00801591	0.017091444	0.001633543	0.0000664	1.96191E-05		
14	0.664	0.386717333	4.17892E-05	0.098111111	0.009521982	0.022089156	0.002118074	0.0000665	1.96191E-05		
15	0.719	0.386721	4.02865E-05	0.114222222	0.011167081	0.027948111	0.002688861	6.66667E-05	1.96144E-05		
16	0.775	0.386724667	3.97157E-05	0.131377778	0.012931672	0.034728222	0.003352749	0.0000668	1.96191E-05		
17	0.83	0.386728	3.84318E-05	0.149577778	0.014794043	0.042487422	0.004116503	6.70667E-05	1.95717E-05		
18	0.885	0.386732	3.751E-05	0.168777778	0.016790253	0.051281889	0.004986765	6.73333E-05	1.9624E-05		
19	0.941	0.386735667	3.60185E-05	0.188955556	0.018884718	0.061173311	0.005982628	6.76333E-05	1.9624E-05		
20	0.996	0.386739333	3.54448E-05	0.210044444	0.021104221	0.072207644	0.007084368	0.000068	1.95768E-05		
21	1.051	0.386743333	3.45302E-05	0.232022222	0.023455048	0.0844	0.008297791	6.84333E-05	1.9582E-05		
22	1.107	0.386747	3.30454E-05	0.254844444	0.025973006	0.097866667	0.009674939	6.89667E-05	1.95873E-05		
23	1.162	0.386751	3.21403E-05	0.278511111	0.028554068	0.112622222	0.011178617	6.95333E-05	1.95403E-05		

Figure C-3: Screenshot of the Results Worksheet in LPILE MC Simulator

Macro Code

```
Public myFile As String
Public FrontEnd As String
```

```
'-----
'*****
'-----
```

```
Function SoilParams(modelNum As Integer, order As Integer, myUnits As String) As String
```

```
'-----
' This function determines which soil parameters should appear based on the selected model
number
'-----
```

```
Dim myString As String
Dim English As Boolean
Dim StrengthUnits, DensityUnits, FrictionUnits, ModUnits, YoungsUnits, RQDUnits As String
```

```
If myUnits = "E" Then
```

```
    English = True
    StrengthUnits = "psi"
    DensityUnits = "pci"
    FrictionUnits = "deg"
    ModUnits = "pci"
    YoungsUnits = "psi"
    RQDUnits = "%"
```

```
Else
```

```
    English = False
    StrengthUnits = "kN/m^2"
    DensityUnits = "kN/m^3"
    FrictionUnits = "deg"
    ModUnits = "kN/m^3"
    YoungsUnits = "kN/m^2"
    RQDUnits = "%"
```

```
End If
```

```
Select Case modelNum
```

```
Case 1 'Soft Clay (Matlock, 1970)
```

```
    If order = 1 Then
        myString = "Unit wt, " + DensityUnits
    ElseIf order = 2 Then
        myString = "Cohesion, " + StrengthUnits
    ElseIf order = 3 Then
```

```

    myString = "Strain Factor, E50"
Else
    myString = ""
End If
Case 2 'Stiff Clay with Free Water (Reese)
    If order = 1 Then
        myString = "Unit wt, " + DensityUnits
    ElseIf order = 2 Then
        myString = "Cohesion, " + StrengthUnits
    ElseIf order = 3 Then
        myString = "P-Y Modulus, K, " + ModUnits
    ElseIf order = 4 Then
        myString = "Strain Factor, E50"
    Else
        myString = ""
    End If
Case 3 'Stiff Clay w/out Free Water (Reese)
    If order = 1 Then
        myString = "Unit wt, " + DensityUnits
    ElseIf order = 2 Then
        myString = "Cohesion, " + StrengthUnits
    ElseIf order = 3 Then
        myString = "Strain Factor, E50"
    Else
        myString = ""
    End If
Case 4 'Sand (Reese)
    If order = 1 Then
        myString = "Unit wt, " + DensityUnits
    ElseIf order = 2 Then
        myString = "Friction Angle, " + FrictionUnits
    ElseIf order = 3 Then
        myString = "P-Y Modulus, K, " + ModUnits
    Else
        myString = ""
    End If
Case 6 'Strong Rock (Vuggy Limestone)
    If order = 1 Then
        myString = "Unit wt, " + DensityUnits
    ElseIf order = 2 Then
        myString = "Compress Strength, " + StrengthUnits
    Else
        myString = ""
    End If
Case 7 'Silt (cemented c-phi soil)
    If order = 1 Then

```



```

    myString = "Unit wt, " + DensityUnits
ElseIf order = 2 Then
    myString = "Cohesion, " + StrengthUnits
ElseIf order = 3 Then
    myString = "Friction Angle, " + FrictionUnits
ElseIf order = 4 Then
    myString = "P-Y Modulus, K, " + ModUnits
Else
    myString = "Strain Factor, E50"
End If
Case 8 'API Sand
    If order = 1 Then
        myString = "Unit wt, " + DensityUnits
    ElseIf order = 2 Then
        myString = "Friction Angle, " + FrictionUnits
    ElseIf order = 3 Then
        myString = "P-Y Modulus, K, " + ModUnits
    Else
        myString = ""
    End If
Case 9 'Weak Rock
    If order = 1 Then
        myString = "Unit wt, " + DensityUnits
    ElseIf order = 2 Then
        myString = "Youngs Modulus, " + YoungsUnits
    ElseIf order = 3 Then
        myString = "Compress Strength, " + StrengthUnits
    ElseIf order = 4 Then
        myString = "RQD, " + RQDUnits
    ElseIf order = 5 Then
        myString = "K_rm"
    Else
        myString = ""
    End If
Case 10 'Liquefied Soil (Rollins et al, 2005)
    If order = 1 Then
        myString = "Unit wt, " + DensityUnits
    ElseIf order = 2 Then
        myString = "P-Multiplier"
    Else
        myString = ""
    End If
Case 11 'Liquefied Soil (Brandenberg et al. 2007)
    If order = 1 Then
        myString = "Unit wt, " + DensityUnits
    ElseIf order = 2 Then

```

```

        myString = "Friction Angle, " + FrictionUnits
    ElseIf order = 3 Then
        myString = "P-Y Modulus, K, " + ModUnits
    ElseIf order = 4 Then
        myString = "P-Multiplier"
    Else
        myString = ""
    End If
End Select

SoilParams = myString

End Function

'-----
'*****
'-----
Sub GetInitialFile()

'-----
' This subroutine prompts the user to select the initial .LPD file that will serve as the base
' file for the Monte Carlo Simulation
'-----

Dim Filetoopen As Variant

Filetoopen = Application.GetOpenFilename _
(Title:="Please choose a file to import", _
FileFilter:="LPILE Files *.lpd (*.lpd),")
"

If Filetoopen = False Then
    ' nothing.....close the dialog box
Exit Sub
Else
'First, Clear the existing file name
Range("Filename").Value = ""

myFile = Filetoopen
Range("Filename").Value = myFile

Call DoTheImport 'Imports the basefile to Worksheet Sheet2 so that it can easily be modified

End If

End Sub

'-----

```

‘*****
‘-----

Public Sub ImportTextFile(FName As String, Sep As String)

.....

' ImportTextFile
' This imports a text file into Excel.
.....

Dim RowNdx As Long
Dim ColNdx As Integer
Dim TempVal As Variant
Dim WholeLine As String
Dim Pos As Integer
Dim NextPos As Integer
Dim SaveColNdx As Integer
Dim rowcounter As Integer

Application.ScreenUpdating = False
'On Error GoTo EndMacro:

SaveColNdx = 1
RowNdx = 1
rowcounter = 1
FrontEnd = ""

'Clear Worksheet Sheet2
Worksheets("Sheet2").Range("A1:M200").Clear

Open FName For Input Access Read As #1

While Not EOF(1)
 Line Input #1, WholeLine
 If Right(WholeLine, 1) <> Sep Then
 WholeLine = WholeLine & Sep
 End If
 If rowcounter < 7 Then
 FrontEnd = FrontEnd + WholeLine & vbCrLf
 ColNdx = SaveColNdx
 Pos = 1
 NextPos = InStr(Pos, WholeLine, Sep)
 While NextPos >= 1
 TempVal = Mid(WholeLine, Pos, NextPos - Pos)
 Worksheets("Sheet2").Cells(RowNdx, ColNdx).Value = TempVal

```

        Pos = NextPos + 1
        ColNdx = ColNdx + 1
        NextPos = InStr(Pos, WholeLine, Sep)
    Wend
Else
    ColNdx = SaveColNdx
    Pos = 1
    NextPos = InStr(Pos, WholeLine, Sep)
    While NextPos >= 1
        TempVal = Mid(WholeLine, Pos, NextPos - Pos)
        Worksheets("Sheet2").Cells(RowNdx, ColNdx).Value = TempVal
        Pos = NextPos + 1
        ColNdx = ColNdx + 1
        NextPos = InStr(Pos, WholeLine, Sep)
    Wend
End If
RowNdx = RowNdx + 1
rowcounter = rowcounter + 1
Wend

```

```

EndMacro:
On Error GoTo 0
Application.ScreenUpdating = True
Close #1
.....
' END ImportTextFile
.....

```

'Now, save the base soil parameter values on different cells on the worksheet so they can be pasted back at the end of the Monte Carlo run
Call StoreInitial

'Clear the initial input sheet
Call ClearInputSheet

```

'Now set the model numbers for the user based on the initial input file
Dim numLayers As Integer, x As Integer, y As Integer, finished As Boolean
Dim PropertyCount As Integer
PropertyCount = Worksheets("Sheet2").Range("B4").Value
numLayers = Worksheets("Sheet2").Cells(5 + PropertyCount, 1).Value
finished = False
x = 0
y = 1
For y = 1 To numLayers
    Cells(10 + x, 5).Value = Worksheets("Sheet2").Cells(5 + PropertyCount + y, 1).Value
    x = x + 4

```

Next

End Sub

Sub DoTheImport()

ImportTextFile FName:=Range("Filename").Value, Sep:=vbTab

End Sub

```
'-----  
'*****  
'-----
```

Sub GetOutputFile()

```
'-----  
' This subroutine prompts the user to select the initial .LPD file that will serve as the base  
' file for the Monte Carlo Simulation  
'-----
```

Dim Filetoopen As Variant
'First, Clear the existing file name
Range("Output").Value = ""

Filetoopen = Application.GetOpenFilename _
(Title:="Please choose a file to import", _
FileFilter:="LPILE Files *.lpo (*.lpo)," _
)

If Filetoopen = False Then
 ' nothing.....close the dialog box

Exit Sub

Else

myFile = Filetoopen

Range("Output").Value = myFile

Call DoTheImportOutput 'Imports the Output file to Worksheet Sheet3 so that it can be easily
read

End If

End Sub

```
'-----  
'*****  
'-----
```

Public Sub ImportOutputFile(FName As String)

```
'-----
```

' This function reads the output file from LPILE and records it onto Sheet3

```
Dim sFileName As String
Dim iFileNum As Integer
Dim sBuf As String
Dim x As Integer
Dim NextLine As Boolean
Dim TempVal As Double
Dim ReadValues As Boolean
Dim nonlinear As String
If Worksheets("Sheet1").Range("E7").Value = "y" Then
    nonlinear = "yes"
Else
    nonlinear = "no"
End If

'Clear existing values
Worksheets("Sheet3").Range("A1:F300").Clear

' edit this:
sFileName = FName

' does the file exist? simpleminded test:
If Len(Dir$(sFileName)) = 0 Then
    Exit Sub
End If

x = 1
NextLine = False
ReadValues = True

iFileNum = FreeFile()
Open sFileName For Input As iFileNum

Do While Not EOF(iFileNum)
    Line Input #iFileNum, sBuf
    ' now you have the next line of the file in sBuf
    ' do something useful:
    Debug.Print sBuf

    Select Case nonlinear
        'Identify which type of output LPILE is using: nonlinear analysis or
        linear elastic
```

Case "yes" ' Uses nonlinear output format

If sBuf = "" Then

 If NextLine = True Then

 ReadValues = False

 End If

End If

If NextLine = True Then

 If ReadValues = True Then

 'Read the depth of the nodes

 TempVal = Val(Mid(sBuf, 1, 8))

 Worksheets("Sheet3").Cells(x, 1).Value = TempVal

 'Read the deflections of the nodes

 TempVal = Val(Mid(sBuf, 10, 9))

 Worksheets("Sheet3").Cells(x, 2).Value = TempVal

 'Read the moments of the nodes

 TempVal = Val(Mid(sBuf, 20, 9))

 Worksheets("Sheet3").Cells(x, 3).Value = TempVal

 'Read the shear of the nodes

 TempVal = Val(Mid(sBuf, 30, 9))

 Worksheets("Sheet3").Cells(x, 4).Value = TempVal

 'Read the slope of the nodes

 TempVal = Val(Mid(sBuf, 40, 9))

 Worksheets("Sheet3").Cells(x, 5).Value = TempVal

 x = x + 1

 End If

End If

If sBuf = "-----" Then

 NextLine = True

End If

Case "no" 'Use linear elastic LPILE output format

If sBuf = "" Then

 If NextLine = True Then

 ReadValues = False

 End If

End If

```

If NextLine = True Then
  If ReadValues = True Then
    'Read the depth of the nodes
    TempVal = Val(Mid(sBuf, 1, 8))
    Worksheets("Sheet3").Cells(x, 1).Value = TempVal

    'Read the deflections of the nodes
    TempVal = Val(Mid(sBuf, 10, 9))
    Worksheets("Sheet3").Cells(x, 2).Value = TempVal

    'Read the moments of the nodes
    TempVal = Val(Mid(sBuf, 19, 12))
    Worksheets("Sheet3").Cells(x, 3).Value = TempVal

    'Read the shear of the nodes
    TempVal = Val(Mid(sBuf, 32, 12))
    Worksheets("Sheet3").Cells(x, 4).Value = TempVal

    'Read the slope of the nodes
    TempVal = Val(Mid(sBuf, 45, 10))
    Worksheets("Sheet3").Cells(x, 5).Value = TempVal
    x = x + 1
  End If
End If

If sBuf = "-----" Then
  NextLine = True
End If

End Select

Loop

' close the file
Close iFileNum

End Sub

'-----
'*****
'-----

Public Sub CopyIt()

```



```
'-----  
' Sub to copy the new lpile input file from the Excel worksheet and put it on the clipboard  
'-----
```

```
'I made a variable to hold the text from the cells.  
Dim Txt As String
```

```
'I created a data object to use with the clipboard.  
'You must have 'Microsoft Forms 2.0 Object Library' checked in "Tools" - "References"  
'in order to use the 'DataObject' type.  
Dim MyData As New DataObject
```

```
'Count the number of rows in the output file  
Dim mycounter, x As Integer  
Dim finished As Boolean
```

```
finished = False  
mycounter = 1  
x = 1  
Do While finished = False  
    If Worksheets("Sheet2").Cells(x, 1).Value <> "" Then  
        mycounter = mycounter + 1  
        x = x + 1  
    Else  
        finished = True  
    End If  
Loop
```

```
'Clear the text.  
Txt = ""
```

```
'Add each cell in the sheet to the text variable using the cells function.  
'I just put numbers in this one the numbers you have will depend on where the data is  
'in your form. ( the vtab tells it to move over by one column before the next data is added. )  
Dim y As Integer
```

```
y = 1  
x = 1  
For x = 1 To mycounter  
    For y = 1 To 6  
        If Worksheets("Sheet2").Cells(x, y) <> "" Then  
            If Worksheets("Sheet2").Cells(x, y + 1) <> "" Then  
                Txt = Txt & Worksheets("Sheet2").Cells(x, y) & vbTab  
            Else
```

```

        Txt = Txt & Worksheets("Sheet2").Cells(x, y)
    End If
End If
Next y
    Txt = Txt & vbCrLf
    y = 1
Next x

```

'This uses the Data Object to put the collected text on the clipboard.

```
Application.CutCopyMode = False 'clear the clipboard
```

```
MyData.SetText Txt
```

```
MyData.PutInClipboard
```

```
Dim DataObj As New MSForms.DataObject
```

```
Dim S As String
```

```
DataObj.GetFromClipboard
```

```
S = DataObj.GetText
```

```
Debug.Print S
```

'You are now ready to paste !

```
'Clear the LPILE File
```

```
Open Range("Filename").Value For Output As #1
```

```
Close #1
```

```
'Overwrite with the new file
```

```
'first set a string which contains the path to the file you want to create.
```

```
'this example creates one and stores it in the root directory
```

```
myFile = Range("Filename").Value
```

```
'set and open file for output
```

```
fnum = FreeFile()
```

```
Open myFile For Output As fnum
```

```
'use Print when you want the string without quotation marks
```

```
Print #fnum, S
```

```
Close #fnum
```

```
End Sub
```

```

'-----
'*****
'-----

```

```
Sub StoreInitial()
```

```
'-----
' This subroutine copies and pastes the base soil parameter values in Sheet2 so that the original
' base file can be restored upon completion of the Monte Carlo simulation.
'-----
```

```
Dim x, y, myCount As Integer
Dim PropertyCount As Integer, SoilCount As Integer, DensityCount As Integer,
SoilPropertyCount As Integer, InputCount As Integer, PmultCounter As Integer
PropertyCount = Worksheets("Sheet2").Range("B4").Value
SoilCount = Worksheets("Sheet2").Cells(5 + PropertyCount, 1).Value
DensityCount = Worksheets("Sheet2").Cells(5 + PropertyCount, 2).Value
SoilPropertyCount = Worksheets("Sheet2").Cells(5 + PropertyCount, 3).Value
InputCount = Worksheets("Sheet2").Cells(5 + PropertyCount, 4).Value
PmultCount = Worksheets("Sheet2").Cells(5 + PropertyCount, 5).Value

x = 1
y = 1
myCount = SoilCount + DensityCount + SoilPropertyCount + InputCount + PmultCount
Dim finished As Boolean
finished = False
x = 1
Do While finished = False
  For y = 1 To 6
    Worksheets("Sheet2").Cells(x, 8 + y).Value = Worksheets("Sheet2").Cells(x, y).Value
  Next
  y = 1
  x = x + 1
  If Worksheets("Sheet2").Cells(x, 1).Value = "" Then
    finished = True
  End If
Loop

End Sub
```

```
'-----
'*****
'-----
```

```
Sub myMonteCarlo()
```

```
'-----
' this subroutine performs the monte carlo simulation with LPILE 5.0
'-----
```

```
'First, count the number of layers in the model
Dim numLayers, numPmults As Integer
```

```

Dim PropertyCount As Integer, SoilCount As Integer, DensityCount As Integer,
SoilPropertyCount As Integer, InputCount As Integer, PmultCounter As Integer
Dim boguscount As Integer      'Variable to count the number of LPILE runs that had errors
and are not included in the averaging
PropertyCount = Worksheets("Sheet2").Range("B4").Value
SoilCount = Worksheets("Sheet2").Cells(5 + PropertyCount, 1).Value
DensityCount = Worksheets("Sheet2").Cells(5 + PropertyCount, 2).Value
SoilPropertyCount = Worksheets("Sheet2").Cells(5 + PropertyCount, 3).Value
InputCount = Worksheets("Sheet2").Cells(5 + PropertyCount, 4).Value
PmultCount = Worksheets("Sheet2").Cells(5 + PropertyCount, 5).Value
numLayers = Worksheets("Sheet2").Cells(5 + PropertyCount, 1).Value
numPmults = Worksheets("Sheet2").Cells(5 + PropertyCount, 5).Value

```

```

'Next, store the depths of the P-multipliers in an array
Dim myPmultDepths() As Double, y As Integer, myCount As Integer

```

```

myCount = SoilCount + DensityCount + SoilPropertyCount
y = 1
If numPmults > 0 Then
    ReDim myPmultDepths(numPmults)
    For y = 1 To numPmults
        myPmultDepths(y) = Worksheets("sheet2").Cells(5 + PropertyCount + myCount + y, 1)
    Next
Else
    'nothing
End If

```

```

'Next, identify if we need to consider a pile group with a rotational spring
Dim SpringRow As Integer
Dim InitialSpring As Double
Dim completed As Boolean
completed = False
y = 1
If Worksheets("Group Effects").Range("D2").Value = "y" Then
    InitialSpring = Worksheets("Group Effects").Range("D3").Value
    Do While completed = False
        If Worksheets("Sheet2").Cells(y, 3).Value = InitialSpring Then
            SpringRow = y
            completed = True
        End If
        y = y + 1
    If y = 500 Then '.....something wrong.....should have found the value.....abort!!
        MsgBox "Bad initial rotational spring specified. Please verify that the value input on the
'Group Effects' worksheet matches the initial spring in the base LPILE input file.", vbCritical,
"Error.....Bad Input"
        Exit Sub
    End If

```

```
End If
Loop
End If
```

'Then, identify the p-multiplier layers that are associated with liquefiable layers (i.e. random variables)

```
Dim Pmult() As Double, CountasLiquefied() As Boolean, LayerTop(), IsLiq() As Boolean,
PmultTop() As Double
```

```
Dim m As Integer, numLiqLayers As Integer
```

```
ReDim Pmult(numPmults) As Double
```

```
ReDim CountasLiquefied(numPmults) As Boolean
```

```
ReDim LayerTop(numLayers)
```

```
ReDim IsLiq(numLayers) As Boolean
```

```
ReDim PmultTop(numPmults) As Double
```

```
m = 1
```

```
y = 0
```

```
numLiqLayers = 0
```

```
For m = 1 To numLayers
```

```
LayerTop(m) = Worksheets("Sheet2").Cells(5 + PropertyCount + m, 2).Value
```

```
If Cells(10 + y, 5).Value = 11 Then
```

```
numLiqLayers = numLiqLayers + 1
```

```
IsLiq(m) = True
```

```
ElseIf Cells(10 + y, 5).Value = 10 Then
```

```
numLiqLayers = numLiqLayers + 1
```

```
IsLiq(m) = True
```

```
Else
```

```
IsLiq(m) = False
```

```
End If
```

```
y = y + 4
```

```
Next
```

```
Dim LiqLayerTop() As Double, LiqLayerNumber() As Double, n As Integer
```

```
ReDim LiqLayerTop(numLiqLayers) As Double, LiqLayerNumber(numLiqLayers) As Double
```

```
m = 1
```

```
n = 1
```

```
For m = 1 To numLayers
```

```
If IsLiq(m) = True Then
```

```
LiqLayerTop(n) = LayerTop(m)
```

```
LiqLayerNumber(n) = m
```

```
n = n + 1
```

```
End If
```

```
Next
```

```
m = 1
```

```
n = 1
```

```

For m = 1 To numPmults
If myPmultDepths(m) = LiqLayerTop(n) Then
    CountasLiquefied(m) = True
    m = m + 1
    CountasLiquefied(m) = True
    n = n + 1
    If n > numLiqLayers Then
        n = numLiqLayers
    End If
Else
    CountasLiquefied(m) = False
    m = m + 1
    CountasLiquefied(m) = False
End If
Next

```

'Next, define the temporary arrays where each simulated random variable will be stored

```

Dim Strength() As Double, Density() As Double, Friction() As Double, Strain() As Double,
Modulus() As Double, RQD() As Double
ReDim Strength(numLayers) As Double, Density(numLayers) As Double, Friction(numLayers)
As Double, Strain(numLayers) As Double, Modulus(numLayers) As Double, RQD(numLayers)
As Double

```

'Next, redefine the final arrays where the combined values will be stored

```

Dim numIterations As Integer, numDepths As Integer, j As Integer
numIterations = Range("Iter").Value
numDepths = Worksheets("Sheet2").Range("A4").Value + 1
Dim Depth() As Double, Deflect() As Double, Moment() As Double, Shear() As Double, Slope()
As Double
ReDim Depth(numDepths) As Double
ReDim Deflect(numIterations, numDepths) As Double
ReDim Moment(numIterations, numDepths) As Double
ReDim Shear(numIterations, numDepths) As Double
ReDim Slope(numIterations, numDepths) As Double

```

'Now, iterate through each monte carlo iteration

```

Dim x As Integer
Dim modelNum As Integer

```

```

j = 1
x = 0
y = 0
Dim h As Integer
h = 1
boguscount = 0
For j = 1 To numIterations

```

```

Range("Counter") = j
'Now, Iterate through each soil layer
h = 1
x = 0
For h = 1 To numLayers
  If Cells(10 + x, 5).Value <> "" Then
    modelNum = Cells(10 + x, 5).Value
    Select Case modelNum
      Case 1 'Soft Clay (Matlock, 1970)
        Modulus(h) = 0
        Density(h) = GenerateParam(Cells(10 + x, 7).Value, Cells(11 + x, 7).Value, Cells(12 +
x, 7).Value)
        Strength(h) = GenerateParam(Cells(10 + x, 9).Value, Cells(11 + x, 9).Value, Cells(12
+ x, 9).Value)
        Friction(h) = 0
        Strain(h) = GenerateParam(Cells(10 + x, 11).Value, Cells(11 + x, 11).Value, Cells(12
+ x, 11).Value)
        RQD(h) = 0
      Case 2 'Stiff Clay with Free Water (Reese)
        Modulus(h) = GenerateParam(Cells(10 + x, 11).Value, Cells(11 + x, 11).Value,
Cells(12 + x, 11).Value)
        Density(h) = GenerateParam(Cells(10 + x, 7).Value, Cells(11 + x, 7).Value, Cells(12 +
x, 7).Value)
        Strength(h) = GenerateParam(Cells(10 + x, 9).Value, Cells(11 + x, 9).Value, Cells(12
+ x, 9).Value)
        Friction(h) = 0
        Strain(h) = GenerateParam(Cells(10 + x, 13).Value, Cells(11 + x, 13).Value, Cells(12
+ x, 13).Value)
        RQD(h) = 0
      Case 3 'Stiff Clay w/out Free Water (Reese)
        Modulus(h) = 0
        Density(h) = GenerateParam(Cells(10 + x, 7).Value, Cells(11 + x, 7).Value, Cells(12 +
x, 7).Value)
        Strength(h) = GenerateParam(Cells(10 + x, 9).Value, Cells(11 + x, 9).Value, Cells(12
+ x, 9).Value)
        Friction(h) = 0
        Strain(h) = GenerateParam(Cells(10 + x, 11).Value, Cells(11 + x, 11).Value, Cells(12
+ x, 11).Value)
        RQD(h) = 0
      Case 4 'Sand (Reese)
        Modulus(h) = GenerateParam(Cells(10 + x, 11).Value, Cells(11 + x, 11).Value,
Cells(12 + x, 11).Value)
        Density(h) = GenerateParam(Cells(10 + x, 7).Value, Cells(11 + x, 7).Value, Cells(12 +
x, 7).Value)
        Strength(h) = 0

```

Friction(h) = GenerateParam(Cells(10 + x, 9).Value, Cells(11 + x, 9).Value, Cells(12 + x, 9).Value)
 Strain(h) = 0
 RQD(h) = 0
 Case 6 'Strong Rock (Vuggy Limestone)
 Modulus(h) = 0
 Density(h) = GenerateParam(Cells(10 + x, 7).Value, Cells(11 + x, 7).Value, Cells(12 + x, 7).Value)
 Strength(h) = GenerateParam(Cells(10 + x, 9).Value, Cells(11 + x, 9).Value, Cells(12 + x, 9).Value)
 Friction(h) = 0
 Strain(h) = 0
 RQD(h) = 0
 Case 7 'Silt (cemented c-phi soil)
 Modulus(h) = GenerateParam(Cells(10 + x, 13).Value, Cells(11 + x, 13).Value, Cells(12 + x, 13).Value)
 Density(h) = GenerateParam(Cells(10 + x, 7).Value, Cells(11 + x, 7).Value, Cells(12 + x, 7).Value)
 Strength(h) = GenerateParam(Cells(10 + x, 9).Value, Cells(11 + x, 9).Value, Cells(12 + x, 9).Value)
 Friction(h) = GenerateParam(Cells(10 + x, 11).Value, Cells(11 + x, 11).Value, Cells(12 + x, 11).Value)
 Strain(h) = GenerateParam(Cells(10 + x, 15).Value, Cells(11 + x, 15).Value, Cells(12 + x, 15).Value)
 RQD(h) = 0
 Case 8 'API Sand
 Modulus(h) = GenerateParam(Cells(10 + x, 11).Value, Cells(11 + x, 11).Value, Cells(12 + x, 11).Value)
 Density(h) = GenerateParam(Cells(10 + x, 7).Value, Cells(11 + x, 7).Value, Cells(12 + x, 7).Value)
 Strength(h) = 0
 Friction(h) = GenerateParam(Cells(10 + x, 9).Value, Cells(11 + x, 9).Value, Cells(12 + x, 9).Value)
 Strain(h) = 0
 RQD(h) = 0
 Case 9 'Weak Rock
 Modulus(h) = GenerateParam(Cells(10 + x, 9).Value, Cells(11 + x, 9).Value, Cells(12 + x, 9).Value)
 Density(h) = GenerateParam(Cells(10 + x, 7).Value, Cells(11 + x, 7).Value, Cells(12 + x, 7).Value)
 Strength(h) = GenerateParam(Cells(10 + x, 11).Value, Cells(11 + x, 11).Value, Cells(12 + x, 11).Value)
 Friction(h) = 0
 Strain(h) = GenerateParam(Cells(10 + x, 15).Value, Cells(11 + x, 15).Value, Cells(12 + x, 15).Value)


```

    RQD(h) = GenerateParam(Cells(10 + x, 13).Value, Cells(11 + x, 13).Value, Cells(12 +
x, 13).Value)
    Case 10 'Liquefied Soil (Rollins et al, 2005)
        Modulus(h) = 0
        Density(h) = GenerateParam(Cells(10 + x, 7).Value, Cells(11 + x, 7).Value, Cells(12 +
x, 7).Value)
        Strength(h) = 0
        Friction(h) = 0
        Strain(h) = 0
        RQD(h) = 0
    Case 11 'Liquefied Soil (Brandenberg et al. 2007)
        Modulus(h) = GenerateParam(Cells(10 + x, 11).Value, Cells(11 + x, 11).Value,
Cells(12 + x, 11).Value)
        Density(h) = GenerateParam(Cells(10 + x, 7).Value, Cells(11 + x, 7).Value, Cells(12 +
x, 7).Value)
        Strength(h) = 0
        Friction(h) = GenerateParam(Cells(10 + x, 9).Value, Cells(11 + x, 9).Value, Cells(12 +
x, 9).Value)
        Strain(h) = 0
        RQD(h) = 0
    End Select
End If
x = x + 4
Next

```

'Modify the P-multipliers

```

    n = 1
    y = 1
    For y = 1 To numPmults
        If CountasLiquefied(y) = True Then
            If Worksheets("Group Effects").Range("D2").Value = "n" Then
                Pmult(y) = GenerateParam(Cells(10 + (4 * LiqLayerNumber(n) - 4), 13).Value,
Cells(11 + (4 * LiqLayerNumber(n) - 4), 13).Value, Cells(12 + (4 * LiqLayerNumber(n) - 4),
13).Value)
                y = y + 1
                Pmult(y) = Pmult(y - 1)
                n = n + 1
            Else
                Pmult(y) = GenerateParam(Cells(10 + (4 * LiqLayerNumber(n) - 4), 13).Value,
Cells(11 + (4 * LiqLayerNumber(n) - 4), 13).Value, Cells(12 + (4 * LiqLayerNumber(n) - 4),
13).Value)
                Pmult(y) = Pmult(y) * Worksheets("Group Effects").Range("B22").Value
                y = y + 1
                Pmult(y) = Pmult(y - 1)
                n = n + 1
            End If
        End If
    Next

```

```

Else
    Pmult(y) = Worksheets("Sheet2").Cells(5 + PropertyCount + myCount + y,
2).Value
    y = y + 1
    Pmult(y) = Pmult(y - 1)
End If
Next

```

'Now, write the values in the arrays to the spreadsheet and copy it to the new file

```

x = 1
For x = 1 To numLayers
    'Modulus values
    Worksheets("Sheet2").Cells(5 + PropertyCount + x, 4).Value = Modulus(x)
    Worksheets("Sheet2").Cells(5 + PropertyCount + x, 5).Value = Modulus(x)

    'Densities
    Worksheets("Sheet2").Cells(5 + PropertyCount + SoilCount + 2 * x - 1, 2).Value =
Density(x)
    Worksheets("Sheet2").Cells(5 + PropertyCount + SoilCount + 2 * x, 2).Value = Density(x)

    'Other Soil Parameters
    Worksheets("Sheet2").Cells(5 + PropertyCount + SoilCount + DensityCount + 2 * x - 1,
2).Value = Strength(x)
    Worksheets("Sheet2").Cells(5 + PropertyCount + SoilCount + DensityCount + 2 * x - 1,
3).Value = Friction(x)
    Worksheets("Sheet2").Cells(5 + PropertyCount + SoilCount + DensityCount + 2 * x - 1,
4).Value = Strain(x)
    Worksheets("Sheet2").Cells(5 + PropertyCount + SoilCount + DensityCount + 2 * x - 1,
5).Value = RQD(x)
    Worksheets("Sheet2").Cells(5 + PropertyCount + SoilCount + DensityCount + 2 * x,
2).Value = Strength(x)
    Worksheets("Sheet2").Cells(5 + PropertyCount + SoilCount + DensityCount + 2 * x,
3).Value = Friction(x)
    Worksheets("Sheet2").Cells(5 + PropertyCount + SoilCount + DensityCount + 2 * x,
4).Value = Strain(x)
    Worksheets("Sheet2").Cells(5 + PropertyCount + SoilCount + DensityCount + 2 * x,
5).Value = RQD(x)

```

'If analyzing a pile group, then modify the parameters to update the rotational spring and then update the input file

```

If Worksheets("Group Effects").Range("D2").Value = "y" Then
    Worksheets("Group Effects").Cells(25 + x, 6).Value = Strength(x)
    Worksheets("Group Effects").Cells(25 + x, 5).Value = Friction(x)
    Worksheets("Group Effects").Cells(25 + x, 3).Value = Density(x)
If SpringRow > 1 Then

```

```

Worksheets("Sheet2").Cells(SpringRow, 3).Value = Round(Worksheets("Group
Effects").Range("D71").Value, 0)
End If
End If
Next

```

```

'Now do the p-multipliers
x = 1
For x = 1 To numPmults
Worksheets("Sheet2").Cells(5 + PropertyCount + x + SoilCount + DensityCount +
SoilPropertyCount, 2).Value = Pmult(x)
Next

```

```

'Now, overwrite the base LPILE file with the new one
Call CopyIt

```

```

'Run the Analysis in LPILE
Dim ss
Dim starttime, waittime, currenttime

```

```

Filename = Range("Filename")
If j = 1 Then
waittime = 4
'Set ss = CreateObject("WScript.Shell")
'ss.Run "Cmd"
ss = Shell("c:\program files\ensoft\lpilep5\lpilep5.exe", 1)
AppActivate ss
starttime = Timer()
currenttime = starttime
Do Until currenttime - starttime > waittime
'Do nothing
currenttime = Timer()
Loop
SendKeys "%F", True
DoEvents
SendKeys "o", True
DoEvents
waittime = 0.3
starttime = Timer()
currenttime = starttime
Do Until currenttime - starttime > waittime
'Do nothing
currenttime = Timer()
Loop
SendKeys Filename, True

```

```

DoEvents
starttime = Timer()
currenttime = starttime
Do Until currenttime - starttime > waittime
    'Do nothing
    currenttime = Timer()
Loop
SendKeys "{ENTER}", True
DoEvents
starttime = Timer()
currenttime = starttime
Do Until currenttime - starttime > waittime
    'Do nothing
    currenttime = Timer()
Loop
SendKeys "{Enter}", True
DoEvents
waittime = 0.1
starttime = Timer()
currenttime = starttime
Do Until currenttime - starttime > waittime
    'Do nothing
    currenttime = Timer()
Loop
waittime = 0.3
SendKeys "{Enter}", True
DoEvents
starttime = Timer()
currenttime = starttime
Do Until currenttime - starttime > waittime
    'Do nothing
    currenttime = Timer()
Loop
SendKeys "%c", True
DoEvents
starttime = Timer()
currenttime = starttime
Do Until currenttime - starttime > waittime
    'Do nothing
    currenttime = Timer()
Loop
SendKeys "r", True
DoEvents
starttime = Timer()
currenttime = starttime
Do Until currenttime - starttime > waittime

```

```

    'Do nothing
    currenttime = Timer()
Loop
SendKeys "{enter}", True
DoEvents
starttime = Timer()
currenttime = starttime
Do Until currenttime - starttime > waittime
    'Do nothing
    currenttime = Timer()
Loop
Set ss = Nothing

Else
    waittime = 0.35

    SendKeys "%F", True
    DoEvents

    SendKeys "o", True
    DoEvents

    starttime = Timer()
    currenttime = starttime
    Do Until currenttime - starttime > waittime
        'Do nothing
        currenttime = Timer()
    Loop

    SendKeys Filename, True
    DoEvents

    SendKeys "{ENTER}", True
    DoEvents

    waittime = 0.1
    starttime = Timer()
    currenttime = starttime
    Do Until currenttime - starttime > waittime
        'Do nothing
        currenttime = Timer()
    Loop
    SendKeys "{Enter}", True
    DoEvents

    waittime = 0.3

```

```

starttime = Timer()
currenttime = starttime
Do Until currenttime - starttime > waittime
    'Do nothing
    currenttime = Timer()
Loop
SendKeys "{Enter}", True
DoEvents

SendKeys "%c", True
DoEvents

SendKeys "r", True
DoEvents

waittime = 0.4
starttime = Timer()
currenttime = starttime
Do Until currenttime - starttime > waittime
    'Do nothing
    currenttime = Timer()
Loop
SendKeys "{enter}", True
DoEvents
waittime = 0.3
starttime = Timer()
currenttime = starttime
Do Until currenttime - starttime > waittime
    'Do nothing
    currenttime = Timer()
Loop
Set ss = Nothing

If j = numIterations Then
    starttime = Timer()
    currenttime = starttime
    Do Until currenttime - starttime > waittime
        'Do nothing
        currenttime = Timer()
    Loop
    SendKeys "%F", True
    DoEvents
    SendKeys "x", True
    DoEvents
End If
End If

```

```

Dim bogus As Boolean
If j = 3 Then
bogus = True
End If

'Retrieve the results from LPILE and store them in the appropriate array
Dim myOutput As String
Dim myDenominator As Double
If Worksheets("Group Effects").Range("D2").Value = "y" Then
    myDenominator = (Worksheets("Group Effects").Range("B9").Value * Worksheets("Group
Effects").Range("B10").Value)
End If
myOutput = Worksheets("Sheet1").Range("Output").Value
ImportOutputFile (myOutput)
x = 1
If Worksheets("Sheet3").Cells(1, 1).Value = "" Then 'If there was an error in the LPILE
analysis, then do not include the faulty results
    boguscount = boguscount + 1
    j = j - 1
Else
    'The LPILE analysis was successful so include the results
    For x = 1 To numDepths
        'Record the depths .....(only once)
        If j = 1 Then
            Depth(x) = Worksheets("Sheet3").Cells(x, 1).Value
        End If

        'Record the Displacements
        Deflect(j, x) = Worksheets("Sheet3").Cells(x, 2).Value

        'Record the Moment
        Moment(j, x) = Worksheets("Sheet3").Cells(x, 3).Value

        'Record the Shear
        Shear(j, x) = Worksheets("Sheet3").Cells(x, 4).Value

        'Record the Slope
        Slope(j, x) = Worksheets("Sheet3").Cells(x, 5).Value
    Next
End If
Next
'Completed all the iterations

'Compute the Means and Std Deviations for deflect, moment, shear, and slope at all the nodes
and record them
'Clear the existing results

```

```

Worksheets("Results").Range("A2:I400").Clear
'Write the depths
x = 1
For x = 1 To numDepths
    Worksheets("Results").Cells(x + 1, 1) = Depth(x)
Next

'correct the number of iterations to discount the LPILE runs which had errors
numIterations = numIterations - boguscount

'Compute and write the means
Dim TempDeflect As Double, TempMoment As Double, TempShear As Double, TempSlope
As Double
TempDeflect = 0
TempMoment = 0
TempShear = 0
TempSlope = 0
x = 1
y = 1
For x = 1 To numDepths
    If x = 74 Then
        bogus = True
    End If
    For y = 1 To numIterations
        TempDeflect = TempDeflect + Deflect(y, x)
        TempMoment = TempMoment + Moment(y, x)
        TempShear = TempShear + Shear(y, x)
        TempSlope = TempSlope + Slope(y, x)
    Next
    y = 1
    If Worksheets("Group Effects").Range("D2").Value = "n" Then
        Worksheets("Results").Cells(x + 1, 2).Value = TempDeflect / numIterations
        Worksheets("Results").Cells(x + 1, 4).Value = TempShear / numIterations
        Worksheets("Results").Cells(x + 1, 6).Value = TempMoment / numIterations
        Worksheets("Results").Cells(x + 1, 8).Value = TempSlope / numIterations
        TempDeflect = 0
        TempShear = 0
        TempMoment = 0
        TempSlope = 0
    Else
        Worksheets("Results").Cells(x + 1, 2).Value = TempDeflect / numIterations
        Worksheets("Results").Cells(x + 1, 4).Value = TempShear / numIterations /
myDenominator
        Worksheets("Results").Cells(x + 1, 6).Value = TempMoment / numIterations /
myDenominator
        Worksheets("Results").Cells(x + 1, 8).Value = TempSlope / numIterations

```



```

    TempDeflect = 0
    TempShear = 0
    TempMoment = 0
    TempSlope = 0
End If
Next

'Compute and write the Standard Deviations
Dim AvgDeflect As Double, AvgMoment As Double, AvgShear As Double, AvgSlope As
Double
AvgDeflect = 0
AvgMoment = 0
AvgShear = 0
AvgSlope = 0
TempDeflect = 0
TempMoment = 0
TempShear = 0
TempSlope = 0
x = 1
y = 1

For x = 1 To numDepths

    AvgDeflect = Worksheets("Results").Cells(x + 1, 2).Value
    AvgShear = Worksheets("Results").Cells(x + 1, 4).Value
    AvgMoment = Worksheets("Results").Cells(x + 1, 6).Value
    AvgSlope = Worksheets("Results").Cells(x + 1, 8).Value
    If Worksheets("Group Effects").Range("D2").Value = "n" Then
        For y = 1 To numIterations
            TempDeflect = TempDeflect + (Deflect(y, x) - AvgDeflect) ^ 2
            TempMoment = TempMoment + (Moment(y, x) - AvgMoment) ^ 2
            TempShear = TempShear + (Shear(y, x) - AvgShear) ^ 2
            TempSlope = TempSlope + (Slope(y, x) - AvgSlope) ^ 2
        Next
        y = 1
    Else
        For y = 1 To numIterations
            TempDeflect = TempDeflect + (Deflect(y, x) - AvgDeflect) ^ 2
            TempMoment = TempMoment + (Moment(y, x) / myDenominator - AvgMoment) ^ 2
            TempShear = TempShear + (Shear(y, x) / myDenominator - AvgShear) ^ 2
            TempSlope = TempSlope + (Slope(y, x) - AvgSlope) ^ 2
        Next
        y = 1
    End If
    Worksheets("Results").Cells(x + 1, 3).Value = Sqr(TempDeflect / (numIterations - 1))
    Worksheets("Results").Cells(x + 1, 5).Value = Sqr(TempShear / (numIterations - 1))

```

```

Worksheets("Results").Cells(x + 1, 7).Value = Sqr(TempMoment / (numIterations - 1))
Worksheets("Results").Cells(x + 1, 9).Value = Sqr(TempSlope / (numIterations - 1))
TempDeflect = 0
TempShear = 0
TempMoment = 0
TempSlope = 0
Next

```

'Write the original (mean) values back into the LPILE input file and resave

```
finished = False
```

```
x = 1
```

```
y = 1
```

```
Do While finished = False
```

```
  For y = 1 To 6
```

```
    Worksheets("Sheet2").Cells(x, y).Value = Worksheets("Sheet2").Cells(x, 8 + y).Value
```

```
  Next
```

```
  y = 1
```

```
  x = x + 1
```

```
  If Worksheets("Sheet2").Cells(x, 9).Value = "" Then
```

```
    finished = True
```

```
  End If
```

```
Loop
```

Call CopyIt 'Rewrite the original base LPILE file

```
End Sub
```

```

'-----
'*****
'-----

```

```
Function GenerateParam(mean As Double, Sigma As Double, Distribution As Integer) As Double
```

```
'-----
```

```
' this function generates a randomized parameter for the given unknown corresponding to the given
```

```
' mean, standard distribution, and probabilistic distribution function
```

```
'-----
```

```
Dim max As Double, min As Double
```

```
Dim logmean As Double
```

```
Dim logmin As Double
```

```
Dim logmax As Double
```

```
Dim x As Double
```

If Sigma = 0 Then 'No uncertainty.....just return the mean value

GenerateParam = mean

Else

Select Case Distribution

Case 1 'Linear

max = mean + 3 * Sigma

min = mean - 3 * Sigma

If min < 0 Then

min = 0

End If

GenerateParam = (max - min) * Rnd + min

Case 2 'Normal

max = mean + 3 * Sigma

min = mean - 3 * Sigma

If min < 0 Then

min = 0

End If

GenerateParam = normal_dist(mean, Sigma, min, max)

Case 3 'Lognormal

logmean = Log10(mean)

max = mean + 3 * Sigma

min = mean - 3 * Sigma

If min <= 0 Then

min = 0.01

End If

logmin = Log10(min)

logmax = Log10(max)

x = normal_dist(logmean, Sigma, logmin, logmax)

GenerateParam = 10 ^ x

End Select

End If

End Function

Static Function Log10(x)

Log10 = Log(x) / Log(10#)

End Function

'*****
'-----

* Returns random numbers from a Truncated & Scaled Normal Distribution

Function normal_dist(mean, stdev, min, max)

Dim x As Double

```

Do
    x = gauss * stdev + mean
Loop While x < min Or x > max
normal_dist = x
End Function

'-----
'*****
'-----

'*****
'*   Return random numbers from Standard Normal Distribution
'*****

Function gauss()
    Dim fac As Double, r As Double, V1 As Double, V2 As Double
    Do
        V1 = 2 * Rnd - 1
        V2 = 2 * Rnd - 1
        r = V1 ^ 2 + V2 ^ 2
    Loop While (r >= 1)
    fac = Sqr(-2 * Log(r) / r)
    gauss = V2 * fac
End Function

'-----
'*****
'-----

Sub ClearInputSheet()
'-----
' This function clears all of the input values on the main sheet when you import a new file
'-----
Dim x As Integer, y As Integer

x = 1
y = 1

For x = 1 To 6
    For y = 1 To 12
        Cells(10 + (y * 4) - 4, 5 + (x * 2) - 2).Value = ""
        Cells(11 + (y * 4) - 4, 5 + (x * 2) - 2).Value = ""
        Cells(12 + (y * 4) - 4, 5 + (x * 2) - 2).Value = ""
    Next
Next
End Sub

```

```
'-----  
'*****  
'-----
```

```
Sub RunLPILE()
```

```
'-----  
' This Subroutine opens and runs LPILE v5.0 multiple times using the specified input file by  
the user  
'-----
```

```
Dim ss  
Dim starttime, waittime, currenttime  
Dim Filename As String
```

```
Filename = Range("Filename")  
waittime = 4  
'Set ss = CreateObject("WScript.Shell")  
'ss.Run "Cmd"  
ss = Shell("c:\program files\ensoft\lpilep5\lpilep5.exe", 1)  
AppActivate ss  
starttime = Timer()  
currenttime = starttime  
Do Until currenttime - starttime > waittime  
    'Do nothing  
    currenttime = Timer()  
Loop  
SendKeys "%F", True  
DoEvents  
SendKeys "o", True  
DoEvents  
SendKeys Filename, True  
DoEvents  
SendKeys "{ENTER}", True  
DoEvents  
SendKeys "{Enter}", True  
DoEvents  
SendKeys "%c", True  
DoEvents  
SendKeys "r", True  
DoEvents  
SendKeys "{enter}", True  
SendKeys "%F", True  
DoEvents  
SendKeys "x", True
```

```
DoEvents
Set ss = Nothing
```

```
End Sub
```

```
'-----
'*****
'-----
```

```
Function GroupFactor(dD As Double, phi As Double) As Double
```

```
'-----
' This function estimates the pile group efficiency factor for sand presented by
' Kishida and Meyerhoff (1965)
'-----
```

```
Dim n30 As Double, n35 As Double, n40 As Double, n45 As Double
```

```
'compute the n30 parameter
```

```
If dD <= 2 Then
```

```
    n30 = 3
```

```
ElseIf dD >= 7 Then
```

```
    n30 = 1
```

```
Else
```

```
    n30 = 5.341 * dD ^ (-0.876)
```

```
End If
```

```
'compute the n35 parameter
```

```
If dD <= 1 Then
```

```
    n35 = 2.1
```

```
ElseIf dD >= 7 Then
```

```
    n35 = 1
```

```
Else
```

```
    n35 = -0.0032 * dD ^ 3 + 0.069 * dD ^ 2 - 0.5517 * dD + 2.5698
```

```
End If
```

```
'compute the n40 parameter
```

```
n40 = 1
```

```
'compute the n45 parameter
```

```
If dD <= 1 Then
```

```
    n45 = 0.5
```

```
ElseIf dD >= 6.5 Then
```

```
    n45 = 1
```

```
Else
```

```
    n45 = 0.2662 * Application.WorksheetFunction.Ln(dD) + 0.5058
```

```
End If
```

```
If phi < 30 Then
```

```

    GroupFactor = n30
ElseIf phi < 35 Then
    GroupFactor = InterpolateValue(phi, 30, 35, n30, n35)
ElseIf phi < 40 Then
    GroupFactor = InterpolateValue(phi, 35, 40, n35, n40)
ElseIf phi < 45 Then
    GroupFactor = InterpolateValue(phi, 40, 45, n40, n45)
Else
    GroupFactor = n45
End If

```

End Function

```

'-----
'*****
'-----

```

Function InterpolateValue(xTarget As Double, xUpper As Double, xLower As Double,
myUpper As Double, myLower As Double) As Double

```

'-----
'    Function performs simple linear interpolation to find a data point
'-----

```

```

Dim denominator As Double, numerator As Double, ratio As Double
denominator = xUpper - xLower
numerator = xTarget - xLower
ratio = numerator / denominator

```

```

InterpolateValue = myLower + ratio * (myUpper - myLower)

```

End Function

APPENDIX D. PERFORMANCE-BASED PILE RESPONSE SOFTWARE

Introduction

A computer application for performing many of the performance-based lateral spread and pile response computations was developed as part of this study and is called Performance-based Pile Response Software or PPRS (pronounced ‘peppers’). It enables a user to conveniently and relatively rapidly perform the performance-based liquefaction, lateral spread, and pile response procedures described in Chapter 6.

Developmental Environment used to Create PPRS

In order to overcome many of the obstacles that exist when developing a cross-platform program, it was decided to develop PPRS in the Microsoft .NET environment. When Microsoft announced the idea of .NET in late 1999, it was positioned as a platform for building and consuming Extensible Markup Language (XML) Web services. Because XML transfers data using established standard protocols that exist today (i.e. SOAP, HTTP, SMTP, etc.,) programs that utilize XML can be used cross-platform with little or no modification to their source code. The Microsoft .NET environment also caters to applications meant to be used over the internet because the XML format of the application allows it run on any type of computer system and to consume data from any type of server (Beres, 2003).

The actual development of PPRS was performed using Microsoft Visual Studio .NET (Microsoft Visual Studio, 2003). Visual Studio .NET incorporates *object-oriented programming*,

which is a convenient and powerful way to develop applications. Events and objects of the applications are divided into classes and subclasses, which can be easily called, utilized, and terminated. Programming this way takes away much of the repetition that can make the source code of many applications lengthy in size and difficult to understand. The actual programming language that was used to develop PPRS was Visual Basic .NET.

PPRS Overview

PPRS was developed for three main purposes: 1) to develop performance-based liquefaction triggering profiles using the Kramer and Mayfield (2007) procedure, 2) to compute performance-based lateral spread displacements using empirical models in accordance with the Kramer et al. (2007) procedure, and 3) to compute performance-based pile response from user-defined input in accordance with the procedure described in Chapter 6. To achieve these purposes, PPRS is organized according to six general tabs: the Loading Tab, the Soil Profile Tab, the Slope Geometry Tab, the Lateral Spread Tab, and the Pile Tab. These tabs were developed and modeled after LS Displacement Tool, a simplified software tool developed to compute performance-based lateral spread displacements (Franke, 2005). A screenshot of PPRS is shown in Figure D-1.

The Loading Tab

In order to characterize earthquake loading considering all combinations of magnitude and distance across all return periods, PPRS allows the user to either import site-specific deaggregation files from EZ-FRISK (Performance-based Analysis) or import approximated deaggregation files from the USGS 2008 interactive deaggregation website (Weighted Analysis).

Either approach requires that the user import deaggregation files corresponding to seven different return periods: 108 years, 225 years, 475 years, 975 years, 2475 years, 4975 years, and 100000 years. If using the USGS option, ground motions are not available at 100000 years. However, the user can substitute ground motions corresponding to a 1-percent probability of exceedance in 200 years (i.e. return period of 20000 years) instead to account for very rare earthquake events.

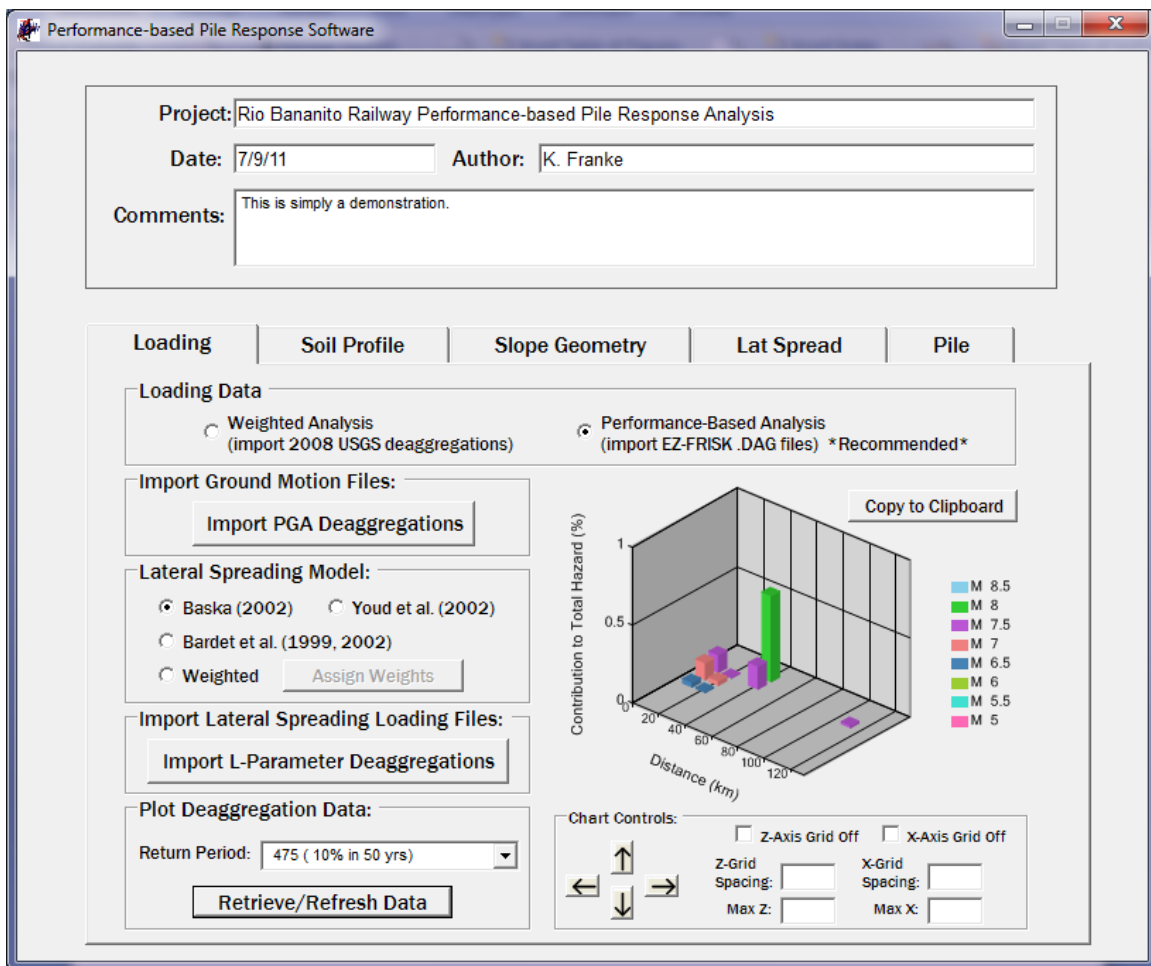


Figure D-1: Screenshot of Performance-Based Pile Response Software (PPRS)

Import 2008 USGS Deaggregation Files (Weighted Analysis)

If the user does not have access to the site-specific seismic hazard analysis software EZ-FRISK, then the probabilistic values of the lateral spread loading parameter \mathcal{L} can be approximated by using the magnitude/distance distributions corresponding to the peak ground acceleration (PGA) made available by the USGS as a proxy. This approach will introduce some bias into the results because there will inherently be differences between the lateral spread loading parameter \mathcal{L} and the PGA.

*Import EZ-FRISK *.DAG File (Performance-based Analysis)*

PPRS allows the user to perform site-specific analyses on a much finer grid than that incorporated in the program itself by importing the loading data directly from EZ-FRISK deaggregation output files (i.e. *.DAG files). When performing this type of analysis, the user must enter deaggregation files corresponding to both the PGA and the desired lateral spread loading parameter(s) \mathcal{L} .

Lateral Spread Model

PPRS allows some flexibility to the user in selecting which empirical lateral spread model(s) to incorporate into the computation of performance-based lateral spread displacements. The user may either specify the Youd et al. (2002) model, the Bardet et al. (1999, 2002) model, the Baska (2002) model, or a weighted combination of multiple models. If using the Performance-based Analysis option in conjunction with a single lateral spread model, then the seven lateral spread loading parameter deaggregation files can be specified by pressing the “Import L-Parameter Deaggregations” button. However, if using a weighted option, then the user

will import the deaggregation loading parameter files when the lateral spread hazard curve is being computed.

Deaggregation Plot

Once loading parameter deaggregation values have been imported, the user has the option to view any of the seven deaggregations in a simplified plot on the Loading Tab. The plot incorporates a basic plotting package made available for free use by Dundas Chart Software. The user has the flexibility to rotate the plot either horizontally or vertically to provide an ideal view of the magnitude/distance distribution on the plot. In addition, the user can control axis grid spacing, maximum value, and minimum value on the plot. Finally, the user can copy the deaggregation plot for pasting in other applications by pressing the “Copy to Clipboard” button. An example of the deaggregation plot is shown in Figure D-2.

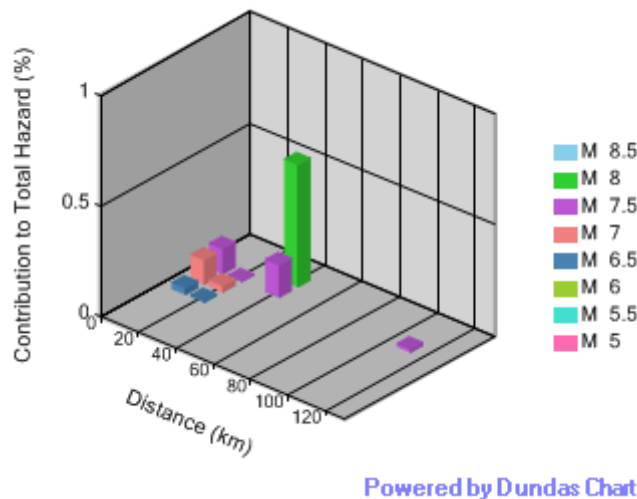


Figure D-2: Example of a Deaggregation Plot Produced by PPRS

The Soil Profile Tab

The Soil Profile Tab allows the user to characterize the native soil layering for the performance-based liquefaction and lateral spread analyses. The user may define the number of sublayers and manually enter the soil information, or import a .txt file containing the soil layer information. The information included in the soil table includes depth to mid-layer, sublayer thickness, corrected SPT blowcount for the sublayer (i.e. $(N_1)_{60}$), plasticity index (%) for the sublayer, fines content (%) for the sublayer, mean grain size diameter for the sublayer (mm), moist unit weight of the sublayer, and sublayer susceptibility to liquefaction (yes or no). The user may specify either metric units (default), or English units. A screenshot of the Soil Profile Tab is shown in Figure D-3.

The user must also specify the depth of the water table for the analysis as well as the average shear wave velocity in the upper 12 meters (40 feet) of the native soil profile (i.e. $V_{s,12}$). The specified water table depth must fall between two sublayers in the soil table; otherwise, PPRS will provide the user with a warning message instructing the user to correct the water table depth. For $V_{s,12}$, a default value of 175 meters/second (574 feet/second) is programmed into PPRS, but the user may adjust this value if site-specific shear wave velocity information is available.

Liquefaction Setup Window

PPRS offers the user some flexibility in performing the performance-based liquefaction triggering analysis. If the user would like to account for higher uncertainty in the soil data due to an inadequate soil investigation, he/she may click on the appropriate checkbox. Doing so will incorporate a higher standard deviation in the computation of probability of

liquefaction triggering (Kramer and Mayfield, 2007). If the user is using PGA ground motions which correspond to bedrock accelerations, then he/she may choose to incorporate generic soil amplification factors as recommended by Stewart et al. (2003) by selecting the appropriate checkbox. Otherwise, the user may wish to incorporate the results of a site-specific site response analysis and manually specify a soil amplification factor to apply to the PGA values. If the user would like to specify a certain factor of safety for liquefaction triggering, then he/she may enter that value into the appropriate the textbox. The default factor of safety for liquefaction triggering is set at 1.2, which is the standard specified by many current design codes such as AASHTO LRFD Seismic Bridge Design Recommendations. Finally, the user may choose to incorporate the Idriss and Boulanger (2010) probability of liquefaction triggering model in the performance-based analysis instead of the Cetin et al. (2004) model by selecting the appropriate checkbox. While this substitution has not yet been validated in literature, the performance-based framework for evaluating liquefaction triggering as presented by Kramer and Mayfield (2007) is quite flexible, and the substitution can be made without critically altering the framework. A screenshot of the Liquefaction Setup Window is shown in Figure D-4.

The Slope Geometry Tab

The Slope Geometry Tab is most simple tab in PPRS. It prompts the user to select whether ground-slope or free-face conditions exist at the site of interest. Depending on which case is selected, the user must then enter the corresponding slope parameter (i.e. gradient or free-face ratio, both as percentages). The tab also includes simple diagrams to help the user understand the definitions of the ground-slope gradient and the free-face ratio. A screenshot of the Slope Geometry Tab is presented in Figure D-5.

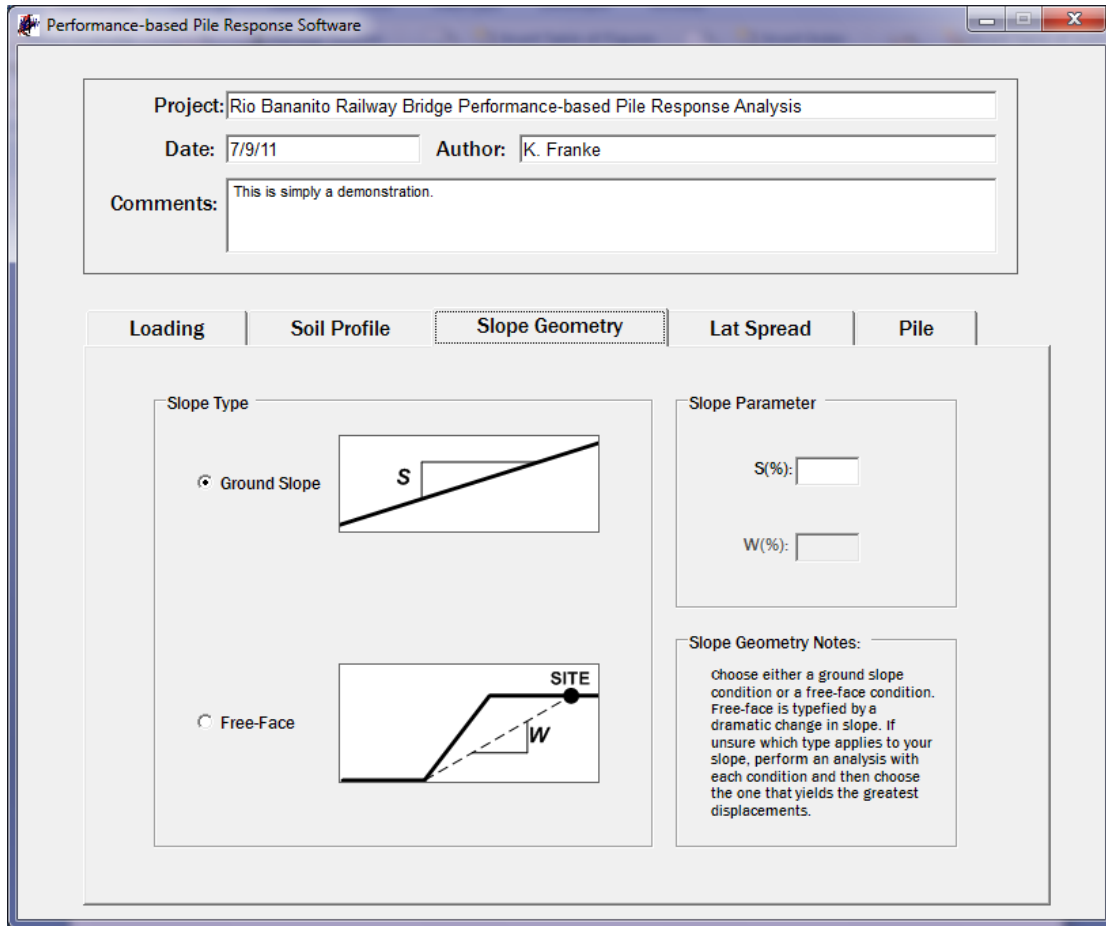


Figure D-5: Screenshot of the Slope Geometry Tab

If a free-face condition is selected by the user, PPRS queries the user as to the height of the free-face. This height is used by PPRS to compute depth limitations for the lateral spread analysis as recommended in the personal communication with Youd (2009) and summarized in Section 3.7 of this dissertation.

Because some slope geometries may be very complex, it can be difficult to determine whether a site should be modeled as a ground-slope case or as a free-face case. There is no definitive answer to this problem, and it is recommended that if any confusion exists as to which

slope geometry type should be used for a given site, then the user should run two separate analyses – one as a ground-slope case, and the other as a free-face case. It is then recommended that the user compare the calculation results of the two analyses and choose the more conservative of the two for use in design.

The Lat Spread Tab

The Lat Spread Tab is used to compute performance-based lateral spread displacements and performance-based liquefaction triggering. A screenshot of the Lat Spread Tab is shown in Figure D-6.

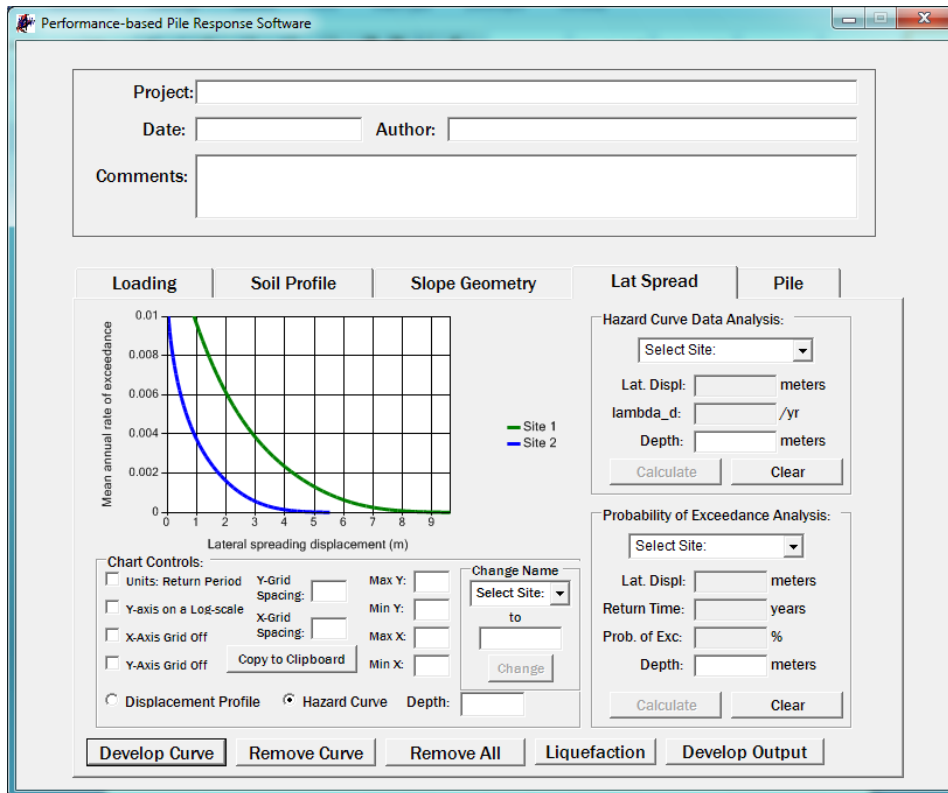


Figure D-6: Screenshot of the Lat Spread Tab

The Hazard Curve Buttons

The buttons that control adding and removing lateral spread hazard curves or probabilistic lateral spread profiles from the plot are called the hazard curve buttons. They are comprised of the buttons labeled *Develop Curve*, *Remove Curve*, and *Remove All*. Pushing the *Develop Curve* button causes PPRS to take the loading, soil profile, and slope geometry data specified by the user to develop the lateral spread hazard curve for the site of interest. The default depth for the lateral spread hazard curve is the ground surface (i.e. depth = 0), but the user may specify a different depth for additional hazard curves. If the user selects the *Profile* option instead of the *Hazard* option, then pressing the *Develop Curve* button will compute the probabilistic lateral spread displacement profile versus depth for the specified annual rate of exceedance or return period. Once developed, the curve is added to the Lat Spread Tab plot for viewing and evaluation. If the user would like to add additional curves for other sites or loading/soil conditions, then he/she needs only to modify the model input and push the *Develop Curve* button again. If the user would like to remove a curve from the analysis, he/she may push the *Remove Curve* button, which removes the most recently-added curve from the plot and *Results* tab. The user may also push the *Remove All* button, which removes all of the hazard curves from the hazard curve plot and *Results* tab – essentially starting the analysis over.

The Hazard Curve Plot

The hazard curve plot contains the lateral spread hazard curves and displacement profile curves. It empowers users by providing them with a powerful set of controls located in the *Chart Controls* groupbox which allows the user to adjust the view of the plot. These controls allow the user to change the units on the hazard curve plot from frequency to return period, apply a

logarithmic scale on the y-axis, remove or adjust the grids for both axes on the plot, and copy the chart to other computer applications. Another useful functionality contained in the *Chart Controls* groupbox is the ability to rename the curves for the plot legend. Figure D-7 demonstrates a hazard curve plot with user-designated names.

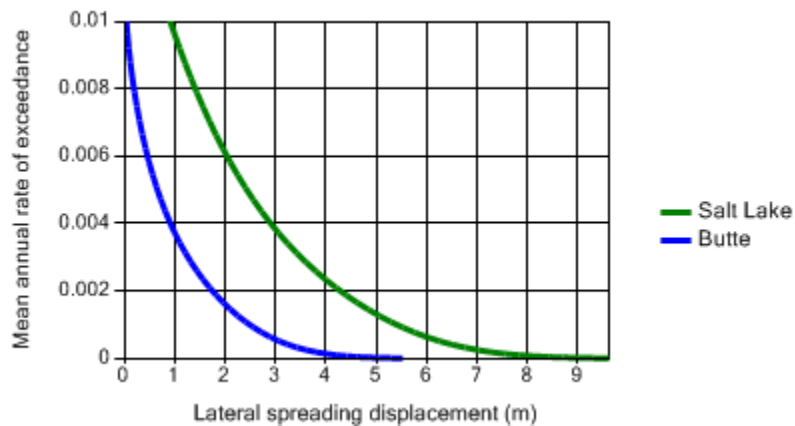


Figure D-7: Demonstration of the Ability to Designate Site Names in PPRS

The Liquefaction Results Window

When the user presses the *Develop Curve* button, PPRS automatically performs a performance-based liquefaction triggering analysis. The user may view the results of the liquefaction triggering analysis by pressing the *Liquefaction* button. Doing so opens the Liquefaction Results Window. A screenshot of the Liquefaction Results Window is shown in Figure D-8.

The plot control box on the Liquefaction Results Window allows the user to view either a factor of safety profile for a specified return period or a liquefaction hazard curve for a specified

depth. The user may also adjust the x- and y-axes, copy the plot to the clipboard for pasting into other computer applications, or use units of return period.

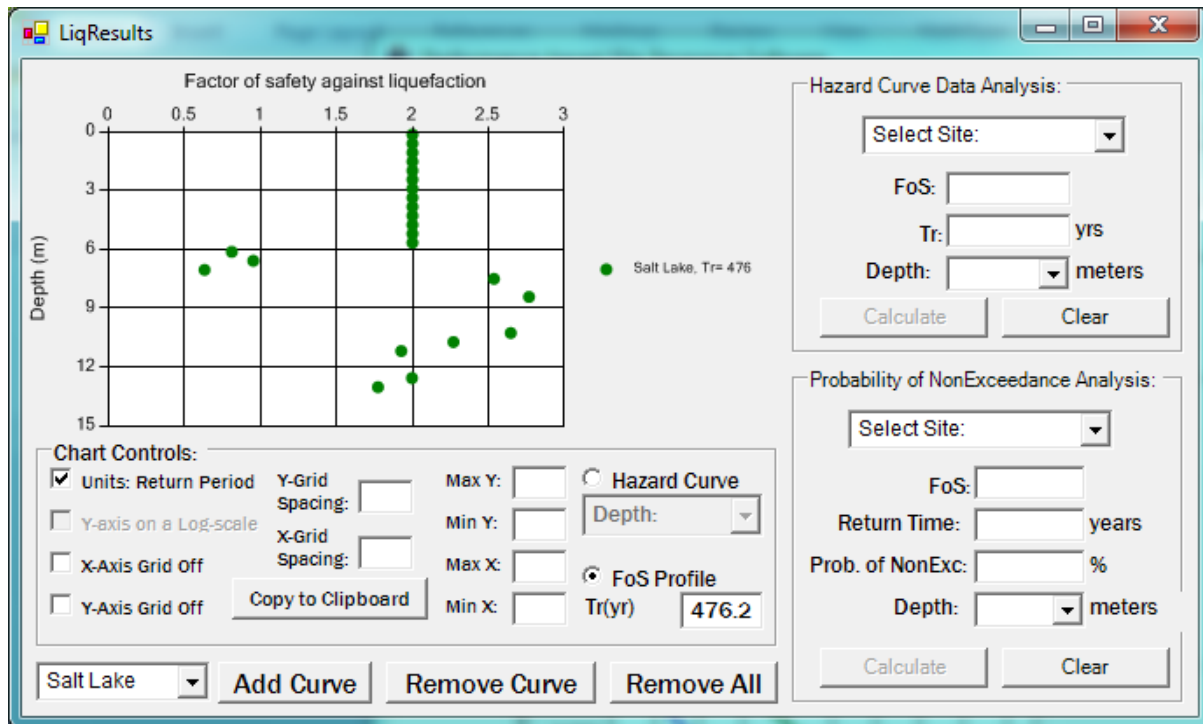


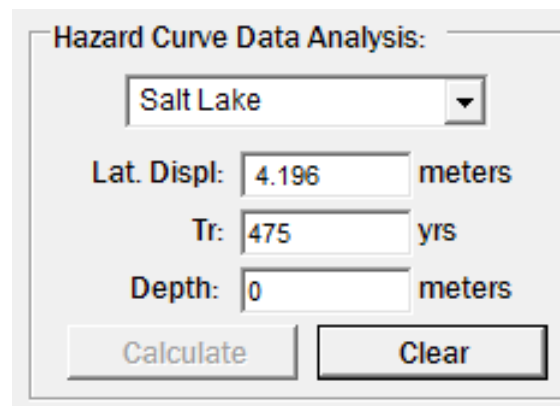
Figure D-8: Screenshot of the Liquefaction Results Window

The Hazard Curve Data Analysis Groupbox

The upper right-hand corner of both the Lat Spread Tab and the Liquefaction Results Window contains the *Hazard Curve Data Analysis Groupbox*. An example of this groupbox is shown in Figure D-9.

The groupbox can be used to obtain specific values of interest from the hazard curves. By selecting the hazard curve of interest from the combo box, the user can obtain either values of

rate of exceedance/return period (depending on the selected units on the hazard curve plot) or lateral spread displacement by pressing the *Calculate* button. The program is designed to solve for the variable for which no value has been entered (i.e. if the user enters a value for lateral displacement, then the program will solve for annual rate of exceedance/return period).



The image shows a software dialog box titled "Hazard Curve Data Analysis:". It contains a dropdown menu with "Salt Lake" selected. Below the menu are three input fields: "Lat. Displ:" with the value "4.196" and the unit "meters", "Tr:" with the value "475" and the unit "yrs", and "Depth:" with the value "0" and the unit "meters". At the bottom of the dialog are two buttons: "Calculate" and "Clear".

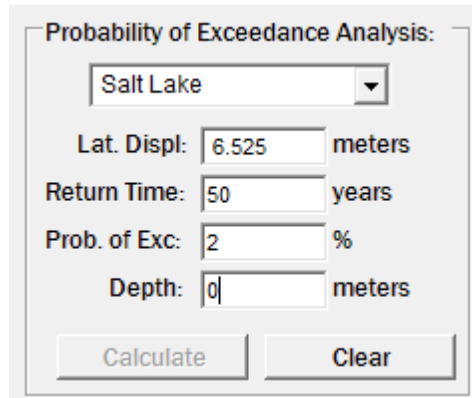
Figure D-9: The Hazard Curve Data Analysis Groupbox

The Probability of Exceedance Analysis Groupbox

The lower right-hand corner of both the LS Spread Tab and the Liquefaction Results Window contains the *Probability of Exceedance Analysis Groupbox*. A screenshot of the groupbox is shown in Figure D-10.

This groupbox applies the Poisson probability model to the hazard curve of interest at the depth specified by the user. Using the analysis tools provided in this groupbox, the user can determine the probability of exceeding a certain lateral spread displacement or factor of safety in a given time period for any selected hazard curve at any depth of interest. The groupbox allows

the user to solve for either the probability of exceedance, exposure time, or lateral spread displacement. The user must provide values for two of the three variables in the groupbox to solve for the third variables. Once the user has provided these values, he/she solves for the third variable by pressing the *Calculate* button in the groupbox.



Probability of Exceedance Analysis:

Salt Lake

Lat. Displ: 6.525 meters

Return Time: 50 years

Prob. of Exc: 2 %

Depth: 0 meters

Calculate Clear

Figure D-10: Screenshot of the Probability of Exceedance Analysis Groupbox

Developing Lateral Spread Output

Many users may wish to incorporate the lateral spread results developed by PPRS into other engineering analyses (e.g. the performance-based kinematic pile response analysis presented in this dissertation). The user may manually obtain the displacements from all of the required depths across all return periods of interest, but doing so may be tedious and time-consuming. By pressing the *Develop Output* button, PPRS will query the user where he/she would like to save the output .txt file. PPRS then writes the summary .txt file providing performance-based liquefaction triggering and empirical lateral spread results corresponding to return periods of 108, 225, 475, 975, 2475, 4975, and 100000 years.

The Pile Tab

The Pile Tab is the last tab on the PPRS program, and it is used to convolve the individual pile response results corresponding to multiple return periods and provided by the user to develop probabilistic estimates of kinematic pile response. A screenshot of the Pile Tab is shown in Figure D-11.

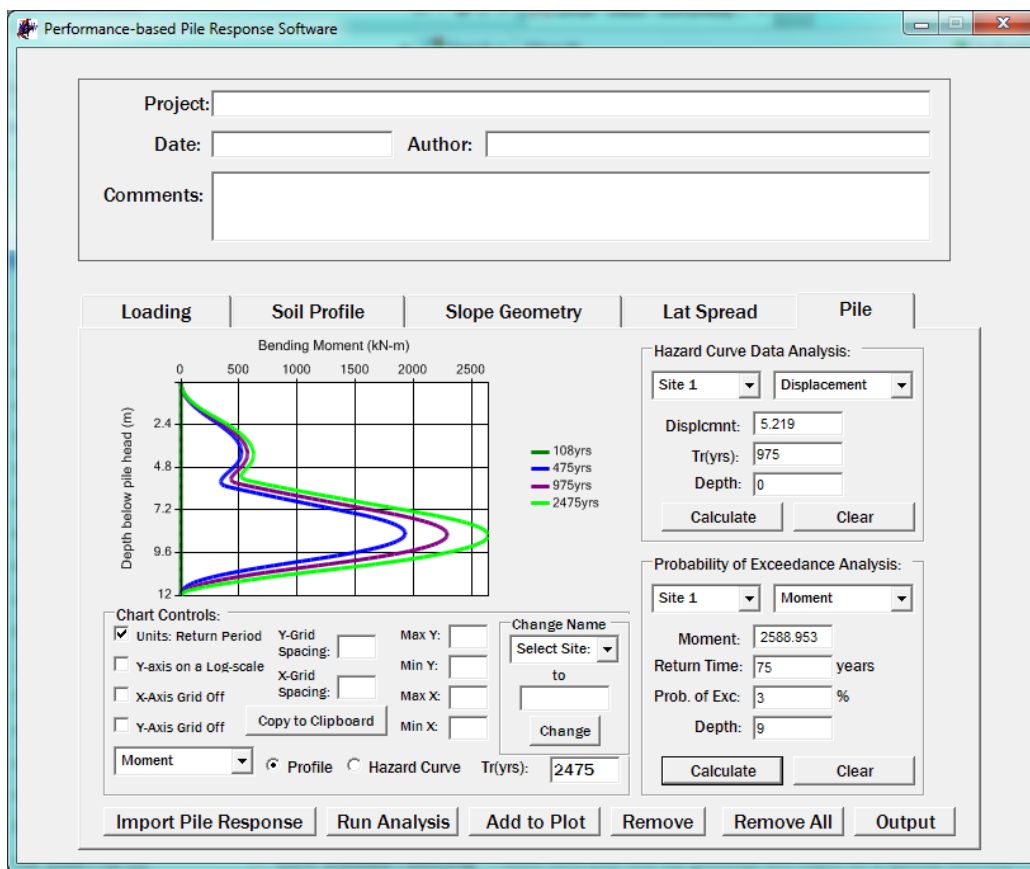


Figure D-11: Screenshot of the Pile Tab in PPRS

The Pile Tab was developed as a separate entity from the other tabs in PPRS to accommodate the users who may wish to perform probabilistic computations of lateral spread

using an approach other than empirical models (e.g. Newmark displacement models, FEM numerical modeling, etc.). Pile Tab by itself does not perform any pile response analysis. Rather, it utilizes the pile response results provided by the user in the performance-based framework described in Chapters 5 and 6 of this dissertation to develop probabilistic estimates of kinematic pile response. As such, the user has the flexibility to apply whichever kinematic pile response analysis method he/she prefers (e.g. p-y soil springs, limit equilibrium, FEM numerical models, etc.) to develop the individual pile response results imported into PPRS.

The Hazard Analysis Buttons

Like the Lat Spread Tab, the main functionality of the Pile Tab is governed by the Hazard Analysis Buttons, which are comprised of the *Import Pile Response*, *Run Analysis*, *Add to Plot*, *Remove*, and *Remove All* buttons.

The *Import Pile Response* button is used by the user to import the individual pile response results for the performance-based computation of kinematic pile response. The user will be asked to specify seven pile response .txt files corresponding to return periods of 108, 225, 475, 975, 2475, 4975, and 100000 years. The .txt file should contain the mean and standard deviation values for the displacement, shear force, bending moment, and curvature from all of the pile nodes of interest. An example of a proper .txt input file that can be read by PPRS is presented in Figure D-12. If using the LPILE MC Simulator spreadsheet described in Appendix C, the Results worksheet on that spreadsheet already develops the pile response results in the appropriate format.

Once all seven pile response input files have been imported by the user, the performance-based pile response algorithm can be initiated by pressing the *Run Analysis* button. Once the

button is pressed, PPRS will utilize Equation (6-23) across all depths of the pile to develop probabilistic estimates of pile deflection, shear force, bending moment, and curvature (all absolute values). Because the algorithm is very computation-intensive, it may take up to a minute or so to complete the analysis. Once the analysis is complete, the user will be notified that the analysis was performed successfully, and hazard and/or profile curves can be added to the plot. If, after analyzing the first set of pile response files, the user would like to analyze a different set of pile response file (perhaps pertaining to a different site or utilizing different site assumption), he/she can simply import the new pile response files by pressing the *Import Pile Response* button again. If, after importing new files, the user presses the *Run Analysis* button again, another performance-based analysis will be performed. PPRS will classify the results from the first analysis as ‘Site 1’, and the results of the second analysis as ‘Site 2’, and so on. Up to 20 sites may be analyzed at a single time using PPRS software.

Depth (m)	Deflection (m)	Sig_Deflect (m)	Shear (kN)	Sig_Shear (kN)	Moment (kN-m)	Sig_Moment (kN-m)	Slope (rad)	Sig_Slope (rad)
0	3.871681395	0.025725707	-8.05535E-11	4.29917E-09	8.2487E-10	3.14806E-08	-0.412165269	0.025937049
0.08	3.838711628	0.02411106	-8.959651395	2.096707221	-0.354647692	0.083717815	-0.412166334	0.025936683
0.16	3.805762791	0.022617	-18.10141907	4.200803911	-1.43354348	0.335473989	-0.41217171	0.025935743
0.24	3.772774419	0.021246095	-27.4138286	6.311749308	-3.250873953	0.755818278	-0.412185785	0.025932904
0.32	3.739811628	0.019910273	-36.88217209	8.426827308	-5.819757674	1.345242847	-0.412213041	0.025927427
0.4	3.706797674	0.018757401	-46.49019744	10.54296127	-9.152024419	2.103826881	-0.412258029	0.025918419
0.48	3.673830233	0.017743091	-56.22075186	12.6587392	-13.25818721	3.031523763	-0.412325369	0.025904988
0.56	3.640837209	0.016983923	-66.05394512	14.7729872	-18.14734651	4.128128881	-0.412419738	0.02588623
0.64	3.607834884	0.016391714	-75.96791535	16.88532598	-23.8268186	5.393375487	-0.412545864	0.025861242
0.72	3.574855814	0.016091309	-85.94057256	18.99481476	-30.30221279	6.826956679	-0.412708515	0.025829117
0.8	3.541818605	0.016064109	-95.94901279	21.10091162	-37.57731023	8.428410351	-0.412912484	0.02578895
0.88	3.508769767	0.016253399	-105.9676058	23.20312647	-45.65405209	10.19731907	-0.413162582	0.025739849
0.96	3.475718605	0.016719052	-115.9689509	25.30041297	-54.53212628	12.13313172	-0.413463627	0.025680901
1.04	3.442632558	0.017407762	-125.9241635	27.39178445	-64.20980349	14.2352764	-0.413820433	0.02561123
1.12	3.409497674	0.018337009	-135.799846	29.47365264	-74.67999256	16.50304958	-0.414237775	0.025529949
1.2	3.37634186	0.019390885	-145.5604323	31.54199007	-85.93706047	18.93538146	-0.41472041	0.02543619
1.28	3.343153488	0.020588423	-155.1677093	33.59431999	-97.96965977	21.53100861	-0.415273027	0.025329102
1.36	3.309895349	0.021920937	-164.5762456	35.62890534	-110.7638956	24.28847383	-0.415900246	0.025207851
1.44	3.276581395	0.023364281	-173.7323121	37.64381311	-124.3018621	27.20629836	-0.416606585	0.025071614
1.52	3.24324186	0.024861333	-182.569914	39.63661845	-138.5610633	30.2828193	-0.417396453	0.024919598
1.6	3.20982093	0.026433591	-191.0031765	41.60671304	-153.5130456	33.51626575	-0.418274099	0.024751019
1.68	3.176313953	0.028023991	-198.9132377	43.56104882	-169.1215737	36.90503399	-0.419243575	0.024565128
1.76	3.142716279	0.02966917	-206.0818098	45.58249535	-185.3391623	40.44857407	-0.420308682	0.024361167
1.84	3.109053488	0.031304571	-211.9215486	48.03886066	-202.0946614	44.15805069	-0.421472871	0.02413835
1.92	3.075306977	0.032978819	-215.1876735	51.14408216	-219.2466133	48.08913855	-0.422738947	0.02389565
2	3.041448837	0.034674053	-214.4922188	53.9635773	-236.5246879	52.27946155	-0.424108482	0.023631594
2.08	3.007460465	0.036339401	-209.95794	55.24187014	-253.5653663	56.62944637	-0.425581139	0.023344662
2.16	2.973330233	0.038043807	-203.0471002	55.15030312	-270.1179586	60.99075431	-0.42715474	0.023034096

Figure D-12: Screenshot of an Example Pile Response Input .txt File

The user may view and evaluate various aspects of the pile response by using the Pile Response Plot. If the user would like to plot a hazard curve, he/she must specify the site number, the type of pile response (i.e. displacement, shear, moment, or curvature) and the depth of interest. If the user would like to plot a response profile curve, he/she must specify site number, the type of pile response and the return period/annual rate of exceedance of interest. The curve is added to the Pile Response Plot by pressing the *Add to Plot* button. Once a curve is added, the user may toggle back and forth between various types of pile response, as well as between hazard curves and response profile curves. In addition, the user may adjust the axes, grid, and legend of the plot as desired. A picture of the plot may be copied to the clipboard to be pasted into other computer applications.

The user may remove the most recently-added curve from the plot by pressing the *Remove* button. If he/she would like to completely clear the curve, then the *Remove All* button should be pressed.

Additional Tools

Like the Lat Spread Tab and the Liquefaction Results Window, the Pile Tab contains groupbox tools designed to compute specific pile response values corresponding to various levels of hazard/performance and to compute the probability of exceeding a specified pile response value within a given time frame. In addition, the Pile Tab allows the user to export a summary of the performance-based pile response to a .txt file by pressing the *Output* button. Pile response values corresponding to return periods of 108, 225, 475, 975, 2475, 4975, and 100000 years are included on the output .txt file.

